EXPERIMENTAL ANALYSIS OF THE VORTICITY AND TURBULENT FLOW DYNAMICS OF A PITCHING AIRFOIL AT REALISTIC FLIGHT (HELICOPTER) CONDITIONS

A Dissertation

by

DIPANKAR SAHOO

Submitted to the Office of Graduate Studies of
Texas A&M University
in partial fulfillment of the requirements for the degree of

DOCTOR OF PHILOSOPHY

May 2008

Major Subject: Aerospace Engineering

EXPERIMENTAL ANALYSIS OF THE VORTICITY AND TURBULENT FLOW DYNAMICS OF A PITCHING AIRFOIL AT REALISTIC FLIGHT (HELICOPTER) CONDITIONS

A Dissertation

by

DIPANKAR SAHOO

Submitted to the Office of Graduate Studies of
Texas A&M University
in partial fulfillment of the requirements for the degree of

DOCTOR OF PHILOSOPHY

Approved by:

Chair of Committee,	Rodney Bowersox
Committee Members,	Othon Rediniotis
	Paul Cizmas
	Simon North
Head of Department,	Helen Reed

May 2008

Major Subject: Aerospace Engineering

ABSTRACT

Experimental Analysis of the Vorticity and Turbulent Flow Dynamics of a Pitching Airfoil at Realistic Flight (Helicopter) Conditions. (May 2008)

Dipankar Sahoo, B.E., National Institute of Technology, Trichy; M.S., University of Alabama

Chair of Advisory Committee: Dr. Rodney Bowersox

Improved basic understanding, predictability, and controllability of vortex-dominated and unsteady aerodynamic flows are important in enhancement of the performance of next generation helicopters. The primary objective of this research project was improved understanding of the fundamental vorticity and turbulent flow physics for a dynamically stalling airfoil at realistic helicopter flight conditions. An experimental program was performed on a large-scale (C = 0.45 m) dynamically pitching NACA 0012 wing operating in the Texas A&M University large-scale wind tunnel. High-resolution particle image velocimetry data were acquired on the first 10-15% of the wing. Six test cases were examined including the unsteady (k>0) and steady (k=0) conditions.

The relevant mechanical, shear and turbulent time-scales were all of comparable magnitude, which indicated that the flow was in a state of mechanical non-equilibrium, and the expected flow separation and reattachment hystersis was observed. Analyses of

the databases provided new insights into the leading-edge Reynolds stress structure and the turbulent transport processes. Both of which were previously uncharacterized.

During the upstroke motion of the wing, a bubble structure formed in the leading-edge Reynolds shear stress. The size of the bubble increased with increasing angle-of-attack before being diffused into a shear layer at full separation. The turbulent transport analyses indicated that the axial stress production was positive, where the transverse production was negative. This implied that axial turbulent stresses were being produced from the axial component of the mean flow. A significant portion of the energy was transferred to the transverse stress through the pressure-strain redistribution, and then back to the transverse mean flow through the negative transverse production. An opposite trend was observed further downstream of this region.

ACKNOWLEDGEMENTS

I would like to express my sincerest gratitude and appreciation to my advisor Dr. Rodney Bowersox for his valuable guidance throughout the progress of this research. I am grateful to him for motivating me during my tough times. I thank Dr. Othon Rediniotis, Dr. Paul Cizmas, and Dr. Simon North for their participation as members of my supervisory committee. I also thank Dr. Tom Doligalski from Army Research Office (ARO) for providing financial support for this research. I would like to thank Aerospace Department staff members, Karen Knabe, Andrea Loggins, and Colleen Leatherman for their help with official paper work which saved me a lot of time.

I extend my gratitude to all employees at the Oran W Nicks Low Speed Wind Tunnel for their valuable assistance. I would like to single out tunnel director Jorge Martinez for his technical assistance and willingness to install the Dynamic Stall Facility into his facility along with Will Seward, for his assistance in constructing the DSF.

I am thankful to Dr. Isaac Ekoto, Michael Semper, Nathan Tichenor, TJ Fuller, Jason Garcia and Dr. Ravichandra Srinivasan for their help in installing the DSF and in testing assistance. I would like to thank all my friends who have supported me throughout. Finally, I am grateful to my parents and family for keeping my spirits high.

NOMENCLATURE

c	Airfoil chord length (0.457 m)
f	Pitching Frequency (Hz)
k	Reduced Airfoil Pitching Frequency ($\pi fc/U_\infty$)
P_{xx}	Production of the *xx*-component of the Reynolds Stress
P_{yy}	Production of the *yy*-component of the Reynolds Stress
P_{xy}	Production of the *xy*-component of the Reynolds Shear Stress
M	Mach number
S_{xy}	*xy*-component Shear Strain Rate
u, v	Instantaneous velocity Components
u', v'	Fluctuating velocity Components
U, V	Mean velocity Components
U_∞	Freestream Velocity
x, y, z	Cartesian Coordinates
α	Angle of Attack
$\Delta\alpha$	Amplitude of the Airfoil Pitching Motion about the ¼-chord
σ_u	$[\overline{u'^2}]^{1/2} / U_\infty^2$

σ_v	$[\overline{v'^2}]^{1/2} / U_\infty^2$
ω_z	*z-component of vorticity*
τ_{xy}^T	$-\overline{u'v'}$
τ_{xy}	$-\overline{u'v'} / U_\infty^2$
τ_{xx}^T	Axial stress
τ_{yy}^T	Transverse stress

TABLE OF CONTENTS

Page

Page

LIST OF FIGURES

FIGURE Page

FIGURE Page

FIGURE Page

FIGURE Page

FIGURE Page

FIGURE Page

FIGURE Page

FIGURE Page

FIGURE Page

FIGURE Page

FIGURE Page

LIST OF TABLES

TABLE Page

CHAPTER I

INTRODUCTION

1.1 The Problem of Helicopter Rotor Dynamic Stall

Dynamic stall is a complicated aerodynamic phenomenon. The complications include unsteady flow, separation, hysteresis, compressibility, shock-waves and non-equilibrium (mechanical) boundary layers. The dynamic stall problem has affected helicopters, fighter aircraft, jet engines and wind turbines, and has resulted in major research programs attempting to identify the mechanisms that combine to delay separation and stall on rapidly pitching aerodynamic surfaces. It has been a problem for helicopter designers, for which the abrupt pitching moment variations have forced restrictions on the flight envelope. It has been solution for fighter aircraft, where the dynamically induced lift offers an opportunity for enhancement of aircraft maneuverability.

Dynamic stall occurs on the ‘retreating’ side of the helicopter rotor (the side where the rotating helicopter blade is traveling away from the direction of flight). The retreating blade must produce sufficient lift to balance the lift produced by the advancing blade in order to maintain level flight. However, the maximum dynamic pressure on the retreating blade can be dramatically less than that found on the advancing blade.

This dissertation follows the style of *Journal of Propulsion and Power*.

Therefore the lift coefficient for the retreating blade must increase in order to maintain the required lift. This imbalance in dynamic pressure increases rapidly as the speed of the helicopter increases, ultimately requiring dynamic excursions of angle of attack of the rotating blade beyond the angle of attack at which the blade would stall in steady flow, thus leading to dynamic stall conditions.

The airfoil is subjected to two fundamental periodic oscillations: pitching and plunging. A plunging oscillation is a periodic translation of the airfoil in a direction normal to the free stream. A pitching motion is a periodic variation of the angle of attack. The most important parameters affecting the dynamic behavior of an airfoil under periodic variations of inflow conditions are: amplitude of the oscillation, mean angle of attack, reduced frequency, Reynolds and Mach numbers, airfoil shape (thickness, leading edge radius, etc.), surface roughness, and free stream turbulence. With so many factors affecting dynamic stall, the flow field is very complicated. Hence very limited data is available at true flight (helicopter) conditions.

A detailed background review is given in Chapter II. A main theme that emerged from the literature review is the need for high fidelity experiments directed at improved flowfield understanding and predictability at realistically high Reynolds numbers ($\sim 10^6$) and Mach numbers ($\sim 0.2 - 0.4$). The importance of the flight conditions is highlighted in Chandrasekhara[33] (1998), where the dynamic separation processes were documented to change in fundamental manners with both Reynolds number and Mach number.

1.2 Army Research Office Interests

The Army Research Office [Dr. T. Doligalski, *DAAD19-00-R-0010*] identified improved understanding, predictability and controllability of vortex-dominated and unsteady aerodynamic flows as important for the development of future Army weapon systems. It was also noted that the physics of these flows are Mach and Reynolds numbers dependent, and hence research in this area needs to be performed at realistic flight conditions. Detailed experimental non-intrusive measurements of velocity were also listed as needed in the separating region to yield new phenomenological understanding.

In order to understand the Army research requirements, the Texas A&M University Researchers consulted with Drs. L. Carr and W. McCroskey from the U.S. Army Aeromechanics Laboratory and the NASA Ames Research Center. In summary, specific issues that limit the development of dynamic stall control strategies include (1) a lack of understanding of the basic vortex dynamics with large pressure gradients, (2) the uncertainties of applying quasi-steady turbulence models to dynamic stall problems, (3) the influence of strong adverse pressure gradients on the turbulence models, and (4) the quantification and prediction of transition from laminar to turbulence flow. The present research project was focused on the first three of these Army research requirements.

1.3 Research Objectives and Approach

The primary objective of this research project was improved understanding of the fundamental vorticity and turbulent flow physics for a dynamically stalling airfoil at realistic helicopter flight conditions.

In order to meet the objective, an experimental program using high-resolution Particle Image Velocimetry (PIV) was performed to provide an empirical characterization of the leading-edge (first 10-15% of the chord) flow structure. A dynamically pitching NACA 0012 wing operating in the Texas A&M University large-scale wind tunnel was studied. The region of interest is shown schematically in Fig. 1. The data resolution was approximately 0.25 mm (0.06% of the airfoil chord) between data points, and data were acquired to within 0.5 – 1.0 mm from the airfoil surface. The sample sizes consisted of nominally 1000 image pairs to ensure statistical convergence of the measurements. The test matrix is given in Table 1.

The measurements included planar contours of the mean velocity (*u*- and *v*-components), vorticity, strain rates, turbulence intensities (*u*- and *v*-components), the Reynolds shear stress, and production of the turbulent stresses (axial, transverse and shear). The vorticity and turbulent transport equations are described in Chapter III.

1.4 Research Contributions and Scientific Impact

The primary scientific impact is documentation and improved understanding of the fundamental flowfield processes for a dynamically pitching airfoil at realistic helicopter flight conditions. The specific research contributions include (1) the extensive and highly resolved dynamic stall experimental database obtained under realistic flight conditions, (2) the subsequent mean flow analyses and (3) the analysis of the turbulence and the production thereof under the dynamic flow conditions.

1.5 Overview of the Dissertation

Summarized in Chapter II are the results from a detailed literature review. Listed in Chapter III are the relevant transport equations. The facilities and instrumentation that were employed to perform the current research are presented in Chapter IV. Described in Chapter V are the experimental and data reduction techniques that were used and/or developed in this research. A detailed interrogation of the flow structure is presented in Chapter VI. The overall flow structure was similar for all six cases examined. Hence, Case 1 served as the representative case for the discussion in Chapter VI. Summarized in Chapter VII are the conclusions and recommendations for future research needs. A description of the installation procedures for the Dynamic Stall Facility is presented in Appendix A. The remaining Appendices serve as a data repository for Cases 2 – 6.

CHAPTER II

REVIEW OF DYNAMIC STALL LITERATURE

Unsteady airfoil aerodynamics has numerous military and civilian applications. Some examples include rotor blades, high-angle of attack aircraft and wind turbines. Hence, unsteady airfoils have been the subject of considerable theoretical, experimental and numerical research; most of which has occurred since the late 1940s. Presented in the first section of the review is a brief synopsis that highlights the current state of understanding and prediction of the dynamic stall problem. Given in the second section is a detailed chronological review of the progress in the field starting in 1948 and ending in 2007.

2.1 Overview of the Dynamic Stall Problem

2.1.1 Phenomenological Description

Dynamic stall occurs on the ‘retreating side of the helicopter rotor (the side where the rotating helicopter blade is traveling away from the direction of flight). The retreating blade must produce sufficient lift to balance the lift produced by the advancing blade in order to maintain level flight. However, the maximum dynamic pressure on the retreating blade can be dramatically less than that found on the advancing blade. Therefore, the lift coefficient for the retreating blade must increase in order to maintain the required lift. This imbalance in dynamic pressure increases rapidly as the speed of the helicopter increases, ultimately requiring dynamic excursions of angle of attack of

the rotating blade beyond the angle of attack at which the blade would stall in steady flow, thus leading dynamic stall. The problem of dynamic stall has been a topic of great interest to aerodynamicists and scientists. This problem presents a unique combination of unsteady effects, flow non-linearity and strong viscous-inviscid interaction. These challenging and difficult features have stimulated coordinated effort in analytical, experimental and computational research areas. Review articles include McCroskey[1], Carr[2], Carr and McCroskey[3], and Ekaterinaris and Platzer[4]. Literally hundreds of articles are included in these reviews. A brief synopsis is given here.

McCroskey[1] points out that one of the reasons that dynamic stall is so difficult to analyze is that it depends on a large number of parameters. He listed airfoil shape, Mach number (> 0.2), reduced frequency, mean angle and oscillation amplitude as having large effects on dynamic stall. He also indicated that Reynolds number had an unknown effect at high Mach numbers. Two general stages of dynamic stall, light and deep, have been defined. Light and deep dynamic stall flows are compared in Fig. 2. Light dynamic stall occurs for lower maximum angle of attacks than are typically associated with the deep stall. One of the distinguishing features of light dynamic stall is the relatively small vertical extent of the viscous region, as compared to deep stall, and the stall behavior is closely related to the boundary layer separation behavior. Deep stall occurs when the maximum angle-of-attack significantly exceeds the static stall angle, and the flow separation is initiated with formation of a strong vortex-like structure in the leading-edge region of the flow.

Shown in Fig. 3 are sketches (boxed images on the right-hand-side) of the canonical low-Mach flow deep stall events. Dynamic stall generally refers to complex unsteady flow processes that lead to dynamic delay of stall on aerodynamic bodies Carr[2]. Following Carr[2], Ekaterinaris and Platzer[4] and Greenblatt *et al*.[5], state (a) corresponds to the event where the airfoil dynamically pitches beyond the static stall. Stages (b)-(d) indicate initiation of the vortex formation starting with viscous disturbances. State (e) corresponds to the initial vortex development near the airfoil leading edge as the angle of attack is rapidly increased past the static stall angle. This vortex then convects downstream near the airfoil surface, which causes an increase in lift and strong pitching-moments due to suction created by the vortex [stages (f) through (i)]. The magnitude of the lift depends on the strength and location of the vortex. The streamwise movement of the vortex depends on the airfoil shape and pitch rate. Full dynamic stall occurs at stage (j) and continues until the airfoil angle-of-attack has reduced such that attached flow state re-occurs. As a result of this sequence of events, the unsteady lift, drag and moment coefficients show a large degree of flow hysteresis when plotted versus angle of attack (plot on the left-hand-side of Fig. 3). The sequence of events, amount of hysteresis and the shape of the hysteresis loop depend nonlinearly on amplitude of oscillation, mean angle of attack, reduced frequency ($k = \omega c/2u_\infty$), Mach number and Reynolds number.

2.1.2 Prediction Methods and Limitations

Two basic methodologies exist for predicting dynamic stall. The first method uses semi-empirical relations founded in oscillating thin airfoil theory for the prediction of forces and moments McCroskey[1], Ekaterinaris and Platzer[4] and Leishman[6]]. The

second, more modern, approach is founded in computational fluid dynamic (CFD) solutions of the Navier-Stokes equations. CFD methods have become increasing popular since the mid 1980's with the continual advancement of computational capabilities. These tools have provided very valuable insight into the flow processes [e.g., see Ekaterinaris and Platzer[4] and Choudhuri *et al.*[7]] especially for laminar flow. However, Ekaterinaris and Platzer[4] note that predictions of dynamic stall on helicopters and wings, involving realistically high Reynolds number turbulent flows, will only contribute toward improved flowfield understanding if progress is made toward improving the ability to numerically predict turbulent flow and transition.

The computational requirements for direct numerical simulation, or even large-eddy simulation, of realistic turbulence problems are prohibitive. Hence, engineers and scientists must rely on approximate averaged forms of the Navier-Stokes equations that involve turbulence modeling. Ekaterinaris and Platzer[4] summarize the performance of the available range of turbulence models (algebraic, half-equation, one-equation and two-equation) all of which invoke the Boussinesq[8] approximation. The results were found to strongly depend on the turbulence model. Hence, accurate models are required. Furthermore, the available models could not be tuned to produce accurate prediction of the lift, moment and drag loops; instead, the models could only be tuned to produce accurate prediction of one. Barakos *et al.*[9] and Ko and McCroskey[10] also confirmed these general conclusions.

The poor performance of the available eddy-viscosity type models is not surprising. First, the deficiencies of the Boussinesq[8] approximation are well

documented. Wilcox (2000)[11] reports that this approximation fails for (1) flows with sudden changes in the mean strain rates, (2) flow over curved surfaces, (3) flows in ducts with secondary motion, (4) rotating flow, (5) three-dimensional flow and (6) flows with boundary layer separation. Referring to flowfield in Fig. 2, it is not surprising that the available models fail for the present class of flows. Second, Ekaterinaris and Platzer[4] reported that none of the current turbulence models were validated for dynamic stall.

The development and validation of turbulence models requires empirical information. Although quantitative flowfield studies have been performed [e.g., Carr *et al*. [12] and Shih *et al.*[13]], detailed turbulent field data for a dynamically stalling airfoil is lacking, as discussed in Ekaterinaris and Platzer[4].

2.2 Chronological Description of the Dynamic Stall (1948 To 2007)

The goal of this section is to present an overview of the chronology of progress in key focus areas. For more exhaustive reviews see McCroskey[1], Carr[2], Carr and McCroskey[3], and Ekaterinaris and Platzer.[4]

Harper and Flanigan[14] showed that the lift on an aircraft can be significantly increased if the aircraft is pitched at a rapid rate. Carta[15] was able to identify a pressure field on oscillating, two-dimensional airfoil that was indicative of the passage of a vortex. The importance of unsteady aerodynamics was considered by Harris and Pruyn[16]. It was observed that the extra lift on the helicopter rotor could be explained if lift on the blade was greater than that predicted by steady flow during the time when the blade was moving opposite to the direction of flight (the retreating-blade condition). Ham and Garelick[17] observed that the extra lift could be created by rapid pitching of airfoils, and

this extra lift was associated with a vortex formed on the airfoil during the unsteady motion. This was modeled by Ham[18] to reproduce the same form of dynamic overshoot that was observed in helicopter flight tests. Liiva and Davenport[19] also observed this vortex passage and the corresponding dynamic pressure distribution.

McCroskey and Fisher[20] explored dynamic stall on a model rotor and verified that the dynamic effects were indeed a result of a vortex dominated flow field that occurred during blade motion into the low-dynamic- pressure environment of the third and fourth quadrants of the helicopter rotor. This model rotor test, and further two-dimensional airfoil wind tunnel tests, then produced more quantitative information about dynamic stall.

Experiments were performed by Martin *et al.*[21] using flow-visualization techniques to again demonstrate the presence of vortex. These data reveal a number of interesting Reynolds number, amplitude, and reduced frequency effects on dynamic stall. They intended to point out the importance of testing under actual helicopter rotor operating conditions and that this approach can eventually describe the mechanism of dynamic stall. The angle for stall initiation decreases with increasing *Re,* while the angle for maximum lift increases with increasing *Re*. Hot-wire anemometry data indicated the occurrence of a short bubble during both the upstroke and down stroke. The angle of bubble passage, for a given *x/c*, decreases as *Re* increases. They concluded that decrease in pressure at the leading-edge and peaking of leading-edge velocity is the surest indicator that the process of stall initiation has begun. Increasing reduced frequency increases the stall delay.

McCroskey, McAlister and Carr[22] performed dynamic stall experiments on oscillating airfoils. They studied dynamic stall and unsteady-boundary layer separation in incompressible flow at moderately large Reynolds numbers. By varying the leading-edge geometry of an NACA 0012 airfoil, three different types of stall were produced, and the vortex shedding phenomenon was found to be the predominant feature of each. In most cases, including the leading-edge stall on the basic NACA 0012 profile, dynamic stall was found not to originate with the bursting of a laminar separation bubble, as is commonly believed, but with a breakdown of the turbulent boundary layer. Results in this experimental investigation can be summarized as 1) trailing edge stall developing from a relatively gradual progression of boundary-layer flow reversal and separation, from the trailing edge toward the leading edge; 2) leading-edge stall caused by an abrupt breakdown of the turbulent flow on the forward portion of the airfoil, following an initial progression of flow reversal from the trailing edge, and 3) two forms of leading-edge stall due to the abrupt bursting of a leading-edge laminar separation bubble.

Sankar and Tassa[23] solved the unsteady two-dimensional Navier-Stokes equations for laminar compressible flow around a NACA 0012 airfoil. They presented the governing equations in a strong conservation form in a body-fitted coordinate system, and solved them using an alternating direction implicit procedure. The technique was applied to the dynamic stall of a NACA 0012 airfoil, for several combinations of Mach number, Reynolds number and reduced frequency. They concluded compressibility has an inhibiting effect on the formation of the leading edge vortex. The decrease in reduced frequency increases the intensity of the dynamic stall vortex

shedding, and a lower reduced frequency also leads to an earlier formation and growth of the leading-edge vortex. They found the Reynolds number to be a weak parameter.

Lorber and Carta[24] performed experiment to study the aerodynamics of dynamic stall penetration at constant pitch rate and high Reynolds number, in an attempt to model more accurately conditions during aircraft poststall maneuvers and during helicopter high-speed forward flight. The results demonstrate the influence of the leading-edge vorticity on the unsteady aerodynamic response during and after stall. The vortex is strengthened by increasing the pitch rate and is weakened by increasing the Mach number and by starting the motion close to the steady-state stall angle. The level of understanding required to make proper use of this effect has yet to be achieved. Consistent control of unsteady, separated flow will be required if fighter pilots are to make full use of the expanded aerodynamic boundaries that will be made available by unsteady aerodynamics; this emphasizes the need for basic research in three-dimensional dynamic-stall effects, compressibility effects on dynamic stall, and positive control of unsteady separated flow, as well as in other fundamental areas of unsteady aerodynamics.

Chandrasekhara and Carr[25] studied compressibility effects on dynamic stall of a NACA 0012 airfoil undergoing sinusoidal oscillatory motion using a stroboscopic schileren system. Their study showed that a dynamic stall vortex always forms and convects over the airfoil upper surface at approximately 0.3 times the freestream velocity for all cases studied. The results also demonstrate that occurrence of deep stall is delayed to higher angles of attack with increased reduced frequency, even when compressibility

effects are present, but increasing Mach number alone has the opposite effect. They concluded dynamic stall vortex is present at all Mach numbers and reduced frequencies. However, its strength and initiation angle appear to vary with Mach number. Increasing the reduced frequency helps in holding the dynamic stall vortex on the airfoil surface to higher angles of attack, for high Mach numbers as well. Compressibility effects are significant beyond M = 0.3. Dynamic stall occurs at lower angles of attack as the Mach number exceeds 0.3. However, the origin of the vortex was not clear from the tests. They were also not able to find out the shock near the leading edge.

Carr, Platzer, Chandrasekhara, and Ekaterinaris[26] performed experimental and computational studies on dynamic stall. The dynamic overshoot of lift that characterizes the dynamic stall process is the key characteristic that is of interest to the aircraft designer; the strong pitching moment is the reason why the helicopter designer avoids dynamic stall. Review of past studies of dynamic stall demonstrates that compressibility will play a major role in effective use of dynamic lift. In particular, it has been shown that as the free stream Mach number exceeds 0.2, local supersonic flow develops around the leading edge of airfoils that pitch rapidly past the static stall angle. This region of supersonic flow can dramatically change the way that airfoil stall develops, changing a trailing-edge stall at low Mach number to a leading-edge stall at higher Mach number $(M \approx 0.3)$. They concluded 1) the dynamic stall vortex appeared for all cases studied experimentally, but its initiation occurred at significantly lower angles of attack as the Mach number increased. The vortex could be delayed by increasing the oscillation frequency across the full Mach number range of the experiment, 2) the stroboscopic

schlieren offers the first truly instantaneous visualization of the dynamic stall vortex, since it is sensitive only to density gradients at the time of the photograph, 3) the Navier-Stokes model of dynamic stall initiation shows good agreement with lift and pitching moment magnitudes, but requires prior knowledge of the state of the flow turbulence in order to model the details of the flow field after stall begins, 4) viscous-inviscid interaction techniques offer a way to analyze the dynamic stall onset at a computational cost which could be practical for design purposes.

Shih, Lourenco, Van Dommelen, and K Rothapalli[13] investigated unsteady flow past a NACA 0012 airfoil in pitching-up motion in a water towing tank using the particle image displacement velocimetry (PIDV) technique. The Reynolds number based on the free stream velocity and the chord length is 5000. The airfoil pitching motion was from 0 to 30 deg angle of attack at a dimensionless pitch rate of 0.131. They observed boundary-layer separation near the airfoil leading edge leads to the formation of a vertical structure. The evolution of this vortex along the upper surface dominates the aerodynamic performance of the airfoil. Complete stall emerges when the boundary layer near the leading edge detaches from the airfoil, under the influence of the vortex. This vortex triggers the shedding of a counter-rotating vortex near the trailing edge.

Wilder, Chandrasekhara, Carr[27] studied transition effects on compressible dynamic stall of transiently pitching airfoils. They concluded the laminar separation bubble present in the untripped flow was found to have a beneficial effect on dynamic stall delay. Dynamic stall onset moves closer to the leading edge in the presence of a trip, which eventually leads to stall at lower angles of attack (by about 1 – 1.5 degrees)

than observed in untripped airfoil dynamic stall. The leading-edge adverse pressure gradient and the peak suction pressure coefficient were lower in value on the tripped airfoil. The behavior of the flow is grossly different under compressibility conditions with a trip. The shock/boundary layer interactions are modified by the trip, as also is the leading edge pressure gradient. The sensitivity of the flow to the state of the boundary layer turbulence points to a need for highly refined computational flow modeling.

Knight and Chowdhury[28] studied 2-D unsteady leading edge separation on a pitching airfoil. The Reynolds number considered was 10000, Mach number 0.2 and the dimensionless pitching rate as 0.2. They performed computations using two separate algorithms for the compressible laminar Navier-Stokes equations. Their results revealed that the appearance of the primary recirculating region has been traced to the emergence of a pair of critical points (saddle and center) in the flow at approximately the 18% chord location at an angle of attack close to 15 degrees. The primary recirculating region (center) has a clockwise sense of fluid rotation, and grows with increasing angle of attack. Secondary and tertiary recirculating regions form after the appearance of the primary recirculating region. The sense of fluid rotation is counter-clockwise and clockwise respectively. Subsequent to the formation of secondary and tertiary recirculating regions, the boundary layer erupts due to the interaction of the recirculating regions. The primary recirculating region detaches from the airfoil surface and forms the dynamic stall vortex. The appearance of the primary recirculating region does not signify separation. For higher Mach number compressibility affects the process of stalling.

Compressibility effects can and do play a significant role in the development of the unsteady flowfield on rapidly pitching airfoils.

Carr, Chandrasekhara, and Broke[12] performed a quantitative study of unsteady compressible flow on an oscillating airfoil. Point diffraction interferometry permitted the detailed study of the complex unsteady flow near the leading edge of an oscillating airfoil, and quantitative flow information has been obtained both on the surface and in the surrounding flowfield for a range of frequencies and Mach numbers. A laminar separation bubble was observed in most of the higher angle conditions, although the occurrence of the bubble can be delayed by unsteadiness. Locally supersonic flow was observed near the leading edge, but the region of supersonic flow was quite small. Unsteadiness significantly relieves the pressure gradient that occurs in this region. The performance limitation of a helicopter stemmed from the leading-edge flow separation causing dynamic stall on the retreating blade of the helicopter during the pitch up stroke. The flow eventually reattached during the pitch down cycle. Depending on the mean angle of attack, amplitude, and frequency of oscillations, a hysteresis loop of varying size developed. This loop determines aerodynamic damping. An understanding of this reattachment process may help in modifying flow. For example, if the process can be completed rapidly, the airfoil will be able to generate more lift through the cycle, thus altering its performance. The damping can be negative during certain parts of the cycle, resulting in an increase in the amplitude of oscillation causing stall flutter. An understanding of the reattachment process is therefore essential to alleviate the stall flutter and to improve the dynamic lift characteristic of an oscillating airfoil.

Niven, Galbraith, and David[29] made the first attempt to analyze the reattachment of separated flow of a two-dimensional wing undergoing ramp down motion through surface pressure measurements. This study showed that the reattachment process occurs over a finite length of time and the airfoil incidence at reattachment was found to be close to the static stall angle. However, no flowfield measurements were available to understand the physics of the flow field.

Ahmed and Chandrasekhara[30] studied the reattachment of an oscillating airfoil dynamic stall flow field using the techniques of stroboscopic schlieren, two-component laser Doppler velocimetry, and point diffraction interferometry, for a freestream Mach number 0.3 and reduced frequency 0.05. The major conclusions from their studies were as follows. Reattachment of the dynamic stall flow is a continuous process, unlike that in a steady flow. The process includes development of larger than freestream velocities near the airfoil surface as the process advances over it. Reattachment begins at or near the static stall angle even in unsteady flow. As the flow begins to reattach, the suction pressure coefficient rises rapidly, but its values are different from those in the steady flow and the unsteady flow during the upstroke at the same angle of attack. For the Reynolds number of the experiment, reattachment process progresses through a separation bubble, which changes size during the process and disappears at a low angle of attack. Reasonable agreement was found between LDV and PDI studies, enhancing the confidence level of the measurements. Lift enhancement by unsteady airfoil motion through the production of coherent vorticity is a problem of both fundamental and practical interest. The potential benefits of dynamically delaying stall of an airfoil offers

possibilities for expanding the flight envelope of full-scale aircraft systems. The dynamic stall of an oscillating (or a transiently pitching) airfoil originates from the failure of the laminar separated flow to reattach as the angle of attack increases, resulting in the formation of the dynamic stall vortex from the bursting of a separation bubble. Since the separation bubble is a consequence of transition of the laminar separated shear layer, it can be concluded that transition physics plays a major role in the dynamic stall process. Additional complexity is introduced by the ever-changing transition behavior such as reduction of transition length with increasing pressure gradient (as the airfoil pitches to a higher angle of attack). Thus, it is desirable to remove the transition effects by predetermining the transition point and fixing it so that the effects of compressibility due to the large local fluid velocities around the leading edge can be clearly isolated. Traditionally, fluid dynamicists have tripped the boundary layer in the hope of achieving Reynolds number similarity and removing transition effects as a parameter in low-Reynolds number studies.

Chandrasekhara, Wilder, and Carr[31] presented results of boundary-layer tripping studies of compressible dynamic stall flow. The criteria for successful tripping were established as the elimination of the laminar separation bubble that otherwise forms, delay of dynamic stall onset angle, and production of larger suction peaks at corresponding angles of attack when compared with an untripped airfoil dynamic stall flow. The results showed that the dynamic stall flow was extremely sensitive to the trip used and hence to the state of turbulence in the flow immediately downstream of the trip. The optimum trip was determined to consist of a distributed roughness whose height was

comparable to (but less than) the boundary-layer thickness in the adverse pressure gradient region and upstream of the point where the dynamic stall vortex forms over untripped airfoil. The large variability in the details of the dynamic stall process of an untripped airfoil was removed by fixing the transition point. The data generated thus are believed to be useful in validating compressible dynamic stall flow computations.

Ko and McCroskey[10] studied computations of unsteady separating flows over an oscillating airfoil. The primary objective of their study was to identify the most accurate, robust and economic turbulence model for dynamic stall computations. In dynamic stall computations, a two-dimensional, body-fitted C-type computational grid moves in a sinusoidal pitching motion about an airfoil's quarter chord in the inertial reference frame. They selected Baldwin-Lomax (B-L) model because of its popularity as a zero-equation model. The Spalart-Allmaras (S-A) model is chosen among one-equation model because of its excellent performance. Finally, the $\kappa - \varepsilon$ model is selected because it is the most popular two equation model. The predictions by S-A and the $\kappa - \varepsilon$ models agree very well with the measured data for all three force coefficients C_l, C_d, and C_m. The B-L model shows fairly good agreement with the measurements for C_l, C_d but not for C_m.

Geissler, Carr, Chandrasekhara, Wilder, and Sobieczky[32] performed a computational study of compressible dynamic stall flow which includes the role of boundary layer transition. They also considered variable geometry airfoils. The study addressed the inadequacies of modeling the dynamic stall flow without incorporating the effects of transition. Fairly good agreement was obtained between the experiments and

calculations for the NACA 0012 airfoil at a Reynolds number of $1.1x10^6$ despite the fact the flow experienced the large scale flow separation associated with deep dynamic stall. This prompted the extension of the model to the DDLE airfoil where the nose radius is very large. In this case, both experiment and calculation shows the negative pressure peak on the airfoil upper surface continues to increase as the angle of attack increases to 17^0. This is in strong contrast to the NACA 0012 results, where bubble bursting and dynamic stall onset occur at 14^0 angle of attack. Earlier experiments have documented the onset of compressible dynamic stall either from the bursting of a leading-edge laminar separation bubble or from a leading-edge shock, depending on the Reynolds number and Mach number. However, for certain combinations of conditions, the supersonic flow and the bubble dynamics compete with each other. The consequent complex interactions lead to a newly discovered mechanism of dynamic stall onset.

Details of these various mechanisms were discussed by Chandrasekhara, Wilder, and Carr[33]. They concluded that compressible dynamic stall is influenced by three different, competing factors at low and moderate Reynolds numbers. Dynamic stall is caused by the bursting of the laminar separation bubble at low Reynolds numbers and moderate Mach numbers. As the Mach number is increased, the interaction between the supersonic flow and the bubble can initiate the dynamic stall process. At still higher Mach numbers, shock induced boundary-layer is the cause of dynamic stall process. The dynamic stall flow and vortex evolve under a supersonic external flow. Depending on local flow conditions, the fluid dynamic interactions vary, thus strongly influencing the dynamic stall onset process. All of these aspects need to be modeled properly if attempts

to compute the flow are to be successful. The strong pitching moment that accompanies dynamic stall is well known to be highly detrimental to helicopter performance. Furthermore, compressibility effects induce a premature onset of dynamic stall at freestream Mach numbers as low as 0.3, which greatly limits the performance of a rotor. The phenomenon of unsteady flow separation also limits the operational envelope of fixed-wing aircraft when it is encountered during airfoil flutter, buffet, etc. control of both steady and unsteady flow will expand the flight envelopes of future aircraft designs. Recent studies have shown that compressible dynamic stall can be caused either by an extremely strong adverse pressure gradient in the flow near the leading edge or by a shock-induced separation occurring in this region. Because both phenomena are a consequence of the fixed-airfoil geometry, there appears no simple way to significantly alter these conditions. However, the use of smart materials and actuator offers the possibility of designing wings that can continuously and rapidly adapt to changes in local flow conditions, thereby enabling these wings to deliver optimum performance at each instantaneous flow condition.

Upon recognizing that dynamic stall at practical Mach numbers is induced by rapid flow acceleration followed by abrupt deceleration around the leading edge, Chandrasekhara, Wilder, and Carr[34] developed a control strategy to modify the flow gradients by suitably shaping the airfoil leading edge. The goal was to reduce the local Mach number in the leading-edge region and to favorably alter the leading-edge pressure distribution, thereby introducing possible delays or elimination of the onset and effects of dynamic stall. In other words the aim was to achieve control of flow separation and to

eliminate dynamic stall vortex through dynamic airfoil leading-edge curvature change and, thus, effect vorticity management in the flow. This approach in turn leads to the concept of dynamically deforming leading edge. Dynamically changing the airfoil curvature showed that it is preferable to change the curvature slowly for the flow to adjust to the instantaneous geometry if control is to be effective. DDLE airfoils with shape 8.5 at M=0.3 and shape 6 at M=0.4 both were dynamic stall free, and the leading edge flow was always attached, even though there was some trailing-edge separation present in the flow. This remarkable result, thus, validated the use of the DDLE airfoil concept for achieving dynamic stall control. Changing the leading-edge curvature of an NACA 0012 airfoil was effective in producing significant stall delay (about 5 deg at M=0.3) through decreasing leading-edge flow acceleration. The extreme sensitivity of the airfoil peak suction pressure to the flow acceleration around the airfoil leading edge resulted in reduced peak suction levels when the nose radius was increased. Rounding the leading-edge also distributed the low pressure region over a wider extent on the airfoil upper surface, reducing the leading edge adverse pressure gradient, thus making it possible for the airfoil to reach higher angles of attack before stalling, in both steady and unsteady flows.

Greenbalt, Nishri, Darabi, and Wygnanski[35] presented some recent developments in separation control. Specifically, the effects of net mass-flux superposition, curvature, large flap deflection and extended reduced frequency range were considered on static configurations. Additionally, the bases of dynamic stall, as well as the means to affect its control, were emphasized. The superposition of blowing, together with periodic

excitation, was found to detrimental to separation control, while suction was beneficial. Specifically, the length and transverse height of the ubiquitous separation bubble were increased while suction initiated the bubble formation closer to the slot and shortened its length. Considerations of streamline curvature confirmed the effectiveness of these reduced frequencies but emphasized the importance of actuator location on separation control with curvature. Due to the nature of momentum transfer by the large eddies, under certain conditions, form drag was found to exceed total drag- indicating negative net skin friction. The effect of reduced frequency on lift enhancement indicated that the most effective frequencies for separation control are in the approximate range $0.3 \le F^{+} \le 4$, confirming the findings of many in-house and other investigations. Small amplitude excitation in this range dramatically reduces the lift and moment oscillations resulting from unsteady separation and vortex shedding. Simulated dynamic stall on a stationary flap, compared with an airfoil undergoing dynamic stall at rotorcraft reduced frequencies, demonstrated the principle of time-scale disparity between the destructive dynamic stall vortex (DSV) and the controlling large coherent structures (LCS).

A study of the mechanisms of dynamic stall control on an airfoil revealed that excitation effectively removed the DSV and rendered the aerodynamic coefficients independent of airfoil oscillation rate, *k.* moreover, the generation and advection of LCS's over the airfoil surface at maximum incidence was similar for both dynamic and static cases. Consequently, the resultant oscillations in aerodynamic coefficients were

negligibly small and large instantaneous post-stall excursions, typical of the baseline data, were all but eliminated.

Chandrasekhara, Wilder, and Carr[36] performed experiments focusing on controlling the flow over a sinusoidally oscillating airfoil by determining the dynamic shape variations that produced the right nose curvature at each instantaneous flow condition, thus producing the most attached flow over the range of angles of attack interest. They chose a sharp to round shape profile, while always maintaining the airfoil shapes within the range of a previously determined attached flow envelope, to achieve the desired flow control effect. They concluded compressible dynamic stall can successfully be controlled using dynamic shape adaptation. This required a very small (0.6 mm) change in the chord length of a dynamically adaptive airfoil that produced a nearly 150% change in the leading-edge radius of curvature. The flow was found to be dynamic stall vortex free for M = 0.3, k = 0.5 and $\alpha(\text{deg}) = 10 + 10 \sin(\omega t)$. The favorable effects of dynamic shape adaptation realized through changes in the instantaneous potential flow resulted in broader pressure distributions with lower peak suction values and led to a redistribution of the unsteady flow vorticity. The vorticity level decreased to values where the dynamic stall vortex did not form. The peak suction variation loop over the oscillation cycle was found to be the smallest for the adapting airfoil. The deformation rate, the initial angle of attack, and the amount of nose curvature change affect the success of the approach significantly. The most benefit is produced while remaining within the attached flow envelope for a given Mach number during dynamic shape adaptation.

Greenbalt, Nishri, Darabi, and Wygnanski[37] discussed the parameters governing steady separation control and the time resolved mechanisms that affect the control. They also described the classical DSV development and the analogy between dynamic stall simulation (and its control) on a stationary deflected flap with classical aerodynamic stall. This characterization illustrates the pivotal importance of the different time scales associated with dynamic stall vs. those of the controlling LCSs. The principal objective of their work was to study the mechanisms that affect dynamic stall and its control. They concluded excitation effectively removed the DSV and significantly attenuated trailing-edge separation. Phase-averaged dynamic pressure distributions at maximum incidence were almost identical to static under the same excitation conditions. The comparisons improved further with increasing excitation frequency. The generation and advection of LCSs over the airfoil surface at maximum incidence were similar, with differences in amplitude and phase velocity diminishing with increasing excitation frequency. Excitation rendered the aerodynamic coefficients effectively independent of airfoil oscillation rate *k.* Oscillations in the aerodynamic coefficients induced by the excitation were insignificantly smaller when compared to the phase-averaged quantities. Excitation effectively eliminated the large instantaneous post-stall excursions, typical of the baseline aerodynamic coefficients, resulting in small differences between instantaneous and phase averaged data.

Greenbalt and Wygnanski[5] performed a parametric study to investigate the effect of periodic excitation (with zero net mass flux) on a NACA 0015 airfoil undergoing pitch oscillations at rotorcraft reduced frequencies under incompressible conditions. The

primary objective of the study was to maximize airfoil performance while limiting moment excursions to typical pre-stalled conditions. Their study yielded following principal conclusions. Light stalls, as well as deep stall, were effectively controlled by oscillatory excitation. The beneficial effects of excitation were more pronounced at higher airfoil oscillation rates and effectively independent of Reynolds number. Flap-shoulder excitation, in conjunction with pre-stall pitch excursions, was more aerodynamically efficient than excitation employed in the post-stall regime. As more information about and greater understanding of the dynamic stall process has been developed, efforts have focused on ways to delay formation of the dynamic stall vortex to higher angles of attack, or even to eliminate it from the operating environment of the helicopter. The dynamic stall study of slotted airfoil configuration demonstrated that there is indeed a way to suppress the dynamic stall vortex. Suppression of the dynamic stall vortex resulted in elimination of the pitching moment excursions that are the primary reason that dynamic stall conditions must be avoided.

Carr, Chandrasekhara, Wilder, and Noonan[38] tested a multi-element airfoil designed for helicopter applications for compressible dynamic stall behavior and proved to be a robust dynamic stall-free concept. This slotted airfoil has operated into post-stall areas without the dynamic stall vortex that is normally present whenever airfoils are tested beyond their static stall boundary. One of these slotted airfoils, operated throughout the range of Mach numbers representative of helicopter flight without experiencing a dynamic stall vortex at any condition tested, thus demonstrating the value of such a configuration for application to future helicopters. A detailed discussion of the

flow on the optimum slot design showed that the design was effective in suppressing the dynamic stall vortex, even at the high Mach numbers that have negated the effectiveness of many flow control concepts. Significant compressibility effects were observed, including a strong shock appearing in the slot for certain dynamic conditions. This shock played an important role in the development of the flow at high angle of attack and shows the type of flow condition that only occurs during dynamic motion at compressible flow conditions. Flow separation on the slat and main airfoil element progressively increased as the Mach number increased, but no dynamic stall vortex was observed at any of the conditions tested. A comparison with the basic single-element airfoil, as well as a second slat design, showed the improvements that can be attained through effective slat design. The slot-jet continued to energize the main element boundary layer even after the slat stalled. This suggests the possibility that there may be some special slot geometries that are the most efficient for this task. However, the many conflicting requirements of the main element leading-edge geometry for the wide ranging conditions of the rotor need to be considered carefully if this effort is to succeed. Instantaneous pressure distributions were presented showing the influence of slat design on the suction peak that occurs in the pressure distribution. A discussion of Reynolds number effects was presented that indicated that the dynamic stall suppression resulting from use of the slat concept also seems to be insensitive to changes in Reynolds number.

CHAPTER III

VORTICITY AND TURBULENCE TRANSPORT EQUATIONS

3.1 Vorticity Transport Dynamics

The mean vorticity (Helmoholtz) transport equation is written for Reynolds averaged turbulent flow following Bowersox[42] as

$$\frac{D\vec{\omega}}{Dt} = -\vec{\omega}(\nabla\cdot\vec{V}) + (\vec{\omega}\cdot\nabla)\vec{V} + \frac{1}{\overline{\rho}}\nabla x(\nabla\cdot\Pi) - \nabla x\left(\frac{1}{\overline{\rho}}\nabla\overline{p}\right) + \nabla\left(\frac{1}{\overline{\rho}}\right)x(\nabla\cdot\Pi) \qquad (3.1)$$

The left-hand side of Eq. (1) contains the local unsteady and convective vorticity transport. The first two terms on the right-hand side depict the familiar compressibility and three-dimensional vortex stretching. The third term denotes the molecular diffusion and anisotropic turbulent transport, where the tensor Π includes both the molecular and turbulent (Reynolds or Favre averaged) shear stresses. The fourth term is the baroclinic torque, and the last term represents an anisosteric (i.e., variable density) molecular and turbulent diffusion. Direct calculation of ensemble-averaged contours of the vorticity (z-component), convection, compressibility, and vortex stretching terms are possible with the acquired data.

3.2 Turbulence Transport Equation

The turbulent shear stress transport is given by [Wilcox[11]]:

$$\begin{aligned}\tau^T_{ij,t} + (\overline{u}_j\tau^T_{ij})_{,j} = &-\tau^T_{ik}\overline{u}_{j,k} - \tau^T_{jk}\overline{u}_{i,k} + \overline{u''_j}\overline{p}_{,i} + \overline{u''_i}\overline{p}_{,j} - \overline{\tau}_{ik,k}\overline{u''_j} - \overline{\tau}_{jk,k}\overline{u''_i} - \overline{p'(u''_{i,j} + u''_{j,i})} \\ &-[\overline{(\rho u''_i u''_j u''_k)} - \overline{p'u''_i}\delta_{jk} - \overline{p'u''_j}\delta_{ik} + \overline{(\tau'_{ik}u''_j + \tau'_{jk}u''_i)}]_{,k} + \overline{\tau'_{ik}u''_{j,k} + \tau'_{jk}u''_{i,k}}\end{aligned} \qquad (3.2)$$

The left-hand side of Eq. (2) contains the local unsteady and convective turbulent shear stress transport. The first two terms on the right-hand side are the turbulent shear stress production; the third and fourth are the pressure-work; the fifth and sixth are the "viscous-work;" the seventh term is the pressure-strain redistribution; the eight term is diffusion, and the last is the dissipation. Direct measurement of the production was achieved.

CHAPTER IV

EXPERIMENTAL FACILITIES

To accomplish the dynamic stall measurements, a Dynamic Stall Facility (DSF) was constructed. The DSF included the combination of area reducing inserts to the Oran Nicks Low-Speed Wind Tunnel and a hydraulic actuation apparatus to dynamically move the wing. The inserts were designed to increase the flow velocity and to transfer the wing loads to the tunnel support structure. A large-scale NACA 0012 wing was constructed for the present study. A detailed description of the facilities is given below.

4.1 Oran Nicks Low-Speed Wind Tunnel

The Oran W. Nicks Low Speed Wind Tunnel at Texas A&M University (TAMU) is a self-contained research facility. It is a closed circuit tunnel with a rectangular test 2.1 m high, 3.0 m wide and 3.7 m long (7 ft x 10 ft x 12 ft) fabricated of structural steel lined with marine plywood. The corners have 0.3 m (12 in) fillets. The maximum Mach number is 0.25, which corresponds to a velocity of 85 m/s (200 mph). Three inch wide vertical venting slots in the side walls at the test section exit maintain near atmospheric static pressure. The test section side walls diverge about 0.083 m per meter distance in along the stream wise direction to account for boundary layer growth. Fig. 4 shows the facility schematic and photographs of the test section.

4.1.1 The DSF Inserts

The DSF consisted of inserts to increase the flow velocity in the Orin Nicks Tunnel and to support the loads during dynamic actuation of the wind tunnel model (described in the next section). A Mach number of 0.3 was achieved in the present test. However, with additional modifications to the diffuser, Mach 0.4 is believed possible. The inserts were designed to reduce the test section to 2.1 m x 2.1 m (7 ft x 7 ft). The flow conditions are listed in Table 1. A detailed description of the insert design is given below.

4.1.2 Tunnel Flow

Computation Fluid Dynamics (CFD) was employed to design the inserts to achieve uniform flow in the reduced area test section. Preliminary CFD analysis was done on the current wind tunnel (Oran W Nicks Low Speed Wind Tunnel) to validate the design methods. The physical dimension of the tunnel was measured and incorporated into SolidWorks. The SolidWorks drawing was used to generate the grid in GAMBIT. The physical dimension of the tunnel that was simulated was divided into 3 sections: a 1.83 m (6 ft) inlet, a 4.87 m (16 ft) test section, and a 12.2 m (40 ft) long diffuser. Total length of the wind tunnel simulated was 18.9 m (62 ft). The CFD code FLUENT was used to compute the flow. Due to the symmetric nature of the wind tunnel only one-quarter of the grid was simulated. This feature helped in reducing the computational time. The boundary conditions were as follows:

1. Inlet

2. Outflow
3. Wall
4. X – Symmetry
5. Y – Symmetry

Fig. 5 shows the drawings of the current tunnel with the test section. Fig. 6 shows the grid for the current tunnel along with the boundary conditions.

Above flow problem was solved to get the pressure data on the wall and the floor. The goal was to compare the results obtained by CFD to pressure data obtained by experimental methods. To record pressure data on the floor and wall of the tunnel following procedure was employed.

Pressure data was obtained at every 15.24 cm (6 in) of the tunnel wall and floor starting from the inlet. Data was recorded for a length of almost 18.3 m. A pin hole was made on the vinyl tubing (0.04 mm. diameter) with one end connected to the pressure sensor and the other end was a closed end. To keep the tubes together they were taped on to the thin aluminum sheet which in turn was taped to the wind tunnel wall/floor. Sample images with the vinyl tubes taped to the floor are shown in Fig. 7. Fig. 7 (a) shows vinyl tubes taped on to the floor and Fig. 7 (b) shows vinyl tubes taped on to the wall of the modified wind tunnel.

A comparison of experimental pressure data (Pexp) to the computations (Pcompu.) is given in Fig. 8. Also shown are the simple 1-D theoretical results, both incompressible (Pincomp.) and compressible (Pcomp.)]. The 1-D incompressible theory was based on conservation of mass and Bernoulli’s equation given by:

$$p_1 + \frac{1}{2}\rho v_1^2 = p_2 + \frac{1}{2}\rho v_2^2 \tag{4.1}$$

The 1-D compressible is given by the equation:

$$\frac{p_0}{p} = \left(1 + \frac{\gamma - 1}{2} M^2\right)^{\frac{\gamma}{(\gamma-1)}} \tag{4.2}$$

Fig. 9 shows the comparison of pressure data on the wind tunnel floor. The dip in the plot is the test section region where the pressure is almost constant as expected. The pressure decreased in the inlet, remained constant in the test section and finally increased in the diffuser section. The pressure data for all methods fell on top of each other as shown. This exercise ensured that the boundary conditions used in FLUENT gave right results.

Presented in Fig. 10 is a comparison of the CFD results and the 1-D theory for the reduced 2.1 m x 2.1 m (7 ft x 7 ft) test section. As shown in the plot, they agreed very well. Fig. 11 shows the pressure data on the wall as obtained by CFD (Pcomp) and the compressible 1-D calculations (Pcompr). As shown in the plot they both match well. These results demonstrated that the test section flow was uniform and the static pressure was expected to be 50 psf, which was used for structural design.

4.1.3 Mechanical Design

In a similar test section reduction of the Orin Nicks Wind Tunnel, Noak and Norton[39] constructed a set of inserts from wood. However, for the present DSF facility, large loads static pressure loads, as well as large unsteady wing loads (described later) were expected. Hence, the wind tunnel inserts were made from a steel frame and

aluminum plate skin structure. Type 5052 AL was chosen for cost reasons. Detailed load analyses were performed using the stress analysis program CosmosX, which is part of the autocad program SolidWorks program. A factor of safety of 5.0 was chosen for all designs. Thus, the design load was set to 12,000 Pa (250 psf). The dynamic loads are described in the following section.

Looking up stream, the left side of the wind tunnel insert consisted of six panel structures. All of the panels were made from steel frames with AL 5052 sheets screwed (10-32 steel screws) to them to from the wall. Shown in Fig. 12 is a drawing of a panel. The frame for each panel was made from 5.08 cm x 2.54 cm (2 in x 1 in) C-channels. The exception being the middle panel (3rd) frame which was made out of 12.70 cm x 4.45 cm (5 in x 1.75 in) C-channel. This frame was the primary support for the wing. The aluminum plate thickness was 4.8 mm (3/16 in), which was selected to withstand the test section suction pressure with minimal displacements.

The 3rd panel holds the wing and encounters the large unsteady load. Hence, to transfer this load to the wind tunnel structures and eventually to the concrete structure underneath, the 3rd panel was made stronger. The panels were inserted into the tunnel one at a time. The panels were then all bolted together using 1.27 cm (½ in) steel bolts. The hole-pattern of the C-channel is shown in Fig. 12. The 3rd panel C-channel (Fig. 13) had more holes as this frame is bolstered by additional structures (Fig. 14).

Special care was taken to design the additional structures shown in Fig. 14. There was an 20.32 cm x 20.32 cm x 10.16 cm (8 in x 8 in x 4 in) block used to hold top

structure (NDSP3-Ti)[1] and the bottom structure (NDSP3-Bi) together. The block acts as a bearing housing. The shaft of the wing went through this bearing as shown in Fig. 15. The design of the wing along with the shaft is described later in the Chapter. In the structures NDSP3-Ti and NDSP3-Bi, the smaller I-beams were welded to the larger I-beam at angle of 45° as shown. The bottom structure (NDSP3-Bi) was welded to the steel frame of the 3rd panel as shown in Fig. 15. The top structure (NDSP3-Bi) was screwed to the steel frame so that it can slide up and down for the convenience of installing the wing. The bearing was set in place in the bearing housing. Depending on the load acting on the shaft of the wing due to lift and drag, the bearing was chosen to have a minimum factor of safety of 5. Taper roller bearing was chosen as it could handle the maximum load for the fixed inner diameter (ID) of 3.05 cm (1.5 in). Once the block was set in place between NDSP3-Bi and NDSP3-Ti and bolted, 4 threaded rods [2.54 cm (1 in) diameter and 60.1 cm (2 ft long)] were used to further secure them as shown in Fig. 15. The right wall was built exactly the same as left wall except for optical access. Presented in Fig. 16 is a view of the additional structures from inside of the modified wind tunnel.

Provisions were made on the left wall of the modified wind tunnel to have glass windows in order to perform Stereo Particle Image Velocimetry (SPIV) experiments in the future. A door was made on the 6th. panel of the left wall. Adjustable vents were included on both the walls to control the pressure inside the wind tunnel. Fig. 17 shows the glass windows, structures to hold the wing, vent and the door. A circular section was

[1] Structure identification number defined during the design construction of the facility.

cut to make an optical glass window on the right wall to perform 2D Particle Image Velocimtery (PIV) experiments, which was used in the present experiments. Fig. 18 shows the optical glass window for 2D PIV experiment. Fig. 19 shows the optical glass window with the camera acquiring images during the experiment.

A new steel frame of roof was made of 7.62 cm x 6.35 cm (3 in x 2.5 in) steel I-beams. This roof was designed to transfer the tunnel loads to the support structure. The design of the roof is shown in Fig. 20. The 5052 AL sheets were bolted to the roof using 10-32 screws. A section of the roof was fit with a Plexiglas window. The PIV laser was directed through this window on to the wing. The grey frame around the Plexiglas was made out of AL 5052. The roof was bolted to the side walls of the modified wind tunnel. Thus the roof was set in place as shown in Fig. 21.

The inlet of the wind tunnel insert was a curved section that mated the reduced test section width to the original tunnel contraction. Templates were constructed to define the shape as shown in Fig. 22. The actual structure was constructed from a formed steel frame and $1/8^{th}$ thick aluminum plate. The steel frames were made from 2.54 cm x 1.27 cm (1 in x ½ in) C-channel. The frame was anchored to the concrete contraction of the current wind tunnel. Fig. 22 – 26 show the sequence of building the inlet. For inlet section 8-32 screws were used to attach aluminum sheet to the frame in stead of 10-32 screws as the sheet was thinner. All of the screws were countersunk.

The final section of the modified wind tunnel was the diffuser section. As was done for inlet section, the diffuser section mated the end of the test section to the existing diffuser. The diffuser was anchored to the concrete diffuser. Unlike the inlet section, the

diffuser walls were straight. The diffuser was arbitrarily selected to be 3.05 m (10 ft) long. The frame was fabricated from 2.54 x 1.27 cm (1 in x ½ in) thick steel C-channels with 3.18 mm (1/8 in) aluminum sheet screwed on to the frame. Fig. 27 shows the left diffuser wall.

Vortex generators were used at the end of the test section to help minimize diffuser separation. The Vortex generators help in mixing the high momentum fluid away from the wall with the low momentum fluid near the wall. The present vortex generators were built to the shape of NACA 0012 profile and screwed to the test section as shown in Fig. 28.

The next step was to run the tunnel and verify the test section Mach number. Fig. 29 (a) and (b) show the plots of Mach number and static pressure in the modified 7 ft x 7 ft tunnel. With this configuration, the peak Mach number was 0.28. This was limited by both diffuser performance and tunnel power.

The original goal was a freestream Mach number of 0.4. Power calculations (Fig. 30) demonstrated that a smaller test section was required to achieve this speed with the available 1200 kW of propeller power. Furthermore, the diffuser included divergence angle also needed to be reduced to approximately 10°, which translates into 10 – 12 m long achieve efficient diffusion at mach 0.4. A second reduced area test section (5 ft x 7ft) was constructed, and the diffuser will be installed during the follow-on project.

To achieve a 1.5 m x 2.1 m (5 ft x 7 ft) test section, inserts were designed to lower roof and raise the floor each by 1.0 ft. The design included detailed load

calculations to size roof and ceiling inserts. As shown in the Fig. 31, 7.62 cm x 7.62 cm (3 in x 3 in) C-channels were bolted to the steel frames of the 7 ft x 7 ft modified wind tunnel test section. For the floor, 4 panels were designed and fabricated. These panels were bolted together. Each panel had a steel frame made out of 5.08 cm x 2.54 cm (2 in x 1 in) C-channel. Aluminum 5052 sheets [4.8 mm (3/16 in)] thick were screwed on to them as was done for the wall. These 4 panels were slid through the gap between the C-channels shown in Fig. 32. The floor of the 5 ft x 7 ft test section is shown in Fig. 33. The roof was designed and fabricated as was done for the floor. The only difference was the roof was designed to have a glass window through which the laser can be shot on the test section model. Figs. 33 – 36 show the floor, roof, right side view and left side view of the 5 ft x 7 ft test section, respectively. Fig. 37 – 43 show images of the modified wind tunnel insert (7 ft x 7ft). After the installation of the modified wind tunnel all the seams were taped.

4.2 NACA 0012 Wind Tunnel Model

A NACA 0012 airfoil was selected for the current research. This airfoil is a good compromise between high maximum lift, low pitching moment and high drag divergence Mach number, and this airfoil has been the subject of numerous previous studies. The choice of this airfoil was driven by the fact that numerous researchers have used this profile, which translates into an available database for comparison.

4.2.1 Mechanical Design

The airfoil chord length was selected as 18 in and the model spanned the wind tunnel. A clearance of 3.2 mm (1/8 in) was maintained between the wing and the wind tunnel wall on both sides. Hence the wing was designed to have a span of 2.1 m (6 ft 11¾ in). The maximum flow blockage at the highest planned angle of attack with this arrangement was approximately 7.3%. An 11.4 cm (4.5 in) section of the airfoil was machined from Plexiglas. The Plexiglas piece was 2.54 (1 in) wide. Plexiglas is an optically transmitting material. Hence the laser sheet passes through the Plexiglas piece and minimizes any reflection issue during Particle Image Velocimetry (PIV) experiments. A shaft ran through the quarter chord of the wing. One end of the shaft was held by the hydraulic actuator to flap the wing at the desired frequency. Quarter chord point was the choice because the coefficient of aerodynamic moment C_m created at this point is of the order of 0 ~ 0.1. Hence the wing was flapped with minimum power requirement.

As mentioned in the above paragraph, a shaft was designed to run through the quarter chord of the wing, which was supported by bearings at both the ends. Stainless steel was chosen due to its high strength. The following calculation procedure was used to design the shaft:

$$L = C_L Qcb \tag{4.3}$$

where, C_L = Lift Coefficient = 1.6 (for a dynamically stalled NACA 0012); L = Lift acting on the airfoil, Q = Dynamic Pressure [= 13,400 Pa (280 psf)]; c = Chord length of

the airfoil [= 0.457 m (1.5 ft.)], and b = Width of the airfoil [=2.1 m (6 ft 11 ¾ in)]. With these values, L = 20,200 N (4540 lbf). A factor of safety 4 was chosen for all design purposes. Hence, the design load was estimated as $F = 4L$ [= 80,800 N (18,200 lbf)]. The minimum shaft diameter was based on the allowable shear stress of stainless steel of 2.3 x 10^8 Pa (33,000 psi). The shear stress is given by $\tau = F/A$, where $A = \pi d_s^2/4$ and the d_s is the shaft diameter. For the present design the minimum shaft diameter for failure was 2.1 cm (0.84 in). However, the shaft diameter was set at 3.81 cm (1.5 in) to maintain the maximum deflection to less than 6.35 mm (¼ in).

The thickness distribution for the NACA 0012 is given by the following equation.

$$\pm y_t = \frac{t}{0.2}\left(0.29690\sqrt{x} - 0.12600x - 0.35160x^2 + 0.28430x^3 - 0.10150x^4\right) \qquad (4.4)$$

where y_t is the thickness of the airfoil, t = maximum thickness expressed as a fraction of the chord, x is the axial coordinate along the airfoil center line per c.

The numbering system for NACA wing sections of the four digit series is based on the section geometry. The first integer indicates the maximum value of the mean-line ordinate y_t in percent of the chord. The second integer indicates the distance from the leading edge to the location of the maximum camber in tenths of the chord. The last two integers indicate the section thickness in percent of the chord. Thus the NACA 0012 wing section has 0 percent camber at 0.0 of the chord from the leading edge and is 12 percent thick.

Airfoil stress analysis was performed with the finite elements program ABAQUS. The airfoil cross-section was created using the profile equation 4.4 and then was extruded to the full span. The points on the profile were joined by 18 straight lines so that the airfoil surface had 18 regions both on the upper and lower surface to apply the varying pressure as the load. The loading[40] (varying pressure) is shown in Fig. 44. Table 2 shows the other input parameters used in ABAQUS.

In terms of boundary condition, the shaft was pinned at the ends and was constrained from having any movement with respect to the airfoil by using tie constraint condition.

Figs. 45 – 47 show the contour plots of deflection, reaction forces and stress acting on the wing and shaft. As can be seen in these plots, the deflection, stress and reaction force acting were well within the design limits.

The NACA 0012 wing used in the current research was built in two halves. Dowels pins [11.43 cm (4.5 in) long and 4.8 mm (3/16 in) diameter) were used to prevent any axial motion of the shaft as shown in Fig. 48. The detailed drawing of the wing with the screws and the shaft attachment dowel pins is given Fig. 48. The cross sectional drawing of bottom half of the wing is shown in Fig. 49. The two halves are screwed on to each other using 53 screws. Stress analysis was done on these screws (3/8 in diameter). The wing was counter sunk to accommodate the nuts and the bolt heads. The empty area in the counter sunk portion is filled with putty. Finally the wing surface was polished to have a smooth surface as any unevenness on the surface would trip the boundary layer and eventually affect the flow field. The length of the shaft was 3.05 m

(10 ft). Approximately 0.55 m (1.813 ft) of the shaft extends out on both sides of the wing. The shaft is concentric with the quarter chord of the wing as mentioned earlier. Fig. 50 shows the wing with the shaft and the Plexiglas piece.

The final NACA 0012 wing used in the present research is summarized below:

Chord of the wing	=	0.457 m (18 in)
Span of the wing	=	2.13 m (83.75 in)
Weight of the wing	=	104 kg (230 lb)
Mass Moment of Inertia of the wing	=	1.79 N-m (1.32 ft-lb)

4.3 DSF Hydraulic Actuation Apparatus

A hydraulic actuation apparatus was designed to pitch the airfoil about ¼-line. The advantage of hydraulic system over the originally proposed electric motor system was safety, where the electric motor system would require a large flywheel. A Parker Hannifin system was purchased from TEX A DRAULICS.

The hydraulic pump was driven by a 29.8 kW (40 HP) electric motor. The flow was 36.1 GPM @ 1800 rpm. The hydraulic reservoir held 80 gallons of *Chevron Rykon aw ISO 46* hydraulic fluid. The maximum pressure of the system was 20.67 MPa (3000 psi). A suction strainer/filter was used to keep the oil free of impurities before it goes to the accumulator bladder. The unit also has an oil level gauge with thermometer. The accumulator had a 9.46 liter (2.5 gallon) storage capacity, and was connected to the main pump reservoir with high pressure hoses [29.3 MPa (4250 psi). The accumulator maximum pressure was 20.67 MPa (3000 psi). During operation, the accumulator

supplied the required amount of hydraulic fluid through the servo valve. During downward movement of the piston, oil returned to the accumulator through a similar high pressure hose.

A Parker Hannifin servo valve controlled the amount of hydraulic fluid required for the pitching of the airfoil. Hence, one end of the valve was connected to the inlet of the hydraulic actuator and the other end to the outlet of the actuator as shown in Fig. 52. An algorithm was developed to control the opening/closing of the valve to allow required flow rate of hydraulic fluid in order to move the actuator.

The hydraulic valve was operated by a PID controller program implemented in RMCWin software. RMCWin software is RMC100 motion controller software by Delta computer systems. The RMC100 is a modular, high performance motion controller appropriate for a wide range of industrial applications for position and velocity control. Judicial choice of the Proportional, Integral, Differential gains, extended feed forward/backward and acceleration feed forward/backward make sure that the target command follows the actual command. An algorithm was developed to control the opening/closing of the valve to allow required flow rate of hydraulic fluid in order to move the actuator.

The final major component of the actuation system was the hydraulic cylinder with actuator as shown in Fig. 53. The inlet port, which was connected to the servo valve, was on the bottom of the cylinder. The outlet of the cylinder, which was also connected to the servo valve, was on the top of the cylinder.

A moment arm acted as a link between the wing and the hydraulic actuator. Hence, the linear motion of the actuator was converted to the pitching motion of the wing. The linear motion of the hydraulic actuator was then converted to sinusoidal motion of the airfoil.

The hydraulic cylinder actuator was connected to a moment arm by a clevis as shown in Fig. 54. The wing shaft was connected to the other side of the moment arm by a power lock. The power lock is a keyless locking device used to transfer torque. The inner diameter of the power lock matched the 3.81 cm (1.5 in) diameter of the stainless steel shaft. With this configuration of hydraulic system a range of 0° - 20° of the airfoil motion can be achieved at a maximum frequency of 12-15 Hz. The hydraulic cylinder had a bore of 6.35 cm (2.5 in). The actuator diameter was 2.54 cm (1 in). The range of linear motion of hydraulic actuator was 3.81 cm (1.5 in). However for the current test matrix the actuator was operated within a distance of 1.27 cm (0.5 in). A linear position sensor (MTS temposonics sensor) was mounted to the bottom end of the actuator as shown in Fig. 55. This sensor provided accurate non-contact position sensing in a wide array of output configurations. With this specification, the hydraulic actuator could sustain 6000 lbs of force.

To work out the algorithms used to operate hydraulic valve, it was decided to simulate the pitching of the wing without the wind load. Hence, a stand was made as shown in Fig. 56. As a first step, only the shaft was loaded. Once the program worked well with that the wing was loaded and the program was tweaked to produce the right result. This exercise helped to build experience with the general dependence of gains on

loads acting on the piston. Hence, with the wind load, it was an easy task to tweak the gains so actual command precisely followed the target command. This simulation also helped in building some additional structures required to prevent vibration in the wing and also in designing the stand for the hydraulic cylinder as shown in Fig. 57.

One of the major advantages of simulating the pitching experiment without wind load was the discovery of a vibration issue of the shaft. This vibration propagated to the wing and could have caused a failure of the wing. Hence, an additional support was built to hold the actuating end of the shaft as shown in Fig. 58. The shaft goes through the center steel block as shown. A lock collar was used at the end of the shaft to prevent any axial movement. The top and bottom I-beam structures were bolted to the modified wind tunnel steel frame. Thus, the load was transferred to the structure. This additional structure eliminated vibration in the shaft and also bolstered the support. Also, an additional structure was designed and built to bolt the hydraulic actuator support as shown in Fig. 59. This structure helped in transmitting the unsteady load to the large C-channels supporting the 7 ft x 10 ft low speed wind tunnel as shown. Fig. 60 shows the additional structures explained above. Given in Fig. 61 is an image of the hydraulic actuator drive system placed in the ready room along with the computer that was used to control the program. Presented in Fig. 62 is a comparison of the target sine wave to that measured during operation with the above mentioned LVDT. As indicated, the system worked very well.

4.3.1 Wing Angle Calibration and Coordinate System

The wing position (angle-of-attack) was related to the hydraulic piston motion through a linear calibration (see Fig. 63). The average variance between the calibration and the measured angle was 0.2 deg. The angle resolution for the control system was 55 counts per degree, which translates into steps of 0.018 deg.

The wing coordinate system for the experiments was defined as follows. The origin was fixed at the wing ¼-chord; *x* was defined as pointing in the upstream direction parallel to the tunnel floor; *y* was defined as vertically up, and *z* completed the right hand system.

The installation procedure of the DSF in the OWN Low Speed Wind Tunnel is described in the Appendix B.

CHAPTER V

EXPERIMENTAL APPARATUS AND DATA REDUCTION TECHNIQUES

The leading-edge region of the flowfield was documented using Particle Image Velocimetry (PIV). A detailed description of the PIV system is presented below. This is followed by a summary of the remaining instrumentation used to provide the tunnel flow conditions. The uncertainty analysis results are presented in the last section.

A new film, developed by ISSI, Inc., was tested to measure the surface shear stress and pressure. The S3F methods are proprietary to ISSI. The S3F data were too preliminary to draw conclusions. Hence, only a brief overview of the system with example results for the flapping wing is described in the last section of this Chapter.

5.1 Particle Image Velocimetry

5.1.1 Overview of the Operating Principles

Particle Image Velocimetry (PIV) is a non-intrusive diagnostic technique to measure the velocity in a plane. The technique has emerged into one of the most popular methods to quantify fluid flow. The primary reason is that PIV provides detailed instantaneous velocity measurements on plane. Both 2-D and 3-D measurements are possible on the measurement plane. For the present study, PIV was used to document the field near the leading edge during dynamic stall of a NACA 0012 airfoil operating the Dynamic Stall Facility described in the previous Chapter.

In summary, the PIV technique measures the velocity of a fluid element indirectly by measuring the velocity of tracer particles seeded into the flow. A schematic of a typical wind tunnel application is shown in Fig. 64. The tracer (or seed) particles are usually illuminated by a series of two short pulse lasers, separated by a specified time increment. The light scattered by the particles from the two pulses is recorded. Charge-Coupled Devices (CCD) cameras are generally used to record the two images. For most applications, interline transfer cameras are used, where both pulses are independently recorded on two separate images acquired on the same CCD in succession. The displacement of particles between the two images and the time increment between the light pulses determine the velocity of the flow.

Qualitatively three different types of image density can be distinguished. Low image density (Fig. 65a) is used for Particle Tracking Velocimetry (PTV), where individual particles are tracked. In the case of a medium density image (Fig. 65b), the individual particles can be detected. However, it is not possible to identify image pairs by visual inspection of the recording. For this case statistical correlation methods are used. This case has been termed PIV. The advantage of PIV over PTV is the better spatial resolution per image. In the case of high particle density (Fig. 65c) it is not even possible to detect individual images as they overlap in most cases and form speckles. This is called Laser Speckle Velocimetry (LSV). LSV requires large seed volumes, which was not available for the present study. Hence, PIV was used.

To evaluate the velocity, a digital PIV recording is divided in small sub-areas called interrogation areas. The local displacement vector for the images of the tracer

particles of the first and second illumination is determined for each interrogation area by means of statistical auto- or cross-correlation methods. The underlying assumption is that all of the particles within one interrogation area have moved homogeneously between the two illuminations. The projection of the vector of the local flow velocity into the plane of the light sheet (2-component velocity vector) is calculated taking into account the time delay between the two illuminations and the magnifications at imaging. The process is usually performed in a sequence starting with relatively large interrogation windows and then subsequently reducing the size of the window. The larger windows contain more samples and thus have higher correlation coefficients.

5.1.2 Texas A&M University PIV System

The PIV system used in the present experiment is an in-house designed system. A description of the system is given below.

A New Wave Solo 120 XT Dual Head Nd:YAG Laser (frequency doubled to $\lambda = 532\,\text{nm}$) provide the two laser pulses. The available repetition rate is 15 Hz. Each laser head has a maximum energy output of 120 mJ at 532 nm. The pulse width is 4 ns with an $\pm 1\,\text{ns}$ jitter. The beams emerge with parallel polarization. The polarization for one of the beams was rotated 90 degrees with a ½-wave plate. The plate is crystal quartz optic designed to differentially retard the phase of polarized beam. The beams were them overlapped in space with a high energy polarizing cube beam splitter that provides efficient narrow band polarization. The polarizer consists of a pair of precision right-angle prisms optically contacted together and has a damage threshold up to 10 J/cm^2.

This process provided two coincident beams; one with parallel polarization and the other with perpendicular polarization.

The laser system and corresponding optics were mounted onto the roof of the wind tunnel as shown in Fig. 66. The laser beams were guided into the test section using 90^0 prisms constructed of BK7 glass with AR coatings. A laser sheet (1.5 to 2 cm wide) was formed on the model using a BK7 Plano-concave cylindrical lens. A BK7 focusing lens with a focal length of 900 – 1000 mm is used to focus the beam so that the waist is located just above the test section model, precisely just above the Plexiglas portion of the NACA 0012 wing. The thickness of the laser sheet was less than 1.0 mm.

Vibrations were present when the wind tunnel ran at high-speeds. To stabilize the beans, two 10.2 cm x 10.2 cm (4in x 4 in) I-beams were used as shown in Fig. 66. The two I-beams run perpendicular to the direction of freestream and spanned across the wind tunnel test section. They were supported onto the current wind tunnel concrete roof. Vibration isolation material (rubber pads) was used between the I-beams and the concrete. Four sand bags were placed on the I-beams for further isolation of vibration. This setup proved to be effective to obtain a stable laser beam.

Data were were acquired with two cameras: a Cooke Corporation PCO 1600 Camera, and LaVision Flowmaster Camera. This was a high dynamic range (14bit), thermoelectrically cooled (to -20 deg C) interline transfer CCD camera with a 1600 x 1200 pixel array resolution. The camera has a Nikon f-mount for lenses. For the present set of experiments an exposure time of $5\mu s$ and trigger delay time of $10\mu s$ was used. The interline transfer rate is sufficient for delays down to 300 nsec. The camera frame

grabbing software was Camware version 2.13. A Nikon 70 – 300 mm lens was used to focus the camera onto the illuminated particles. The LaVision PIV camera was UltraSpeedStar Camera. This camera had a 12 bit, 1280x1024 pixel array. This camera was control with the LaVision DaVis software package.

The camera was mounted to an H-shaped stand was that made from aluminum rails (Fig. 67). The camera was mounted on an extension bar which in turn was attached to the middle rail using a mounting plate. The camera was supported by cylindrical posts which in turn were attached to the extension bar as shown in the Fig. 68. Mounting camera on the extension bar helped in moving it in the direction perpendicular to the flow depending on the requirement. For example, for a wide angle view the camera was moved away from the test section, and on the other hand for the zoomed in high resolution data, it moved in close to the test section wall as shown in Figure 68. The mounting plate can be slid on the middle rail thus providing movement of the camera in the direction of flow. Two cylinders were inserted into the middle rails at both ends. The middle rail was attached to the cylinders (running inside the rail) and to the side rails with the help of set screws and mounting plates respectively. This arrangement in turn provided rotational degree of freedom for the camera. Thus, the camera had three degrees of freedom for alignment.

The synchronization of the camera trigger, laser Q-switch, laser flash lamps to the wing motion as indicated from the signal from the hydraulic actuator were all controlled by a Quantum Composer Model 9618 pulse generator. The program ensured the flapping motion of the airfoil, laser sheet and the camera were phase locked to

acquire images at a particular angle of attack. The pulse generator had 8 channels with 100 ns resolution (jitter < 5 ns).

The tunnel was seeded by MDG Max 5000 Fog generator using MDG neutral fluid. The MDG neutral fluid corresponded to mineral oil. The Fog generator has a fog output of 10000 ft^3/min. Fluid consumption was 2.5 liter/hr. at 40 PSI at full volume. The reservoir capacity was 0.66 US gallons. It produced pure white particle diameter of 0.5 to 0.7 μm. The 3 dB frequency response of these particles was estimated at 40-62 kHz[47].

5.1.3 Surface Reflections

Bright laser reflections from a solid (reflective) surface masks the Mie scattering signal from the small seed particles (0.5 – 0.7 μm, here). An additional complication associated with the laser reflection from the surface is image blooming, which a situation where neighboring pixels are saturated with excess charges producing a white band in the image. A balance in the laser power is required optimize scattering from the particles while minimizing blooming.

To address the reflection challenge, a 10.2 cm (4.0 inch section) of the airfoil leading edge was machined from Plexiglas (optically transmitting material). The notch for the Plexiglas insert is visible near the center of the airfoil Fig. 50. The Plexiglas was polished to a clear transmitting surface with Buehler Brand polishing compound (20 micro-inch, followed by 5 micro-inch). This Plexiglas insert transmitted approximately 92% of the laser energy. The purpose of this section was to minimize laser sheet

reflections. To that end, the portion of the wing underneath the Plexiglas was painted black so that laser sheet would not reflect back. The remaining 8% still masked the data below approximately 1.5 mm. Thus, the Plexiglas was coated with a fluorescent (Rhodamine) paint capable of absorbing up to 99% of the incoming light at 532 nm and emitting the light at approximately 590 nm (see Fig. 66). The second benefit was that the emitted light was diffuse, compared to the specular laser reflection. Lastly, the airfoil was painted black approximately one foot on each side of the Plexiglas (see Fig. 66) to minimize additional light reflections. This combination of measures significantly reduced the reflections, and data were acquired as close as 0.5 – 1.0 mm from the wall.

5.1.4 Data Reduction

Each PIV sample consisted of two images; these were labeled image A and image B. For present study, 1000 to 1300 image pairs (samples) were acquired at each angle of attack to assure statistical convergence of the mean and second order statistics. These images were processed as described below.

As described above, considerable effort was put into minimizing vibrations. However, the remaining vibration had an adverse affect on the images. Specifically, the camera vibrations resulted in the airfoil position “jumping” around from one image to the next. The magnitude of the airfoil jumps was approximately 10 to 15 pixels. Thus, the first step in the data analysis was to “de-jitter” the airfoil images. To accomplish this task, an in-house MATLAB code was developed to locate the airfoil edge on each image. All of the images were translated to align all of the airfoil edges with the first image in the sequence. The airfoil position was aligned to within 4 pixels.

The second step in the data analysis was performed to further minimize the reflection effects. Specifically, an in-house MATLAB code was developed average all the shifted image A's and images B's. The averaged image was then subtracted from each image. This algorithm worked very well as shown in Fig. 69. Given in Fig. 69(a) is an original instantaneous image before subtraction. The averaged image is shown Fig. 69(b), and the image after subtraction is given in Fig. 69(c). The contrast in the last image was adjusted to better show the particles.

Velocity fields were created by calculating the displacements of particle ensembles from consecutive images using Innovative Scientific Solutions' Digital Particle Image Velocimetry (DPIV) 32-bit Analysis Code[41]. A four-step adaptive correlation calculation using successive interrogation spot (square) sizes of 128x128, 64x64, 32x32, 16x16 pixel respectively with a 75% overlap was used to determine velocity vectors. The images were correlated to the grid. Hence the grid option was 'on' in the DPIV program. With these settings, data were acquired in 4 pixel increments, which corresponded to approximately 0.06% of the airfoil chord or 0.25 mm. This "hyper fine mesh" is shown in Fig. 70. With this mesh, there were nominally 100,000 velocity vectors in the region of interest.

In order to enhance the intensity of correlation peaks relative to random noise, a correlation multiplication process filter with all four correlation maps was turned on. A consistency post processing filter was turned on to improve the adaptive correlation calculation during the first, second, and third steps and eliminated incorrect vectors during the fourth step. The Consistency filter is the parameter which searches for a

correlation peak around another within a radius of 1 unit. Hence in the settings for consistency filter in DPIV program, the minimum particle was set to 2. The radius was also set to 2, which corresponded to one unit to the left and one unit to the right. A filter refinement study was performed to ensure that the results were independent of the filter settings. As a result of the refinement study, the nearest neighbor option in the DPIV program was turned off as option on did not affect the results and consumed significantly more computation time. An example comparison is shown in Figs 71, where Fig. 71(a) corresponds to the case where the nearest neighbor option was off and 71(b) corresponds to the case where it was on. In this figure, the contour plot of the transverse velocity is shown for the case where the wing was at an angle of attack of 14° during the pitch up stroke; the reduced frequency was k=0.18, and the Mach number was 0.2. The results in Figs. 71(a) and (b) are indistinguishable.

A grid refinement study was also performed between 3 iteration and 4 iterations as shown in Figs. 72(a) and (b), respectively, where contour plots of Mach number are compared. The mesh generated with 3 iterations is named as “coarse” mesh. The correlation to the grid with hyper fine mesh took ~48 more hrs to process than did the coarse mesh. The differences were modest, where the maximum difference was 0.02 in Mach number. The small number of levels used the contours in Fig. 72 exaggerated the difference. The hyper fine mesh was chosen for analysis as the result was resolved to a higher order. In the DPIV program, the vector display option was turned off while processing to decrease the processing time. The data reduction analyses to compute the vector fields from the PIV images required 3000 CPU hrs, which was distributed over

six personal computers running in parallel. An output file consisting of instantaneous velocity data was stored in an ASCII file format for each image pair.

First and second order turbulent statistics are created using an in-house MATLAB code that ensemble averaged the velocity vector fields. In order to minimize the effect of fluctuations in the wind tunnel conditions on statistics, the program binned the average velocity data and computed the fluctuating velocities relative to the average velocity in the corresponding bin. The normalized binned data were then averaged. The equation for the bin mean velocity is given below, where n is the number of samples per bin, and J_{max} is the total number of bins.

$$U_{bin,j} = \frac{1}{n} \sum_{i=(j-1)n+1}^{j \cdot n} u_i, \quad j = 1 \ldots j_{\max} \tag{5.1}$$

The computed mean velocity is then the ensemble average of the bin velocity:

$$U = \frac{i}{J_{\max}} \sum_{j=1}^{J_{\max}} U_{bin,j} \tag{5.2}$$

The fluctuating statistics were computed as

$$\begin{aligned} \overline{u'u'} &= \frac{1}{N-1} \sum_{i}^{N} \left(u_i - \bar{u}_{bin,j} \right)^2 \\ \overline{v'v'} &= \frac{1}{N-1} \sum_{i}^{N} \left(v_i - v_{bin,j} \right)^2 \\ \overline{u'v'} &= \frac{1}{N-1} \sum_{i}^{N} \left(u_i - \bar{u}_{bin,j} \right) \left(v_i - \bar{v}_{bin,j} \right) \end{aligned} \tag{5.3}$$

where $1 \le i \le n \Rightarrow j = 1, \ldots, (J_{\max} - 1)n + 1 \le i \le J_{\max} n \Rightarrow j = J_{\max}$. The z–component of the vorticity and the *xy*-component of the strain tensor were calculated as follows

$$\omega_z = -\left(\frac{du}{dy} - \frac{dv}{dx}\right)$$
$$S_{xy} = \left(\frac{du}{dy} + \frac{dv}{dx}\right) \tag{5.4}$$

The strain rates were computed using second order central differences. The static temperature and Mach number were computed assuming an adiabatic flow. Following equations are used to calculate the Mach number. The static temperature is given by $T = T_t - (u^2 + v^2)/2C_{p,}$ where T_t was the temperature in the tunnel stilling chamber. With the static temperature, the speed of sound, a, was computed assuming a thermally perfect gas, and the Mach number was computed as $M = V/a$, where V is the magnitude of the measured velocity.

Both the axes are normalized with the chord length c. The velocities, normal and shear stress components are normalized with the freestream velocity.

In the post processing code, a 3σ filter was used to discriminate erroneous data points. The 3σ retained 98% of the vectors, where a 2σ retains 92%. The choice of the filter setting was made based on a filter refinement study, which are summarized in Figs. 73. The flow conditions were the same as those described above for Fig. 5.8. Shown in Figs. 73 (a) are contour plots of V velocity and number of velocity vectors remaining after the filter used in the averages, respectively, for the 3σ filter. Given in Figs 73 (b) are the same data with 2σ filtering. The peak difference between the two datasets was less than 3%. The 3σ filtering was used for the present study as it retained the larger number of data points.

5.2 Tunnel Flow Freestream Condition Instrumentation

Test section conditions were measured using a Druck DPI 203 digital pressure gage and an Omega Model 199-temperature gage. The Druck pressure gage measures the set dynamic pressure within ±0.08% of full scale, and the Omega thermometer is accurate to within ±0.2 deg C. A Mensor 14500C digital barometer was used to read the atmospheric pressure, and it is accurate to within ± 4.0 Pa. All of these measurements were read with the motion controller computer.

In addition to the wind tunnel instrumentation, the freestream conditions for the 7 ft x 7ft test section were also examined with the present PIV system. The wing was in the tunnel during the tests, but the angle of attack was set to zero. The mean velocity agreed with the tunnel instrumentation to well within the PIV measurement uncertainty. The freestream turbulence was found to increase from 2.0% at Mach 0.2 to 4.0% at Mach 0.28.

5.3 Uncertainty Estimates

The measurement uncertainties for the present study are summarized in Table 3, and were accumulated with a Euclidean (L_2) norm. The uncertainties in the freestream stagnation conditions include the transducer uncertainty. The position uncertainties were takes as the uncertainty in the airfoil edge, which was nominally 4 pixels after the de-jitter algorithm was applied. The angle-of-attack uncertainty was based on the calibration (described above). The relative position uncertainties used to compute the strain rates was equivalent to the actual position variance of the CCD array pixels, this uncertainty was assumed negligibly small. The calibration (or conversion) error was

nominally 1.0%. The uncertainty analysis of the PIV data (last four rows in Table 3) accounted for correlation mapping error and the conversion error from the physical length scale to the appropriate number of camera pixels. The estimated uncertainty in the statistical quantities was determined using a 95% confidence interval[46]. The variance was determined assuming a normal distribution and a total of 1000 instantaneous velocity vector fields. The uncertainty in the production was the result of a combination of the uncertainties in position, the mean velocity and the associated finite difference scheme. The relatively large values of the fluctuating unsteady flow velocities in the separated regions resulted in the large PIV uncertainties listed in Table 3. These are the worst case results.

5.4 Preliminary Assessment of the S3F Technique

At the time of this study, innovative Scientific Solutions, Inc. (ISSI) was developing a new film technology to directly measure both the surface pressure and surface shear stress during wind tunnel testing. This technology was evaluated during the present dynamic stall study. The operating principle of the film is shown in Fig. 74. In general, the film was designed to deform under both shear and normal pressures. The deformation was recorded in two ways. First, the film was doped with particles which shift position when a shear load was applied. The PIV algorithms described above were then used to record this deformation. Second, the film was also doped with fluorescent molecule. The intensity of the fluorescence varied as the normal load varies the film thickness. The film composition and data reduction software is proprietary to ISSI.

The S3F film was evaluated during two series of dynamic stall tests. Since this was a new technique, it was difficult to predict a priori the correct thickness and stiffness of the film. A range of films were tested. However, most of the data were contaminated by film rippling under the harsh loads associated with the present tests. An example set of preliminary data is present in Fig. 75. Because the method is preliminary, no addition results were presented in this dissertation.

CHAPTER VI

RESULTS FOR *k*=0.10, M=0.2

Data were acquired at all of the angles-of-attack listed in Table 4. Case 1 is described in this Chapter as a representative case to explain the flow structure. For this case, the freestream velocity was 71 m/s (M = 0.20), the pitching frequency was 5 Hz (*k = 0.10*), and the wave form was $10 \pm 10 \sin \omega t$. This case corresponded to Light Dynamic Stall[10]. The results for other cases are presented in the Appendix.

A detailed interrogation of the flow structure is presented in this Chapter. The analysis starts with flow visualizations of the separation and reattachment process. This is followed by the flow hysteresis and time scales associated with the flow field leading to detailed mean and turbulent flow characteristics analyses for the upstroke and downstroke motion of the wing. Boundary layer analysis is presented for a representative angle-of-attack due to change in pressure gradient. Finally, Reynolds shear stress structure in the leading edge region is characterized.

6.1 Flow Visualization

Mie scattering flow visualization images were acquired on an area that was approximately 4 times the region of interest shown in Fig. 1. A qualitative examination of the flow structure based on these images is given in this section. Specifically, the separation and reattachment events are described.

The pitching up Mie-scattering images are shown in Figs. 76 (a) – 80 (a), for angles-of-attack of 10°, 12°, 14°, 16°, and 18°, respectively. As can be seen during the

upstroke motion of the wing, the flow was attached at 10°. As the angle-of-attack was increased, unsteady vortices were created and detached off the surface as shown Fig. 79 (a). These vortices were in the form of small pockets that were void of particles (i.e. the particles were "spun" out due to strong vorticity). The point of origin of these vortices moved up stream with increasing angle-of-attack. Also, the rising of the vortices were not at the same axial location at every "snapshot" of the flow at a given angle-of-attack, which demonstrated the expected unsteady nature of the flow field.

The pitching down images are shown in Figs. 76 (b) – 80 (b), for angles-of-attack of 10°, 12°, 14°, 16°, and 18°, respectively. During the downstroke motion, the flow tended to reattach to the surface of the airfoil. At the highest angle-of-attack, i.e. 18°, a separated shear layer was observed as shown in Fig. 80 (b). As the angle-of-attack was decreased, the thickness of the layer decreased, indicating reattachment. The flow visualization data showed that the flow reattached at a larger angle-of-attack than when separated, which was the expected hysteresis result[30]. The separated shear layer always appeared to emanate from near the leading edge.

To better show the hysteresis, streamline data, from the high resolution PIV data discussed below, for a representative angle-of-attack of 14° are shown in Fig. 81(a) and (b) for the upstroke and the downstroke motion, respectively. It was evident from the direction of the streamlines that the flow separated during the upstroke motion at $x/c \approx 0.22$. However, during the downstroke motion the flow appeared to be attached. A more quantitative discussion of the hysteresis is given in the following section.

6.2 Hysteresis Effects

It is well known that dynamically stalling systems exhibit path dependent hysteresis effects. Separation location data for the oscillation cycle for the present case is summarized in Fig. 82. The angles-of-attack are shown on the abscissa. The axial separation distance from the leading edge is shown in the ordinate. For the coordinate system shown in Fig. 1, positive *x*-axis pointed to the right and positive *y*-axis directed up. For all cases, the leading edge was fixed to $x/c = 0.25$ and $y/c = 0$.[2]

During the upstroke motion of the wing, the average flow separation point was apparent from the contour plots of the axial velocity (U_N). Hence, the average separation point for a particular angle-of-attack was directly read from the contour plot of the corresponding angle-of-attack. For a representative angle-of-attack of 14°, the average separation point is pointed out in Fig. 87.

During the downstroke motion of the wing, the flow was reattaching back to the airfoil surface. The average separation point was inconclusive from the contour plots of the axial velocity. However, the Reynolds shear stress was found to be negative in the separated flow region as will be discussed in the later sections. Hence, the average separation point was read from the contour plot of Reynolds shear stress. For a representative angle-of-attack of 14°, the average separation is pointed out in Fig. 184.

For the current test conditions, the flow was attached at 10° in the region of interest. As shown in the figure, during the upstroke motion of the wing the flow

[2] As mentioned in Chapter V, during the de-jittering data reduction step, the wing position was arbitrarily positioned such that leading edge was at x/c = 0.25 and y/c = 0. The actual wing position was readily computed from the angle of attack and ¼-chord location.

separated with increasing angle-of-attack. The separation point moved upstream towards the leading edge. During the downstroke motion of the wing, the flow tended to reattach to the surface. Hence, the separation point moved downstream i.e. away from the leading edge with decreasing angle-of-attack. The bar shown at 16° for both the upstroke and downstroke motion indicates the unsteadiness in the separation distance, which was estimated to be 5% and 3%, respectively. The hysteresis identified in this section implied that the time scale associated with the wing motion were similar to those of the flow field. Thus, for realistic helicopter flight conditions, the flow is characterized by multiple time scales.

6.3 Time Scales

From the above discussion it was concluded that the flow separated during the upstroke and reattached during the downstroke motion of the wing. Hence, it was important to quantify the time scales of processes. During the upstroke, the flow separated past leading edge. Hence the associated time scales were calculated in the leading edge region (Region I). During the downstroke motion of the wing, the flow tended to reattach in the downstream of the leading edge region (Region II). Hence the associated time scales were calculated in these regions. These regions are shown schematically in Figure 83. The following three time scales were quantified:

- Wing Oscillation Time-scale (Mechanical)
- Mean flow Shear Time-scale
- Turbulence Time-scale

The oscillation time-scale (τ_o) was defined as

$$\tau_o \sim \left(\frac{1}{\Delta\alpha} \frac{d\alpha}{dt} \right)^{-1} \sim \omega^{-1} \tag{6.1}$$

where $d\alpha/dt = \omega\Delta\alpha\cos(\omega t)$, $\cos(\omega t) \sim 1.0$. The shear time-scale (τ_s) was defined as the reciprocal of mean strain rate (S_{xy}). It is given by

$$\tau_s \sim (S_{xy})^{-1} \tag{6.2}$$

The Turbulent time-scale was defined as

$$\tau^t \sim \frac{K}{\varepsilon} \sim \frac{C_\mu S_{xy}}{a_1} \sim (3S_{xy})^{-1} \tag{6.3}$$

where K was the turbulent kinetic energy, ε was the dissipation, and $C_\mu = 0.09, a_1 = 0.3$[43]. The time scale is representative of an eddy-turn over time. It was observed that the flow was attached at 10° and fully separated at 18°. Hence the time scales were calculated for a representative angle-of-attack of 14°, which fell between the two extreme flow conditions. The results are in Table 5 for Regions I and II.

During the upstroke motion of the wing, the flow time and the oscillation time scales were equivalent making indicating that the flow was in a state of mechanical non-equilibrium. There was a strong coupling between the freestream velocity and the wing motion. This in turn resulted in a complex flow behavior. The shear time scale in the leading edge region (Region I) was three times lower than that in the downstream region (Region II). This meant the shear action was high in the favorable pressure gradient region compared to adverse pressure gradient region as expected. As shown in the table, the turbulent time scales were similar in the two regions. As the turbulent time scales were higher than the oscillation and shear time scales, history effects are expected to be

important. During the upstroke motion, the flow was attached in the leading edge region which will be discussed in the later sections. Hence, it was of interest to analyze the turbulent quantities in this region, as the flow in this region directly impacts the separation dynamics.

Similar trends were observed in time scales during the downstroke motion of the wing. However, the shear and turbulent time scales for the downstroke motion were more than three times lower than that during the upstroke motion of the wing. This was the result of flow being attaching during the downstroke motion. The turbulent kinetic energy was expected to be higher in these regions for the downstroke motion compared to the upstroke motion.

In summary, the time scales indicate that the wing motion and flow response times were comparable which indicates that flow history effects are important. Thus, understanding and modeling of flow around helicopter rotor blades at realistic flight conditions are challenging. Hence, empirical characterization is an important step in the analysis.

6.4 Empirical Description of Flow Field

A detailed interrogation of the mean and turbulent flow field during the dynamic stall process is presented in this section. The upstroke motion of the wing is described first, followed by the downstroke motion. The objective is improved understanding of the flow field around the leading edge during dynamic stall for high Reynolds number flow. In order to achieve this objective, it was pertinent to obtain data in the close proximity of the leading edge of airfoil prior to separation event as suggested by the flow

visualization images described in the previous paragraph. Hence, the experiments were limited to the leading edge region of the flow field to maximize resolution.

The region of interest is shown schematically in Fig. 1. The physical dimension of the region of interest was nominally 63 mm x 60 mm. However, the region of interest reduced slightly with increasing angle-of-attack due to optical access limitations. The flow was from right to left. Hence, the U-velocity was negative for the coordinate system shown in Fig. 1. The flow quantities were also non-dimensionalized using the freestream velocity and airfoil chord length.

6.4.1 Airfoil Pitching Up Motion

6.4.1.1 Mean Flow Field

As the heading suggests, the mean flow field comprising of the U-velocity, V-velocity, Mach number, Mean Strain rate and Vorticity are described in this section. The schematic of the flow field during the upstroke motion is shown in Fig. 84. As shown, the flow field was divided into three regions. The flow structure in each region will be discussed below.

The pitching up contour plots of U_N are shown in Figs. 85 – 89, for angles-of-attack of 10°, 12°, 14°, 16° and 18°, respectively. As shown in the plots, the flow accelerated around the leading edge. This was a result of strong favorable pressure gradient around the leading edge. For each angle-of-attack, the U-velocity was found to have a maximum slightly downstream of the leading edge region (Region I in Fig. 84). The average peak magnitude of U_N decreased as the angle-of-attack increased. Also, the axial location of the average peak magnitude moved upstream as shown in the Table 6. It

was believed that the separation process initiated at an angle-of-attack of 12°, although weak in nature, as there was a hint of flow separation at this angle (pointed out in Fig. 86). As expected, the flow separation increased with increasing angle-of-attack, and became fully separated at 18° as shown in Fig. 89. Also, the point of separation moved upstream with increasing angle-of-attack as shown in Table 6. At higher angles-of-attack, eddies were formed in the separated flow as was seen in the flow visualization images. These eddies drew energy from the mean flow. Hence, with increasing angle-of-attack more eddies were formed and the axial velocity decreased. Based on this analysis, it was expected that the large-scale energy of axial turbulent stress would increase with increasing angle-of-attack as more eddies were formed.

The dependence of the flow separation on the angle-of-attack was supported by the line plot of U_N shown in Fig. 90. The axial velocity (U_N) is on the ordinate, and the abscissa shows the distance (s) along the wing, where s is the distance defined in the Fig. 83. The data points were extracted at a distance of 2 mm (0.44% c) above the airfoil surface. The data are shown for three angles-of-attack, 10°, 14°, and 18°. At 10°, the flow was attached. At 14°, the separation event was in the measurement window, and at 18°, the flow was fully separated. The data for other angles-of-attack followed the trend. The oscillatory behavior in the line plots were attributed to the unsteadiness in the flow field.

Focusing first on the angle-of-attack of 10° trace, it was observed that the magnitude of axial velocity U_N increased rapidly from 0.855 at s/c = 0 to 1.65 at s/c = 0.044. Beyond this peak, the axial velocity decreased slightly. The rapid increase was

attributed to strong favorable pressure gradient in Region I (Fig. 84). The downstream decrease was attributed to adverse pressure gradient. At 14°, the axial velocity increased from 0.852 at s/c = 0 to 1.55 at s/c = 0.03. The downstream decrease was slightly larger than that at 10°. The difference in velocities beyond s/c = 0.03 was mainly due to the separation in the flow field. At 18°, the flow was fully separated. The axial velocity increased from 0.5 at s/c = 0 to 1.3 at s/c = 0.032. The downstream decrease was higher compared to the other angles-of-attack. The axial velocity peak decreased with angles-of-attack; the comparison of reductions in the peak magnitude is summarized in Table 7.

The pitching up contour plots of the transverse velocity (V_N) also showed high levels of acceleration around the leading edge. The contour plots are shown in Figs. 91 – 95 for angles-of-attack of 10°, 12°, 14°, 16° and 18°, respectively. The magnitude of the transverse velocity was higher in Region I and Region III. These regions are shown schematically in Fig. 84. For lower angles-of-attack (10° – 14°), Region I was embedded in Region III. However, for higher angles-of-attack (16° and 18°), Region I was discernible from Region III. The average peak magnitude of the V-velocity in dark red area (Region III) and the average height of the region for all angles-of-attack are shown in Table 8. As shown in the table, the magnitude of transverse velocity was almost constant for all the angles-of-attack considered. However, the height of the region of high velocity increased with increasing angle of attack. This implied that the V-velocity was maximum around the leading edge. At the leading edge, the radius of curvature encountered by the flow was at a maximum and hence the V-velocity suddenly changed and was observed to be a maximum. It was believed that the obstruction in the flow

strengthened the transverse velocity in the flow. In the downstream region (Region II in Fig. 84), as the radius of curvature decreased, the V-velocity also decreased. This result was corroborated by the line plots shown in Fig. 96; these velocity traces correspond to the U_N traces in Fig. 90.

Focusing first on the 10° angle-of-attack trace in Fig. 96, it was observed that the transverse velocity V_N increased rapidly from 0.65 at s/c = 0 to 0.955 at s/c = 0.021. Beyond this peak, the transverse velocity decreased rapidly. The rapid increase was attributed to strong favorable pressure gradient as well as the high radius of curvature. The decrease was attributed to adverse pressure gradient and reduced radius of curvature. At 14°, the transverse velocity increased from 0.75 at s/c = 0 to 0.95 at s/c = 0.016. The downstream decrease was slightly larger than that at 10°. At 18°, the transverse velocity increased from 0.43 at s/c = 0 to 0.76 at s/c = 0.015. Like the axial velocity, the transverse velocity also decreased with increasing angles-of-attack. It is important to note that the data were extracted 2 mm away from the surface of the airfoil, and at 18°, the data were present in Region I (Fig. 84). The comparison of reduction in the peak magnitude of the transverse velocity at different angles-of-attack is shown in Table 9. As expected, the location of the peak transverse velocity moved upstream with increasing angle-of-attack.

The pitching up contour plots of Mach number ($M = \sqrt{U^2 + V^2}/a$) are shown in Figs. 97 – 101, for angles-of-attack of 10°, 12°, 14°, 16° and 18°, respectively. The trend

followed the trend observed in contour plots of U_N . The average peak Mach number and the average axial distance of the region of peak Mach number are shown in Table 10.

As shown in Table 10, the average peak Mach number is almost constant at a value of 0.35 – 0.36 for angles-of-attack of 10° - 16°. However, at 18°, the average Mach number decreased by 11%. This result was consistent with the significant reduction in velocities observed due to fully separated flow field at this angle-of-attack. However, the average axial length of the peak Mach number region decreased with the decreasing angle-of-attack as shown in the table. This was an indication of the flow separation. The magnitude of peak Mach number also suggested that the compressibility effects were relatively small.

To understand the effect of axial and transverse velocities on Mach number, it was important to investigate the contribution of magnitude of each component. Hence, the contribution of magnitude of each component is shown in Table 11 for angles-of-attack of 10° - 18°. Eleven data points were extracted along '*s*' at an interval of 0.01 as shown. The ratio *R* denotes the contribution of transverse velocity. As shown in the table for all angles-of-attack, the contribution of V-velocity was maximum in the leading edge region (Region I in Fig. 84). In the downstream region (Region II in Fig. 84), the contribution was negligible. Hence, the axial velocity was dominant in this downstream region. Also, the Mach number was higher in the region slightly downstream of the leading edge region and decreased further downstream for all angles-of-attack. For the attached angle-of-attack 10°, beyond *s*/*c* = 0.06, the Mach number was higher than for the separated cases, e.g., 14° and 18°.

The velocity profiles indicated that the leading edge flow was characterized by strong shear leading to strong strain-rates in both *x*- and *y*- coordinate directions. It was expected that these strain rates strongly influenced the turbulent flow structure described in the later sections. The shear actions along the airfoil surface were also expected to create a rotational flow field with significant vorticity. It was expected that the vorticity influenced flow separation. Hence, the study of mean strain rate along with vorticity was performed. The results for mean strain rate and vorticity are presented in the following paragraphs.

The pitching up contour plots of mean strain rate (S_{xy}) are shown in Figs. 102 – 106, for angles-of-attack of 10°, 12°, 14°, 16° and 18°, respectively. The present focus is on the leading-edge flow prior to separation. Hence the mean strain rate is described with respect to the leading edge Region IA and IB defined in Fig. 107. Collectively, Regions IA and IB merged to Region I shown in Fig. 84. In Region IA, the mean strain rate was found to be negative. In Region IB, mean strain rate was positive as shown in the contour plots. The axial and transverse velocity gradient contributed to the mean strain rate ($S_{xy} = dU/dY + dV/dX$). The contour plots of the axial velocity gradient (*dU/dY*) and the transverse velocity gradient (*dV/dX*) are shown in Figs. 108 – 109, for a representative angle-of-attack of 14°. Upon comparing the contour plots of gradients and mean strain rate at 14°, it was evident that in Region IA, *dU/dY* (negative) was the dominant term and in Region IB, *dV/dX* (positive) was the dominant term. Region IA extended to the downstream location as shown in the contour plots. The thickness of the Region IA increased with increasing angle-of-attack. Eventually at 18°, with the flow

separation at the leading-edge, Region IA detached off the airfoil surface as shown in Fig. 106. The effect of mean strain rate on the turbulent production quantities is described in the later sections.

The vorticity is a powerful concept for flows where viscosity is low; i.e. at high Reynolds numbers. In such cases, even when velocity field is complicated, such as the present study, the vorticity will be essentially zero everywhere except for the viscous regions[44]. This fact was corroborated in the present vorticity contour plots, where it was close to zero everywhere except near the airfoil surface. At high Reynolds number, boundary layers tend to exhibit a strong inclination to abruptly develop a sharp eruption in regions of adverse pressure gradient. This is separation and is a process of boundary layer detachment from the wall. This separation event is mainly the result of unsteady viscous-inviscid interaction. For a high Reynolds number flow, such as the present test condition, boundary layer vorticity is first concentrated into a thin band in the streamwise direction. In terms the flow physics, fluid particles are compressed in the streamwise direction and to keep the mass flow rate constant, the particles must elongate in a direction normal to the wall. The separation event culminates in an unsteady viscous-inviscid interaction environment.

The pitching up contour plots of vorticity ($\omega_z = dV/dX - dU/dY$) are shown in Figs. 110 – 114, for angles-of-attack of 10°, 12°, 14°, 16° and 18°, respectively. For the lower angles-of-attack, such as 10° and 12°, there was a narrow band of concentrated vorticity near the surface. At 14°, the strong viscous-inviscid interaction due to separation appeared (Fig. 112). Vortex breakdown occurred in regions of high localized

stress. Unsteadiness of the flow field also contributed to the vortex breakdown. Because of the velocity gradient signs Regions IA and IB collapsed into one region for the vorticity.

6.4.1.2 Turbulent Flow Field

6.4.1.2.1 Turbulent Stresses

This section describes the turbulence axial stress, transverse stress and Reynolds shear stress. The pitching up contour plots of the axial stress (σ_u) are shown in Figs. 115 – 119, for angles-of-attack of 10°, 12°, 14°, 16° and 18°, respectively. For lower angles-of-attack (10° – 14°), the magnitude of σ_u was highest in the leading edge region (Region I in Fig. 84). For higher angles-of-attack (16° - 18°), there was increase in σ_u in Region II (Fig. 84), owing to separation of the flow as was expected in the flow.

Line plots of σ_u around the airfoil (2 mm above the surface) are shown in Fig. 120. In the line plot shown in Fig. 120, '*s*' is the distance as described before. At 10°, the magnitude of σ_u decreased rapidly from 0.4 at *s*/*c* = 0 to 0.10 at *s*/*c* = 0.03. Beyond this decrease, the magnitude of axial stress remained almost constant with some fluctuations in the plot owing to flow unsteadiness. At 14°, the magnitude of σ_u decreased from 0.38 at *s*/*c* = 0 to 0.18 at *s*/*c* = 0.02. Beyond this point, the axial stress increased to 0.27 at s/c = 0.04. Further downstream the magnitude remained almost constant. At 18°, due to full separation at the leading edge there was significant unsteadiness in the plot from the beginning. However, broadly it can be seen that the magnitude of axial stress decreased from 0.33 at *s*/*c* = 0 to 0.27 at *s*/*c* = 0.018. Beyond this point, the magnitude increased to

0.7 at s/c = 0.07. To sum up the findings from the line plot, from *s*/*c* = 0 to *s*/*c* = 0.2, the axial stress was high but had a decreasing trend. Beyond *s*/*c* = 0.20, for attached flow (10°), the axial stress decreased, and, for separated flow, it increased. At 18°, with the flow fully separated the axial stress was approximately 70% higher than that at *s*/*c* = 0.

The pitching up contour plots of transverse stress (σ_v) are shown in Figs. 121 – 125, for angles-of-attack of 10°, 12°, 14°, 16° and 18°, respectively. It was found the magnitude of σ_v was highest in the leading edge region (Region I in Fig. 84) for all angles-of-attack. In the downstream region, the transverse stress decreased. The turbulence production and transport mechanisms are discussed later.

A line plot of transverse stress is shown in Fig. 126. At 10°, the magnitude of σ_v decreased sharply from 0.35 at *s*/*c* = 0 to 0.08 at *s*/*c* = 0.03. Beyond this decrease, the magnitude of transverse stress remained almost constant with some unsteady peaks. At 14°, the magnitude of σ_v decreased from 0.30 at *s*/*c* = 0 to 0.18 at *s*/*c* = 0.024; beyond this point, σ_v increased slightly in the downstream region. At 18°, the transverse stress was 0.34 at *s*/*c* = 0 and reduced gradually to 0.1 at *s*/*c* = 0.07; beyond this point, σ_v increased.

The final 2nd order turbulent quantity of prime importance from the modeling point of view is the Reynolds shear stress. The pitching up contour plots of Reynolds shear stress (τ_{xy}) are shown in Figs. 127 – 131, for angles-of-attack of 10°, 12°, 14°, 16° and 18°, respectively. Reynolds shear stress was found to be positive in the leading edge region (Region I in Fig. 84). For all cases considered, in Region I, there was a favorable

pressure gradient. In this region, the gradients of the *x*-component of velocity were negative. Positive values of u' occurred when v' was negative and vice versa. However, in the separated flow region, positive values of u' occurred when v' was positive and vice versa making the Reynolds shear stress negative. Above mentioned behavior was observed in the wall bounded flow for all angles-of-attack. This trend of negative shear stress can be considered as an identification of separation process. It can be seen that negative shear stress was a result of energy being fed back to the mean flow. For all angles-of-attack considered, in Region I, there was a positive shear stress which meant that, energy was drawn from the mean flow. As the angle-of-attack increased, the shear stress appeared to diffuse and eventually the flow separated. Separated flow field was very complex and unsteady in nature. Again, the goal of the present experimental analyse was to obtain measurements very close to the wall in the leading edge region.

The line plot of Reynolds shear stress at three different angles-of-attack is shown Fig. 132. At 10°, the shear stress reduced from 0.115 at s/c = 0 to 0.01 at s/c = 0.01. Beyond that point the shear stress increased to 0.03 at s/c = 0.018 and then reduced to zero. At 14°, the shear stress reduced from 0.035 at s/c = 0 to -0.009 at s/c = 0.01. Beyond this point the shear stress again increased gradually to 0.02 at s/c = 0.03 and then reduced gradually. At 18°, the flow was fully separated and the shear stress was positive with higher values.

6.4.1.2.2 Turbulence Transport

In order to assess turbulence production, the magnitudes of turbulent stresses in the leading edge region are summarized in Table 12 for different angles-of-attack.

Studying the table it can be seen that the magnitudes of axial and transverse stress were had similar magnitudes in the leading edge region. However, in the downstream region beyond *s*/*c* = 0.03, differences started to appear. At 10°, the difference was 25% at s/c = 0.03. The difference gradually increased with increasing '*s*'. It was important to bear in mind that in the downstream region, the *y*-compoent of velocity also showed decreasing trend. At 14°, the difference was 33% at *s*/*c* = 0.03. There was a steep increase in the *s*/*c* difference with increasing *s*. This was the result of flow separation.

The turbulent shear stress transport equation was given by Eq. 3.2. The *x*-component and *y*-component of transport equation was obtained by substituting *i,j = 1*, *k = 1,2* and *i,j = 2*, *k = 1,2* respectively. The concise form is given by the following equations.

$$\frac{1}{U_\infty^2}\frac{D\sigma_u^2}{Dt} = P_{xx} + \varepsilon_{xx} - \Pi_{xx} + T_{xx} \tag{6.4}$$

$$\frac{1}{U_\infty^2}\frac{D\sigma_v^2}{Dt} = P_{yy} + \varepsilon_{yy} - \Pi_{yy} + T_{yy} \tag{6.5}$$

The $P_{xx,}$ and P_{yy} symbols denote the production of *xx*-component and *yy*-component of Reynolds Stresses. The dissipation terms are denoted by ε_{xx} and ε_{yy}. The pressure strain terms are given by Π_{xx} and Π_{yy}. The pressure work, viscous work and the diffusion terms are collected T_{xx} and $T_{yy.}$ In this study, we focused our attention on the production terms as they are responsible for the energy exchange between the turbulent and mean flow fields.

$$P_{xx} = -2 * (\tau_{xx}^T \frac{\partial U}{\partial x} + \tau_{xy}^T \frac{\partial U}{\partial y}) \tag{6.6}$$

$$P_{yy} = -2 * (\tau_{yy}^{T} \frac{\partial V}{\partial y} + \tau_{xy}^{T} \frac{\partial V}{\partial x}) \tag{6.7}$$

The pressure-strain distribution terms primarily drive the turbulence towards isotropy[11], and are given by

$$\Pi_{xx} = \overline{2p' \frac{\partial u'}{\partial x}} \tag{6.8}$$

$$\Pi_{yy} = \overline{2p' \frac{\partial v'}{\partial y}} \tag{6.9}$$

The production for an angle-of-attack of 14° (the representative case) is described in this paragraph. As shown in the Table 12, in the leading edge region, prior to separation, the magnitudes of axial and transverse stress were comparable. In this region, there was a positive production of *xx*-component of Reynolds stress (P_{xx}). The production contours are described in a subsequent paragraph. In the same region, there was a negative production of *yy*-component of Reynolds stress (P_{yy}). The similar magnitude turbulence stresses coupled to the production signs indicated that turbulence was being redistributed from the axial to the transverse component through the pressure-strain redistribution terms, which tend to drive the turbulence towards isotropy. The negative transverse production indicated that some of that energy was transferred back to the transverse component of the mean flow kinetic energy.

Further downstream, where separation started to occur (s/c = ~ >0.03), the trend was different. The axial stress was higher than the transverse stress. As expected, there was a positive production of P_{yy} and negative production of P_{xx} in this region. Again energy was being redistributed from the mean to the turbulent and then back to the mean

flow. These energy transfer mechanisms have a direct influence on the flow separation process.

The pitching up contour plots of P_{xx} are shown in Figs. 133 – 137, for angles-of-attack of 10°, 12°, 14°, 16° and 18°, respectively. The magnitude of P_{xx} was found to be a maximum in Region I (Fig. 84) for all angles-of-attack considered. In Region I, there was a favorable pressure gradient, where the flow was attached irrespective of the angle-of-attack. This meant there was a substantial production of *xx*-component of the Reynolds stress. In Region I, as a result of favorable pressure gradient, dU/dx and dU/dy were large and negative. As shown in Eq. 6.3, P_{xx} depended on these velocity gradients. Hence the production was attributed to a high velocity gradient in this region. Comparing the gradient plots, it can be seen $\tau_{xy}^{T}\frac{\partial U}{\partial y}$ was the dominant term. Upstream of the high P_{xx} region at the leading edge, there was a region observed where P_{xx} was negative. In this region it was found that $\tau_{xx}^{T}\frac{\partial U}{\partial x}$ was the dominant term.

The line plot of P_{xx} is shown in Fig. 138 for 10° and 14°. For both angles-of-attack in Fig. 138, the magnitude of P_{xx} was found to be a maximum at the leading edge in Region I. A sharp drop in P_{xx} was observed downstream of Region I for both angles-of-attack. At 10°, the magnitude of P_{xx} reduced from 19.8 at s/c = 0.002 to -3.31 at s/c = 0.01. At 14°, the magnitude of P_{xx} reduced from 3.75 to -3.84 at s/c = 0.01. Further downstream the magnitudes increased slightly to zero. The magnitude was found to be close to zero in the weak and strong adverse pressure gradient region in the downstream.

It was positive in the favorable pressure gradient region. The magnitude of P_{xx} decreased with increasing angle-of-attack in the region I for low angles-of-attack (10° – 14°). However at 18°, it was substantially higher than any other angle-of-attack. It is expected that the unsteadiness in the flow dominated the fluctuation levels.

The pitching up contour plots of production of *xy*-component of Reynolds stress (P_{xy}) are shown in Figs. 139 – 143, for angles-of-attack of 10°, 12°, 14°, 16° and 18°, respectively. At lower angles-of-attack, the red line in the contour plots was the location of the airfoil edge as shown in Figs. 139 – 141. In the leading edge region (Region I in Fig. 84), P_{xy} was found to be negative. The equation for P_{xy} is given below.

$$P_{xy} = -(\tau_{xx}^{T} \frac{\partial V}{\partial x} + \tau_{xy}^{T} \frac{\partial U}{\partial x} + \tau_{xy}^{T} \frac{\partial V}{\partial y} + \tau_{yy}^{T} \frac{\partial U}{\partial y}) \tag{6.10}$$

Out of the four terms in Eq. 6.10, it was found that the terms $\tau_{xx}^{T} \frac{\partial V}{\partial x}$ and $\tau_{yy}^{T} \frac{\partial U}{\partial y}$ were the primary contributions to P_{xy}. This was because $\frac{\partial V}{\partial x}$ and $\frac{\partial U}{\partial y}$ terms were substantially high in this region. Also, as was seen before the axial and transverse stresses were high in the leading edge region.

A narrow region of positive P_{xy} was observed near the wall at *x/c* = 0.225 for 10°. This region moved upstream towards the leading edge with increasing angle-of-attack. Also, the thickness of the region increased in the downstream with increasing angle-of-attack. However, at 18°, it was detached off the airfoil surface. The location of this region was found to be a sensitive indication of flow separation. In this narrow

positive P_{xy} region, the transverse velocity gradients were small although non-negligible. The $\frac{\partial U}{\partial x}$ term had a small effect. Hence, the only significant term was $\tau_{yy}^{T} \frac{\partial U}{\partial y}$. It was also observed that the transverse stress increased in the downstream region with increase angle-of-attack contributing to P_{xy}.

The line plot of P_{xy} is shown in Fig. 144 for 10° and 14°. At angles-of-attack of 10° and 14°, the magnitude of P_{xy} was found to be a maximum at the leading edge in Region I. At 10°, the magnitude of P_{xy} had a positive peak of 2.15 at s/c = 0.001. The value reduced to -6.42 at s/c = 0.01. Beyond this point, the magnitude increased close to zero at s/c = 0.027 and was almost constant in the downstream. However, at 14°, a negative peak of -10.75 was observed at s/c = 0.003. The negative peak reduced very sharply to -1.75 at s/c = 0.01. Beyond this point, the magnitude of P_{xy} increased. Finally P_{xy} changed sign and became positive at s/c = 0.07.

The final coupling term between mean flow and turbulent stress is P_{yy}. The pitching up contour plots of P_{yy} are shown in Figs. 145 – 149, for angles-of-attack of 10°, 12°, 14°, 16° and 18°, respectively. In Region I, P_{yy} was found to be negative for all angles-of-attack considered. Starting from the leading edge, this trend was noticed until about 3% of the chord length, which meant there was a loss of *yy*-component of Reynolds stress where dV/dx and dV/dy were positive. This meant both the right hand terms in Eq. 6.7 having the velocity gradients were equally dominant. This was in

contrast to the behavior exhibited by P_{xx} as shown in Figs. 133 – 137. However, along the wall, downstream of the point *x/c* = 0.22, P_{yy} was noticed to be positive for all angles-of-attack considered. In this region, it was found that dV/dy was negative and dominant. Hence, in this region the term $\tau_{yy}^{T}\frac{\partial V}{\partial y}$ was contributing the most to P_{yy} . The magnitude of P_{yy} decreased with increasing angle-of-attack for lower angles-of-attack (10°-14°). For these angles-of-attack, the flow was not fully separated. At the lowest angle-of-attack considered, there was a large production of *yy*-component of Reynolds stress in the downstream wall region indicating positive P_{yy}. At this angle-of-attack, there was no evidence of formation of eddies. With increasing angle-of-attack, eddies were formed. To maintain the wall shear flow eddies, were formed and there was energy transfer between the boundary layer fluid and these eddies. Eventually at higher angles-of-attack the flow became fully separated. Hence, with increasing angle-of-attack the rate of loss of *yy*-component of Reynolds stress increased.

The line plot of P_{yy} is shown in Fig. 150 for 10° and 14°. As mentioned in the previous paragraph at angles-of-attack of 10° and 14°, the magnitude of P_{yy} was found to be negative at the leading edge in Region I. The line plots were fluctuating in nature. However, between *s*/*c* = 0 to *s*/*c* = 0.02, the magnitude of P_{yy} at 10° was higher than that 14°. Beyond this point, the value of P_{yy} was close to zero for both angles-of-attack.

6.4.2 Airfoil Pitching Down Motion

In the same manner as above, results were analyzed for the airfoil pitching down motion. The following three sections describe the mean flow quantities, turbulence stresses and the turbulence transport.

The flow visualization images suggested reattachment of the flow during the pitching down motion of the wing. This section describes some of the key findings of the flow quantities during pitch down motion of the wing. This helped in understanding the global flow field. The schematic of the flow field is shown in Fig. 151. The flow field was divided into different regions as shown. The mean and turbulent flow quantities are described with respect to regions shown in the schematic.

6.4.2.1 Mean Flow Field

The pitching down contour plots of the axial velocity (U_N) are shown in Figs. 152 – 155, for angles-of-attack of 16°, 14°, 12°, and 10°, respectively. Region I corresponded to the high axial velocity region. In this region, the magnitude of axial velocity decreased with decreasing angle-of-attack. There was a narrow region observed above the airfoil surface. This region is labeled as Region II in Fig. 151. This layer can be thought of as an indication of flow reattachment process. At the highest angle-of-attack considered, this layer was thicker and as the angle-of-attack was decreased this layer became thinner. The average thickness of the region for different angles-of-attack is shown in Table 13. Eventually, the flow was completely attached to the airfoil surface at the lowest angle-of-attack considered. The average peak magnitude of axial velocity for different angles-of-attack is shown in Table 14. For the same angle-of-attack, during

the downstroke motion, the average peak magnitude of axial velocity was higher than that during the upstroke motion of the wing as shown in the table. The 4th column in the table shows the difference between average peak magnitude of axial velocity during the upstroke and downstroke motion of the wing.

As shown in the table, the velocity difference increased with increasing angle-of-attack. At 10°, during the upstroke and downstroke motion, the flow was attached in the region of interest. Hence, the least difference was observed at this angle-of-attack. At higher angle-of-attack, eddies were formed during the upstroke motion. As a result of flow reattachment eddies do not form during the downstroke motion. These eddies drew energy from the mean flow. Hence, the mean axial flow velocity was higher during the downstroke motion.

The line plot of the axial velocity at 14° for the upstroke and downstroke is shown in Fig. 156. The coordinate *s* is the distance as explained earlier. In both cases, magnitude of the axial velocity increased from 0.5 at $s/c = 0$ to 1.6 at $s/c = 0.045$. Until the location $s/c = 0.045$, the magnitudes were almost comparable. However, beyond this point, i.e. between $s/c = 0.045$ and 0.12, a striking difference in magnitude was observed. The magnitude of axial velocity during the downstroke motion was approximately 19% higher than that during the upstroke motion of the wing. At 14°, during the upstroke motion separation had occurred. Hence, the magnitude of the axial velocity was less than that during the downstroke motion. This implied that during the downstroke motion the flow, reattachment process was underway leading to higher axial velocity.

The pitching down contour plots of the transverse velocity (V_N) are shown in Figs. 157 – 160, for angles-of-attack of 16°, 14°, 12°, and 10°, respectively. As shown in these plots, the flow reattached during the downstroke motion of the wing. The magnitude of the transverse velocity was found to be a maximum in Region III and reduced along the chord as was seen in case of the upstroke motion.

The pitching down contour plots of Mach number ($M = \sqrt{U^2 + V^2}/a$) are shown in Figs. 161 – 164, for angles-of-attack of 16°, 14°, 12°, and 10°, respectively. As can be seen, Mach number decreased with decreasing angle-of-attack. Mach number was found to be a maximum in Region I and reduced further downstream. As shown in Figs. 161 and 162, the maximum value was approximately more than twice the freestream Mach number for the higher angles-of-attack (16° and 14°). The average peak Mach number for different angles-of-attack (10°, 14°, and 16°) for the downstroke motion is listed in Table 15. The table also shows the comparison of Mach numbers for the downstroke and upstroke motion. At higher angle-of-attack (14° and 16°) the flow was believed to be separated in case of the upstroke motion. Hence, at these angles the Mach number for the downstroke motion was found to be higher than the upstroke motion. The higher Mach numbers during the downstroke motion suggested that compressibility effects were relatively higher for the downstroke motion compared to the upstroke motion. For a representative angle-of-attack of 16°, the difference in average peak magnitude of axial velocity for the downstroke and upstroke motion was 27.6% and the difference in average Mach number was 20%.

Focusing on Region V, for a representative angle-of-attack of 14° (Fig. 151), the Mach number was found to be 0.01. In the same region for the upstroke motion, the Mach number was found to be 0.2. During the downstroke, Region V appeared to be a stagnation region. Thus, during the downward motion, the stagnation appeared to be on the upper surface of the airfoil for higher angles-of-attack. The axial length of Region V was 2.2 mm. This region narrowed with increasing *y/c*. At 10°, the stagnation region disappeared. This indicated that the flow field was attached and that the stagnation point had moved back to the lower surface of the airfoil.

The pitching down contour plots of mean strain rate (S_{xy}) are shown in Figs. 165 - 168, for angles-of-attack of 16°, 14°, 12°, and 10°, respectively. A narrow band of negative mean strain rate was observed in the wall region starting from the leading edge. This band collapsed into the Regions II and IV in Fig. 151. The contour plots of dU/dy and dV/dx are shown in Figs. 169 – 170 for a representative angle-of-attack of 14°. Comparing these contour plots with the contour plot of mean strain rate at 14° (Fig. 166), it was observed that the dU/dy term contributed mostly to the mean strain rate. This was in contrast to the results observed in case of the upstroke motion at 14° where, in the early part of leading edge region, dV/dx was the dominant term. This meant, for the upstroke motion of the wing, the transverse velocity was higher in this region compared to the downstroke motion.

Quantitatively, in the downstream region close to the wall, the mean strain rate was approximately five times higher during the downstroke motion compared to the

upstroke motion. As the magnitude of transverse velocity was not significant in this region, most likely the axial velocity was higher in this region for the downstroke motion compared to the upstroke motion. Higher magnitude of axial velocity again indicated the reattachment process during the downstroke motion. The high mean strain rate indicated that the fluid was increasingly strained during reattachment process, which in turn enhanced the process. The thickness of Region II is summarized in Table 16 for angles-of-attack of 12°, 14° and 16° during the downstroke motion. The thickness was measured at *x/c = 0.20* (5% of the chord length). As shown in the table, the thickness decreased with decreasing angle-of-attack. The trend demonstrated that the flow was reattaching with decreasing angle-of-attack.

The pitching down contour plots of vorticity (ω_z) are shown in Figs. 171 – 174, for angles-of-attack of 16°, 14°, 12°, and 10°, respectively. Similar to strain field, the magnitude of vorticity was approximately five times higher for the downstroke motion as opposed to the upstroke motion for the same angle-of-attack. The magnitude of ω_z was found to be a maximum in Region II. Because of the velocity gradient signs, the vorticity was positive in this region. However, in this region, $\partial U/\partial y$ term was dominant. As expected, away from the wall, towards the freestream region the vorticity was close to zero.

6.4.2.2 Turbulent Flow Field

6.4.2.2.1 Turbulent Stresses

This section describes the results and analysis of the axial stress, transverse stress and Reynolds shear stress.

The pitching down contour plots of axial stress (σ_u) are shown in Figs. 175 – 178, for angles-of-attack of 16°, 14°, 12°, and 10°, respectively. In Region IV, the magnitude of σ_u was less than that in Region II. This implied that, near the leading edge (i.e., Region IV), the *x*-component of turbulent kinetic energy was less than that in the shear layer in the downstream (i.e. Region II). As the shear layer was formed, the *x*-component of turbulent kinetic energy increased. The magnitude of σ_u was found to be high in Region II for angles-of-attack of 12°, 14° and 16°. Region II corresponded to the shear layer that was observed in the flow visualization images in Figs. 76(b) – 80(b). At 10°, the magnitude of σ_u was lower than the other angles-of-attack, where the flow was attached. The magnitude of axial stress in the shear layer for a representative angle-of-attack of 14° is tabulated in Table 17. The data points were extracted within 1 mm from the airfoil surface to ensure the point was in shear layer. As can be seen in the table, in the downstream region (Region II), the axial stress was high. The magnitude of axial stress for the downstroke motion was higher compared to the upstroke motion as shown in the table.

The pitching down contour plots of transverse stress (σ_v) are shown in Figs. 179 – 182, for angles-of-attack of 16°, 14°, 12°, and 10°, respectively. The magnitude of σ_v was found to be a maximum slightly upstream of Region IV in Region III (Fig. 151) for all angles-of-attack considered. This was attributed to the high radius of curvature encountered by the flow resulting in increased production. It can be recalled that the magnitude of transverse velocity was also maximum in this region. The nominal high

values of σ_v in Region III are listed in Table 18 for different angles-of-attack during the downstroke. As shown in the table, with decreasing angle-of-attack the location of the center also moved downstream, as expected during the downstroke reattachment. In Region IV, the magnitude of σ_u was 80% higher than the magnitude of σ_v.

The pitching down contour plots of Reynolds shear stress (τ_{xy}) are shown in Figs. 183 – 186, for angles-of-attack of 16°, 14°, 12°, and 10°, respectively. In Region IV, as well as in the early part of Region II, the magnitude of τ_{xy} was noticed to be high and positive. In the above mentioned regions the flow was believed to be reattached to the surface of the airfoil. This produced high positive values of shear stress of the order of ~0.1. At 16°, the axial distance of high shear stress region was ~ 4.5% of the chord length. At 10°, the axial distance was ~ 7%. This indicated that the attached flow region increased with decreasing angle-of-attack. In stagnation region introduced earlier (Region V), the magnitude of Reynolds shear stress was of the order of ~0.001.

6.4.2.2.2 Turbulence Transport

This section summarized the results and analysis of Reynolds stress production; namely the P_{xx}, P_{yy} , and P_{xy} . As shown in Eq. 6.6 and 6.7, the mean flow and the turbulent flow are coupled through these terms. Hence, it was of importance to analyze the effect of production to understand the combined effect of mean and turbulent quantities on the flow field.

The focus of this study was to obtain high fidelity data near the leading edge. Hence, attention was given to Regions II and IV as these two regions coincide with the

reattachment process. It was also deemed important to analyze the downstream of Region of II where there was a high axial stress. The high axial stress was expected to contribute in the production terms.

The pitching down contour plots of P_{xx} are shown in Figs. 187 – 190, for angles-of-attack of 16°, 14°, 12°, and 10°, respectively. The magnitude of P_{xx} was found to be a maximum in Region IV and in the early part of Region II (Fig. 151) for all angles-of-attack considered. This meant that there was a substantial production of *xx*-component of the Reynolds stress. In Region IV, as a result of favorable pressure gradient, the dU/dx and dU/dy strain rates were large and negative. As shown in Eq. 6.6, P_{xx} depended on these two velocity gradients. Hence, the production was attributed to a high velocity gradient in this region. Comparing with the gradient plots, it was found in Region IV the terms $\tau_{xy}^{T}\frac{\partial U}{\partial y}$ and $\tau_{xx}^{T}\frac{\partial U}{\partial x}$ were comparable. Earlier it was noticed in Region II, $\frac{\partial U}{\partial y}$ was very high. Also, in this region the axial stress was noticed to be high. Hence, it was concluded that in Region II, the term $\tau_{xx}^{T}\frac{\partial U}{\partial x}$ was substantial but still less than $\tau_{xy}^{T}\frac{\partial U}{\partial y}$. In the region IV and early part of Region II, P_{xx} decreased with decreasing angle-of-attack. It was found in the leading edge region, for the same angle-of-attack the magnitude of P_{xx} for the downstroke motion was higher than the upstroke motion.

The pitching down contour plots of P_{xy} are shown in Figs. 191 – 194, for angles-of-attack of 16°, 14°, 12°, and 10°, respectively. As can be seen in the contour plots, in Region II for all angles-of-attack, the production of *xy*-component of Reynolds stress

was higher compared to other regions. This was attributed to the shear action occurring at the airfoil surface. The formulation for P_{xy} was given in Eq. 6.8. As mentioned earlier, the axial stress and axial/transverse velocity gradients were also high in this region. Thus, both $\tau_{xx}^{T}\frac{\partial V}{\partial x}$ and $\tau_{yy}^{T}\frac{\partial U}{\partial y}$ terms were significant in this region. For the representative angle-of-attack of 14°, the average peak magnitude of P_{xy} was higher in Region II for the downstroke motion compared to the upstroke motion by approximately 85%. However, the difference in magnitude decreased in the downstream of Region II. In this region, the flow reattached or was trying to reattach. For completeness of the analysis, it was noted that in the Region IV, all four terms were comparable.

The final coupling term between mean flow and turbulent stress is P_{yy}. The pitching down contour plots of P_{yy} are shown in Figs. 195 – 198, for angles-of-attack of 16°, 14°, 12°, and 10°, respectively. In Region IV and beginning of Region II, there was a greater loss of *yy*-component of Reynolds stress. In other words P_{yy} was highly and negative. In this region, the flow was believed to be attached. Both the terms shown in Eq. 6.7 were contributing to P_{yy}. However, the contribution of $\tau_{xy}^{T}\frac{\partial V}{\partial x}$ was higher. In the beginning of Region II, it was found the term $\tau_{yy}^{T}\frac{\partial V}{\partial y}$ was dominant as a result of dominant transverse velocity gradient. In the aforementioned regions, the magnitude of P_{xx} was an order higher than the magnitude of P_{yy}.

From the above discussions, it was noticed the Reynolds stress production quantities exhibited similar behavior in the attached flow region for both the upward and downward motion of the wing. However, in this region, these quantities were at least one order higher during the downstroke motion compared to the upstroke motion. The large differences were attributed to the increased turbulent stresses and velocity gradients for the attached flow.

6.5 Boundary Layer Profile Properties

In the leading edge region, there was an attached boundary layer with a strong favorable pressure gradient. In the downstream region there was an adverse pressure gradient. The flow was separated in this region. Thus, it was also of interest to examine the effect of pressure gradients on mean and turbulent flow structure following the boundary layer methods typically utilized in the literature.[43]

6.5.1 Upstroke Motion of the Wing

As discussed in earlier sections, at 10°, the flow was attached during the upstroke motion of the wing. At 18°, the flow was fully separated. At 14°, the flow was between the two extreme conditions. Hence, line plots were drawn at a representative angle-of-attack of 14° to provide an insight into the attached flow in the leading edge region and separated flow in the downstream region.

Line plots of mean and turbulent flow quantities are shown in Figs. 199 – 206. The flow parameter is plotted on the abscissa. The perpendicular distance from the airfoil surface (*n/c*) is plotted on the ordinate. The perpendicular distance was normalized by the chord length '*c*'. Two hundred data points were extracted from the

contour data at two stations x/c = 0.235 (1^{st}) and 0.15 (2^{nd}). The locations corresponded to 1.5 and 10.0 percent of the chord length, respectively, relative to the leading edge. A schematic drawing of the location of these stations is shown in Fig. 83. The 1st and 2nd station data points were extracted in the regions of favorable and adverse pressure gradients, respectively.

The line plot of the magnitude of axial velocity (U_N) is shown in Fig. 199. As shown, the velocity profile resembled a turbulent velocity profile on a flat plate. At the 1st station, there was a favorable pressure gradient. The magnitude of axial velocity rapidly increased from 0 at n/c = 0 to 1.55 at n/c = 0.002. That is the velocity increased from 0 to 110 m/s in 0.9 mm. Beyond this peak, the axial velocity gradually decreased. The convex curvature in the velocity profile between n/c = 0.0007 to n/c = 0.005 suggested that the flow was attached at this point in Region I as shown in Fig. 84. Away from Region I, the velocity gradually reduced. The 2nd station data points were extracted in the region of adverse pressure gradient. The magnitude of axial velocity rapidly increased from 0 at n/c = 0 to 1.17 at n/c = 0.0005. Beyond this point, the axial velocity increased to 1.26 at n/c = 0.005 and stayed almost constant thereafter. Between n/c = 0.0005 to 0.005 the velocity profile exhibited a concave curvature with an inflection point as shown. The concave curvature in the velocity profile at 2nd station identified that, the flow was separated in Region II.

The line plot of the magnitude of transverse velocity (V_N) is shown in Fig. 200. At the 1st station, the magnitude of transverse velocity rapidly increased from 0 at n/c = 0 to 0.8 at n/c = 0.005. Beyond this peak, the transverse velocity gradually decreased. The

convex curvature in the velocity profile was due to the strong favorable pressure gradient. At the 2nd station, the magnitude of transverse velocity rapidly increased from 0 at n/c = 0 to 0.175 at n/c = 0.0005. From n/c = 0.0005 to 0.002, the transverse velocity decreased from 0.175 to 0.05. Beyond this point, the transverse velocity gradually increased. The data point at n/c = 0.002 lied within a concave curvature region. At this point the slope of the velocity profile changed sign. Hence, this point can be termed as the inflection point. Quantitatively, there was a significant difference between the peak transverse velocities at two stations. The difference is shown in Table 19. The difference can be attributed to two reasons. First, at 1st station the radius of curvature was larger than the 2nd station leading to higher velocity. Second, as the flow separated, the magnitude of V-velocity was reduced substantially. The location of the peak magnitude of the V-velocity is shown in the 2nd column of Table 19. The maximum difference in peak magnitude between the two stations is shown in the third column of Table 19. Beyond n/c = 0.005, this difference tended to decrease as shown in the figure. This supported the earlier results that in the adverse pressure gradient region, the transverse velocity does not contribute to the total velocity and in turn to the Mach number. It was noted that, the location of peak magnitude of V-velocity at 1st station occurred further away from the airfoil surface as compared to that at 2nd station.

The line plot of axial stress (σ_u) is shown in Fig. 201. At both the stations, close to the wall at n/c = 0.00074 in Regions I and II (Fig. 83), a peak in the magnitude of the axial stress was observed. At 1st and 2nd station the peak magnitudes were 0.33 and 0.32, respectively. Beyond this peak, at 1st station, the axial stress reduced sharply to 0.12 at

n/c = 0.025. At 2nd station, the axial stress reduced gradually to 0.21 at n/c = 0.025. It can be seen that away from the wall, the axial stress decreased. Beyond n/c = 0.002, the magnitude of axial stress was higher at the 2nd station compared to the 1st station. This meant that, in the downstream region, the *x*-component of turbulent kinetic energy was higher as was expected for separated flow. The maximum difference of the magnitude of axial stress between these two stations was found to be approximately 45%. Also, as expected, the profile of axial stress extracted at 2nd station was oscillatory in nature confirming the unsteadiness in the flow field.

The line plot of transverse stress (σ_v) is shown in Fig. 202. The profile of the transverse stress followed the trend shown by the axial stress as shown in Fig. 200. At both the stations, the transverse stress increased from 0 at n/c = 0 to 0.22 at n/c = 0.002. The maximum difference in the *y*-component of turbulent energy between the two stations was found to be approximately 55%. Beyond n/c = 0.002, the magnitude of axial stress was higher at the 2nd station compared to the 1st station as was seen in case of the axial stress. At n/c = 0.002, for both the stations, the difference between the peaks of *x*-component and *y*-component of turbulent energy was found to be approximately 31%.

The line plot of Reynolds shear stress (τ_{xy}) is shown in Fig. 203. Reynolds shear stress showed strikingly different characteristics as compared to the axial and transverse stress. At the 1st station, shear stress was positive all the way starting from the wall. At the 1st station, the value increased from 0.002 at n/c = 0 to a peak of 0.05 at n/c = 0.0005. Beyond this peak, the shear stress decreased rapidly to 0.005 at n/c = 0.014; it remained constant after this point. The peak was observed very close to the wall and away from

the surface the magnitude decreased. It was believed that the shear stress peak corresponded to the suction peak in the favorable pressure gradient region, which is a feature observed in pressure variations over the airfoil surface by several researchers, and is associated with the acceleration and deceleration of the flow close to the leading edge[45]. At the 2nd station, the magnitude of τ_{xy} was found to be negative as shown in Fig. 203. It was concluded that, in the adverse pressure gradient region, owing to flow separation, the Reynolds shear stress changed sign and there was a reduction in energy. The negative magnitude of shear stress increased from 0 at n/c = 0 to 001 at n/c = 0.003. Beyond this peak, the magnitude decreased to 0.004 at n/c = 0.017. Following this point the magnitude was constant. Close to wall, the magnitude of shear stress was higher than away from the wall. This trend in the shear stress data confirmed there could be secondary flows present at this station. Negative shear stress also indicated flow reversal and hence corresponded to a weaker shear layer. Eventually, with an increase in angle-of-attack the shear layer lifted off completely.

The line plots of production of the *xx*-component, *yy*-component of Reynolds Stress and *xy*-component Reynolds Shear Stress at 14° are shown in Figs. 204 – 206 at two different stations. The line plot of Reynolds axial stress (P_{xx}) is shown in Fig. 204. At both the stations, the Reynolds axial stress was approximately zero at n/c = 0.003. At the 1st station, P_{xx} increased from 14 at n/c = 0.0003 to 145 at n/c = 0.0005. Beyond this peak, the magnitude reduced sharply to 0.21 at n/c = 0.003 and stayed constant after that point. At 2nd station, the negative magnitude of P_{xx} increased from 3.2 at n/c = 0.0003 to 12 at n/c = 0.0006. Beyond this peak, the magnitude reduced to -0.21 at n/c = 0.003 and

stayed constant after point. The magnitude of Reynolds axial stress was about two orders higher than axial turbulent stress at the same station. This was attributed to high velocity gradients in strong favorable pressure gradient region. In the favorable pressure gradient region where the flow was attached, the Reynolds axial stress had a positive value but in the adverse pressure gradient region the magnitude was negative owing to separation. Also, the magnitude of P_{xx} at the 2nd station was found to be about an order of magnitude less than the 1st station.

The line plot of Reynolds transverse stress (P_{yy}) is shown in Fig. 205. The trend shown by P_{yy} was opposite to P_{xx} in the wall region. At the 1st station, there was a negative production of P_{yy}. The negative magnitude of Reynolds transverse stress increased 3.39 at n/c = 0.0004 to 48 at n/c = 0.0005. Beyond this peak the magnitude decreased to 0.41 at n/c = 0.005, further away from the wall. This meant in the favorable pressure gradient region, there was a loss of *yy*-component of Reynolds axial stress to the transverse mean energy and the loss decreased away from the airfoil surface. A reverse trend was observed at 2nd station where, there was production of P_{yy}. The magnitude of Reynolds transverse stress increased -12.5 at n/c = 0.0005 to 9 at n/c = 0.001. Beyond this peak the magnitude decreased to 0.11 at n/c = 0.005, further away from the wall.

The line plot of P_{xy} is shown in Fig. 206. There was a peak observed in the line plots of P_{xy} at both the stations. At 1st station, the magnitude of P_{xy} increased from 0 at n/c = 0 to 13 at n/c = 0.0005. Beyond this peak, the magnitude gradually decreased to -2.6 at n/c = 0.003. Beyond this point, the magnitude increased slightly to -0.48 at n/c =

0.007 and stayed constant afterwards. At 2nd station, the magnitude of P_{xy} increased from 15 at n/c = 0 to 49 at n/c = 0.0005. Beyond this peak, the magnitude gradually decreased to -2 at n/c = 0.001. Beyond this point, the magnitude increased to -0.33 at n/c = 0.007 and stayed constant afterwards. The reduction in the peak magnitude of P_{xy} between 2nd and 1st station at n/c = 0.0005 was found to be 74%. To sum up, between n/c = 0.001 and 0.007, the magnitude of P_{xy} was positive in the adverse pressure gradient region while it was negative in the favorable pressure gradient region.

At the 2nd station, an interesting feature was observed in the line plots of production quantities. All the production terms approached zero between n/c = 0.004 to 0.007. Also the profile of axial velocity had concave curvature that extended the above mentioned distance before reaching a steady value indicating boundary layer characteristic. Hence, it was likely that this distance corresponded to boundary layer thickness at the 2nd station. Physically, this distance corresponded to 1.8 – 3.21 mm, which is similar to the values predicted for a simple flat plate.

6.5.2 Downstroke Motion of the Wing

This section describes the boundary layer profiles of mean and turbulent flow properties during the downstroke motion of the wing. Line plots were drawn at a representative angle-of-attack of 14° during the downstroke motion of the wing.

The line plot of the magnitude of axial velocity (U_N) is shown in Fig. 207. At the 1st station, the magnitude of axial velocity rapidly increased from 0.22 at n/c = 0 to 1.82 at n/c = 0.007. Beyond this peak, the axial velocity gradually decreased. The convex curvature in the velocity profile between n/c = 0.003 to n/c = 0.009 suggested that the

flow was attached. The magnitude of axial velocity rapidly increased from 0.5 at $n/c = 0$ to 1.78 at $n/c = 0.006$. The axial velocity remained almost constant from $n/c = 0.006$ to $n/c = 0.0165$. Beyond this point, the axial velocity gradually reduced. At 1st station, during the downstroke motion, the peak axial velocity was 16% higher than that during the upstroke motion. At 2nd station, the axial velocity was 44% higher than that during the upstroke motion. The higher difference in velocity supported the fact that the flow was attaching during the downstroke motion of the wing.

The line plot of the magnitude of transverse velocity (V_N) is shown in Fig. 208. At the 1st station, the magnitude of transverse velocity rapidly increased from 0 at n/c = 0 to 0.68 at $n/c = 0.014$. Beyond this peak, the transverse velocity gradually decreased. The convex curvature in the velocity profile was due to the strong favorable pressure gradient. At the 2nd station, the magnitude of transverse velocity gradually increased from -0.02 at $n/c = 0$ to close to zero. The negative transverse velocity was an indication of the presence of secondary flows. The transverse velocity became positive at $n/c = 0.018$. Beyond this point, the transverse velocity remained positive. However, the maximum value was found to be close to zero. The difference in peak transverse velocities at both the stations was approximately 70%. This supported the earlier result that in the adverse pressure gradient region, the transverse velocities did not contribute a lot to the total velocity. Hence, in the reattachment region, the axial velocity was of importance. At the 2nd station, during the downstroke motion, the maximum transverse velocity was 10% higher than that during the upstroke motion. On the contrary, at the 1st

station, the transverse velocity was comparable for both the upstroke and downstroke motion of the wing.

The line plot of axial stress (σ_u) is shown in Fig. 209. At both the stations, close to the wall at *n/c* = 0.001 in Regions II and IV (Fig. 151), a peak in the magnitude of the axial stress was observed. At 1st and 2nd station the peak magnitudes were 0.65 and 0.80, respectively. Beyond this peak, at 1st station, the axial stress reduced sharply to 0.30 at *n/c* = 0.0054. At 2nd station, the axial stress reduced sharply to 0.18 at *n/c* = 0.0054. It can be seen that away from the wall, the axial stress decreased. Beyond *n/c* = 0.002, the magnitude of axial stress was higher at the 1st station compared to the 2nd station. This meant that, in the downstream region, the *x*-component of turbulent kinetic energy was lower as was expected for attaching flow. In the shear layer (Region II), the axial stress during the downstroke motion was 150% higher than that during the upstroke emotion. However, away from the shear layer this difference reduced to 6%.

The line plot of transverse stress (σ_v) is shown in Fig. 210. At 1st station, the transverse stress increased from 0.08 at *n/c* = 0 to 0.30 at *n/c* = 0.003. Beyond this point, the transverse stress decreased to 0.21. However, the decreasing trend was oscillatory. At the 2nd station, the transverse stress increased from 0 at *n*/*c* = 0 to 0.16 at *n*/*c* = 0.003. Beyond this point, the transverse stress remained almost constant. Visual inspection suggested that the oscillation in the profile was less than that at the 1st station discussed earlier as a result of the flow stabilization via reattachment. The average transverse stress at the 2nd station was found to be 56% less than that at the 1st station. This reduction in the *y*-component of turbulent energy was attributed to the flow reattachment.

The line plot of Reynolds shear stress (τ_{xy}) is shown in Fig. 211. Reynolds shear stress showed similar characteristics as compared to the upstroke motion of the wing. At the 1st station, shear stress was positive all the way starting from the wall. At the 1st station, the value increased from 0.04 at n/c = 0 to a peak of 0.12 at n/c = 0.001. Beyond this peak, the shear stress decreased rapidly to 0.025 at n/c = 0.0056; it gradually reduced to zero after this point. The peak was observed very close to the wall and away from the surface the magnitude decreased. At the 2nd station, the negative magnitude of τ_{xy} increased from 0 at n/c = 0 to 0.02 at n/c = 0.0004. Beyond this peak, the magnitude decreased to 0.002 at n/c = 0.0036. Following this point the magnitude was constant. It was important to note that at the 2nd station, away from the wall in the shear layer, the magnitude of Reynolds shear stress was positive and approximately 100% higher (at n/c = 0.004) during the downstroke motion compared to the upstroke motion. This supported the fact that during the downstroke motion the shear layer was stronger than during the upstroke emotion.

The Reynolds stress components exhibited similar trend during the downstroke motion as compared to the upstroke motion. However, the magnitudes of these components quantities were higher for the downstroke motion as shown in the Table 20. At x/c = 1.5% and 10%, the magnitude of positive and negative production of Reynolds axial stress was found to be 177% and 483% higher during the downstroke motion as compared to the upstroke motion, respectively. The corresponding magnitudes of the negative and positive production of Reynolds transverse stress was found to be 19% and 80% less during the downstroke motion as compared to the upstroke motion,

respectively. The corresponding positive production of P_{xy} was found to be 85% higher and 68% less during the downstroke motion as compared to the upstroke motion at the two locations, respectively.

6.6 Reynolds Shear Stress Structure in the Leading Edge Region

It was observed that during the upstroke motion of the wing, the flow separated with increasing angle-of-attack. As described earlier, Reynolds shear stress was found to be positive in the leading edge region. From a turbulence modeling prospective, it was important to understand the behavior exhibited by Reynolds shear stress near the leading edge prior to separation. The following section describes the structure of Reynolds shear stress in the leading edge region during the upstroke motion. The discussion is based on the sketch of the leading edge region of the wing shown in Fig. 212. In Regions I and II, shear stress was found to be positive. Physically these regions expanded to approximately 3% of the chord length staring from the leading edge as shown in the contour plots. Region I was observed to be the same size for all angles-of-attack. However, the structure of Region II exhibited interesting characteristics as the angle varied.

The size of the Region II increased with increasing angle-of-attack. This region looked similar to the shape of a “bubble.” This bubble region is indicated on Fig. 212. As shown in the figure, the bubble region lifted off the surface with increasing angle-of-attack, and the size of Region II also increased. In other words, it can be seen that the size of the bubble increased with increasing angle-of-attack. The increase in the transverse (y) dimension of the bubble was higher than the increase in the axial (x)

dimension. Finally, the bubble appeared to have broken down at the highest angle-of-attack (i.e., 18°). At this angle, the flow was fully separated and a free shear layer was formed as shown in the contour plot.

A common line between Regions I and II is annotated on Fig. 212. The length of the line is denoted by *L*. The axial location was at *x/c* = 0.235 which corresponded to 1.5% of the chord length starting from the leading edge. The length 'L' was measured for different angles-of-attack. The results are summarized in Table 21. As shown in Table 20, *L* with increasing angle-of-attack. This is a quantification of the growing size of the bubble with increasing angle-of-attack discussed in the previous paragraph. The sequence of formation of the bubble and eventual diffusion is shown in the contour plots of Reynolds shear stress in Fig. 213. The data indicates that the bubble began to appear at 12°. It grew in size with increasing angle-of-attack and ultimately diffused into the shear layer at 18°.

The bubble was also seen during the downstroke motion of the wing as shown in the contour plots of Reynolds shear stress in Fig. 214. The size of the bubble decreased with decreasing angle-of-attack. Eventually, the bubble disappeared as the flow was fully attached to the airfoil surface at the lowest angle-of-attack (10°) considered.

A second interesting feature was observed in the contour plots of Reynolds shear stress for the upstroke and downstroke motion. For all angles-of-attack, in the attached flow region on the wing surface (Region I and II), the magnitude of Reynolds shear stress was found to be positive. However, at 18°, during the upstroke motion of the wing, Reynolds shear stress was found to be positive in the separated flow as a result of

formation of free shear layer. In the shear layer, Reynolds shear stress diffused and the magnitude decreased with increasing separation.

CHAPTER VII

CONCLUSIONS AND RECOMMENDATIONS

The primary objective of this research project was improved understanding of the fundamental vorticity and turbulent flow physics for a dynamically stalling airfoil at realistic helicopter flight conditions. In order to meet this objective, an experimental program using high-resolution Particle Image Velocimetry (PIV) was performed to provide an empirical characterization of the leading-edge (first 10-15% of the chord) flow structure. A dynamically pitching NACA 0012 wing operating in the Texas A&M University large-scale wind tunnel was studied. The focus of the present study was the leading-edge flow structures prior to, during and after dynamic stall. The data resolution was approximately 0.25 mm (0.06% of the airfoil chord) between data points, and data were acquired to within 0.5 – 1.0 mm from the airfoil surface. The sample sizes consisted of nominally 1000 image pairs to ensure statistical convergence of the measurements. The measurements included planar contours of the mean velocity (*u*- and *v*-components), vorticity, strain rates, turbulence intensities (*u*- and *v*-components), the Reynolds shear stress, and production of the turbulent stresses (axial, transverse and shear). The test matrix consisted of 6 different cases. Case 1 corresponded to $M = 0.2$, $k = 0.1$, $Re_c = 2.0 \times 10^6$, the mean angle-of-attack and amplitude of oscillation was 10°; Case 2 corresponded to $M = 0.28$, $k = 0.1$, $Re_c = 2.8 \times 10^6$, the mean angle-of-attack and amplitude of oscillation was 10°; Case 3 corresponded to $M = 0.2$, $k = 0.18$, $Re_c = 2.0 \times 10^6$, the mean angle-of-attack and amplitude of oscillation was 10° and 5°, respectively.;

Case 4 corresponded to $M = 0.2$, $k = 0.18$, $Re_c = 2.0 \times 10^6$, the mean angle-of-attack and amplitude of oscillation was 15° and 5°, respectively.; Case 5 corresponded to $M = 0.2$, $k = 0$, and $Re_c = 2.0 \times 10^6$. Case 6 corresponded to $M = 0.28$, $k = 0$, and $Re_c = 2.8 \times 10^6$.

The primary scientific impact is documentation and improved basic understanding of the fundamental flowfield processes for a dynamically pitching airfoil at realistic helicopter flight conditions. The specific research contributions include (1) the extensive and highly resolved dynamic stall experimental database obtained under realistic flight conditions, (2) the subsequent mean flow analyses and (3) the analysis of the turbulence and the production thereof under the dynamic flow conditions.

A detailed quantitative interrogation of the mean and turbulent flow structure for Case 1 was presented in Chapter VI for the both the up- and down-stroke motions of the wing. The remaining cases listed in Table 1 are summarized in the Appendix. These analyses lead to new understandings of the basic flow physics. These new understandings are summarized in the subsequent sections.

7.1 Dynamic Stall Flow Physics

7.1.1 Flow Time-Scales and Hysteresis

In the leading-edge wall region, the wing oscillation, the shear and the turbulent time scales were comparable for both the upstroke and downstroke motion of the wing, which indicated that the flow was characterized as being in a state of mechanical non-equilibrium. As such, the flow exhibited the expected hysteresis behavior, where during the upstroke motion of the wing, the separation process initiated at 12°. The average separation point moved upstream with increasing angle-of-attack. At18°, the flow field

was fully separated. During the downstroke motion, reattachment began at 16° with a shear layer near the surface of the wing. The mechanical non-equilibrium and the associated hystersis were found to strongly couple to the mean and turbulent flow structure.

7.1.2 Vorticity and Mean Strain Rates

The vorticity and mean-strain rates are driving factors in the production of turbulence and the energy budget. Schematics of the vorticity and mean-strain processes are given in Figs. 215 and 216, respectively. The following conclusions were drawn from these figures:

- During the upstroke motion of the wing, the high counter-clockwise vorticiy appeared to be concentrated in the wall region (Region I) as shown in Fig. 215. This region swelled with increasing angle-of-attack and eventually, detached off the wing surface as a result of strong viscous-inviscid interaction.
- During the downstroke motion of the wing, the high positive vorticty appeared to be concentrated in the wall region (Region I) as was noticed in case of the upstroke motion. However, the thickness of the region decreased with decreasing angle-of-attack as a result of reattachment process. The magnitude of the vorticity was an order higher during the downstroke motion as compared to the upstroke motion. A “stagnation” region was observed (Region II in Fig. 215) during the downstroke motion where the vorticity was zero.
- During the upstroke motion of the wing, the mean strain rate was found to be positive and negative in Region I and II respectively. The mean flow strain rate

structures are shown in Fig. 216. Region II was swollen with increasing angle-of-attack as shown in the sketch.

- During the downstroke motion of the wing, the mean strain rate was negative in Region I as shown in Fig. 216. This region was compressed to the wall with decreasing angle-of-attack. The magnitude of mean strain rate was one order of magnitude higher than that during the upstroke motion.

7.1.3 Boundary Layer Profiles

For the most part, turbulence models are based on boundary layer theory including pressure gradient and streamline curvature effects. The dependence on pressure gradient of Reynolds axial and transverse components are shown in the flow chart in the Fig. 217. There was positive and negative production of Reynolds axial stress in the favorable and adverse pressure gradient region, respectively. On the contrary, there was negative and positive production of Reynolds transverse stress in the favorable and adverse pressure gradient region, respectively. At 10% of the chord length, the production terms approached zero within 1.8 to 3.2 mm from the wing surface. Also, the velocity profile exhibited boundary layer characteristics within this distance from the surface. Thus, it was likely that the specific distance corresponded to the boundary layer thickness, which is difficult to quantify in highly accelerating flows.

7.1.4 Energy Budget Dynamics

The transport of energy has a direct bearing on the separation process. Thus, an understanding of the energy budget mechanisms is a necessary step for modeling and control separation. The detailed investigations of the mean flow, the turbulence

Reynolds stresses and the production thereof in the leading-edge region for the upstroke and downstroke motion of the wing presented in Chapter VI, lead to the energy budget mechanisms summarized in Fig. 218. The key physical processes are summarized below:

- In Region I, during the both upstroke and downstroke motion of the wing, it was observed that the axial and transverse stresses were of similar magnitudes. However, the overall production axial stress (P_{xx}) was positive and the production (P_{yy}) the transverse stress was negative. These findings suggested the energy flow shown schematically in Fig. 218. Specifically, turbulent energy was extracted from the *x*-component of the mean flow through positive Reynolds axial stress. Part of the axial energy was lost as a result of dissipation (ε) and diffusion (D). However, a significant amount was transferred to the transverse component through the pressure-strain redistribution (Π_{ij}), which drives the turbulence towards isotropy. This was indicated by the relatively large values of the transverse stress component even though the overall production was negative. Without the energy redistribution, this term would be reduced. A part of the transverse component of kinetic energy was again lost as a result of dissipation and diffusion. The remainder was transferred back to the *y*-component of the mean flow through negative (P_{yy}). The resulting energy flow was clockwise as shown in Fig. 218.
- In Region II, during the both upstroke and downstroke motion of the wing, the energy flow process was reversed as compared to Region I. More specifically, energy was extracted from the *y*-component of the mean flow (through positive

P_{yy}), and redistributed to the axial shear stress and then back to the mean flow. Hence, in the downstream region, the direction of energy budget transfer mechanism was counter-clockwise as shown in Fig. 218.

- It can be seen that in the downstream region (Region II), the direction of energy budget transfer mechanism was similar for the upstroke and downstroke motion of the wing. However, in this region, the flow tended to separate during the upstroke and reattach during the downstroke motion. This anomaly in the flow behavior during the downstroke motion was a result of higher energy being fed back to the *x*-component of the mean flow through negative production of Reynolds axial stress (P_{xx}). This in turn increased the magnitude of *x*-component of the mean flow which countered the effect of adverse pressure gradient and eventually lead to the flow reattachment.

7.1.5 Leading-edge Reynolds Shear Stress Structure

In order to properly predict dynamic stall separation under realistic flight conditions, turbulence models must be able to capture the Reynolds shear stress dynamics discussed in detail in Chapter VI. The basic process is sketched in Fig. 219, where during the upstroke motion a bubble shaped structure (Region II) appeared in the Reynolds shear stress contour plots. The size of the bubble (Region II in Fig. 219) increased with increasing angle-of-attack before being diffused into a shear layer at the highest angle-of-attack (18°). Shear stress was found to be positive in Region I and II, where the flow was attached.

The bubble was also present during the downstroke motion. The size of the bubble reduced with decreasing angle-of-attack and eventually was attached to the airfoil surface at the lowest angle-of-attack (10°). In the attached flow region, shear stress was found to be positive.

7.2 Recommendations

The database and improved understanding gleaned from this research provided a detailed characterization of the leading edge flow field prior to dynamic stall event. This study will be a valuable aid to researchers and engineers in the development of semi-empirical relations and turbulence models. However, areas for further investigations using present data set and with new test conditions/model are recommended.

7.2.1 Investigations using Present Data Set

- It was observed that at angles-of-attack of 10°, 14° and 18°, the flow field was well defined. At 10°, the flow was attached. At 18°, the flow was separated. At 14°, the flow field was between the extreme flow conditions. Hence, it would be informative to perform a detailed analysis of the boundary layer properties for both the upstroke and downstroke motion of the wing at these two angles-of-attack.
- The global flow field appeared to have similar mean and turbulent flow structures for unsteady and steady flow conditions (Cases 2-6) presented in Appendix B-D. However, more detailed interrogations should be performed to quantify the flow properties.

- For Case 3 & 4 data were acquired at two locations. The results are summarized for the 1st location in Appendix C. The PIV images were acquired at 2nd location focusing on 15% - 25% of the chord as shown in Fig. 220. The total axial distance corresponded to $x/c = 0$ to $x/c = 0.19$. The PIV recorded images at 2nd location can be processed for further information of the flow field.
- Computational simulations should be performed to assess the limitation of current turbulence models.

7.2.2 New Investigations

- Current research work was focused for *M = 0.2 and 0.28*. Literature review suggests for compressible flow i.e. *M = 0.4* shocks appear at the leading edge of the airfoil. It will be of interest to perform this set of experiments at *M = 0.4*. This Mach no. can be achieved using current DSF at TAMU with a 5' x 7' test section and a longer diffuser (~40 ft.) with an included angle of 6° – 8°.
- It would be of interest to have an insight of the flow field at a reduced frequency of *k = 0.05*. This will provide additional time to observe the flow separation process. A reduced frequency of *k = 0.05* can be achieved at a Mach No. of 0.1. This data will also complete the flight (helicopter) envelope with a range of Mach no. *0.1 ~ 0.4*.
- For the current set of experiments data were acquired on the upper surface of *NACA 0012*. It will be of interest to acquire data at the lower surface. This will provide information about the location and movement of stagnation point at

different angles of attack. An additional advantage to obtain this data is to be able to understand the behavior of flow field around the leading edge.

- It would be of interest to study the leading edge flow separation of a cambered airfoil.
- This experimental work focused on *NACA 0012* wing undergoing sinusoidal motion. It will be of interest to perform this same set of experiment with wing following a cosine function or flapping up the wing using a sine function at a higher frequency and flapping down at a lower frequency. This will provide more time for reattachment process during flapping down motion of the wing.
- It was observed that the flow separation was initiated at 12°. It would be of informative to perform additional measurements in the range of 13° - 17° with higher resolution in terms of angle-of-attack.
- Improve the optical access in the facility and perform Stereo PIV.

REFERENCES

1. McCroskey, W., "Unsteady Airfoils," *Ann. Rev. Fluid Mech.*, Vol. 14, pp. 285-311, 1982.

2. Lawrence, W. Carr, "Progress in Analysis and Prediction of Dynamic Stall," *Journal of Aircraft*, Vol. 25, No 1, pp. 6-17, January 1988.

3. Carr, L., and McCroskey, W., "A Review of Recent Advances in Computation and Experimental Analysis of Dynamic Stall," *International Union of Theoretical and Applied Mechanics on Fluid Dynamics at High Angle of Attack*, Tokyo, Japan, Sept. 1992.

4. Ekaterinaris, J., and Platzer, M., "Computational Prediction of Airfoil Dynamic Stall," *Progress in Aerospace Sciences*, Vol. 33, pp. 759-846, 1997.

5. Greenblatt, D., and Wygnanski, I, "Dynamic Stall Control by Periodic Excitation, Part 1: NACA 0015 Parametric Study," *Journal of Aircraft*, Vol. 38, No. 3, pp. 430-438, May 2001.

6. Leishman, J., *Principles of Helicopter Aerodynamics*, Cambridge Aerospace Series, Cambridge University Press, New York, 2000.

7. Choudhuri, P., Knight, D., and Visbal, M., "Two-Dimensional Unsteady Leading Edge Separation on a Pitching Airfoil," *AIAA Journal*, Vol. 32, pp. 673-681, April 1994.

8. Boussinesq, J., "Theorie de l'ecoulement tourbillonnant et tumultueux," *Mem. Presents par Diveers Savant Acad. Sci Fr.*, Vol. 23, pp. 46-50, 1897.

9. Barakos, G., Drikakis, D., and Leschziner, M., "Numerical Investigation of the Dynamic Stall Phenomenon Using Non-Linear Eddy-Viscosity Models," *AIAA-98-2740*, Applied Aerodynamics Conference, 16th, Albuquerque, NM, June 1998.

10. Ko, Sungho, and McCroskey, W. J., "Computations of Unsteady Separating Flows over an Oscillating Airfoil," *AIAA Journal*, Vol. 35, No. 7: Technical Notes, pp. 1235-1238, July 1997.

11. Wilcox, D., *Turbulence Modeling for CFD*, 2nd. Ed., DCW Industries, Inc., La Canada, CA, 2000.

12. Carr, L. W., Chandrasekhara, M. S., Broke, N. J., "A Quantitative Study of Unsteady Compressible Flow on an Oscillating Airfoil," *Journal of Aircraft*, Vol. 31, No. 4, pp. 892-898, July-August 1994.

13. Shih, C., Lourenco, L., Van Dommelen, L., and Krothapalli, A., "Unsteady Flow Past an Airfoil Pitching at a Constant Rate," *AIAA Journal*, Vol. 30, No. 5, pp. 1153-1161, May 1992.

14. Harper, W. Paul and Roy, E. Flanigan, "Investigation of the Variation of Maximum Lift for a Pitching Airplane Model and Comparison with Flight Results," *National Advisory Committee for Aeronautics*, Technical Note No. 1734, pp. 2-18, Washington 1948.

15. Carta, F.O., "Experimental Investigation of the Unsteady Aerodynamic Characteristics of a NACA 0012 Airfoil," *Res. Rep. M-1283-1*, United Aircraft Corp., July 1960.

16. Harris, F. D. and Pryun, R. R., "Blade Stal-Half Fact, Half Fiction," *Journal of the American Helicopter Society*, Vol. 13, No. 2, pp. 27-48, April 1968.

17. Ham, N. D. and Garelick, M. S., "Dynamic Stall Considerations in Helicopter Rotors," *Journal of the American Helicopter Society*, Vol. 13, No. 2, pp. 49-55, April 1968.

18. Ham, N. D., "Aerodynamic Loading on a Two-Dimensional Airfoil during Dynamic Stall," *AIAA Journal*, Vol. 6, pp. 1927-1934, October 1968.

19. Liiva, J. and Davenport, F. J., "Dynamic Stall of Airfoil Sections for High-Speed Rotors," *Journal of the American Helicopter Society*, Vol. 14, No. 2, pp. 26-33, April 1969.

20. McCroskey, W. J. and Fisher, R. K., "Detailed Aerodynamic Mesaurements on a Model Rotor in the Blade Stall Regime," *Journal of the American Helicopter Society*, Vol. 17, No. 1, pp. 20-30, January 1972.

21. Martin, J. M., Empey, R. W., McCroskey, W. J., and Caradonna, F. X., "AN Experimental Analysis of Dynamic Stall on an Oscillating Airfoil," *Journal of the American Helicopter Society*, Vol. 19, No. 1, pp. 26-32, 1974.

22. McCroskey, W. J., McAlister K. W., and Carr, L. W., "Dynamic Stall Experiments on Oscillating Airfoils," *AIAA Journal*, Vol. 14, pp. 57-63, January 1976.

23. Sankar, N. L., and Tassa, Y., "Compressibility Effects on Dynamic Stall of NACA 0012 Airfoil," *AIAA Journal*, Vol. 19, pp. 557-558, May 1981.

24. Lorber, P. F., and Carta, F. O., "Airfoil Dynamic Stall at Constant Pitch Rate and High Reynolds Number," *Journal of Aircraft*, Vol. 25, No. 6, pp. 548-556, January 1988.

25. Chandrasekhara, M. S., and Carr, L. W., "Flow Visualization Studies of the Mach Number Effects on Dynamic Stall of an Oscillating Airfoil," *Journal of Aircraft*, Vol. 27, No. 6, pp. 516-522, January 1990.

[26.] Carr, L. W., Platzer, M. F., Chandrasekhara, M. S., and Ekaterinaris, J., "Experimental and Computational Studies of Dynamic Stall," *Numerical and Physical Aspects of Aerodynamic Flows IV*, pp. 239-256, August 1990.

[27.] Wilder, M. C., Chandrasekhara, M. S., and Carr, L. W., "Transition Effects on Compressible Dynamic Stall of Transiently Pitching Airfoils," *AIAA Paper*, 93-2978, July 1993.

[28.] Knight, D., and Choudhuri, Ghosh, P., "2-D Unsteady Leading Edge Separation on a Pitching Airfoil," *AIAA Paper*, 93-2977, July 1993.

[29.] Niven, A. J. M., Galbraith, R. A., and David, G. F. H., "Analysis of Reattachment during Ramp Down Tests," *Vertica*, Vol. 13, No. 2, pp. 187-196, 1989.

[30.] Ahmed, S., and Chandrasekhara, M. S., "Reattachment Studies of an Oscillating Airfoil Dynamic Stall Flowfield," *AIAA Journal*, Vol. 32, No. 5, pp. 1006-1012, May 1994.

[31.] Chandrasekhara, M. S., Wilder, M. C., and Carr, L. W., "Boundary Layer Tripping Studies of Compressible Dynamic Stall Flow," *AIAA Journal*, Vol. 34, No. 1, pp. 96-103, January 1996.

[32.] Geissler, W., Carr, L. W., Chandrasekhara, M. S., Wilder, M. C., and Sobieczky, H., "Compressible Dynamic Stall Calculations Incorporating Transition Modeling for Variable Geometry Airfoils," *AIAA Paper*, 1997.

[33.] Chandrasekhara, M. S., Wilder, M. C., and Carr, L. W., "Competing Mechanisms of Compressible Dynamic Stall," *AIAA Journal*, Vol. 36, No. 3, pp. 387-393, March 1998.

[34.] Chandrasekhara, M. S., Wilder, M. C., and Carr, L. W., "Compressible Dynamic Stall Control Using Dynamic Shape Adaptation," *AIAA Journal*, Vol. 39, No. 10, Technical Notes, pp. 2021-2024, June 2001.

[35.] Greenblatt, D., Nishri, B., Darabi, A, and Wygnanski, I, "Some Factors Affecting Stall Control with Particular Emphasis on Dynamic Stall," *AIAA Paper* 99-3504, July 1999.

[36.] Chandrasekhara, M. S., Wilder, M. C., and Carr, L. W., "Compressible Dynamic Stall Control: Comparison of Two Approaches," *Journal of Aircraft*, Vol. 38, No. 3, pp. 448-453, 2001.

[37.] Greenblatt, D., Nishri, B., Darabi, A., and Wygnanski, I., "Dynamic Stall Control by Periodic Excitation, Part 2: Mechanisms," *Journal of Aircraft*, Vol. 38, No. 3, pp. 439-447, May 2001.

[38.] Carr, L. W., Chandrasekhara, M. S., Wilder, L. W., and Noonan, K. W., "Effect of Compressibility on Suppression of Dynamic Stall Using a Slotted Airfoil," *Journal of Aircraft*, Vol. 38, No. 2, pp. 296-309, March 2001.

[39.] Norton, D., and Noak, R., "A Two-Dimensional Flow Insert for the TAMU 7 x 10' LSWT," *TAMU Aerospace Engineering Report for Test 8101 for Bell Helicopter*, January 1981.

[40.] McCroskey, W., McAlister, K., Carr, L., and Pucci, S., "An Experimental Study of Dynamic Stall on Advanced Airfoil Sections," Vol. 2 Pressure and Force Data, *NASA TM-84245*, July 1982.

[41.] dPIV, 32-bit PIV Analysis Code, Software Package, Ver. 2.1, Innovative Scientific Solutions Inc., Dayton, OH, 2005.

42. Bowersox, R., "Turbulent Flow Structure Characterization of Angled Injection into a Supersonic Crossflow," *J. of Spacecraft and Rockets*, Vol. 34, No. 2, 1997.

43. Schetz, J., *Boundary Layer Analysis*, Prentice Hall Inc., 1993.

44. T. L. Doligalski, C. R. Smith, and J. D. A. Walker, "Vortex Interactions with Walls," *Annu. Rev. Fluid. Mech.*, Vol. 26, pp. 573 – 616, 1994.

45. Kiedaisch, J., and Acharya, M., "Investigation of Incipient Dynamic Stall Over Pitching Airfoils Using Hot-Film Sensors," *AIAA Paper*, 1997.

46. Benedict, L.H., and Gould, R. D., "Towards Better Unsteady Estimates For Turbulence Statistics," *Experiments in Fluids*, Vol. 22, pp. 129 – 136, 1996.

47. Menon, R., and Lai, Wing., "Key Considerations in the Selection of Seed Particles for LDV Measurements," *Fourth International Conference on Laser Anemometry*, Cleveland, OH, Aug. 1991.

Supplemental Sources Consulted

Abbott, H.I., and Doenhoff, V.E. Albert, *Theory of Wing Sections*, Dover Publication, Inc., New York, 1949.

Carr, L., *Personal Conversation*, June 2002.

Ekoto, I., "Supersonic Turbulent Boundary Layers With Periodic Mechanical Non-Equilibrium," PhD Dissertation, Texas A&M University, December, 2006.

Glezer, A., "Fluidic Virtual Aerosurfaces for Flow Control Applications," *AFOSR 2002 Contractor's Meeting in Turbulence and Rotating Flows*, Fort Worth, TX, August 2002.

Katz, J., and Meneveau, C., "Measurement and Modeling of Turbulence and Complex Flow Phenomena in Multi-stage Axial Turbomachines," *AFOSR 2002 Contractor's Meeting in Turbulence and Rotating Flows*, Fort Worth TX, August 2002.

Martin, P.B., McAlister, K.W., Chandrasekhara, M.S., and Geissler, W., "Dynamic Stall Measurements and Computations for a VR-12 Airfoil with a Variable Droop Leading Edge," presented at the AHS Forum 59, Phoenix, AZ, May 6-8, 2003.

McCroskey, W., *Personal Conversation*, June 2002.

Pope, A., *Wind Tunnel Testing*, *2nd. Ed.*, John Wiley and Sons Publications, New York, 1954.

Raffel, M., Willert, E.C., and Kompenhans, J., *Particle Image Velocimetry - A Practical Guide*, Springer Publications, Berlin, 1998.

Reynolds, O., "On the Dynamical Theory of Incompressible Viscous Fluids and the Determination of the Criterion," *Phil. Trans. Roy. Soc. London Ser. A*, Vol. 186, pp. 123-164, 1895.

Tennekes, H., Lumley, J., *A First Course in Turbulence*, MIT Press, Cambridge, MA, 1972.

White, F., *Viscous Fluid Flow*, *2nd. Ed.*, McGraw Hill Publications, Boston, 2001.

APPENDIX A

FIGURES AND TABLES

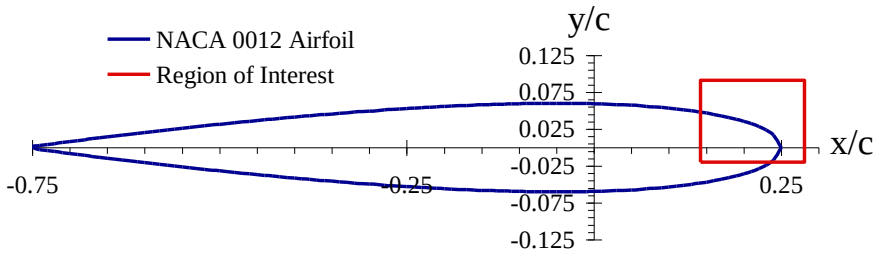

Figure 1: Wing region of interest and coordinate system

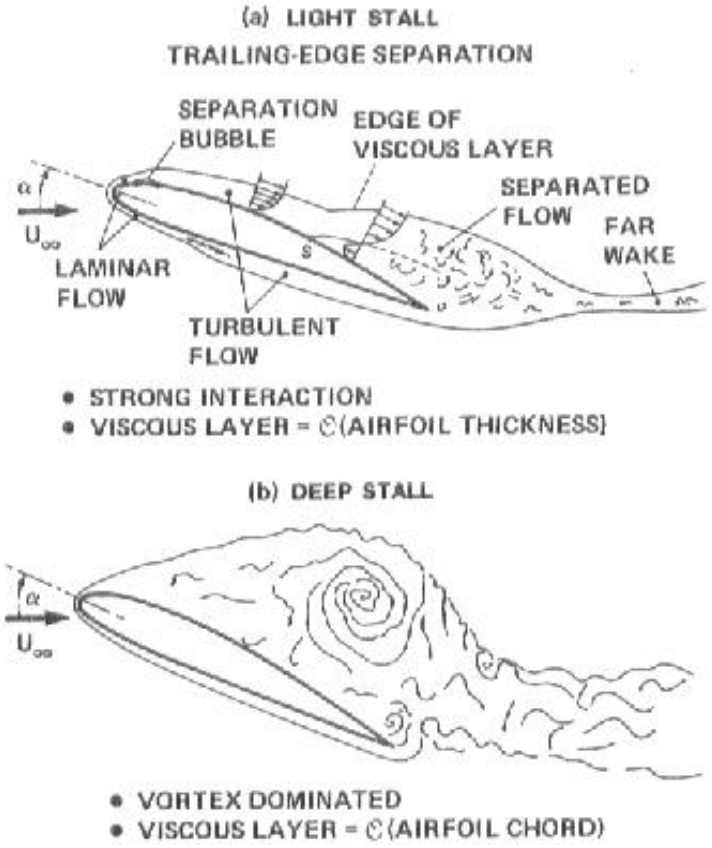

Figure 2: Light and deep dynamic stall flow

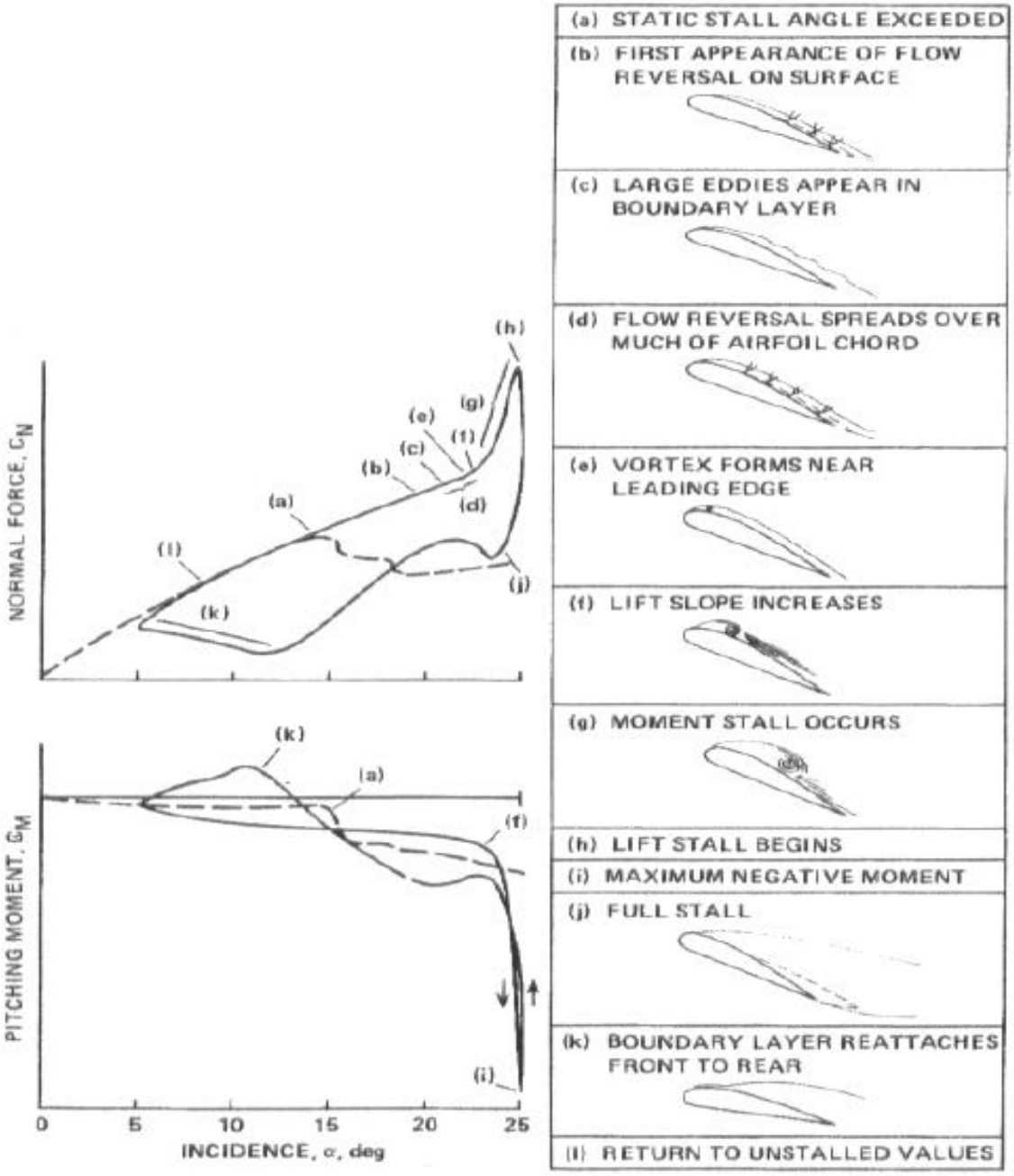

Figure 3: Process of deep dynamic stall on a NACA features [McCroskey[1]]

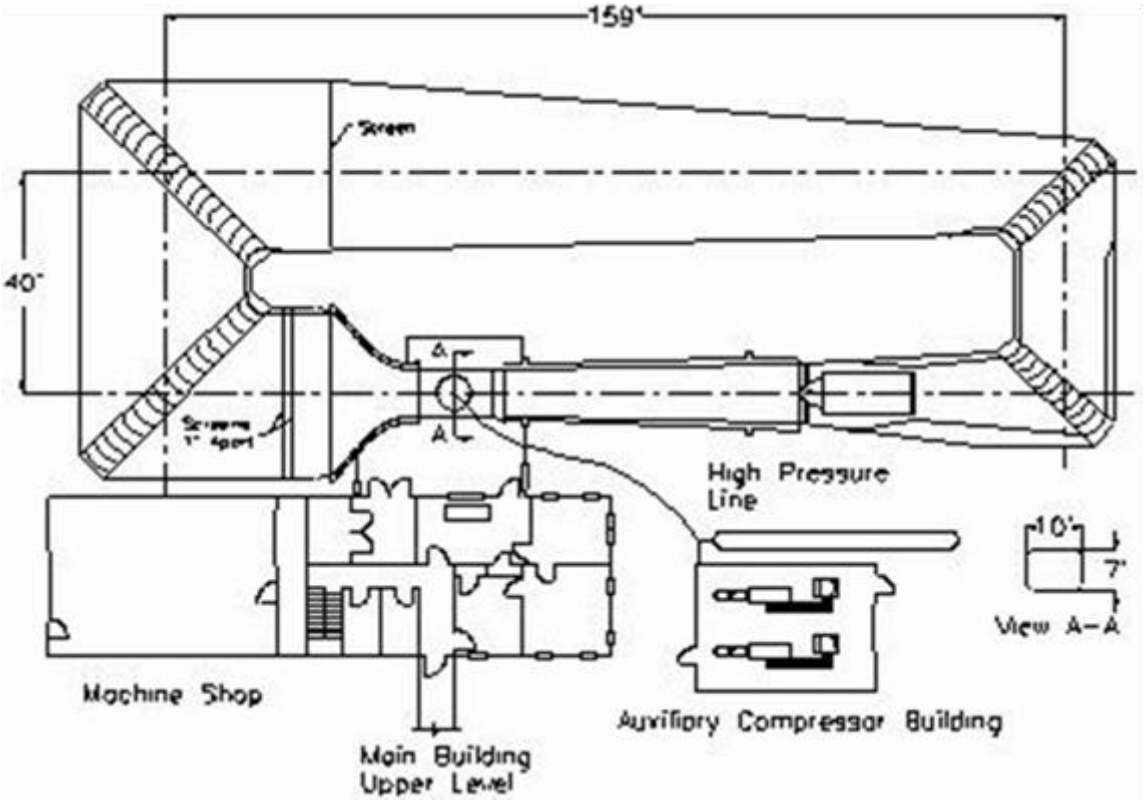

a) Schematic of the wind tunnel

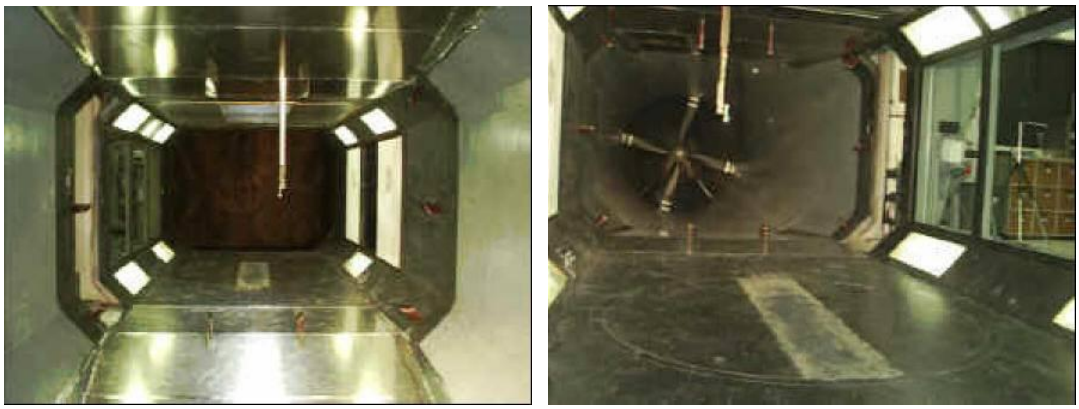

b) Upstream and downstream view of test section

Figure 4: Photographs of the Oran W. Nicks wind tunnel.

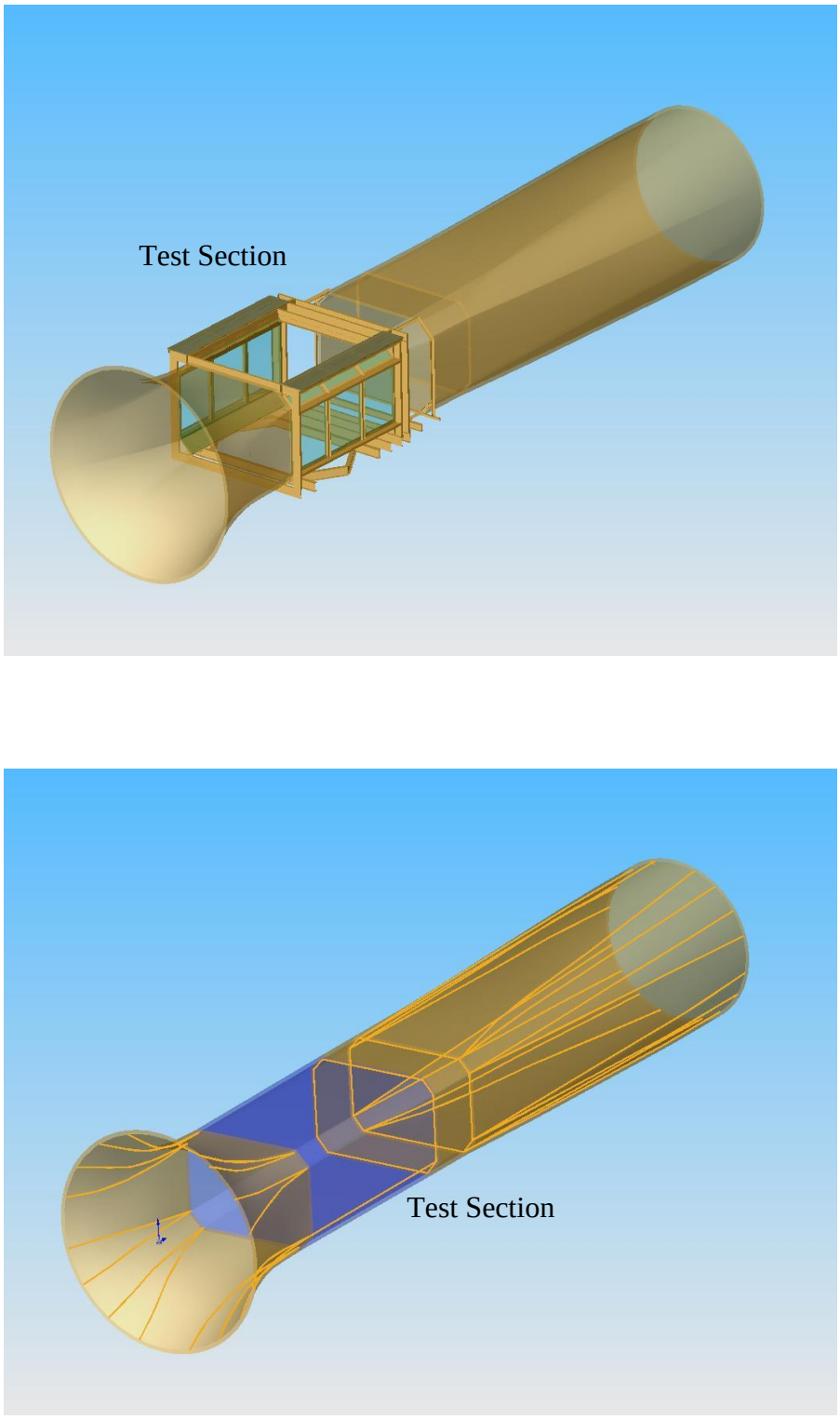

Figure 5: Drawings of the Oran W. Nicks wind tunnel

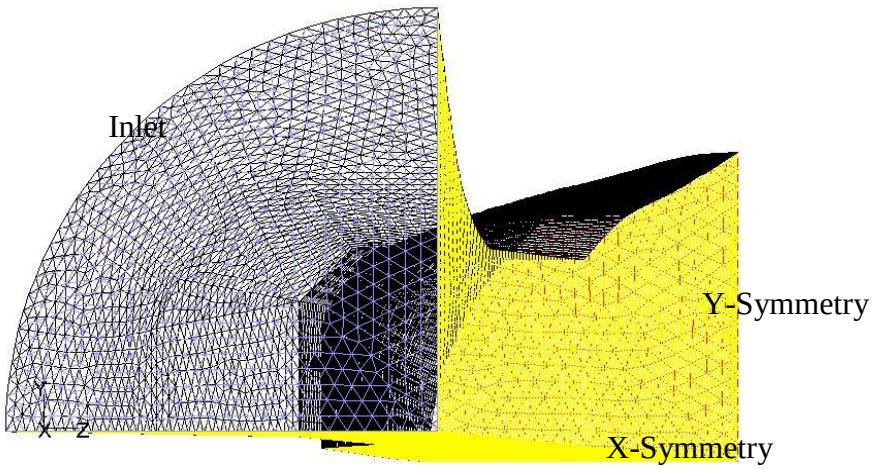

Figure 6: Grid of the Oran W. Nicks wind tunnel

(a) Floor

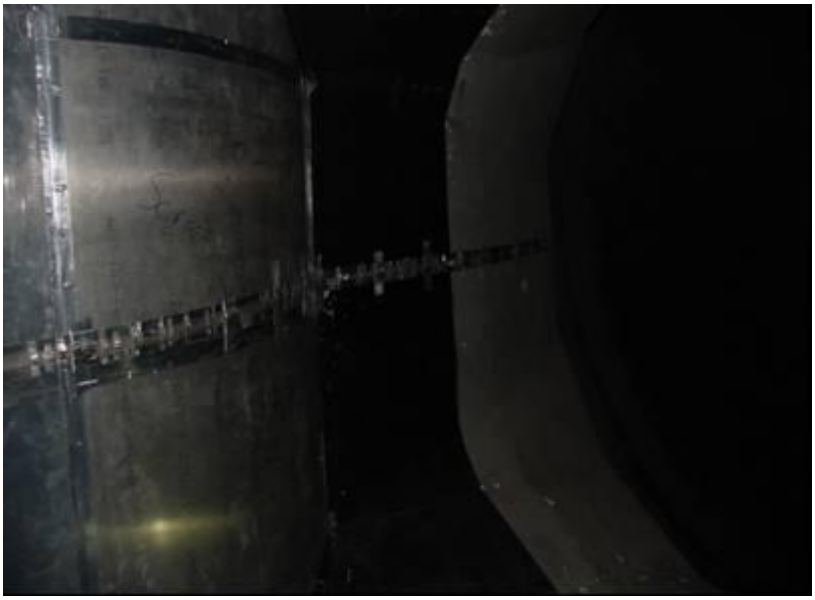

(b) Wall

Figure 7: Vinyl tubes taped to the wind tunnel

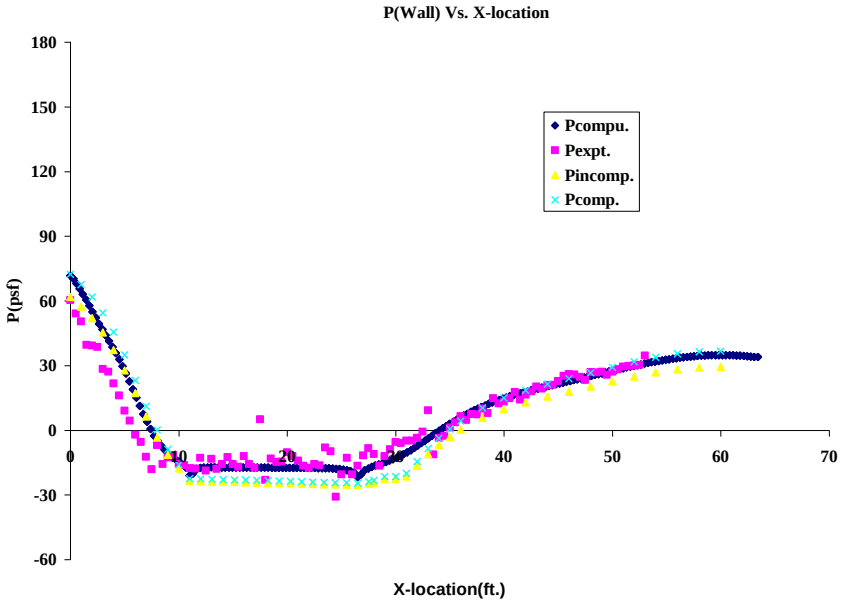

Figure 8: Comparison of pressure data on the wall (7 ft x 10 ft)

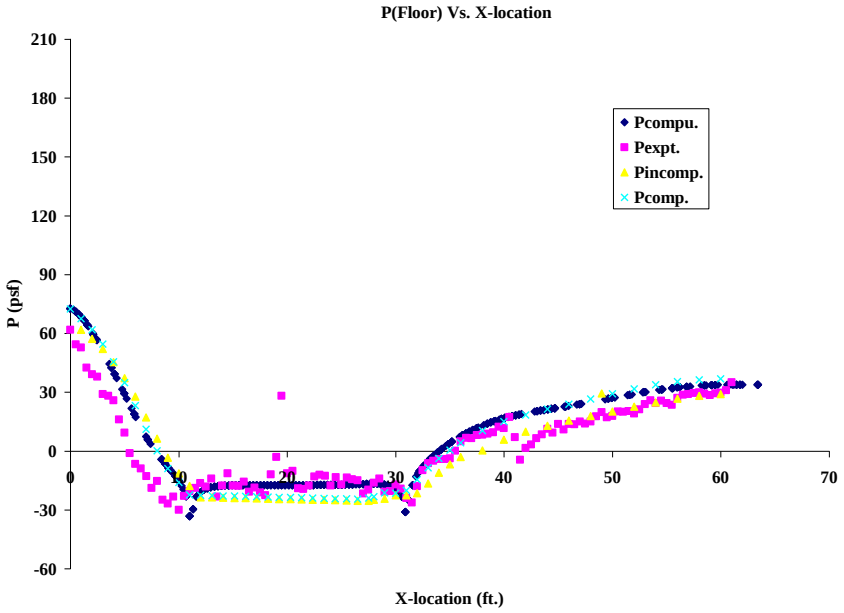

Figure 9: Comparison of pressure data on the floor (7 ft x 10 ft)

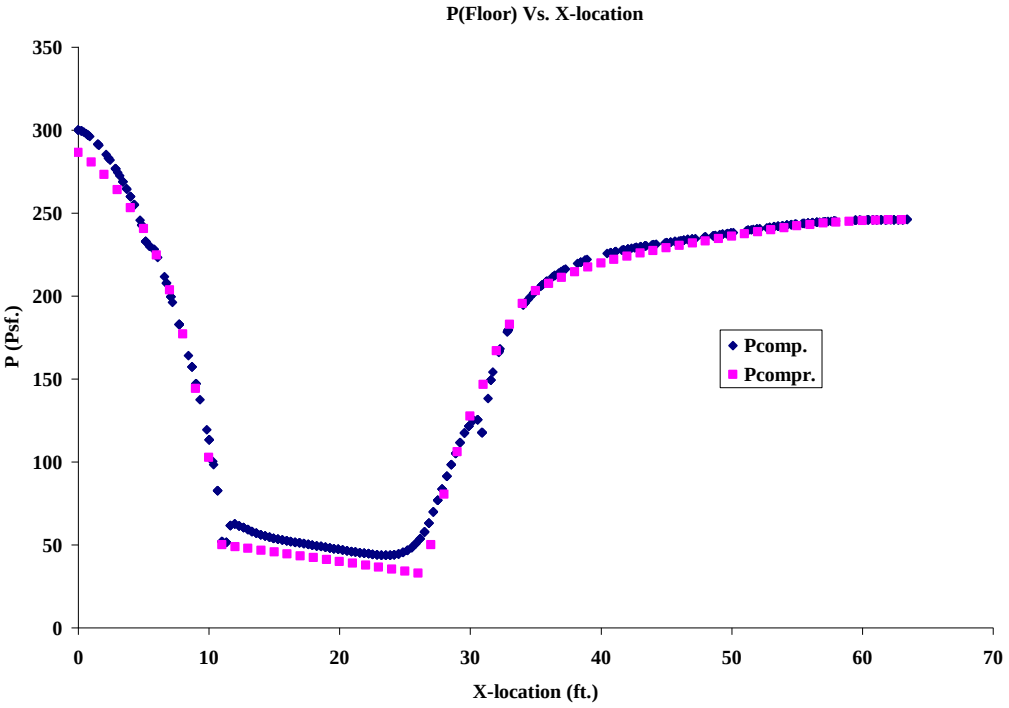

Figure 10: Pressure on the 7 ft x 7ft tunnel floor

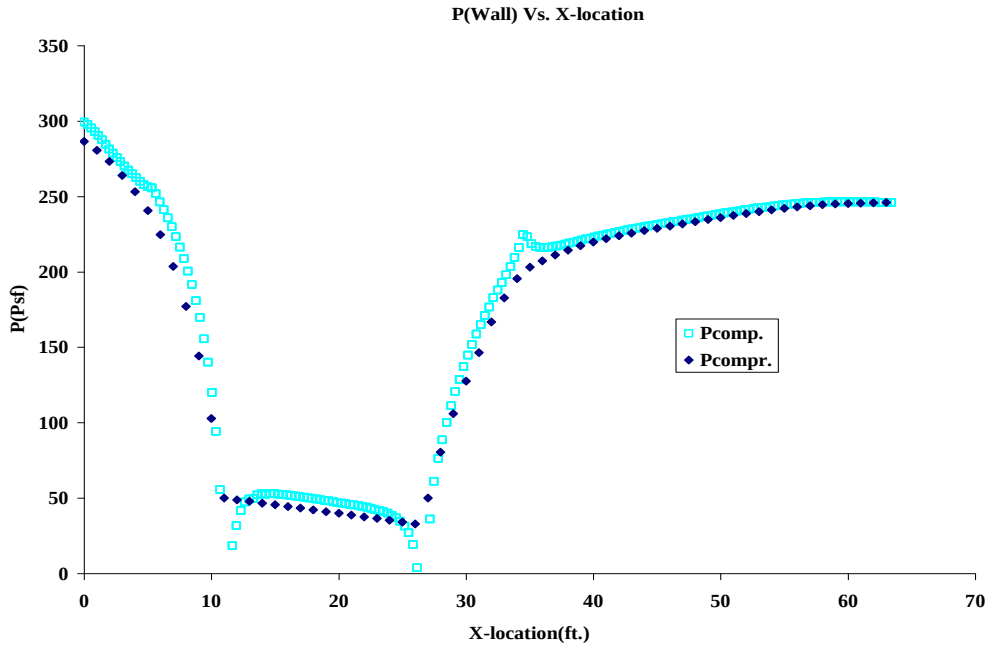

Figure 11: Pressure on the 7 ft x 7ft tunnel wall

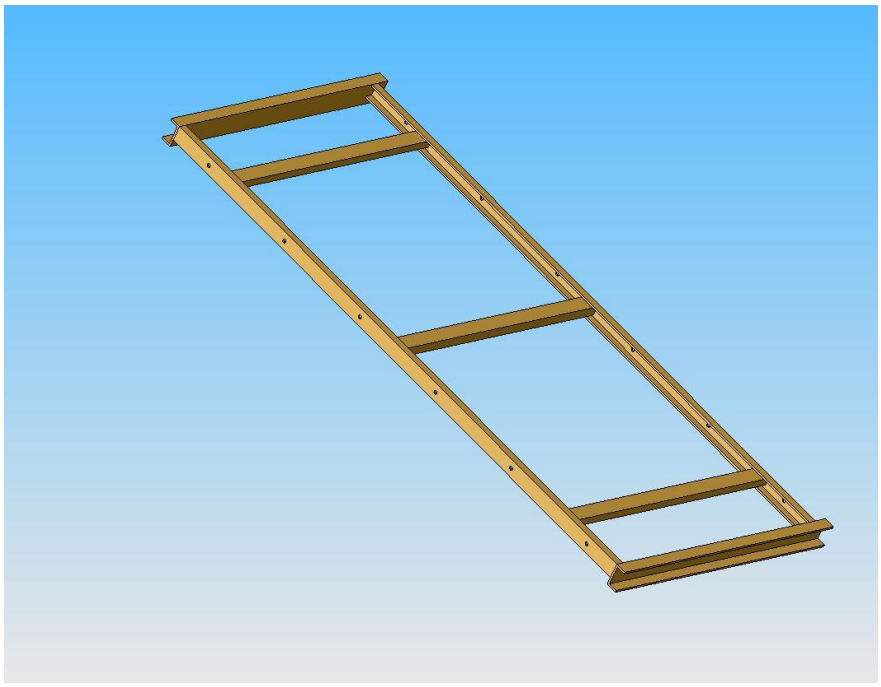

Figure 12: Drawing of wall panel support

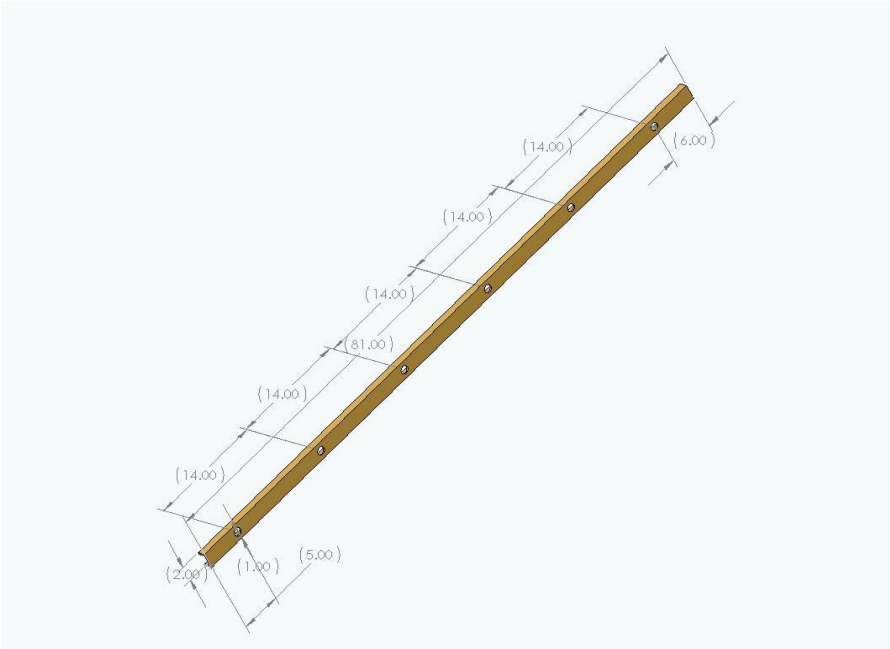

(a) 2 in. x 1 in. C-channel

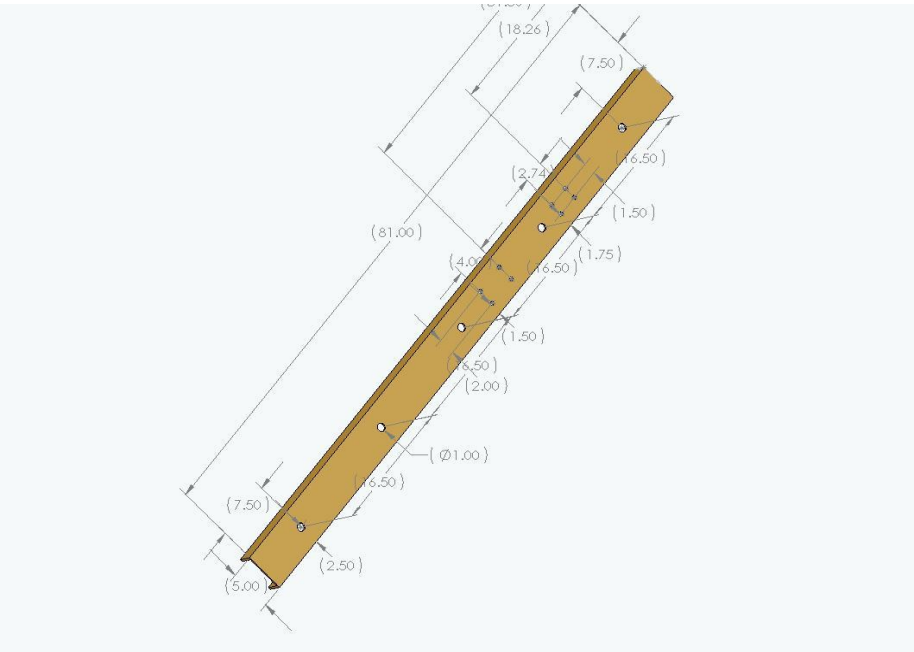

(b) 5 in. x 1.75 in. C-channel

Figure 13: Hole patterns in C-channels

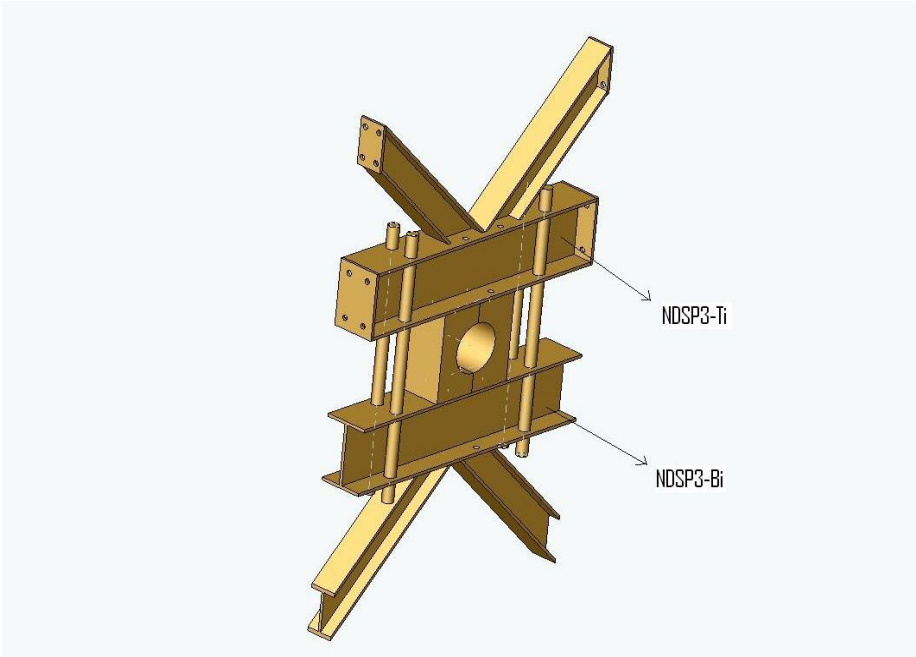

Figure 14: Wing Support structure

Figure 15: Shaft of the wing going through the bearing housing

Figure 16: Additional structures from inside of the modified wind tunnel

Figure 17: Glass windows, structures to hold wing, vent and door on left wall

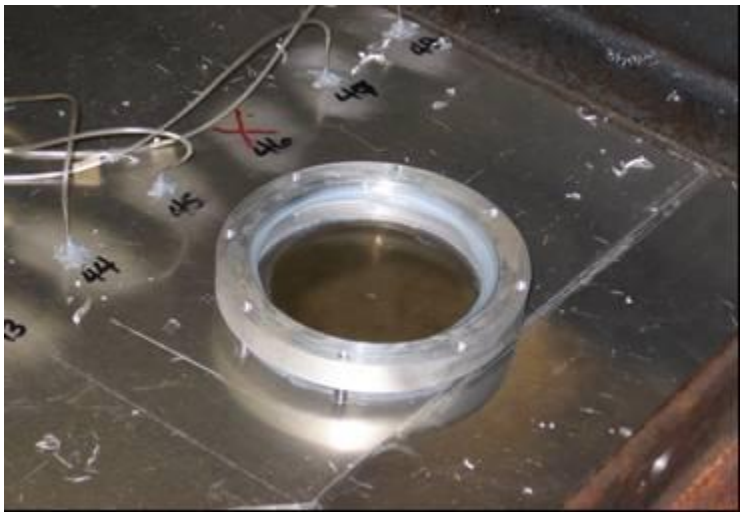

Figure 18: Optical glass windows for 2D PIV experiment

Figure 19: Optical glass window with the camera acquiring images

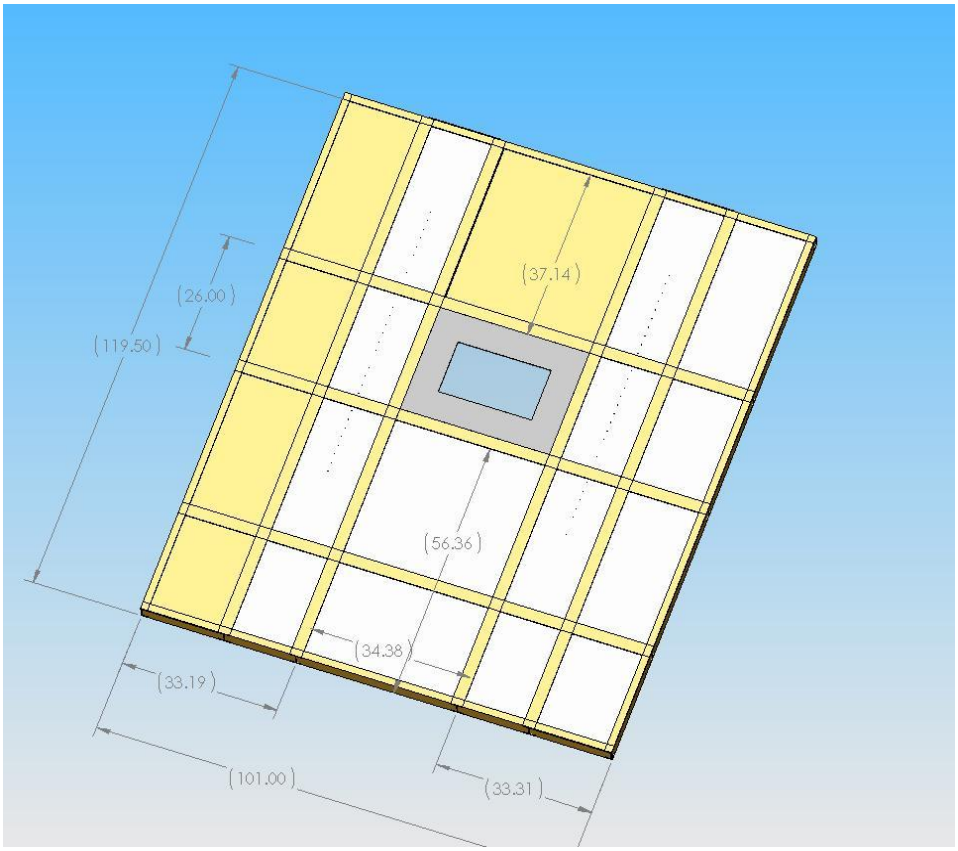

Figure 20: Design of the roof

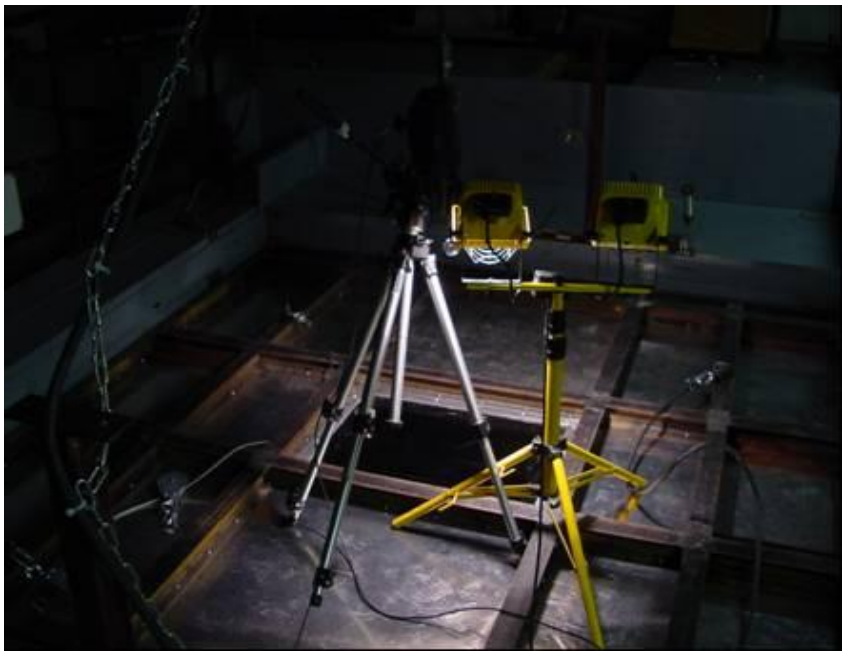

Figure 21: Roof with the plexiglas window

Figure 22: Card board used to define the shape of inlet

Figure 23: Curved steel frame of the inlet

Figure 24: Curved aluminum sheet screwed to steel frame

Figure 25: Steel frame of inlet screwed to the concrete

Figure 26: Inlet section of the modified wind tunnel

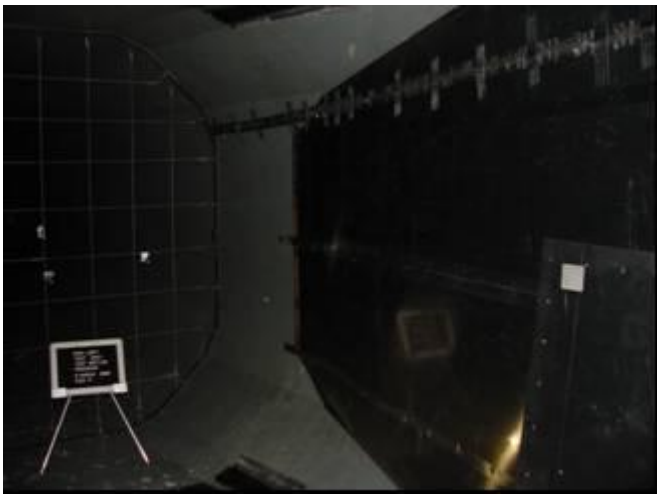

Figure 27: Left diffuser wall of the modified wind tunnel

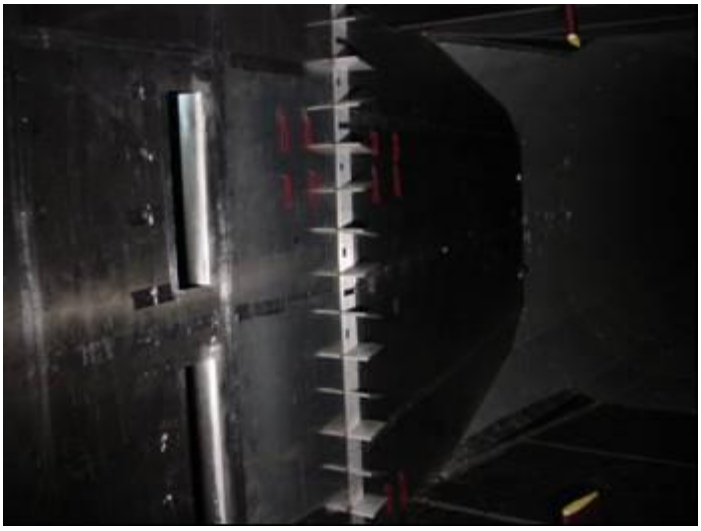

Figure 28: Vortex generators

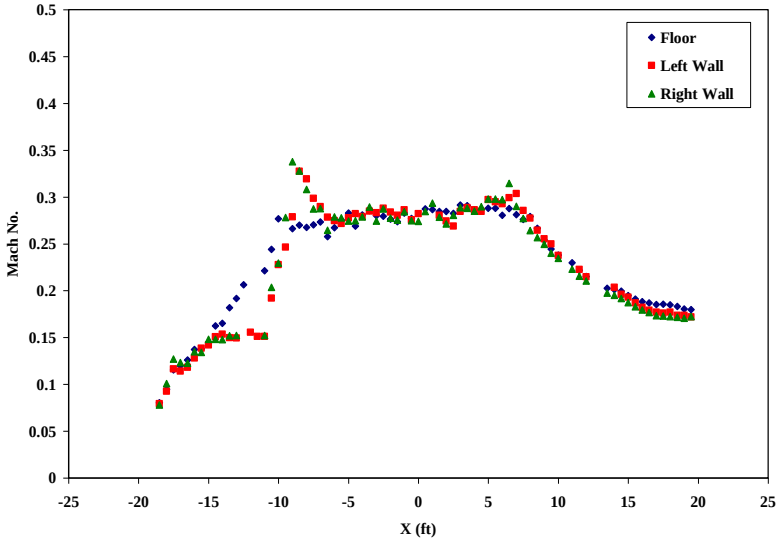

(a) Mach number

Figure 29: Calibration of modified test section

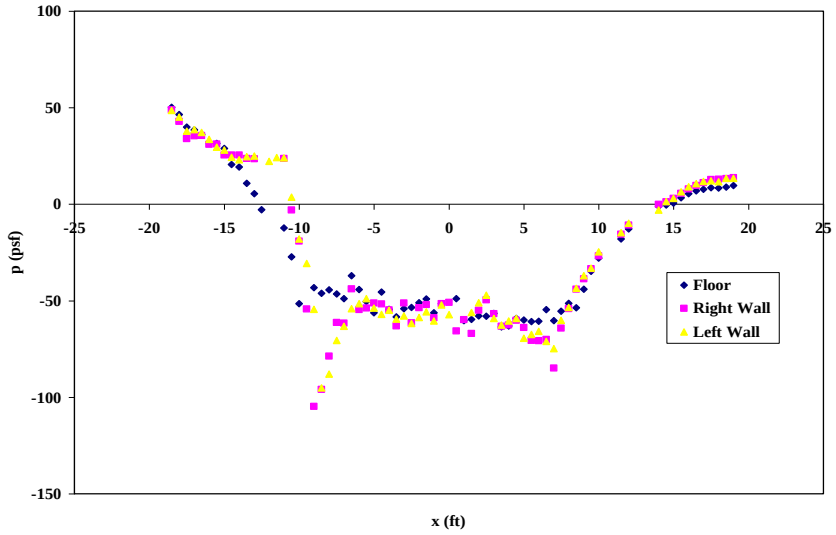

(b) Static pressure

Figure 29: Continued

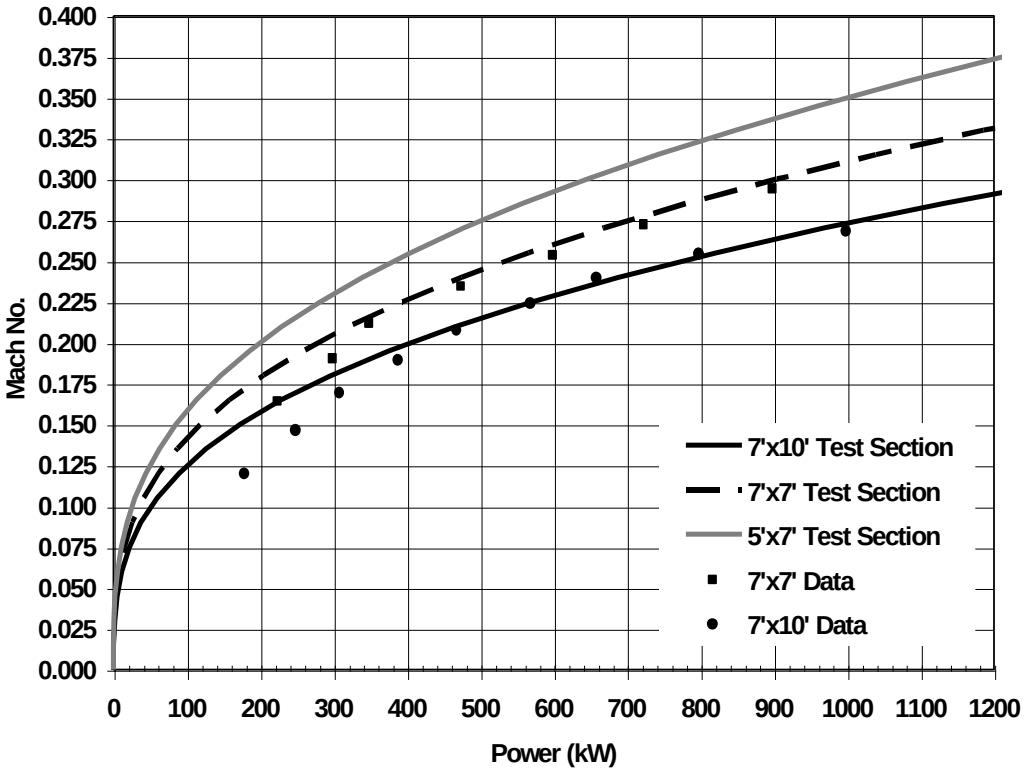

Figure 30: Power requirement calculations

Figure 31: 3 in x 3 in C-channels bolted to the steel frame of 7 ft x 7 ft wind tunnel

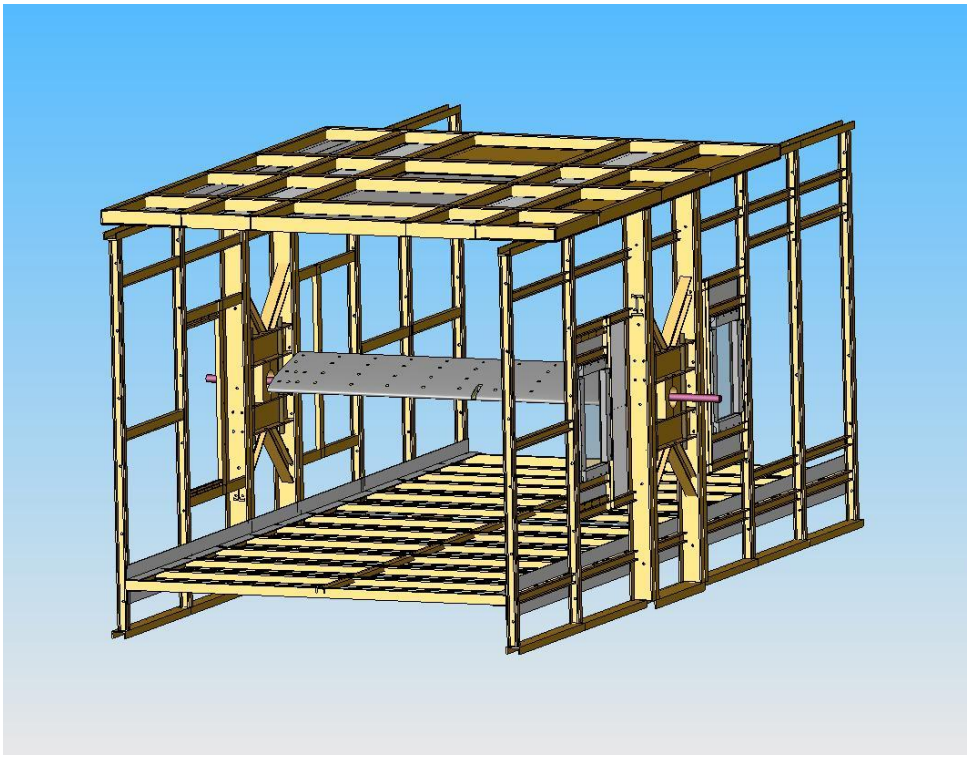

Figure 32: SolidWorks drawing of floor of the 5 ft x 7 ft test section

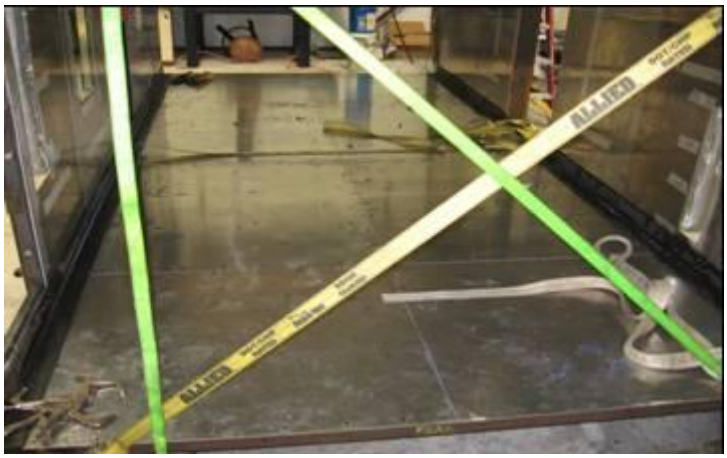

Figure 33: Floor of the 5 ft x 7 ft test section
(Straps were used ensure the facility angles were true)

Figure 34: Roof of the 5 ft x 7 ft test section

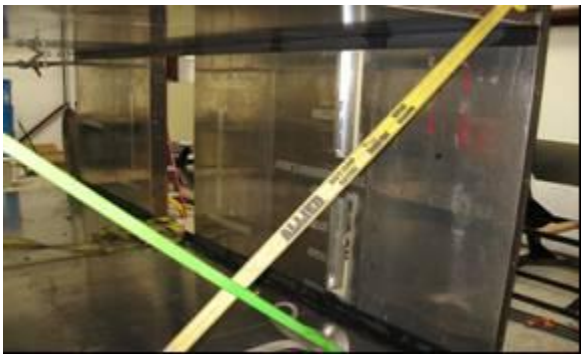

Figure 35: Right side view of the 5 ft x 7 ft test section

Figure 36: Left side view of the 5 ft x 7 ft test section

Figure 37: Left wall of the test section with frames

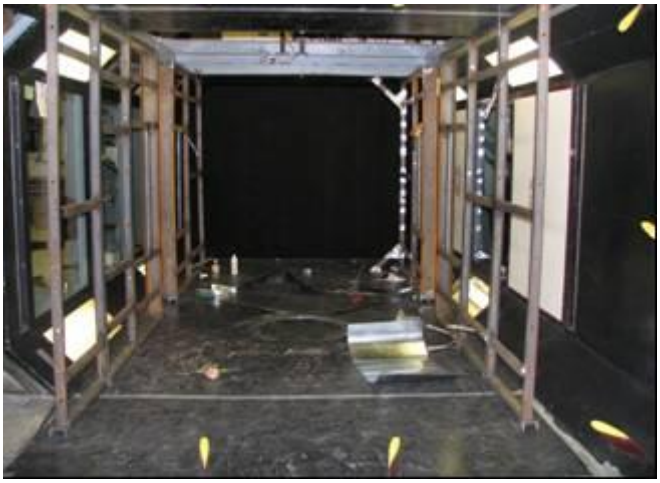

Figure 38: Left and right wall of the test section with frames

Figure 39: Right wall of the test section with aluminum sheet

Figure 40: Roof of the test section with glass window

Figure 41: View of the wind tunnel inserts from stilling chamber

Figure 42: View of the wind tunnel from the ready room

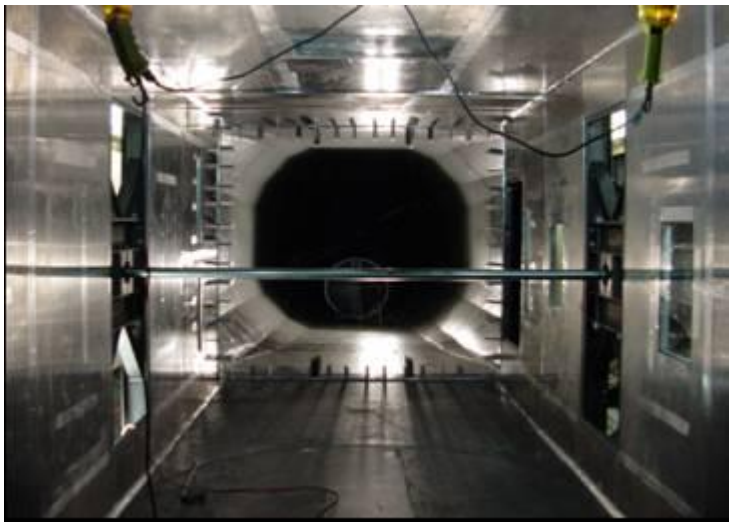

Figure 43: View of the 7ft x 7ft tunnel

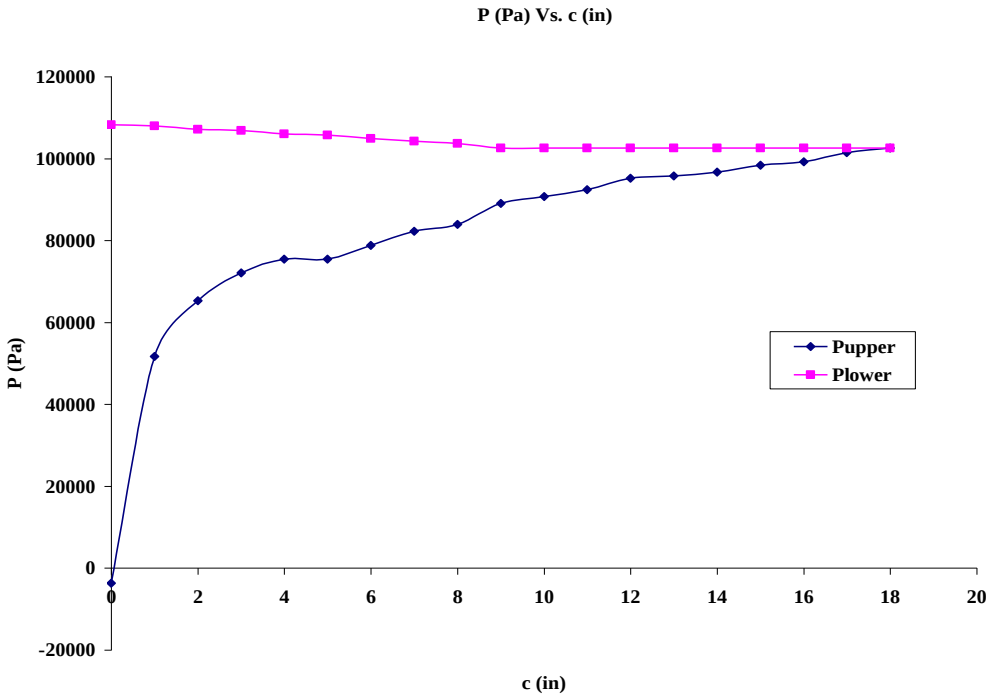

Figure 44: Loading condition applied to the wing in ABAQUS

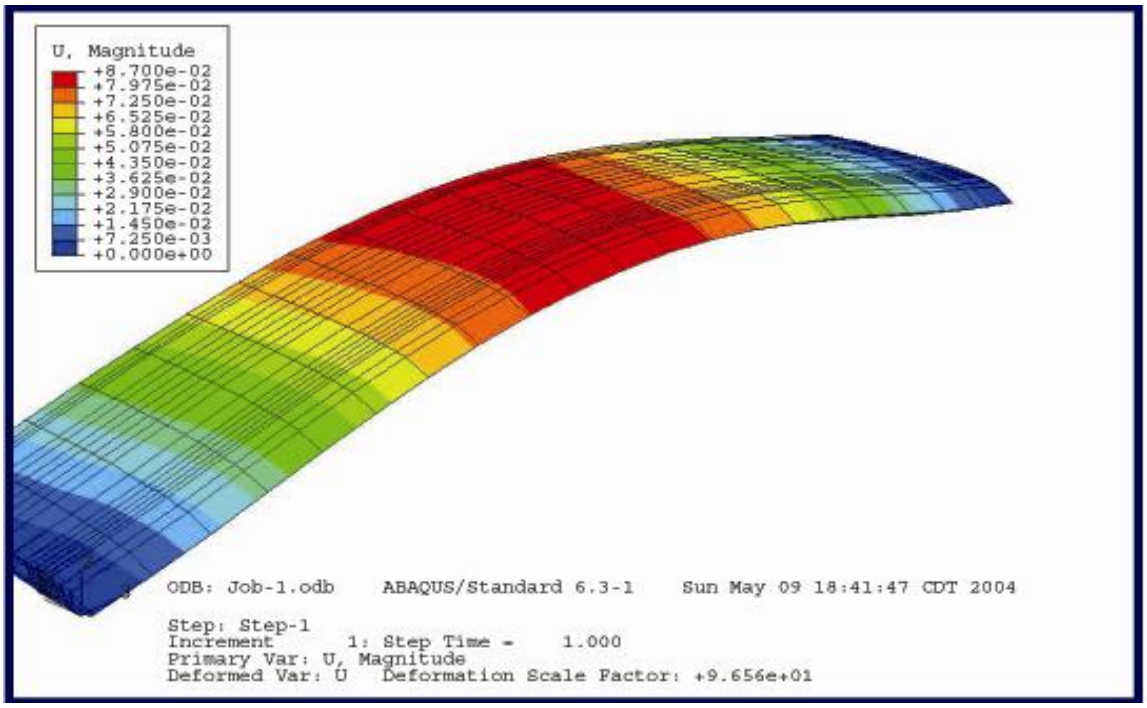

Figure 45: Contour plot of deflection analysis on the wing using ABAQUS

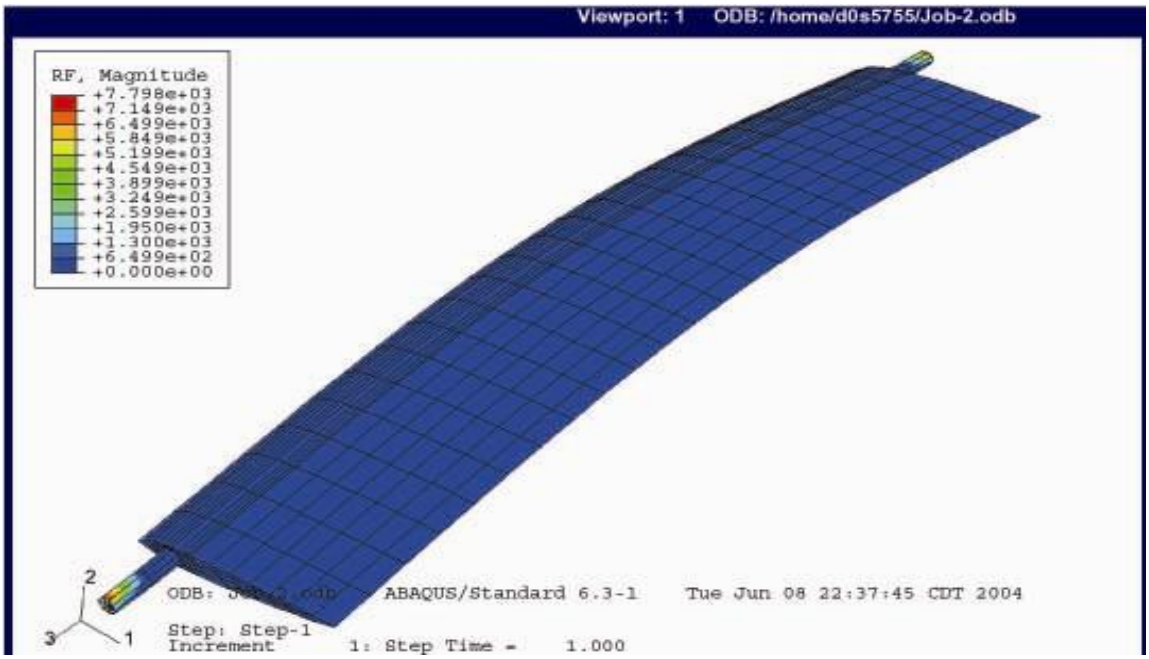

Figure 46: Contour plot of reaction force analysis on the wing using ABAQUS

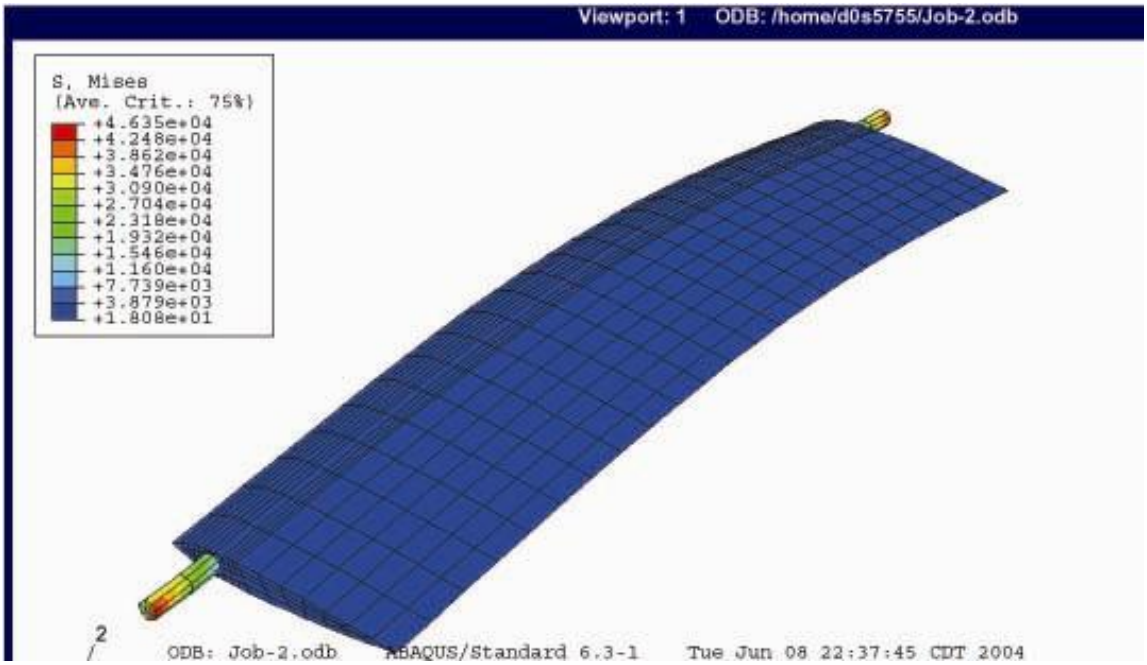

Figure 47: Contour plot of stress analysis on the wing using ABAQUS

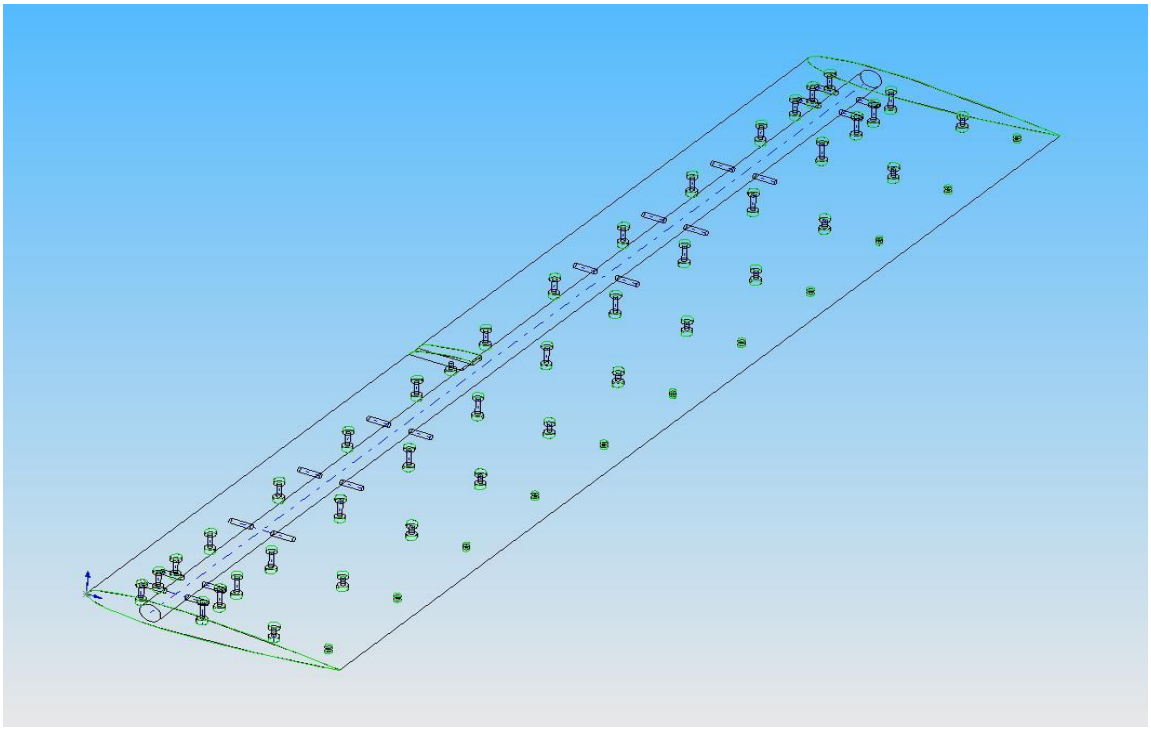

Figure 48: Detail drawing of the wing with screws and dowel pins

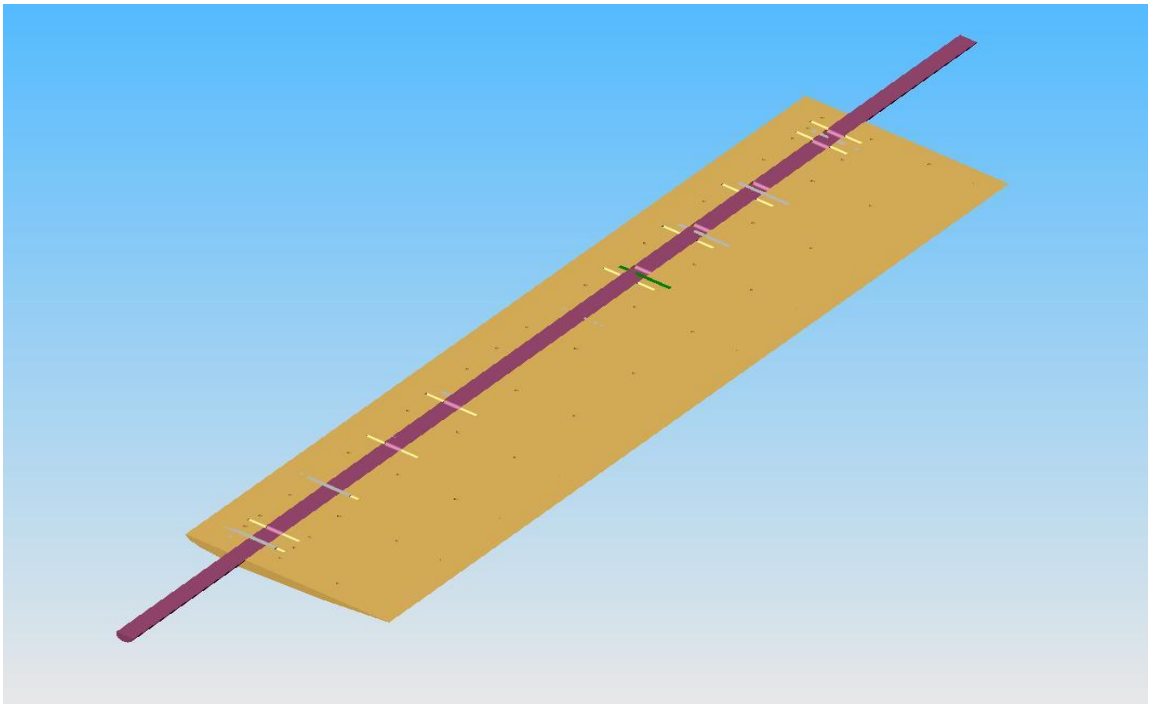

Figure 49: Cross sectional drawing of bottom half of the wing

Figure 50: NACA 0012 model (Plexiglas insert: mid-span at the leading edge)

Figure 51: Hydraulic drive system reservoir

Figure 52: Accumulator with servo valve

Figure 53: Hydraulic actuator with hoses

Figure 54: Actuator and the moment arm

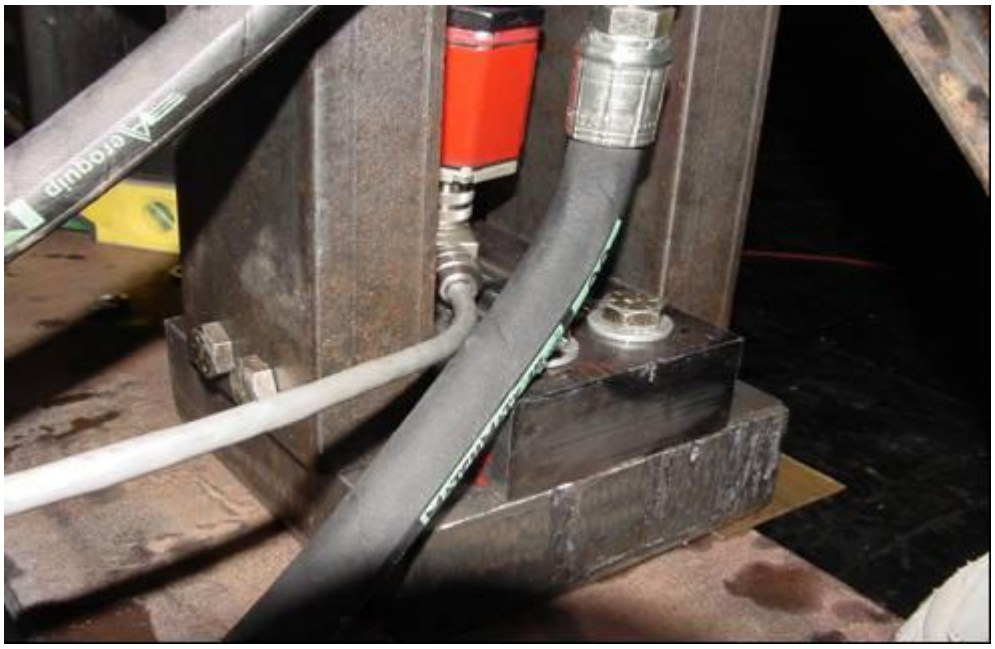

Figure 55: Linear position sensor attached to the hydraulic actuator

Figure 56: Stand to hold the wing during synchronization testing

Figure 57: Stand holding the pitching wing

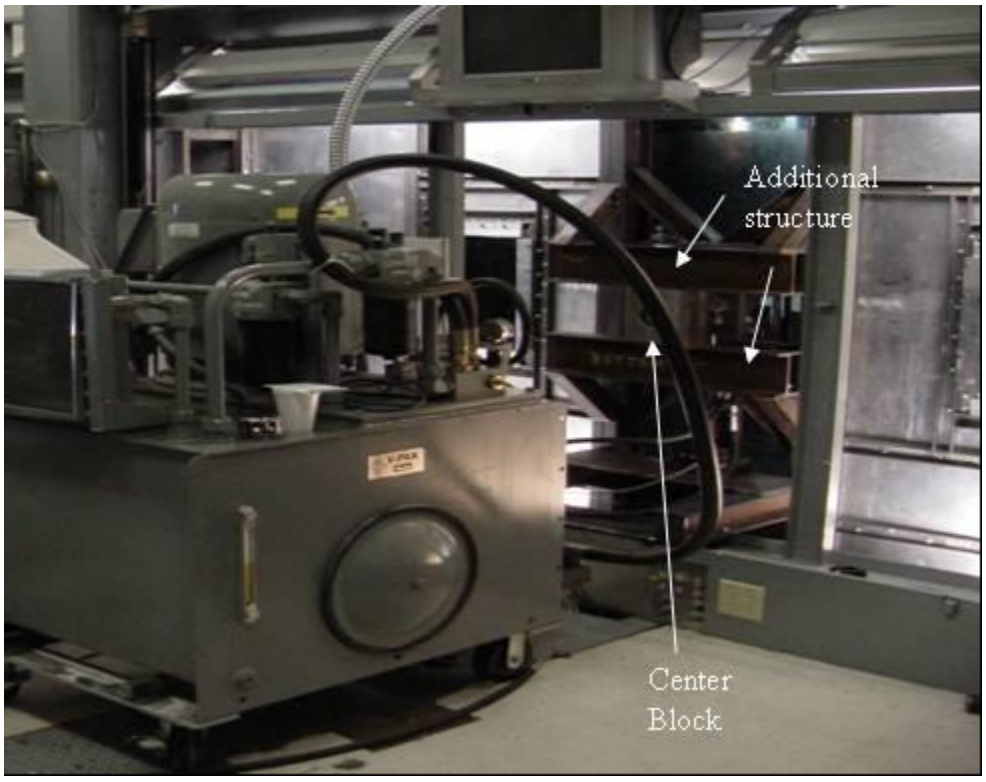

Figure 58: Structures to reduce vibration

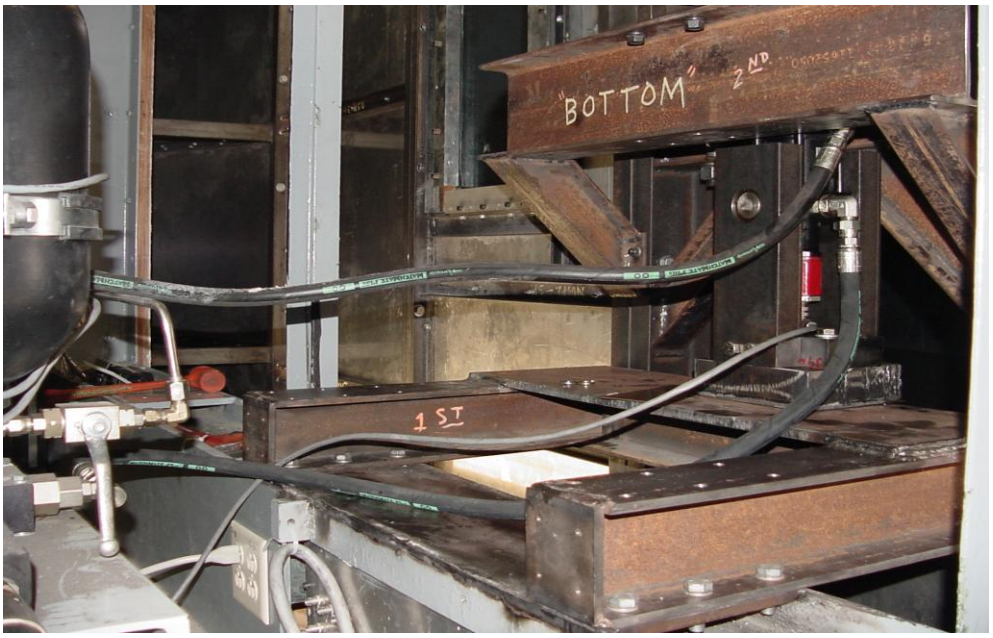

Figure 59: Structure to support the actuator and transfer the load

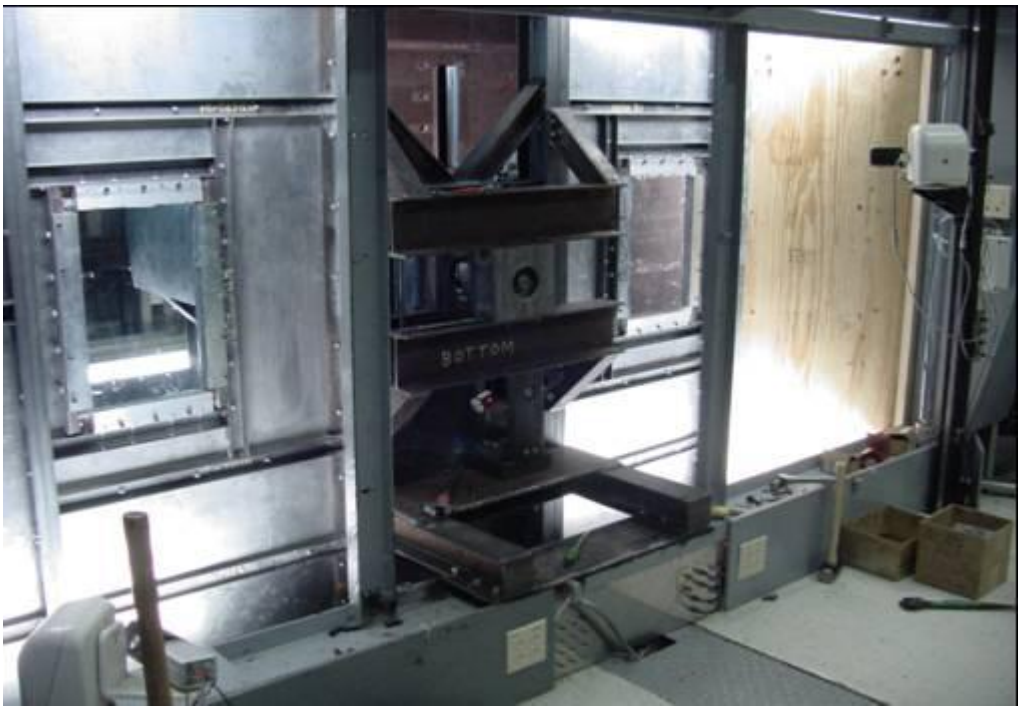

Figure 60: Wing vibration and load support structures in-place

Figure 61: Image of the hydraulic actuator drive system

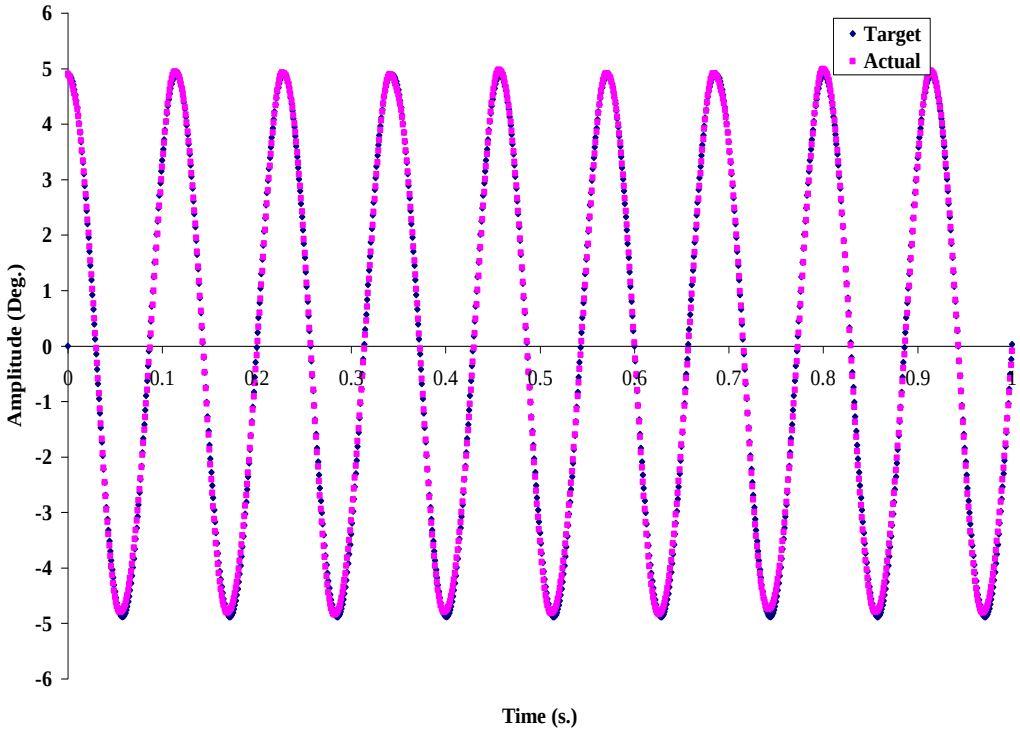

Figure 62: Plot of pitching of the wing following sine function

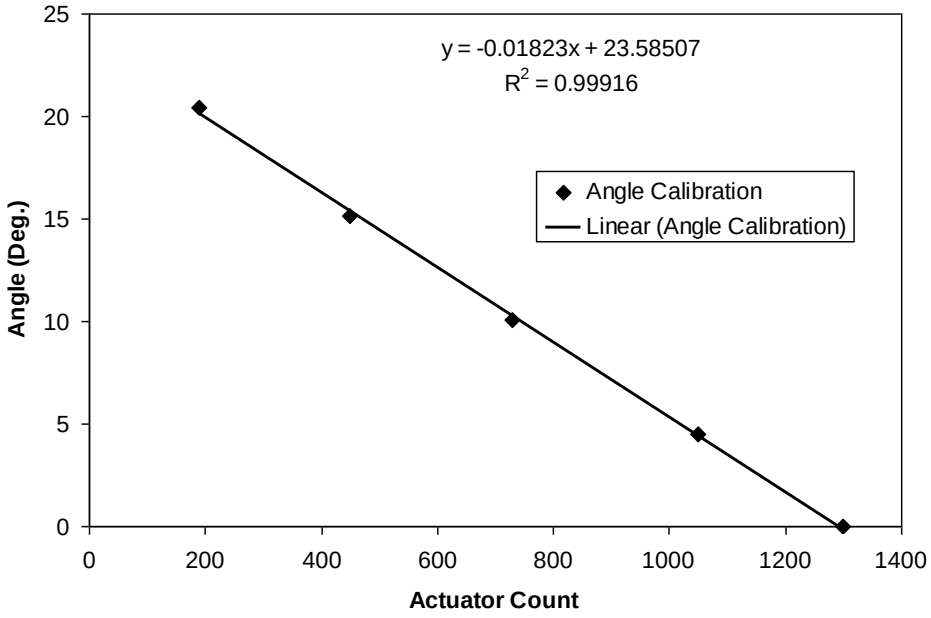

Figure 63: Example wing angle-of-attack calibration

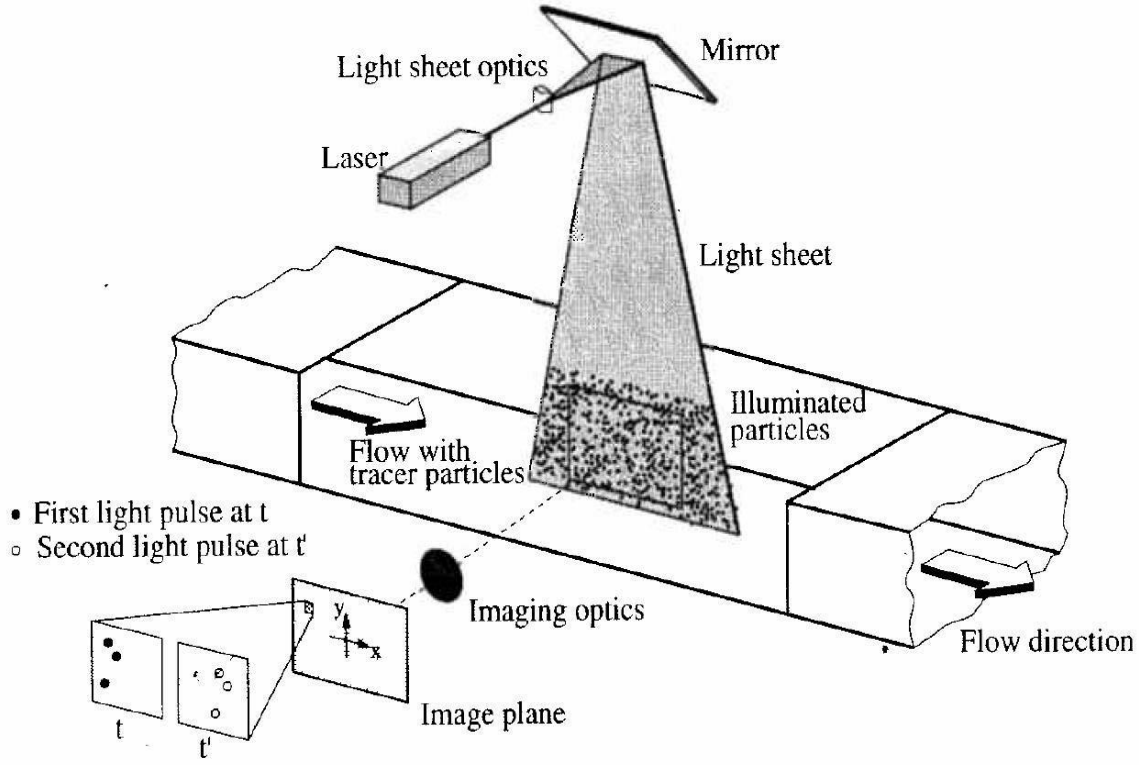

Figure 64: Experimental arrangement of PIV in wind tunnel

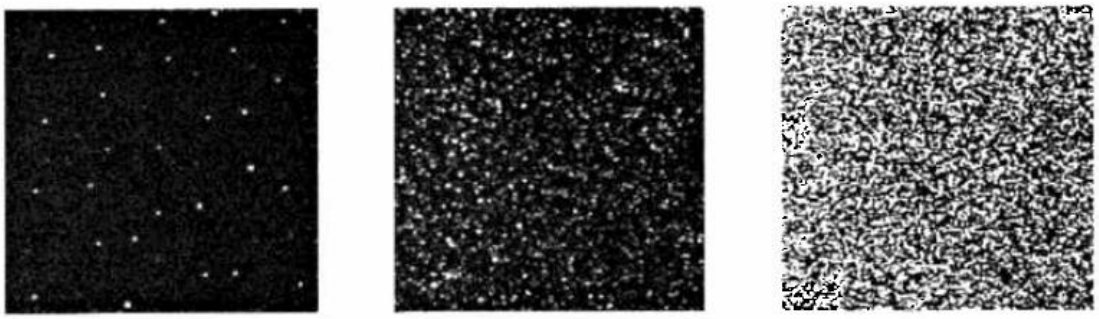

(a) low (PTV) **(b) medium (PIV)** **(c) high (LSV)**

Figure 65: The three modes of particle image density

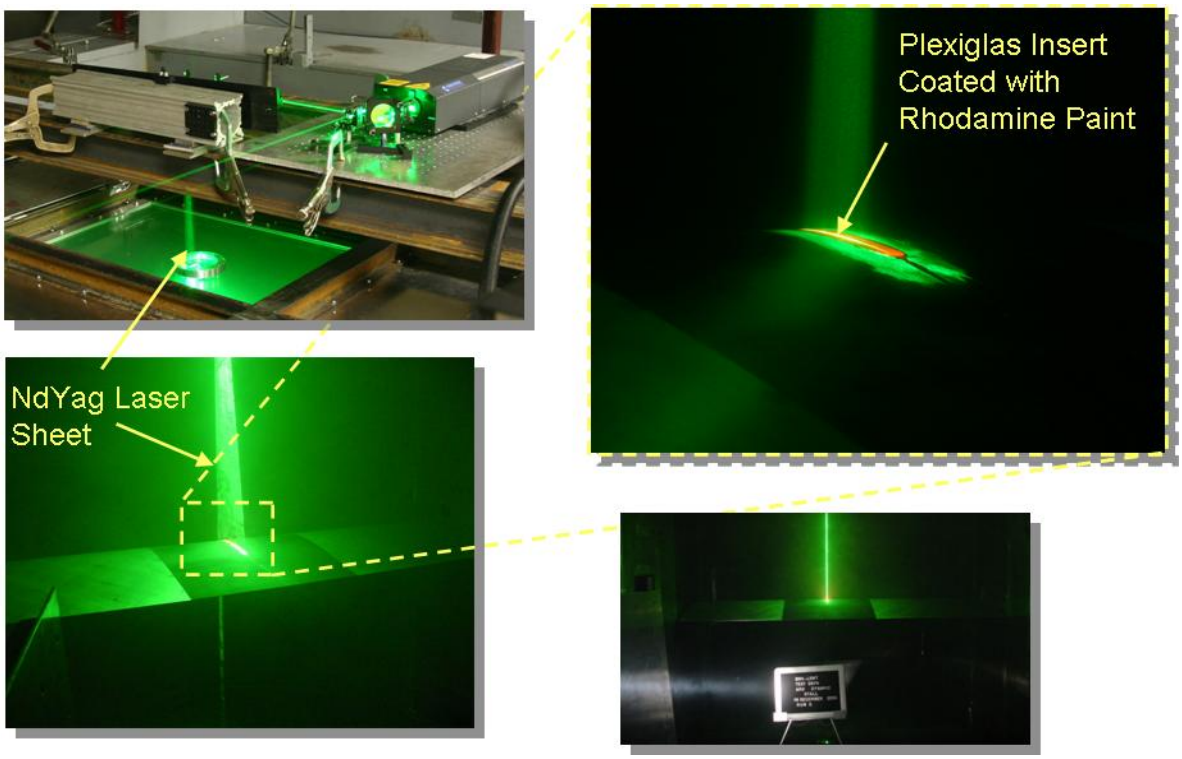

Figure 66: Experimental setup for the laser and the optics

Figure 67: H-shaped stand to support the camera

Figure 68: Experimental setup for the camera

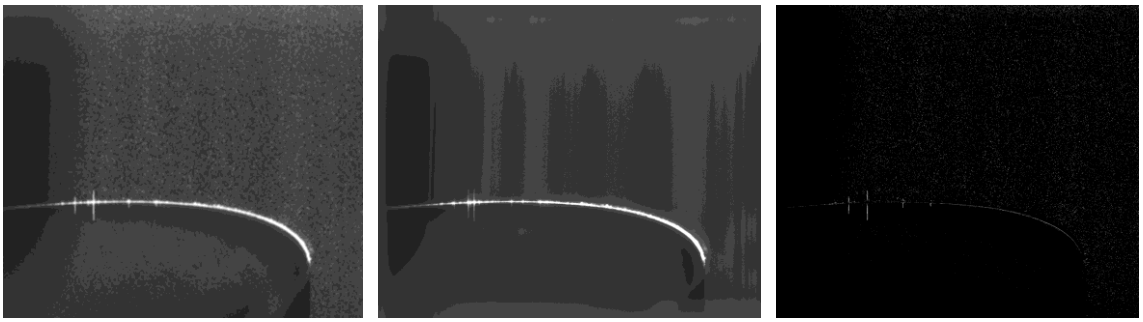

(a) Original Image **(b) Averaged Image** **(c) Subtracted Image**

Figure 69: Image processing steps

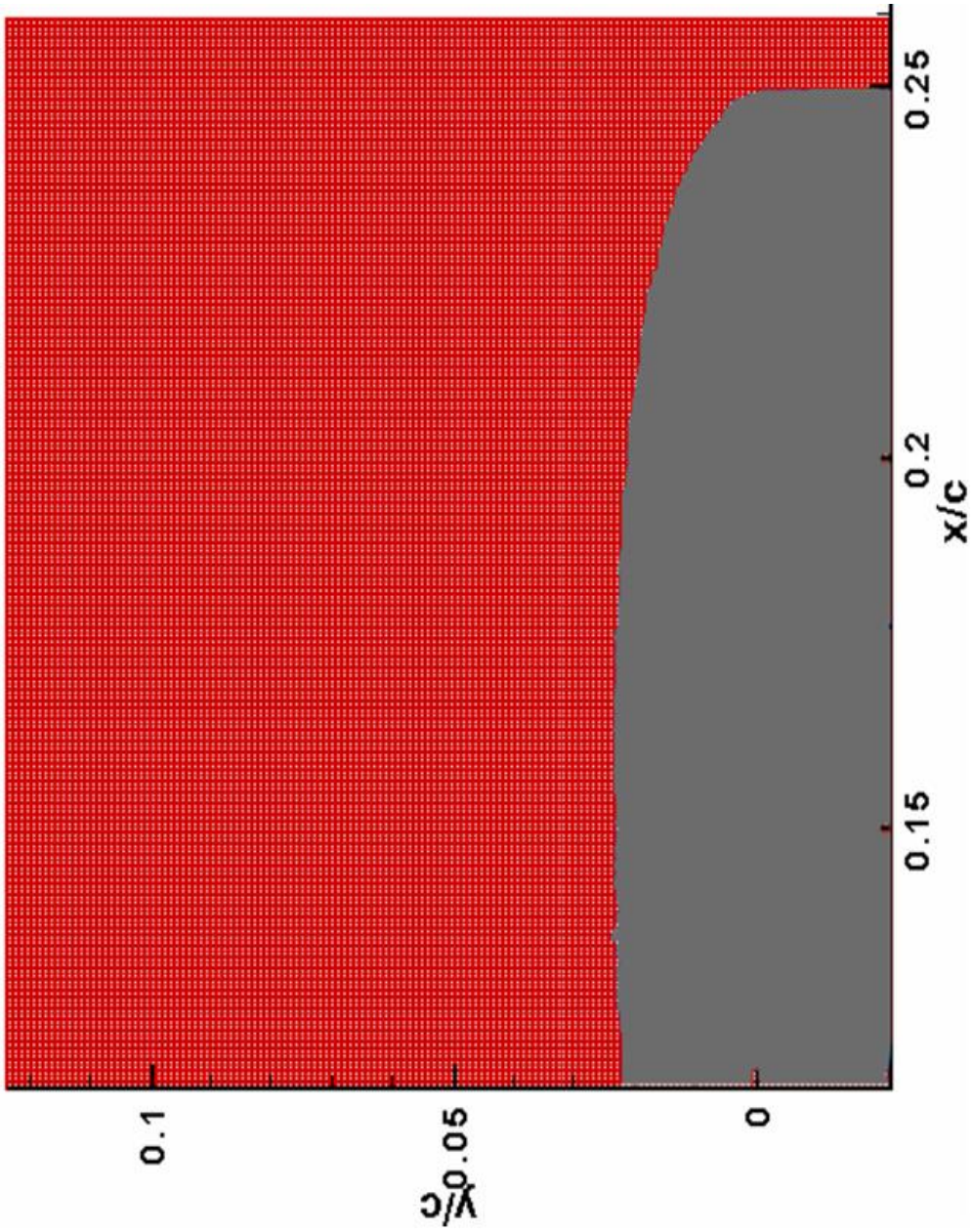

Figure 70: Hyper fine data reduction mesh

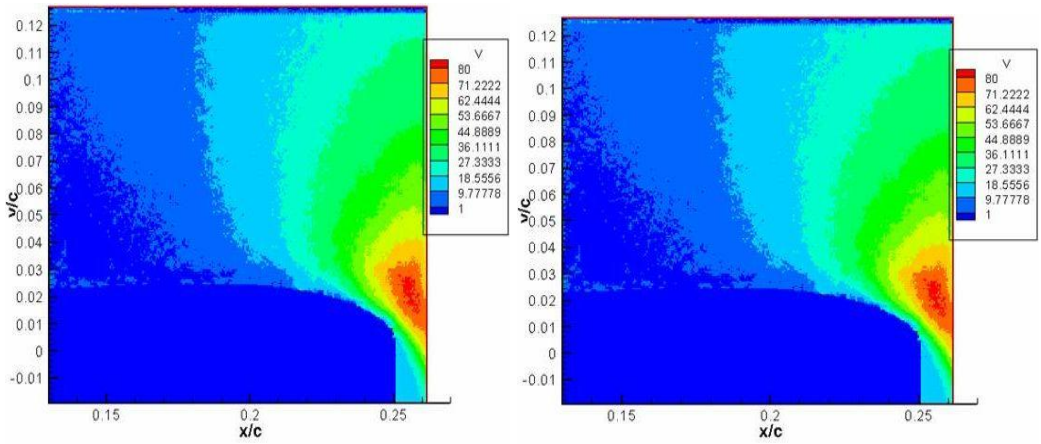

(a) Nearest neighbor option off **(b) Nearest neighbor option on**

Figure 71: Nearest neighbor filter effect

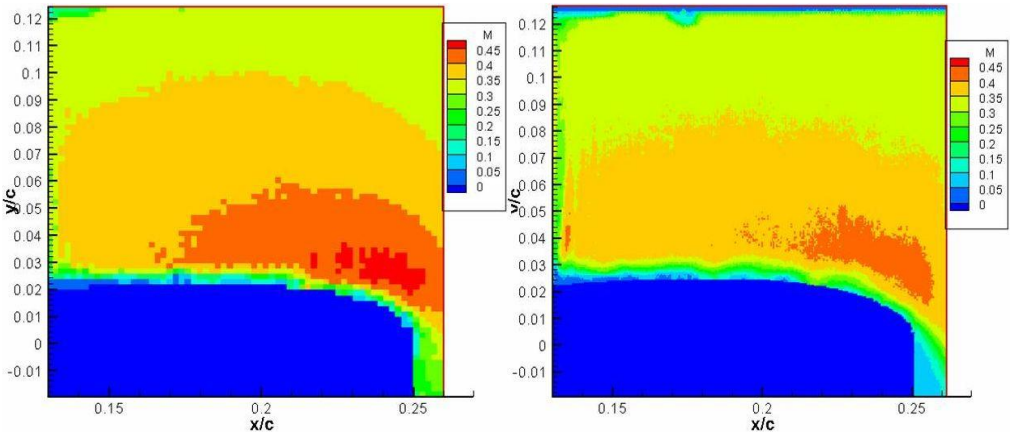

(a) Course Mesh (8 pixel) **(b) Hyperfine (4 pixel)**

Figure 72: Mesh refinement study

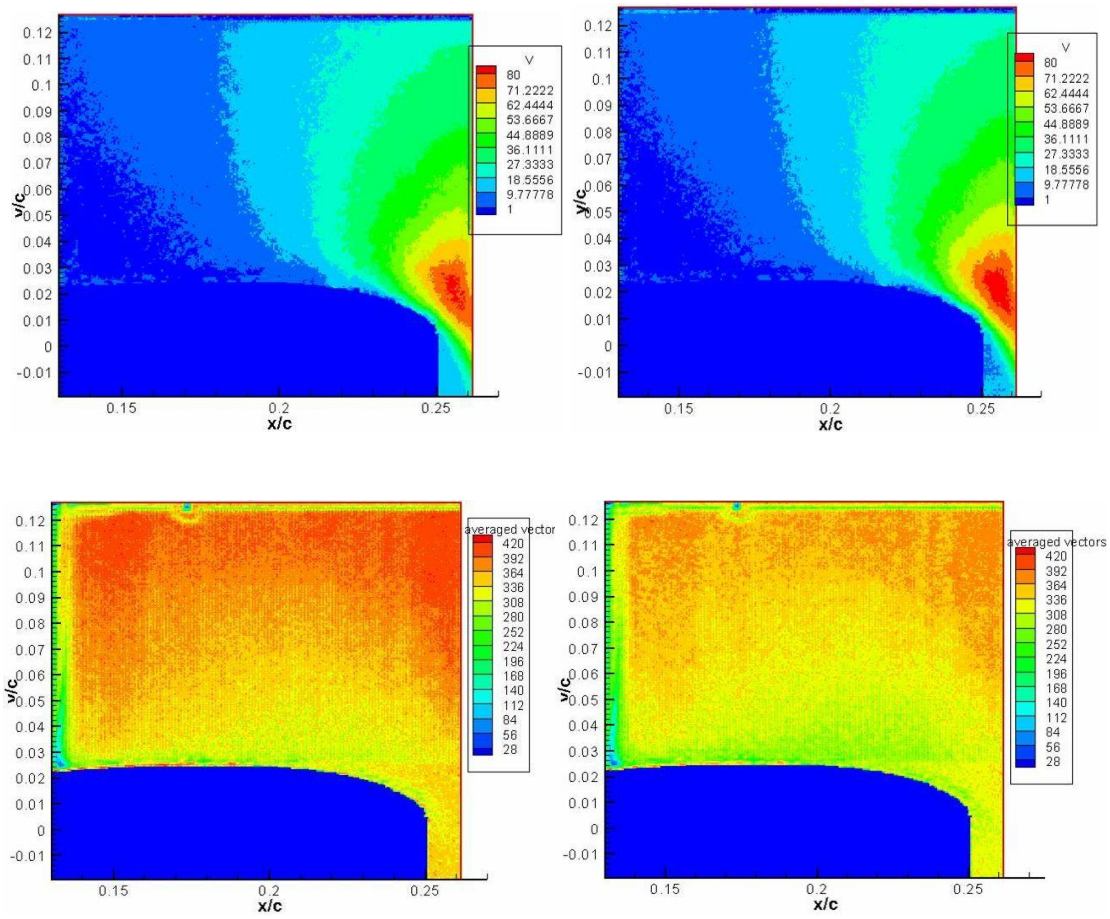

(a) 3σ **(b) 2σ**

Figure 73: Post-processing filter refinement study

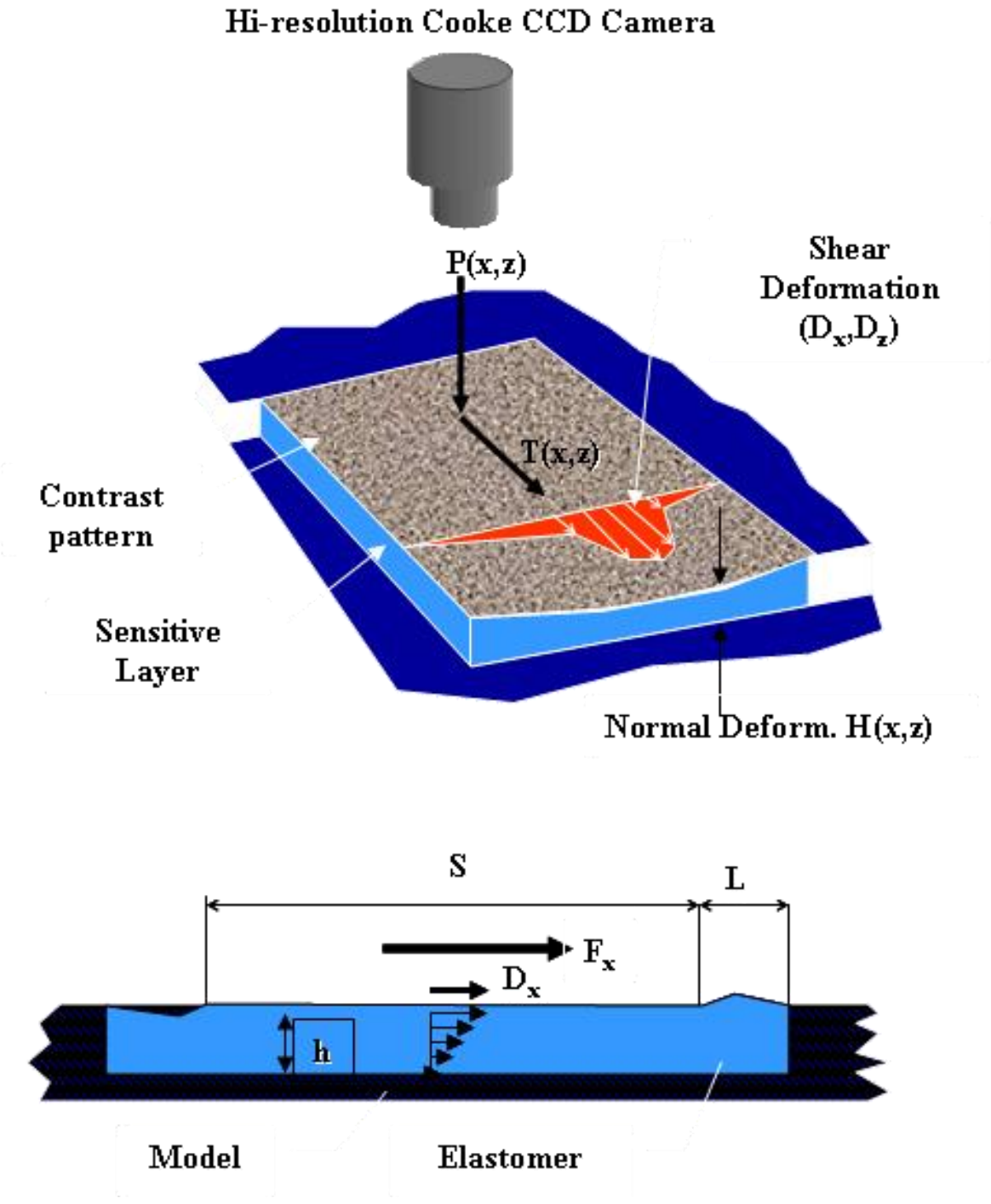

(a) Basic set-up for S3F

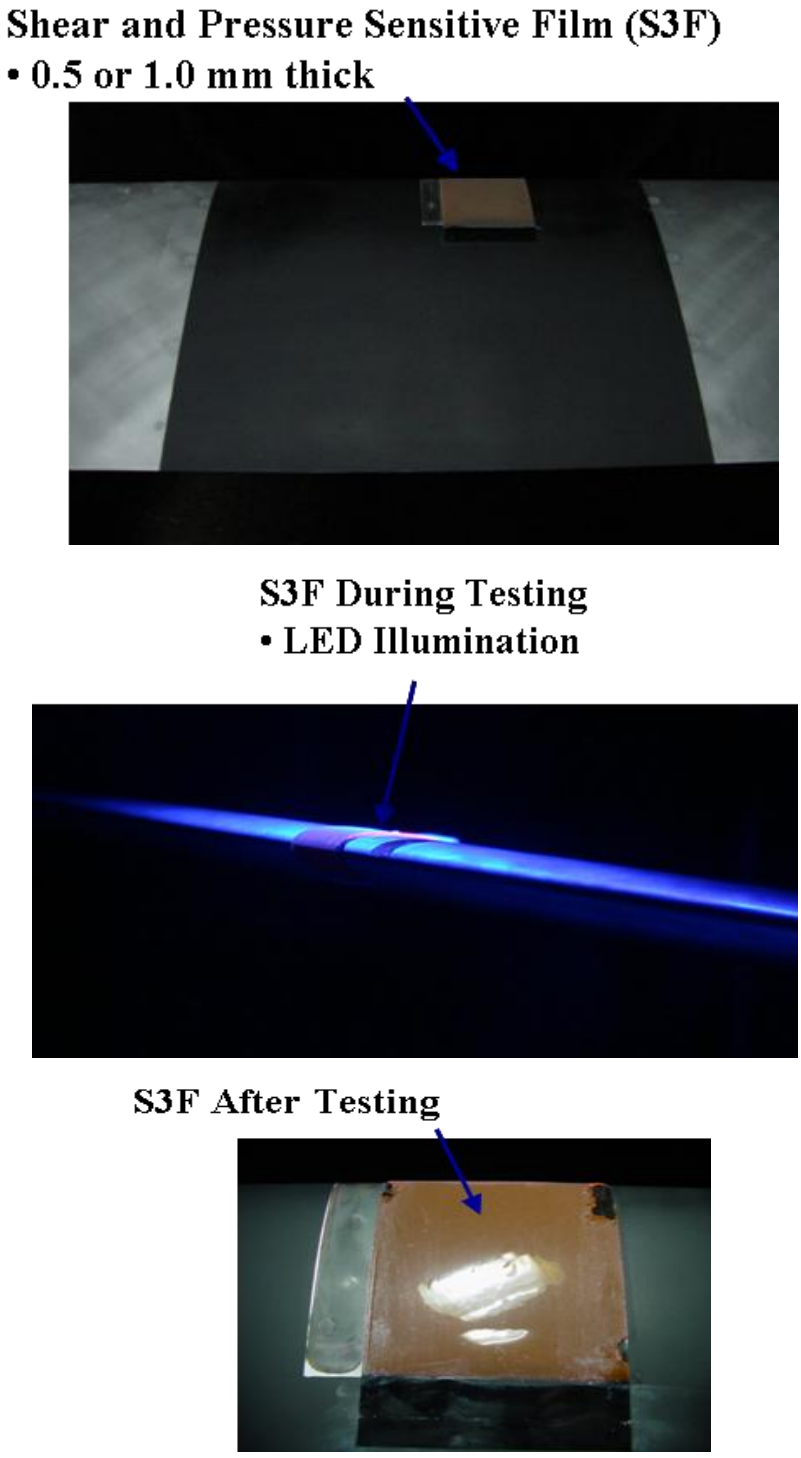

(b) Photographs of the S3F from the present studey

Figure 74: ISSI brand S3F set-up

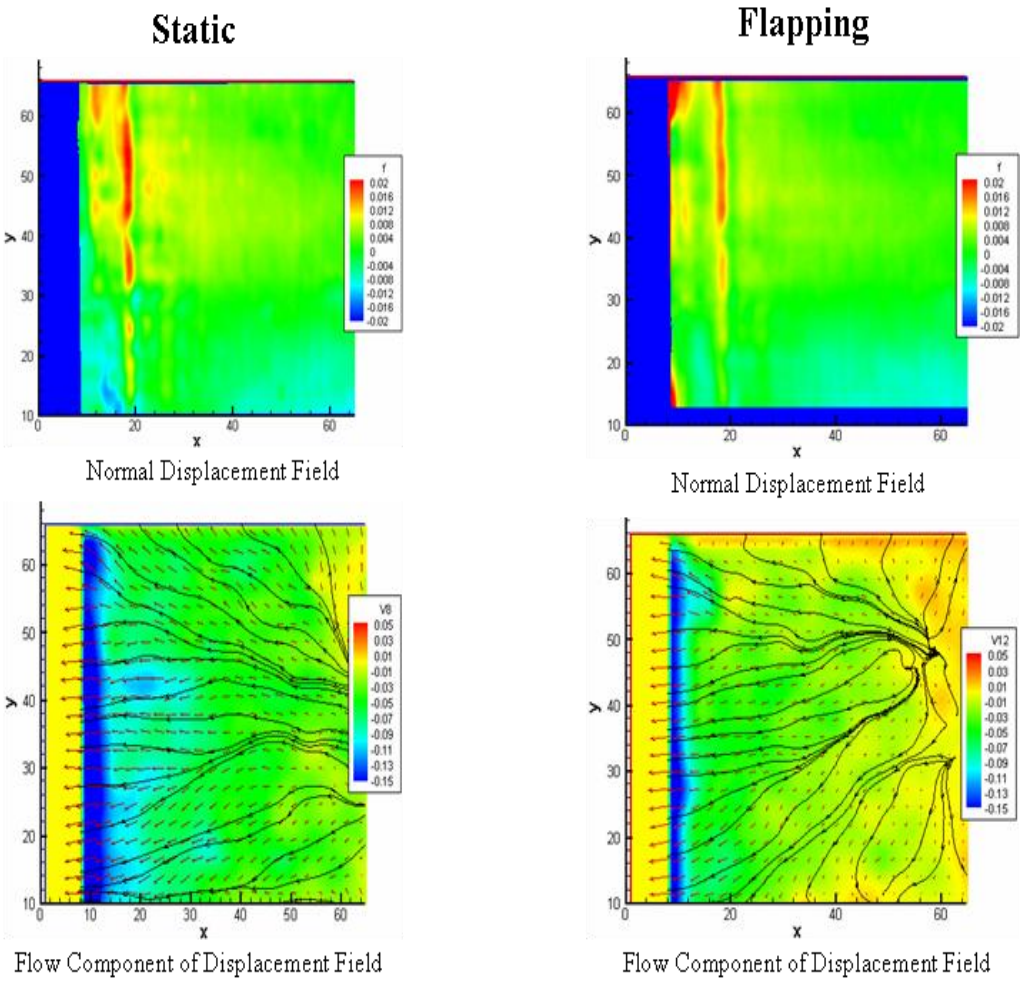

Figure 75: Example S3F Case 4 (M = 0.2, k = 0.18, $\Delta\alpha$ = 5 deg)

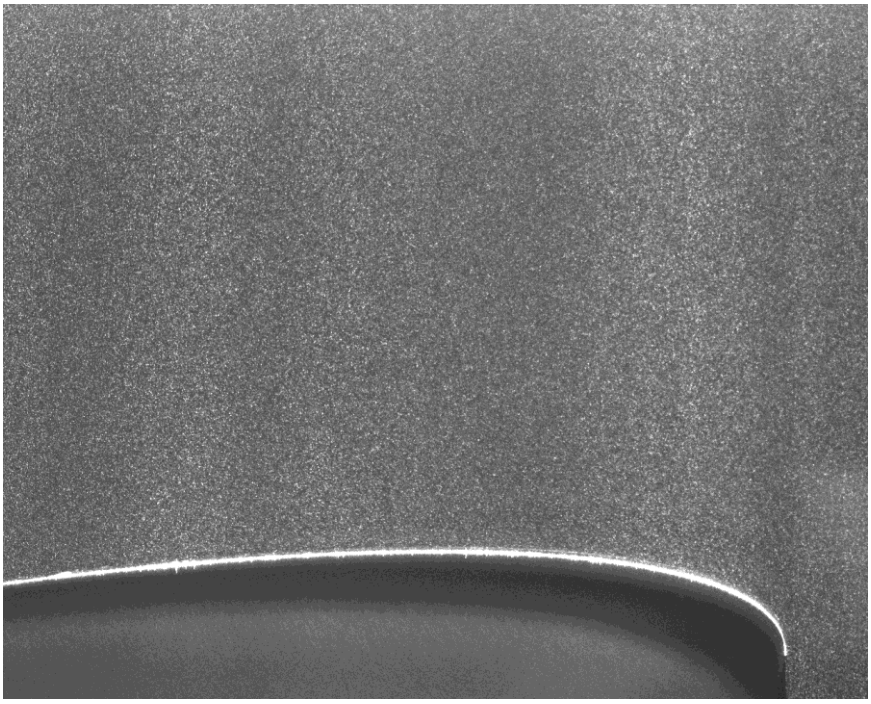

(a)

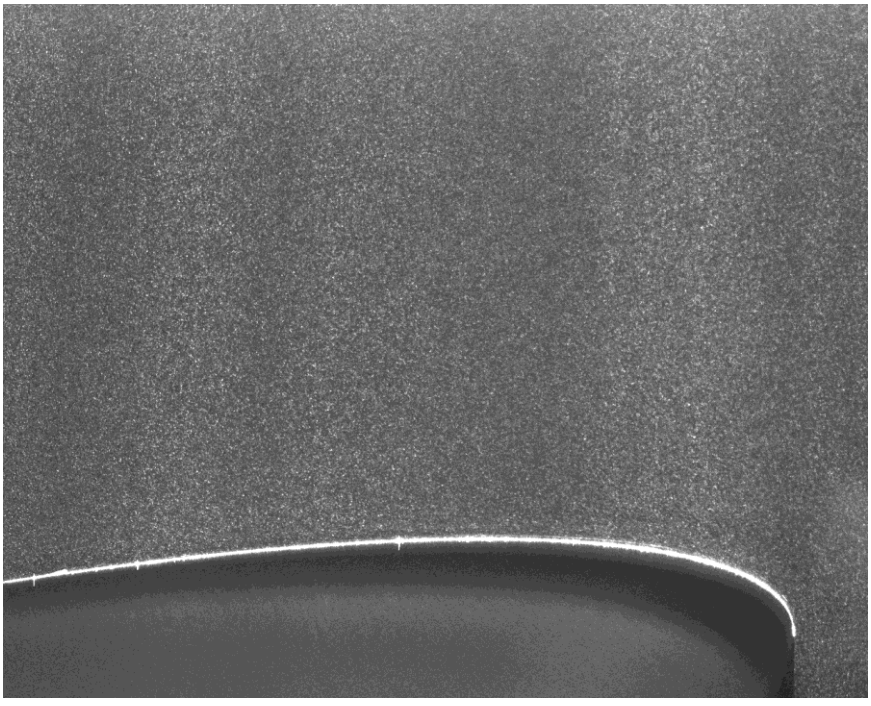

(b)

Figure 76: PIV image acquired at AOA (a) Up stroke (b) Down stroke @10°

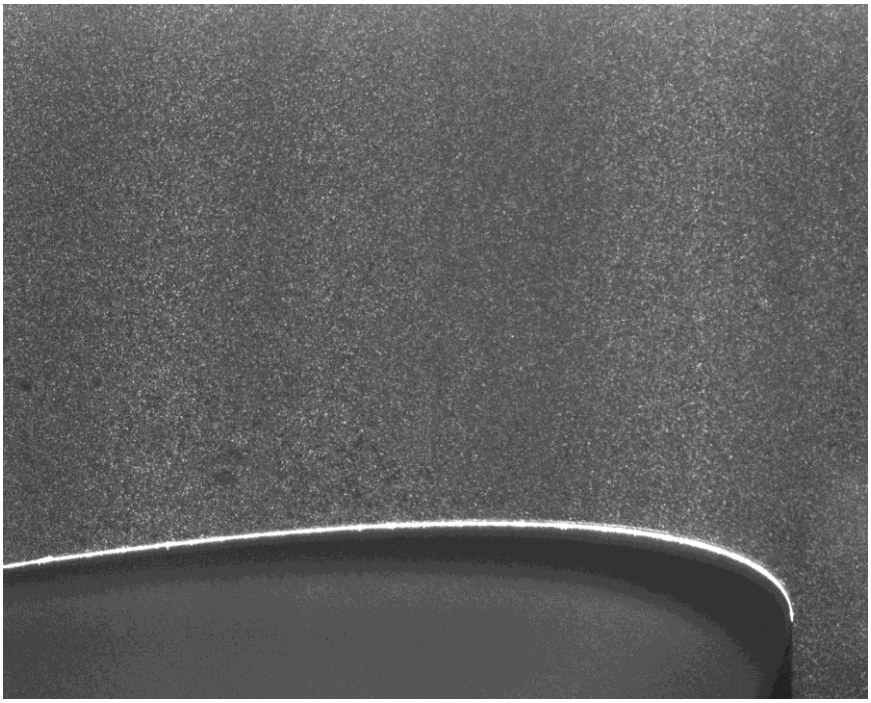

(a)

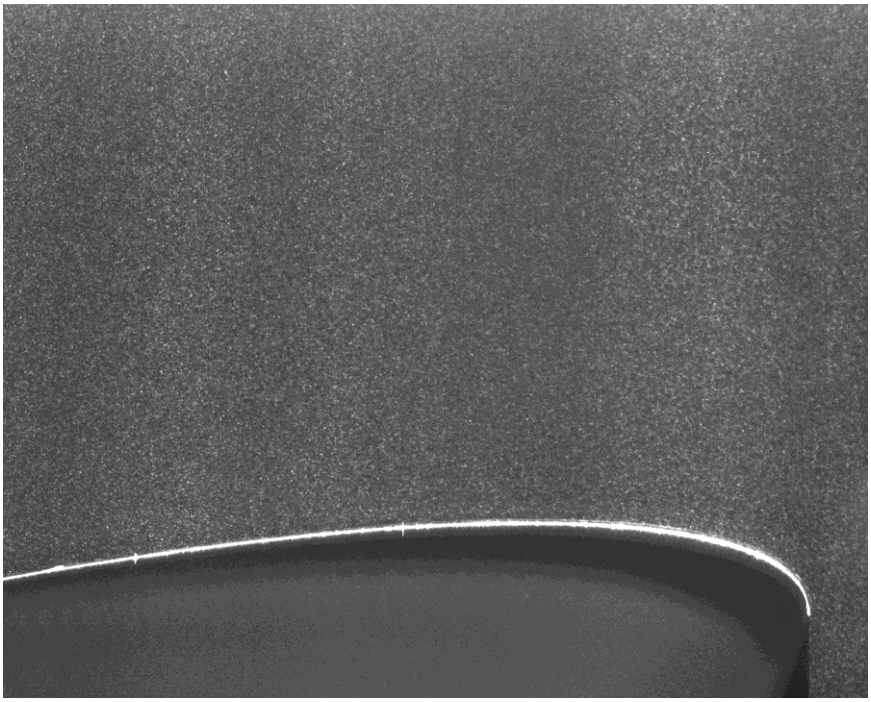

(b)

Figure 77: PIV image acquired at AOA (a) Up stroke (b) Down stroke @12°

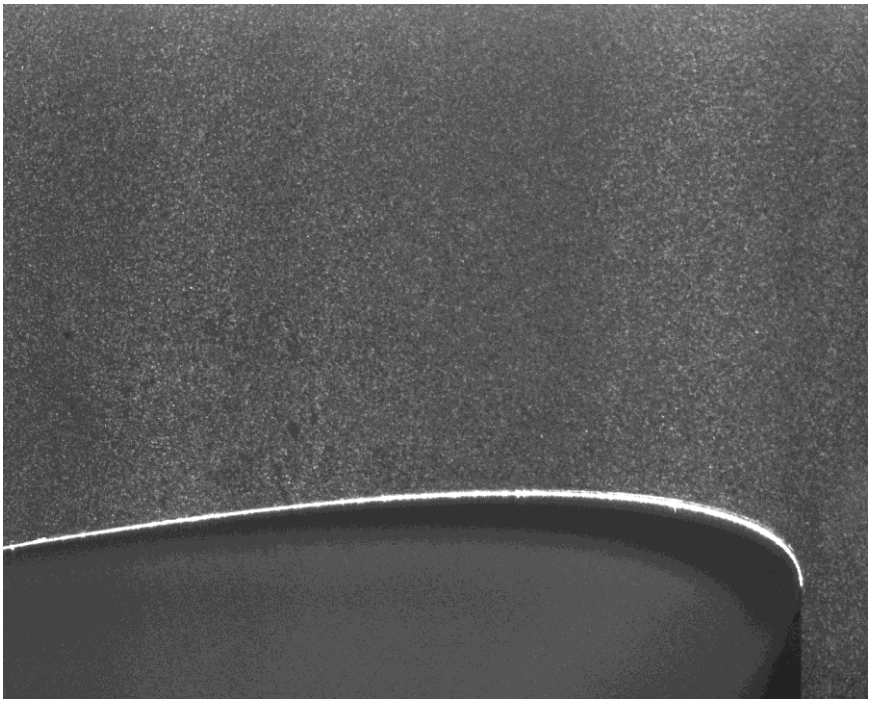

(a)

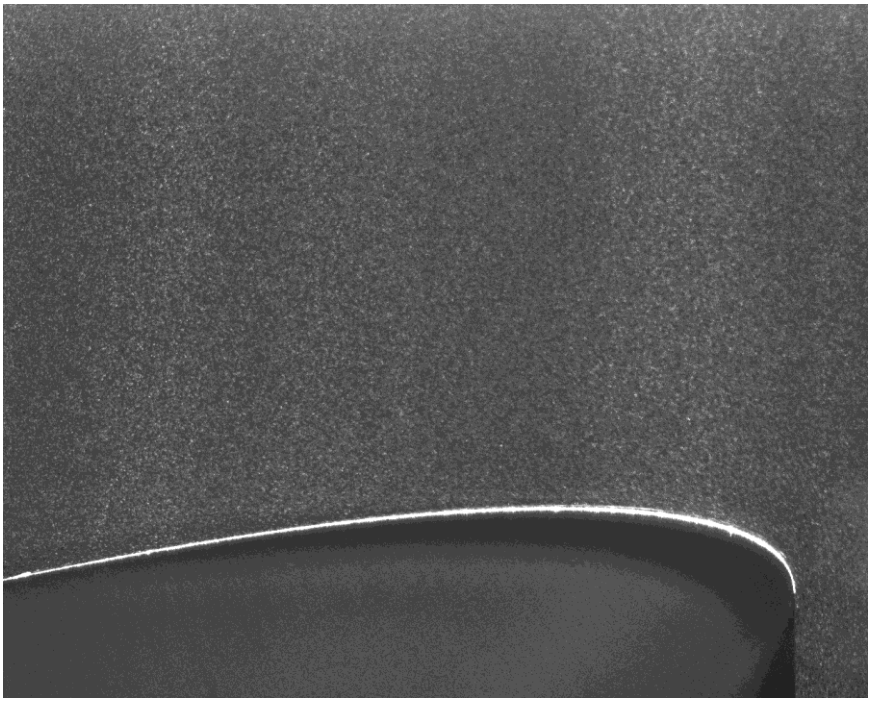

(b)

Figure 78: PIV image acquired at AOA (a) Up stroke (b) Down stroke @14°

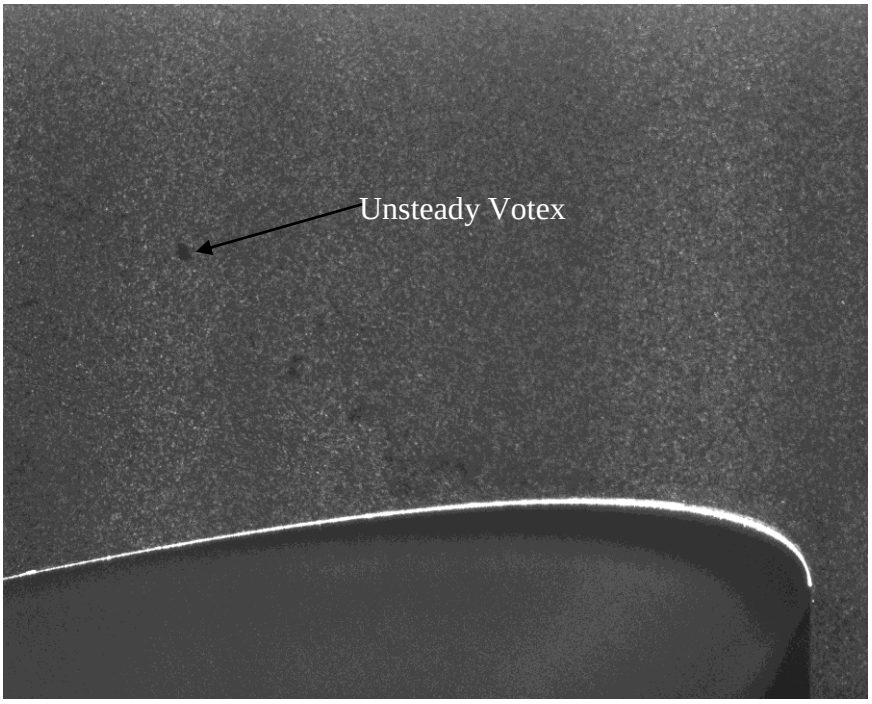

(a)

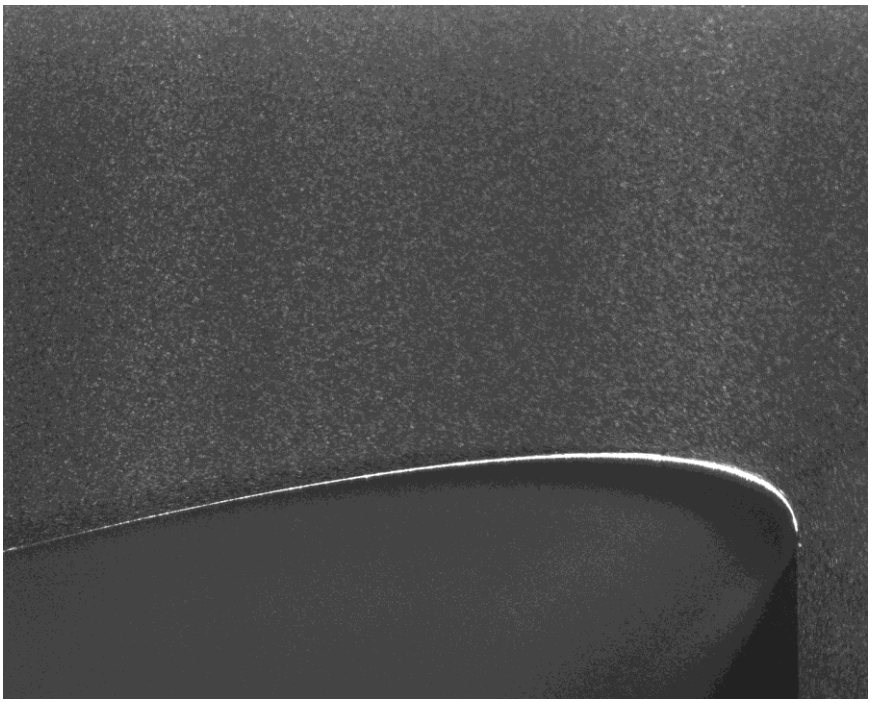

(b)

Figure 79: PIV image acquired at AOA (a) Up stroke (b) Down stroke @16°

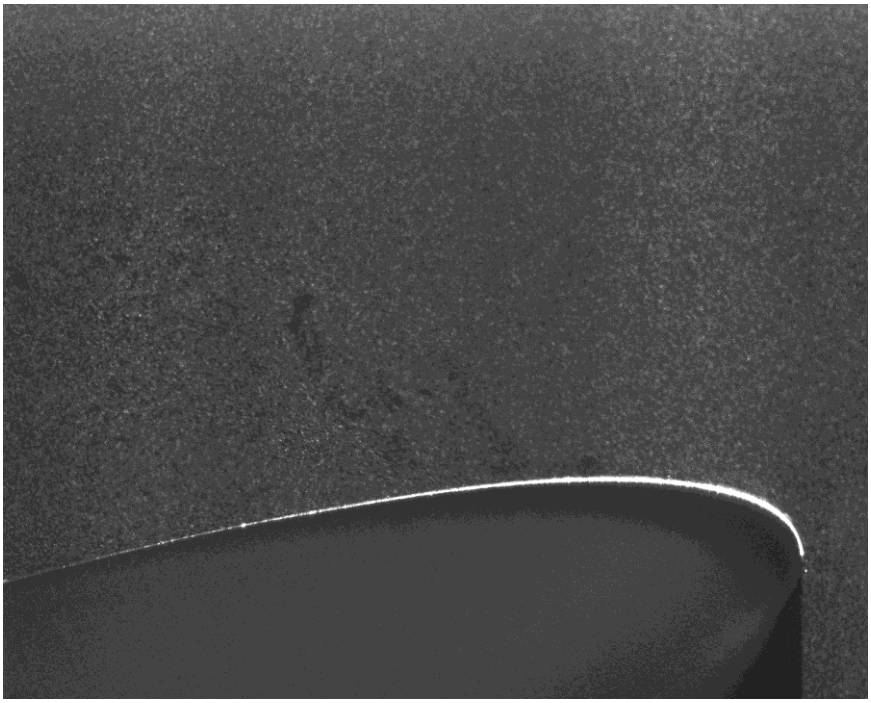

(a)

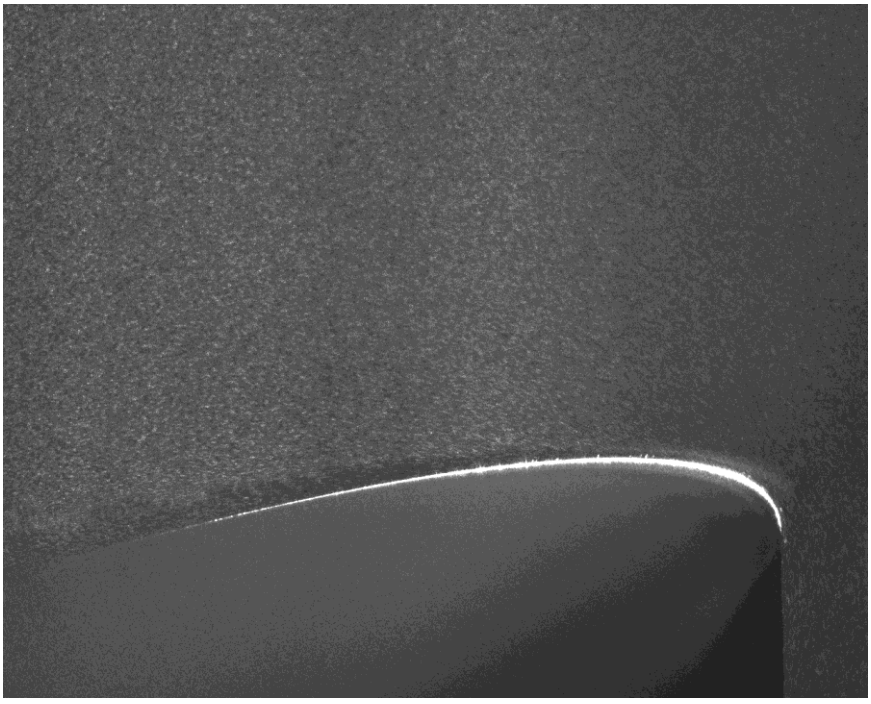

(b)

Figure 80: PIV image acquired at AOA (a) Up stroke (b) Down stroke @18°

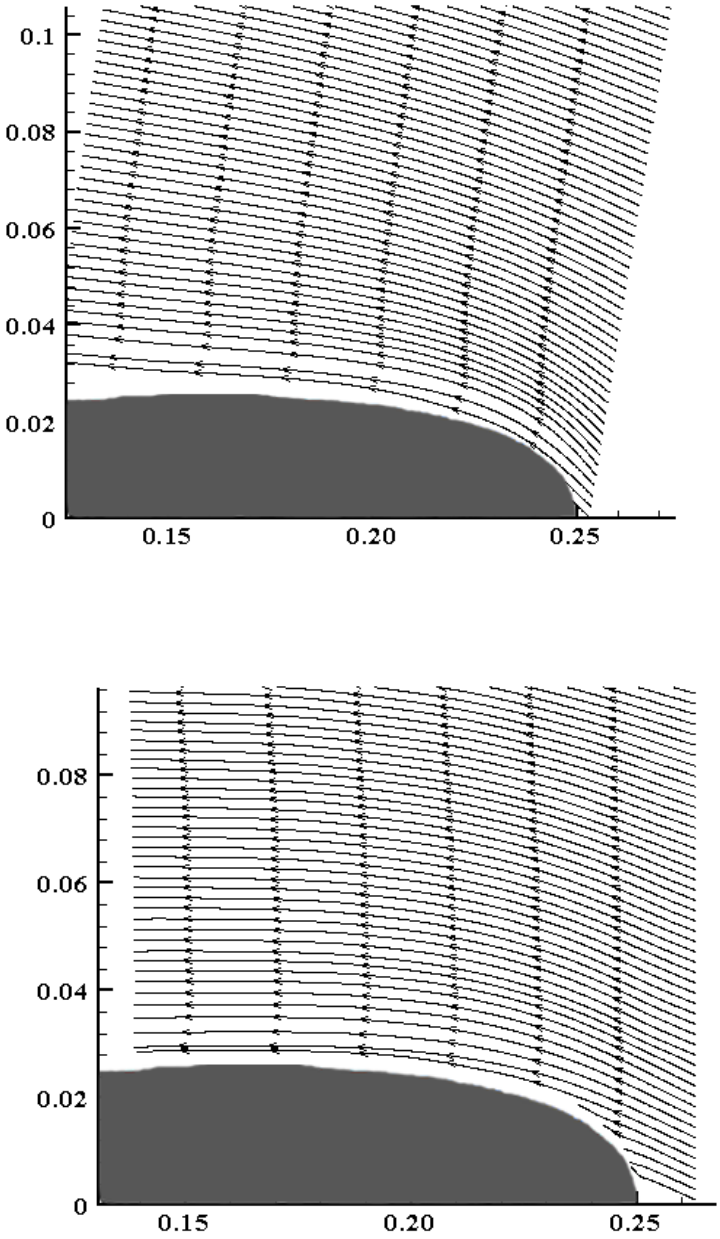

Figure 81: Streamlines during the (a) Upstroke (b) Downstroke motion @ 14°

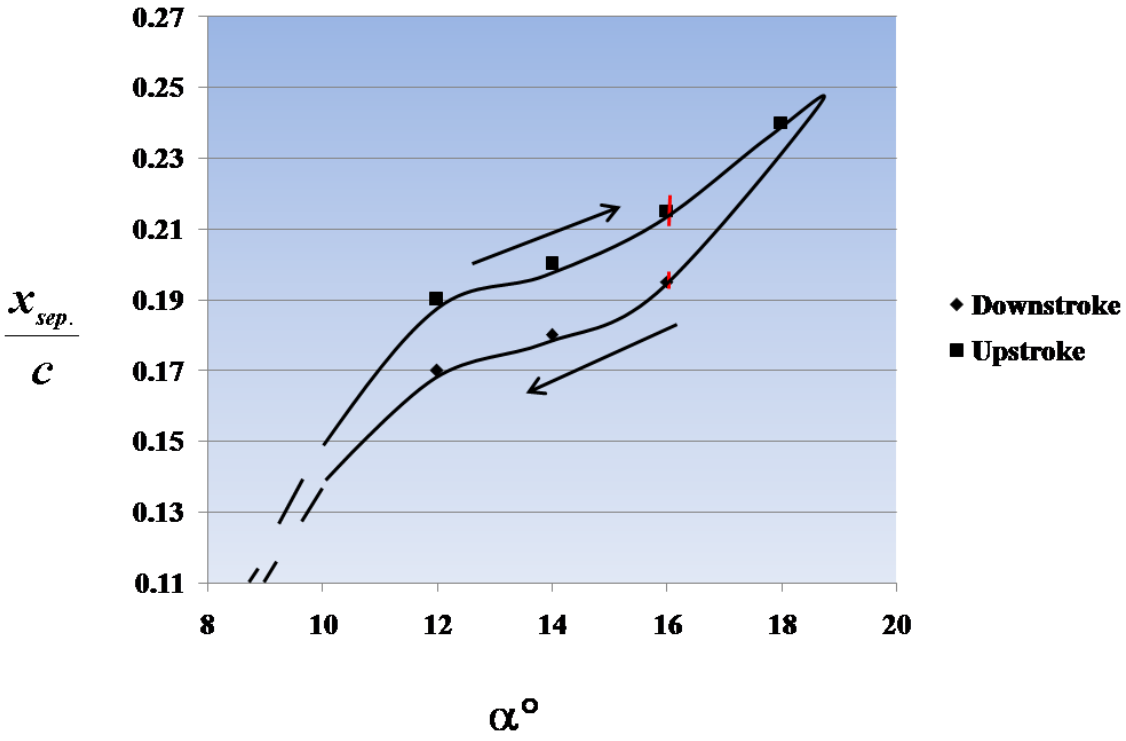

Figure 82: Hysteresis loop during one cycle of the wing motion

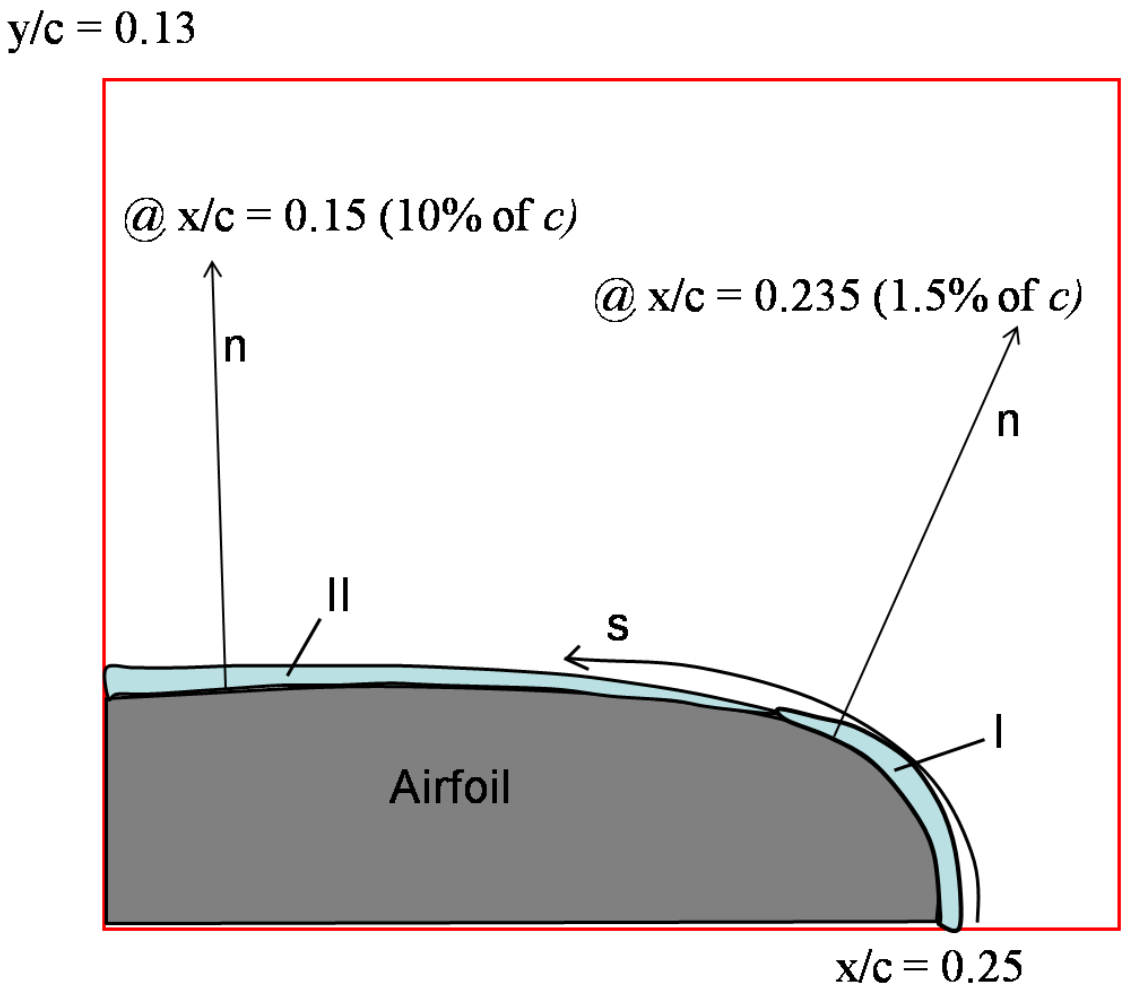

Figure 83: Sketch of regions of time scale calculation along with direction of 's' and 'n'

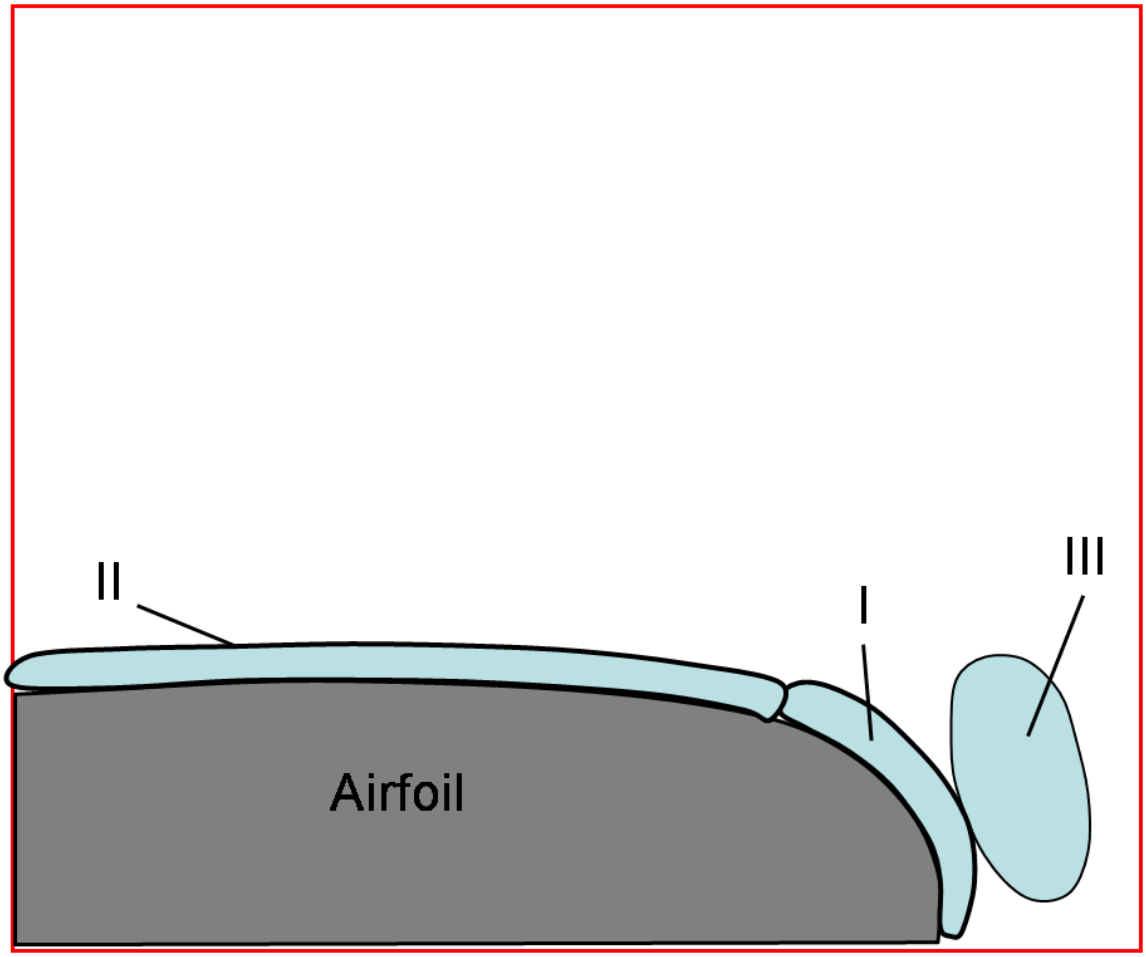

Figure 84: Sketch of regions explained during the upstroke motion of the wing

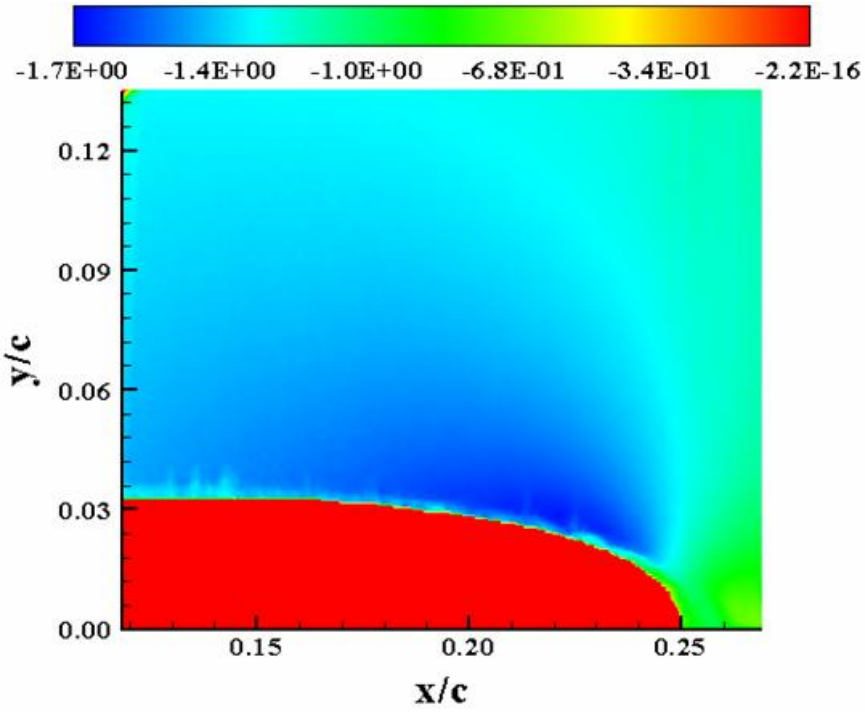

Figure 85: $U_N(M_\infty = 0.2, k = 0.1, Up, \alpha = 10^0)$

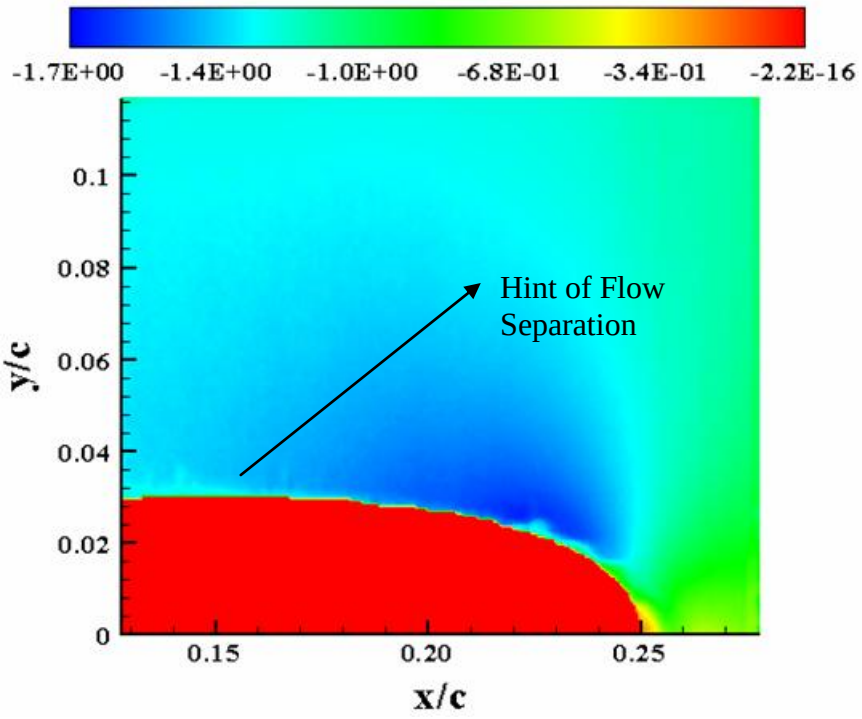

Figure 86: $U_N(M_\infty = 0.2, k = 0.1, Up, \alpha = 12^0)$

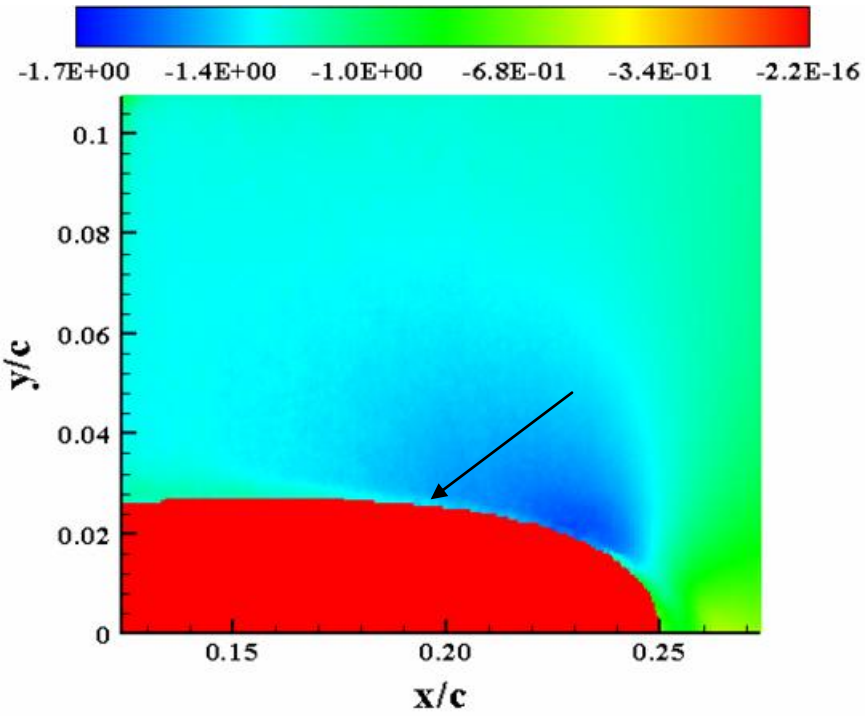

Figure 87: $U_N(M_\infty = 0.2, k = 0.1, Up, \alpha = 14^0)$

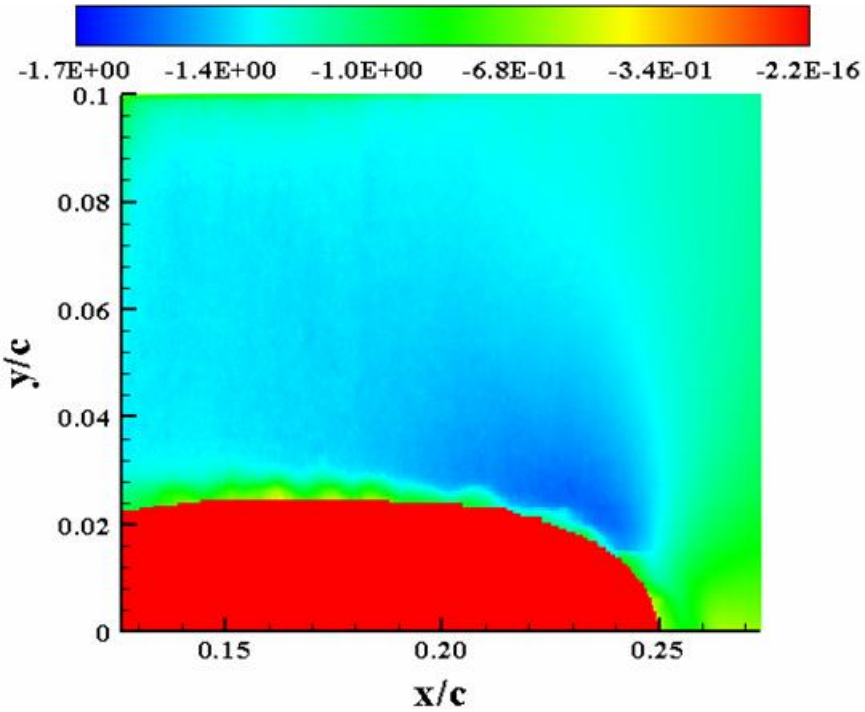

Figure 88: $U_N(M_\infty = 0.2, k = 0.1, Up, \alpha = 16^0)$

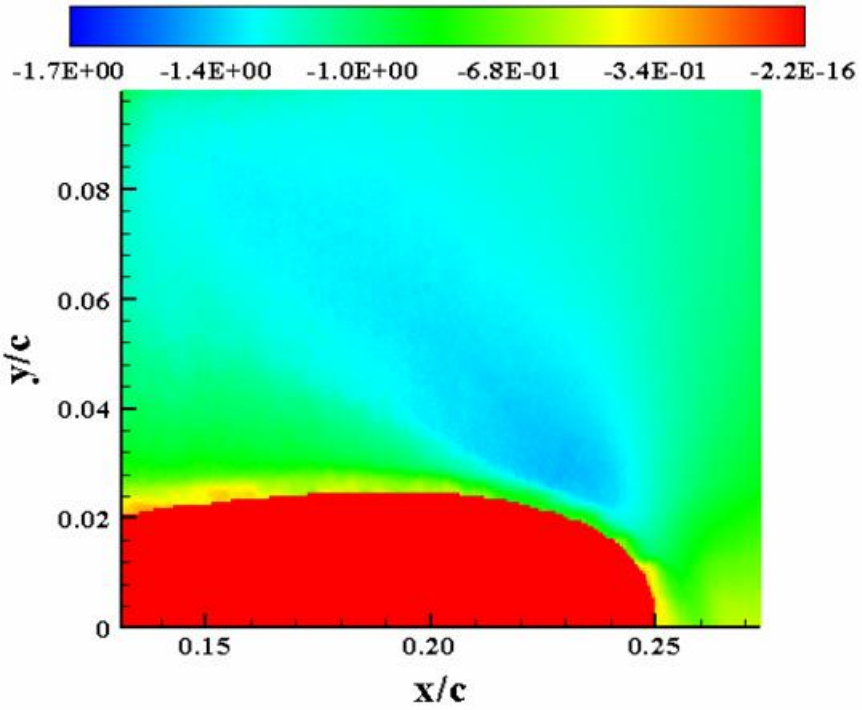

Figure 89: $U_N(M_\infty = 0.2, k = 0.1, Up, \alpha = 18^0)$

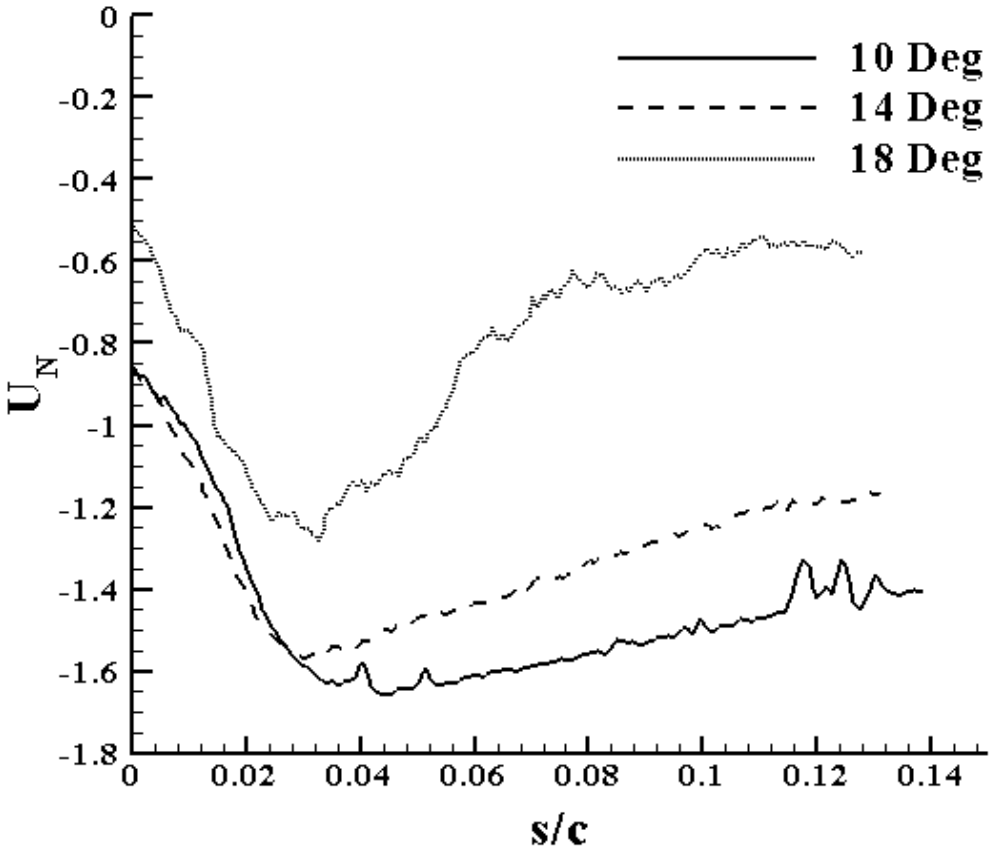

Figure 90: Line plot of U_N for $M_\infty = 0.2, k = 0.1, Up, \alpha = 10^0, 14^0 and 18^0$

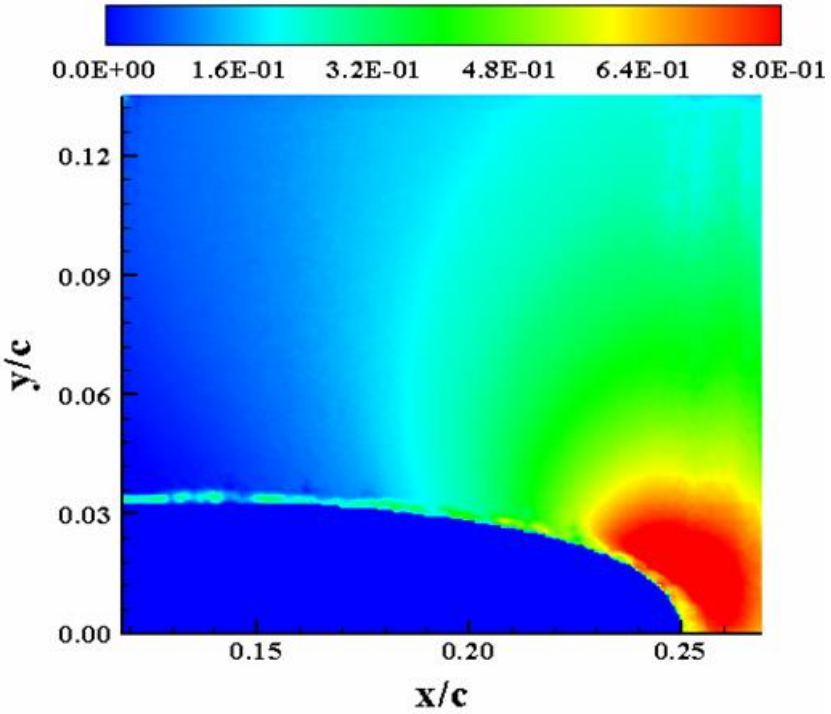

Figure 91: $V_N(M_\infty = 0.2, k = 0.1, Up, \alpha = 10^0)$

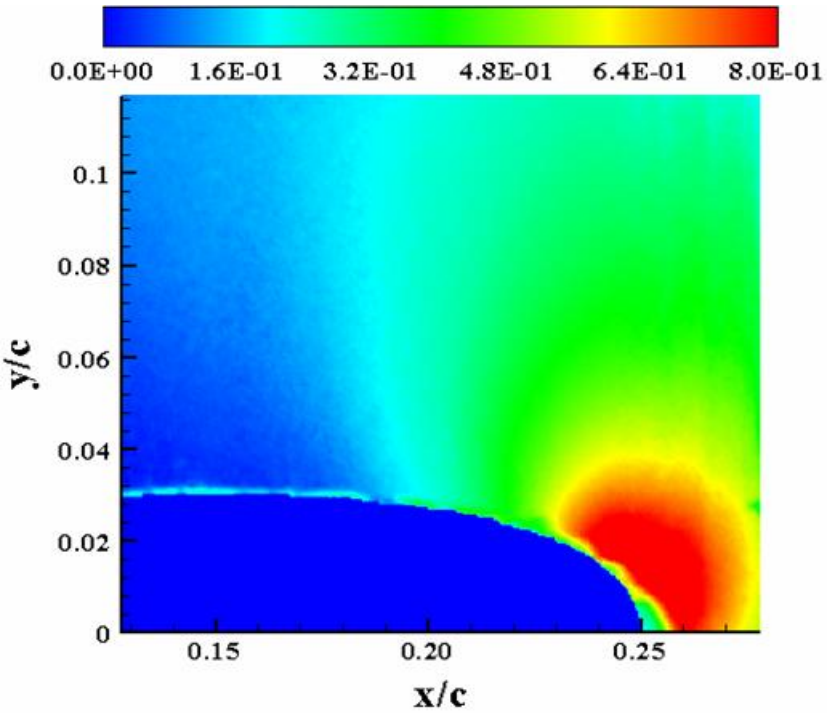

Figure 92: $V_N(M_\infty = 0.2, k = 0.1, Up, \alpha = 12^0)$

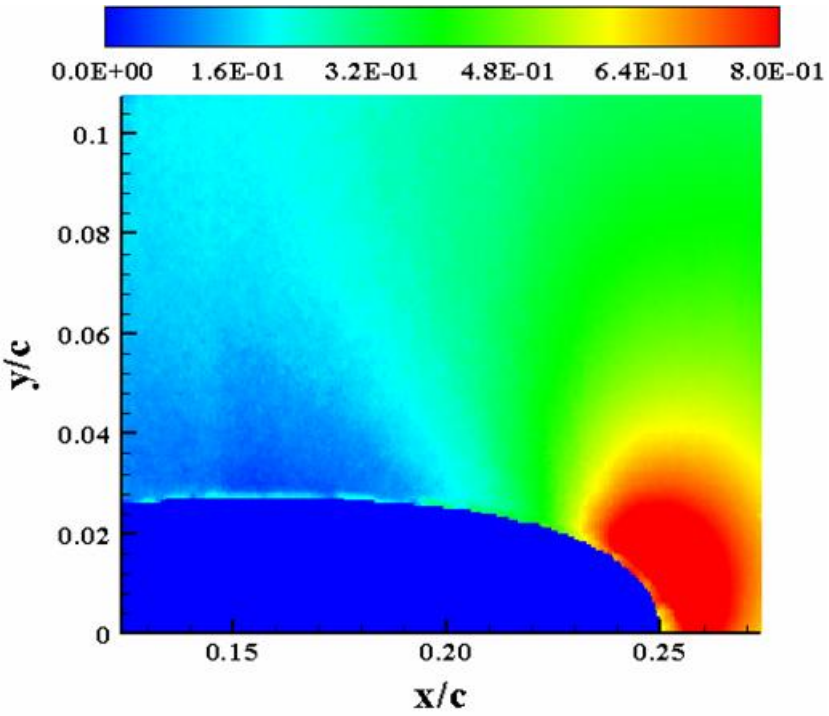

Figure 93: $V_N(M_\infty = 0.2, k = 0.1, Up, \alpha = 14^0)$

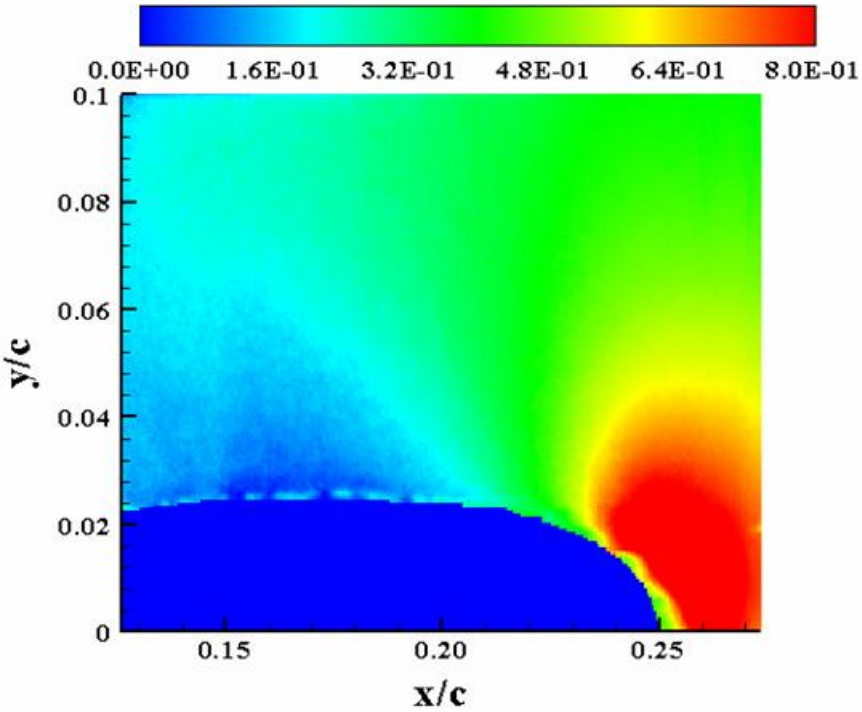

Figure 94: $V_N(M_\infty = 0.2, k = 0.1, Up, \alpha = 16^0)$

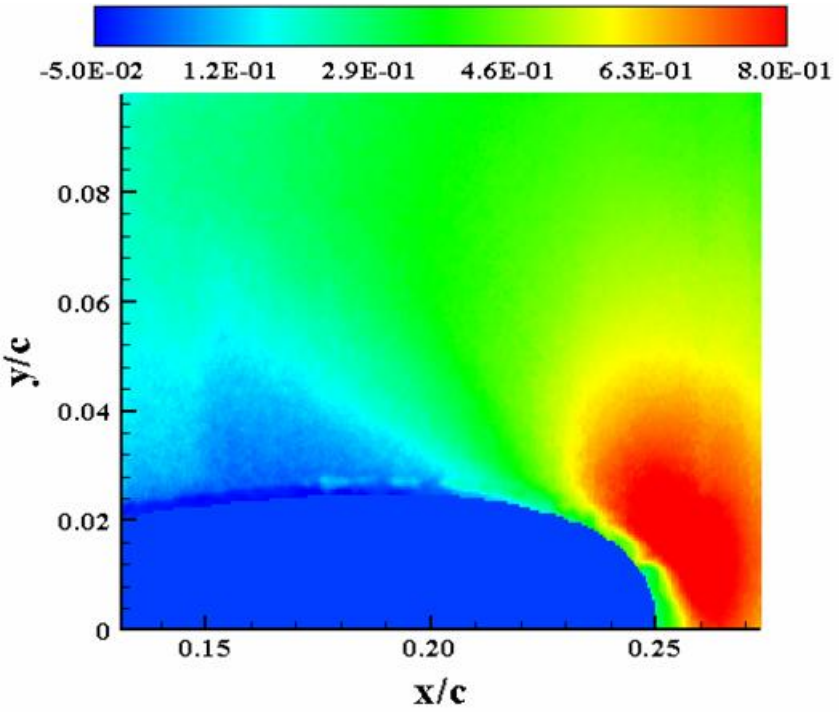

Figure 95: $V_N\,(M_\infty = 0.2, k = 0.1, Up, \alpha = 18^0)$

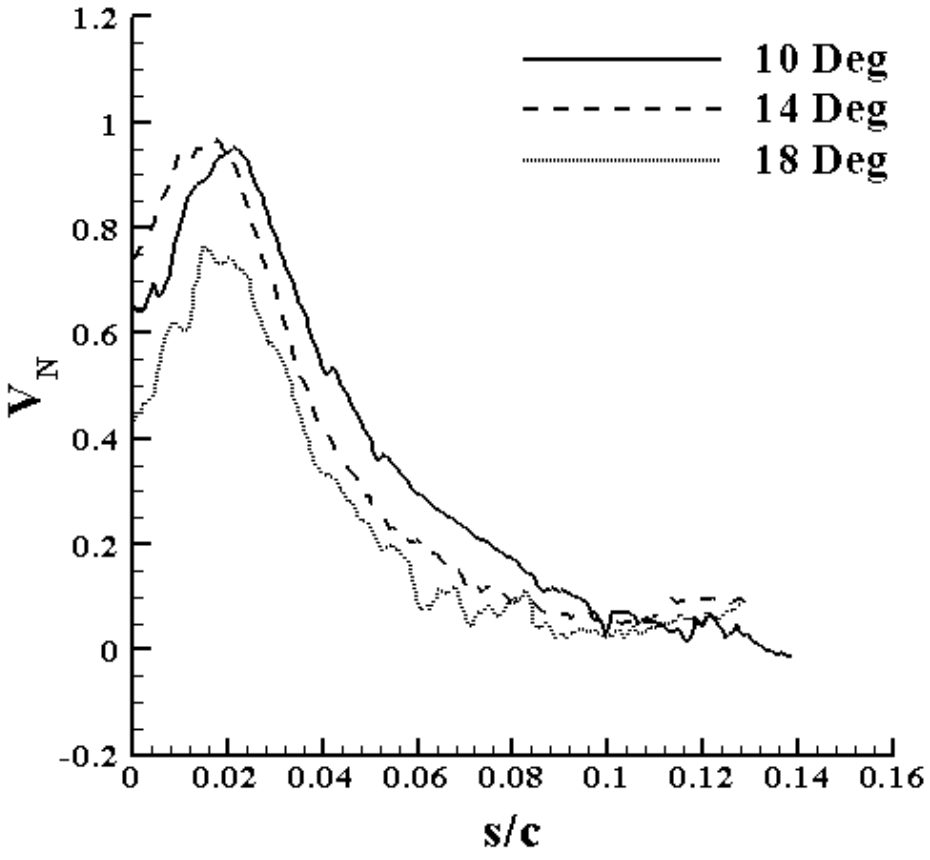

Figure 96: Line plot of V_N for $M_\infty = 0.2, k = 0.1, Up, \alpha = 10^0, 14^0 and 18^0$

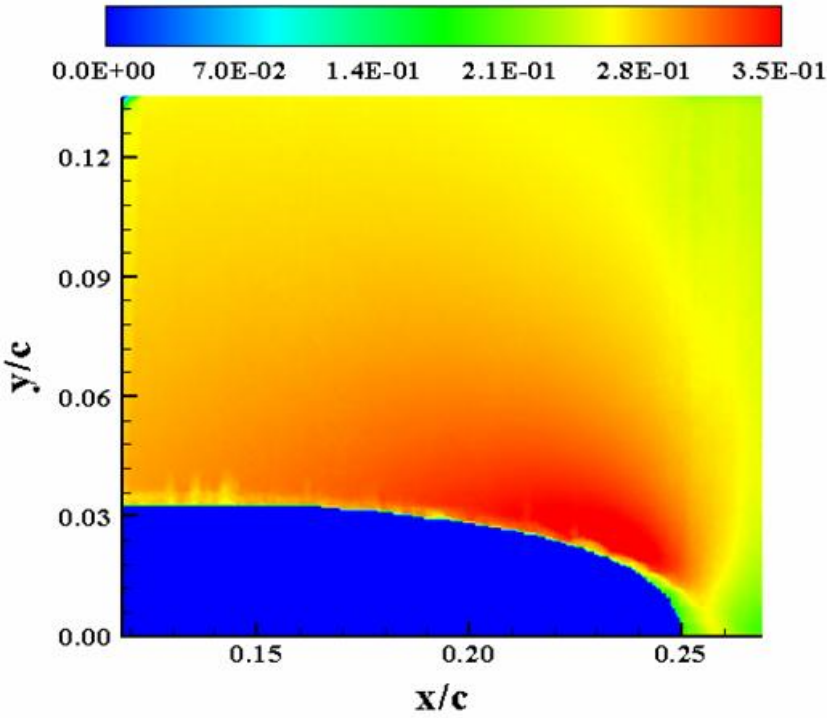

Figure 97: $M(M_\infty = 0.2, k = 0.1, Up, \alpha = 10^0)$

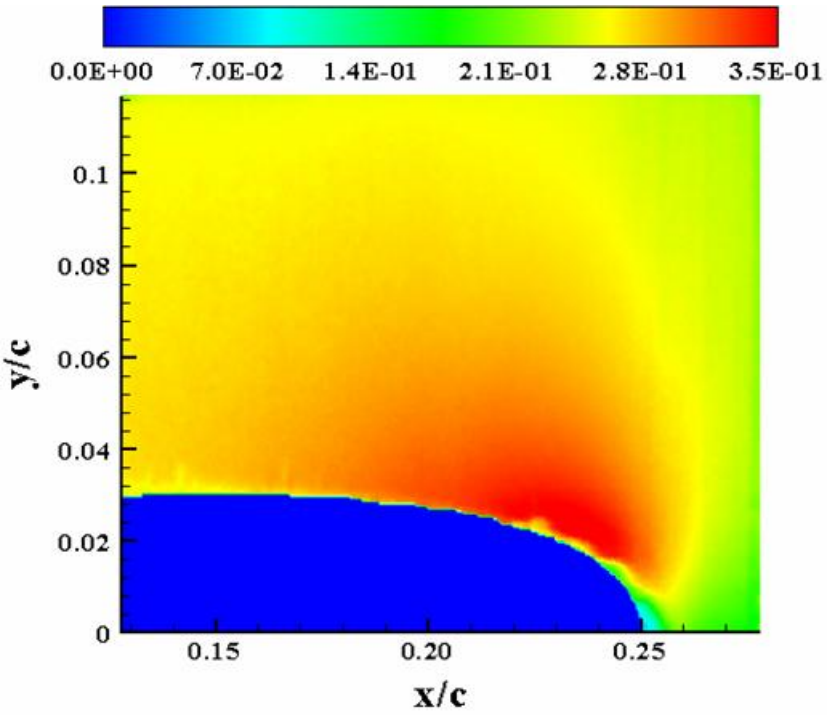

Figure 98: $M(M_\infty = 0.2, k = 0.1, Up, \alpha = 12^0)$

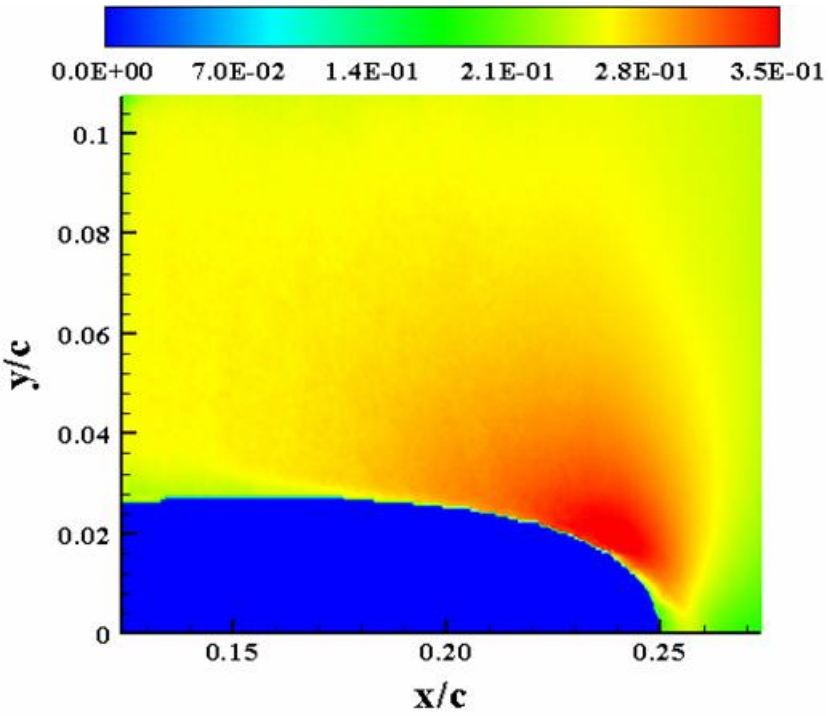

Figure 99: $M(M_\infty = 0.2, k = 0.1, Up, \alpha = 14^0)$

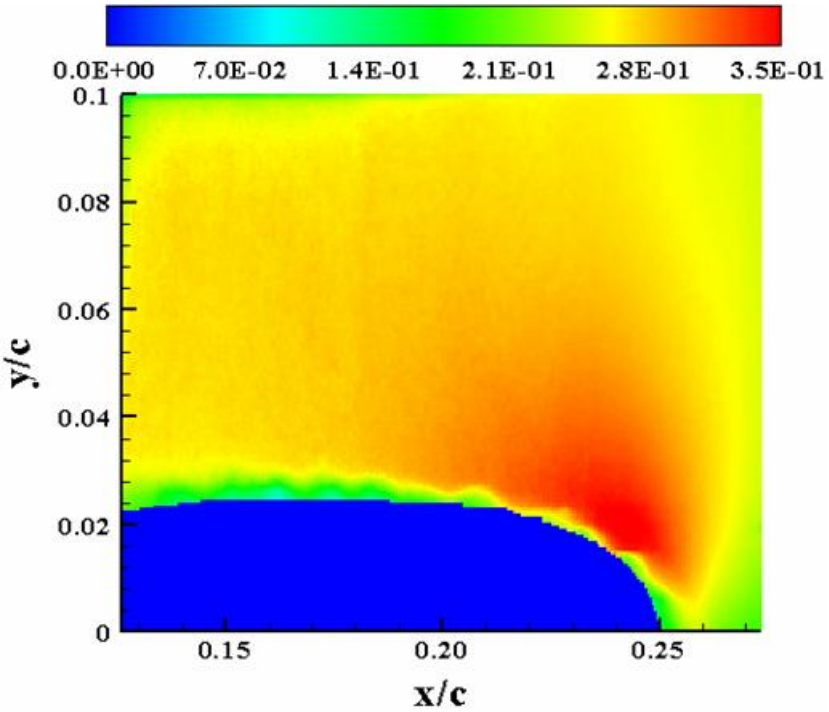

Figure 100: $M(M_\infty = 0.2, k = 0.1, Up, \alpha = 16^0)$

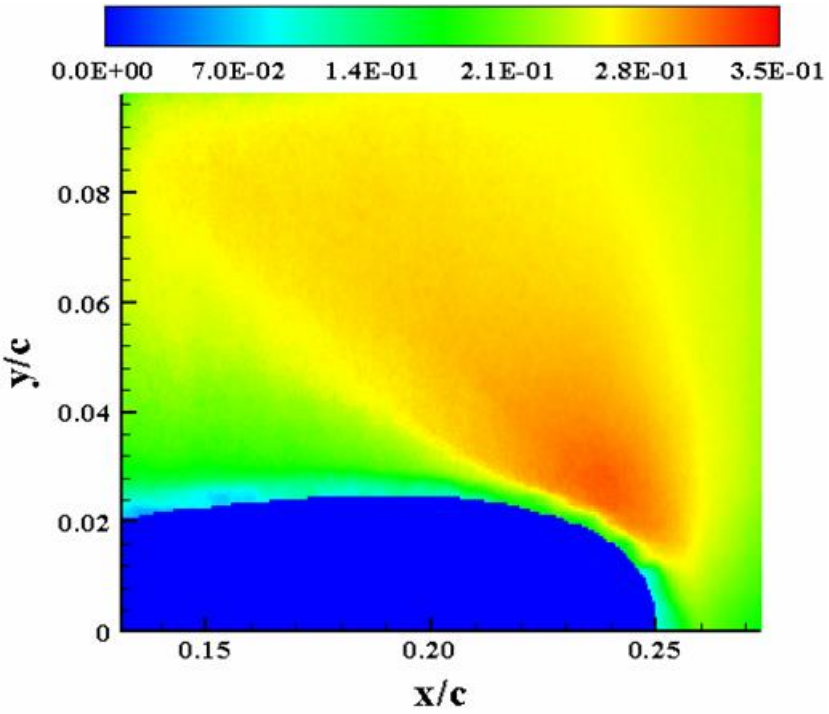

Figure 101: $M(M_\infty = 0.2, k = 0.1, Up, \alpha = 18^0)$

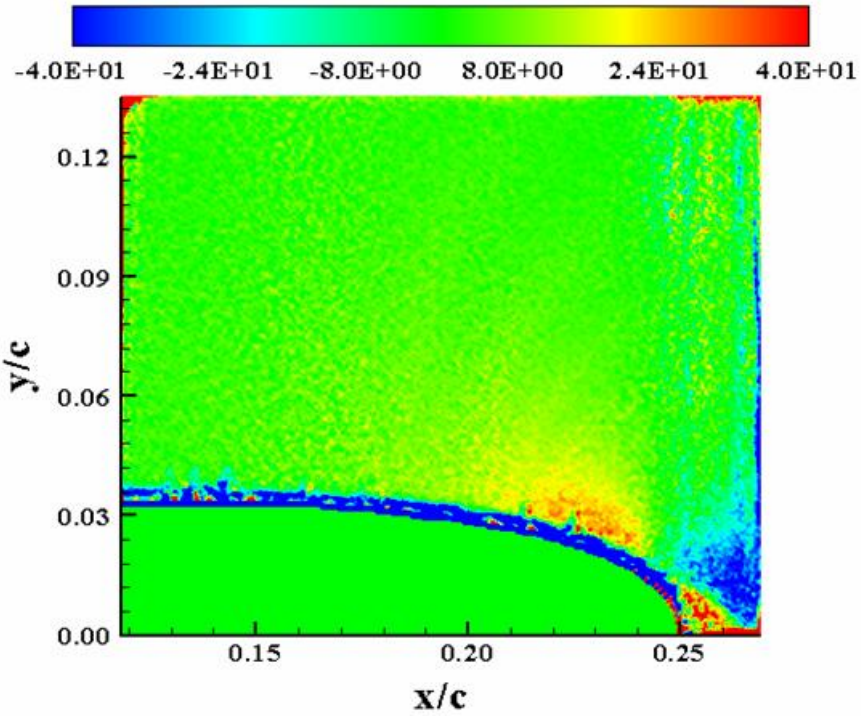

Figure 102: $S_{xy}(M_\infty = 0.2, k = 0.1, Up, \alpha = 10^0)$

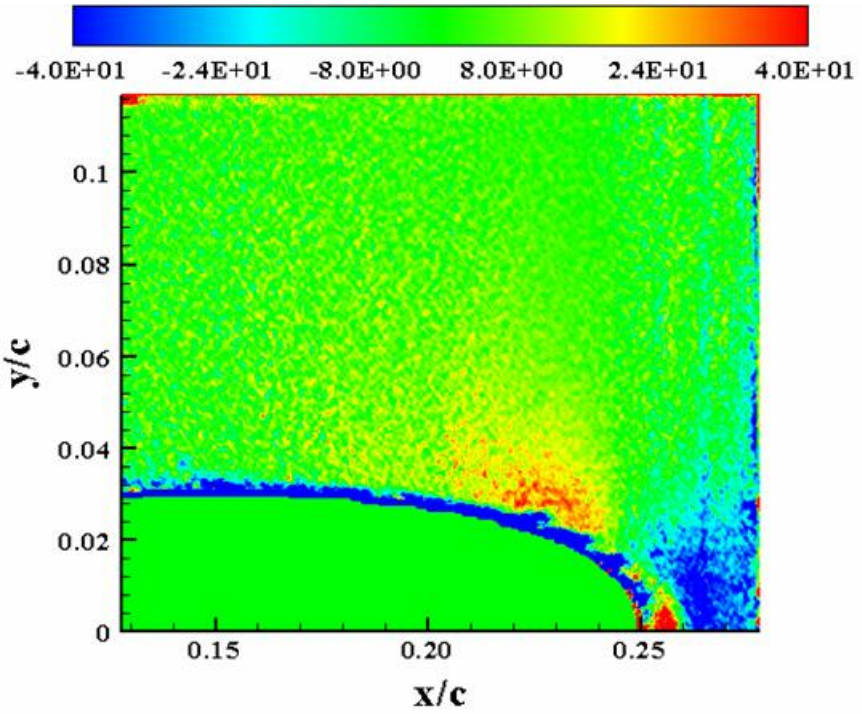

Figure 103: $S_{xy}(M_\infty = 0.2, k = 0.1, Up, \alpha = 12^0)$

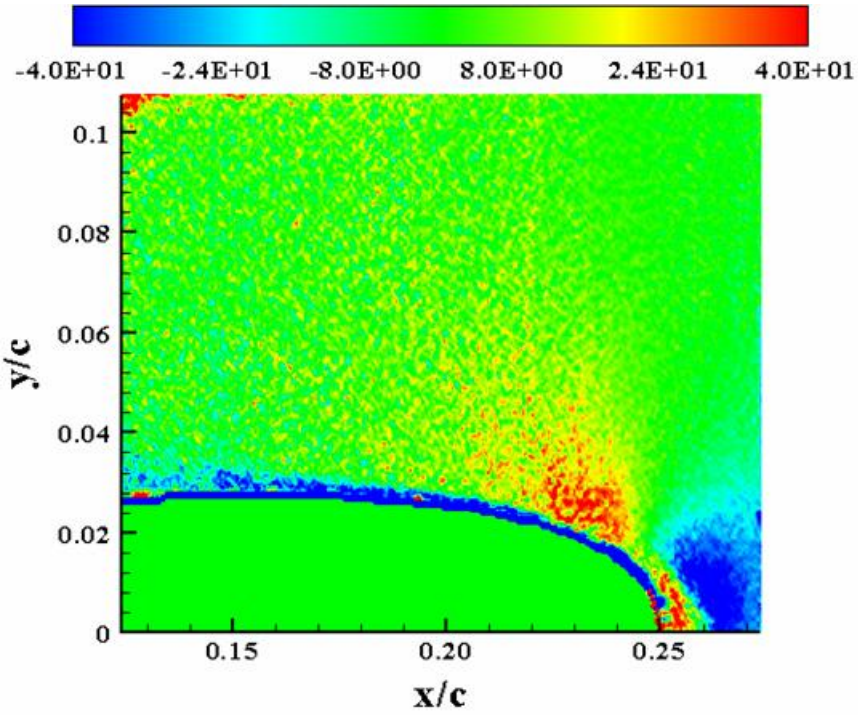

Figure 104: $S_{xy}(M_\infty = 0.2, k = 0.1, Up, \alpha = 14^0)$

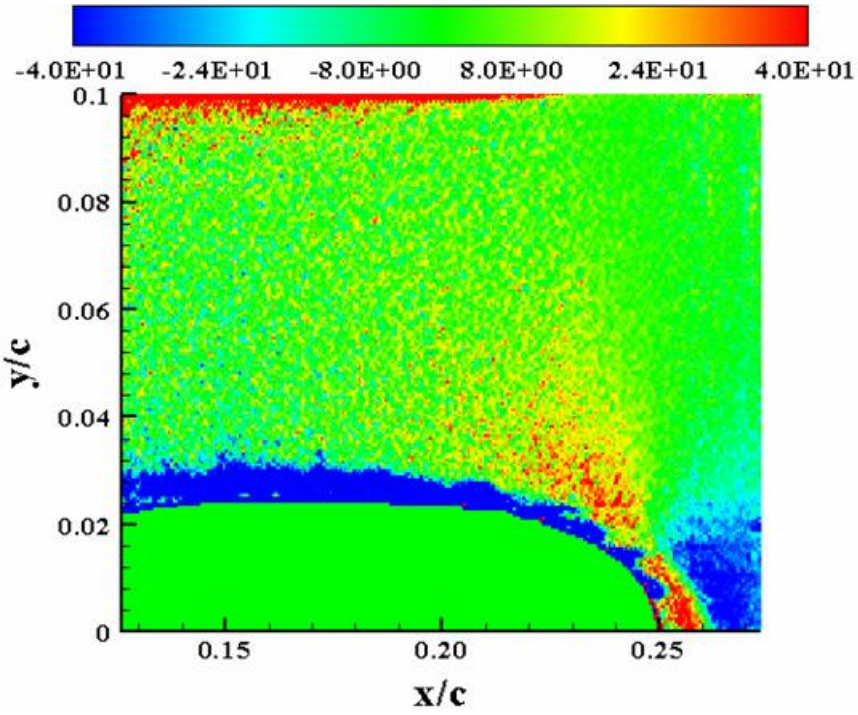

Figure 105: $S_{xy}(M_\infty = 0.2, k = 0.1, Up, \alpha = 16^0)$

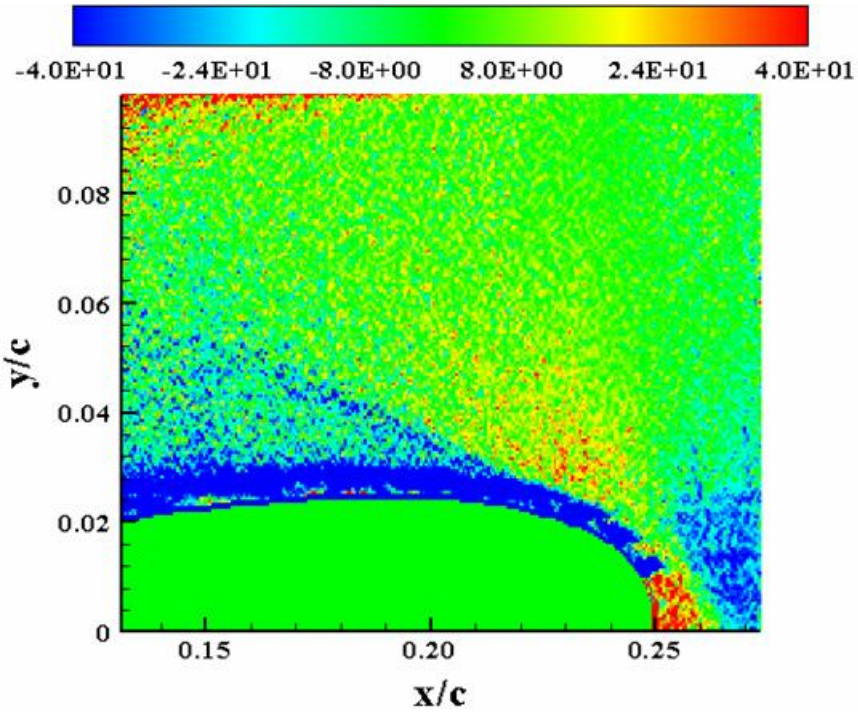

Figure 106: $S_{xy}(M_\infty = 0.2, k = 0.1, Up, \alpha = 18^0)$

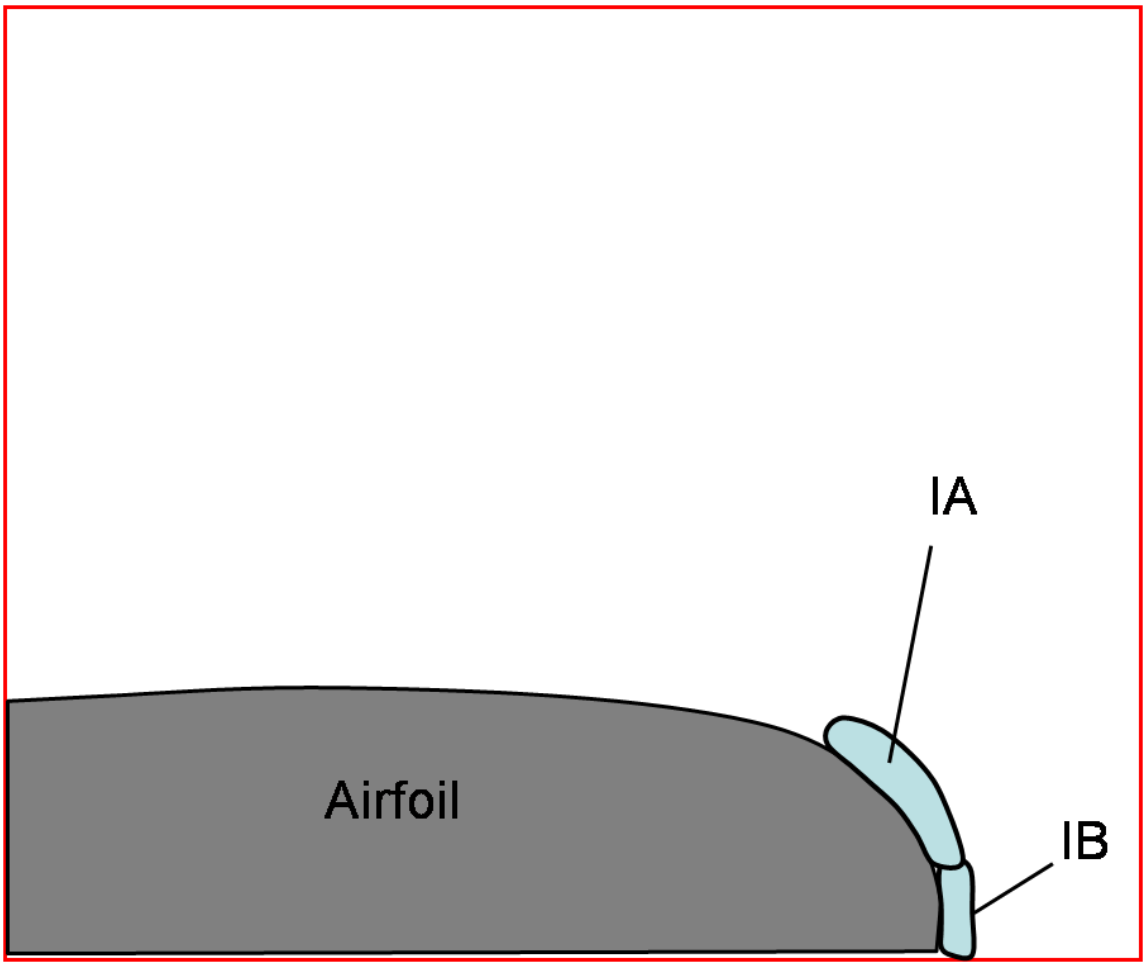

Figure 107: Sketch of regions explained for the mean strain rate during the upstroke motion of the wing

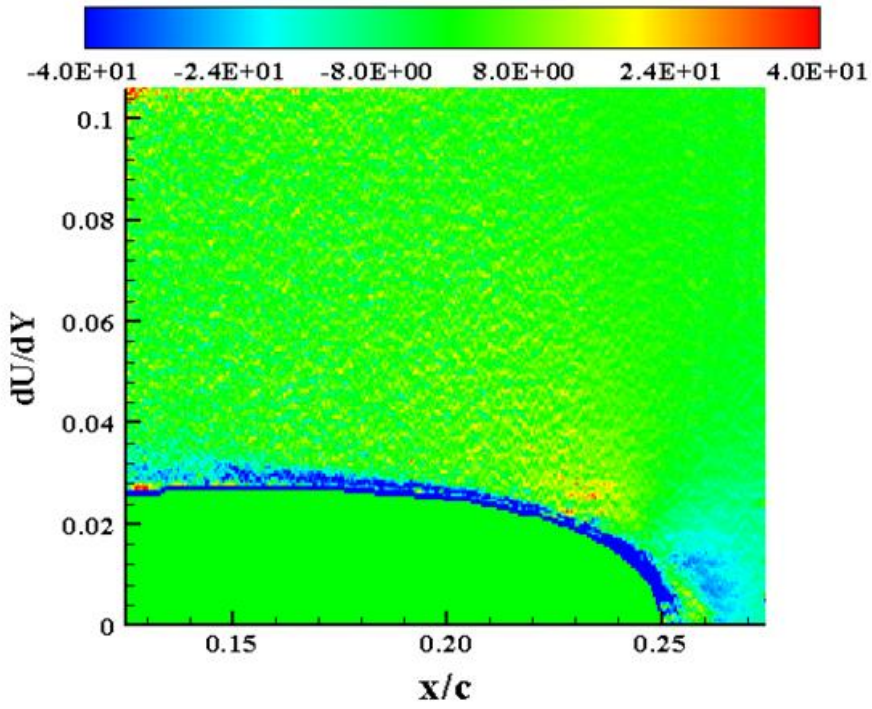

Figure 108: $dU/dY\ (M_\infty = 0.2, k = 0.1, Up, \alpha = 14^0)$

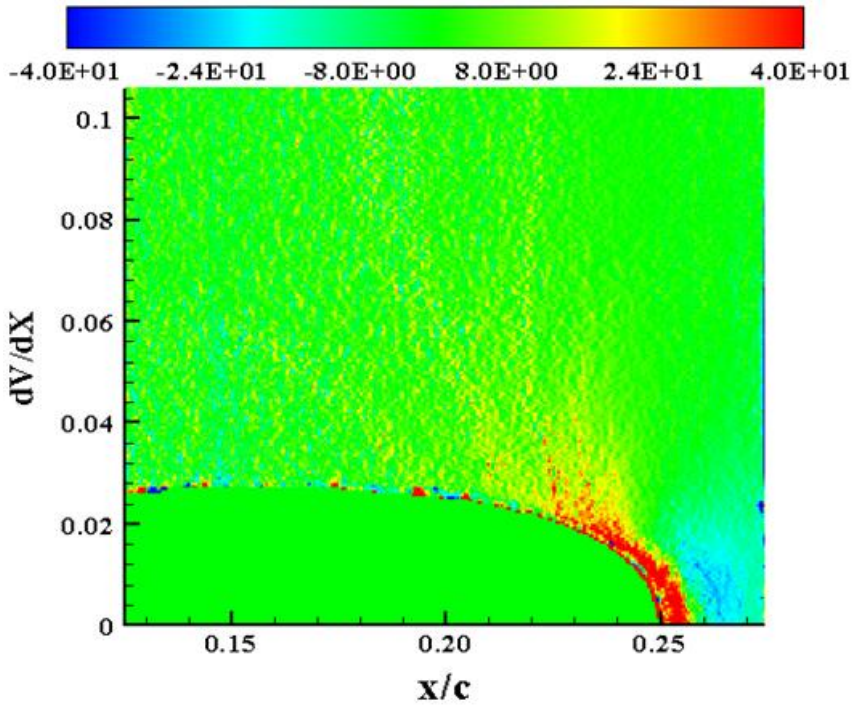

Figure 109: $dV/dX\ (M_\infty = 0.2, k = 0.1, Up, \alpha = 14^0)$

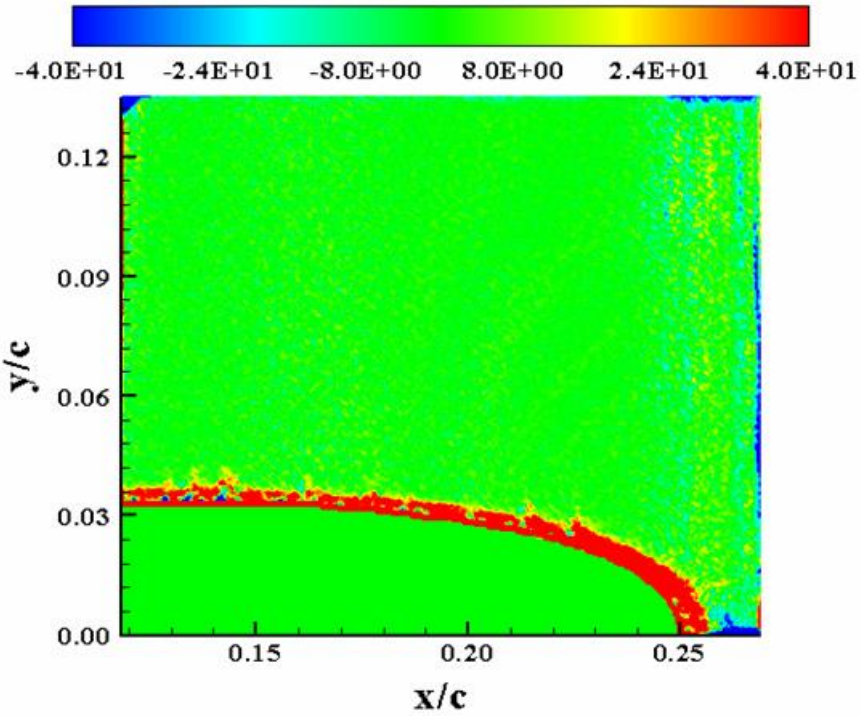

Figure 110: $\omega_z(M_\infty = 0.2, k = 0.1, Up, \alpha = 10^0)$

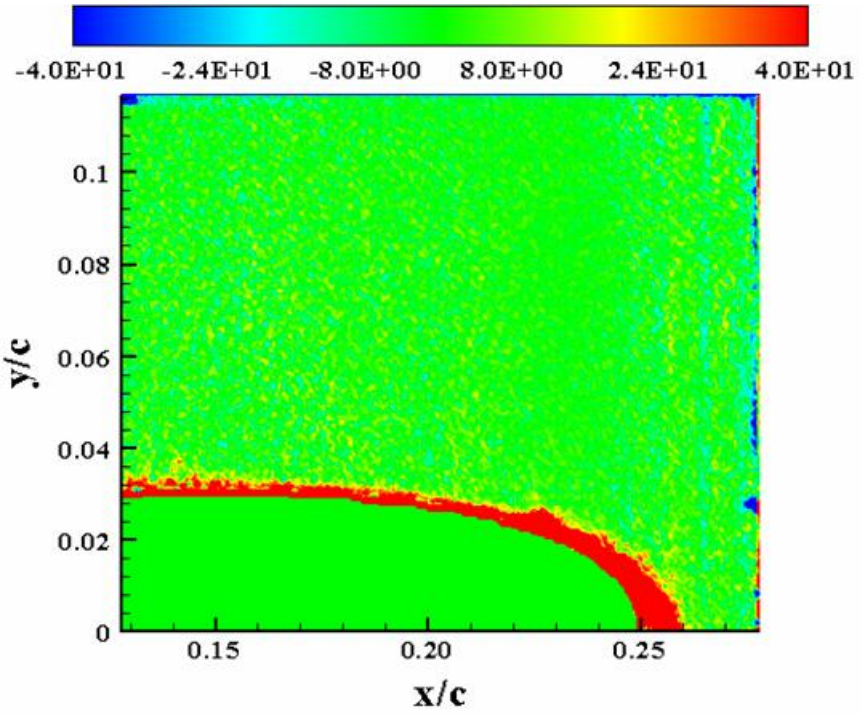

Figure 111: $\omega_z(M_\infty = 0.2, k = 0.1, Up, \alpha = 12^0)$

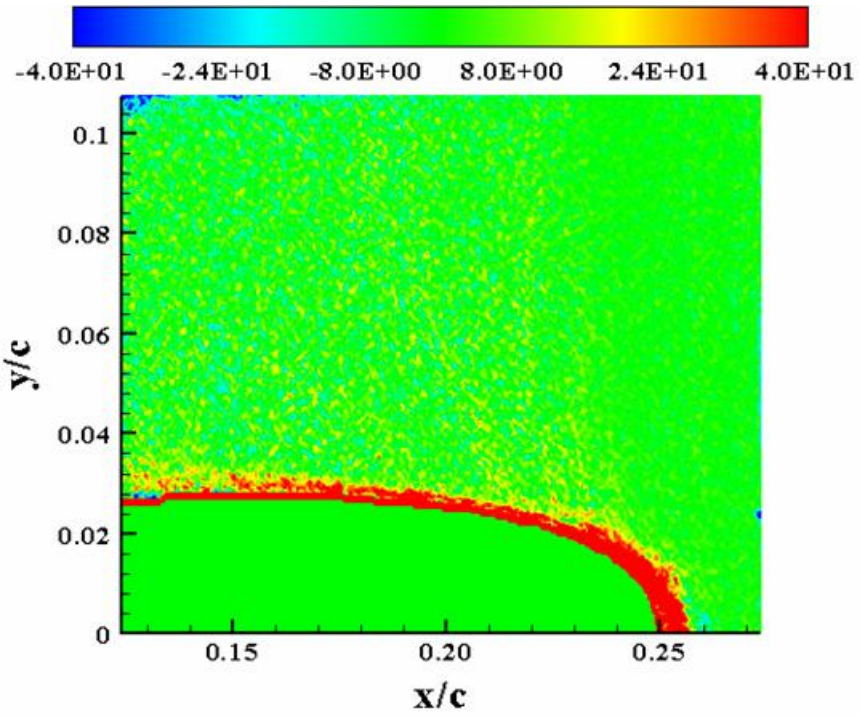

Figure 112: $\omega_z(M_\infty = 0.2, k = 0.1, Up, \alpha = 14^0)$

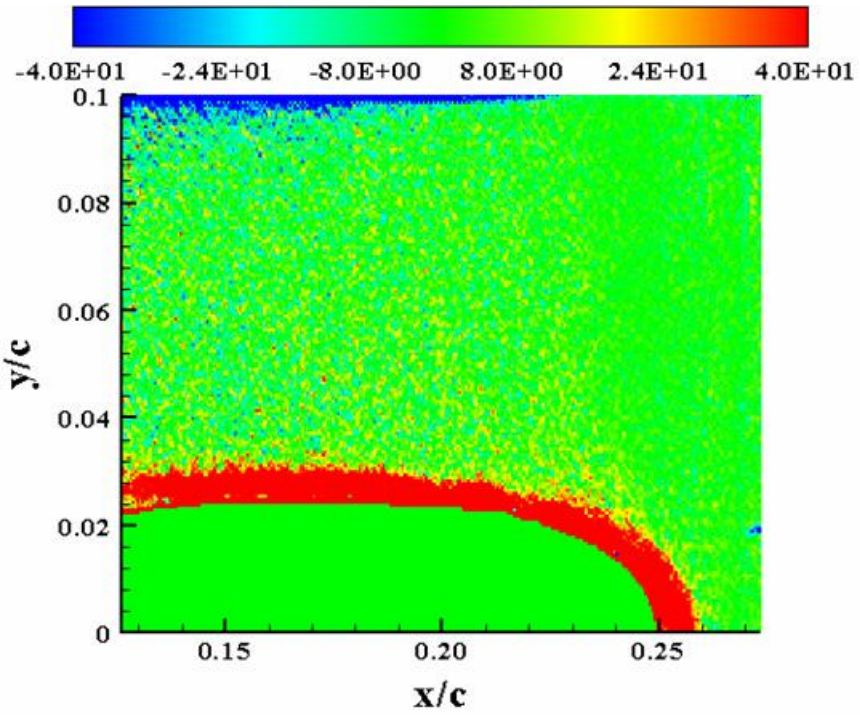

Figure 113: $\omega_z(M_\infty = 0.2, k = 0.1, Up, \alpha = 16^0)$

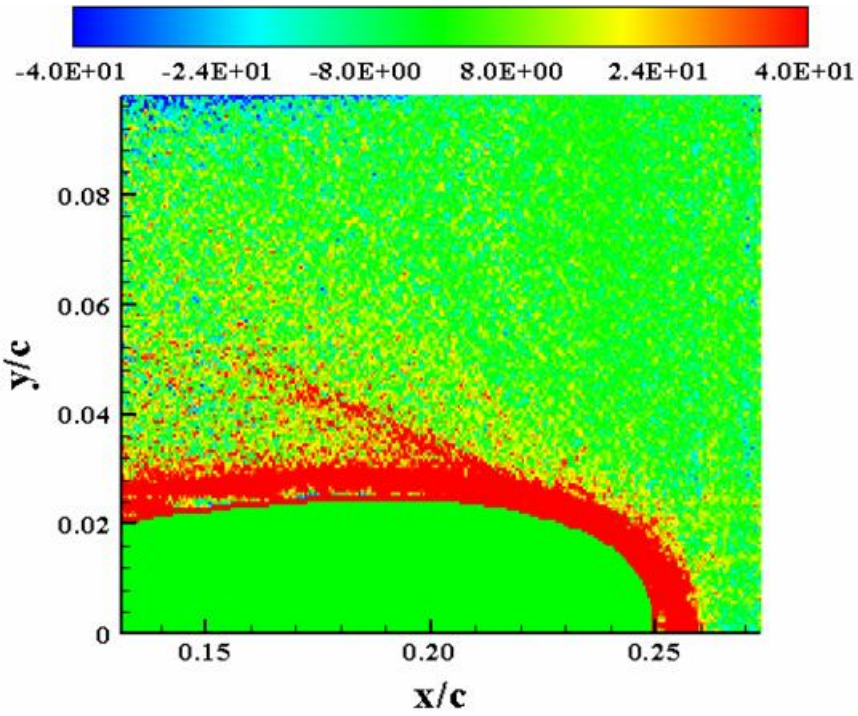

Figure 114: $\omega_z(M_\infty = 0.2, k = 0.1, Up, \alpha = 18^0)$

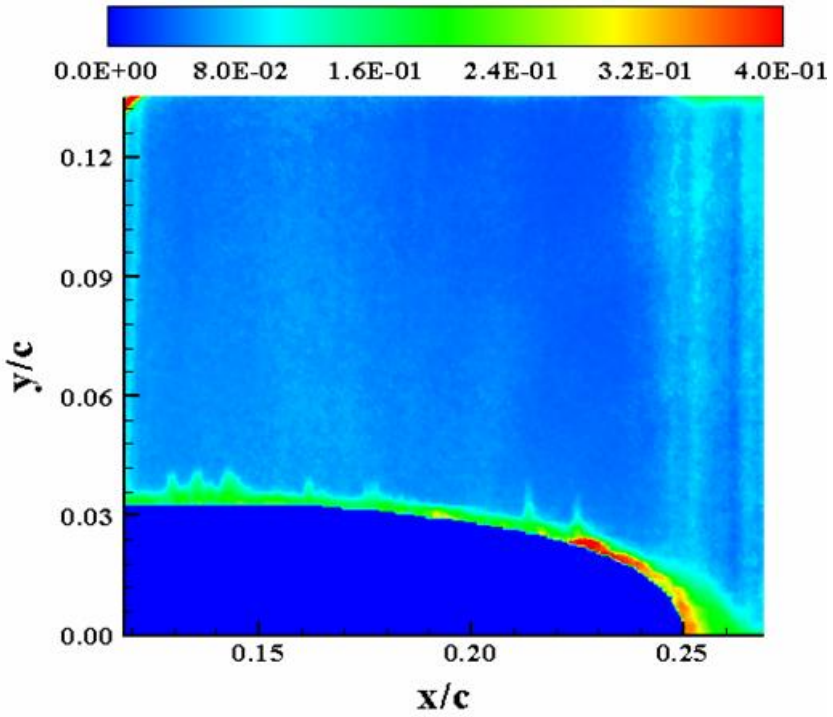

Figure 115: $\sigma_u(M_\infty = 0.2, k = 0.1, Up, \alpha = 10^0)$

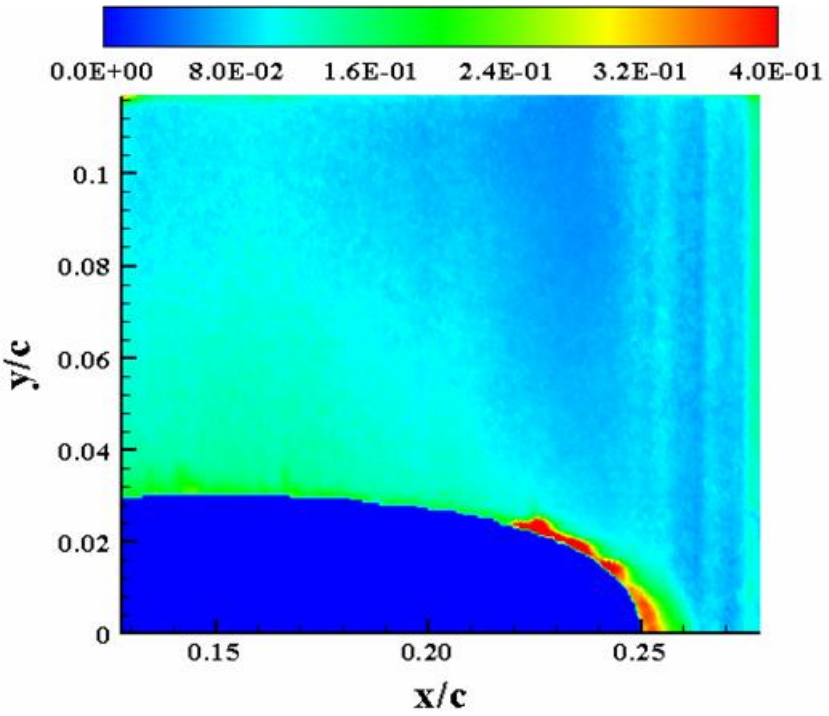

Figure 116: $\sigma_u(M_\infty = 0.2, k = 0.1, Up, \alpha = 12^0)$

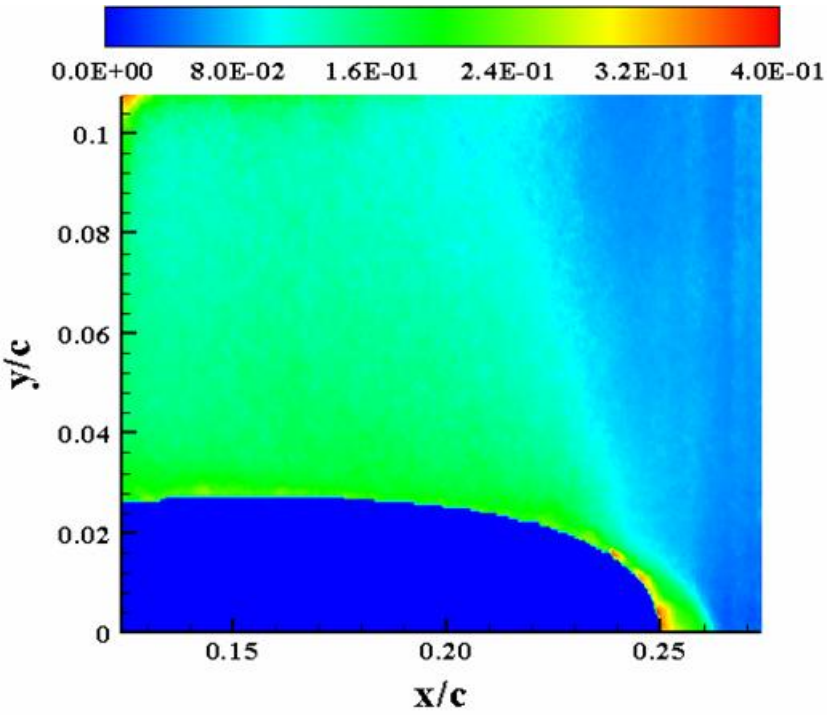

Figure 117: $\sigma_u(M_\infty = 0.2, k = 0.1, Up, \alpha = 14^0)$

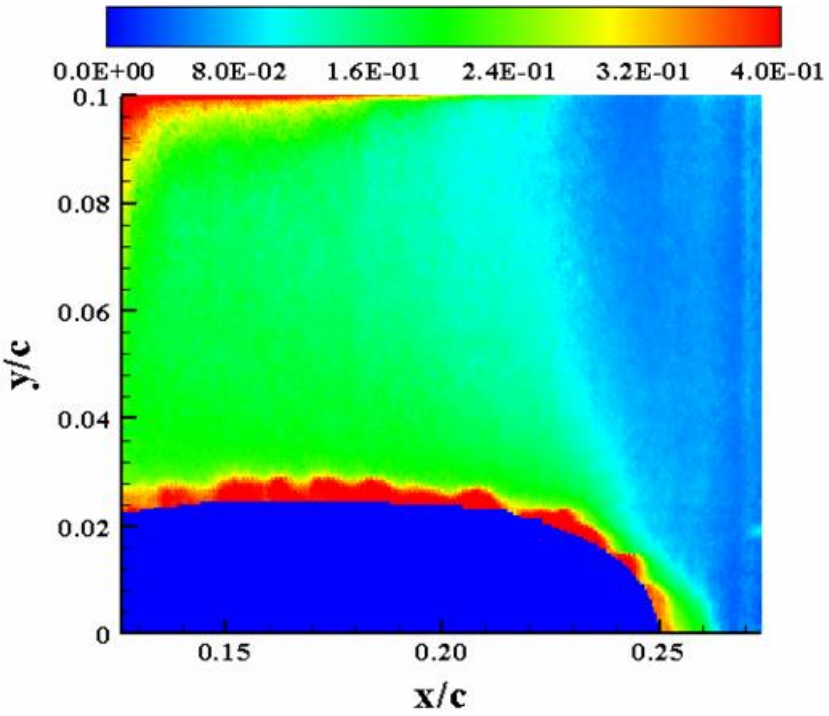

Figure 118: $\sigma_u(M_\infty = 0.2, k = 0.1, Up, \alpha = 16^0)$

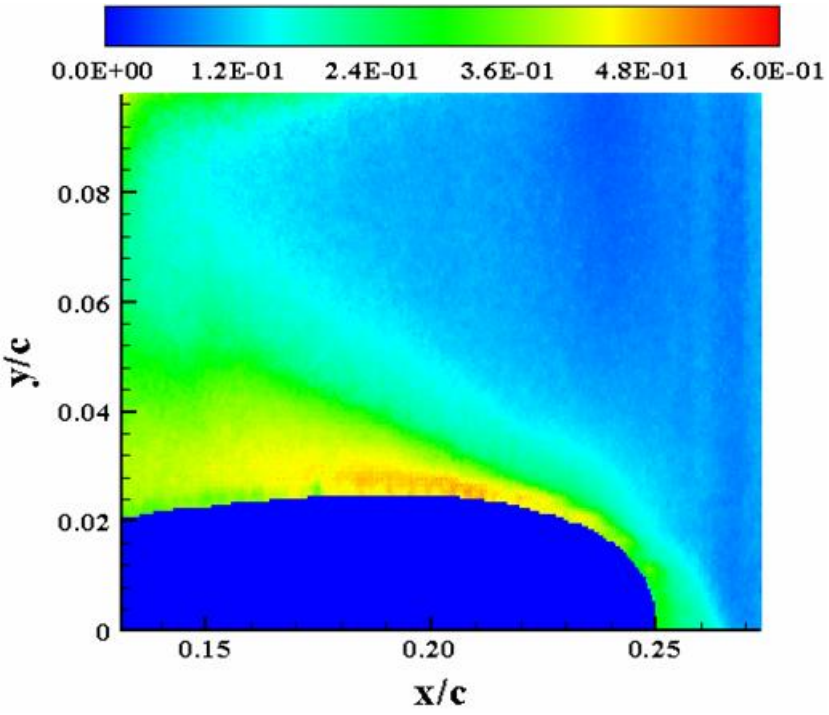

Figure 119: $\sigma_u(M_\infty = 0.2, k = 0.1, Up, \alpha = 18^0)$

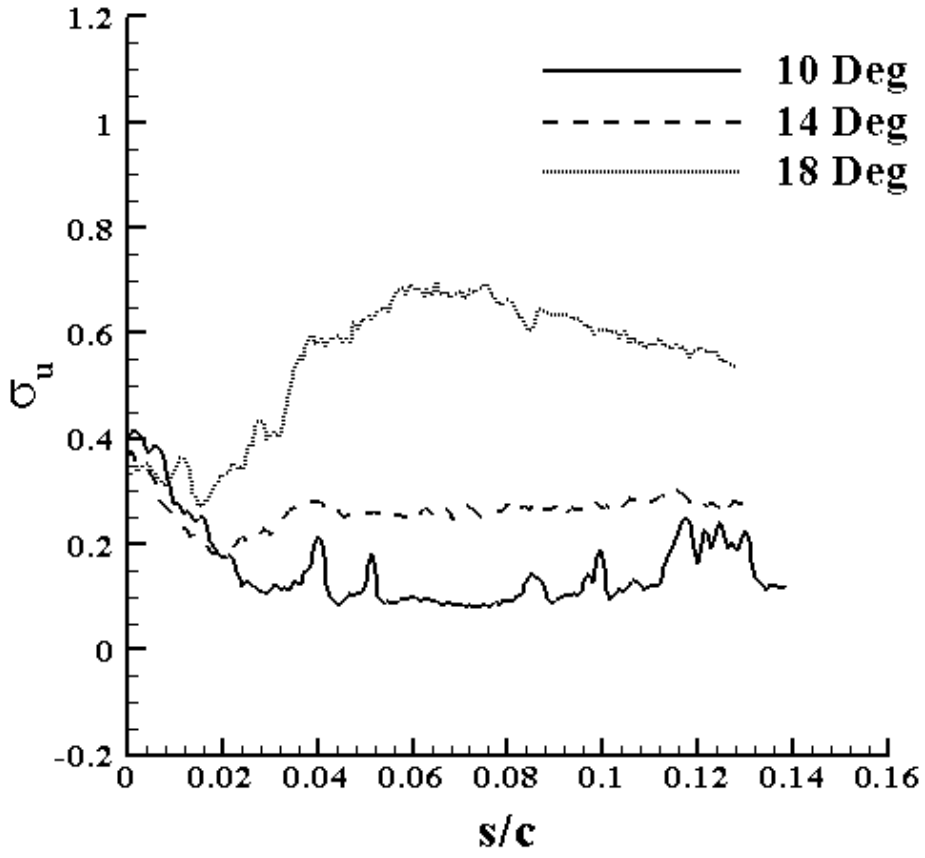

Figure 120: Line plot of σ_u for $M_\infty = 0.2, k = 0.1, Up, \alpha = 10^0, 14^0 \, and \, 18^0$

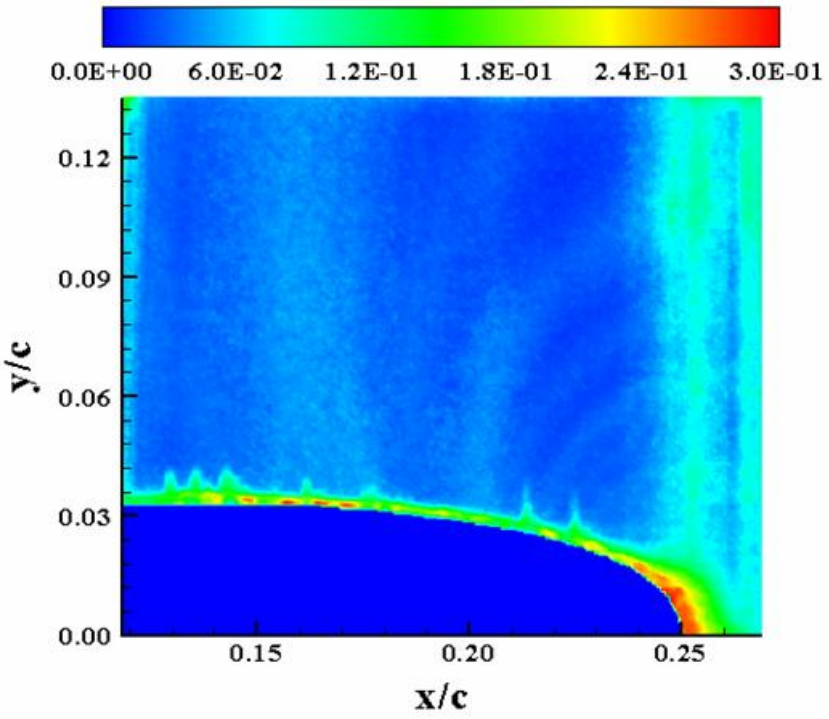

Figure 121: $\sigma_v(M_\infty = 0.2, k = 0.1, Up, \alpha = 10^0)$

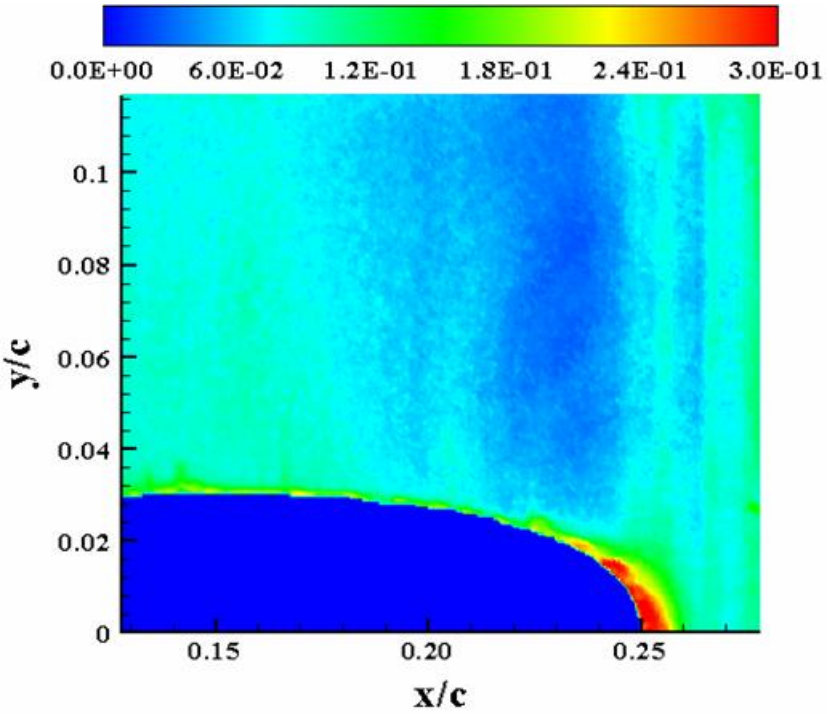

Figure 122: $\sigma_v(M_\infty = 0.2, k = 0.1, Up, \alpha = 12^0)$

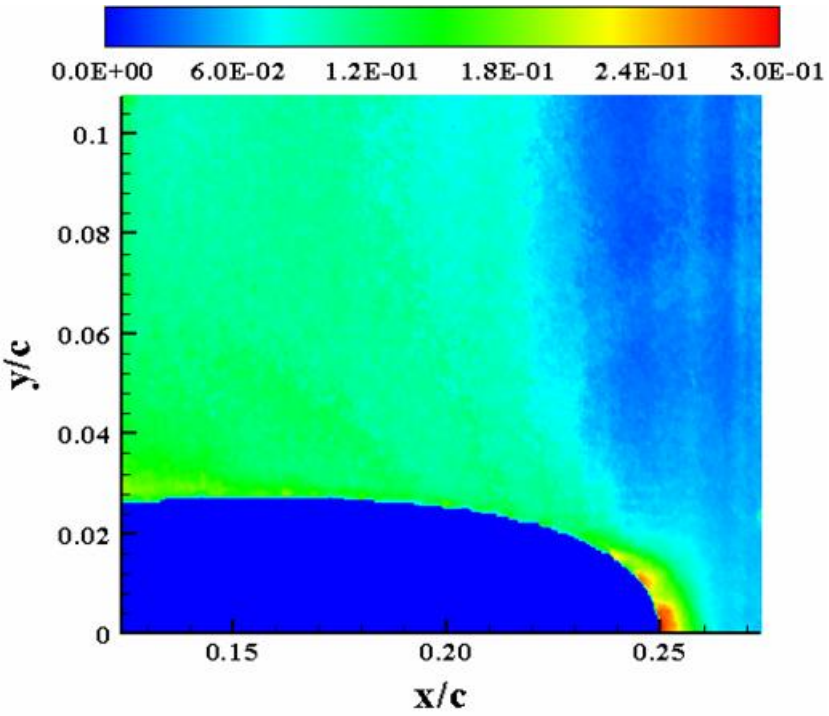

Figure 123 $\sigma_v(M_\infty = 0.2, k = 0.1, Up, \alpha = 14^0)$

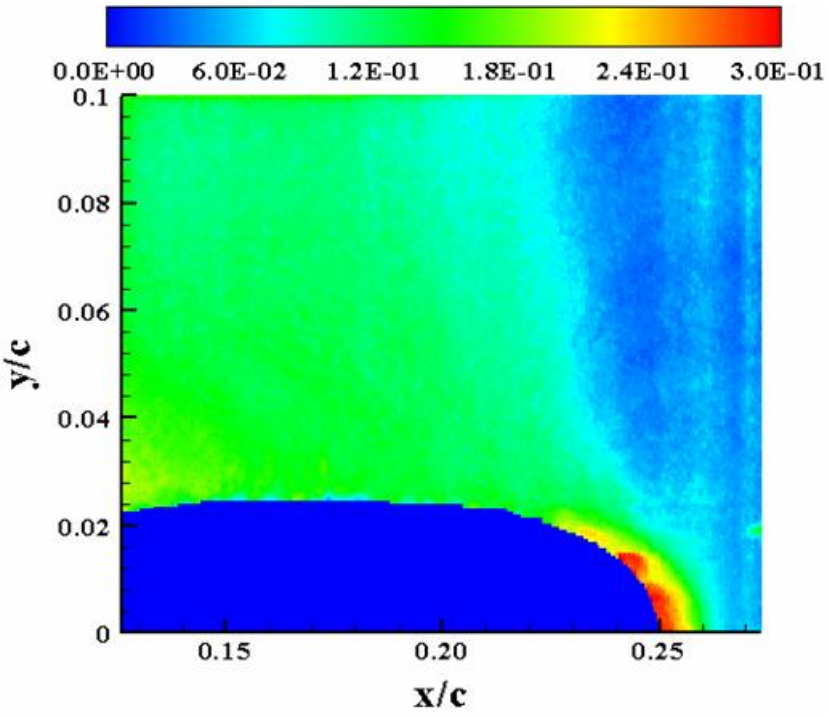

Figure 124: $\sigma_v(M_\infty = 0.2, k = 0.1, Up, \alpha = 16^0)$

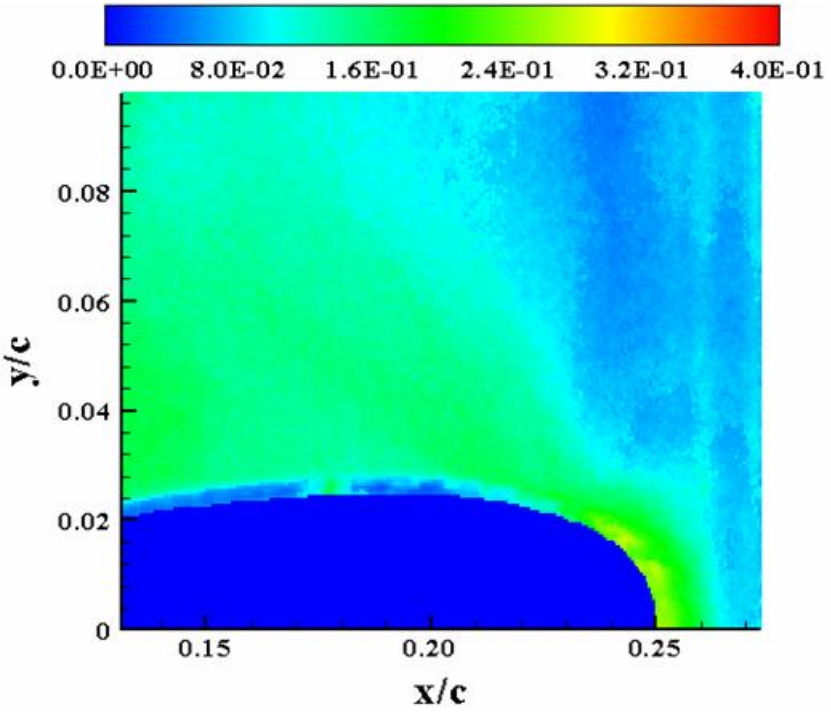

Figure 125: $\sigma_v (M_\infty = 0.2, k = 0.1, Up, \alpha = 18^0)$

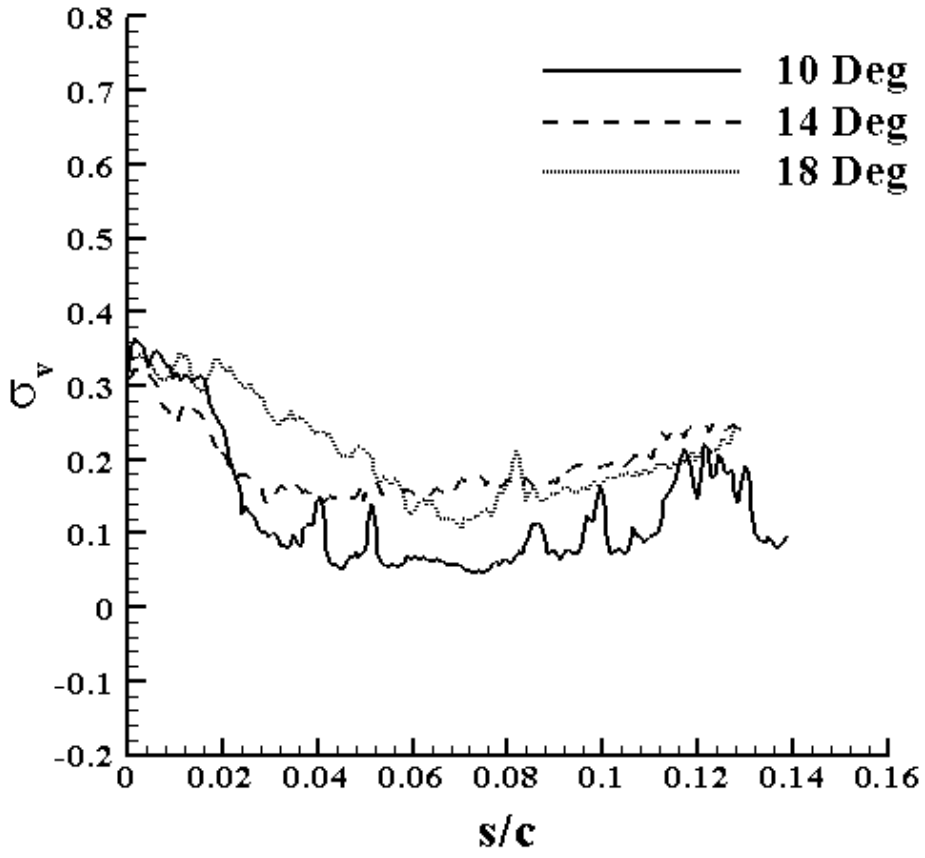

Figure 126: Line plot of σ_v for $M_\infty = 0.2, k = 0.1, Up, \alpha = 10^0, 14^0 \, and \, 18^0$

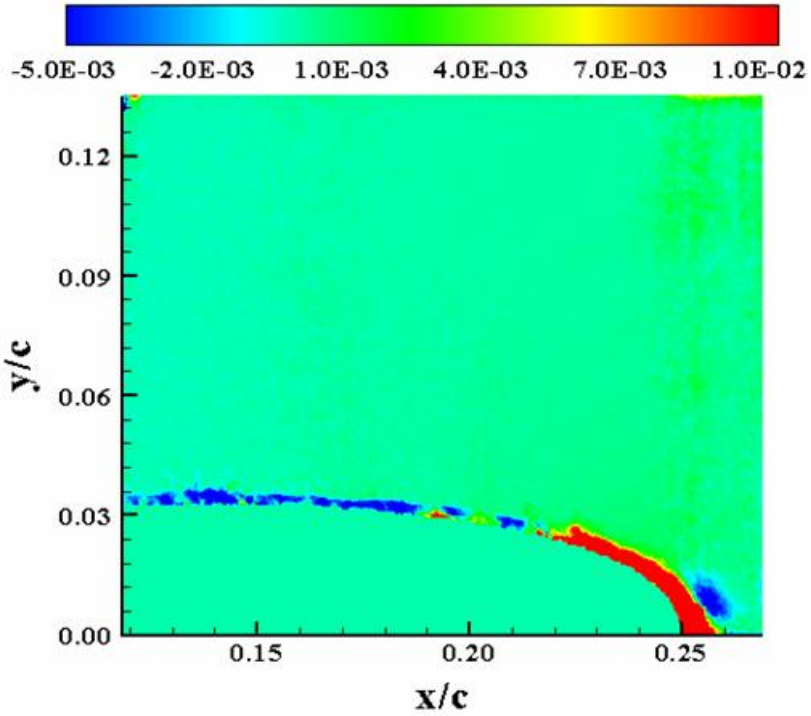

Figure 127: $\tau_{xy}(M_\infty = 0.2, k = 0.1, Up, \alpha = 10^0)$

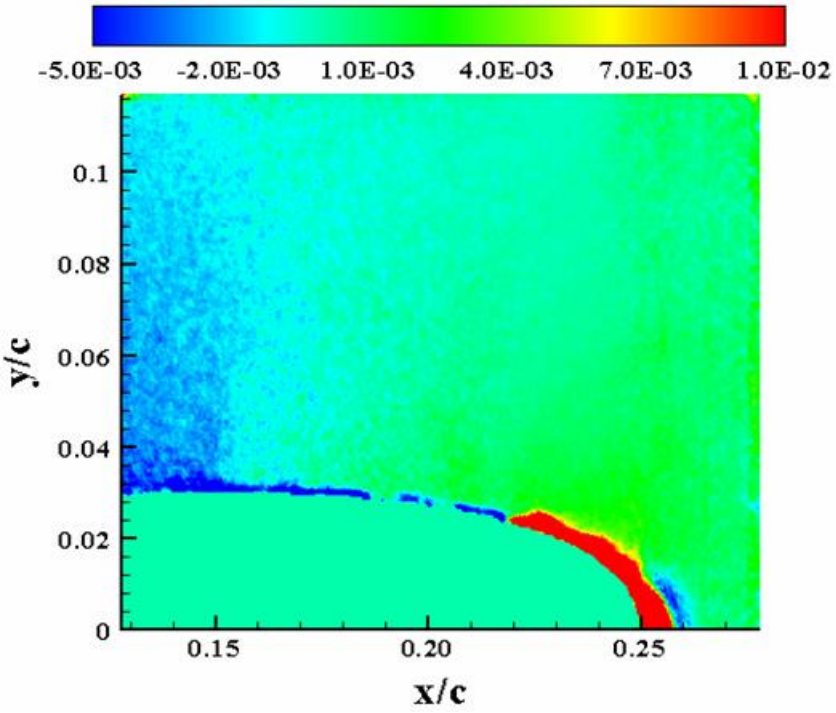

Figure 128: $\tau_{xy}(M_\infty = 0.2, k = 0.1, Up, \alpha = 12^0)$

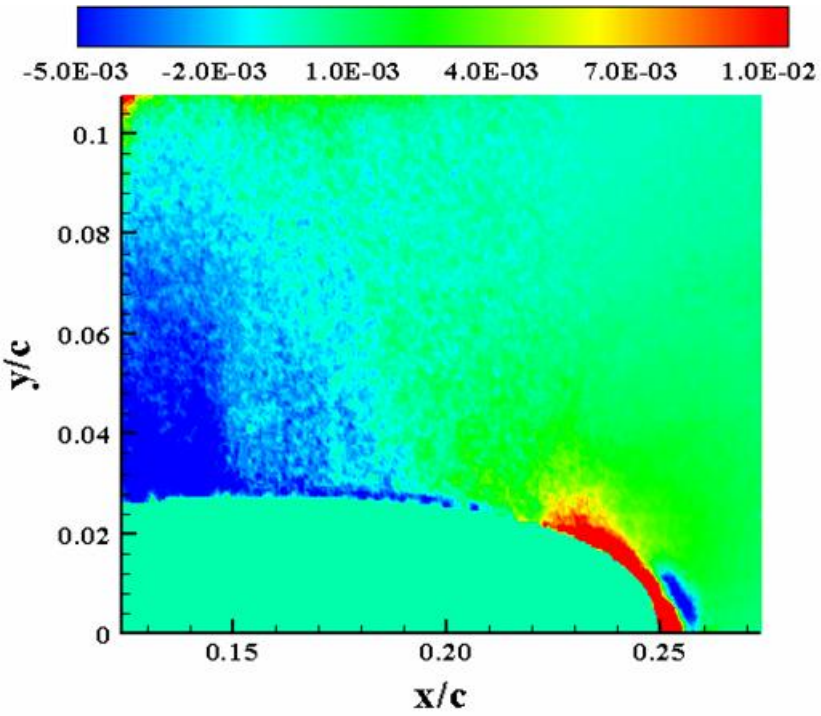

Figure 129: $\tau_{xy}(M_\infty = 0.2, k = 0.1, Up, \alpha = 14^0)$

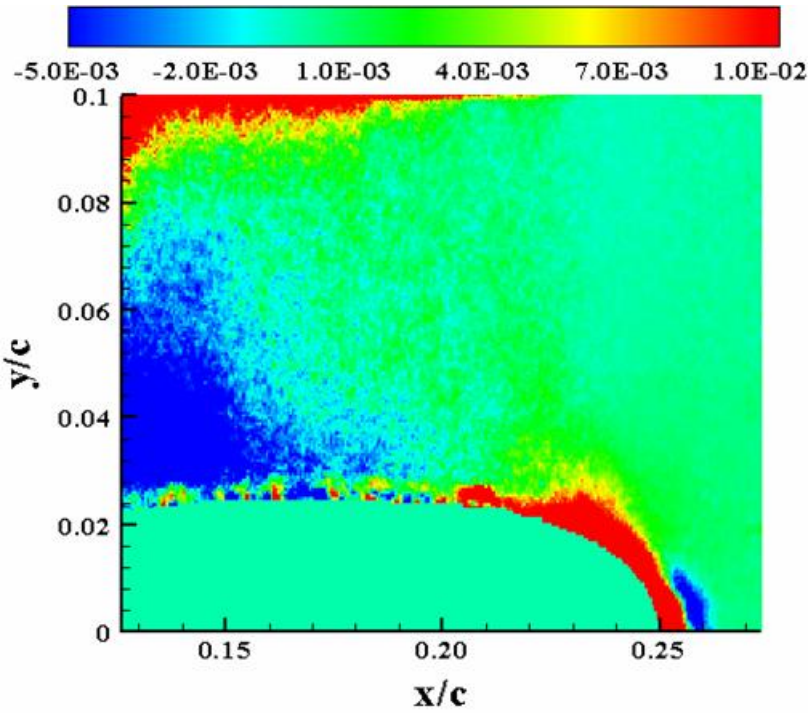

Figure 130: $\tau_{xy}(M_\infty = 0.2, k = 0.1, Up, \alpha = 16^0)$

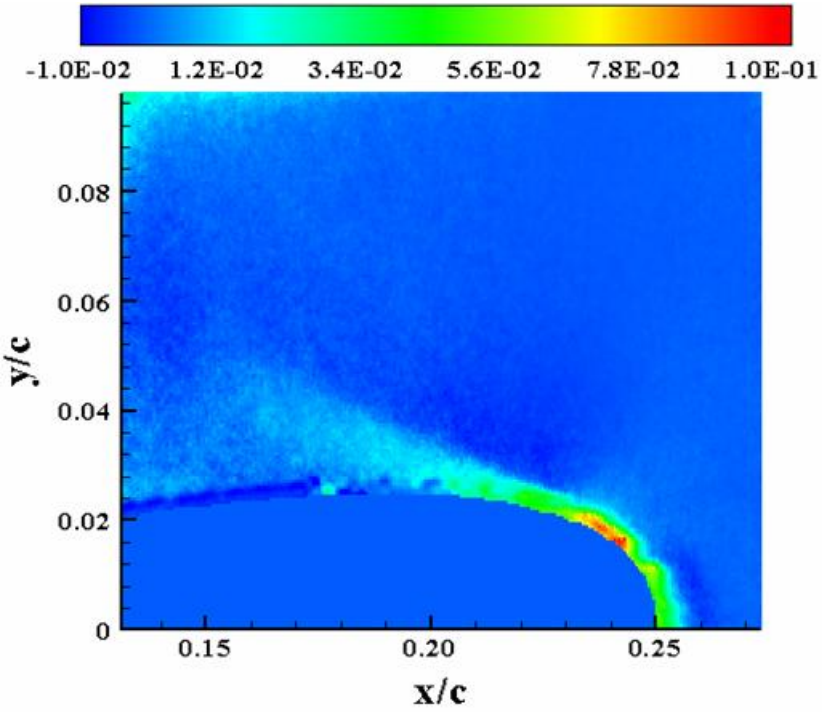

Figure 131: $\tau_{xy}(M_\infty = 0.2, k = 0.1, Up, \alpha = 18^0)$

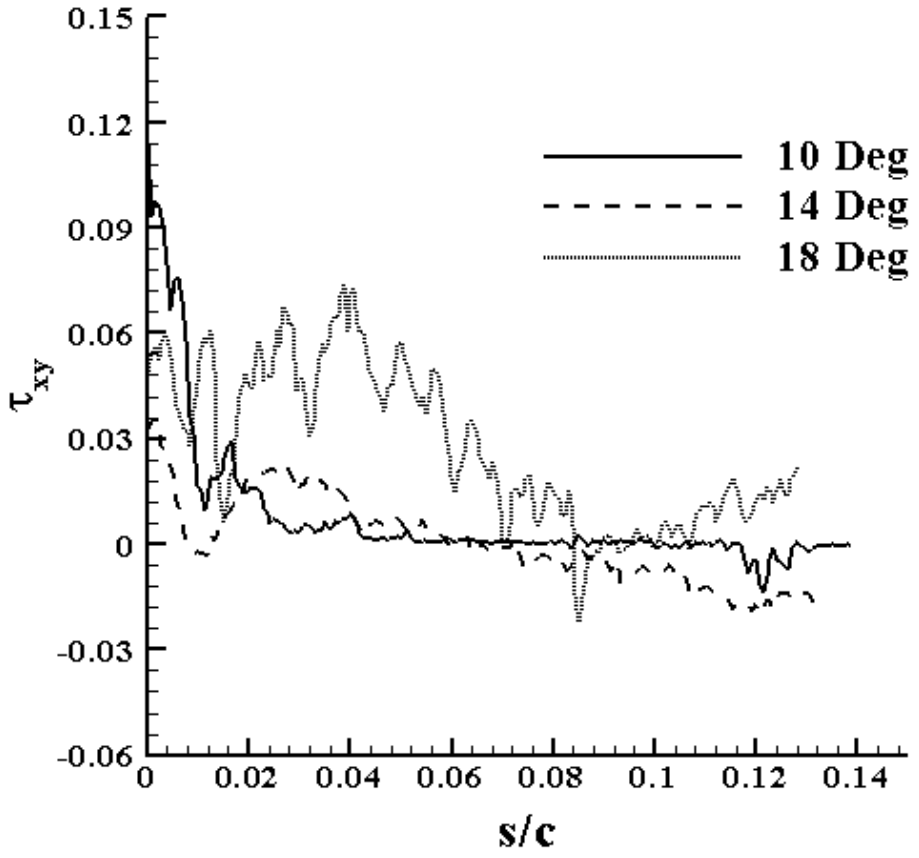

Figure 132: Line plot of τ_{xy} for $M_\infty = 0.2, k = 0.1, Up, \alpha = 10^0, 14^0 and 18^0$

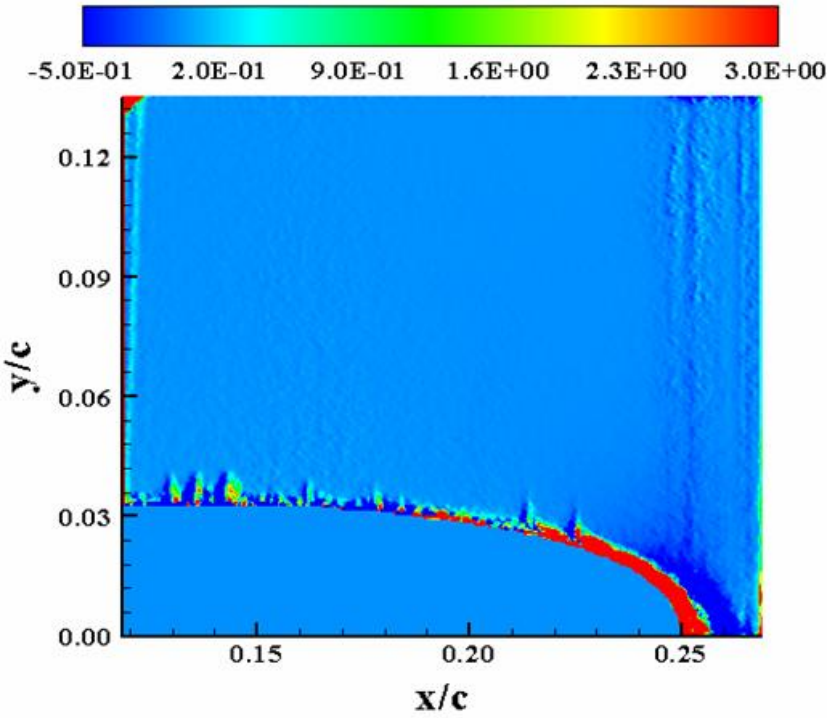

Figure 133: $P_{xx}(M_\infty = 0.2, k = 0.1, Up, \alpha = 10^0)$

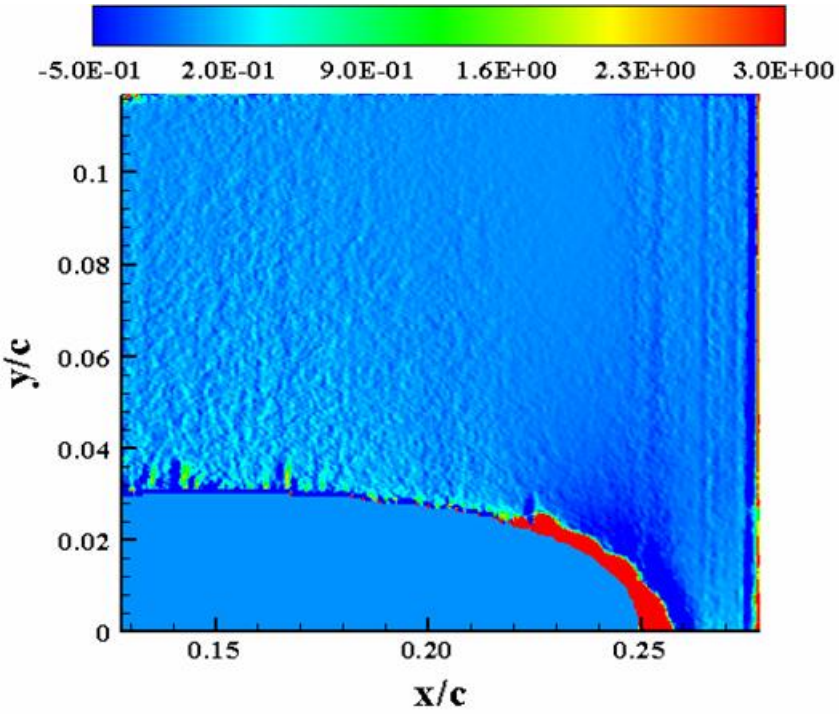

Figure 134: $P_{xx}(M_\infty = 0.2, k = 0.1, Up, \alpha = 12^0)$

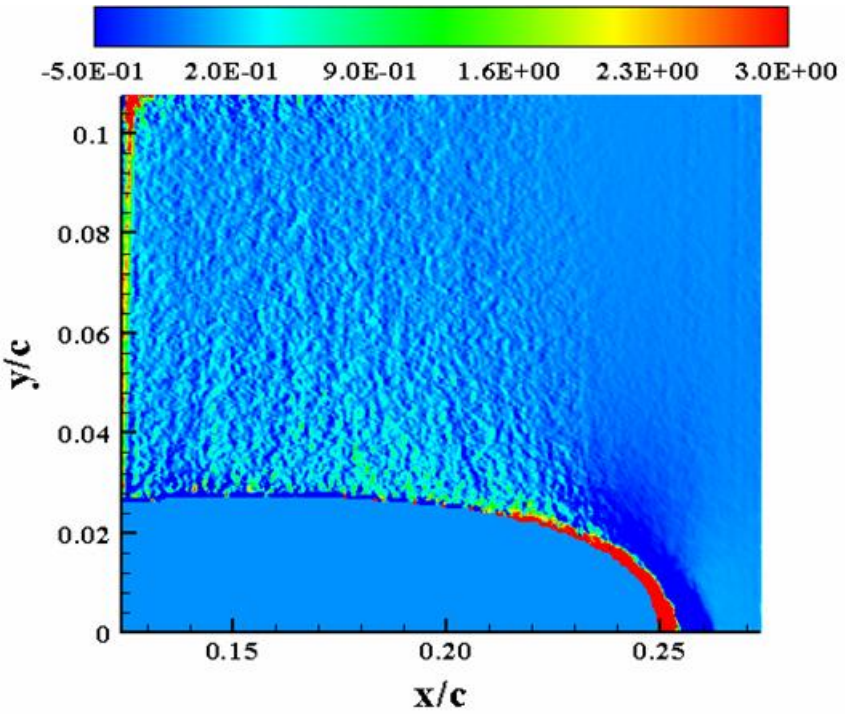

Figure 135: $P_{xx}(M_\infty = 0.2, k = 0.1, Up, \alpha = 14^0)$

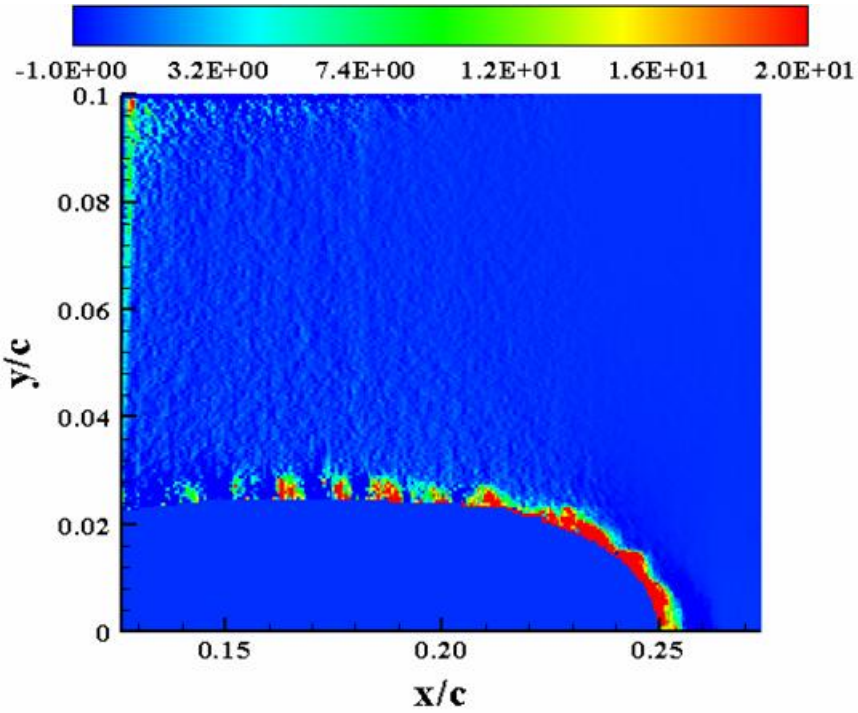

Figure 136: $P_{xx}(M_\infty = 0.2, k = 0.1, Up, \alpha = 16^0)$

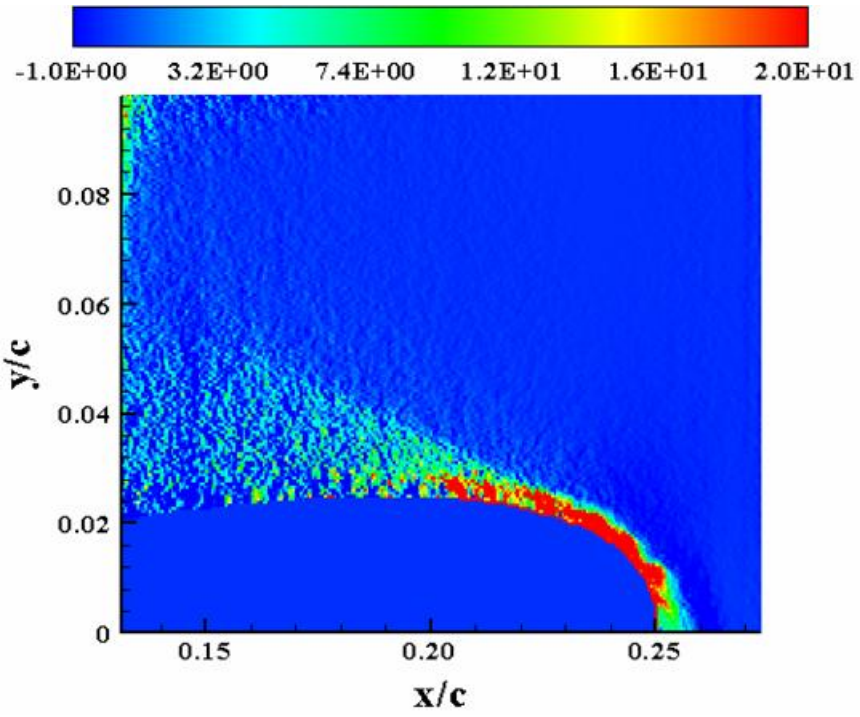

Figure 137: $P_{xx}(M_\infty = 0.2, k = 0.1, Up, \alpha = 18^0)$

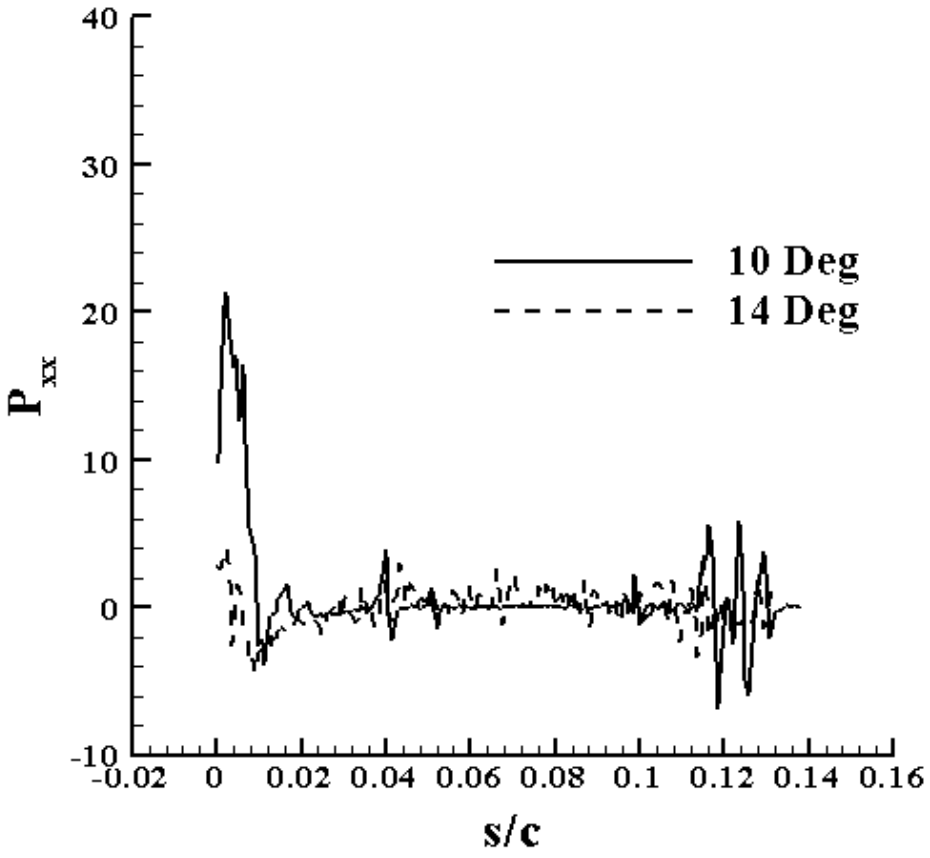

Figure 138: Line plot of P_{xx} for $M_\infty = 0.2, k = 0.1, Up, \alpha = 10^0, 14^0$

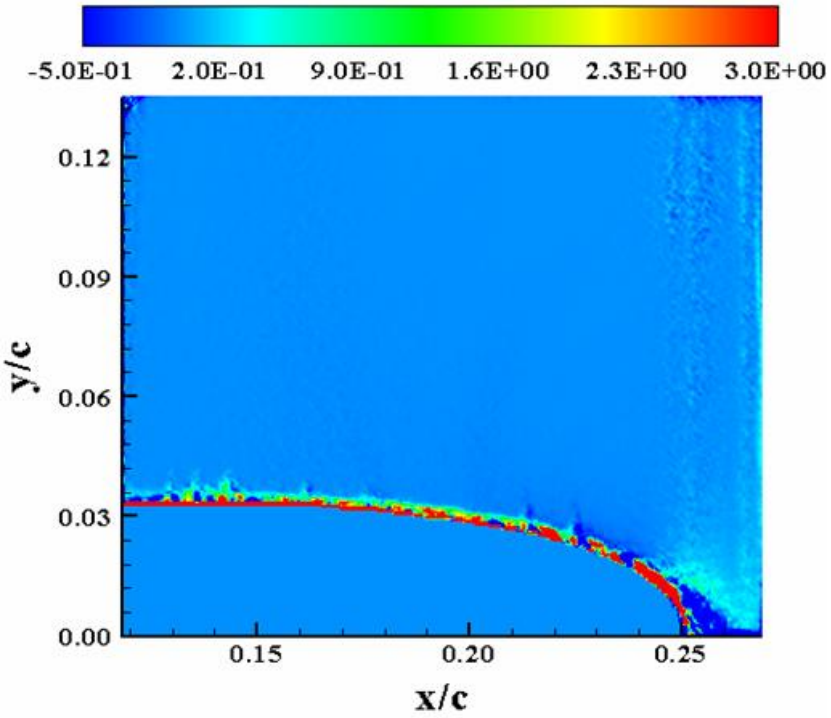

Figure 139: $P_{xy}(M_\infty = 0.2, k = 0.1, Up, \alpha = 10^0)$

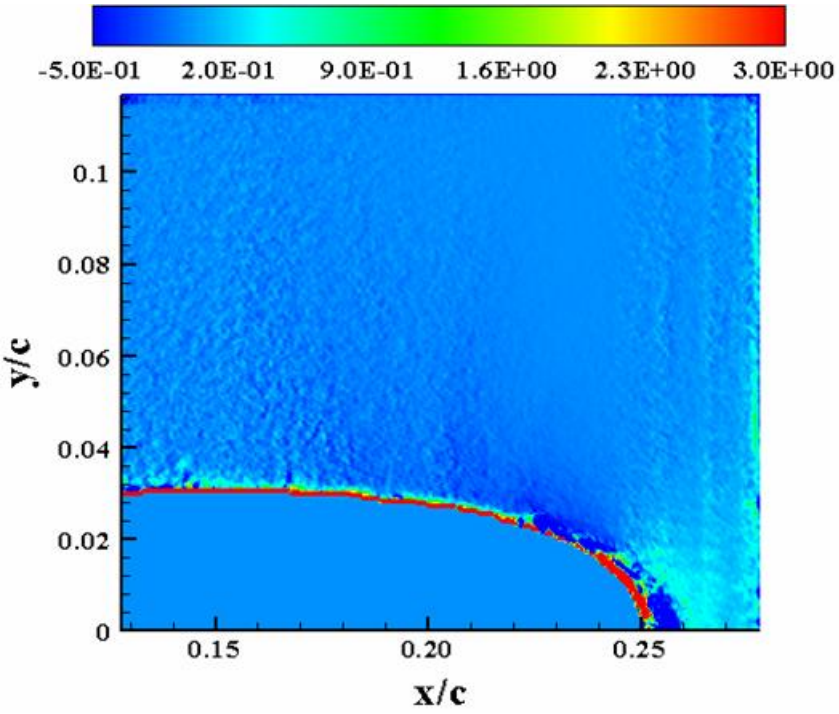

Figure 140: $P_{xy}(M_\infty = 0.2, k = 0.1, Up, \alpha = 12^0)$

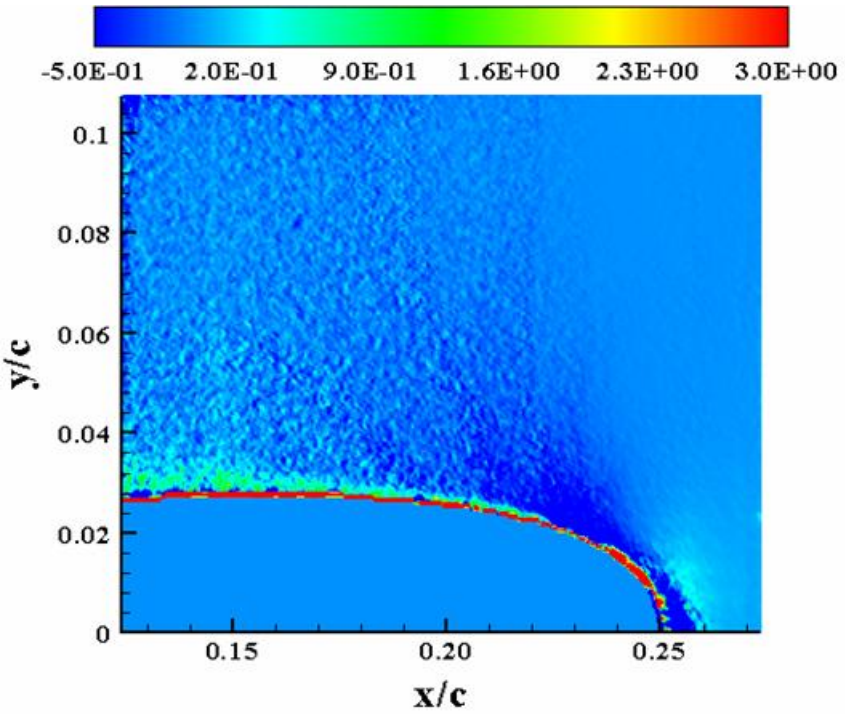

Figure 141: $P_{xy}(M_\infty = 0.2, k = 0.1, Up, \alpha = 14^0)$

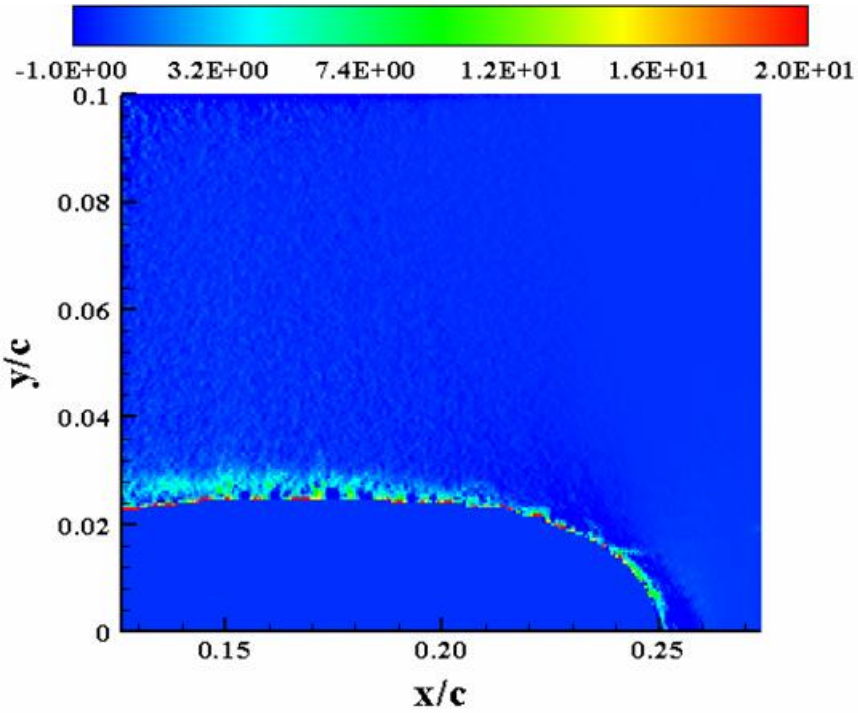

Figure 142: $P_{xy}(M_\infty = 0.2, k = 0.1, Up, \alpha = 16^0)$

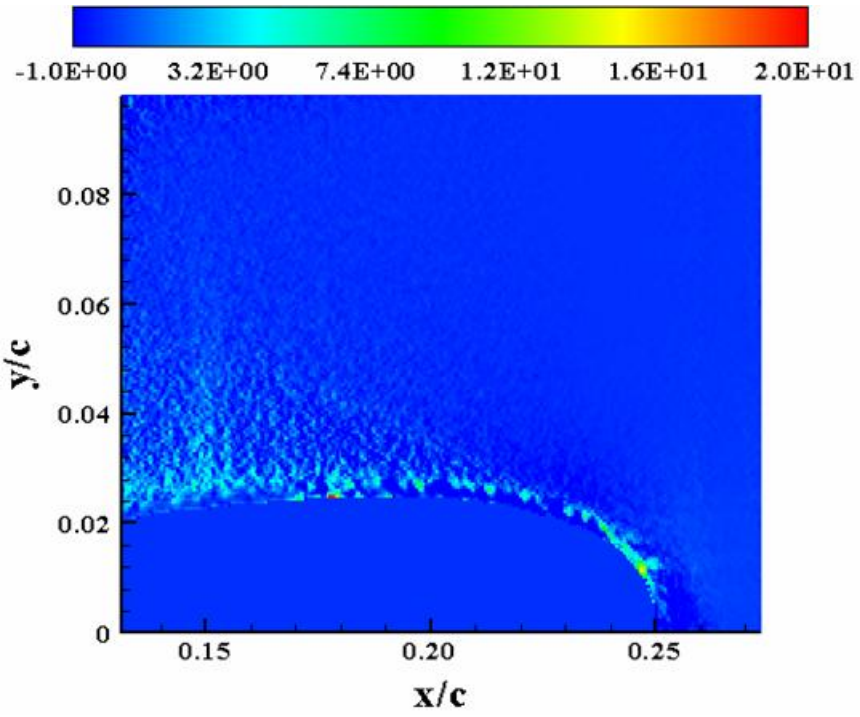

Figure 143: $P_{xy}(M_\infty = 0.2, k = 0.1, Up, \alpha = 18^0)$

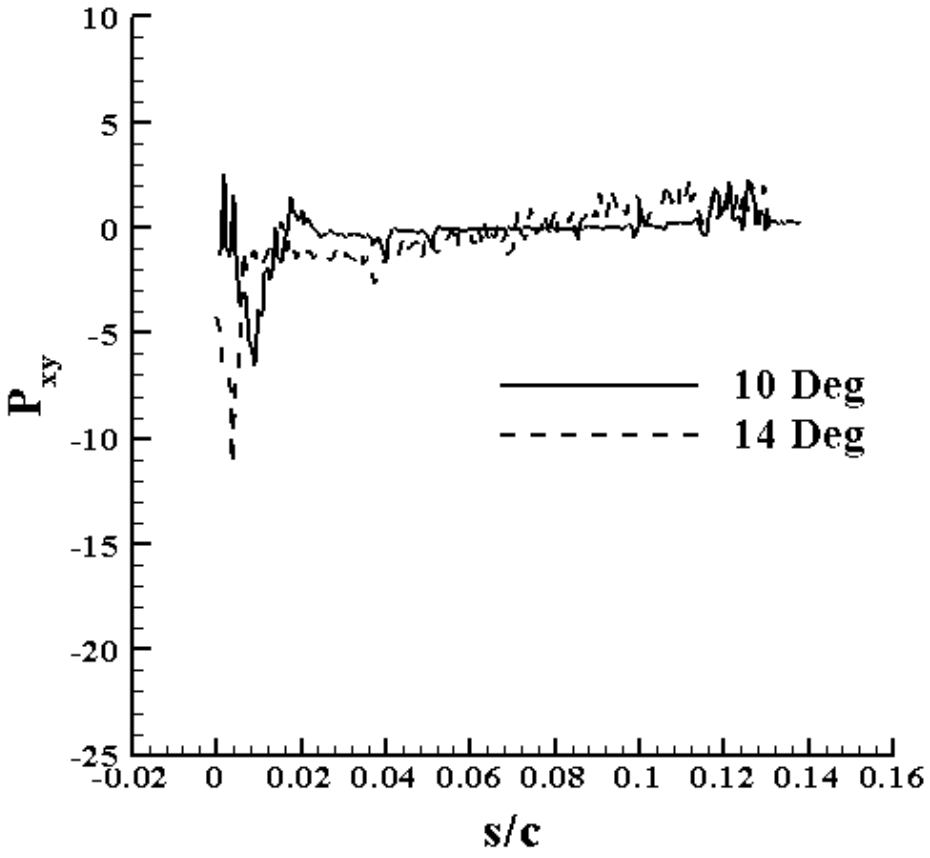

Figure 144: Line plot of P_{xy} for $M_\infty = 0.2, k = 0.1, Up, \alpha = 10^0, 14^0$

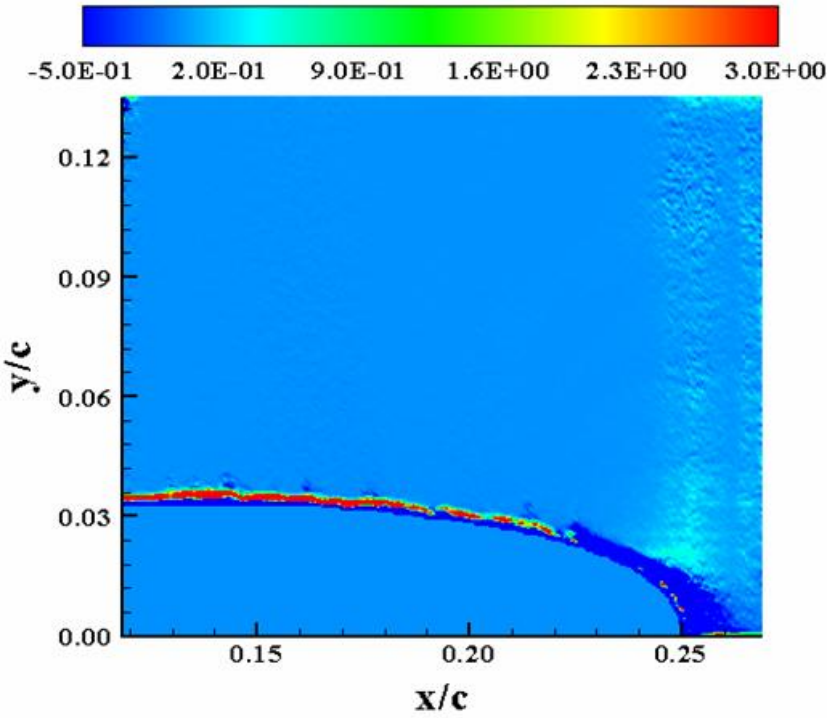

Figure 145: $P_{yy}(M_\infty = 0.2, k = 0.1, Up, \alpha = 10^0)$

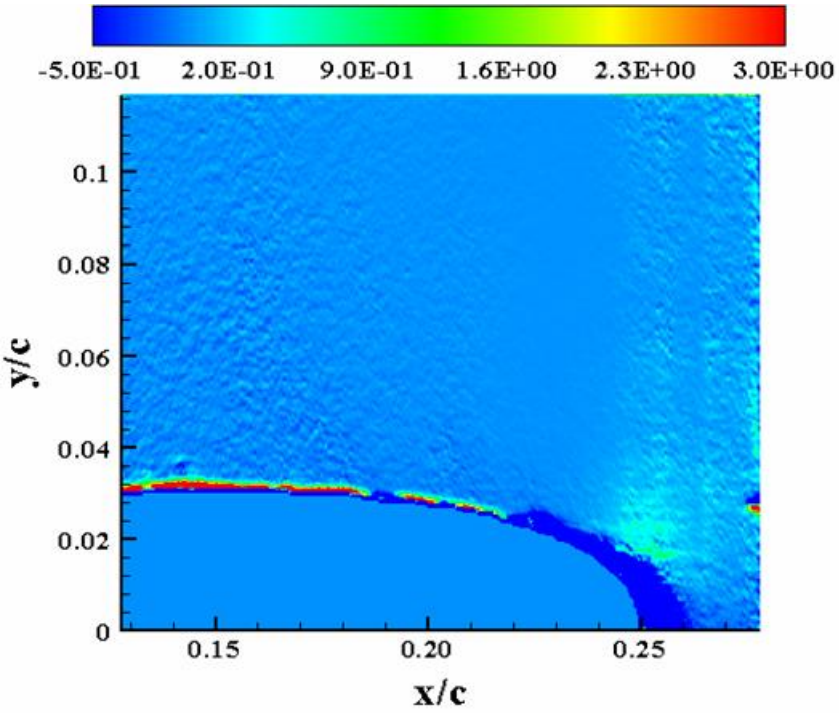

Figure 146: $P_{yy}(M_\infty = 0.2, k = 0.1, Up, \alpha = 12^0)$

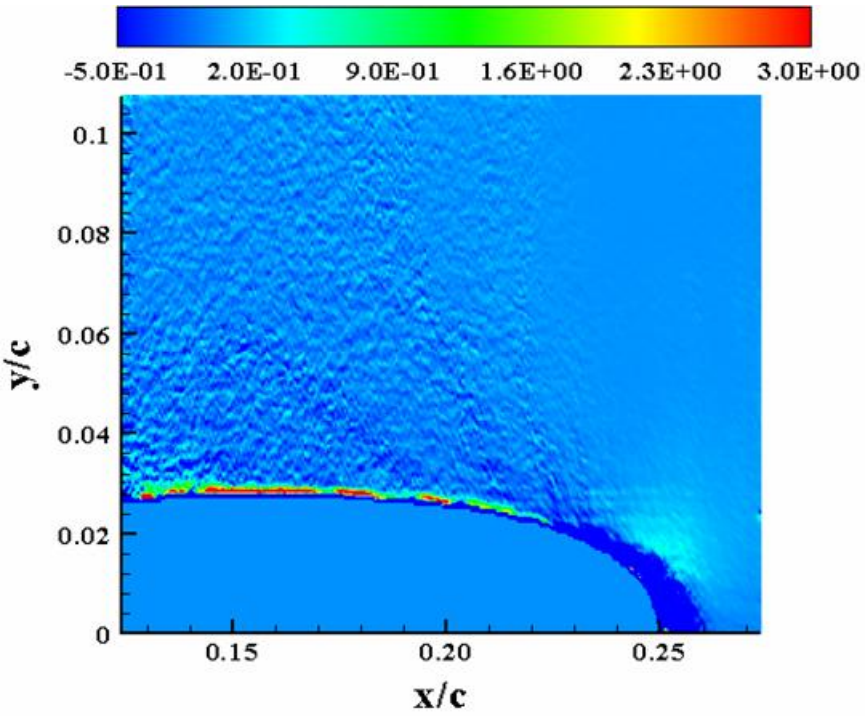

Figure 147: $P_{yy}(M_\infty = 0.2, k = 0.1, Up, \alpha = 14^0)$

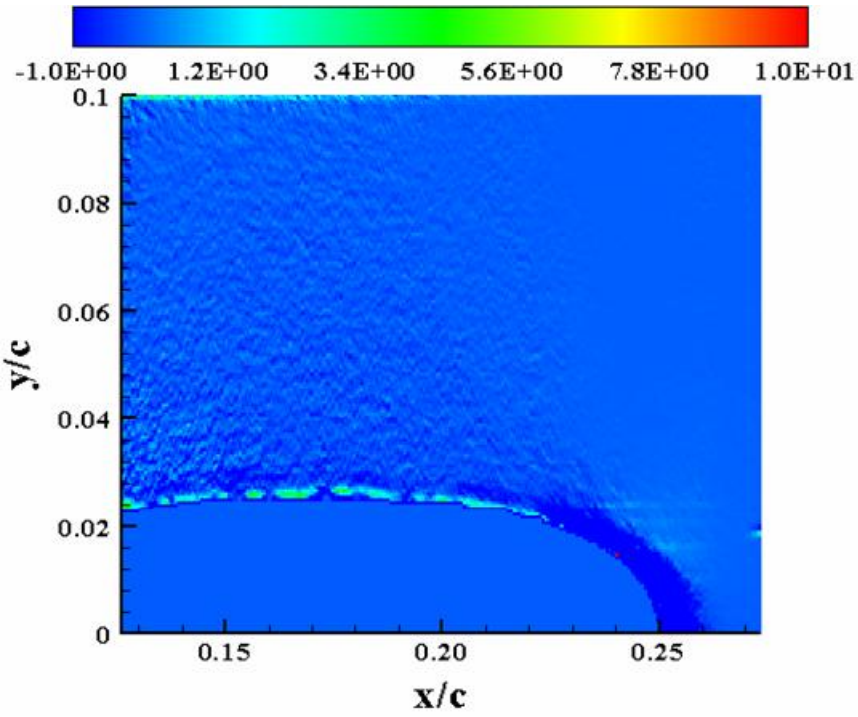

Figure 148: $P_{yy}(M_\infty = 0.2, k = 0.1, Up, \alpha = 16^0)$

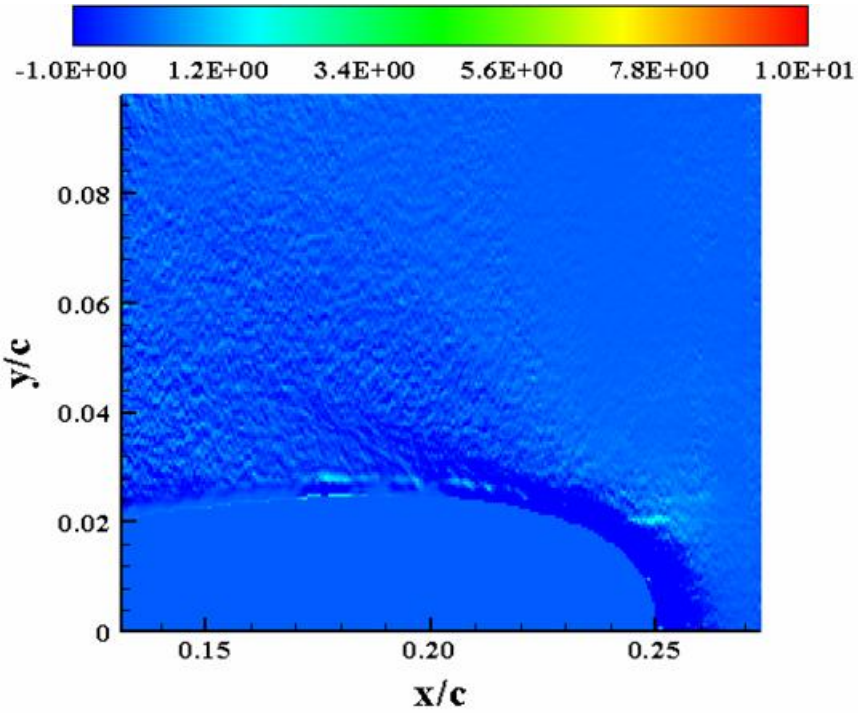

Figure 149: $P_{yy}(M_\infty = 0.2, k = 0.1, Up, \alpha = 18^0)$

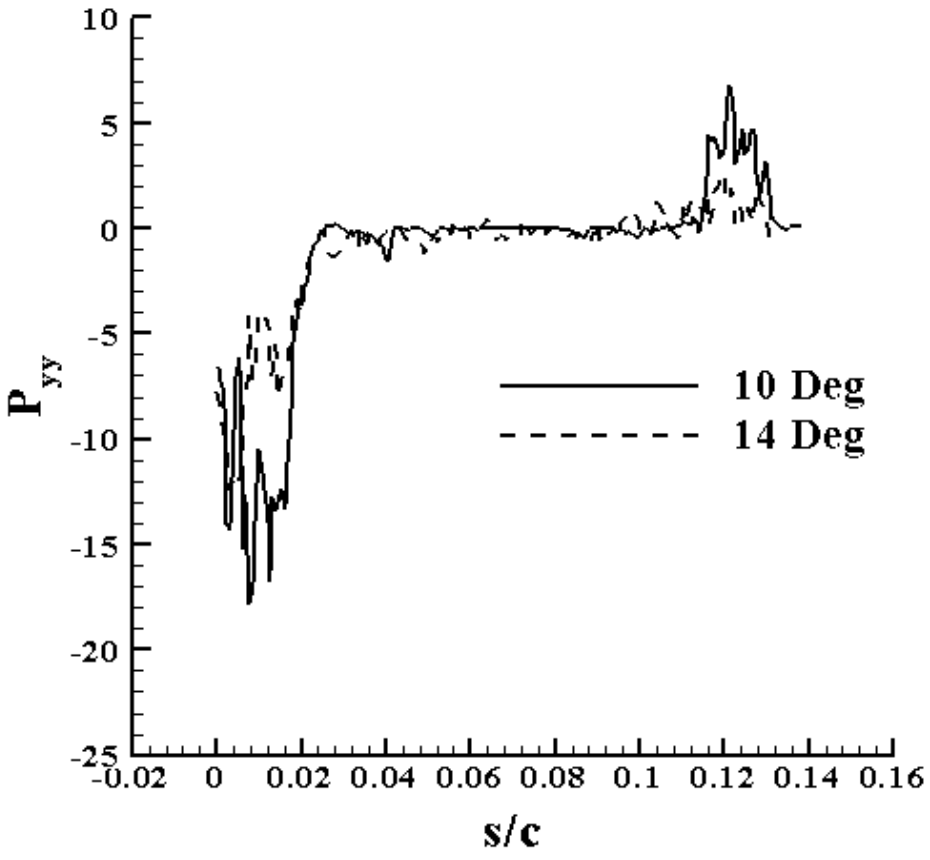

Figure 150: Line plot of P_{yy} for $M_\infty = 0.2, k = 0.1, Up, \alpha = 10^0, 14^0$

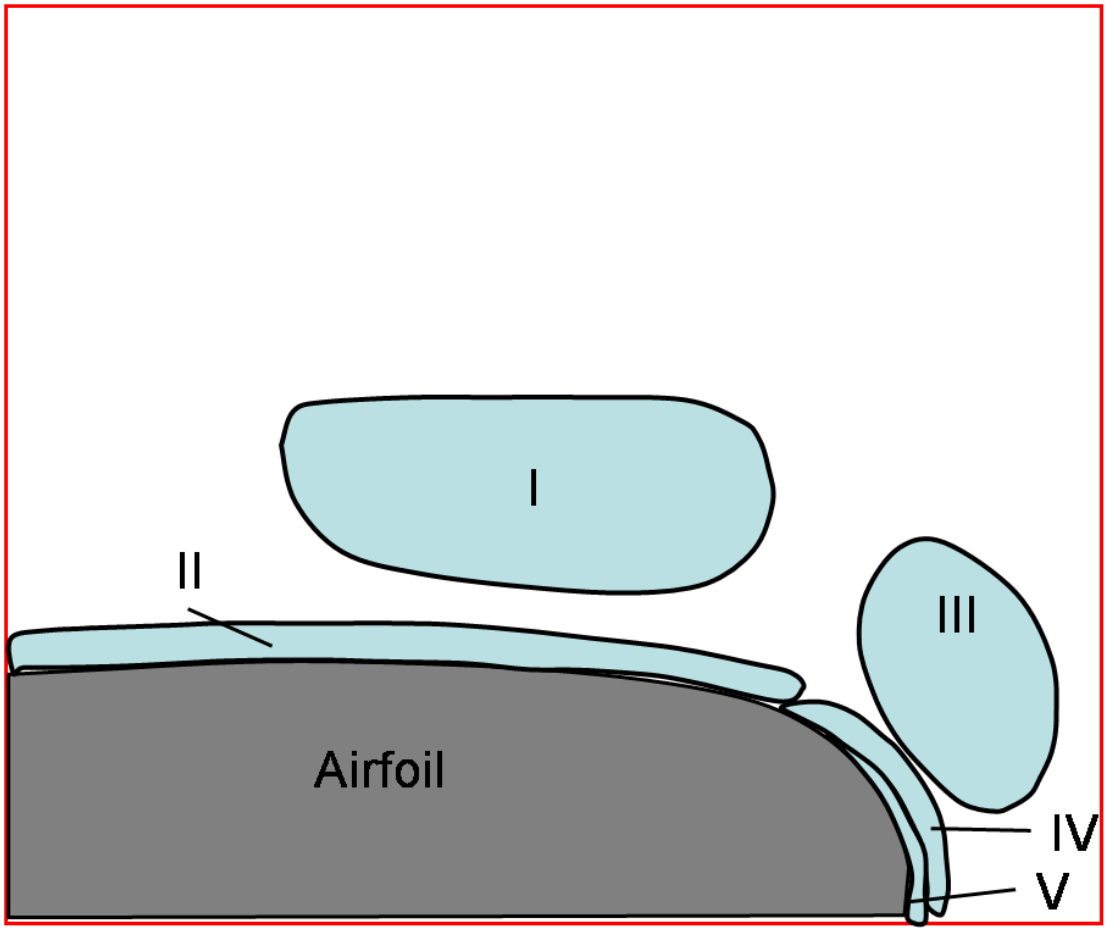

Figure 151: Sketch of regions explained during the downstroke motion of the wing

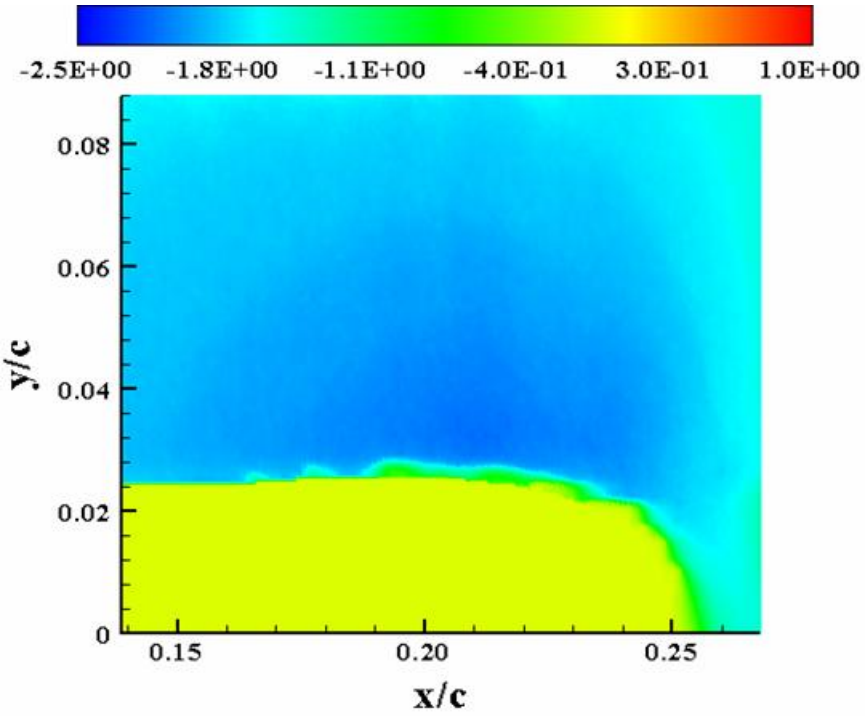

Figure 152: $U_N(M_\infty = 0.2, k = 0.1, Down, \alpha = 16^0)$

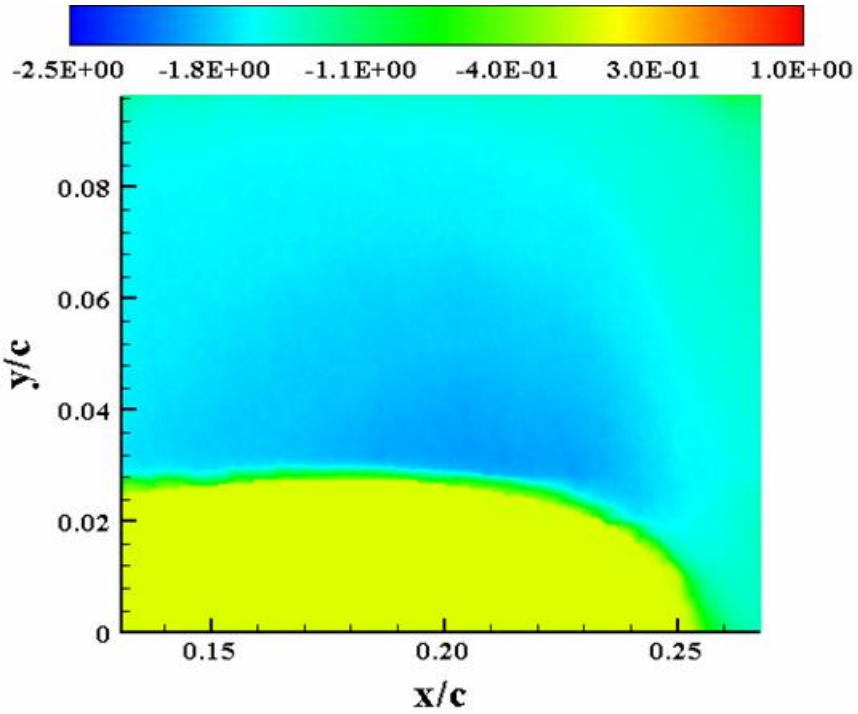

Figure 153: $U_N(M_\infty = 0.2, k = 0.1, Down, \alpha = 14^0)$

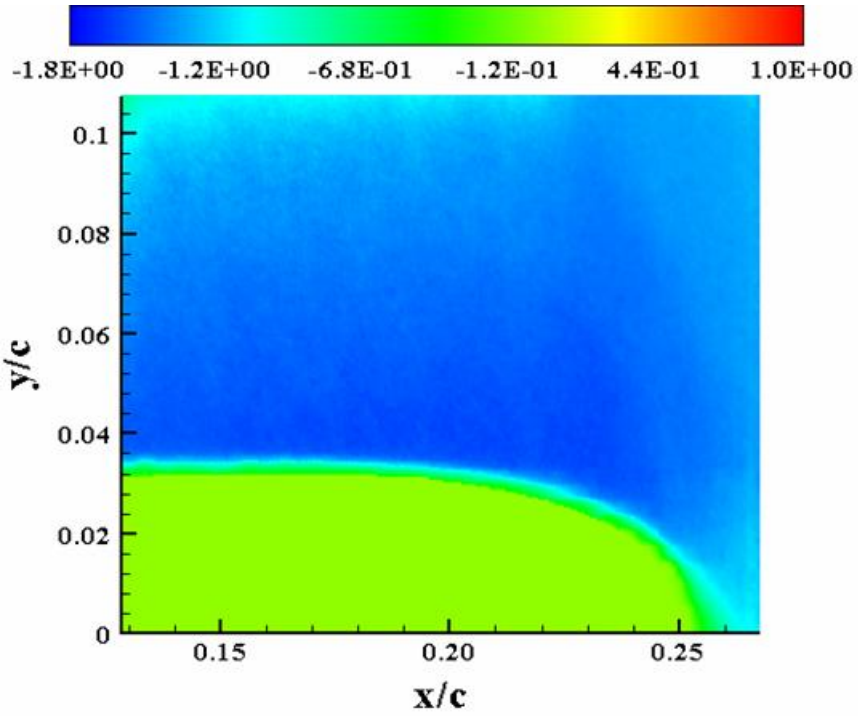

Figure 154: $U_N(M_\infty = 0.2, k = 0.1, Down, \alpha = 12^0)$

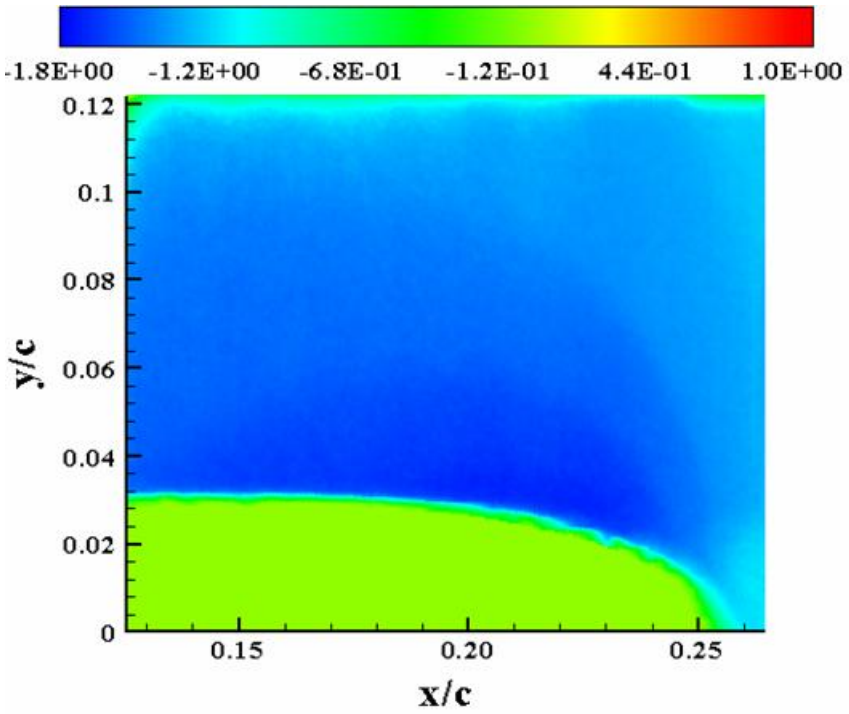

Figure 155: $U_N(M_\infty = 0.2, k = 0.1, Down, \alpha = 10^0)$

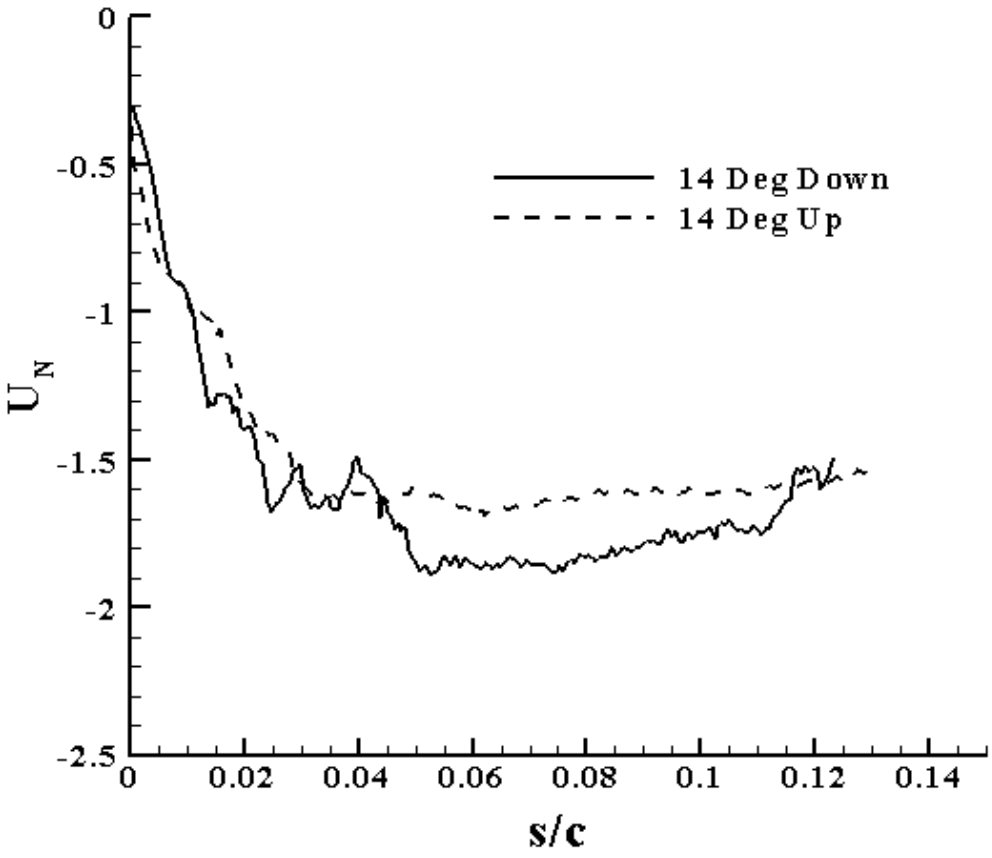

Figure 156: Comparison of U_N during the upstroke and downstroke motion at $\alpha = 14°$

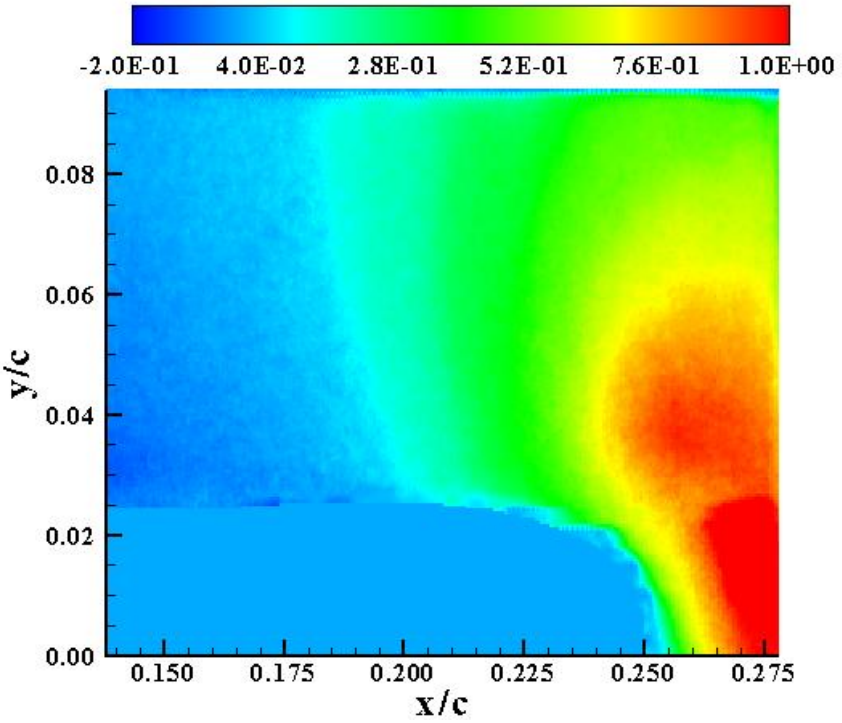

Figure 157: $V_N\,(M_\infty = 0.2, k = 0.1, Down, \alpha = 16^0)$

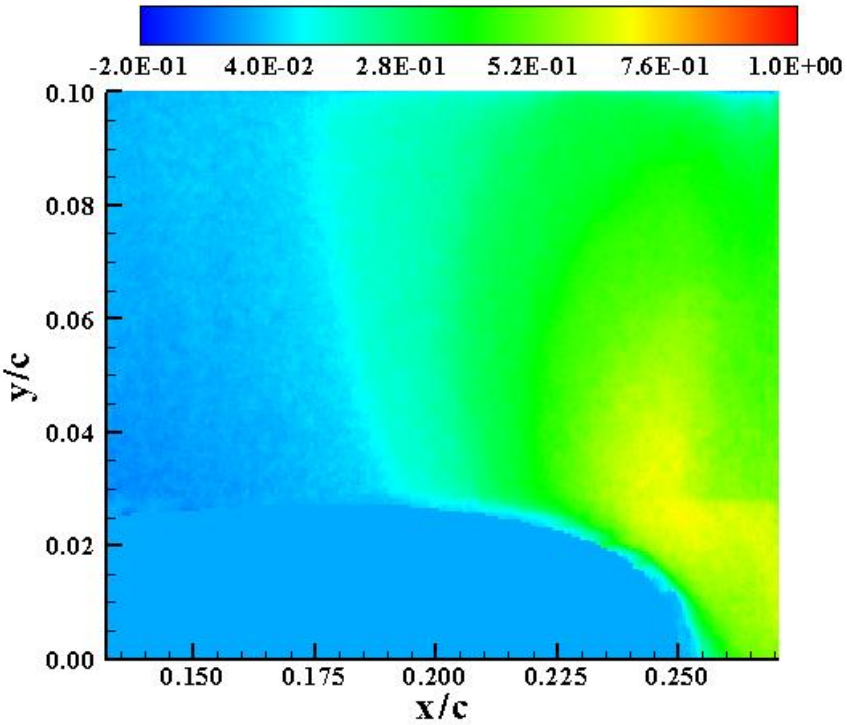

Figure 158: $V_N\,(M_\infty = 0.2, k = 0.1, Down, \alpha = 14^0)$

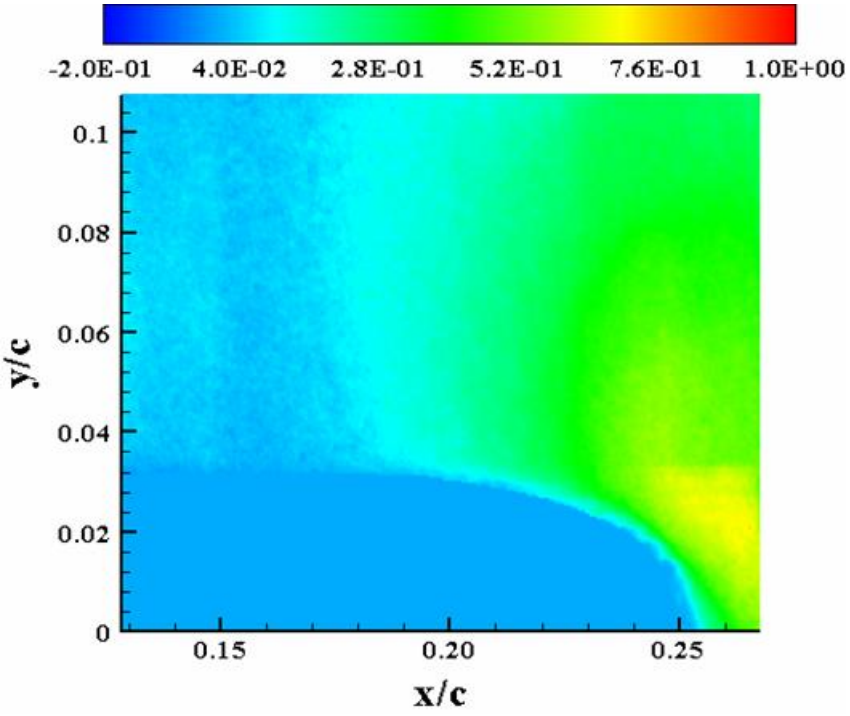

Figure 159: $V_N(M_\infty = 0.2, k = 0.1, Down, \alpha = 12^0)$

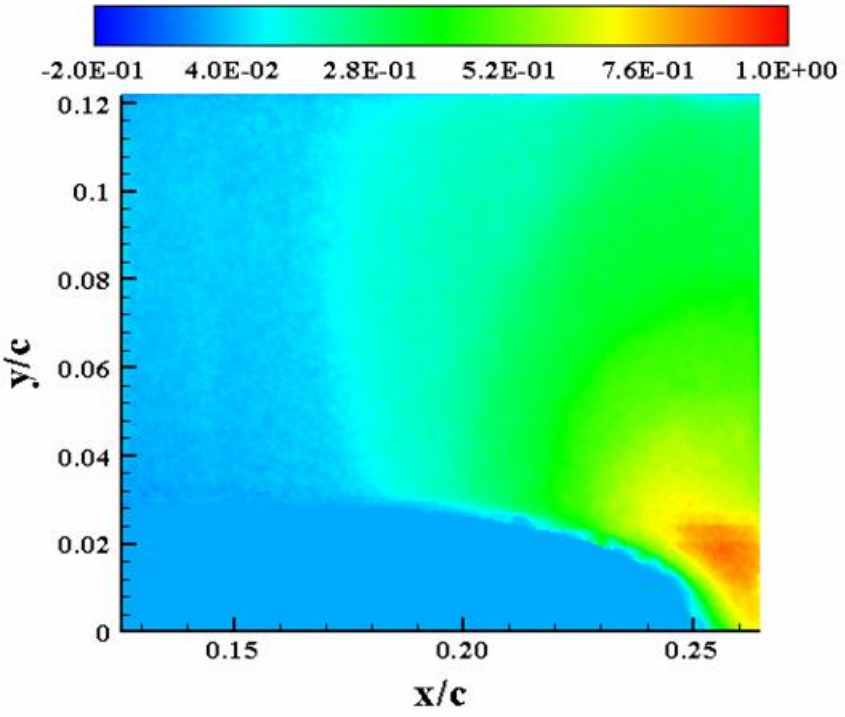

Figure 160: $V_N(M_\infty = 0.2, k = 0.1, Down, \alpha = 10^0)$

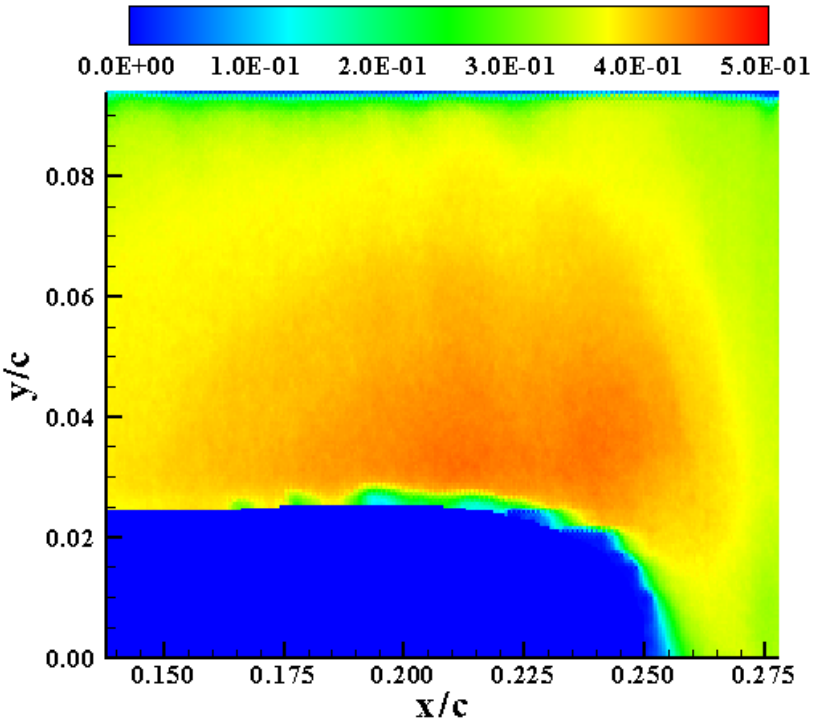

Figure 161: $M(M_\infty = 0.2, k = 0.1, Down, \alpha = 16^0)$

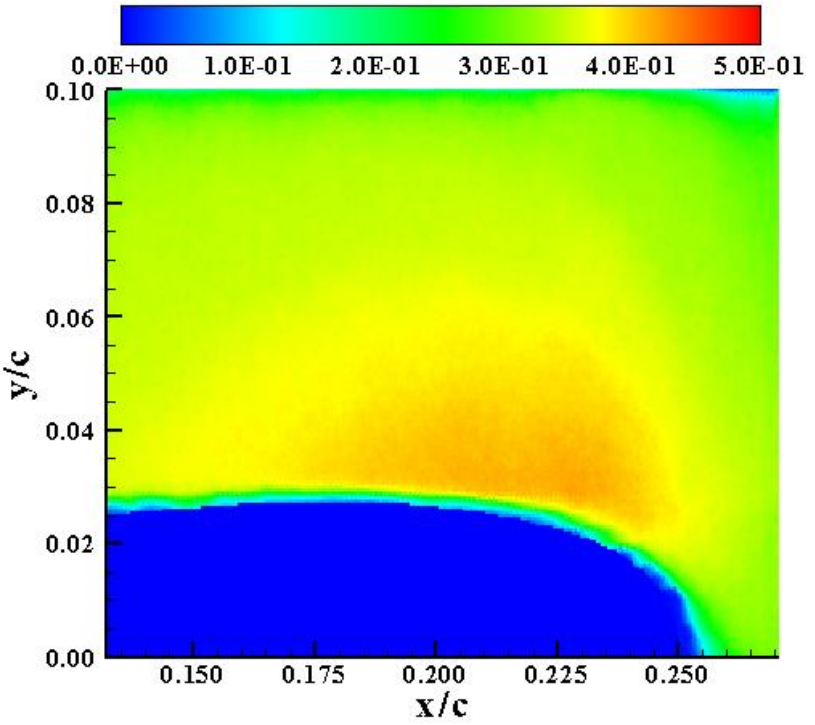

Figure 162: $M(M_\infty = 0.2, k = 0.1, Down, \alpha = 14^0)$

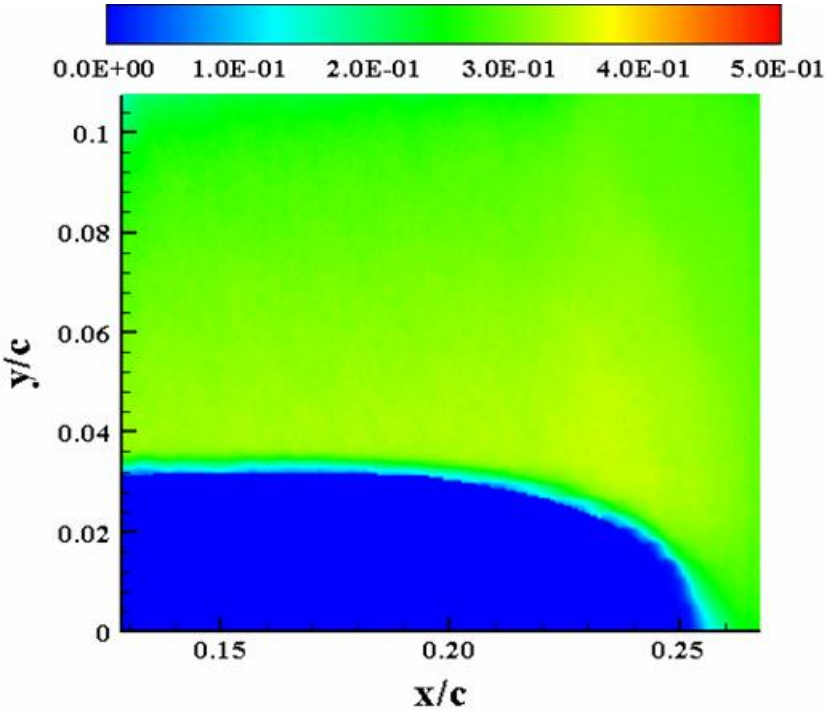

Figure 163: $M(M_\infty = 0.2, k = 0.1, Down, \alpha = 12^0)$

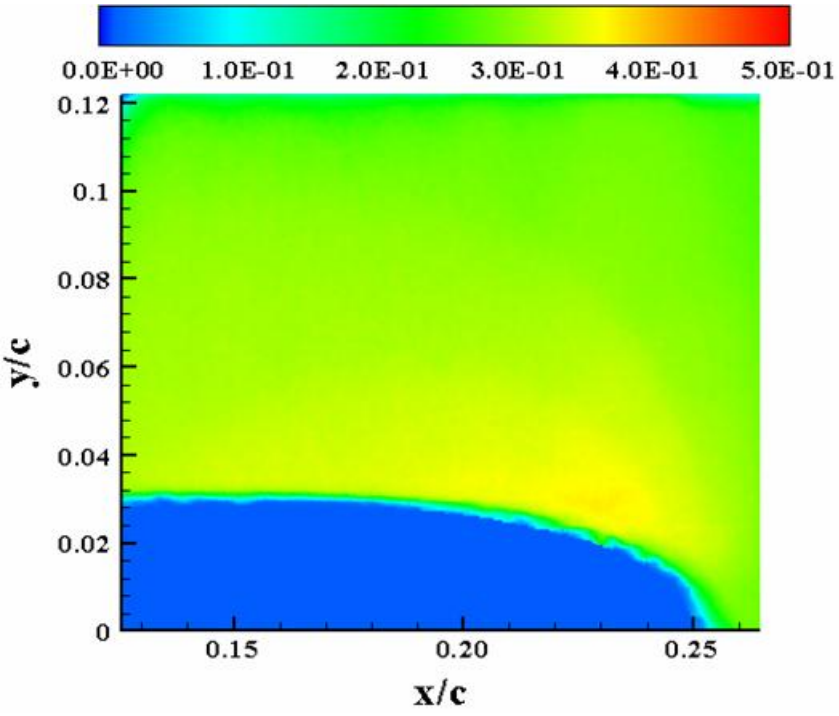

Figure 164: $M(M_\infty = 0.2, k = 0.1, Down, \alpha = 10^0)$

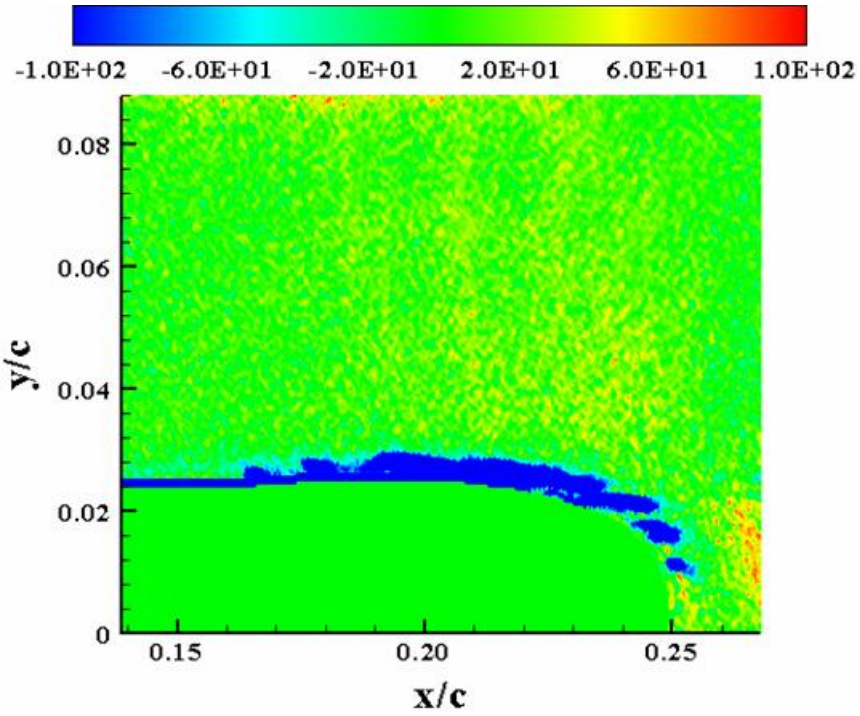

Figure 165: $S_{xy}(M_\infty = 0.2, k = 0.1, Down, \alpha = 16^0)$

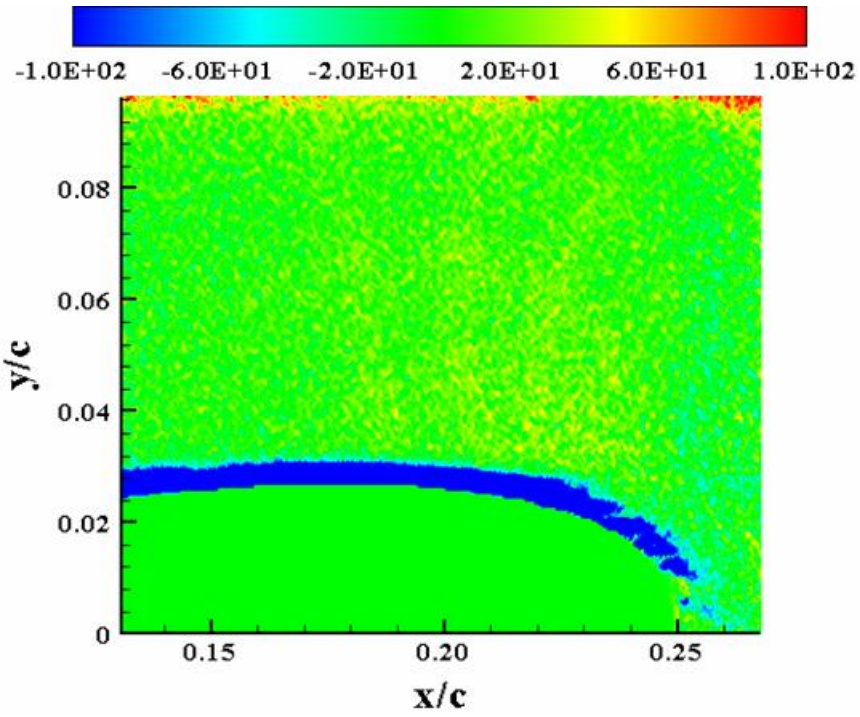

Figure 166: $S_{xy}(M_\infty = 0.2, k = 0.1, Down, \alpha = 14^0)$

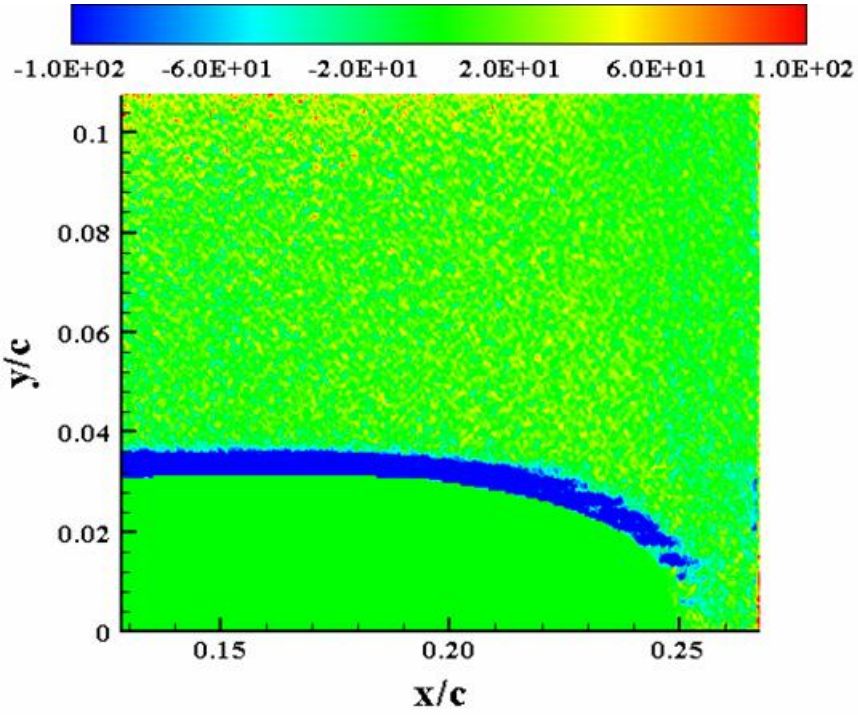

Figure 167: $S_{xy}(M_\infty = 0.2, k = 0.1, Down, \alpha = 12^0)$

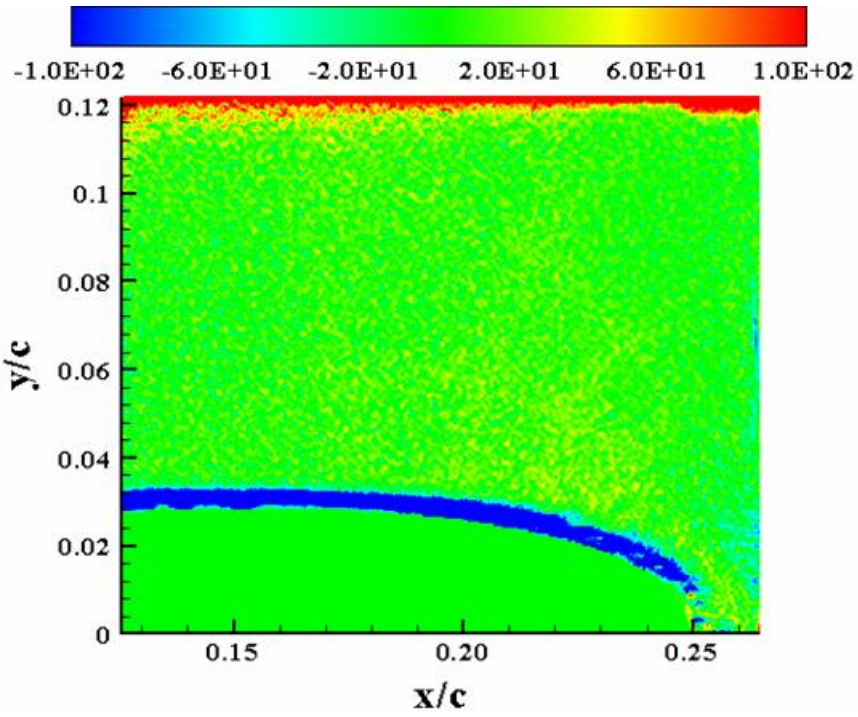

Figure 168: $S_{xy}(M_\infty = 0.2, k = 0.1, Down, \alpha = 10^0)$

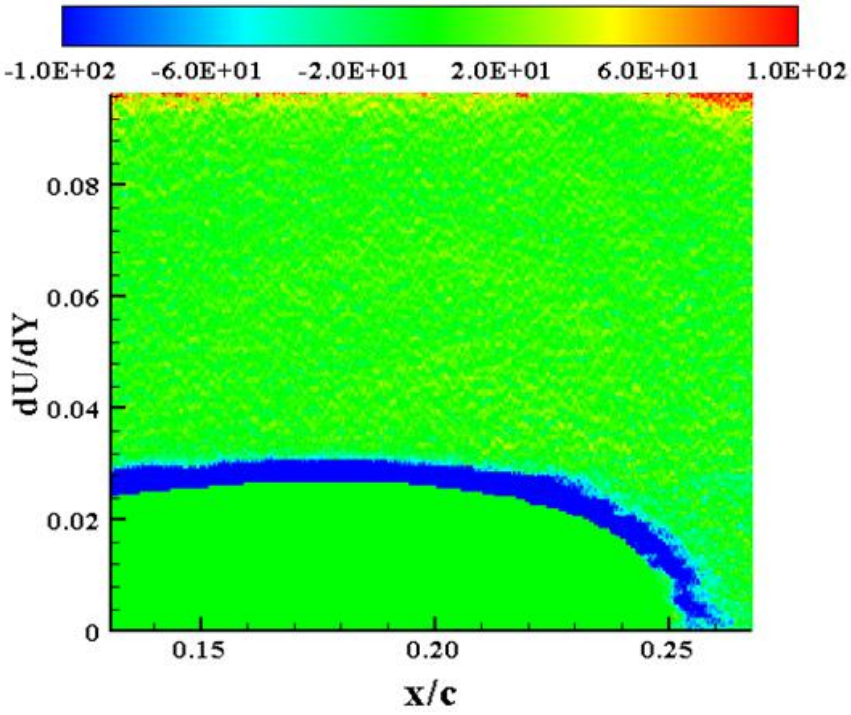

Figure 169: $dU/dY\ (M_\infty = 0.2, k = 0.1, Down, \alpha = 14^0)$

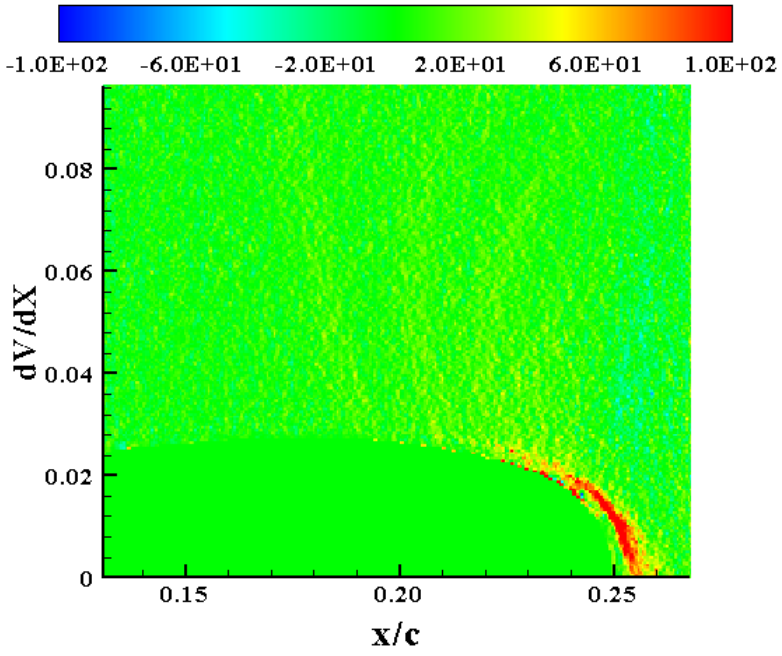

Figure 170: $dV/dX\ (M_\infty = 0.2, k = 0.1, Down, \alpha = 14^0)$

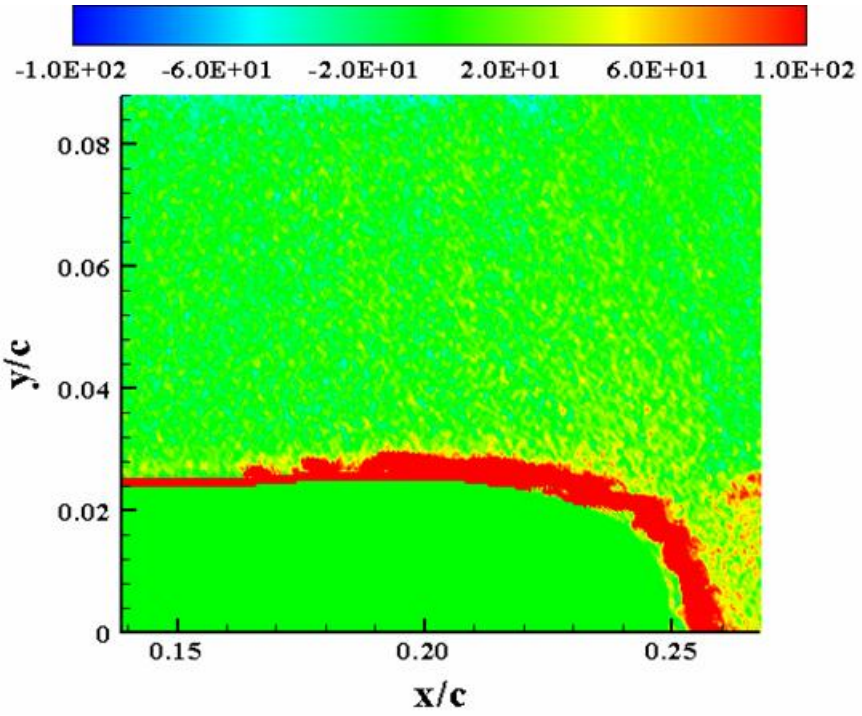

Figure 171: $\omega_z (M_\infty = 0.2, k = 0.1, Down, \alpha = 16^0)$

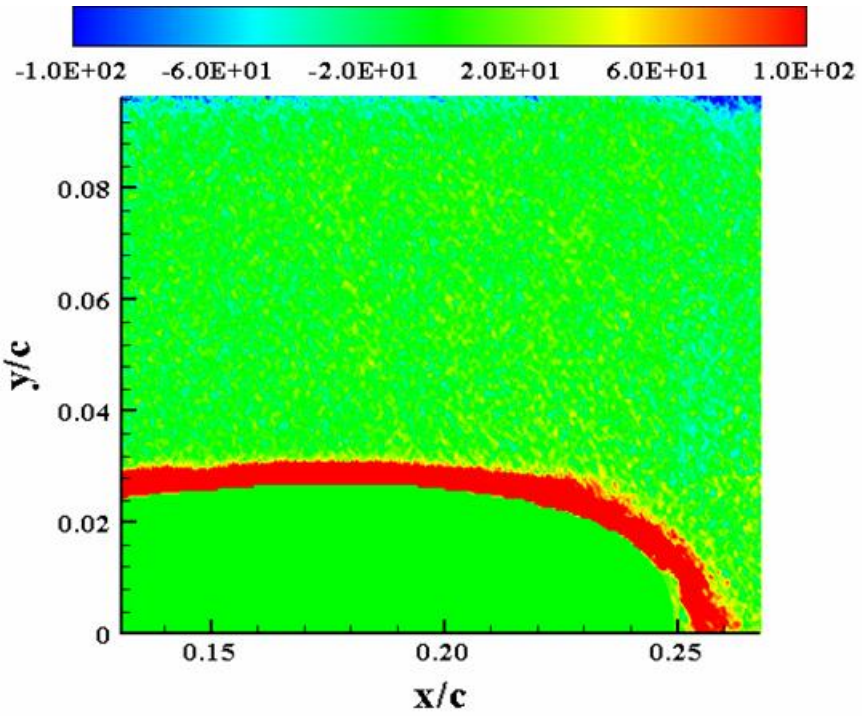

Figure 172: $\omega_z (M_\infty = 0.2, k = 0.1, Down, \alpha = 14^0)$

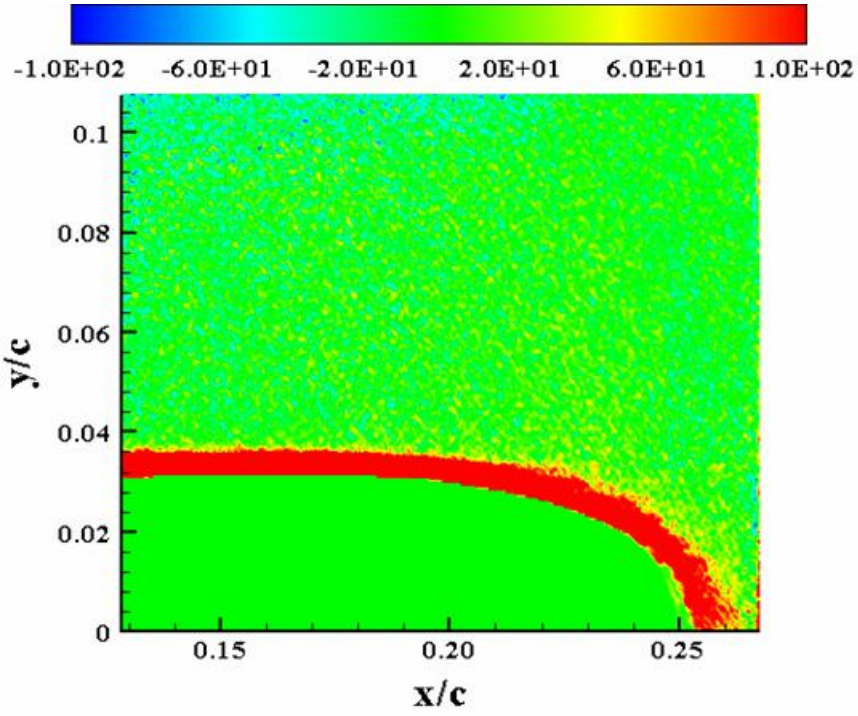

Figure 173: $\omega_z(M_\infty = 0.2, k = 0.1, Down, \alpha = 12^0)$

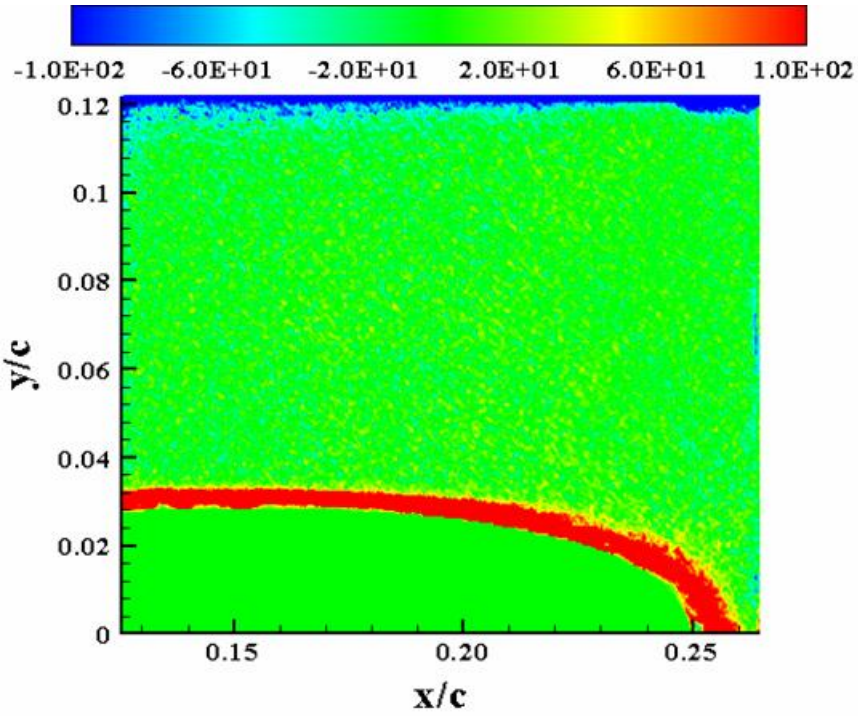

Figure 174: $\omega_z(M_\infty = 0.2, k = 0.1, Down, \alpha = 10^0)$

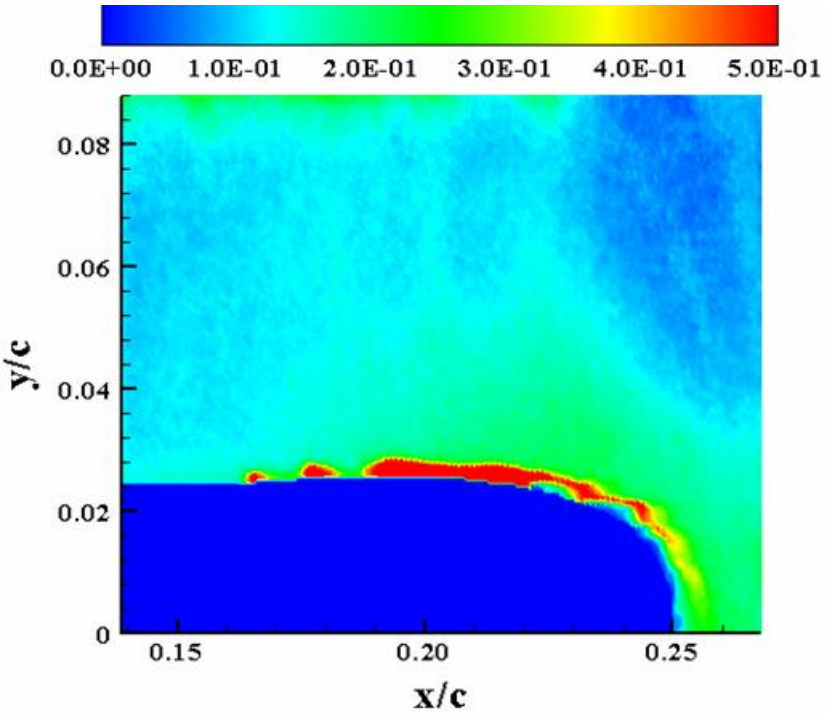

Figure 175: $\sigma_u(M_\infty = 0.2, k = 0.1, Down, \alpha = 16^0)$

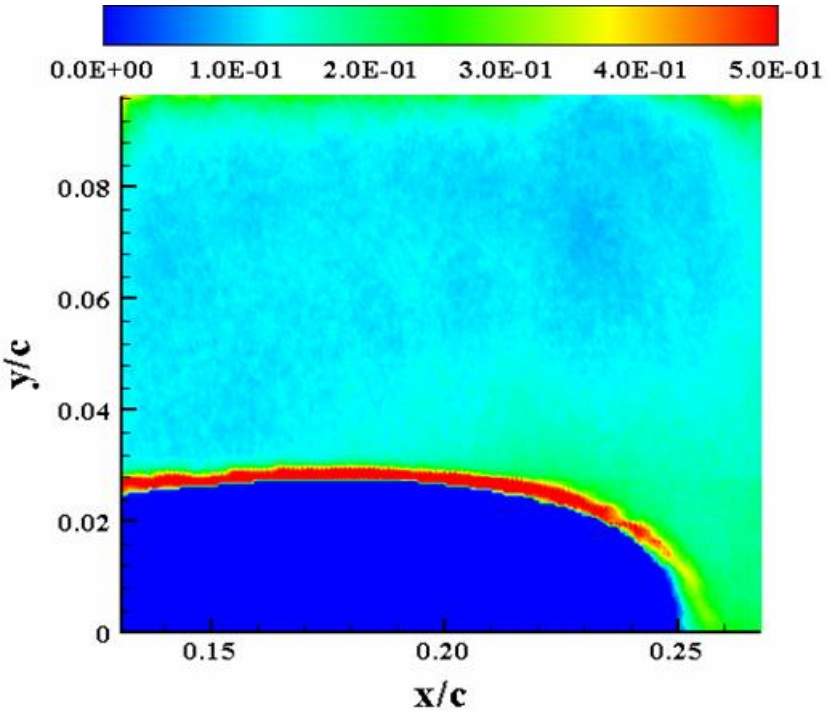

Figure 176: $\sigma_u(M_\infty = 0.2, k = 0.1, Down, \alpha = 14^0)$

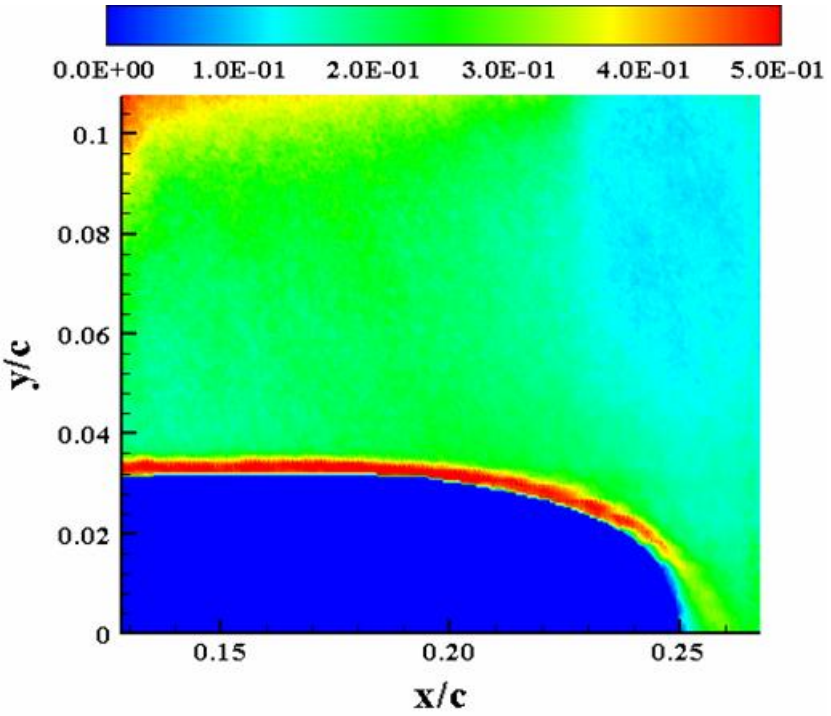

Figure 177: $\sigma_u(M_\infty = 0.2, k = 0.1, Down, \alpha = 12^0)$

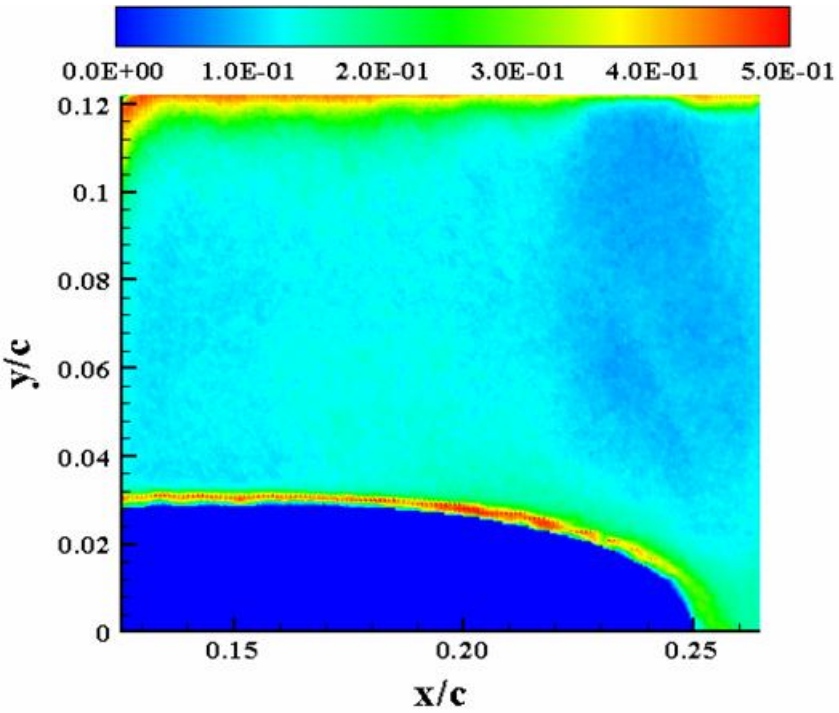

Figure 178: $\sigma_u(M_\infty = 0.2, k = 0.1, Down, \alpha = 10^0)$

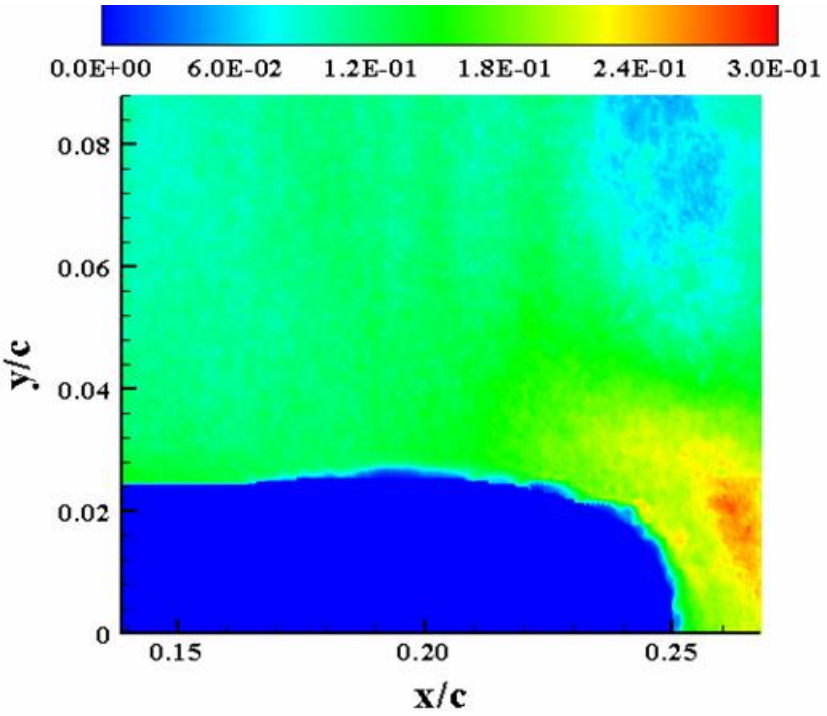

Figure 179: $\sigma_v(M_\infty = 0.2, k = 0.1, Down, \alpha = 16^0)$

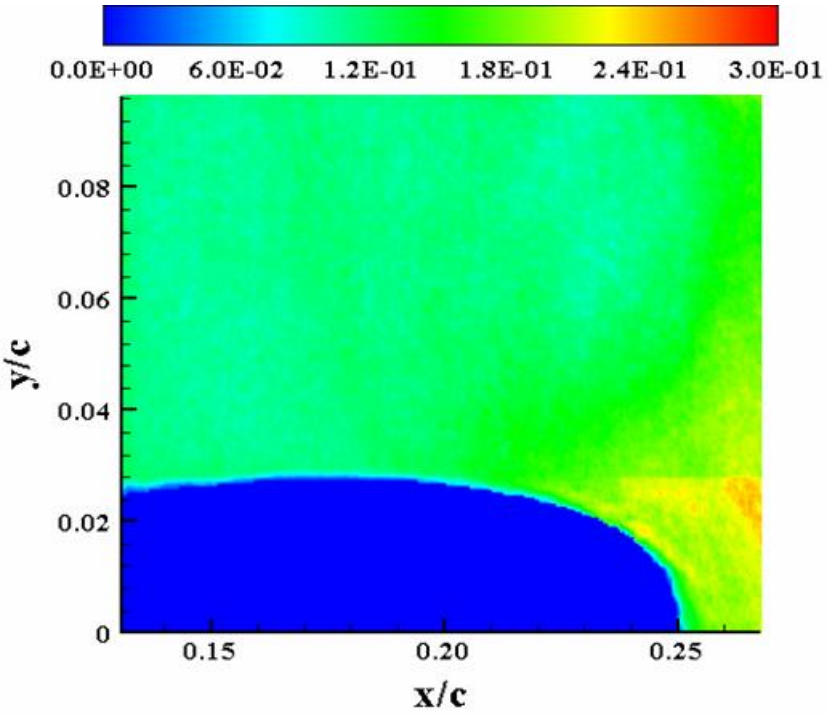

Figure 180: $\sigma_v(M_\infty = 0.2, k = 0.1, Down, \alpha = 14^0)$

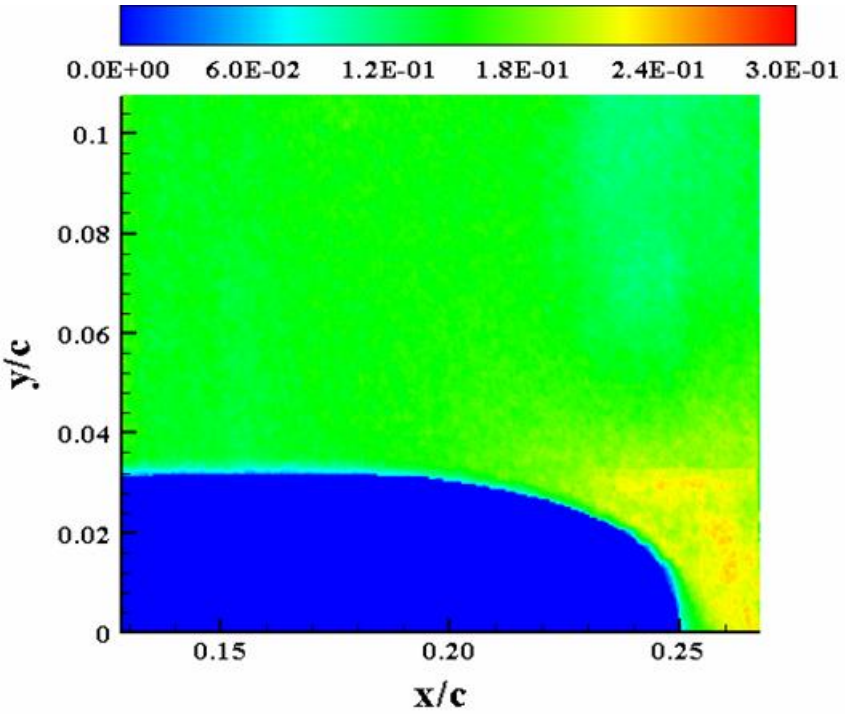

Figure 181: $\sigma_v(M_\infty = 0.2, k = 0.1, Down, \alpha = 12^0)$

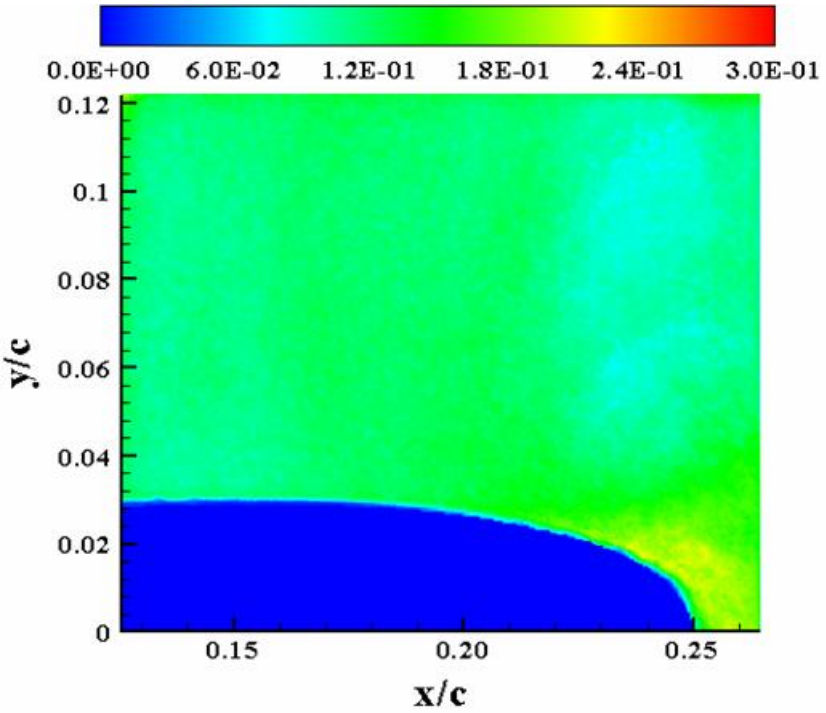

Figure 182: $\sigma_v(M_\infty = 0.2, k = 0.1, Down, \alpha = 10^0)$

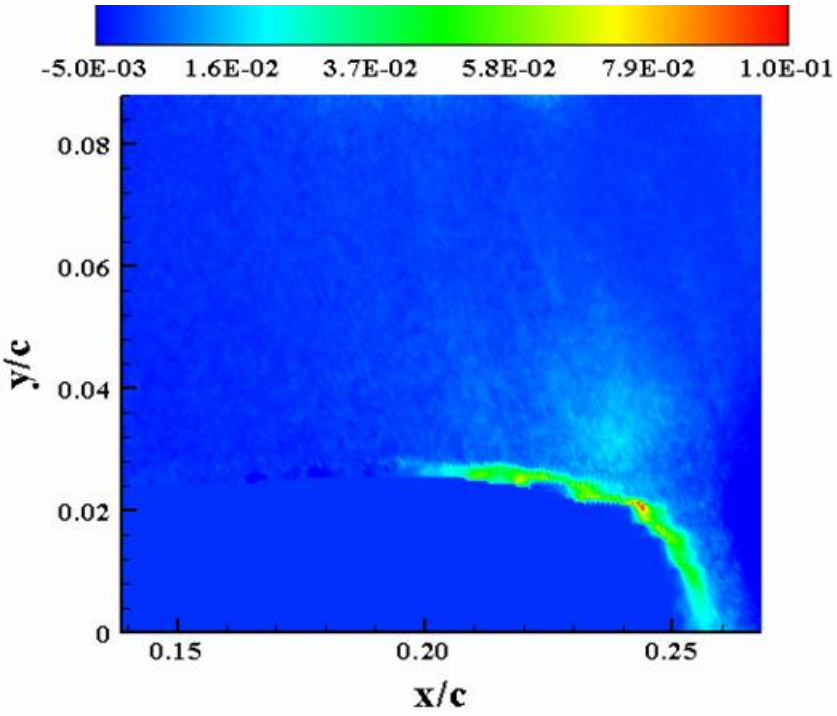

Figure 183: $\tau_{xy}(M_\infty = 0.2, k = 0.1, Down, \alpha = 16^0)$

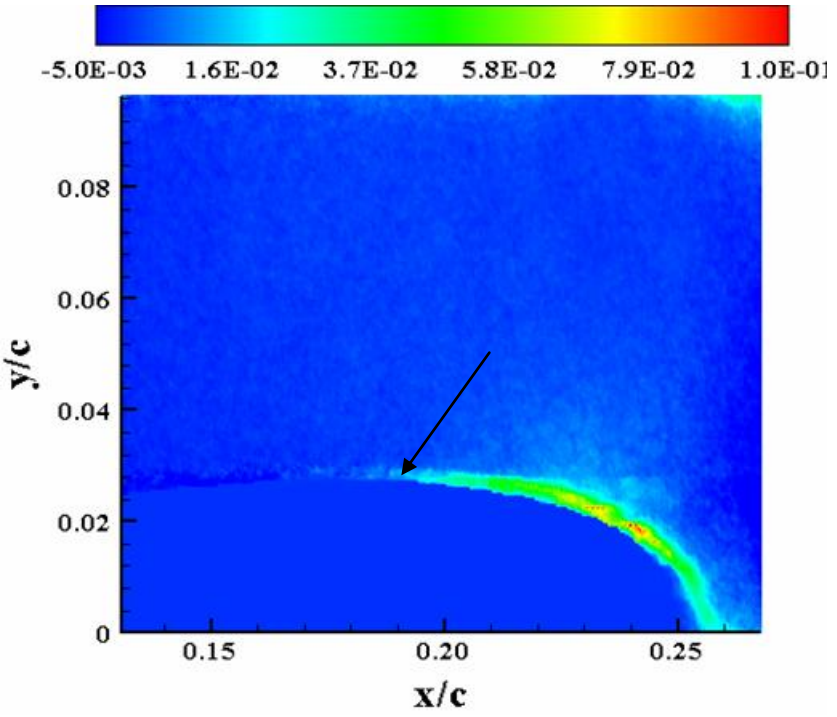

Figure 184: $\tau_{xy}(M_\infty = 0.2, k = 0.1, Down, \alpha = 14^0)$

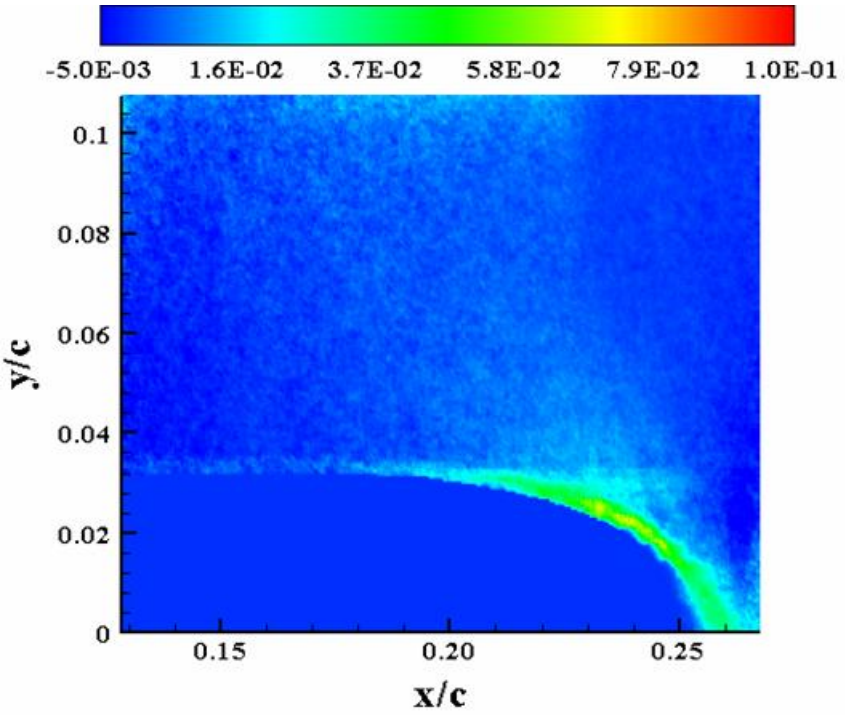

Figure 185: $\tau_{xy}(M_\infty = 0.2, k = 0.1, Down, \alpha = 12^0)$

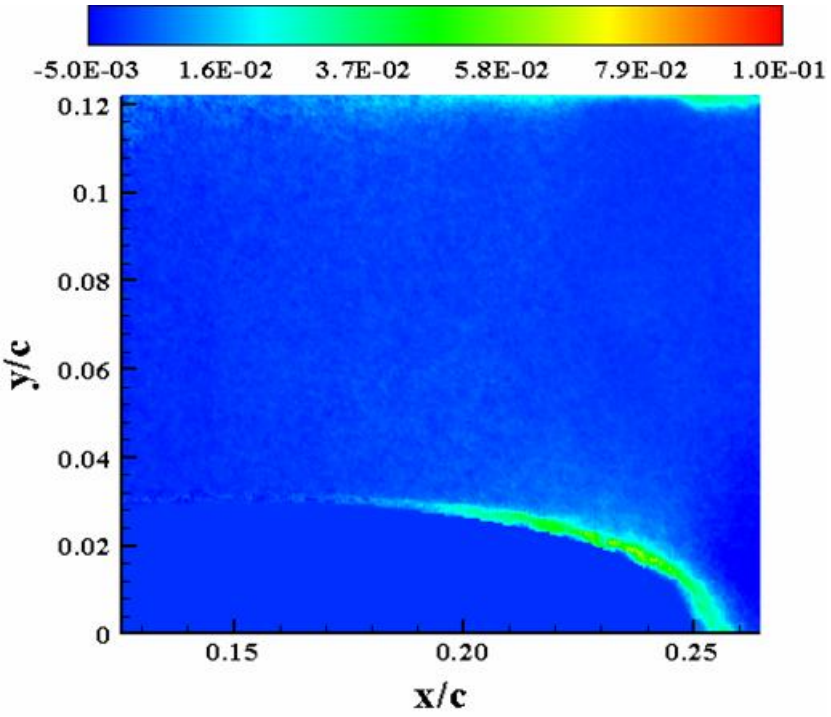

Figure 186: $\tau_{xy}(M_\infty = 0.2, k = 0.1, Down, \alpha = 10^0)$

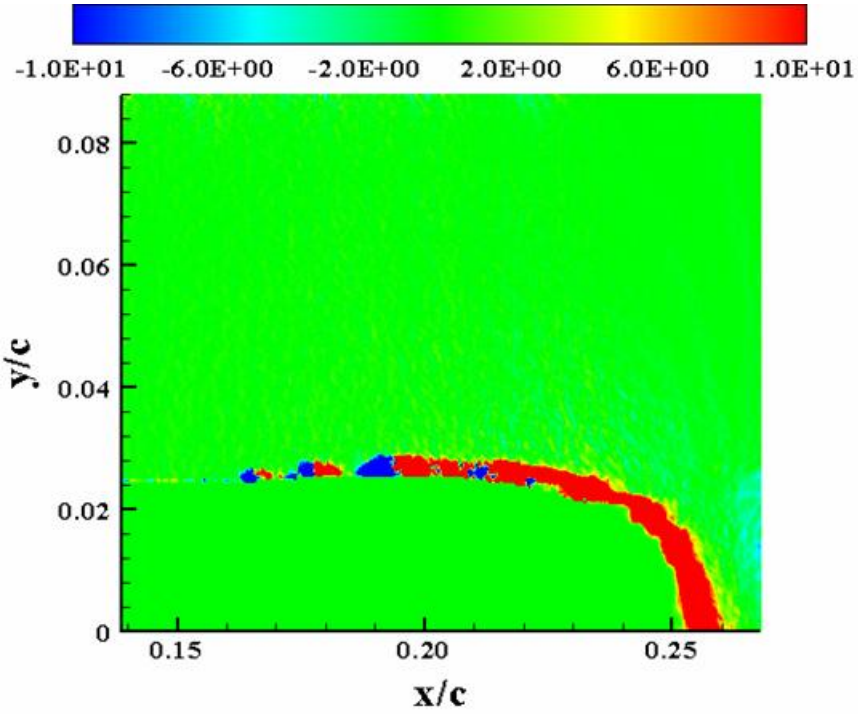

Figure 187: $P_{xx}(M_\infty = 0.2, k = 0.1, Down, \alpha = 16^0)$

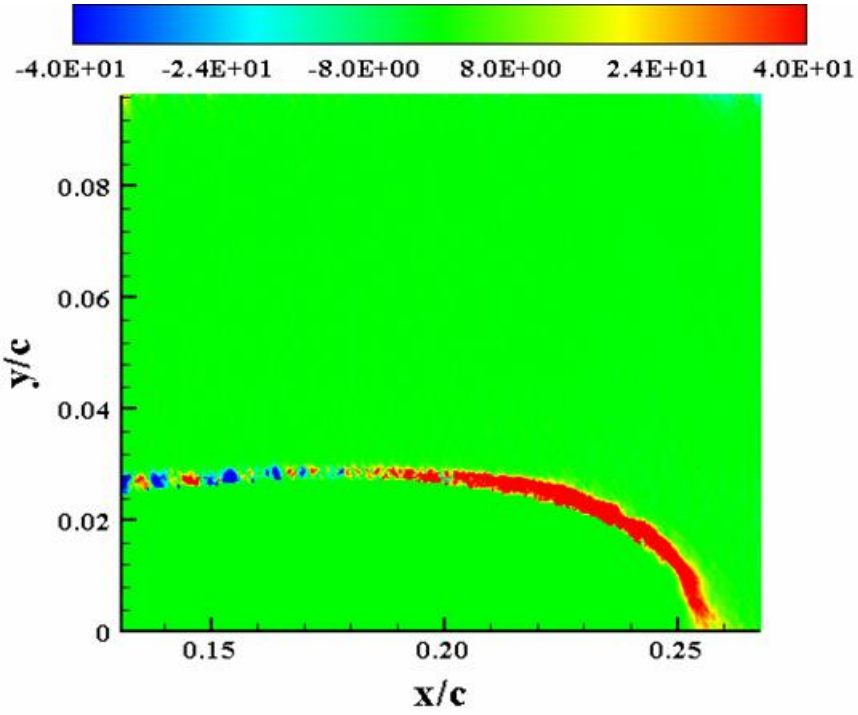

Figure 188: $P_{xx}(M_\infty = 0.2, k = 0.1, Down, \alpha = 14^0)$

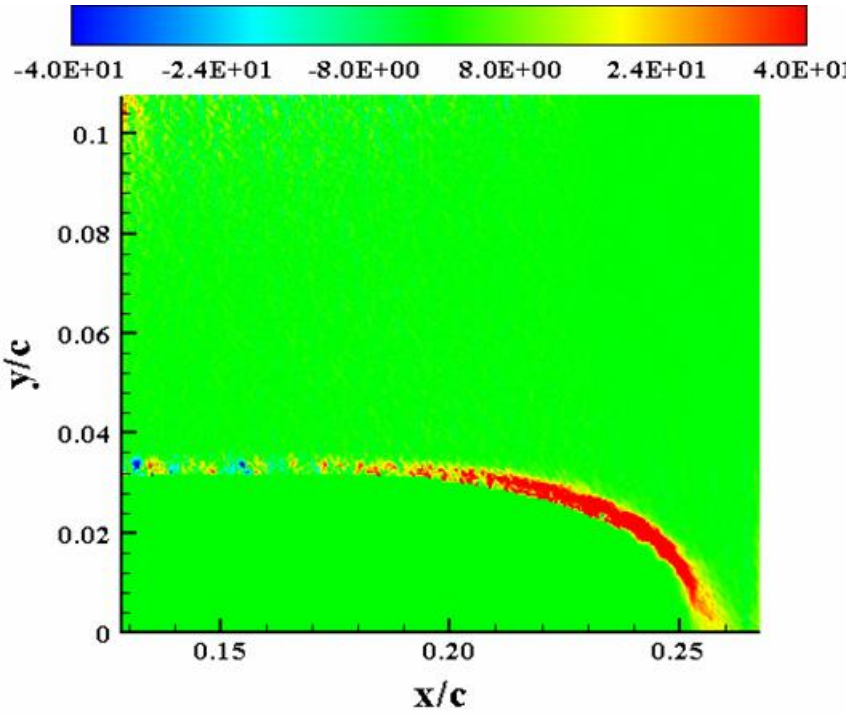

Figure 189: $P_{xx}(M_\infty = 0.2, k = 0.1, Down, \alpha = 12^0)$

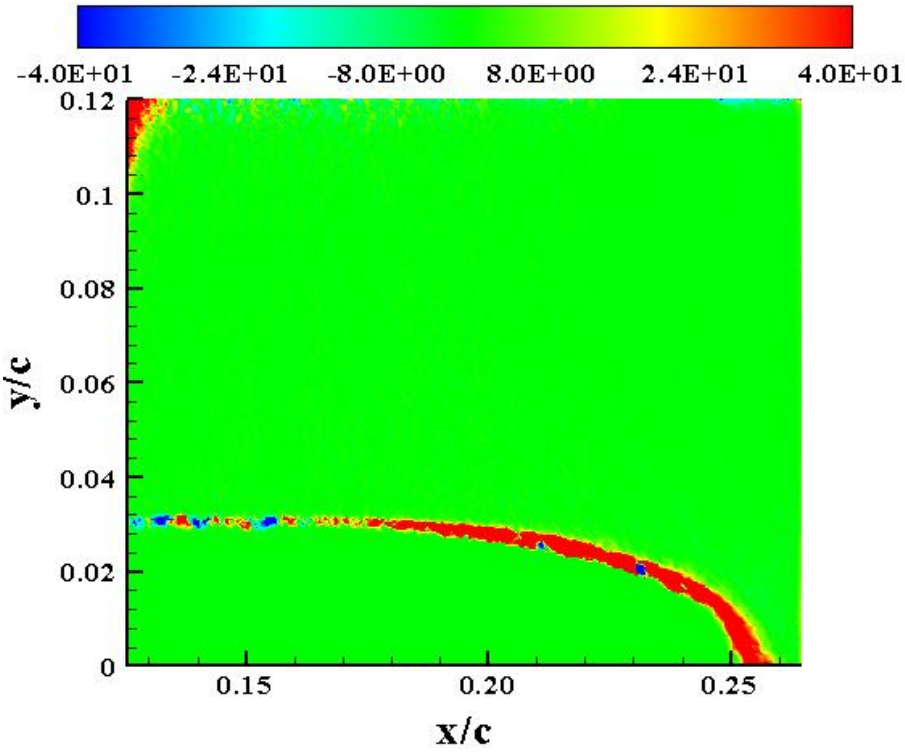

Figure 190: $P_{xx}(M_\infty = 0.2, k = 0.1, Down, \alpha = 10^0)$

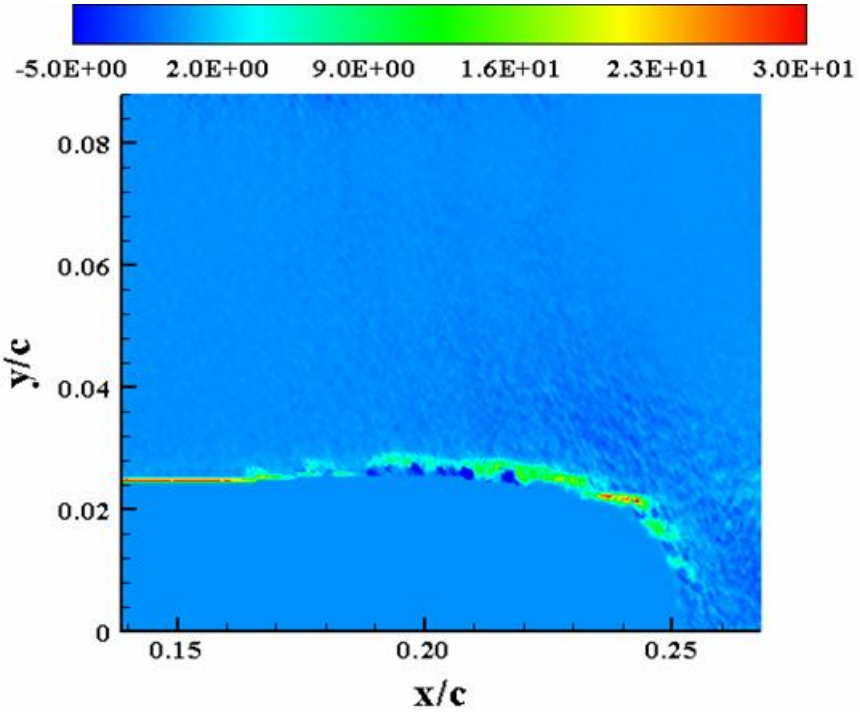

Figure 191: $P_{xy}(M_\infty = 0.2, k = 0.1, Down, \alpha = 16^0)$

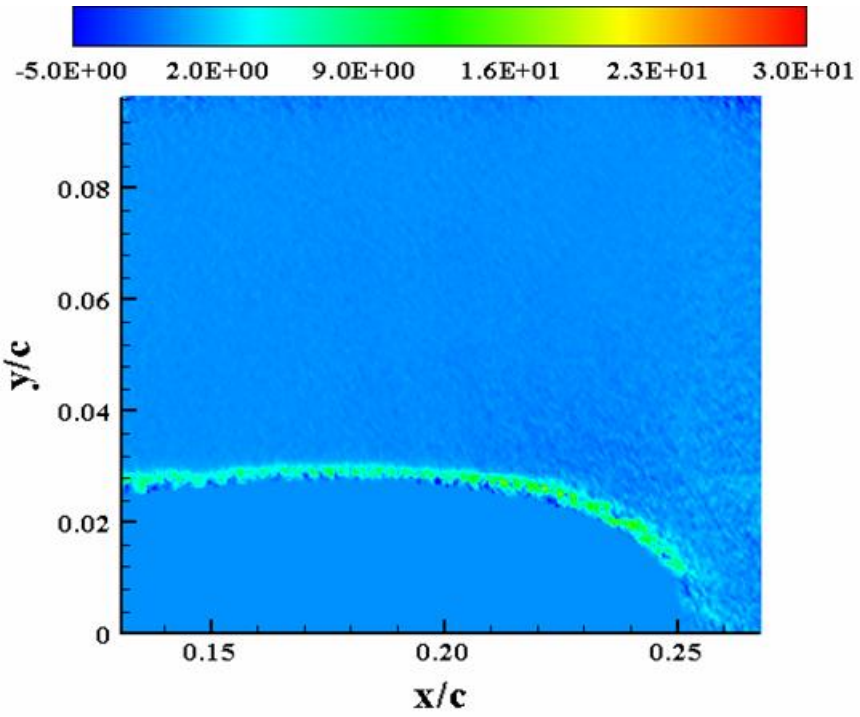

Figure 192: $P_{xy}(M_\infty = 0.2, k = 0.1, Down, \alpha = 14^0)$

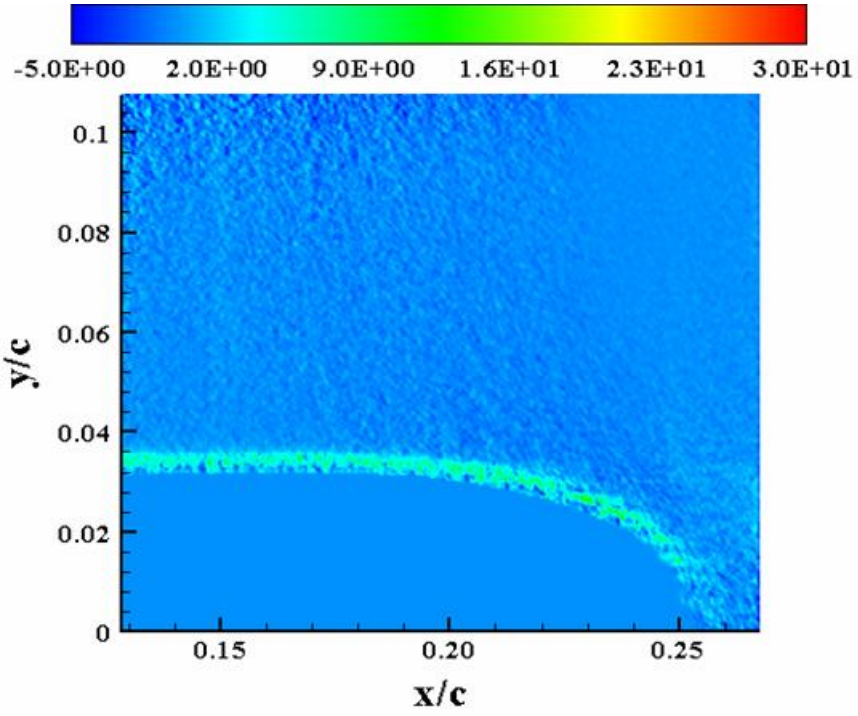

Figure 193: $P_{xy}(M_\infty = 0.2, k = 0.1, Down, \alpha = 12^0)$

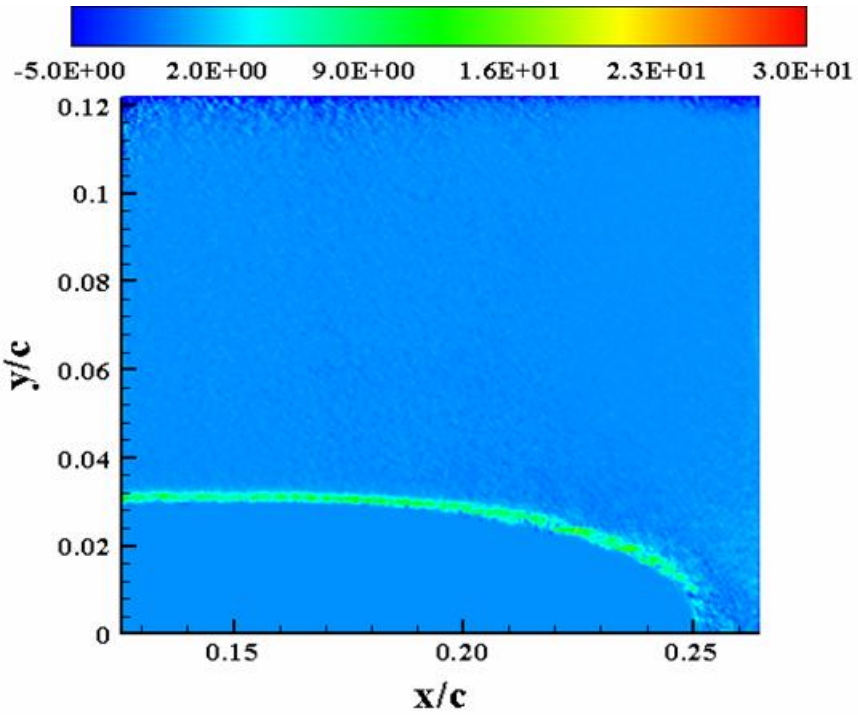

Figure 194: $P_{xy}(M_\infty = 0.2, k = 0.1, Down, \alpha = 10^0)$

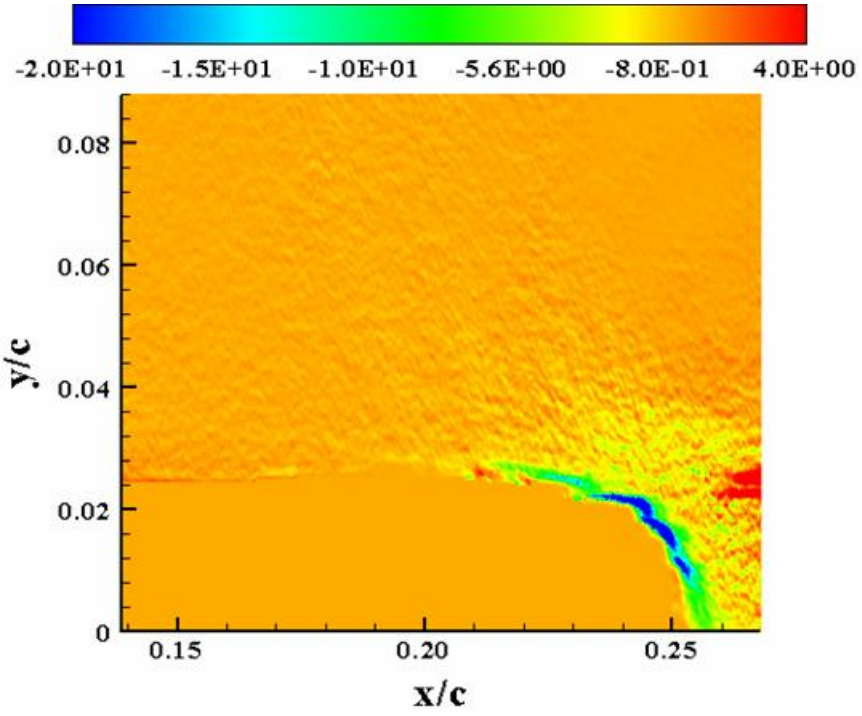

Figure 195: $P_{yy}(M_\infty = 0.2, k = 0.1, Down, \alpha = 16^0)$

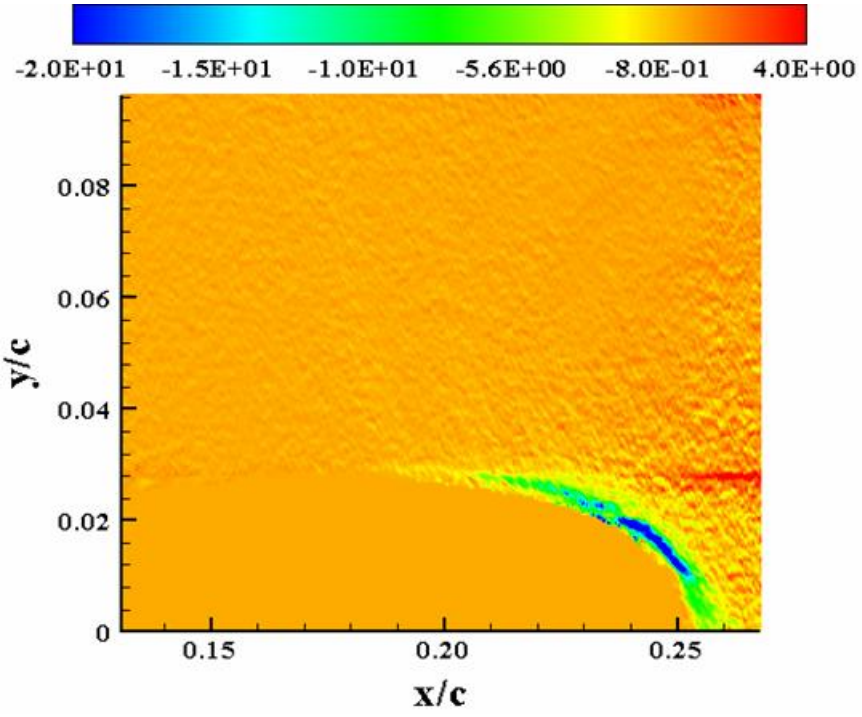

Figure 196: $P_{yy}(M_\infty = 0.2, k = 0.1, Down, \alpha = 14^0)$

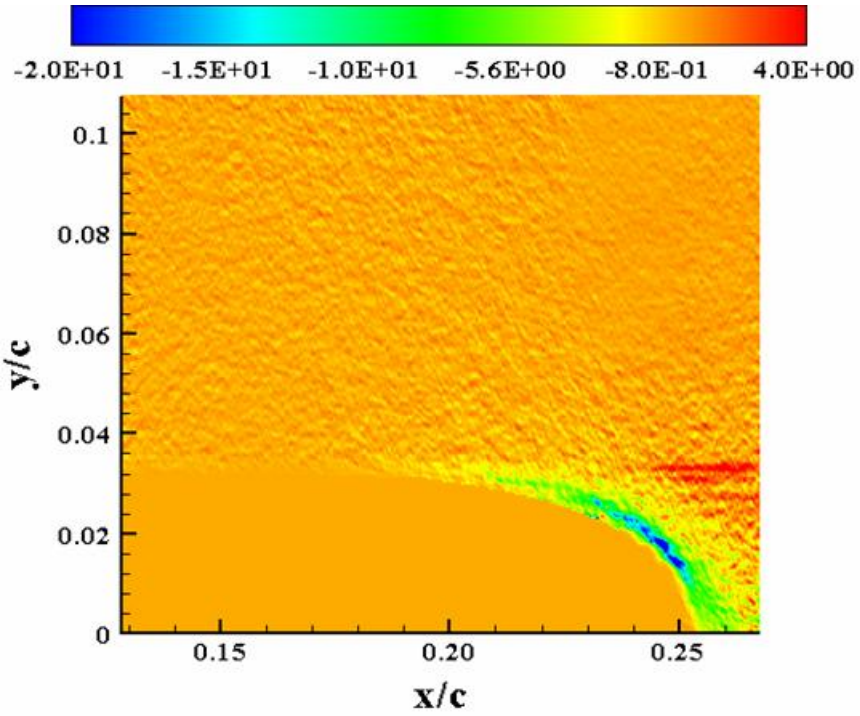

Figure 197: $P_{yy}(M_\infty = 0.2, k = 0.1, Down, \alpha = 12^0)$

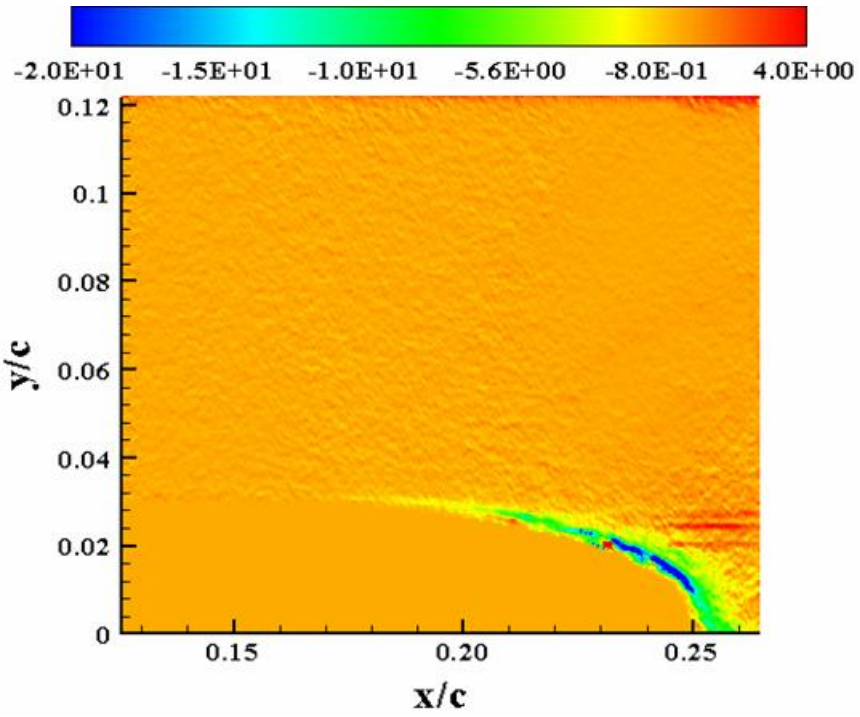

Figure 198: $P_{yy}(M_\infty = 0.2, k = 0.1, Down, \alpha = 10^0)$

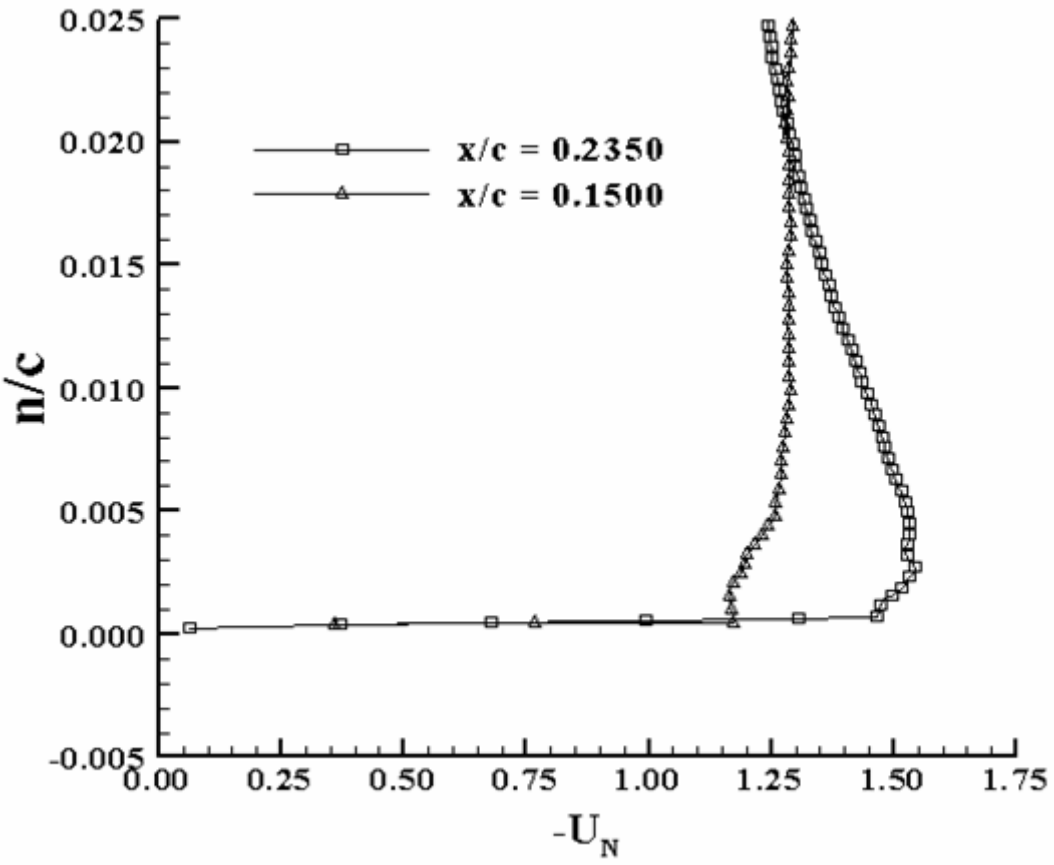

Figure 199: Line plot of -U_N for $M_\infty = 0.2, k = 0.1, Up, \alpha = 14^0$

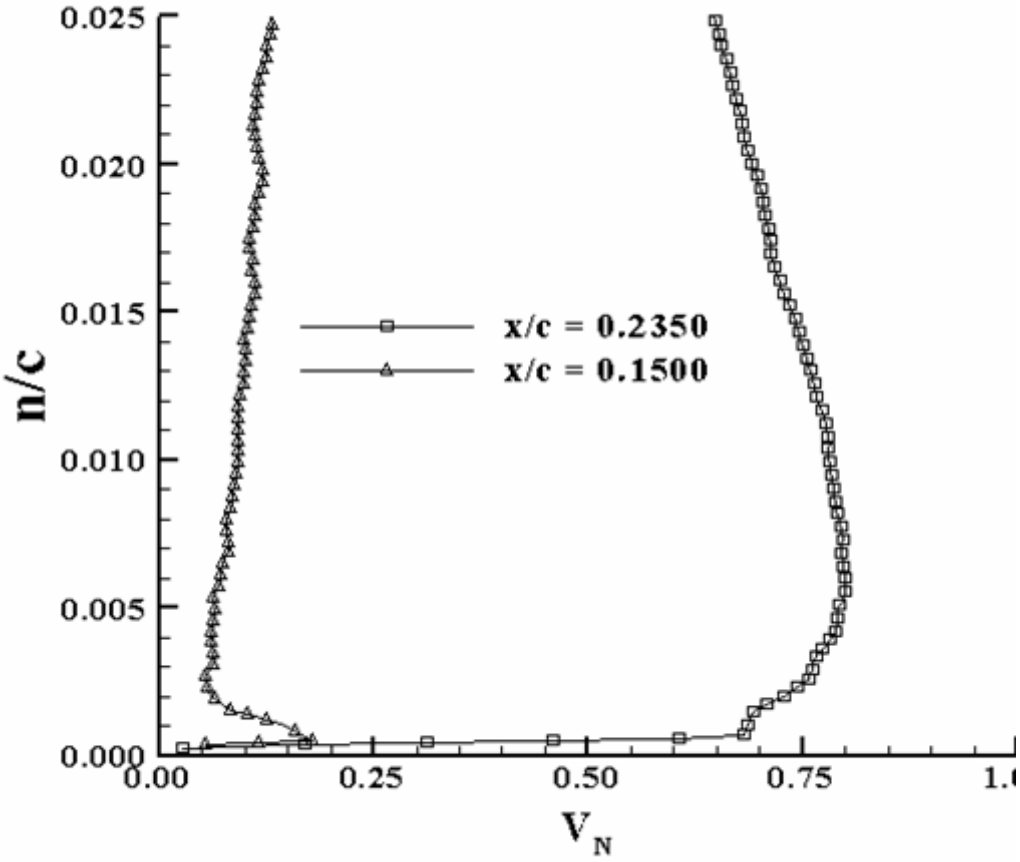

Figure 200: Line plot of V_N for $M_\infty = 0.2, k = 0.1, Up, \alpha = 14^0$

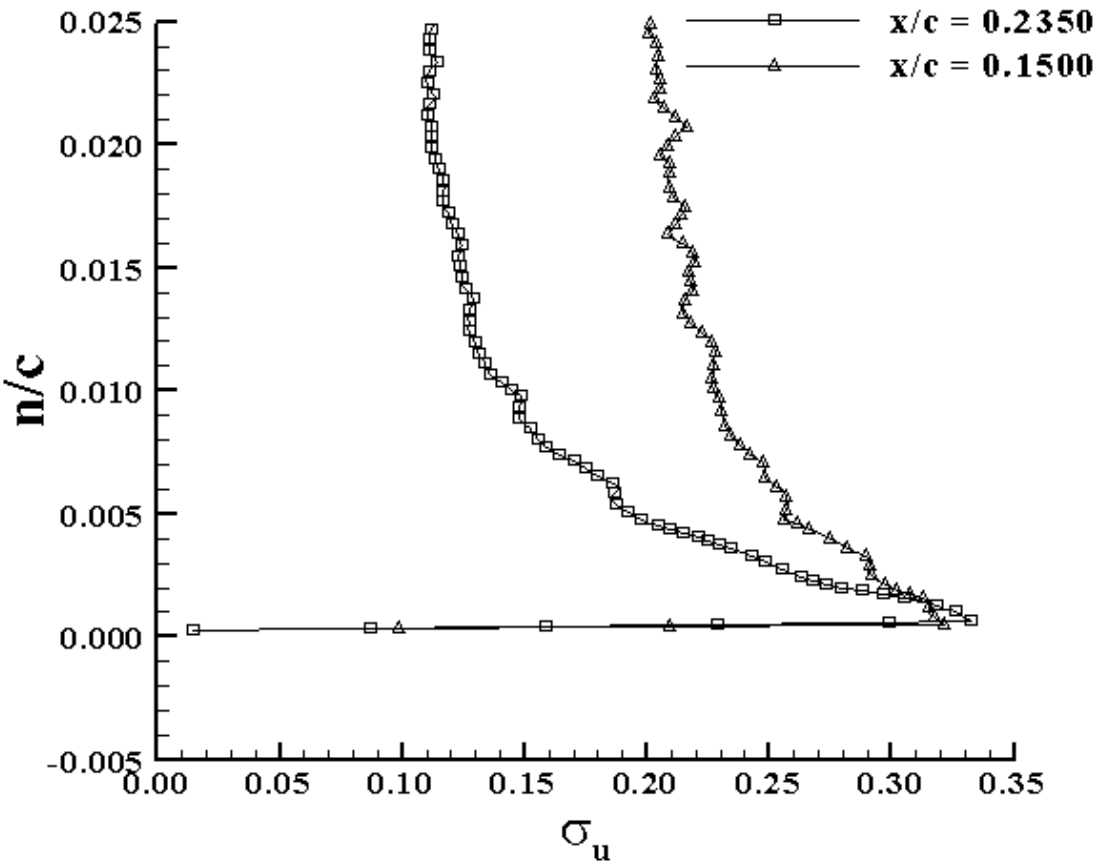

Figure 201: Line plot of σ_u for $M_\infty = 0.2, k = 0.1, Up, \alpha = 14^0$

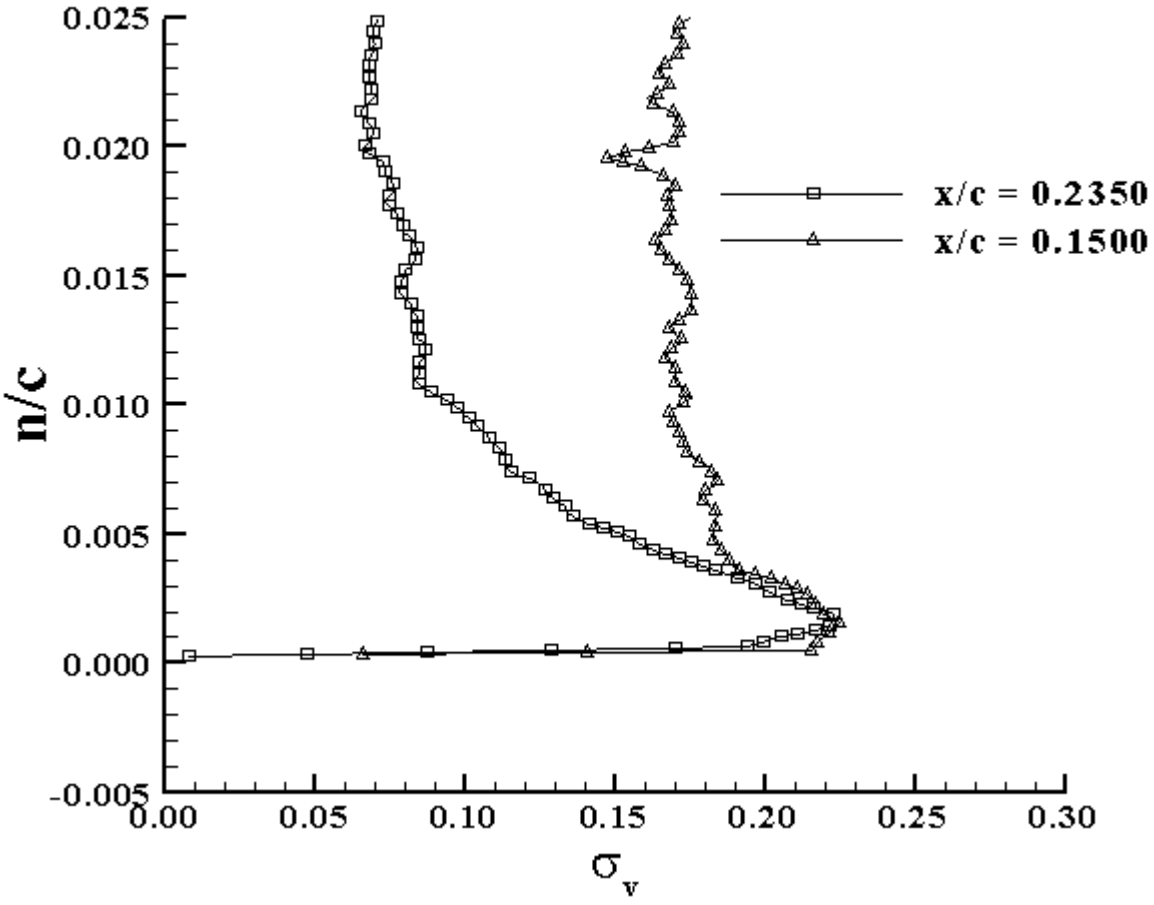

Figure 202: Line plot of σ_v for $M_\infty = 0.2, k = 0.1, Up, \alpha = 14^0$

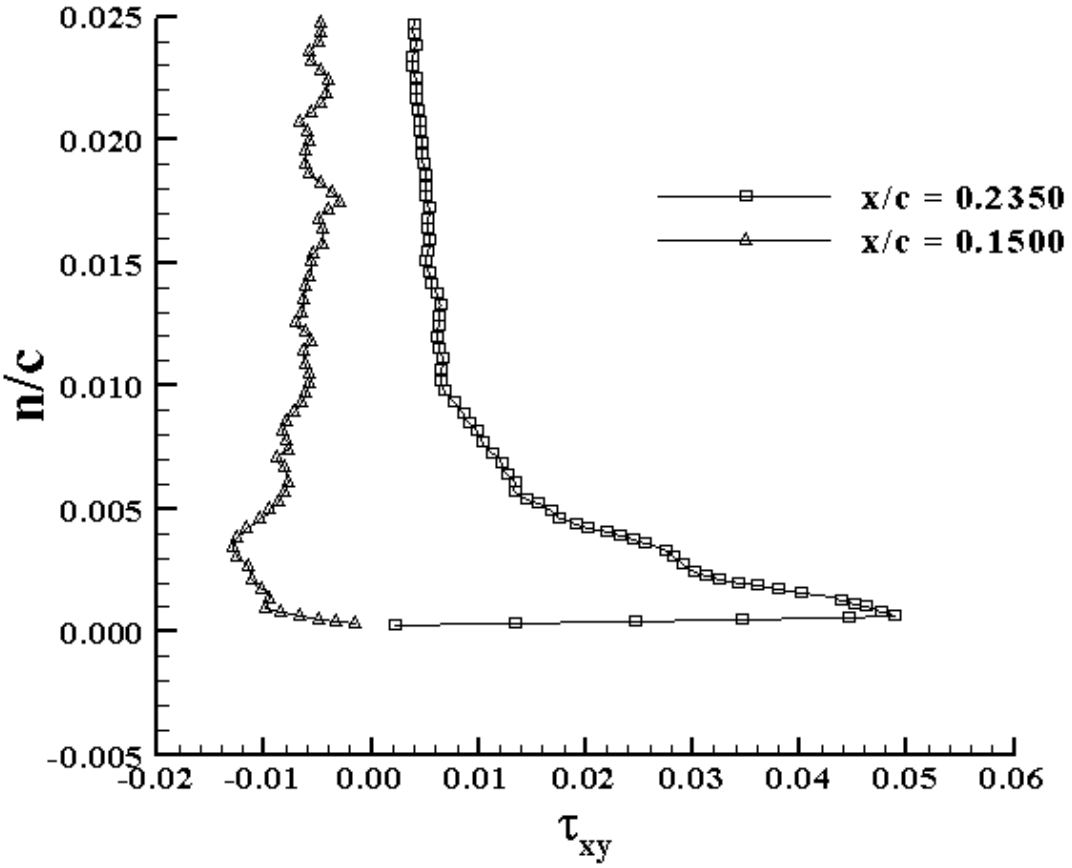

Figure 203: Line plot of τ_{xy} for $M_\infty = 0.2, k = 0.1, Up, \alpha = 14^0$

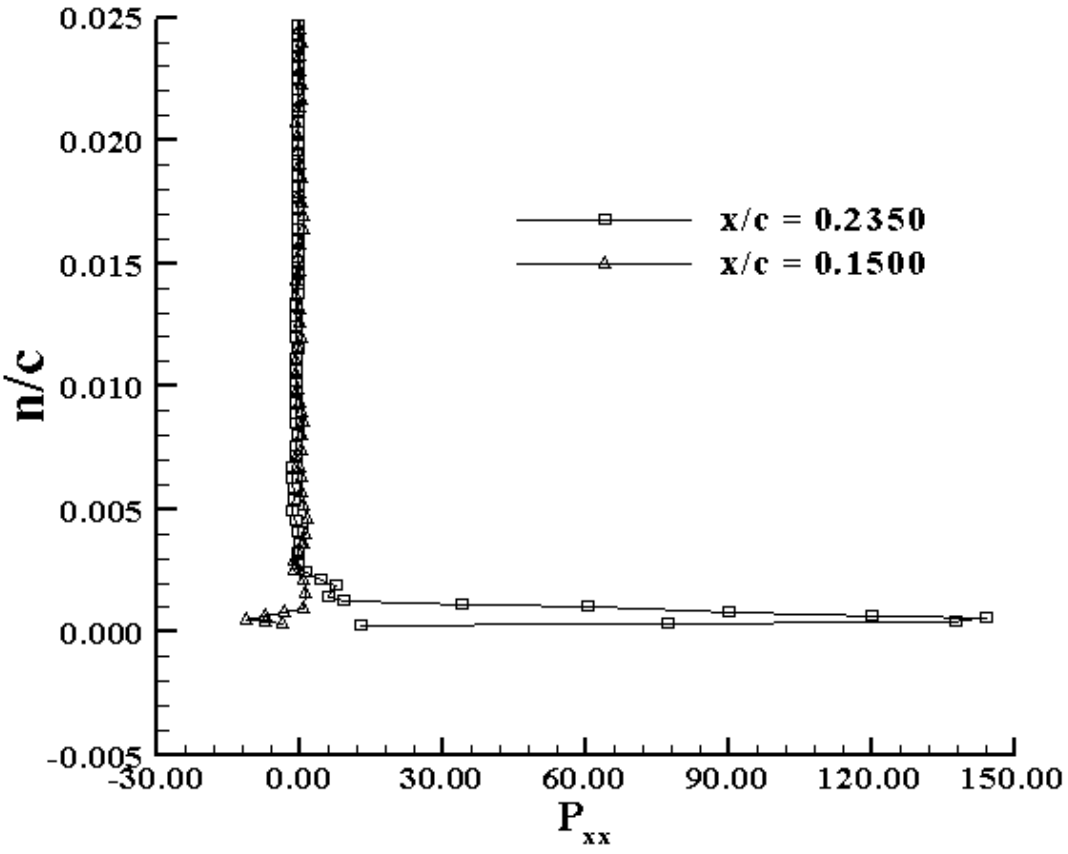

Figure 204: Line plot of P_{xx} for $M_\infty = 0.2, k = 0.1, Up, \alpha = 14^0$

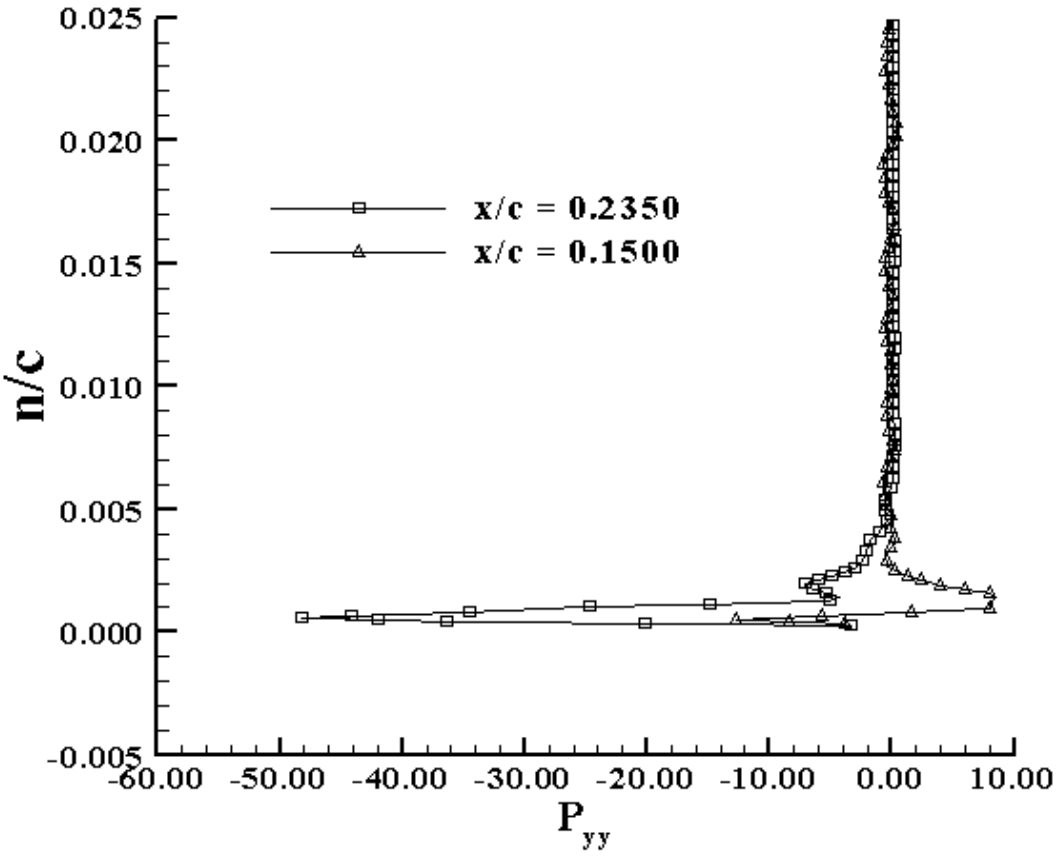

Figure 205: Line plot of P_{yy} for $M_\infty = 0.2, k = 0.1, Up, \alpha = 14^0$

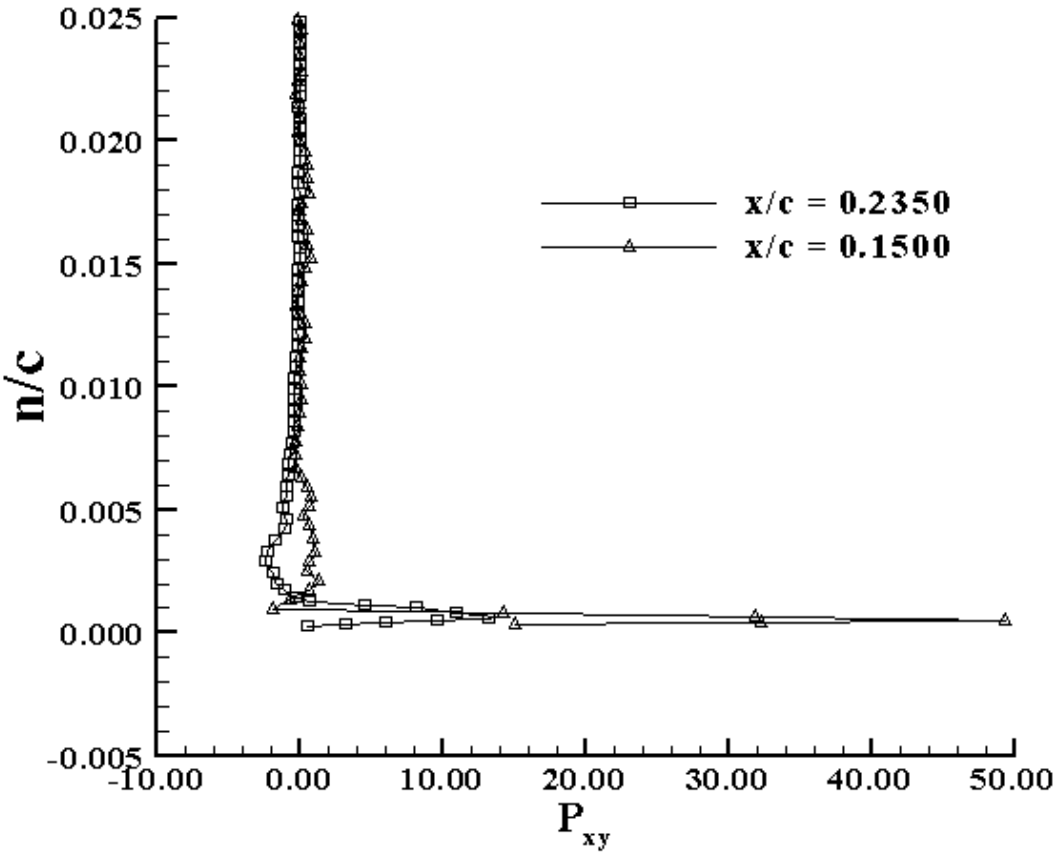

Figure 206: Line plot of P_{xy} for $M_\infty = 0.2, k = 0.1, Up, \alpha = 14^0$

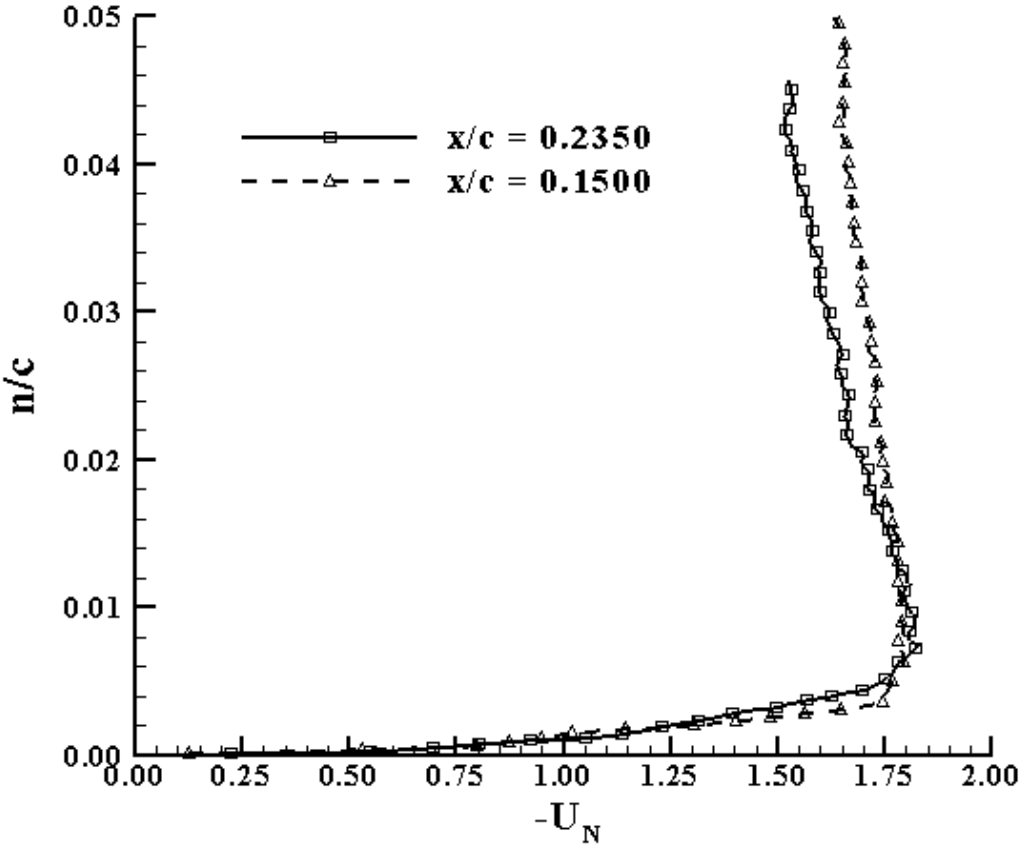

Figure 207: Line plot of -U_N for $M_\infty = 0.2, k = 0.1, Down, \alpha = 14^0$

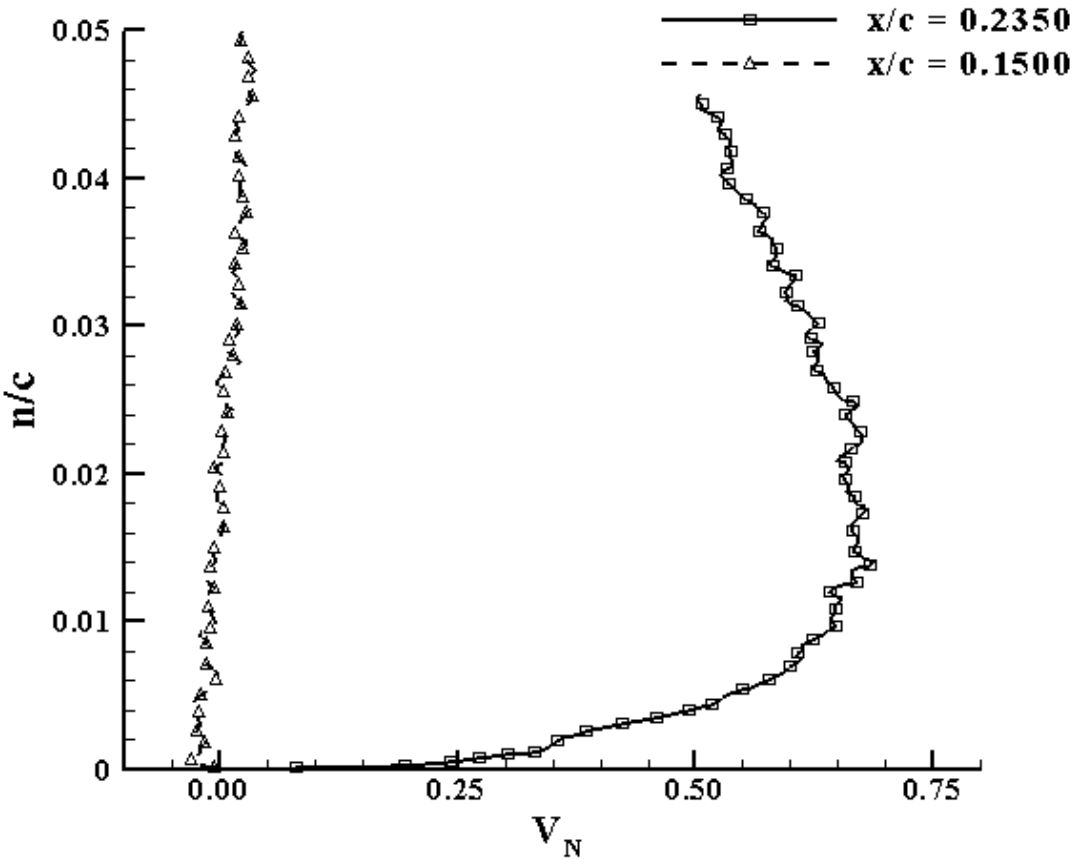

Figure 208: Line plot of V_N for $M_\infty = 0.2, k = 0.1, Down, \alpha = 14^0$

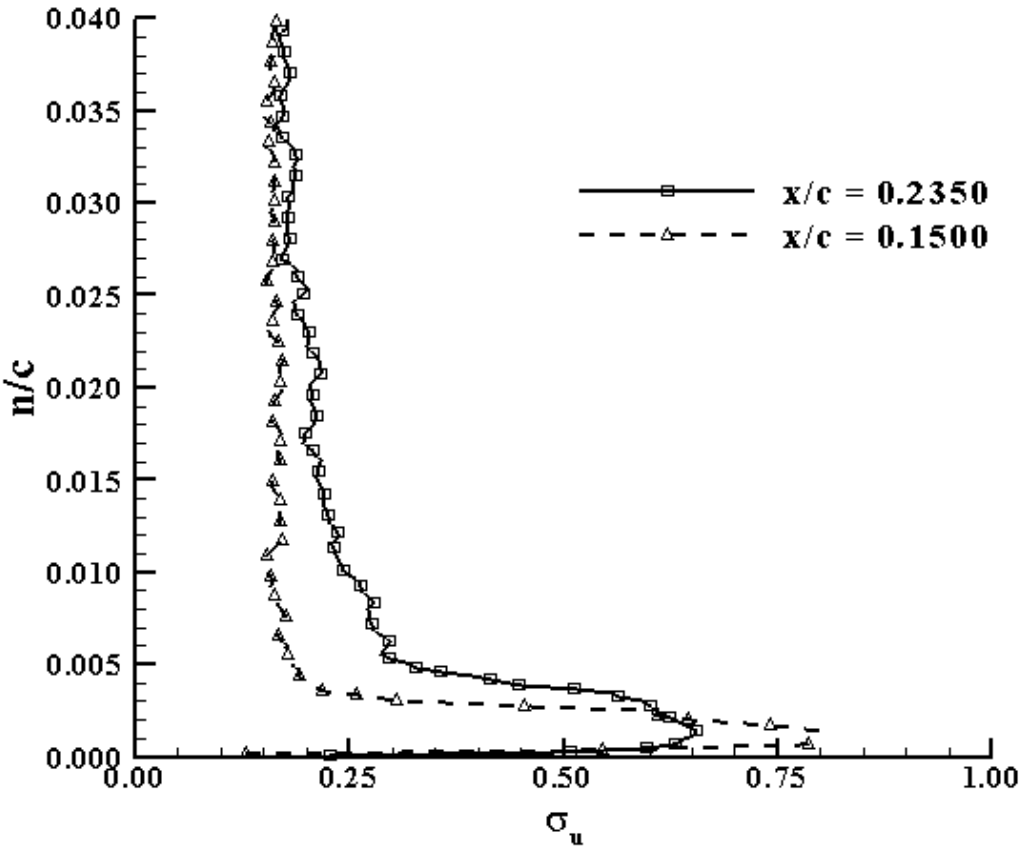

Figure 209: Line plot of σ_u for $M_\infty = 0.2, k = 0.1, Down, \alpha = 14^0$

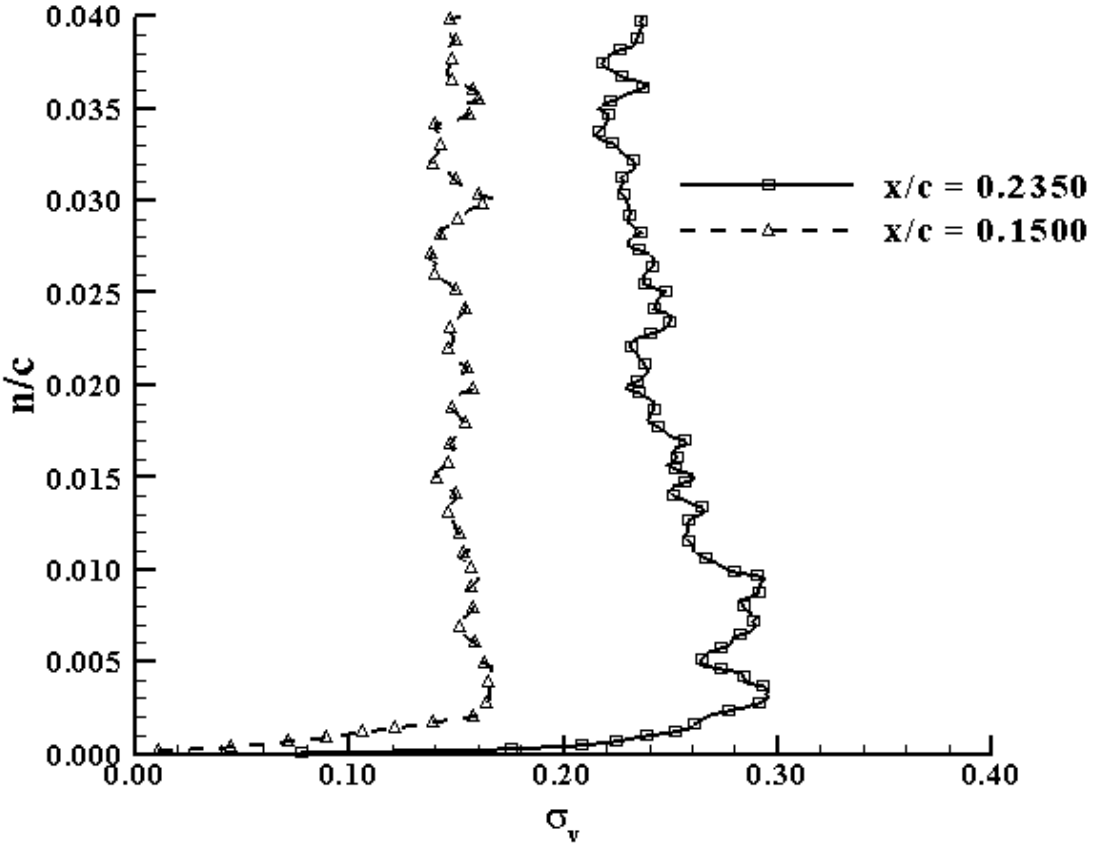

Figure 210: Line plot of σ_v for $M_\infty = 0.2, k = 0.1, Down, \alpha = 14^0$

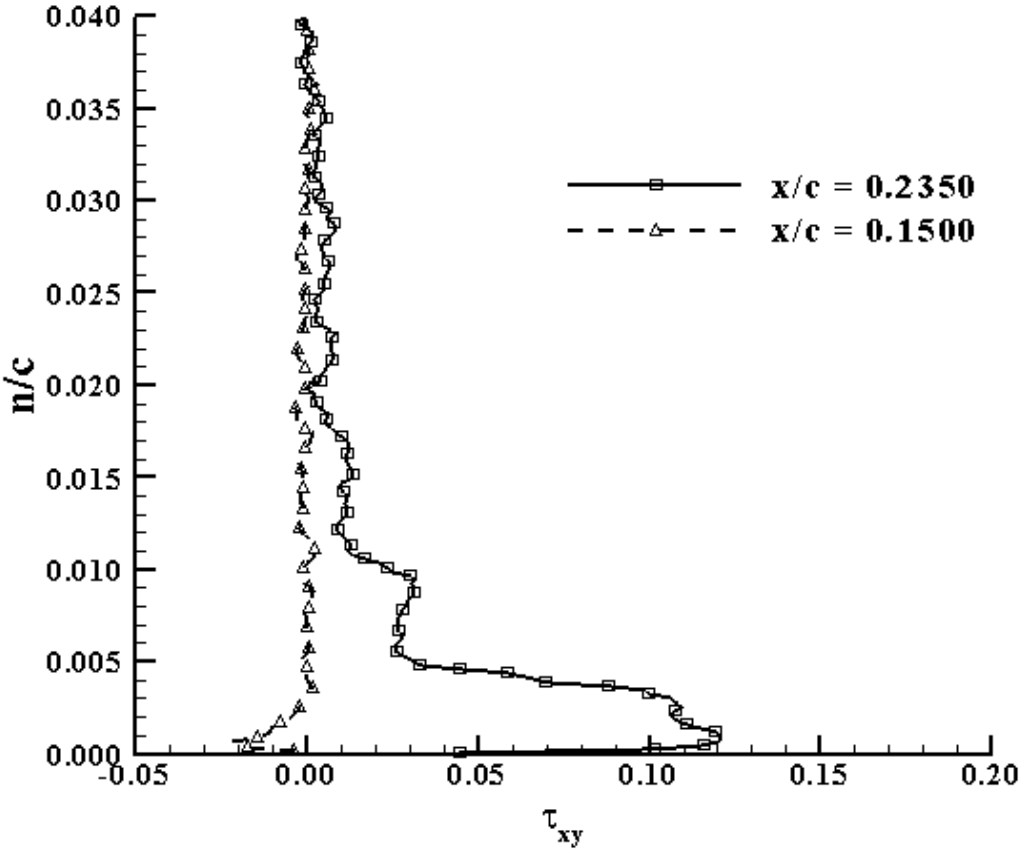

Figure 211: Line plot of τ_{xy} for $M_\infty = 0.2, k = 0.1, Down, \alpha = 14^0$

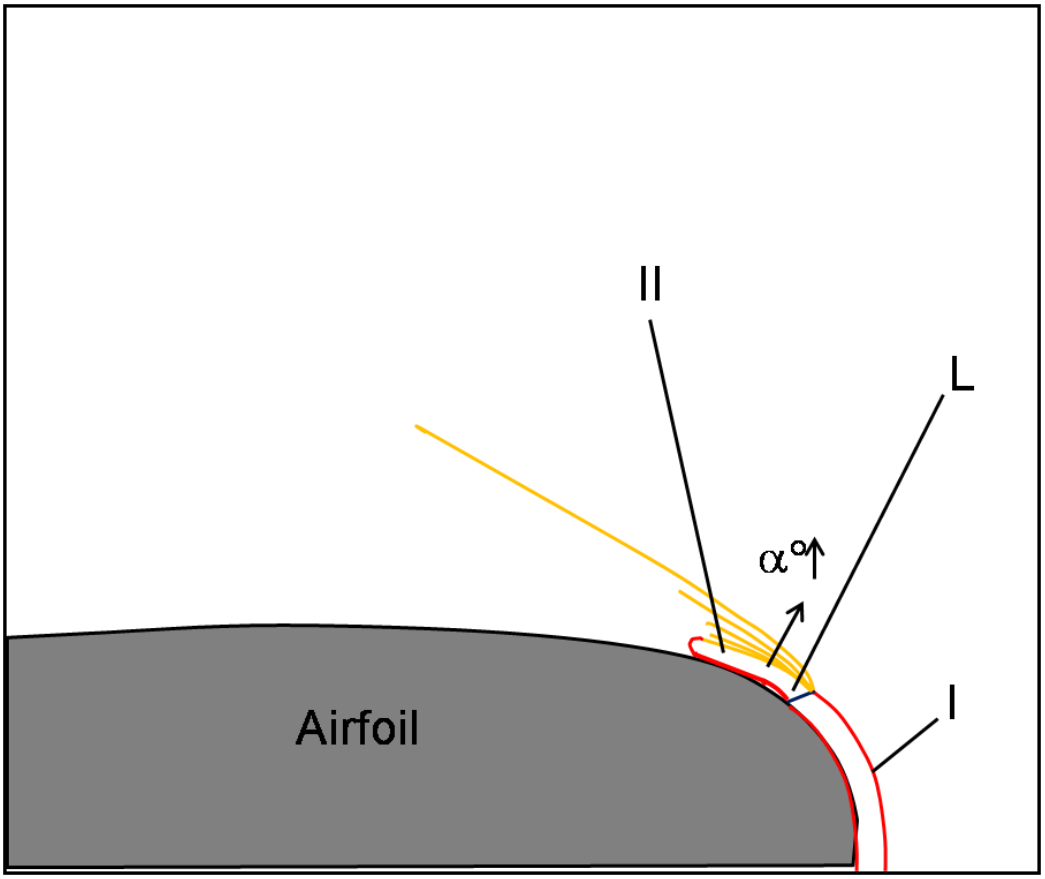

Figure 212: Reynolds shear stress structure in the leading edge region

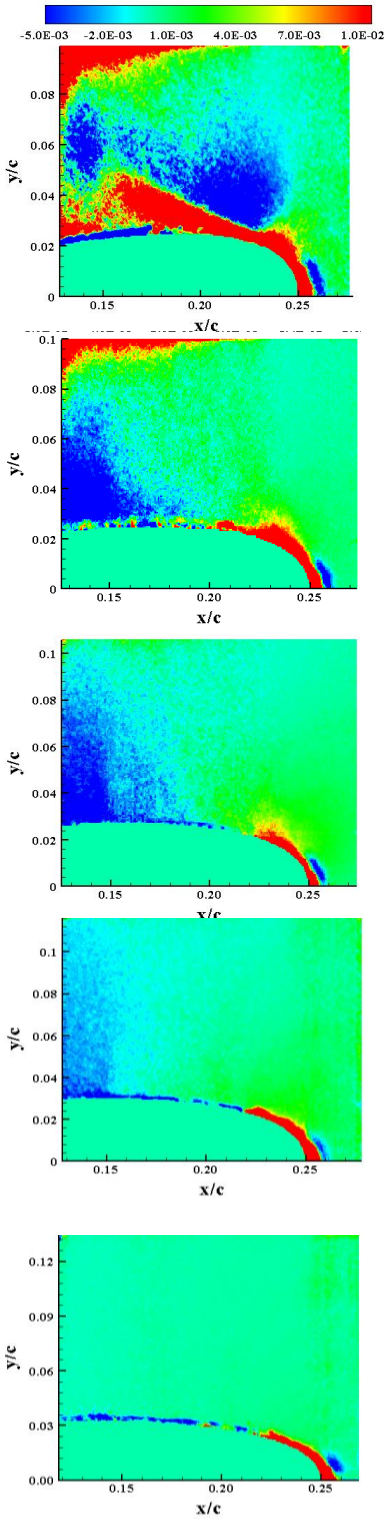

Figure 213: The sequence of formation of the bubble during the upstroke motion

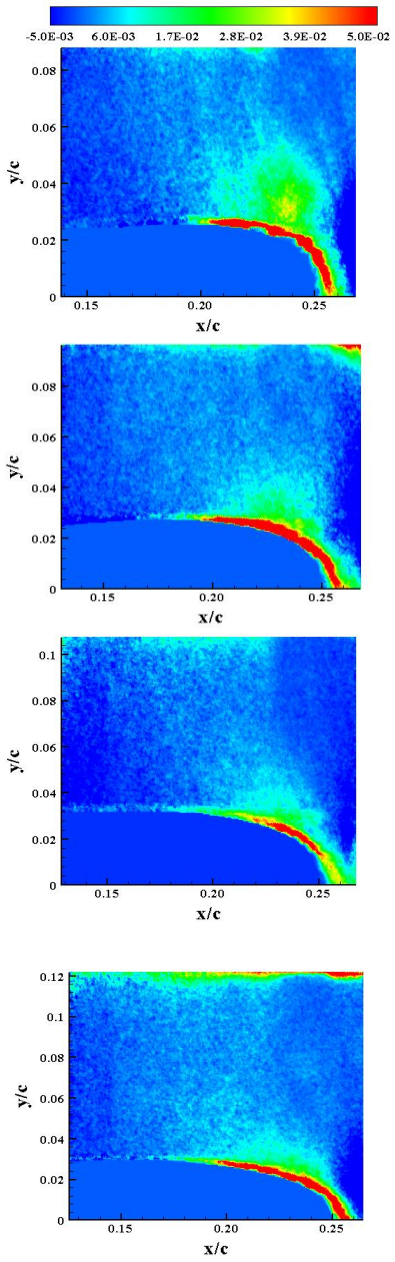

Figure 214: The sequence of formation of the bubble during the downstroke motion

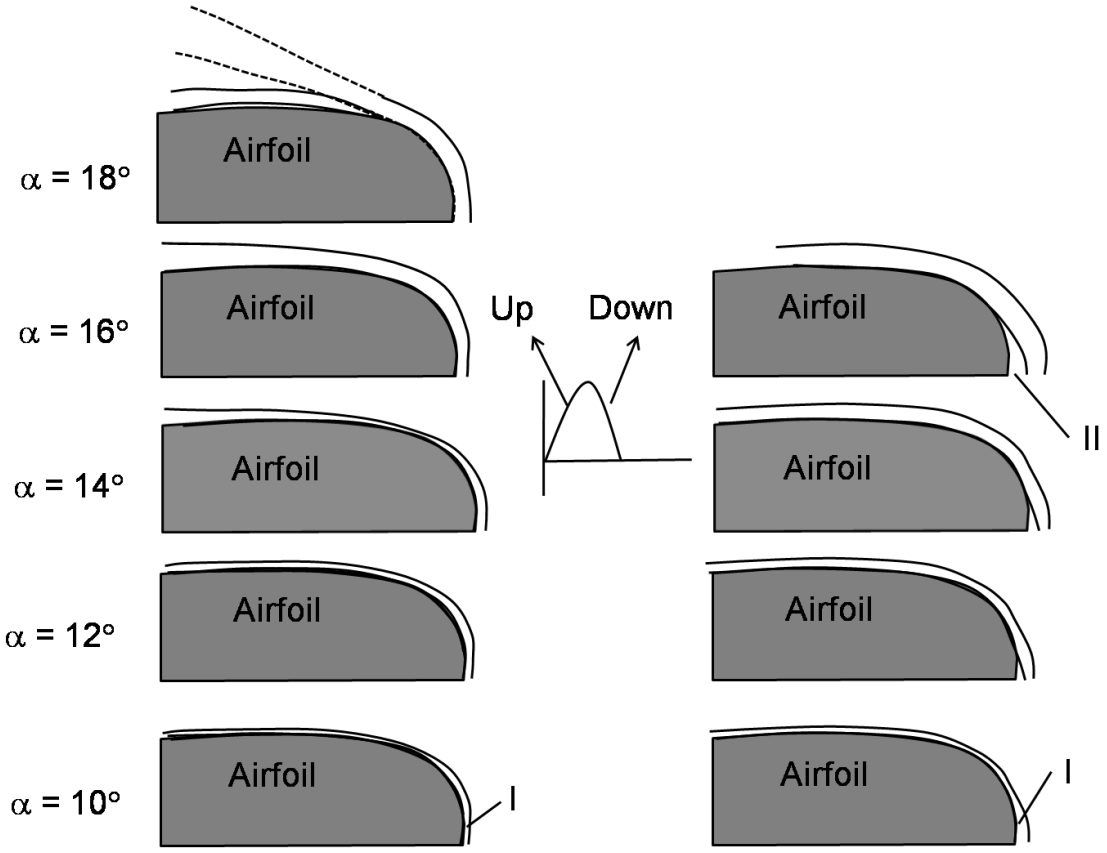

Figure 215: Sketch of the vorticity regions during the upstroke and downstroke motion of the wing

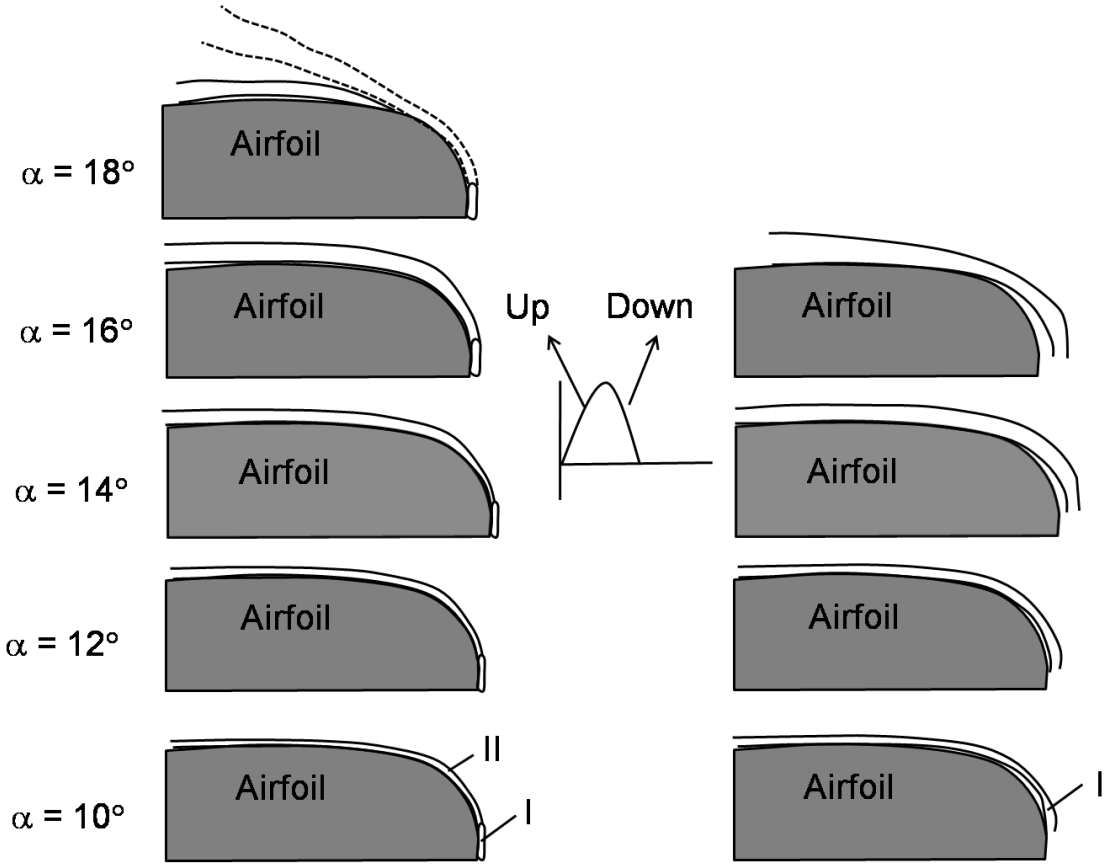

Figure 216: Sketch of the mean strain rate regions during the upstroke and downstroke motion of the wing

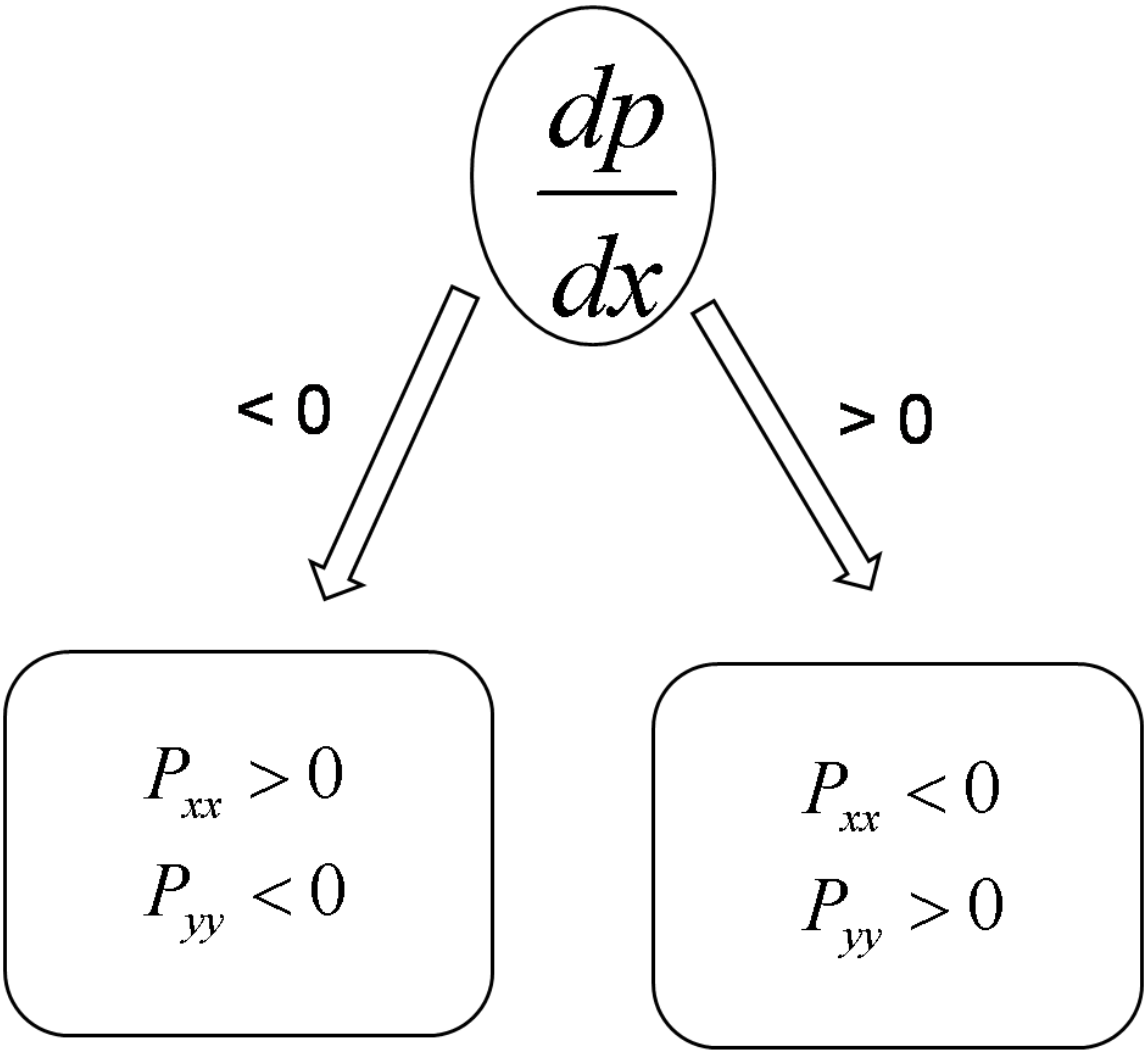

Figure 217: Flow chart depicting the dependence of Reynolds axial and transverse stress components on pressure gradient

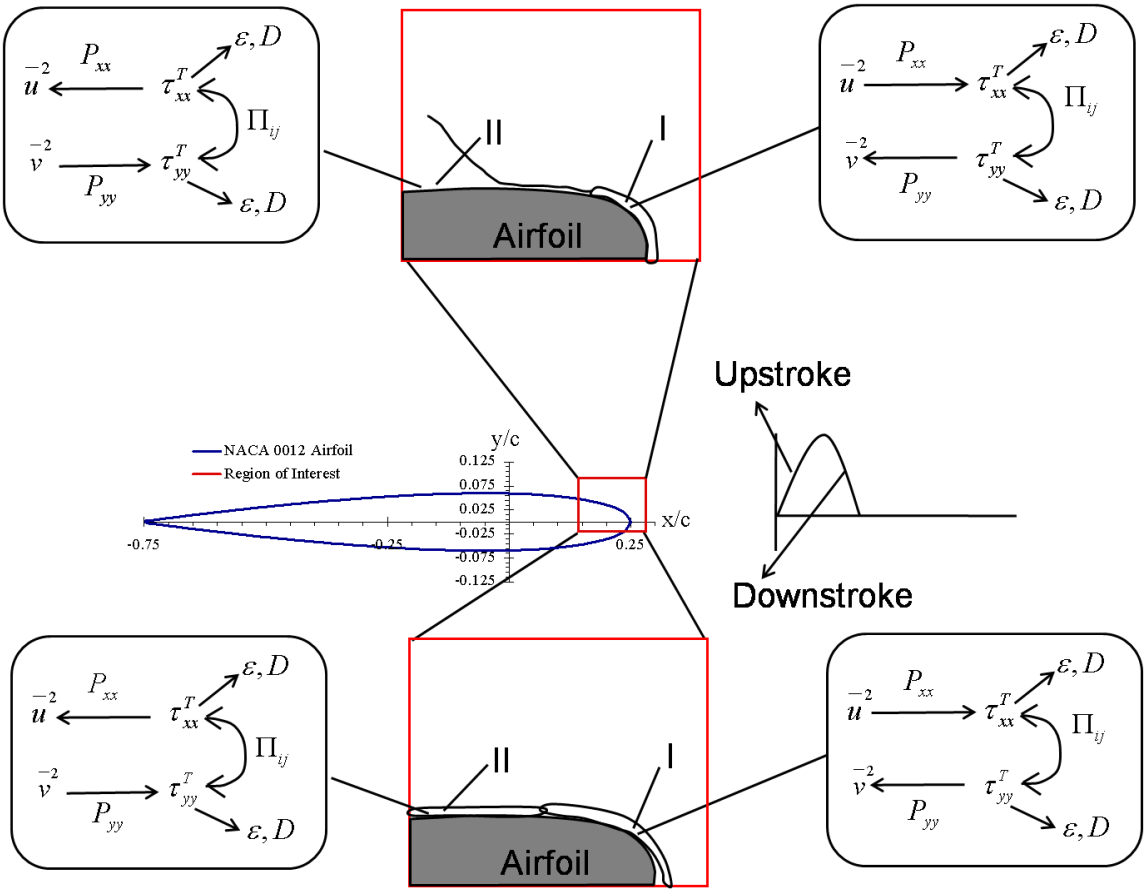

Figure 218: Energy budget sketches during the upstroke and downstroke motion of the wing

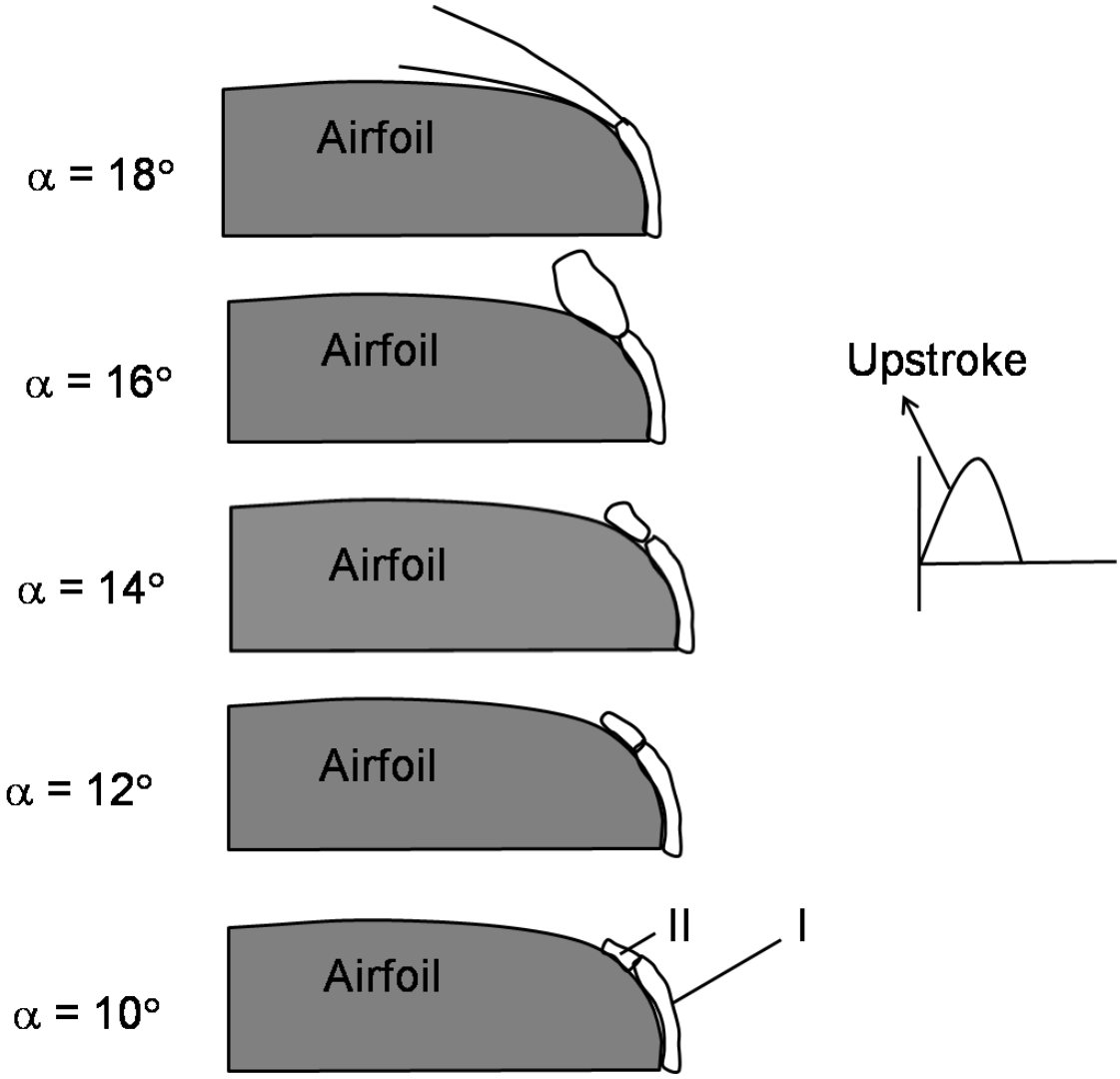

Figure 219: Reynolds shear stress structure

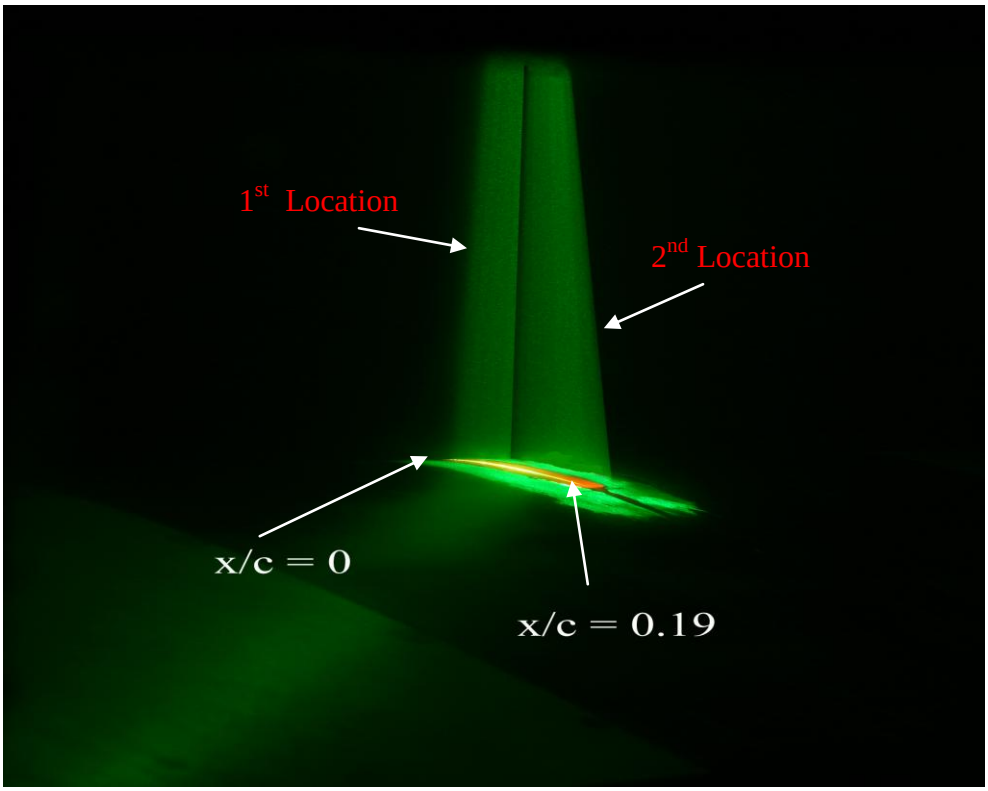

Figure 220: PIV images acquired at 1st and 2nd location corresponding to case 3 and 4

Table 1: Test matrix

Case	*Mach*	Re_c (x10^6)	α(degree)	*K*	*Meas. Angles*
1[1]	0.20	2.0	$\alpha = 10 \pm 10\sin(2\pi ft)$	0.10	10-18[2]
2[1]	0.28	2.8	$\alpha = 10 \pm 10\sin(2\pi ft)$	0.10	10-18[2]
3	0.20	2.0	$\alpha = 10 \pm 5\sin(2\pi ft)$	0.18	9.2, 11.1, 13.0
4	0.20	2.0	$\alpha = 15 \pm 5\sin(2\pi ft)$	0.18	13.7, 16.9
5	0.20	2.0	Static	0.00	10, 14, 18
6	0.28	2.8	Static	0.00	10, 18

[1]PIV movies were acquired for this flow condition. [2]2.0 degree increments

Table 2: Input parameters in ABAQUS[1]

Input Parameters	**Wing**	**Shaft**
Material	Aluminum	Stainless Steel
Density	5.28 slug/in^3	14.74 slug/in^3
Poisson's ratio	0.33	0.30
Young's Modulus	1.0x10^7 Psi	2.1x10^7 Psi
Element type	Hex, independent meshing, Linear 3D stress	Hex, independent meshing, Linear 3D stress

[1]English Units were used in ABAQUS

Table 3: Uncertainties

Variable	***Error***
P	1.0%
T	0.5%
U_{inf}	0.3%
x(mm), y(mm)	0.3
α (degree)	0.3
$\overline{u}$	2.0%
$\sqrt{\overline{u'^2}}$, $\sqrt{\overline{v'^2}}$	10.0%
$\overline{u'v'}$	20.0%
$P_{xx}/\overline{\rho}$, $P_{yy}/\overline{\rho}$, $P_{xy}/\overline{\rho}$	30.0%

Table 4: Angles-of-Attack

Comment	**Pitching Cycle**	**Angle-of-Attack (Degrees)**
Light Dynamic Stall	Up stroke	10 12 14 16 18
Light Dynamic Stall	Down stroke	10 12 14 16

Table 5: Time scales

Regions	Oscillation Time (τ_o)		Shear Time (τ_s)		Turbulent Time (τ_T)	
	Up	**Down**	**Up**	**Down**	**Up**	**Down**
I	0.031	0.031	0.012	0.003	0.042	0.011
II	0.031	0.031	0.036	0.002	0.122	0.008

Table 6: Avg. peak magnitude of U_N along with the axial location

α°	Avg. Peak Magnitude of U_N	Avg. Location of Separation	Avg. Peak Location of U_N
10	1.63	No Separation	0.21*c*
12	1.61	0.185*c*	0.22*c*
14	1.56	0.20*c*	0.23*c*
16	1.52	0.215*c*	0.235*c*
18	1.33	0.235*c*	0.24*c*

Table 7: Percentage reduction in peak axial velocity at different angles-of-attack

Angle-of-Attack (α°)	**Peak ($U_{N,\alpha}$ - $U_{N,10}$)/$U_{N,10}$**
10	0%
14	6%
18	23%

Table 8: Avg. peak magnitude of V_N

α°	**Avg. Peak Magnitude of V_N**	**Avg. Height of Region VI**
10	0.98	0.035*c*
12	0.95	0.037*c*
14	1.02	0.04*c*
16	1.06	0.044*c*
18	0.935	0.047*c*

Table 9: Percentage reduction in peak V-velocity at different angles-of-attack

Angle-of-Attack (α°)	Peak V_α - V_{10}	Location of Peak V_N (s/c)
10	0%	0.021
14	0%	0.016
18	20%	0.014

Table 10: Avg. peak Mach number (*M*)

α°	Avg. Peak *M*	Avg. axial distance of region of peak *M*
10	0.36	0.09*c*
12	0.35	0.06*c*
14	0.35	0.04*c*
16	0.36	0.03*c*
18	0.32	0.02*c*

Table 11: Contribution of axial (U_N) and transverse (V_N) velocities on Mach number

s/c	α = 10°				α = 14°				α = 18°			
	U_N	V_N	R^*	*M*	U_N	V_N	R^*	*M*	U_N	V_N	R^*	*M*
0.00	0.87	0.65	0.74	0.22	0.85	0.74	0.87	0.23	0.87	0.64	0.73	0.13
0.01	1.04	0.84	0.80	0.28	1.09	0.94	0.86	0.30	0.77	0.60	0.78	0.20
0.02	1.39	0.95	0.68	0.35	1.42	0.93	0.65	0.35	1.11	0.74	0.66	0.27
0.03	1.60	0.74	0.46	0.37	1.57	0.68	0.43	0.35	1.24	0.58	0.46	0.28
0.04	1.64	0.53	0.32	0.36	1.53	0.41	0.26	0.32	1.13	0.34	0.30	0.24
0.05	1.63	0.36	0.22	0.35	1.46	0.27	0.18	0.31	1.07	0.24	0.22	0.22
0.06	1.60	0.26	0.16	0.33	1.43	0.20	0.14	0.30	0.83	0.14	0.16	0.17
0.07	1.57	0.19	0.12	0.33	1.37	0.11	0.08	0.28	0.74	0.10	0.13	0.15
0.08	1.52	0.12	0.07	0.31	1.33	0.09	0.06	0.27	0.64	0.07	0.10	0.13
0.09	1.51	0.09	0.05	0.31	1.29	0.06	0.04	0.26	0.66	0.04	0.06	0.13
1.00	1.47	0.05	0.03	0.30	1.24	0.06	0.04	0.25	0.61	0.03	0.04	0.12

*$R = V_N / U_N$

Table 12: Magnitude of axial (σ_u) and transverse (σ_v) stress in the leading edge region

s/c	**α = 10°**		**α = 14°**		**α = 18°**	
	σ_u	σ_v	σ_u	σ_v	σ_u	σ_v
0.00	0.40	0.32	0.37	0.31	0.33	0.33
0.005	0.38	0.34	0.33	0.31	0.34	0.33
0.01	0.27	0.30	0.24	0.24	0.34	0.33
0.015	0.25	0.31	0.20	0.26	0.27	0.29
0.02	0.17	0.18	0.19	0.20	0.33	0.32
0.025	0.12	0.12	0.20	0.18	0.34	0.29
0.03	0.12	0.09	0.21	0.14	0.40	0.26
0.035	0.14	0.10	0.27	0.16	0.48	0.25
0.04	0.1	0.06	0.27	0.15	0.59	0.24

Table 13: Avg. thickness of region II at different angle-of-attack

α°	Average thickness (mm)
10	1.32
12	1.25
14	1.09
16	0.69

Table 14: Avg. peak magnitude of axial velocity (U_N) for different angles-of-attack

α°	Avg. Peak Magnitude of U_N (Pitching Down)	Avg. Peak Magnitude of U_N (Pitching Up)	Difference
10	1.65	1.63	1.2%
12	1.7	1.61	5.3%
14	1.95	1.56	20%
16	2.1	1.52	27.6%

Table 15: Avg. peak magnitude of axial velocity (U_N) for different angles-of-attack

α°	Avg. Peak Mach number & Location (Pitching Down)	Avg. Peak Mach number & Location(x/c) (Pitching Up)
10	0.36	0.36
12	0.35	0.35
14	0.41	0.35
16	0.45	0.36

Table 16: Comparison of the thickness of region II during the downstroke motion of the wing

α	Avg. Thickness of Region II (mm)
12°	0.9
14°	1.82
16°	2.3

Table 17: Magnitude of axial stress in the shear layer at 14° for upstroke and downstroke motion of the wing

x/c	α = 14° (Downstroke)	α = 14° (Upstroke)
0.2475	0.53	0.28
0.245	0.51	0.23
0.2425	0.62	0.21
0.24	0.75	0.23
0.23	0.79	0.29
0.22	0.83	0.29
0.21	0.83	0.27
0.20	0.83	0.26
0.19	0.81	0.26
0.18	0.83	0.27
0.17	0.83	0.28
0.16	0.72	0.29

Table 18: Avg. center coordinates of region III of high σ_v

α	Avg. Center of Region III	
	x/c	**y/c**
10	0.254	0.014
12	0.256	0.015
14	0.258	0.017
16	0.261	0.021

Table 19: Location and difference between peak magnitudes of transverse velocity at stations 1 and 2

Station (*x/c*)	**Location away from wall(mm)**	**Difference**
0.235	2.3	0%
0.15	0.35	77.5%

Table 20: Comparison of magnitude of Reynolds stress components at $\alpha = 14°$

Reynolds Stress Components	Magnitude at 1.5% of '*c*'			Magnitude at 10% '*c*'		
	Down	**Up**	**Difference**	**Down**	**Up**	**Difference**
P_{xx}	400	144	177%	70	12	483%
P_{yy}	42	50	-19%	0	8	-80%
P_{xy}	26	14	85%	10	32	-68%

Table 21: L in mm vs. Angle-of-Attack

α°	L(mm)
10	1.73
12	2.14
14	4.14
16	5.06

APPENDIX B

Installation procedure of the modified 7 ft x 7ft wind tunnel and the wing

- Start with the left side wall (looking upstream). Left side wall includes the inlet and the test section. Put the bolts in position to attach to the floor. Do not tighten them yet.
- Install the right side wall (inlet and the test section). Do not tighten to the floor.
- At this point the panels are also loosely connected.
- Install the roof in position on the side walls.
- A 5 in x 1.75 in C-channel was set against the right side wall on the floor to keep the seams (where panels are bolted) straight.
- Use 2 by 4 wooden blocks to maintain the 7 ft distance between the side walls.
- Put the long spacer between the roof and the top of the side walls in flow direction.
- Once the walls are aligned straight, tighten the all the bolts i.e. bolts attaching the panels of the wall, bolts attaching the side walls to the floor and finally the bolts attaching the side walls to the roof.
- After the side walls are tightened install the diffuser section. Make sure the diffuser is attached to the concrete of current wind tunnel tightly.

Above steps complete the installation of the modified 7 ft x 7ft wind tunnel.

- Insert the NACA 0012 wing into the test section through the 3rd. panel.
- Set the wing on the support structures and tighten all the bolts.

Following figures explain the installation of the wind tunnel along with the wing.

Figure B-1: Installation of the right wall

Figure B-2: Installation of the left wall

Figure B-3 Installation of the roof

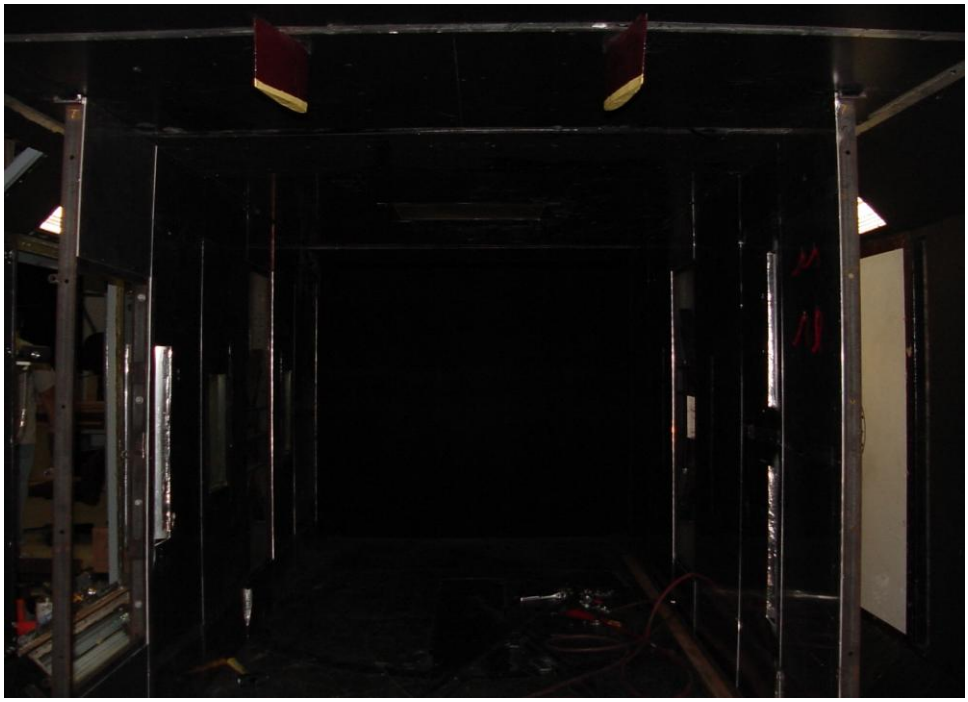

Figure B-4 Installation of side walls and roof - loosely connected

Figure B-5 Installation of left wall with the inlet section

Figure B-6 Installation of right side wall with the C-channel for alignment

Figure B-7 Alignment of side walls with 2 by 4s

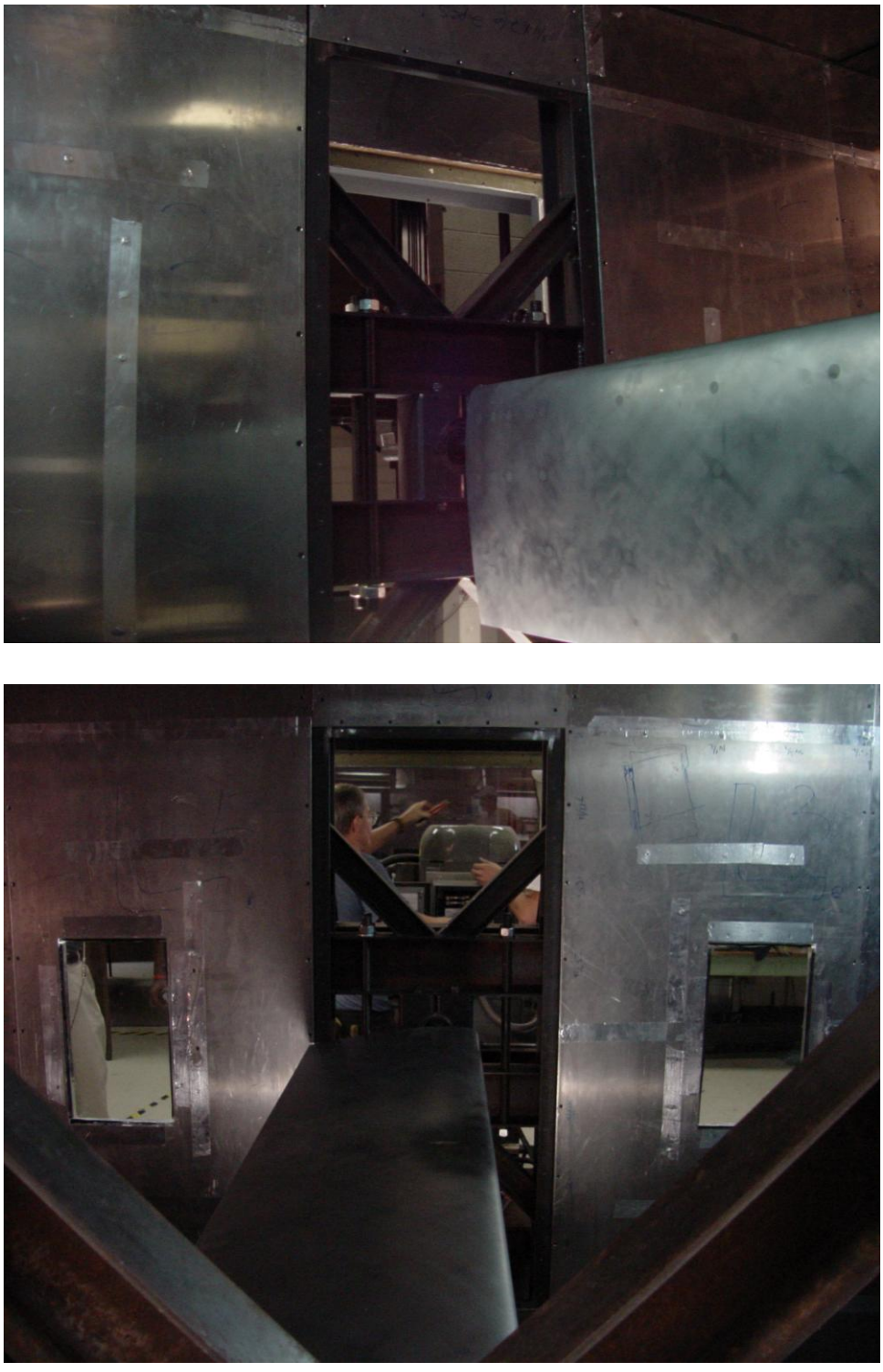

Figure B-8 Installation of the NACA 0012 wing

Figure B-9 View of the wing from outside the wind tunnel (right side)

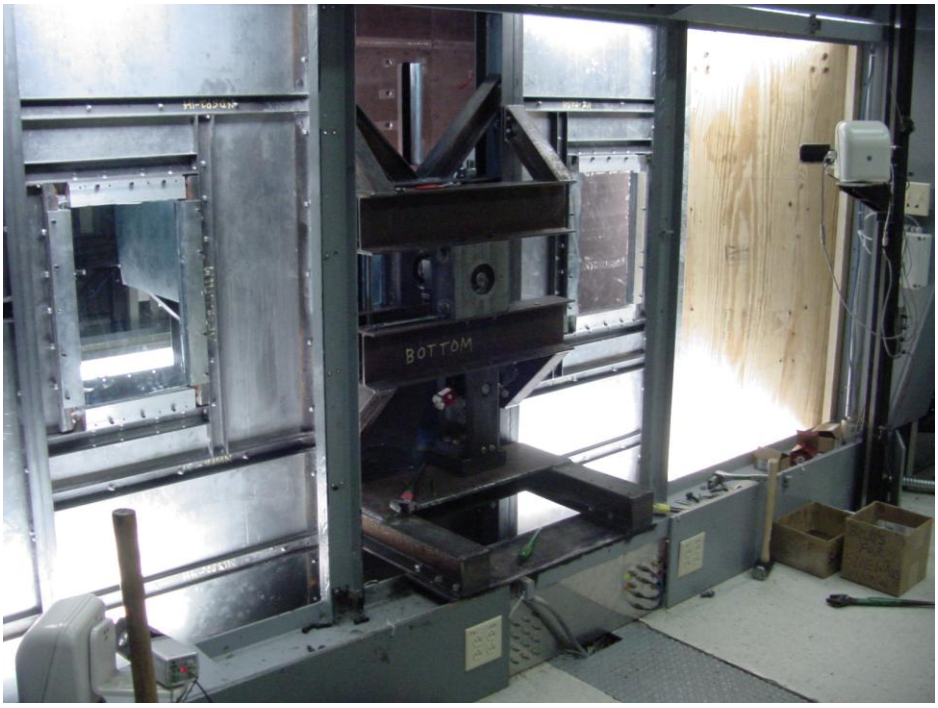

Figure B-10 View of the wing with hydraulic actuator from ready room

Figure B-11 Close up view of the wing with actuator and support structure

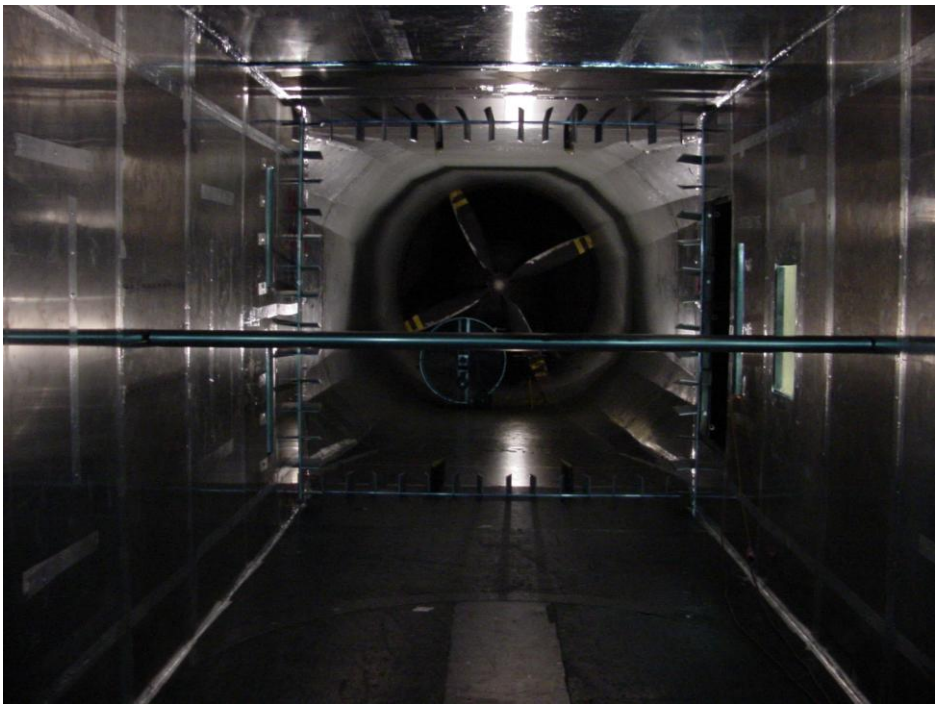

Figure B-12 Modified wind tunnel with the wing and vortex generators

APPENDIX C

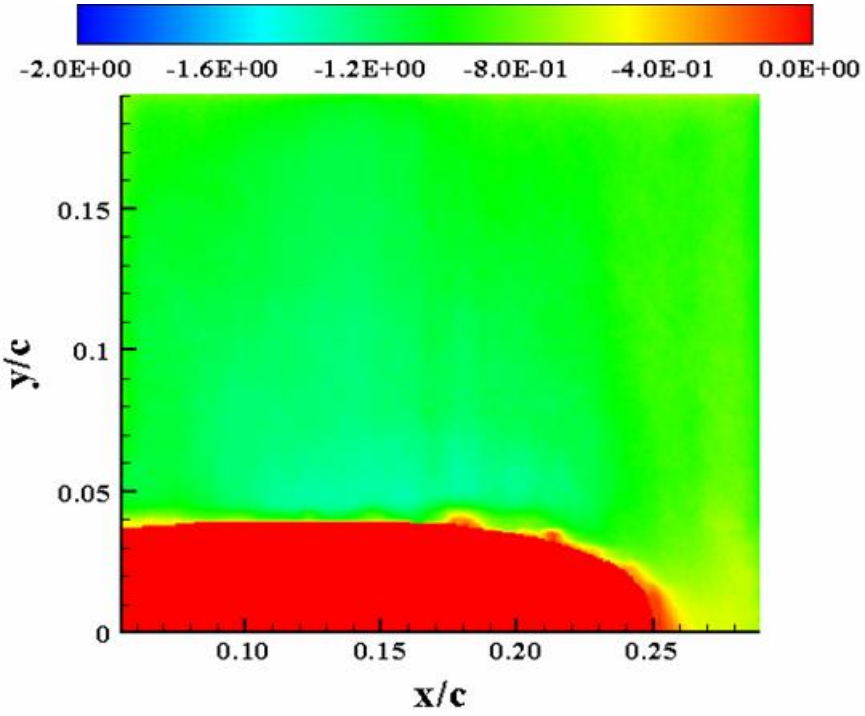

Figure C-1: $U_N(M_\infty = 0.28, k = 0.1, Up, \alpha = 10^0)$

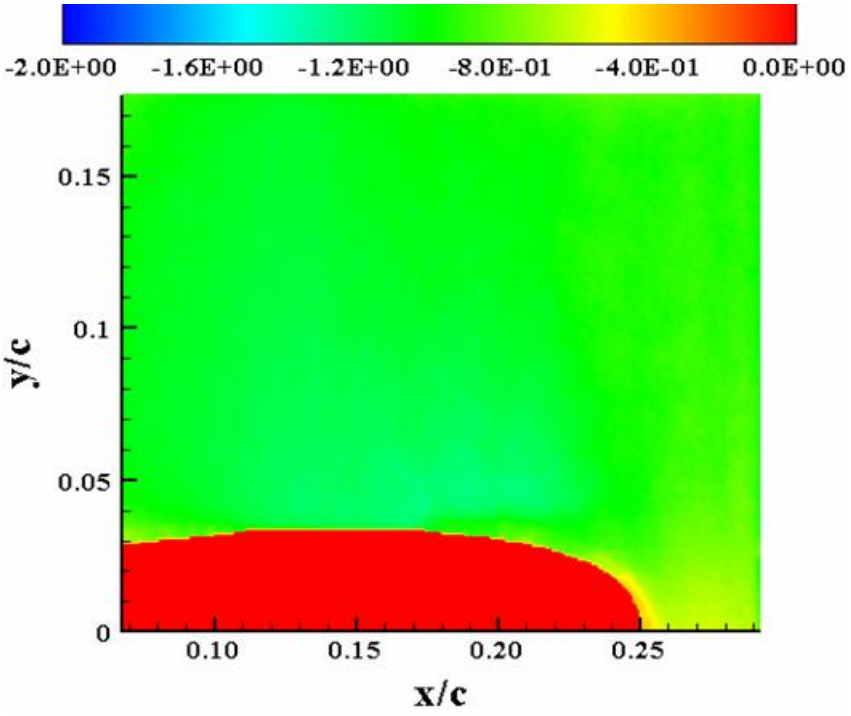

Figure C-2: $U_N(M_\infty = 0.28, k = 0.1, Up, \alpha = 12^0)$

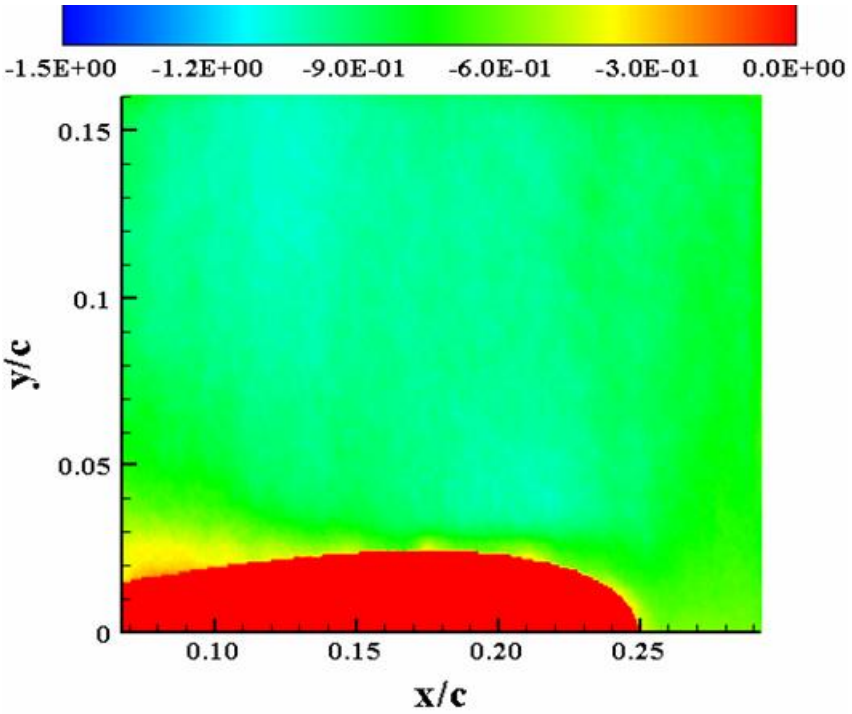

Figure C-3: $U_N(M_\infty = 0.28, k = 0.1, Up, \alpha = 14^0)$

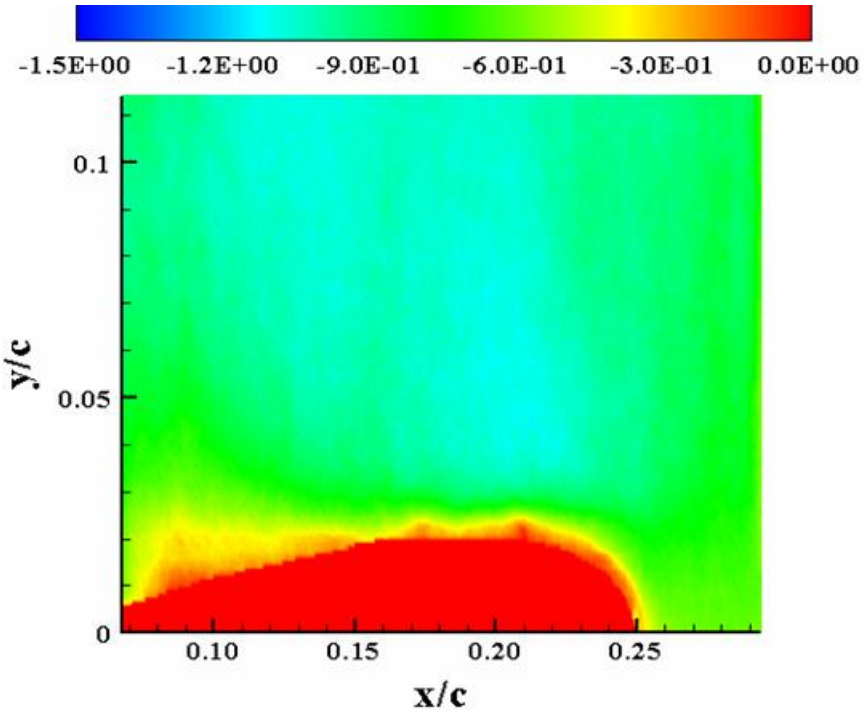

Figure C-4: $U_N(M_\infty = 0.28, k = 0.1, Up, \alpha = 16^0)$

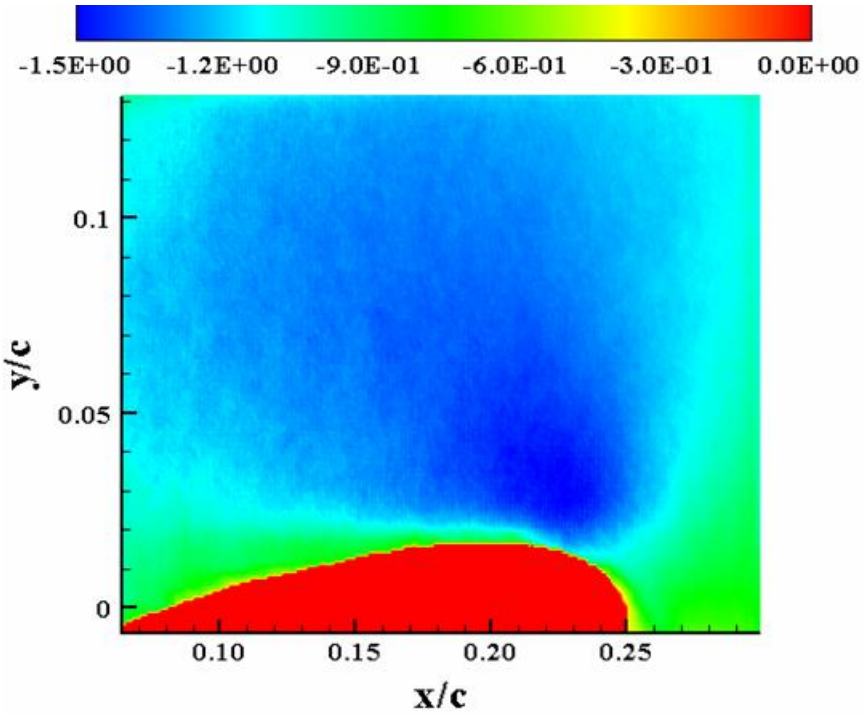

Figure C-5: $U_N(M_\infty = 0.28, k = 0.1, Up, \alpha = 18^0)$

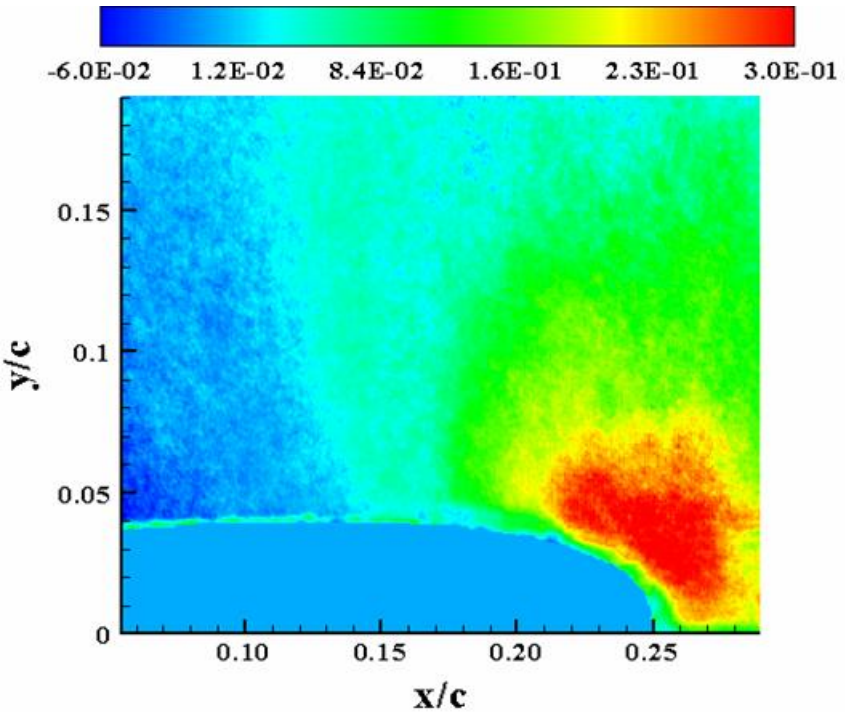

Figure C-6: $V_N(M_\infty = 0.28, k = 0.1, Up, \alpha = 10^0)$

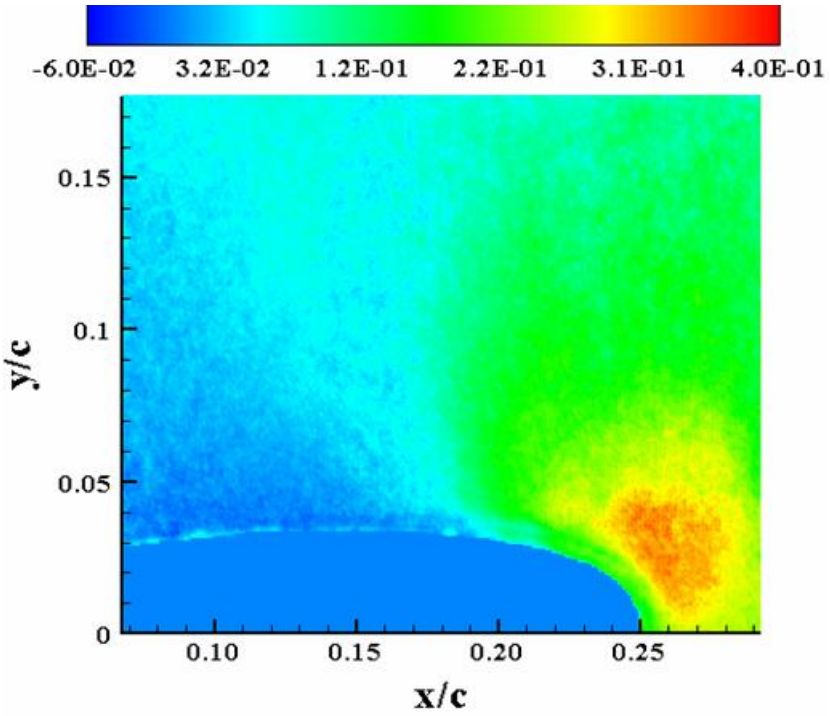

Figure C-7: $V_N(M_\infty = 0.28, k = 0.1, Up, \alpha = 12^0)$

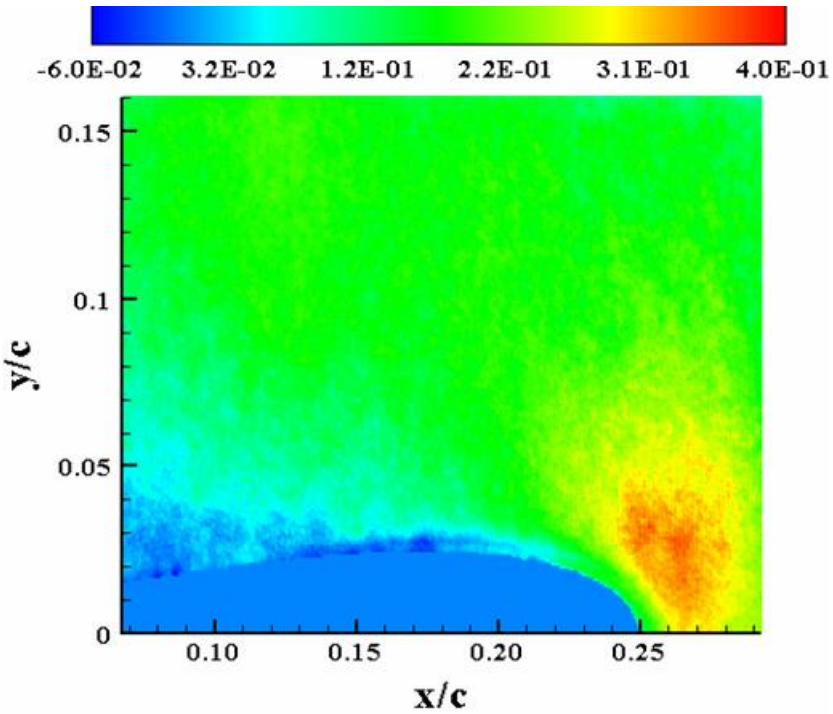

Figure C-8: $V_N(M_\infty = 0.28, k = 0.1, Up, \alpha = 14^0)$

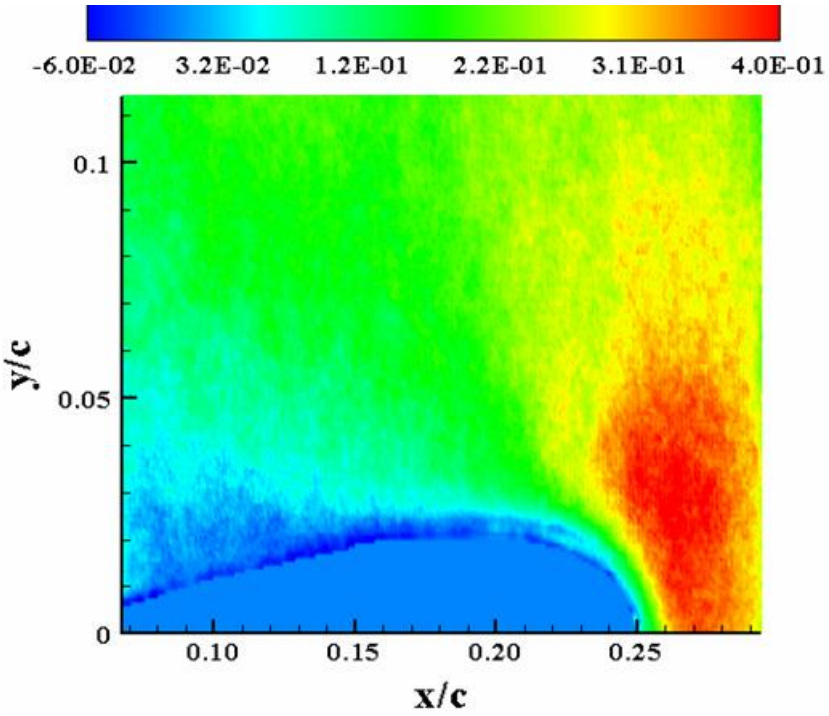

Figure C-9: $V_N(M_\infty = 0.28, k = 0.1, Up, \alpha = 16^0)$

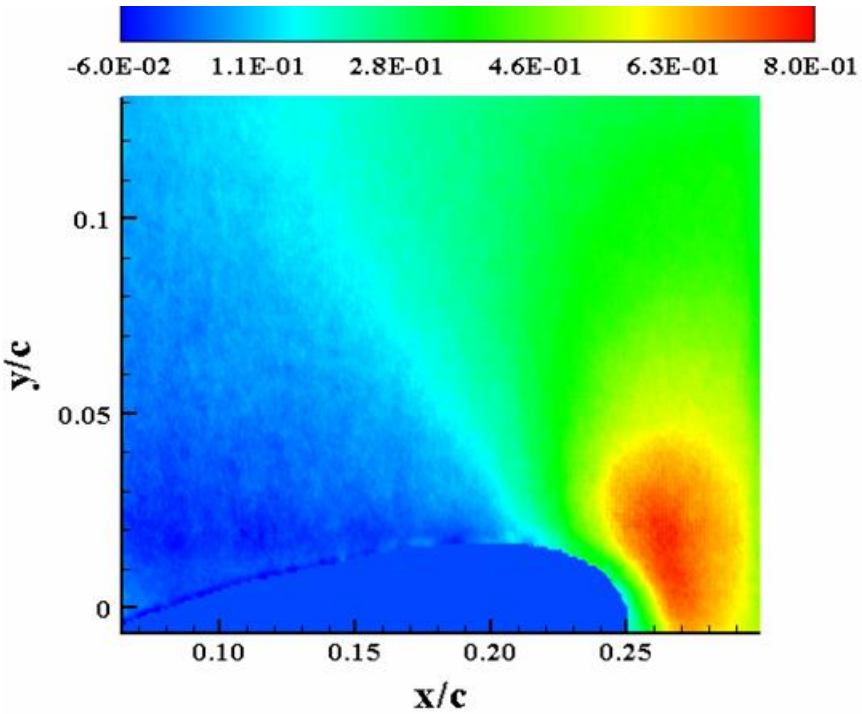

Figure C-10: $V_N(M_\infty = 0.28, k = 0.1, Up, \alpha = 18^0)$

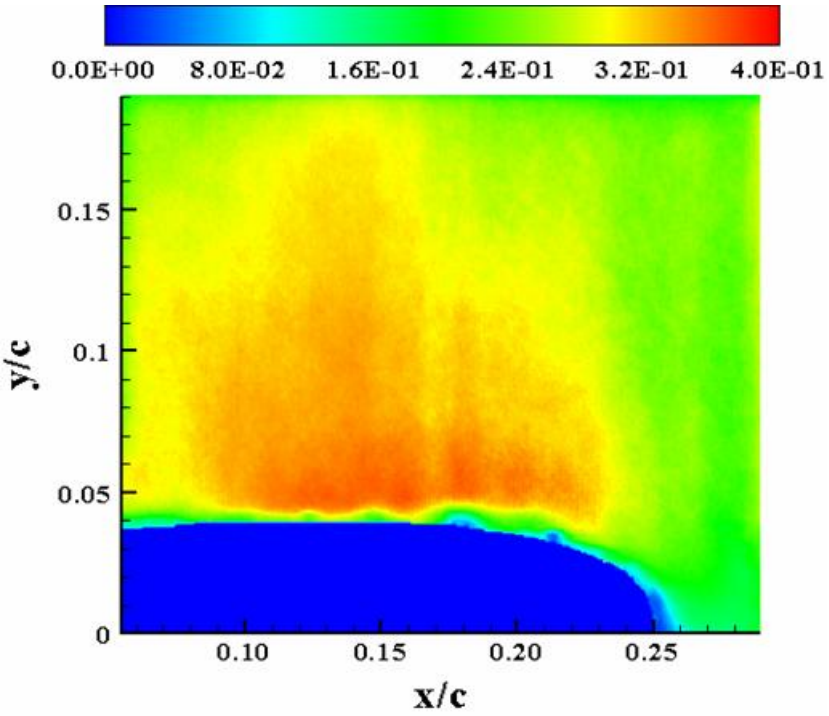

Figure C-11: $M(M_\infty = 0.28, k = 0.1, Up, \alpha = 10^0)$

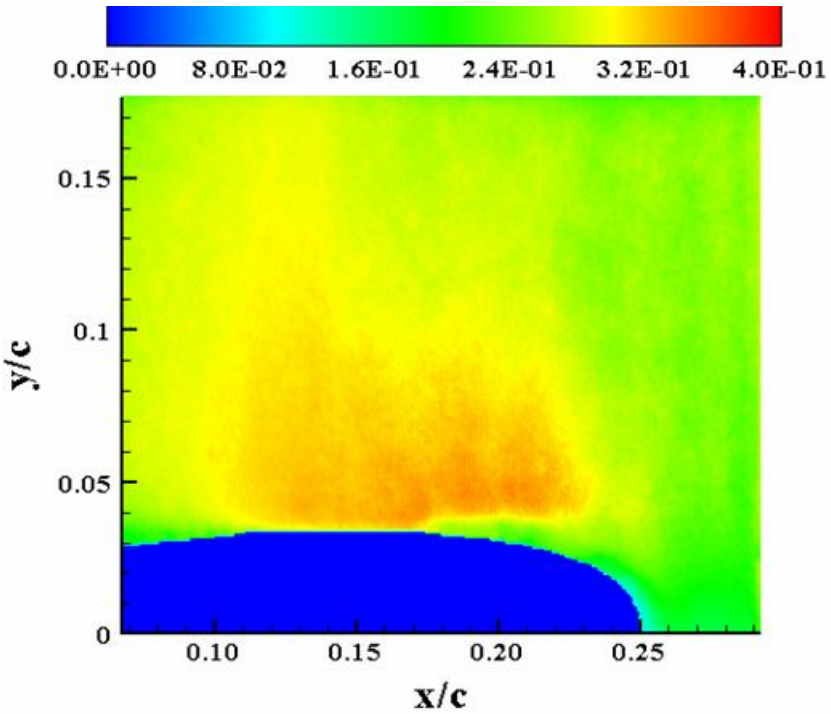

Figure C-12: $M(M_\infty = 0.28, k = 0.1, Up, \alpha = 12^0)$

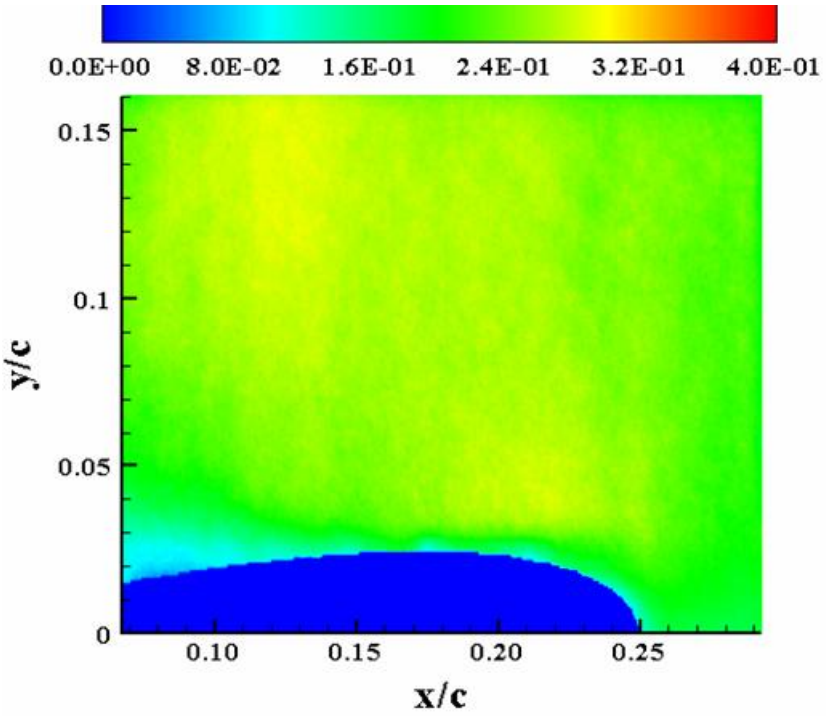

Figure C-13: $M(M_\infty = 0.28, k = 0.1, Up, \alpha = 14^0)$

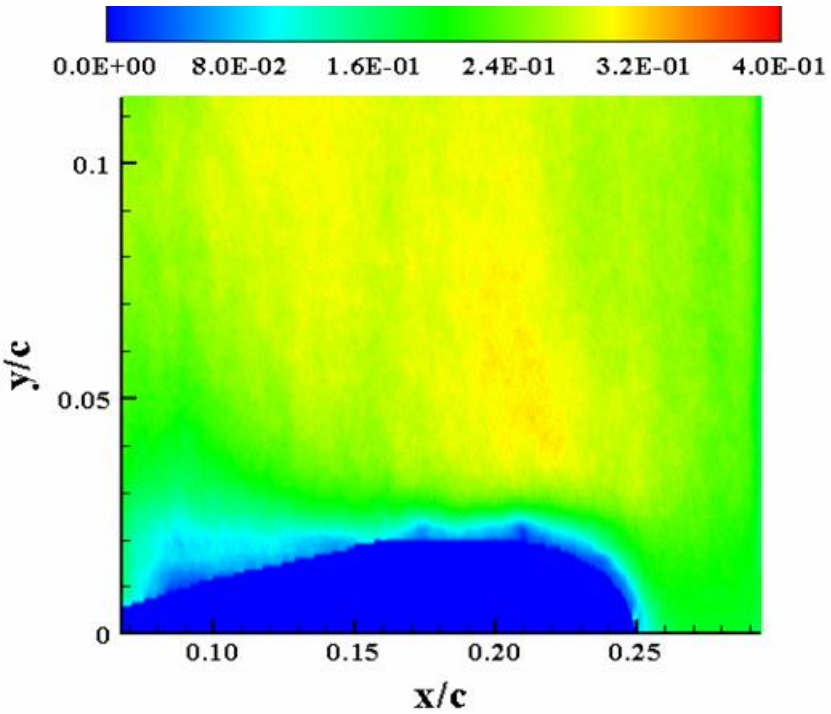

Figure C-14: $M(M_\infty = 0.28, k = 0.1, Up, \alpha = 16^0)$

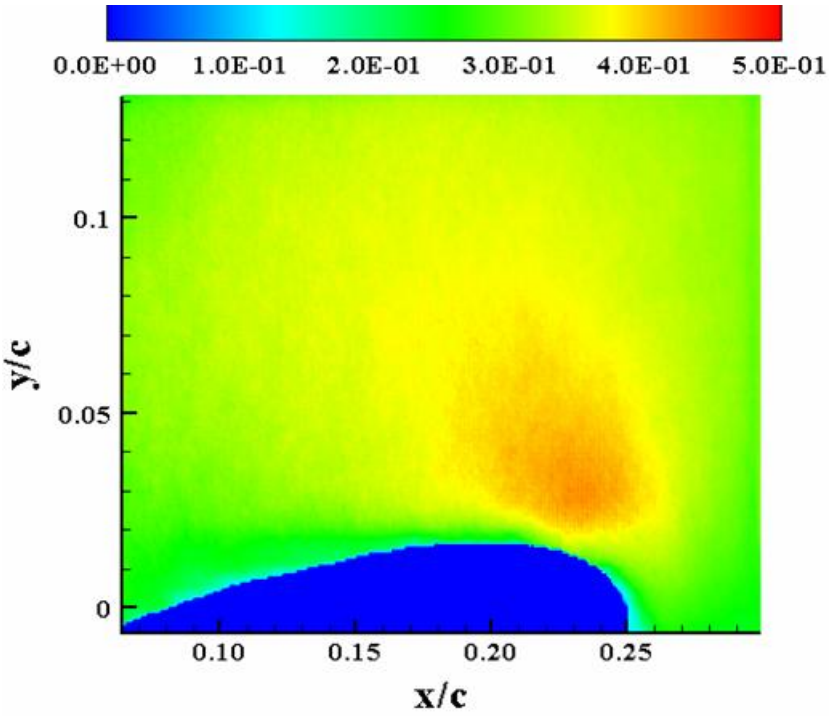

Figure C-15: $M(M_\infty = 0.28, k = 0.1, Up, \alpha = 18^0)$

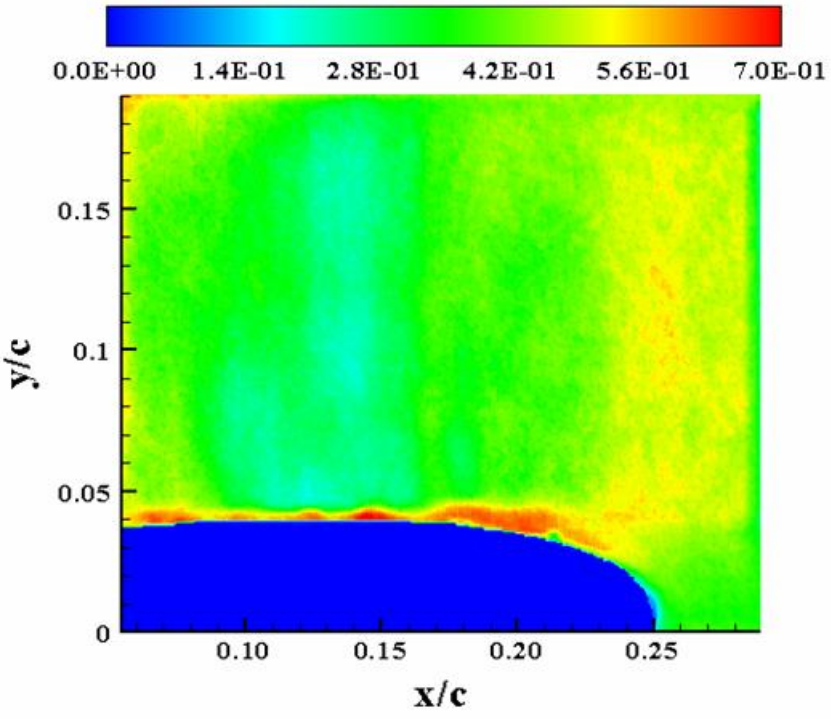

Figure C-16: $\sigma_u(M_\infty = 0.28, k = 0.1, Up, \alpha = 10^0)$

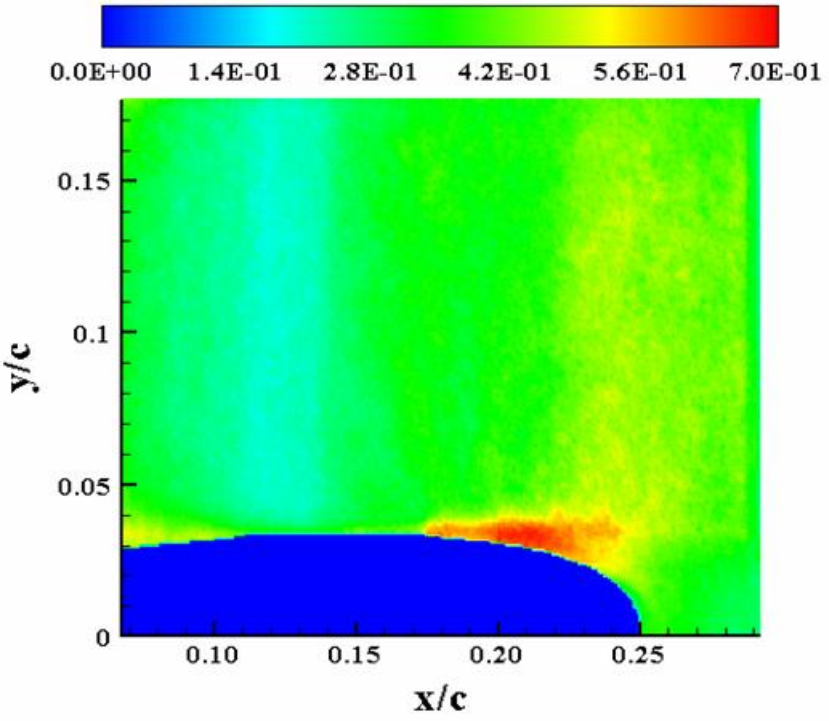

Figure C-17: $\sigma_u(M_\infty = 0.28, k = 0.1, Up, \alpha = 12^0)$

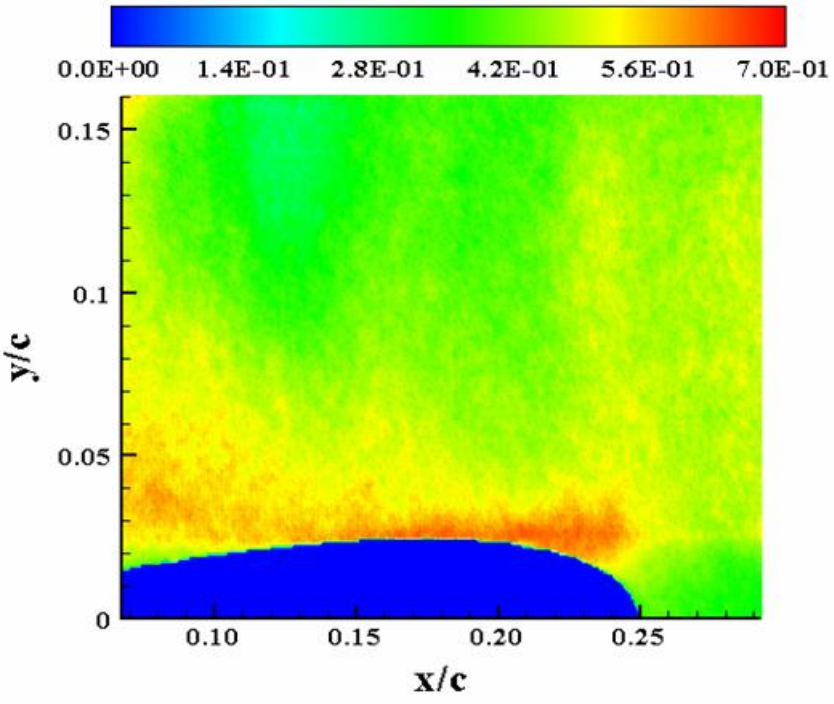

Figure C-18: $\sigma_u(M_\infty = 0.28, k = 0.1, Up, \alpha = 14^0)$

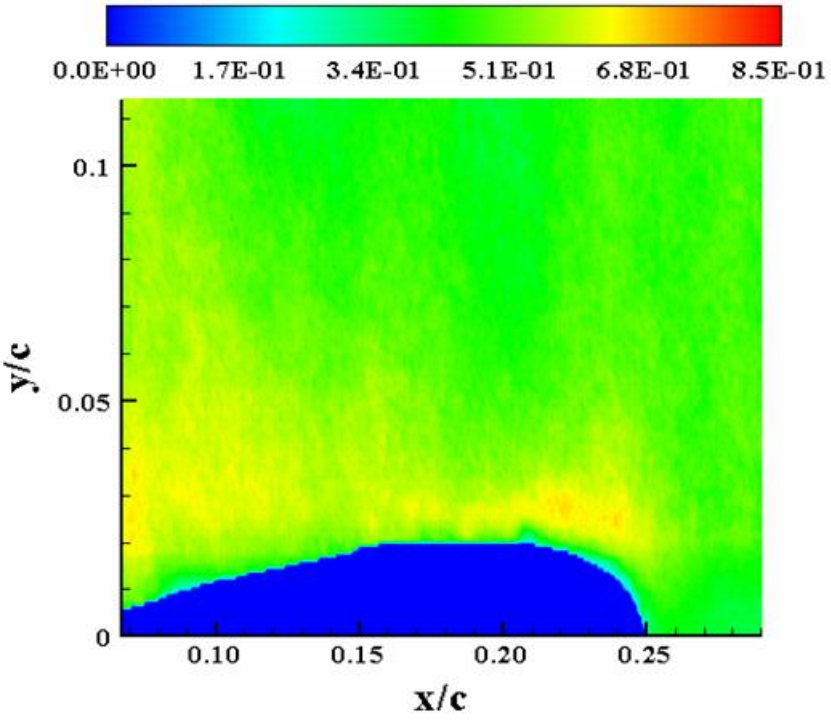

Figure C-19: $\sigma_u(M_\infty = 0.28, k = 0.1, Up, \alpha = 16^0)$

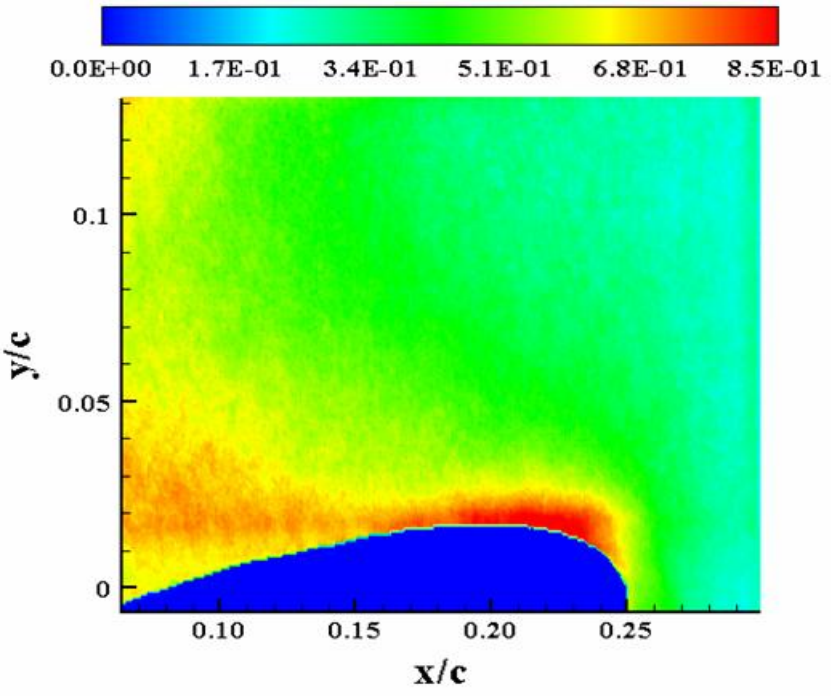

Figure C-20: $\sigma_u(M_\infty = 0.28, k = 0.1, Up, \alpha = 18^0)$

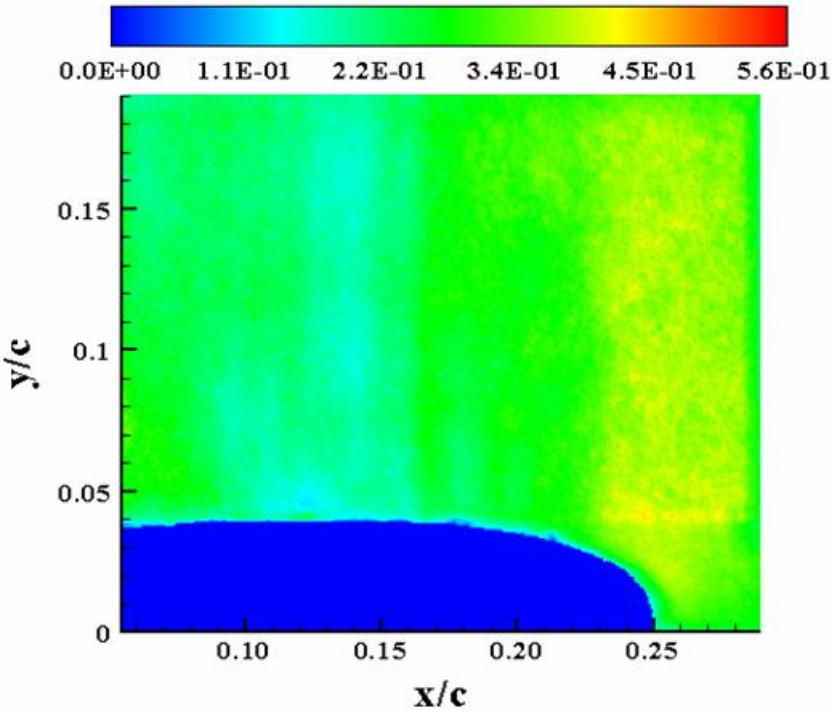

Figure C-21: $\sigma_v(M_\infty = 0.28, k = 0.1, Up, \alpha = 10^0)$

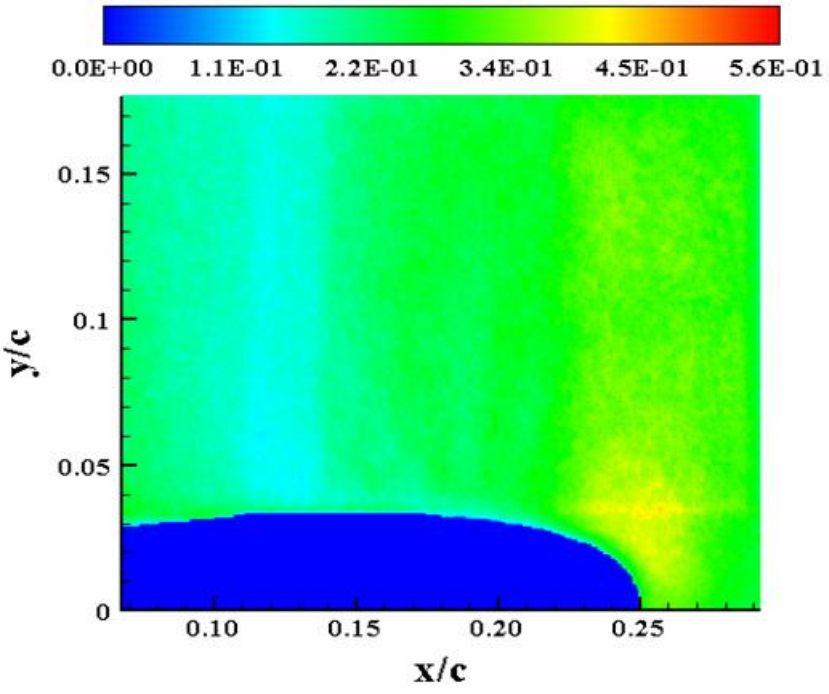

Figure C-22: $\sigma_v(M_\infty = 0.28, k = 0.1, Up, \alpha = 12^0)$

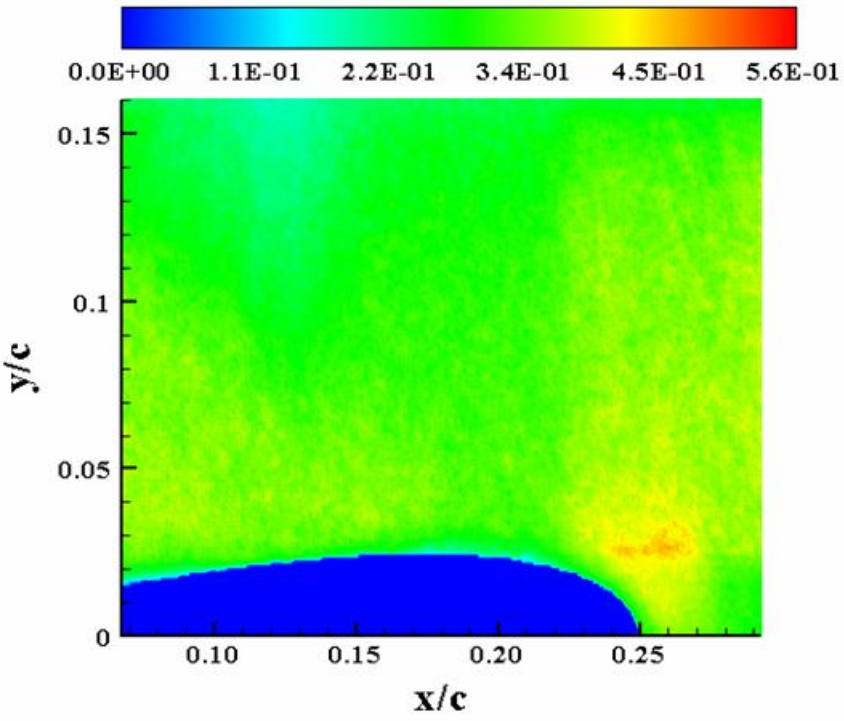

Figure C-23: $\sigma_v(M_\infty = 0.28, k = 0.1, Up, \alpha = 14^0)$

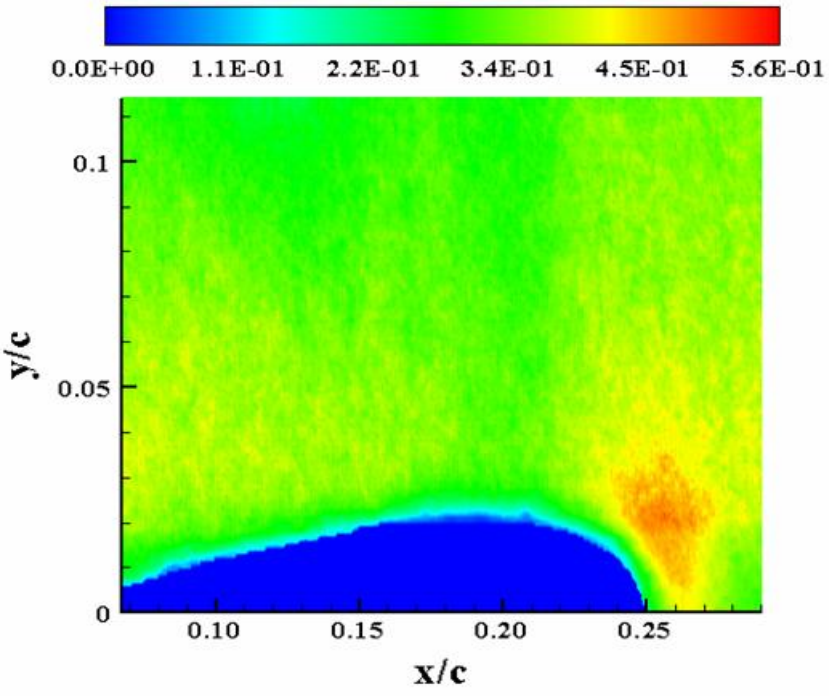

Figure C-24: $\sigma_v(M_\infty = 0.28, k = 0.1, Up, \alpha = 16^0)$

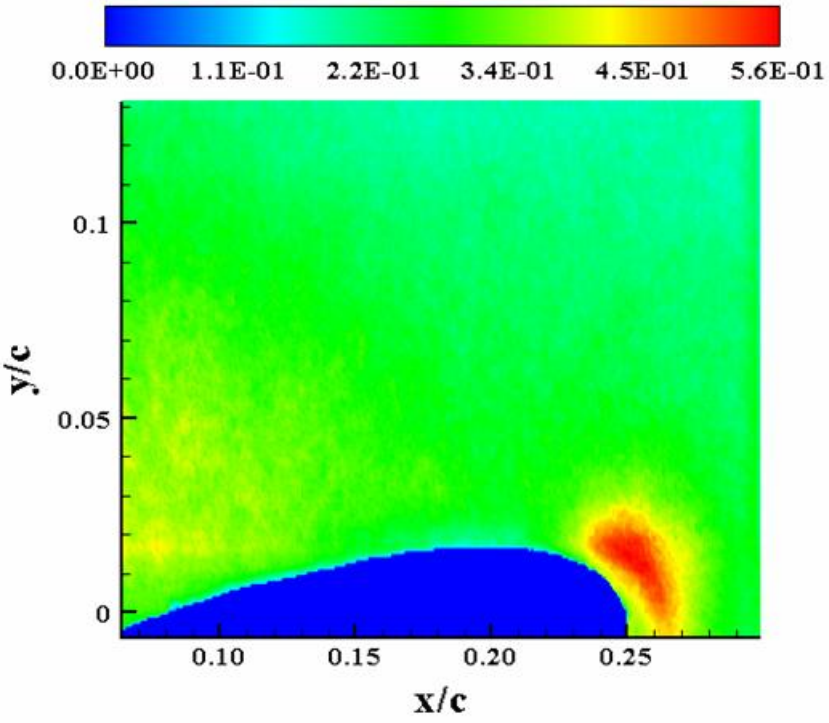

Figure C-25: $\sigma_v(M_\infty = 0.28, k = 0.1, Up, \alpha = 18^0)$

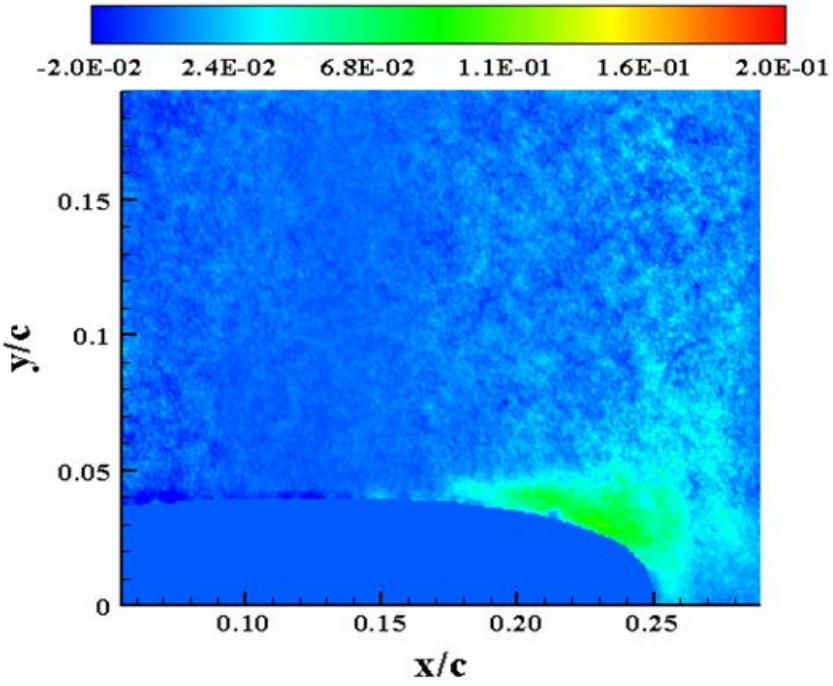

Figure C-26: $\tau_{xy}(M_\infty = 0.28, k = 0.1, Up, \alpha = 10^0)$

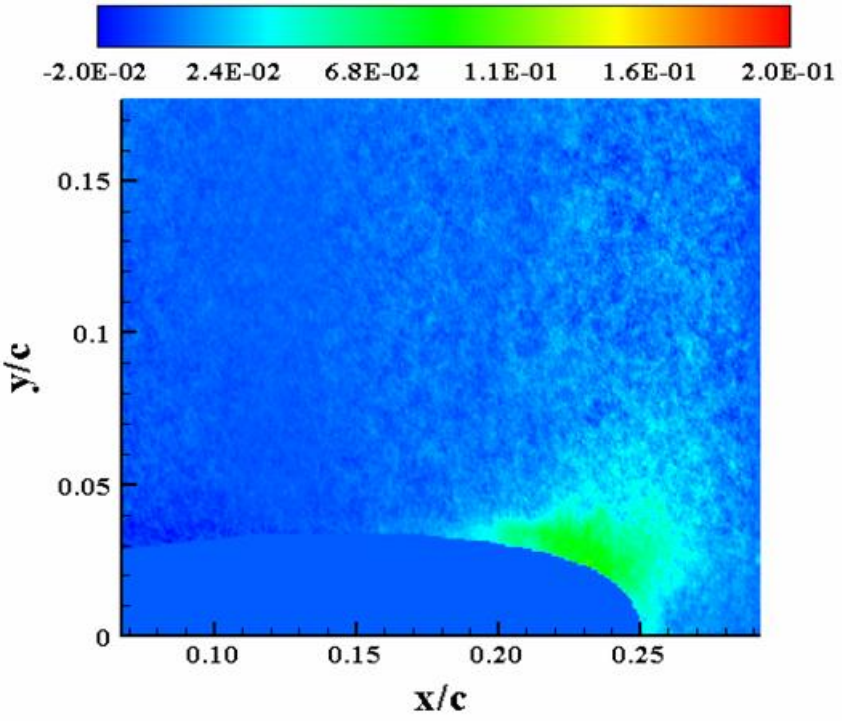

Figure C-27: $\tau_{xy}(M_\infty = 0.28, k = 0.1, Up, \alpha = 12^0)$

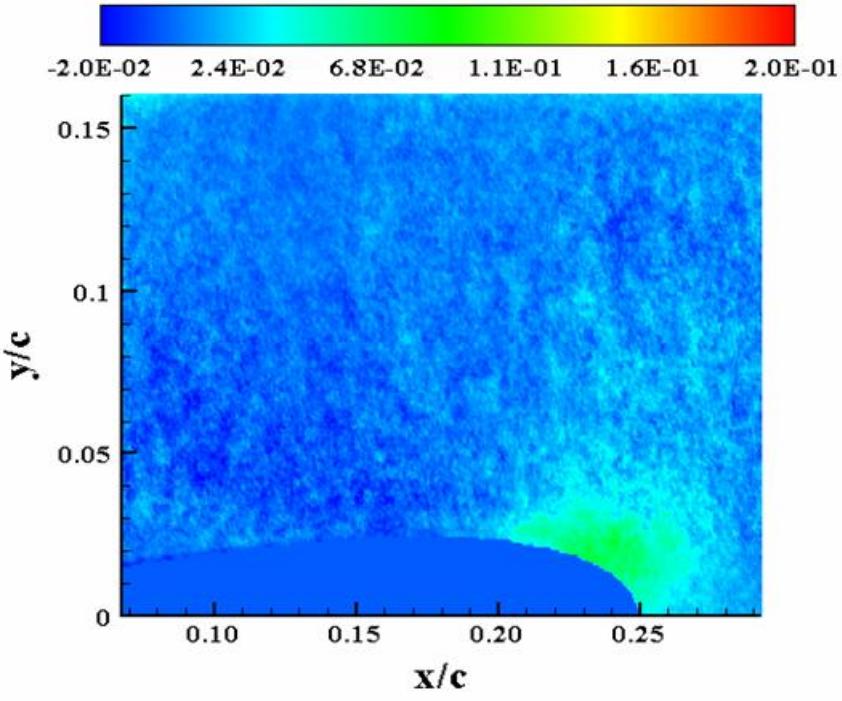

Figure C-28: $\tau_{xy}(M_\infty = 0.28, k = 0.1, Up, \alpha = 14^0)$

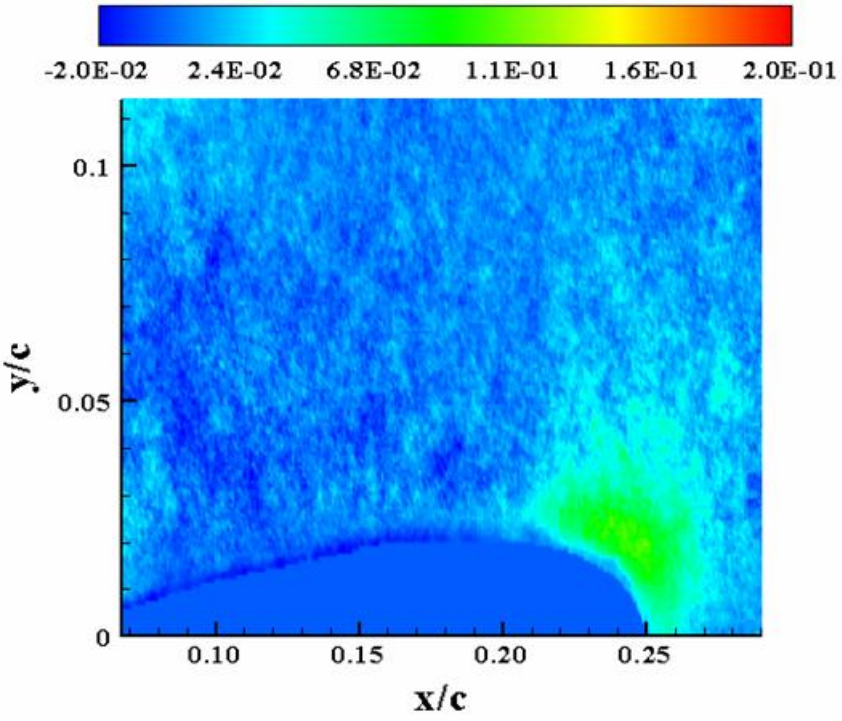

Figure C-29: $\tau_{xy}(M_\infty = 0.28, k = 0.1, Up, \alpha = 16^0)$

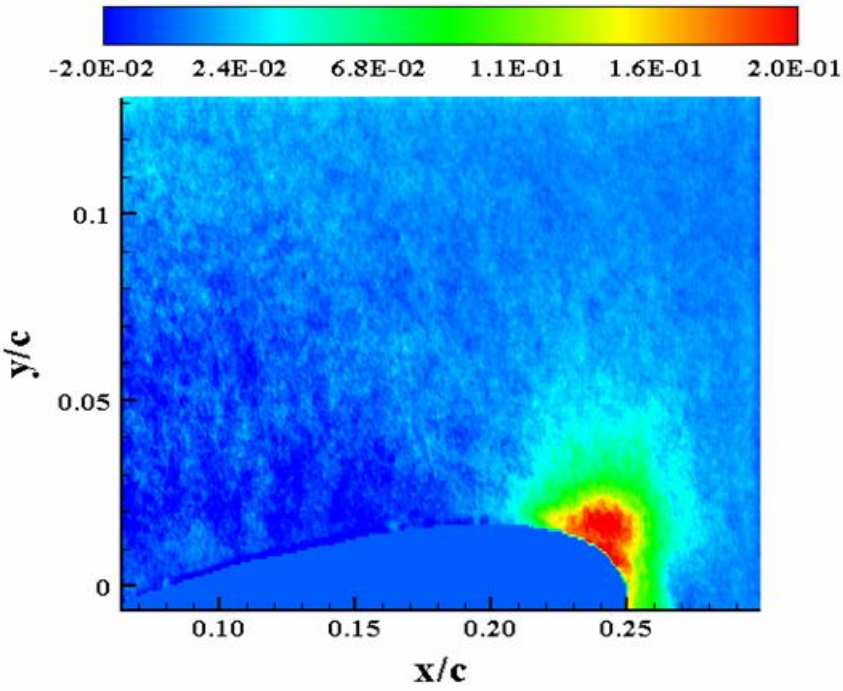

Figure C-30: $\tau_{xy}(M_\infty = 0.28, k = 0.1, Up, \alpha = 18^0)$

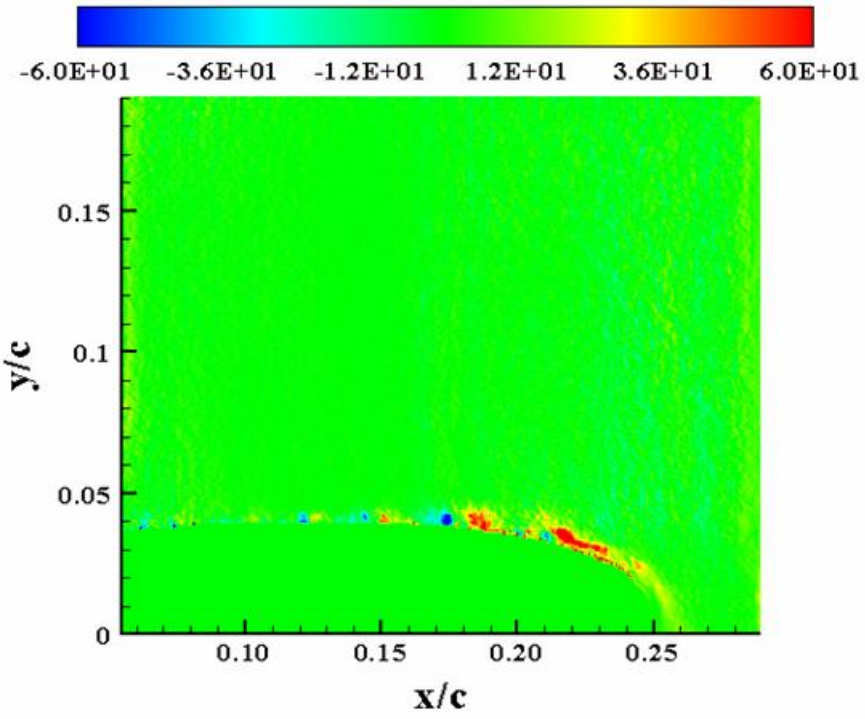

Figure C-31: $P_{xx}(M_\infty = 0.28, k = 0.1, Up, \alpha = 10^0)$

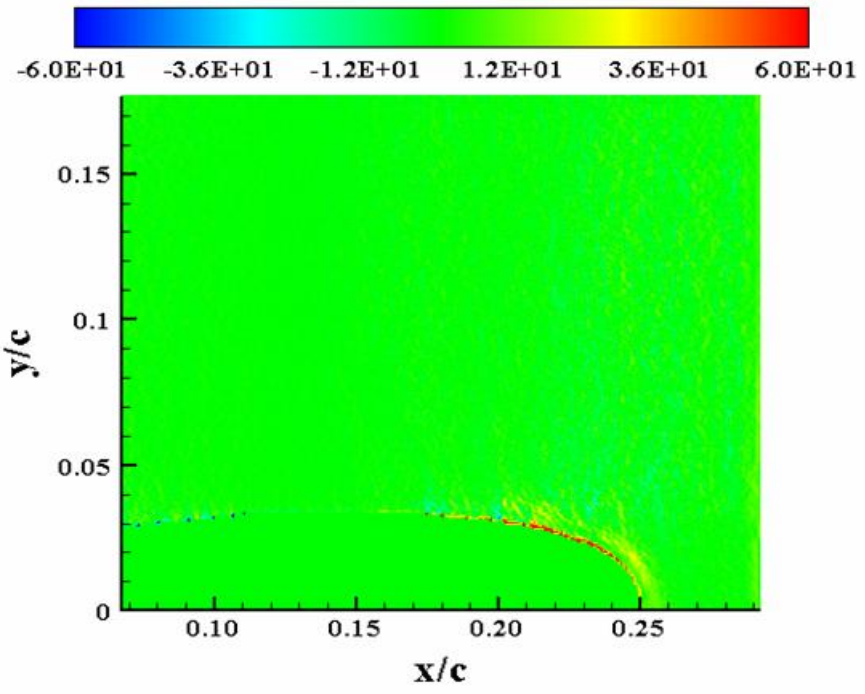

Figure C-32: $P_{xx}(M_\infty = 0.28, k = 0.1, Up, \alpha = 12^0)$

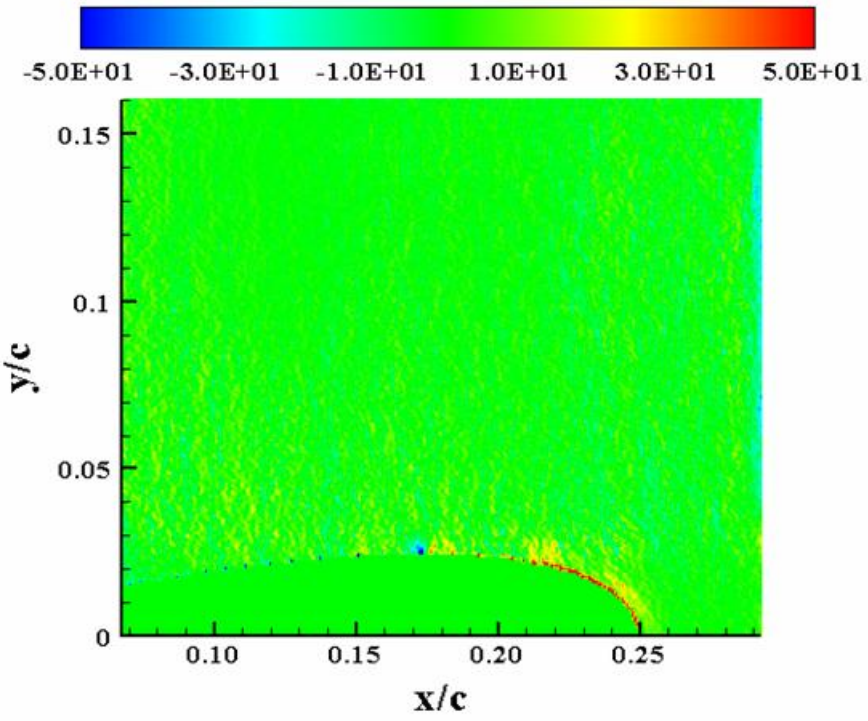

Figure C-33: $P_{xx}(M_\infty = 0.28, k = 0.1, Up, \alpha = 14^0)$

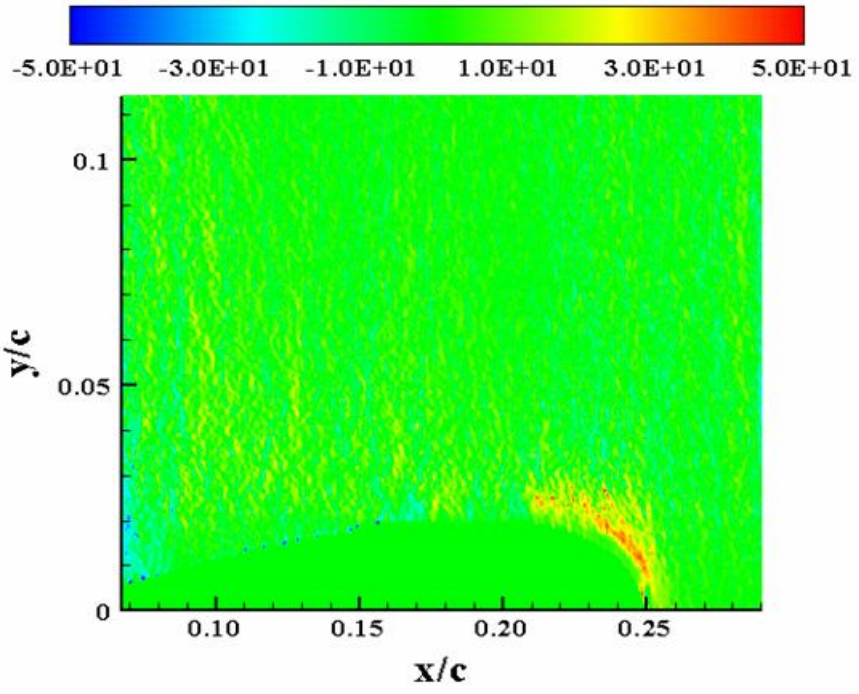

Figure C-34: $P_{xx}(M_\infty = 0.28, k = 0.1, Up, \alpha = 16^0)$

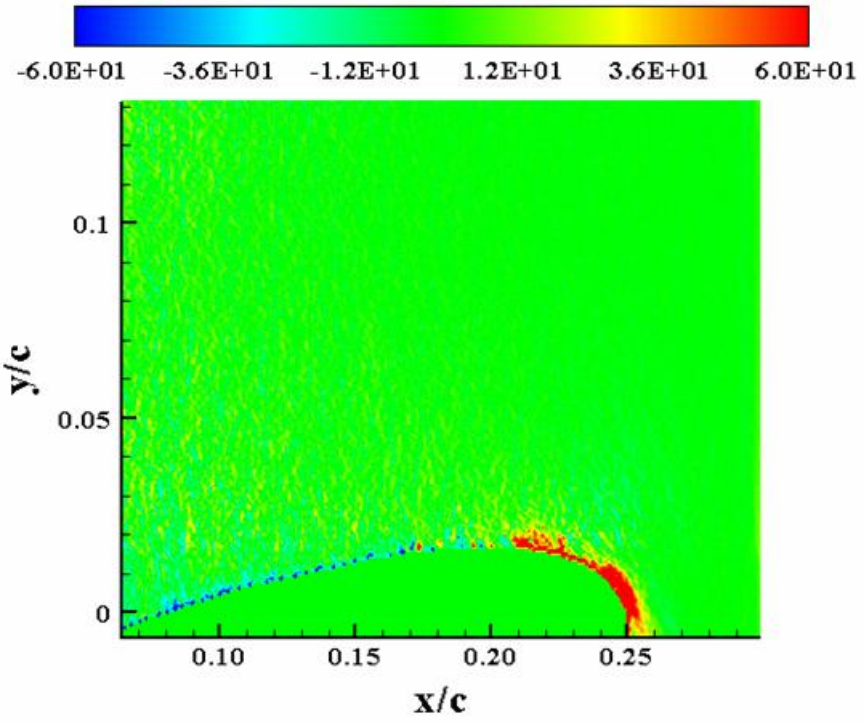

Figure C-35: $P_{xx}(M_\infty = 0.28, k = 0.1, Up, \alpha = 18^0)$

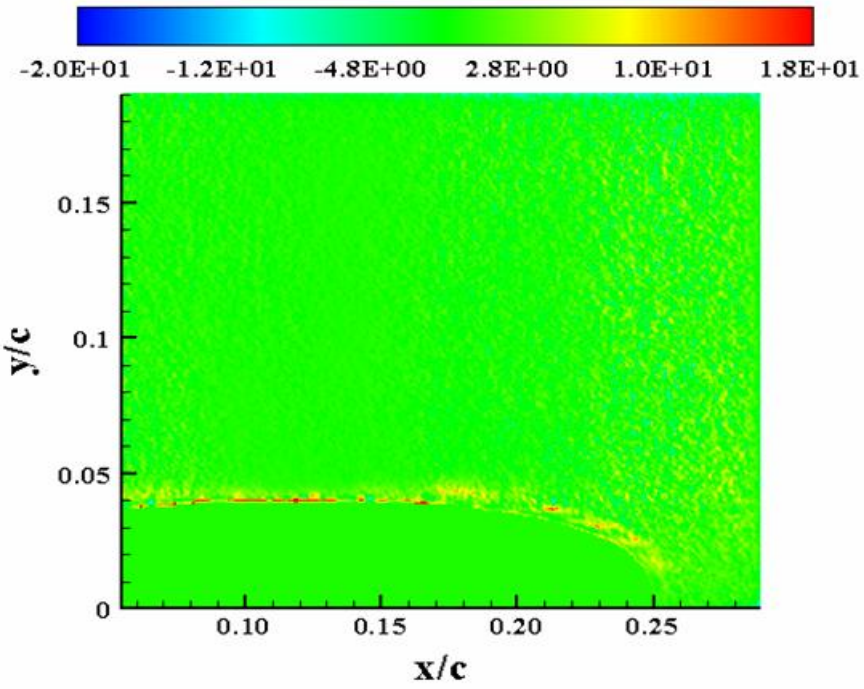

Figure C-36: $P_{xy}(M_\infty = 0.28, k = 0.1, Up, \alpha = 10^0)$

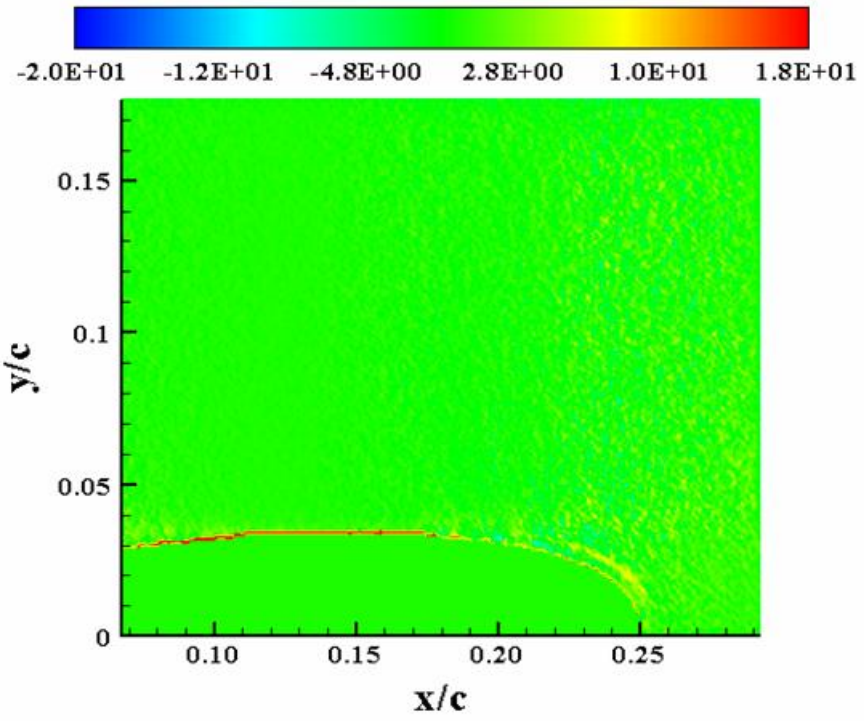

Figure C-37: $P_{xy}(M_\infty = 0.28, k = 0.1, Up, \alpha = 12^0)$

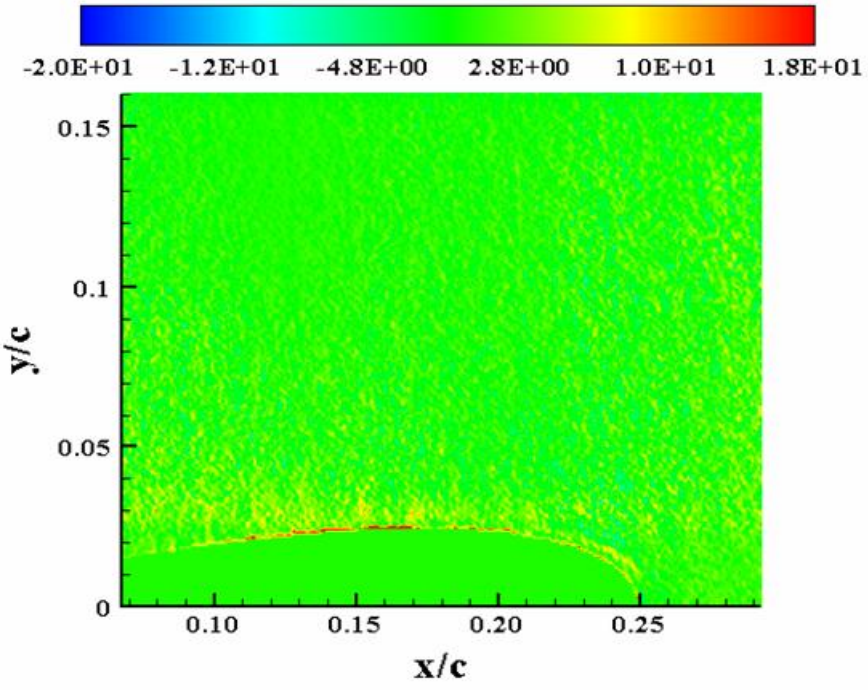

Figure C-38: $P_{xy}(M_\infty = 0.28, k = 0.1, Up, \alpha = 14^0)$

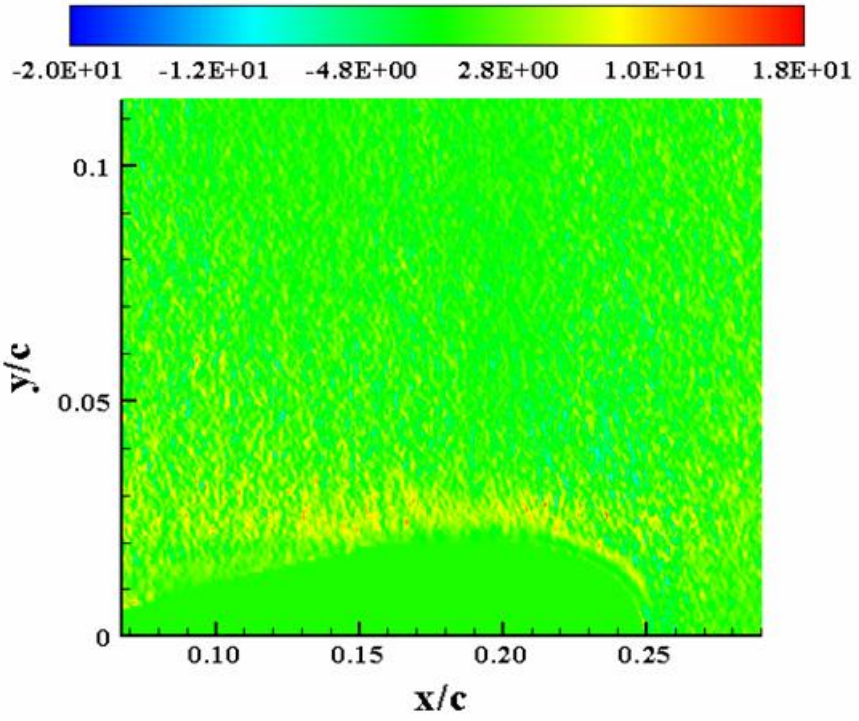

Figure C-39: $P_{xy}(M_\infty = 0.28, k = 0.1, Up, \alpha = 16^0)$

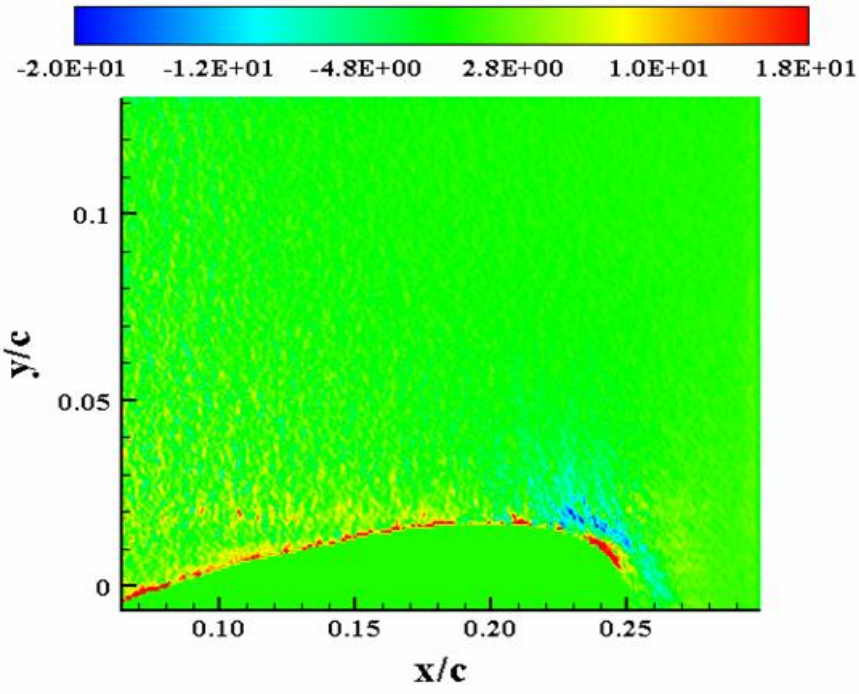

Figure C-40: $P_{xy}(M_\infty = 0.28, k = 0.1, Up, \alpha = 18^0)$

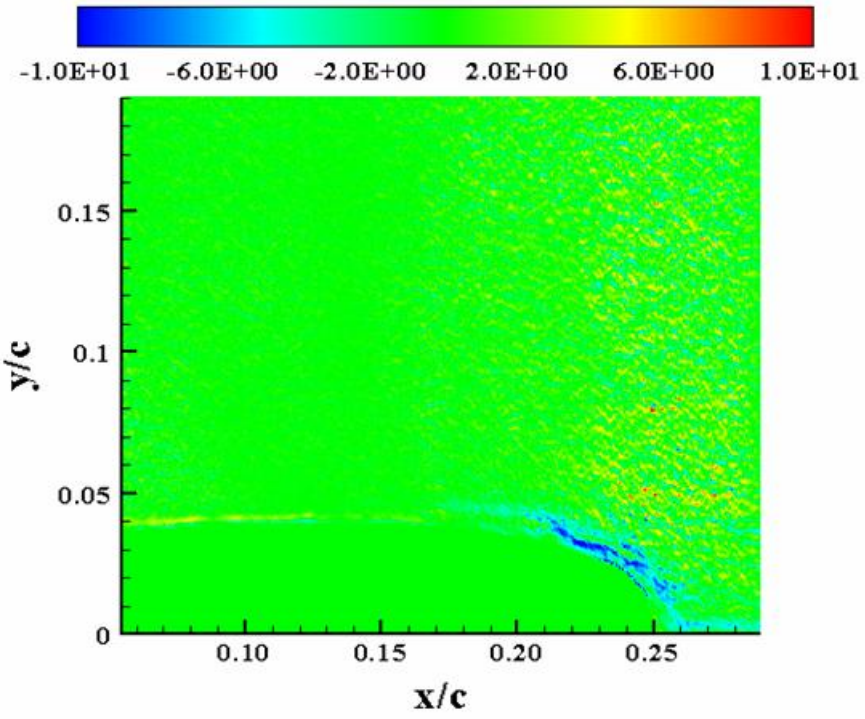

Figure C-41: $P_{yy}(M_\infty = 0.28, k = 0.1, Up, \alpha = 10^0)$

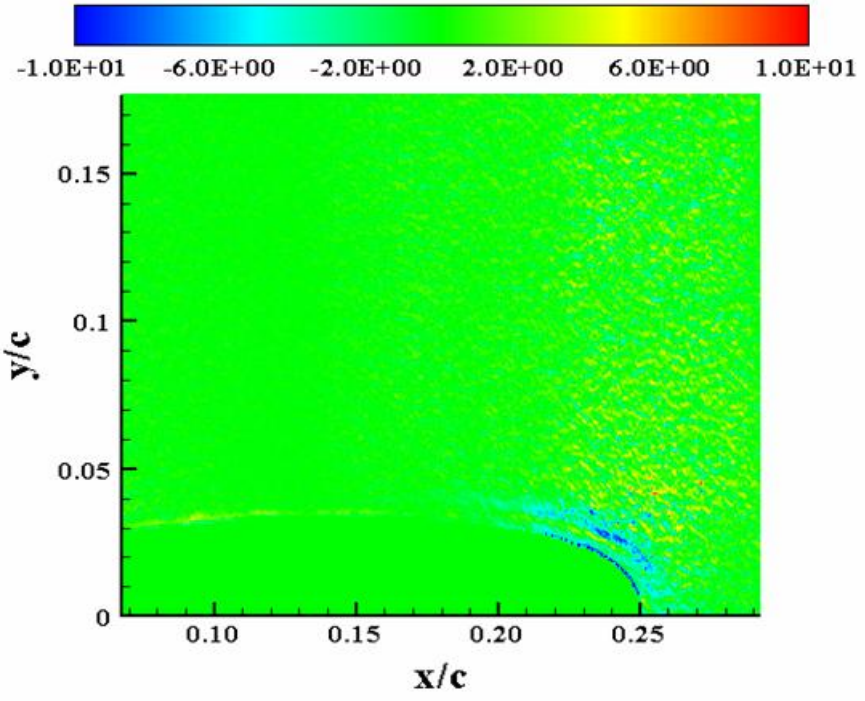

Figure C-42: $P_{yy}(M_\infty = 0.28, k = 0.1, Up, \alpha = 12^0)$

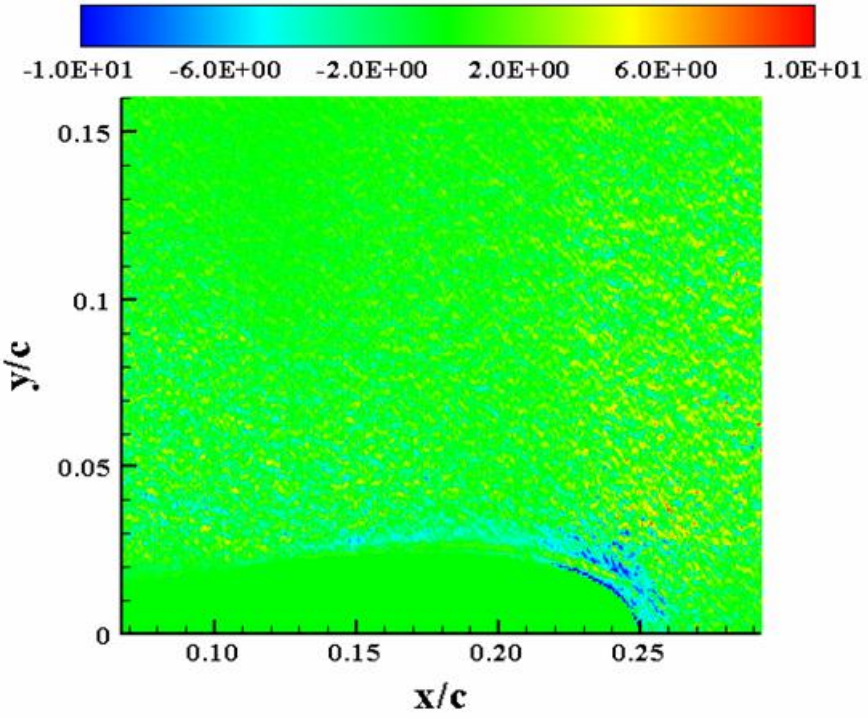

Figure C-43: $P_{yy}(M_\infty = 0.28, k = 0.1, Up, \alpha = 14^0)$

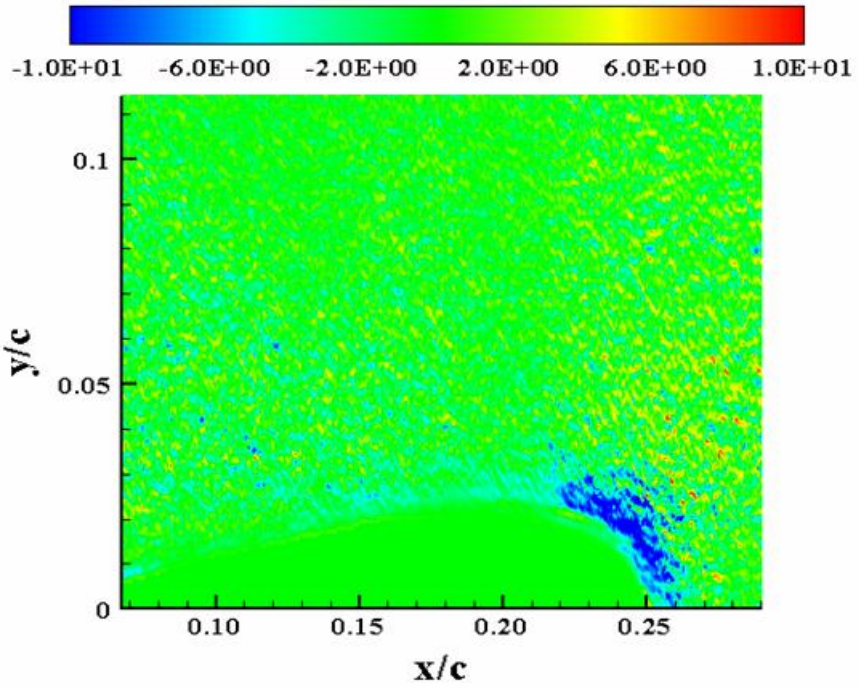

Figure C-44: $P_{yy}(M_\infty = 0.28, k = 0.1, Up, \alpha = 16^0)$

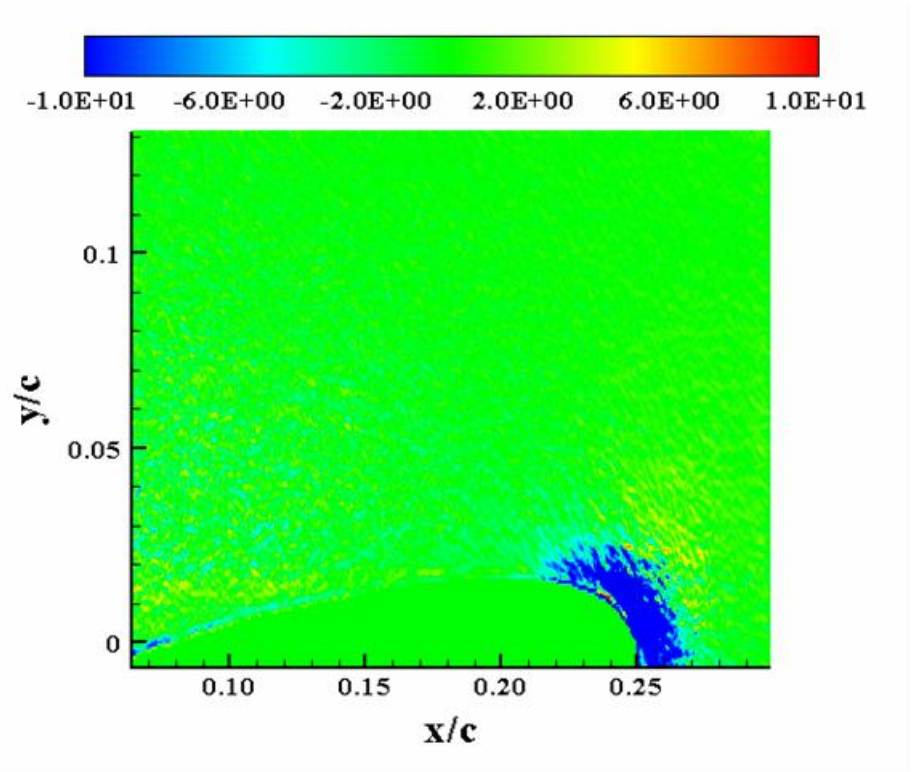

Figure C-45: $P_{yy}(M_\infty = 0.28, k = 0.1, Up, \alpha = 18^0)$

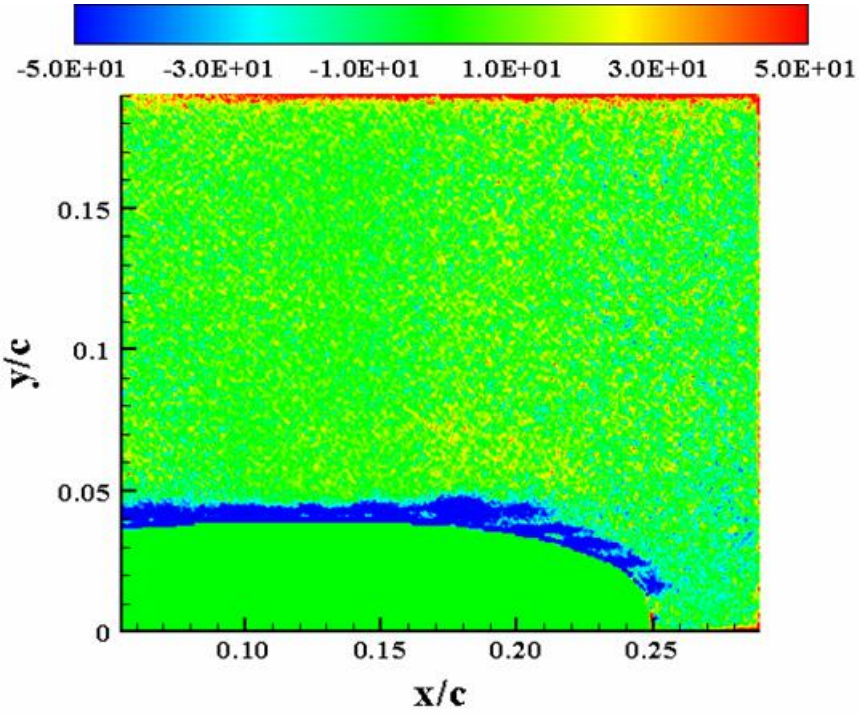

Figure C-46: $S_{xy}(M_\infty = 0.28, k = 0.1, Up, \alpha = 10^0)$

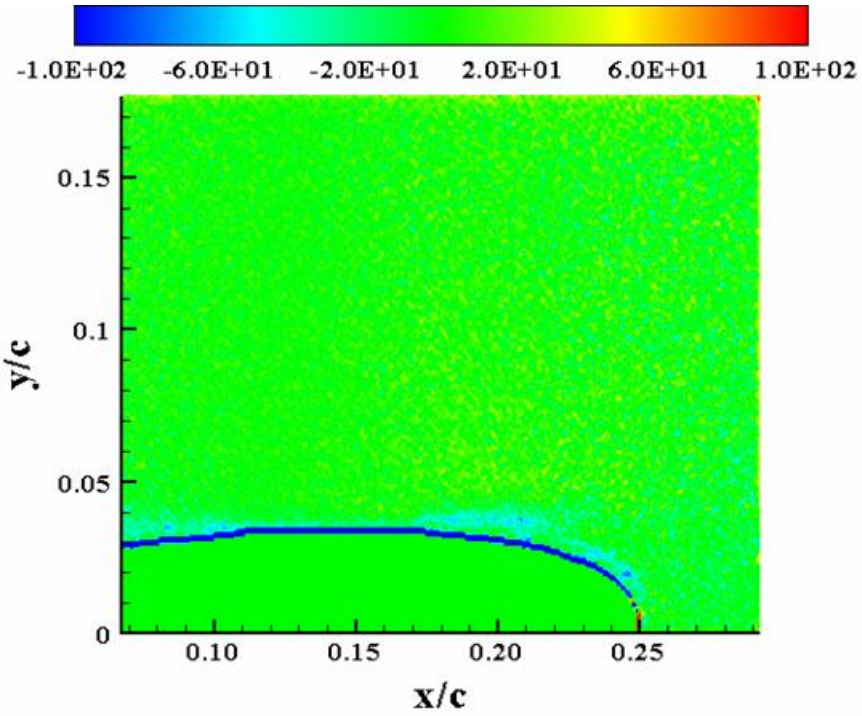

Figure C-47: $S_{xy}(M_\infty = 0.28, k = 0.1, Up, \alpha = 12^0)$

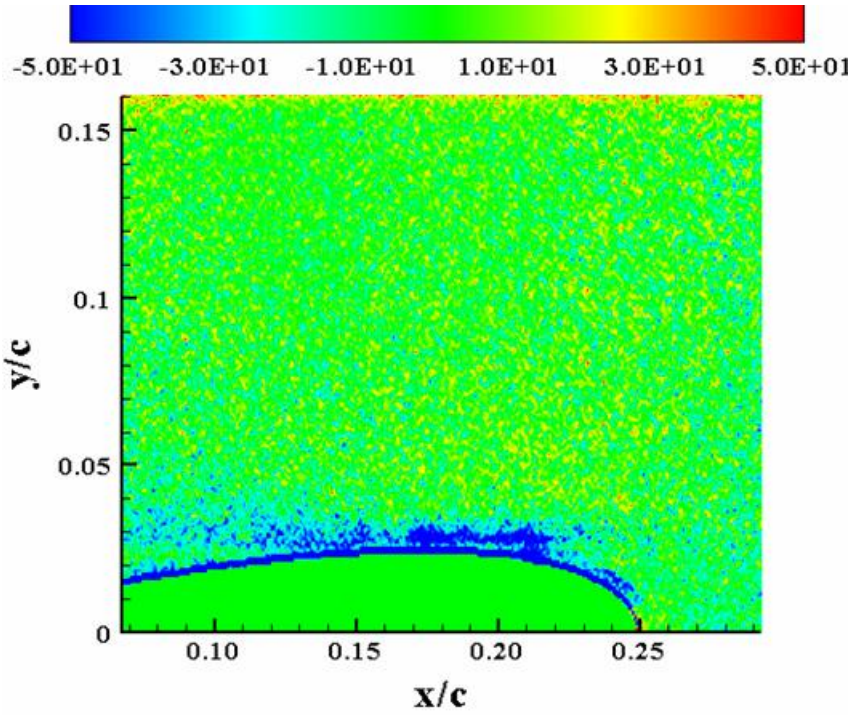

Figure C-48: $S_{xy}(M_\infty = 0.28, k = 0.1, Up, \alpha = 14^0)$

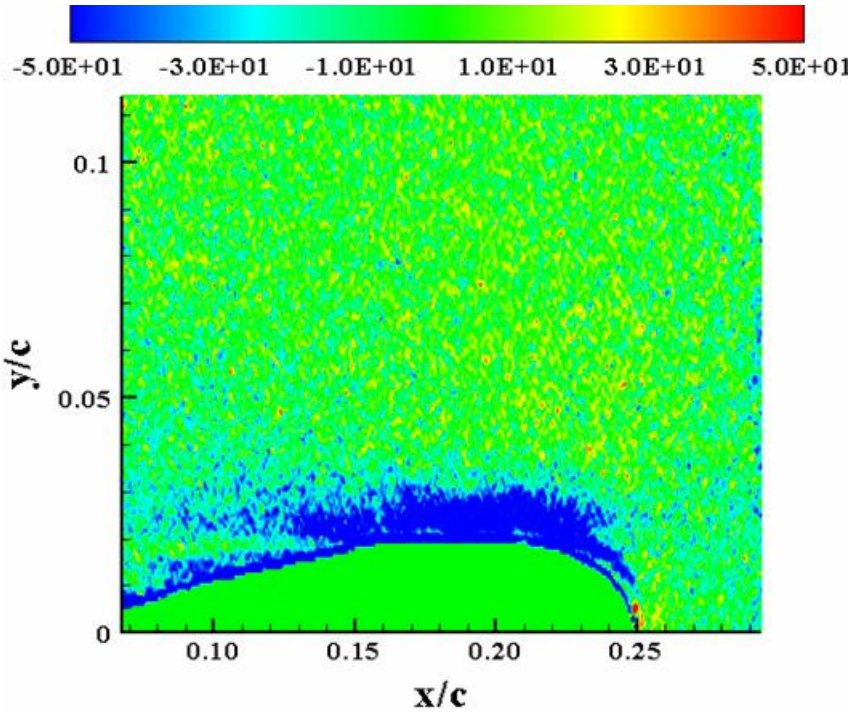

Figure C-49: $S_{xy}(M_\infty = 0.28, k = 0.1, Up, \alpha = 16^0)$

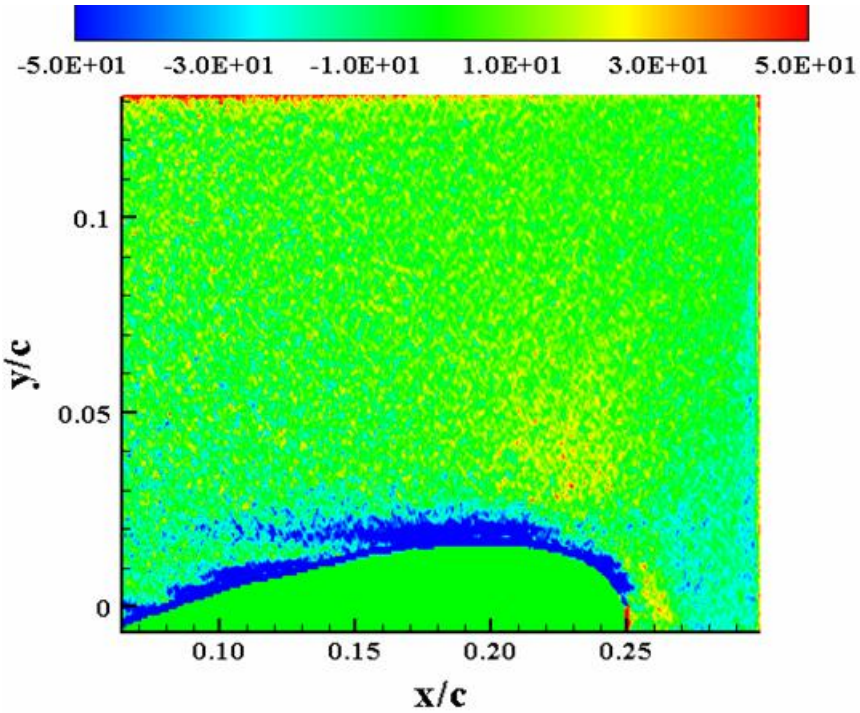

Figure C-50: $S_{xy}(M_\infty = 0.28, k = 0.1, Up, \alpha = 18^0)$

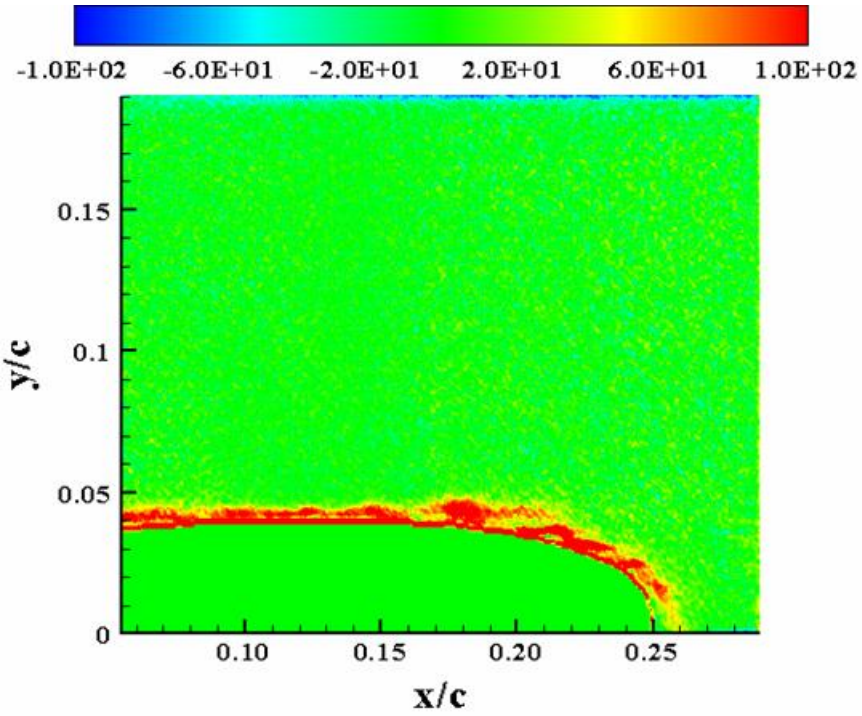

Figure C-51: $\omega_z(M_\infty = 0.28, k = 0.1, Up, \alpha = 10^0)$

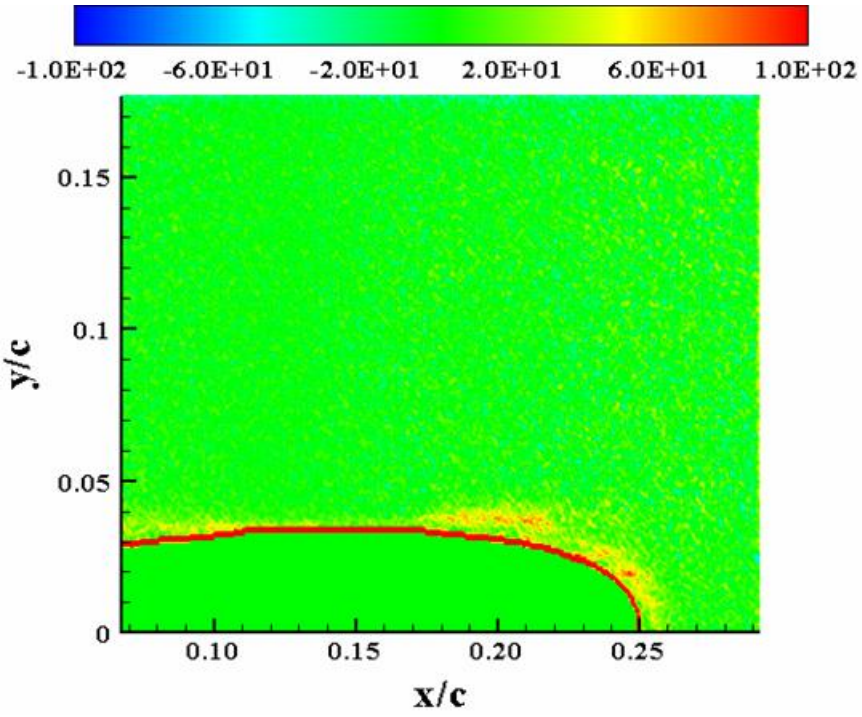

Figure C-52: $\omega_z(M_\infty = 0.28, k = 0.1, Up, \alpha = 12^0)$

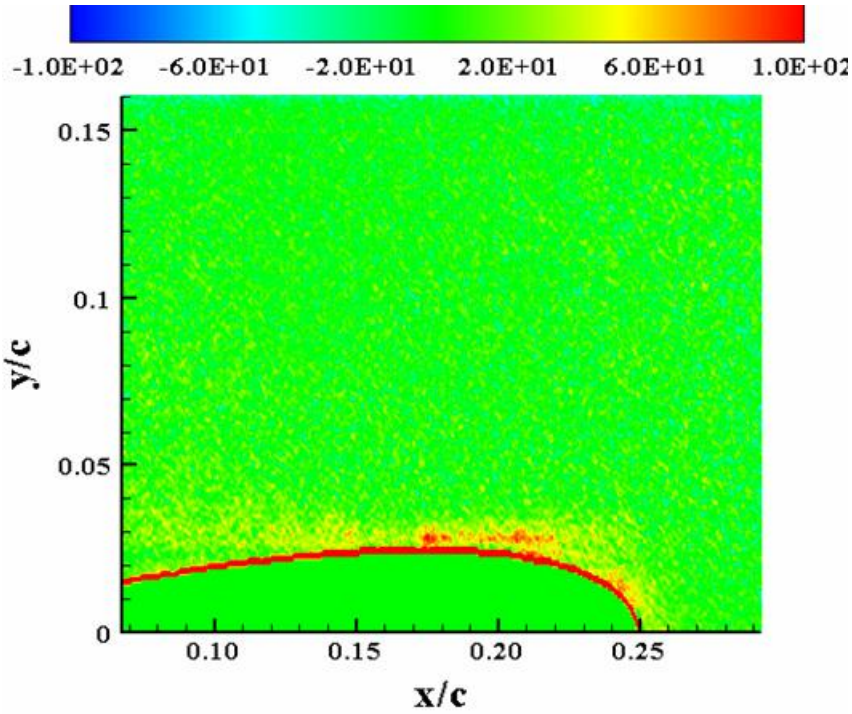

Figure C-53: $\omega_z(M_\infty = 0.28, k = 0.1, Up, \alpha = 14^0)$

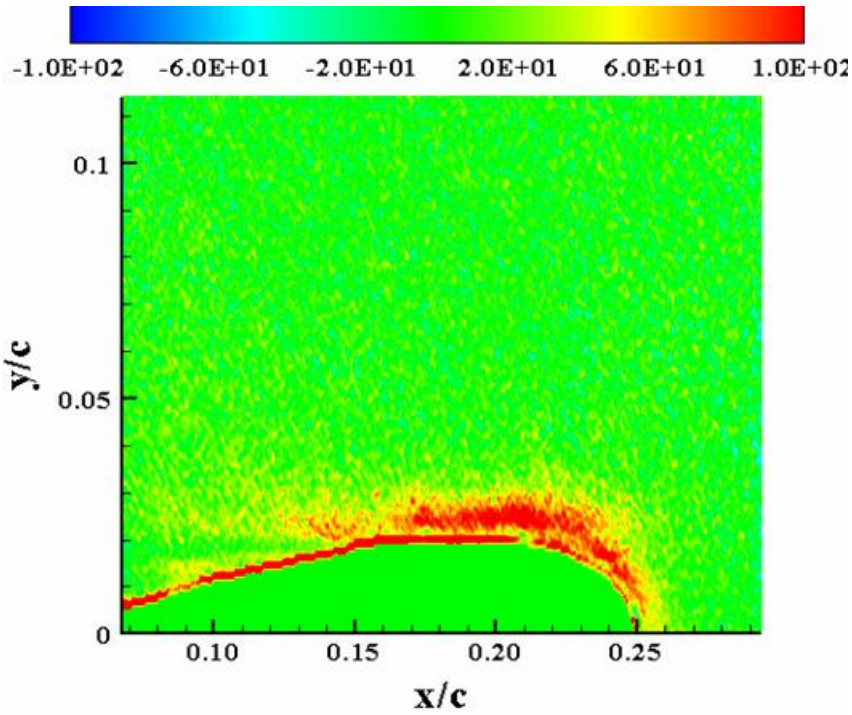

Figure C-54: $\omega_z(M_\infty = 0.28, k = 0.1, Up, \alpha = 16^0)$

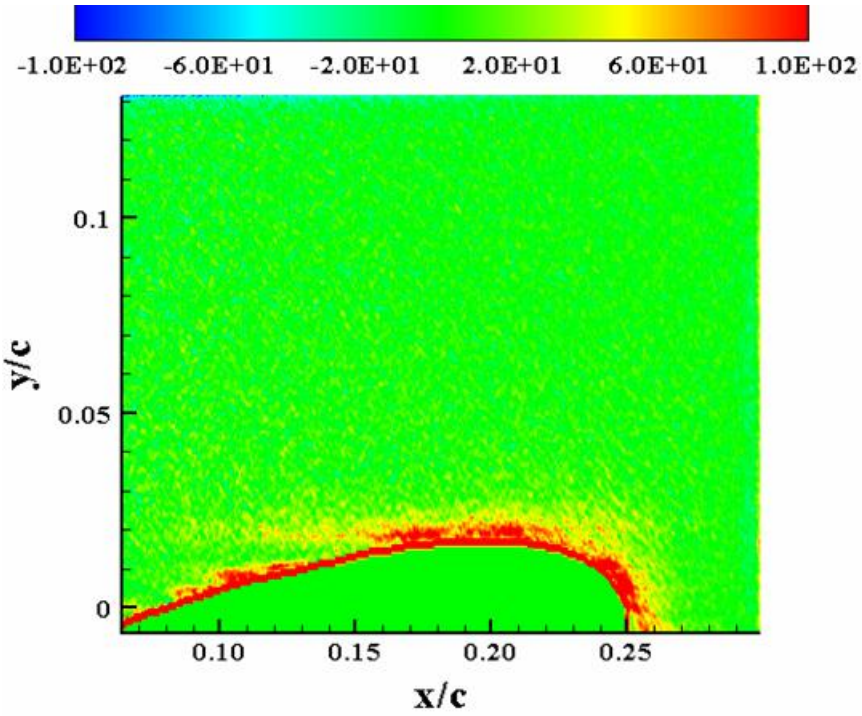

Figure C-55: $\omega_z(M_\infty = 0.28, k = 0.1, Up, \alpha = 18^0)$

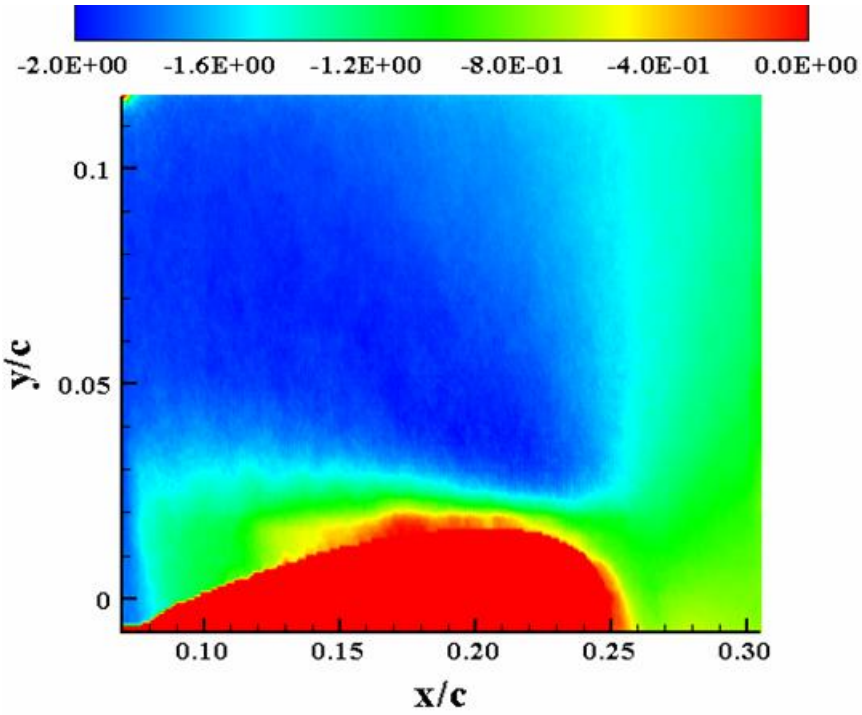

Figure C-56: $U_N(M_\infty = 0.28, k = 0.1, Down, \alpha = 18^0)$

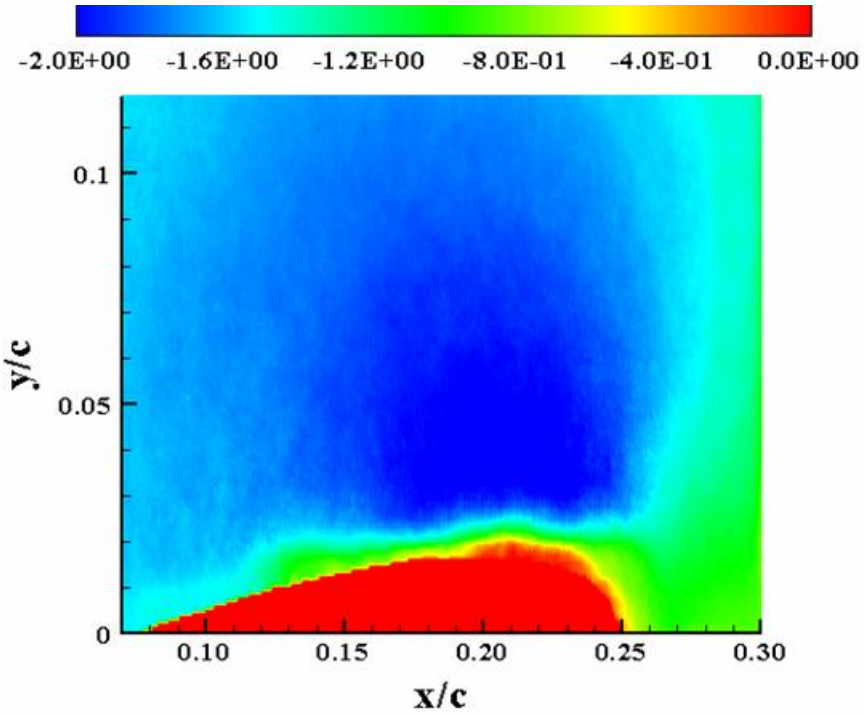

Figure C-57: $U_N(M_\infty = 0.28, k = 0.1, Down, \alpha = 16^0)$

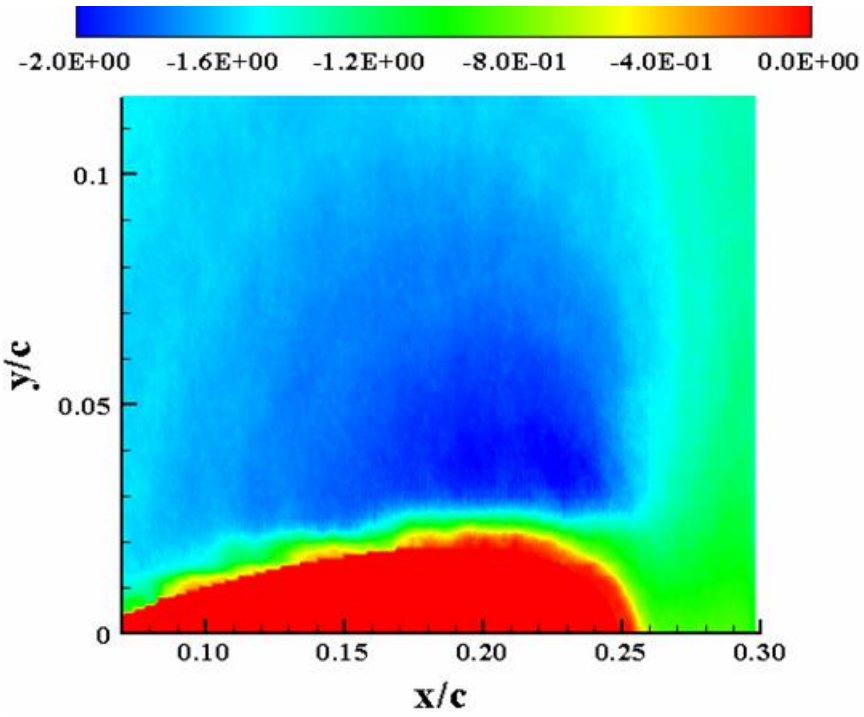

Figure C-58: $U_N(M_\infty = 0.28, k = 0.1, Down, \alpha = 14^0)$

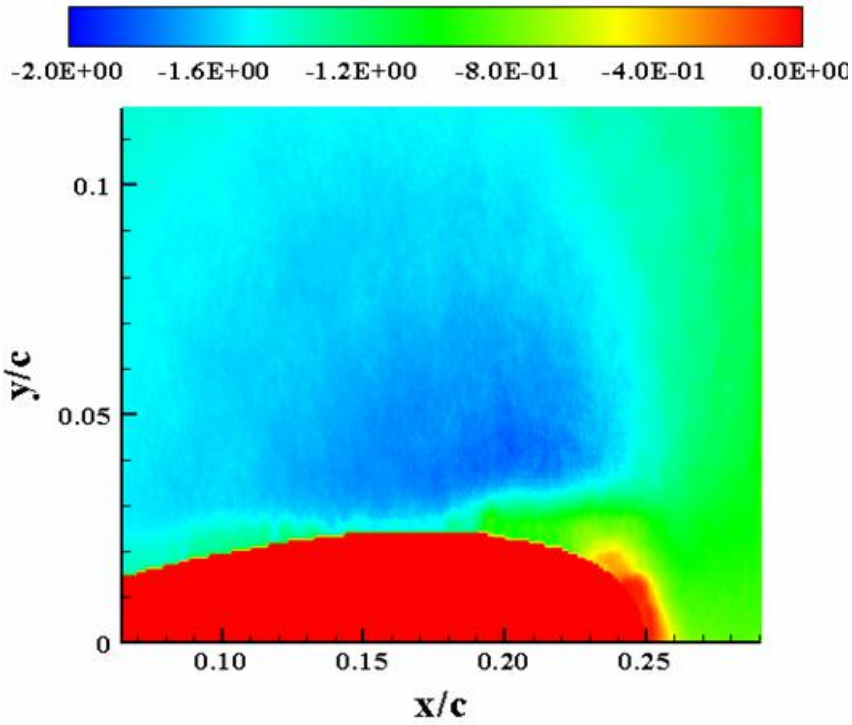

Figure C-59: $U_N(M_\infty = 0.28, k = 0.1, Down, \alpha = 12^0)$

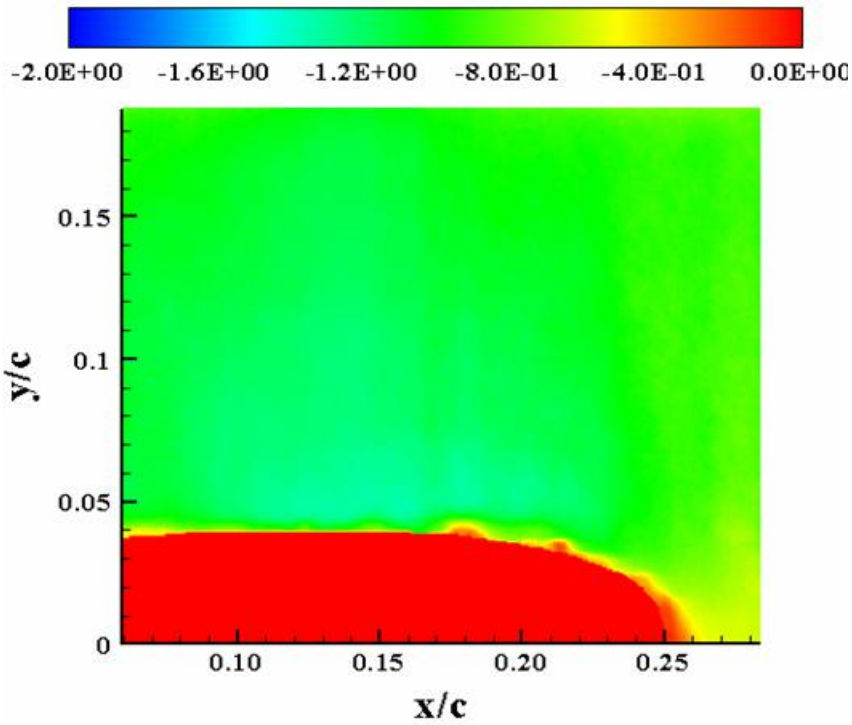

Figure C-60: $U_N(M_\infty = 0.28, k = 0.1, Down, \alpha = 10^0)$

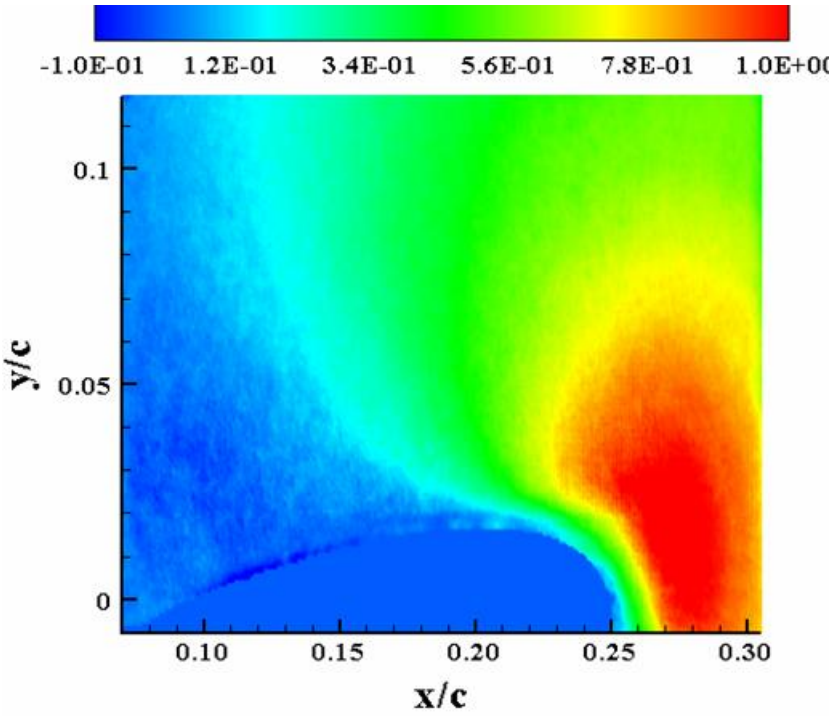

Figure C-61: $V_N\,(M_\infty = 0.28, k = 0.1, Down, \alpha = 18^0)$

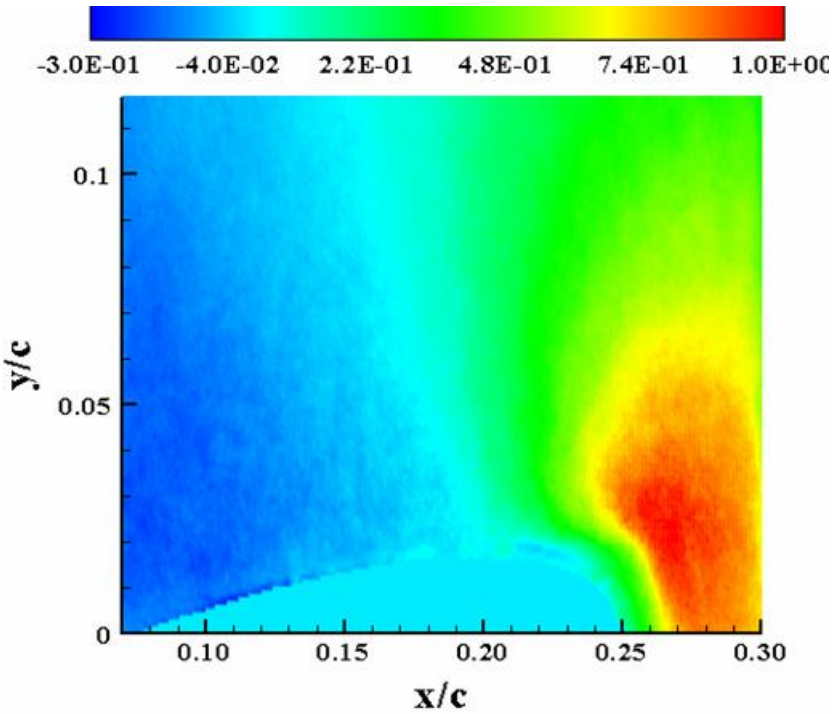

Figure C-62: $V_N\,(M_\infty = 0.28, k = 0.1, Down, \alpha = 16^0)$

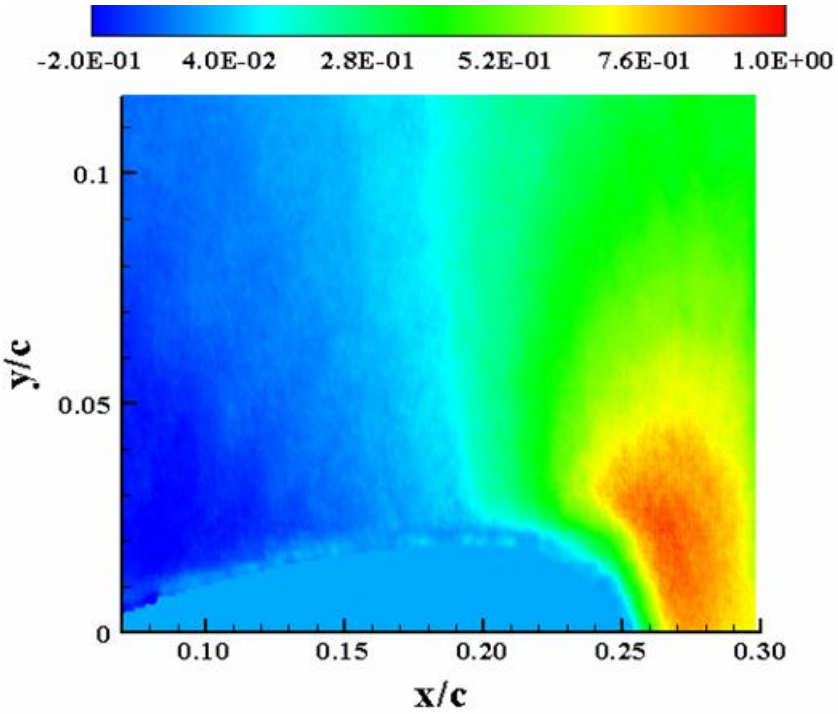

Figure C-63: $V_N\,(M_\infty = 0.28, k = 0.1, Down, \alpha = 14^0)$

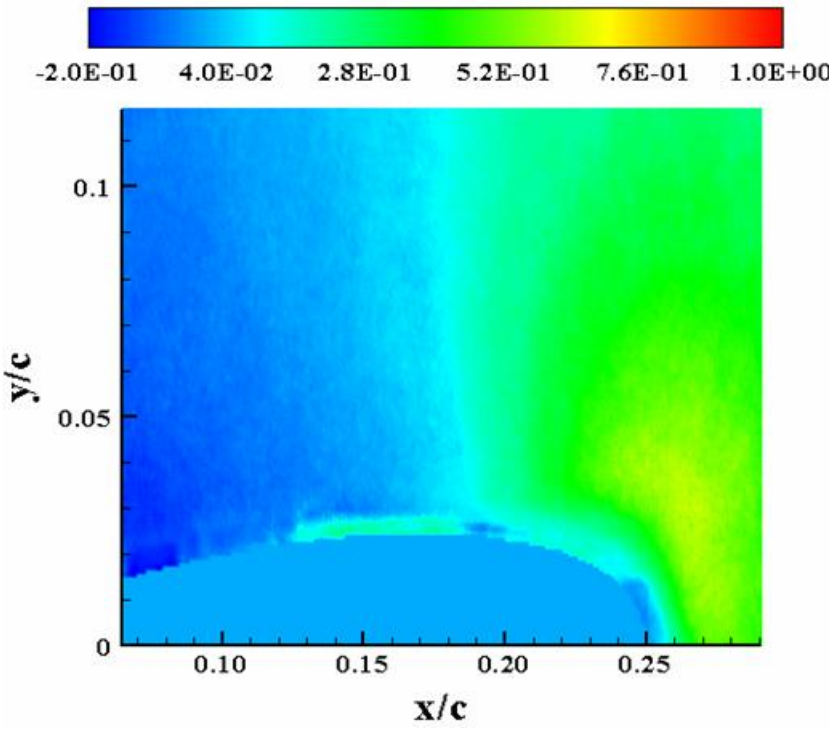

Figure C-64: $V_N\,(M_\infty = 0.28, k = 0.1, Down, \alpha = 12^0)$

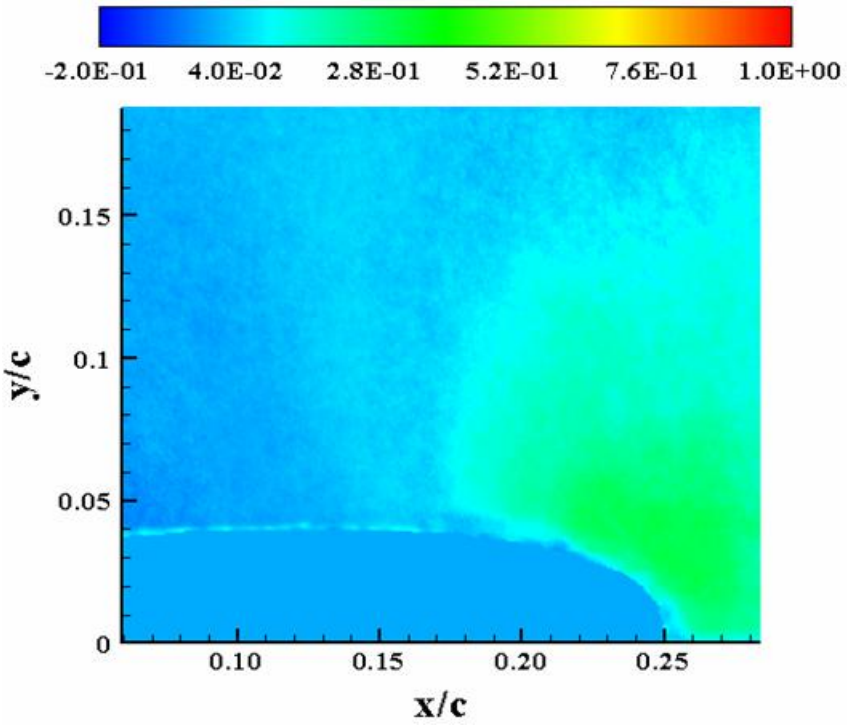

Figure C-65: $V_N\,(M_\infty = 0.28, k = 0.1, Down, \alpha = 10^0)$

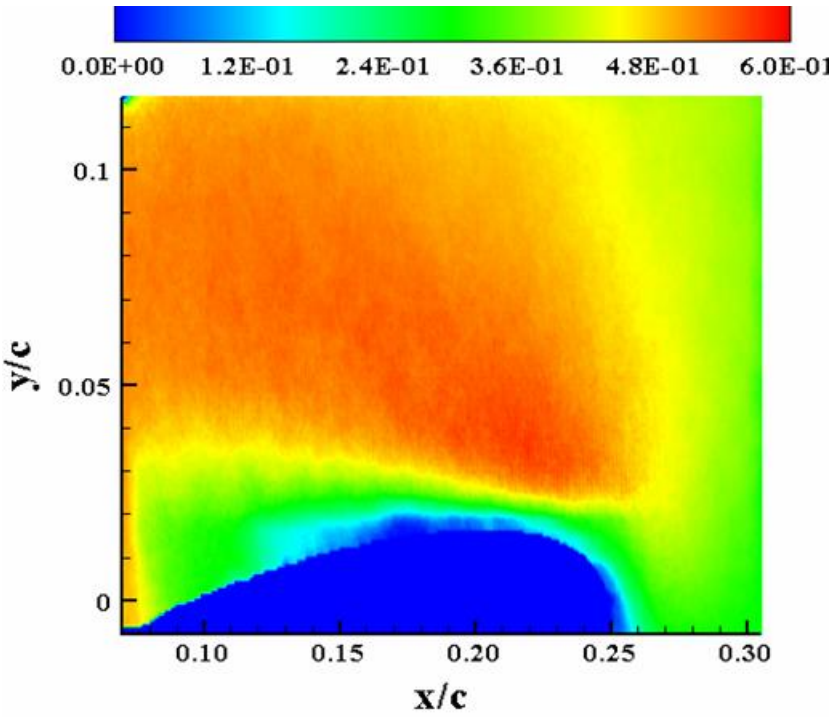

Figure C-66: $M\,(M_\infty = 0.28, k = 0.1, Down, \alpha = 18^0)$

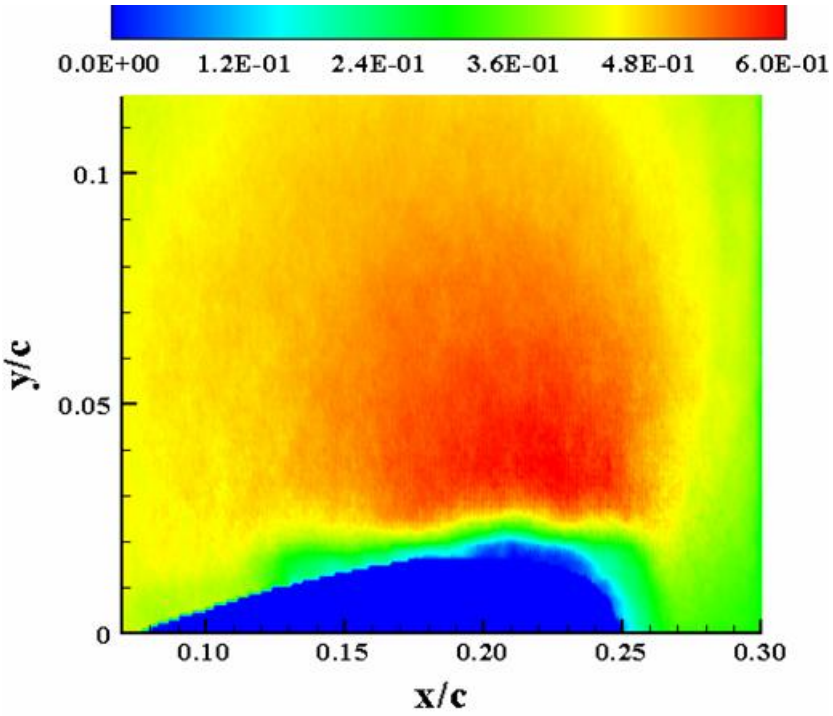

Figure C-67: $M(M_\infty = 0.28, k = 0.1, Down, \alpha = 16^0)$

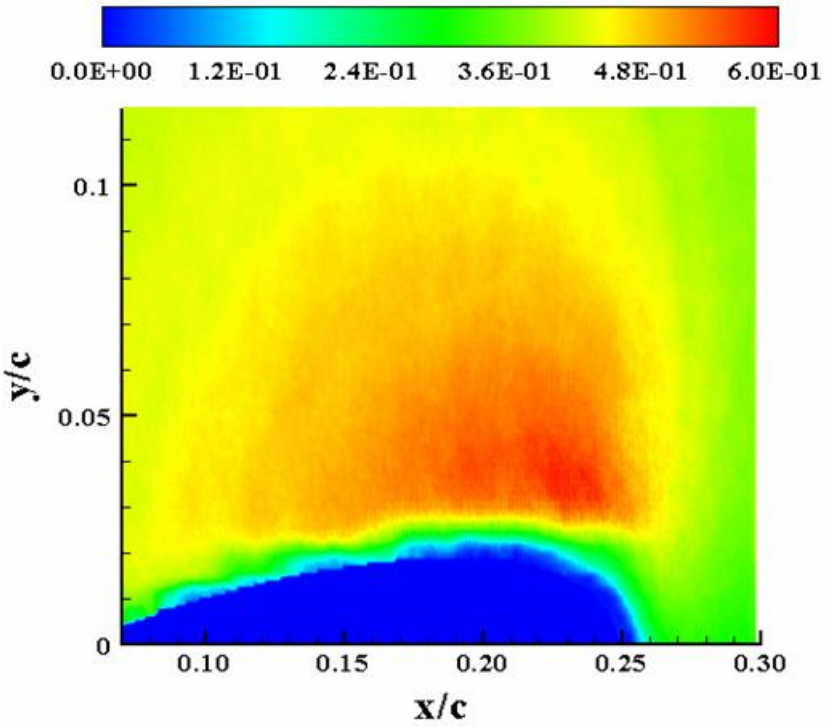

Figure C-68: $M(M_\infty = 0.28, k = 0.1, Down, \alpha = 14^0)$

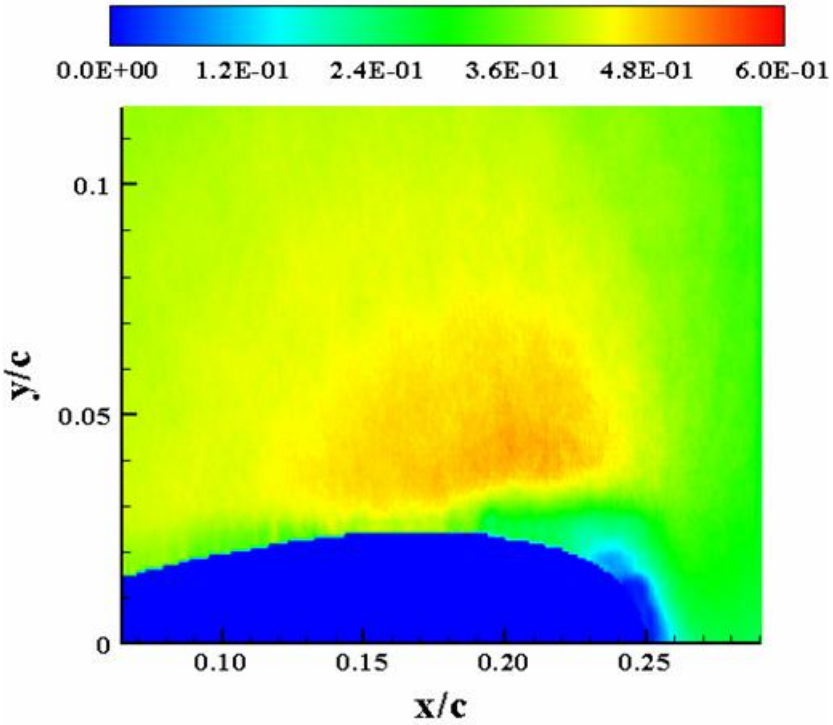

Figure C-69: $M(M_\infty = 0.28, k = 0.1, Down, \alpha = 12^0)$

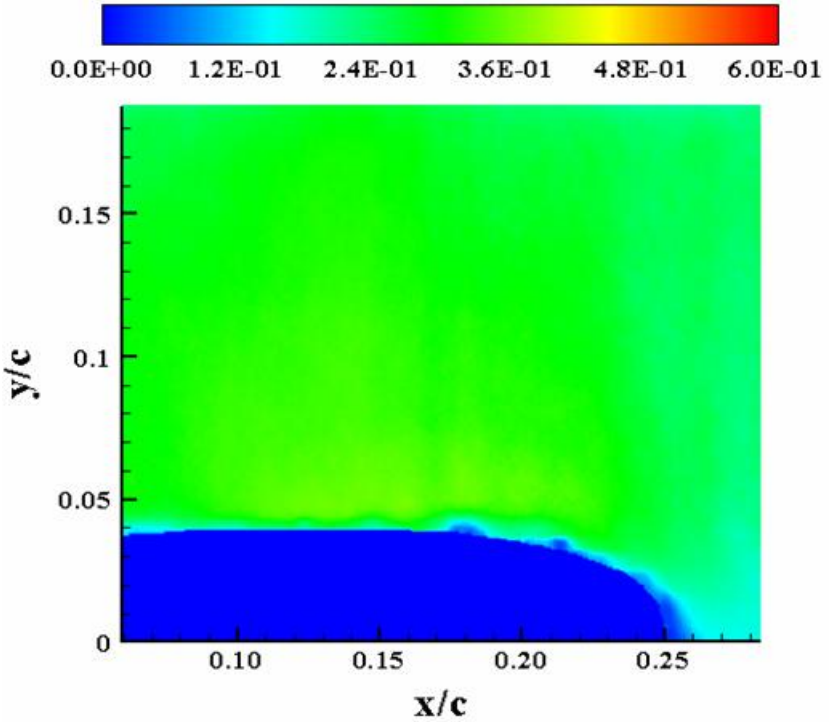

Figure C-70: $M(M_\infty = 0.28, k = 0.1, Down, \alpha = 10^0)$

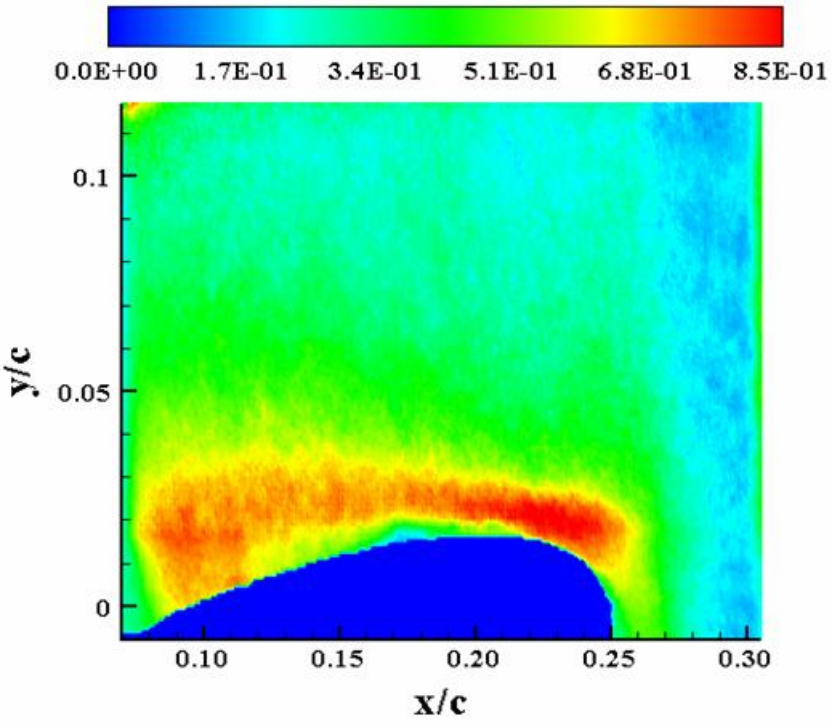

Figure C-71: $\sigma_u(M_\infty = 0.28, k = 0.1, Down, \alpha = 18^0)$

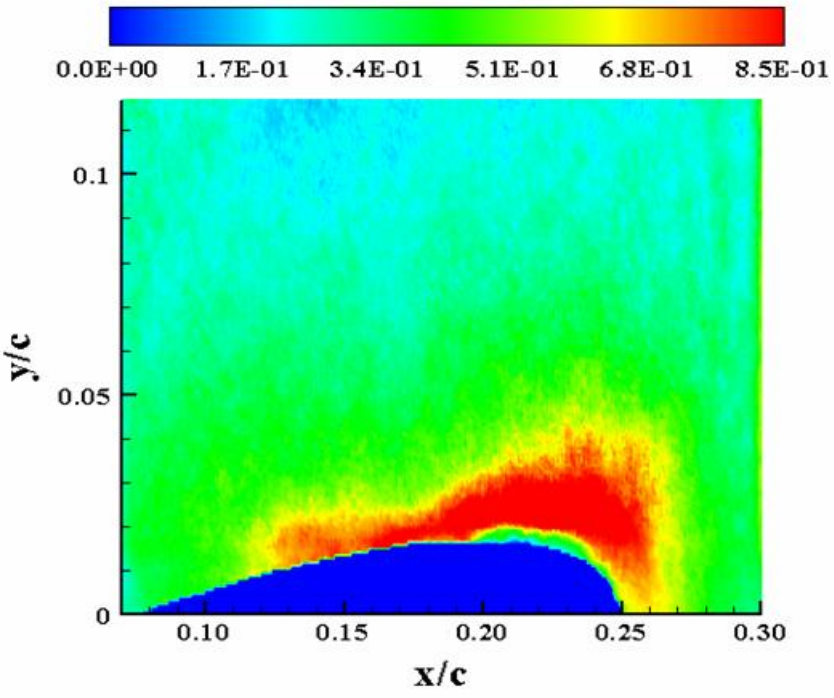

Figure C-72: $\sigma_u(M_\infty = 0.28, k = 0.1, Down, \alpha = 16^0)$

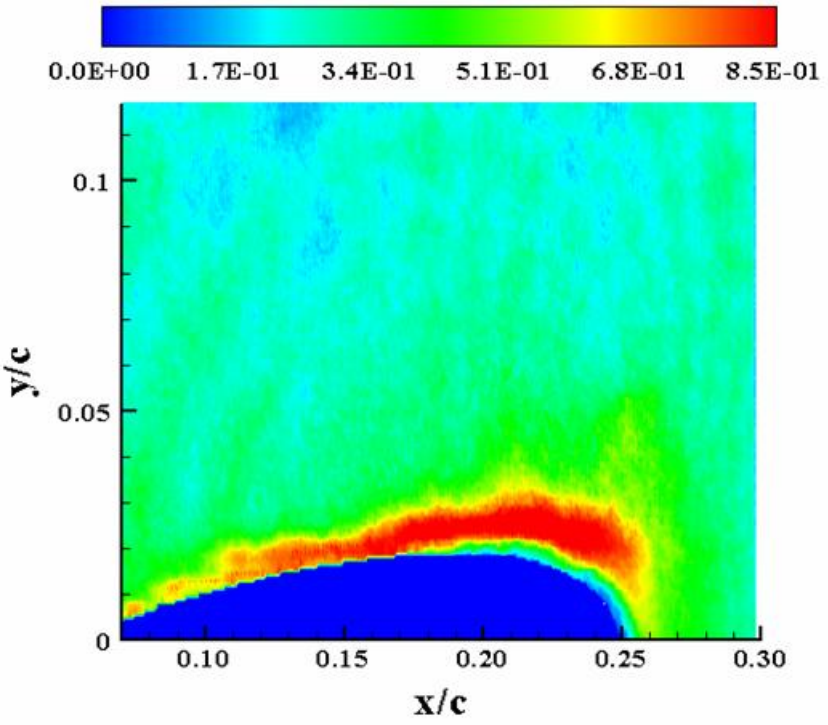

Figure C-73: $\sigma_u(M_\infty = 0.28, k = 0.1, Down, \alpha = 14^0)$

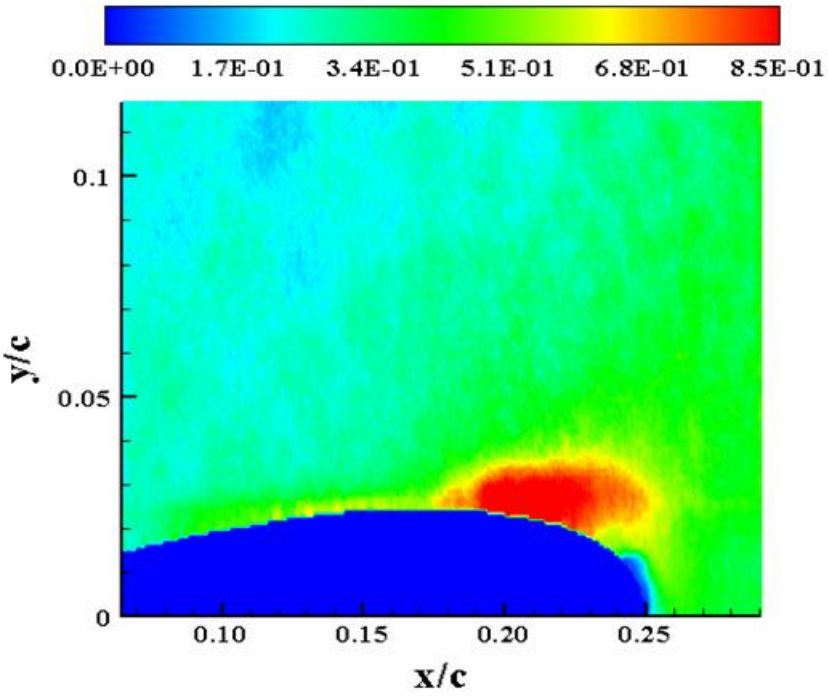

Figure C-74: $\sigma_u(M_\infty = 0.28, k = 0.1, Down, \alpha = 12^0)$

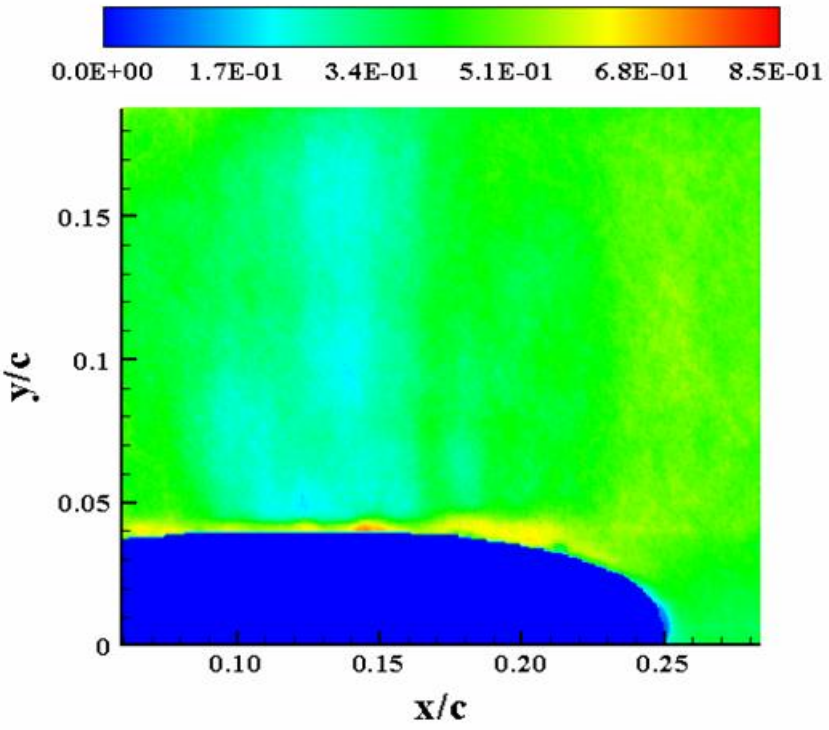

Figure C-75: $\sigma_u(M_\infty = 0.28, k = 0.1, Down, \alpha = 10^0)$

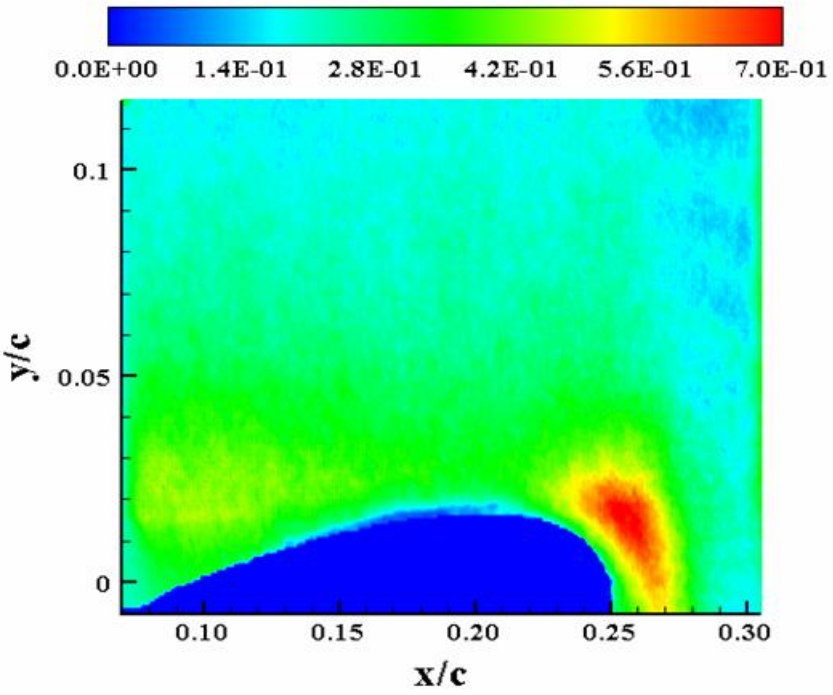

Figure C-76: $\sigma_v(M_\infty = 0.28, k = 0.1, Down, \alpha = 18^0)$

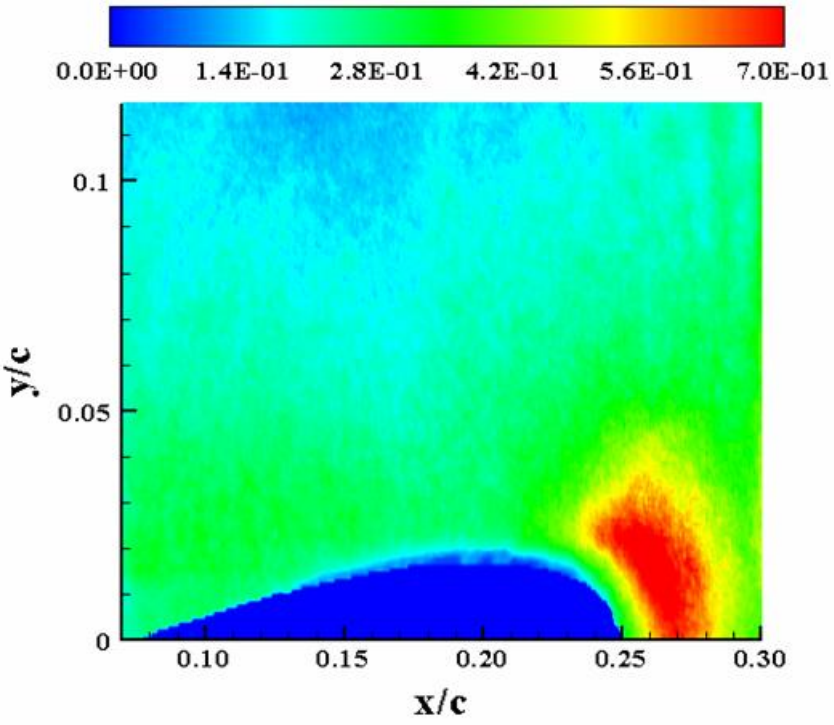

Figure C-77: $\sigma_v (M_\infty = 0.28, k = 0.1, Down, \alpha = 16^0)$

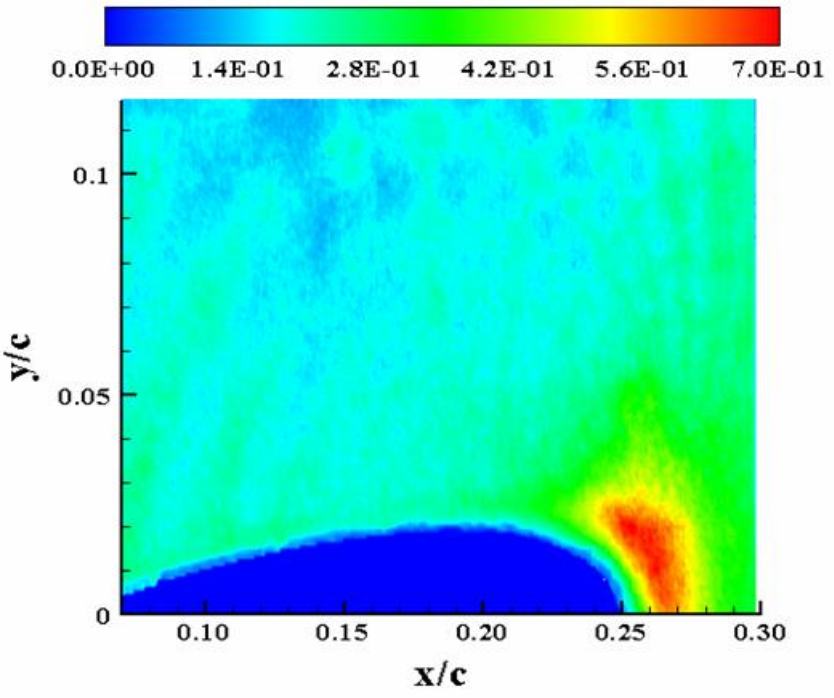

Figure C-78: $\sigma_v (M_\infty = 0.28, k = 0.1, Down, \alpha = 14^0)$

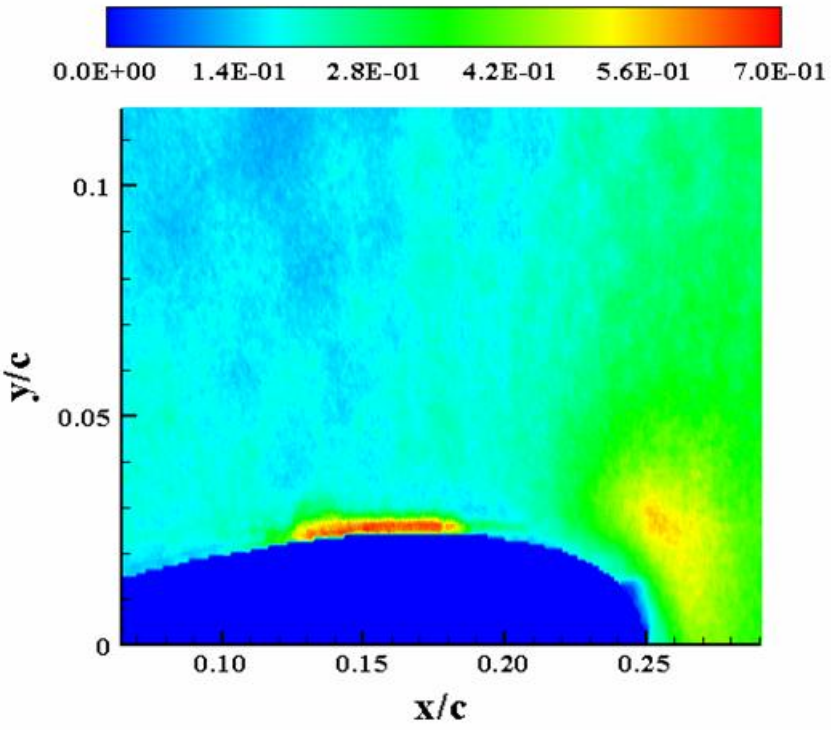

Figure C-79: $\sigma_v(M_\infty = 0.28, k = 0.1, Down, \alpha = 12^0)$

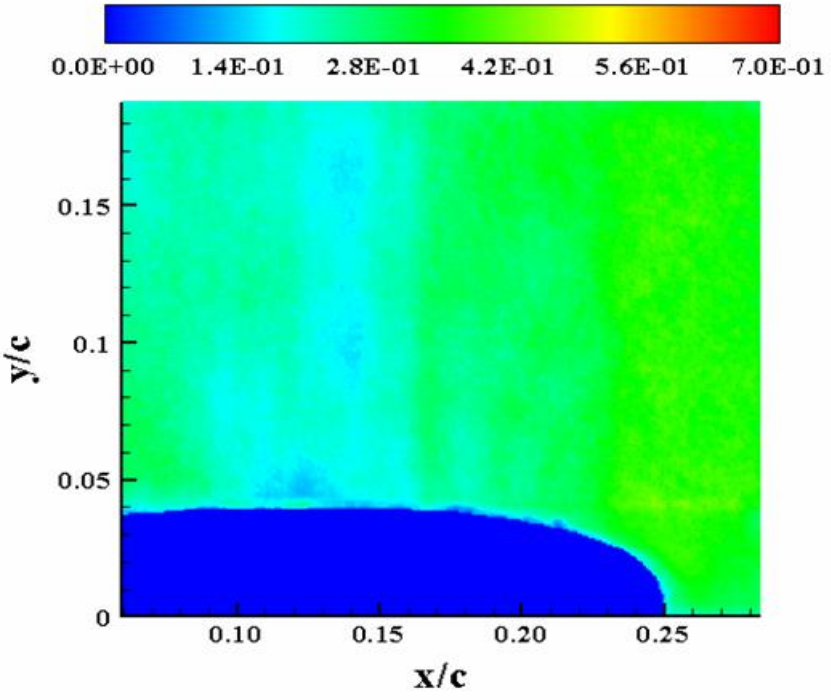

Figure C-80: $\sigma_v(M_\infty = 0.28, k = 0.1, Down, \alpha = 10^0)$

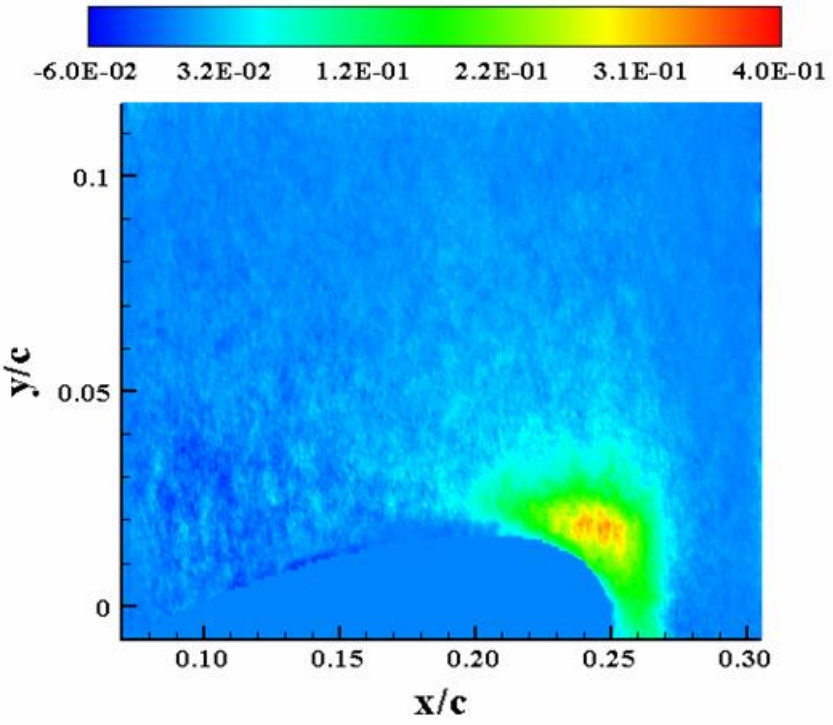

Figure C-81: $\tau_{xy}(M_\infty = 0.28, k = 0.1, Down, \alpha = 18^0)$

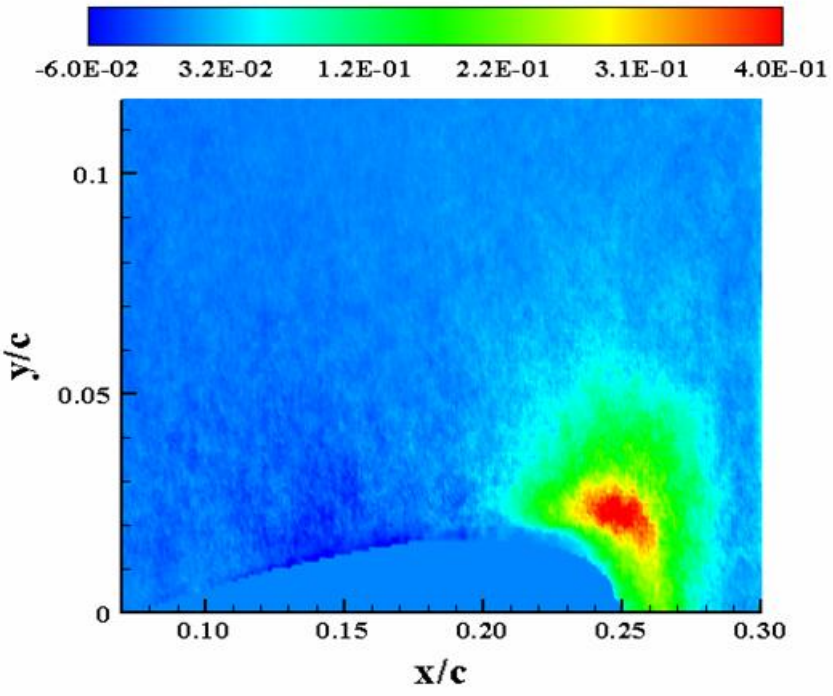

Figure C-82: $\tau_{xy}(M_\infty = 0.28, k = 0.1, Down, \alpha = 16^0)$

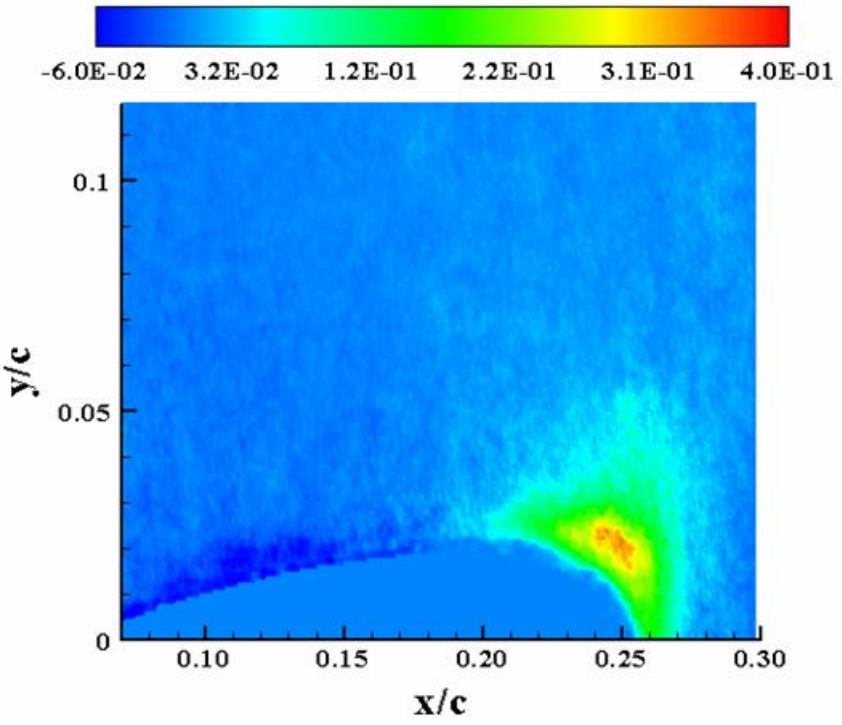

Figure C-83: $\tau_{xy}(M_\infty = 0.28, k = 0.1, Down, \alpha = 14^0)$

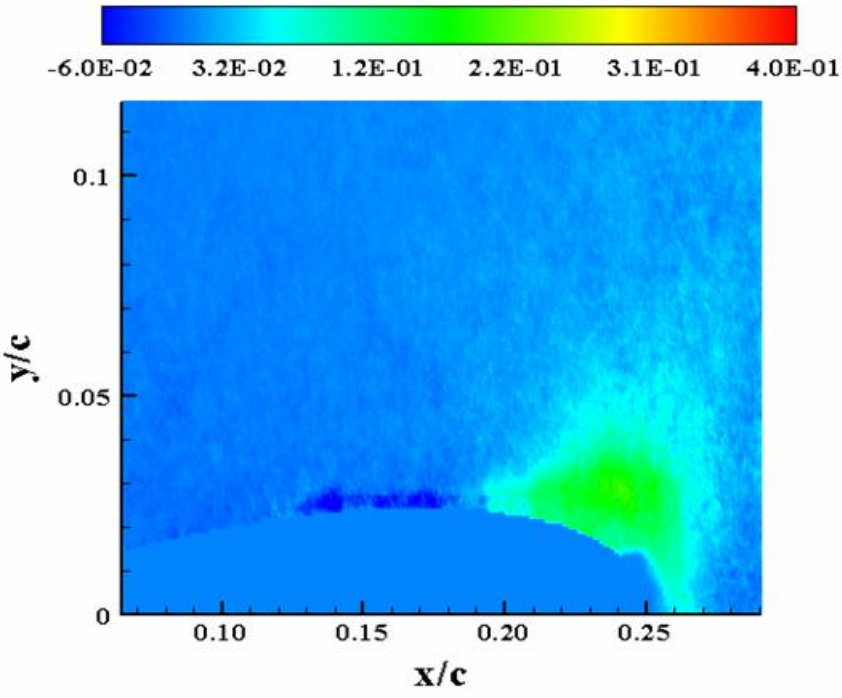

Figure C-84: $\sigma_{uv}(M_\infty = 0.28, k = 0.1, Down, \alpha = 12^0)$

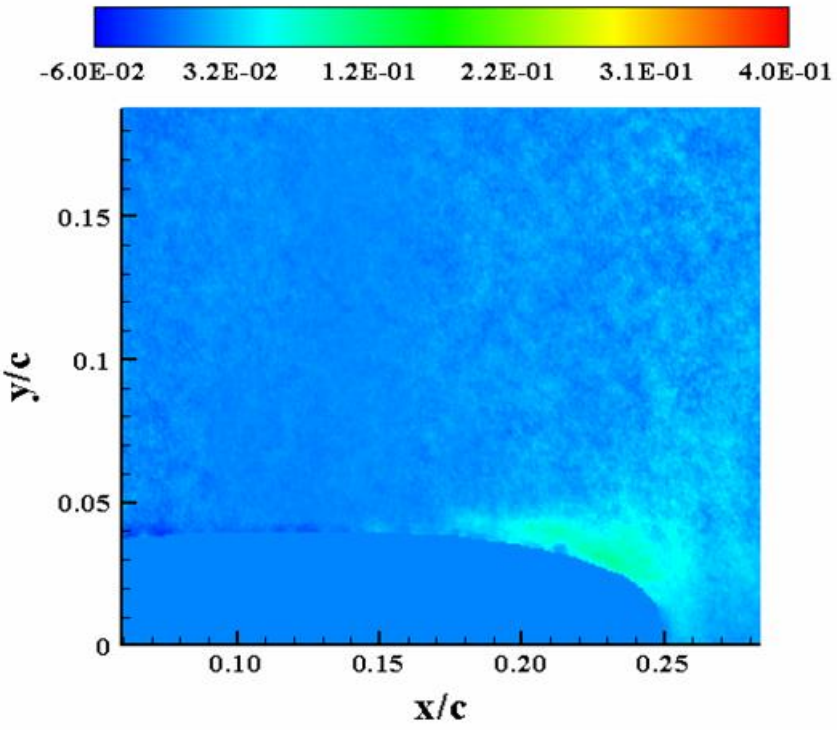

Figure C-85: $\tau_{xy}(M_\infty = 0.28, k = 0.1, Down, \alpha = 10^0)$

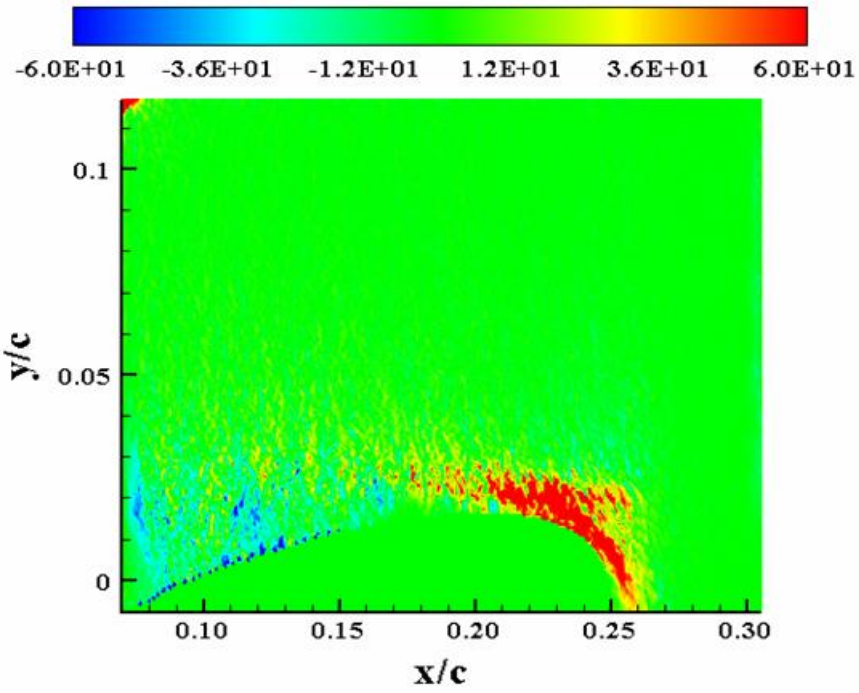

Figure C-86: $P_{xx}(M_\infty = 0.28, k = 0.1, Down, \alpha = 18^0)$

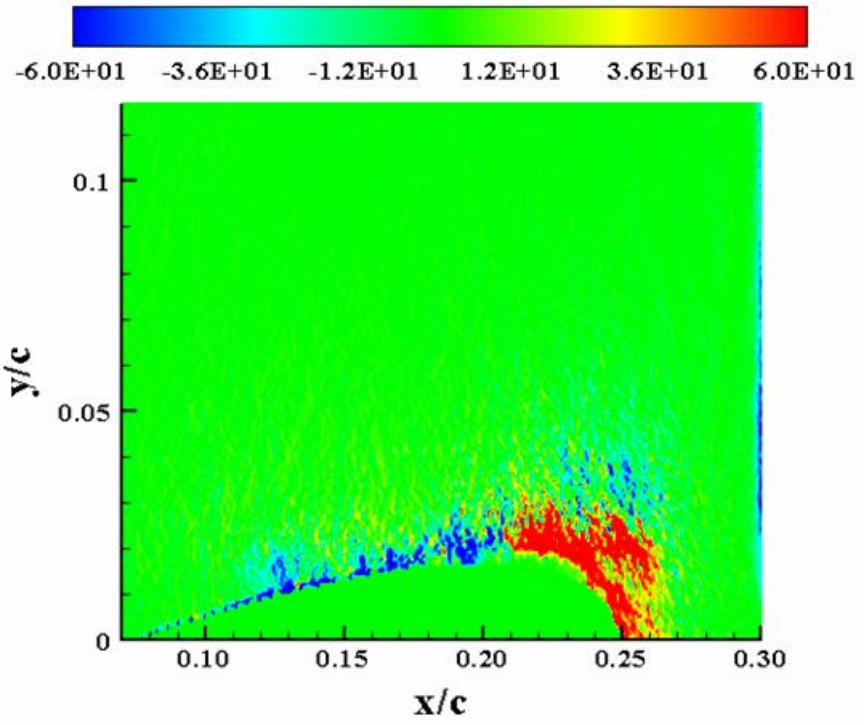

Figure C-87: $P_{xx}(M_\infty = 0.28, k = 0.1, Down, \alpha = 16^0)$

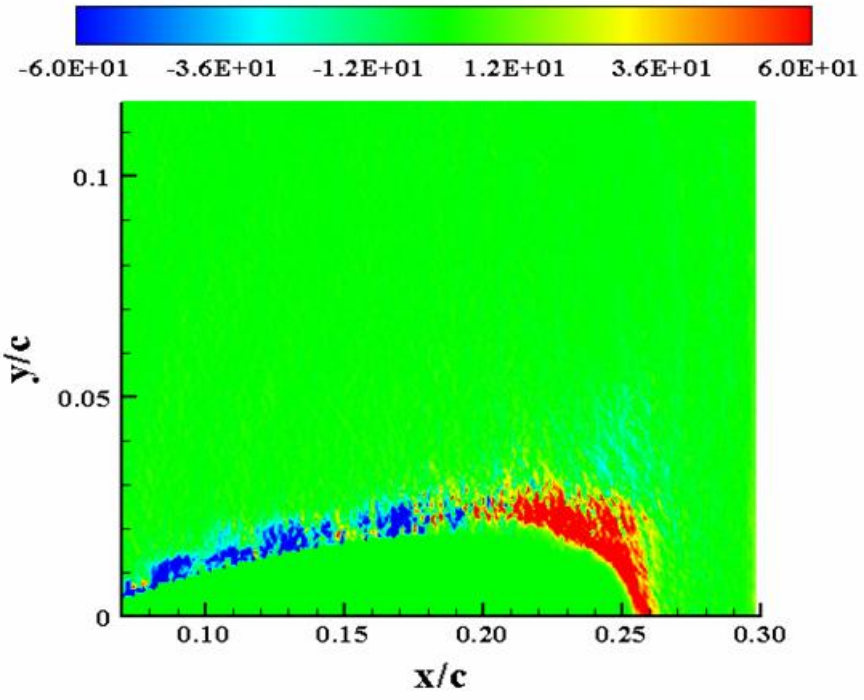

Figure C-88: $P_{xx}(M_\infty = 0.28, k = 0.1, Down, \alpha = 14^0)$

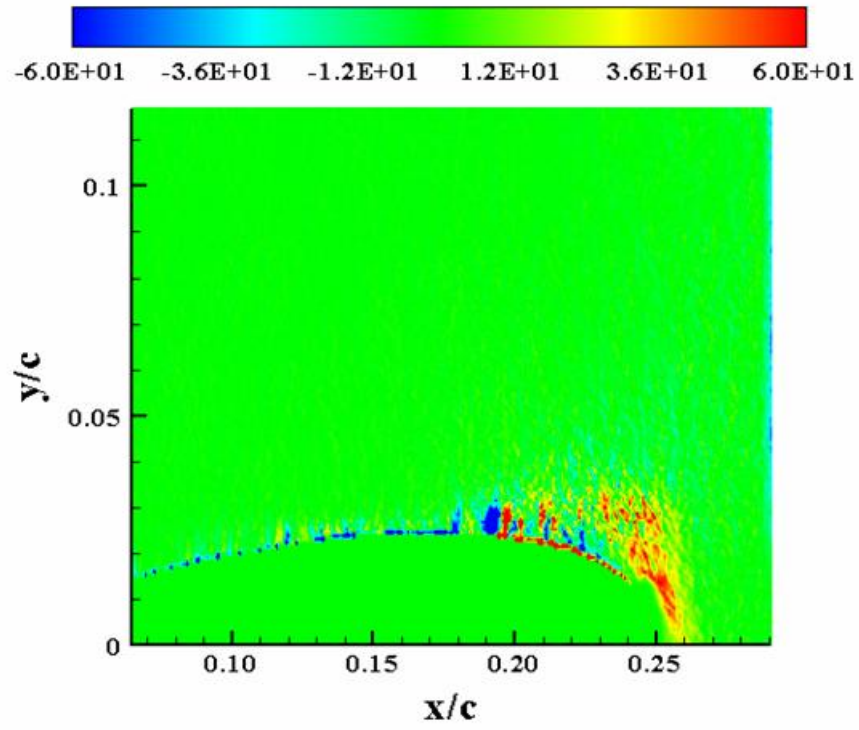

Figure C-89: $P_{xx}(M_\infty = 0.28, k = 0.1, Down, \alpha = 12^0)$

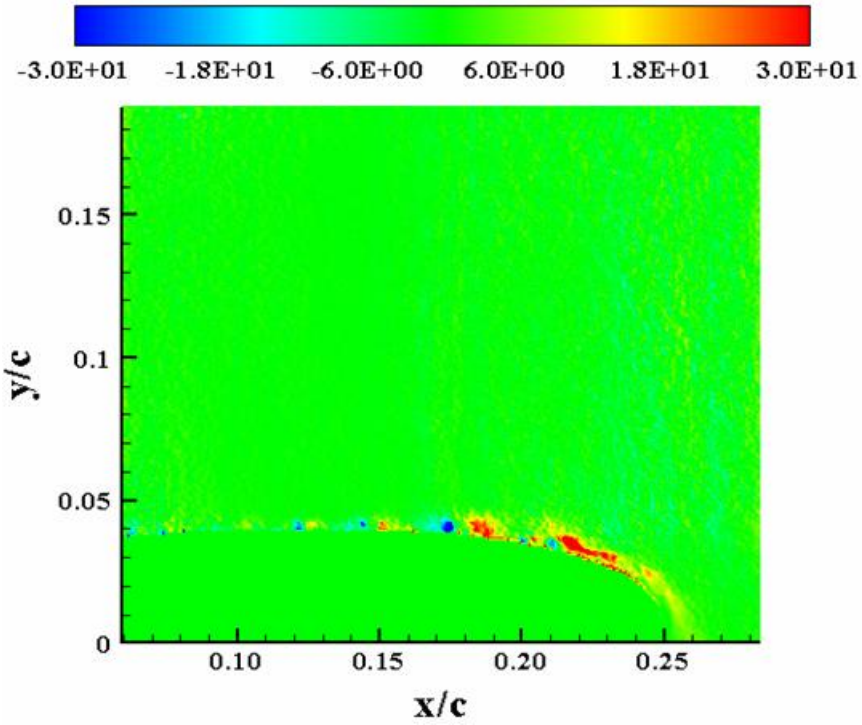

Figure C-90: $P_{xx}(M_\infty = 0.28, k = 0.1, Down, \alpha = 10^0)$

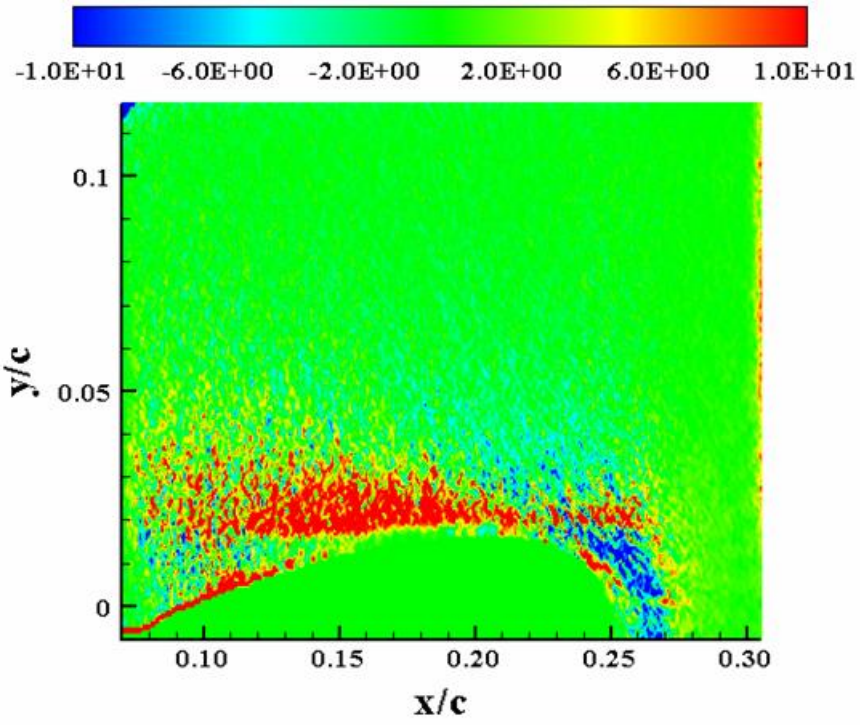

Figure C-91: $P_{xy}(M_\infty = 0.28, k = 0.1, Down, \alpha = 18^0)$

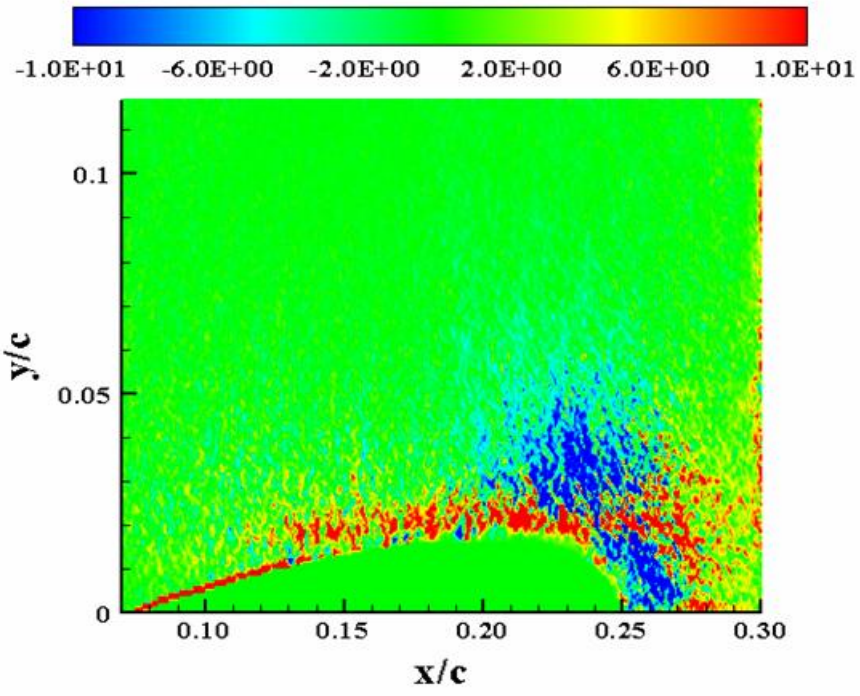

Figure C-92: $P_{xy}(M_\infty = 0.28, k = 0.1, Down, \alpha = 16^0)$

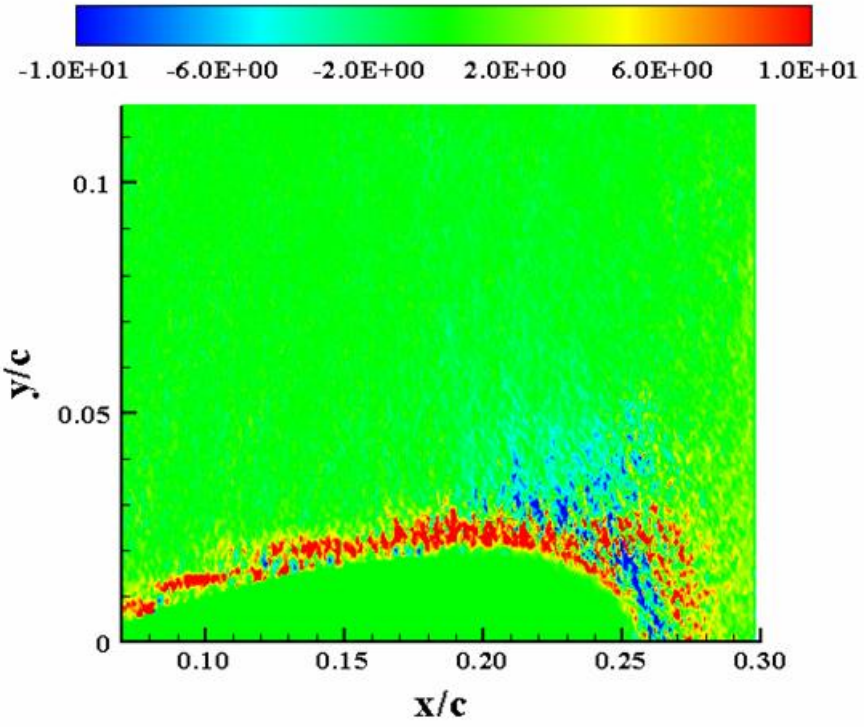

Figure C-93: $P_{xy}(M_\infty = 0.28, k = 0.1, Down, \alpha = 14^0)$

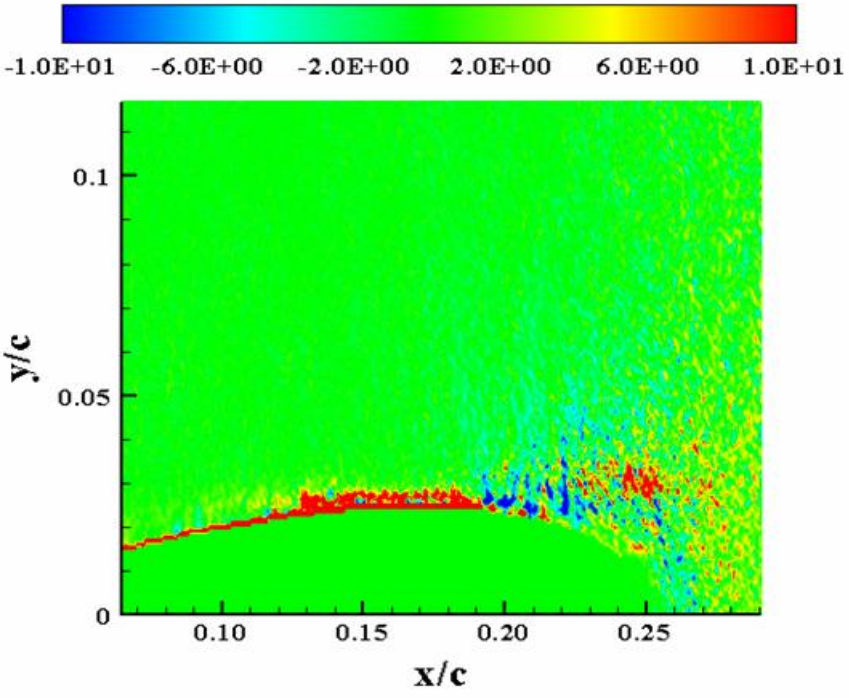

Figure C-94: $P_{xy}(M_\infty = 0.28, k = 0.1, Down, \alpha = 12^0)$

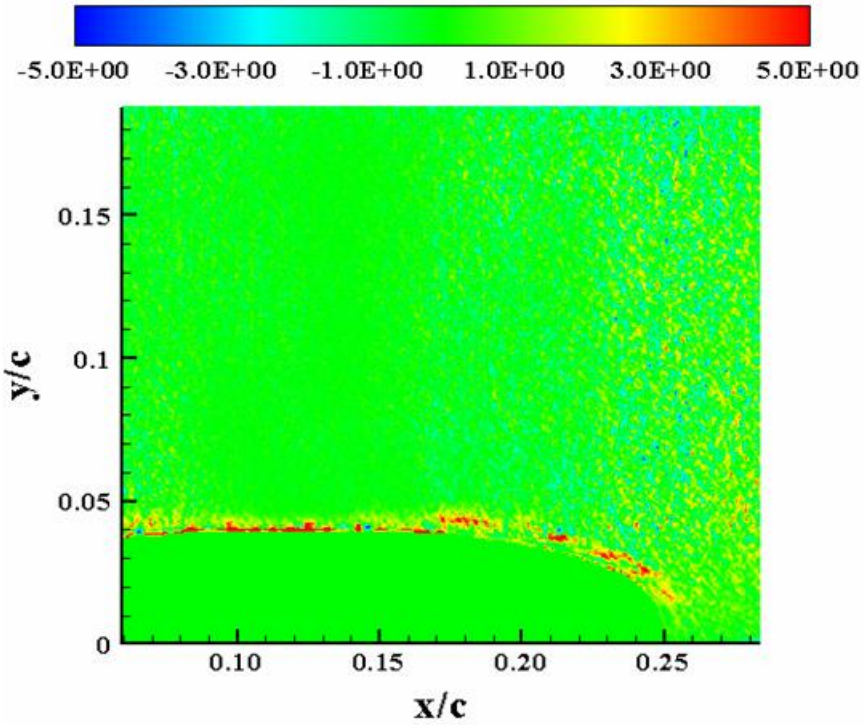

Figure C-95: $P_{xy}(M_\infty = 0.28, k = 0.1, Down, \alpha = 10^0)$

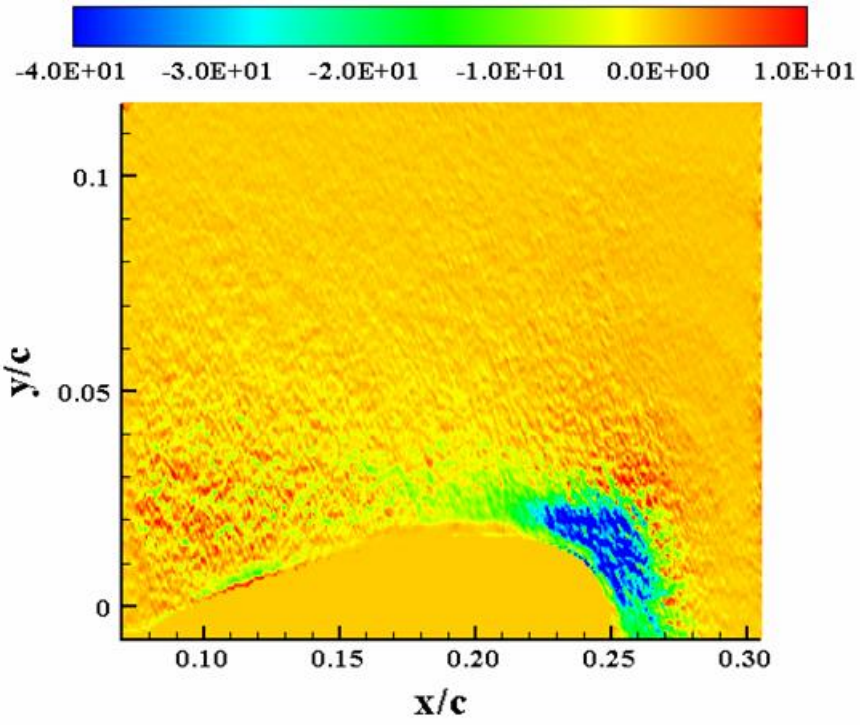

Figure C-96: $P_{yy}(M_\infty = 0.28, k = 0.1, Down, \alpha = 18^0)$

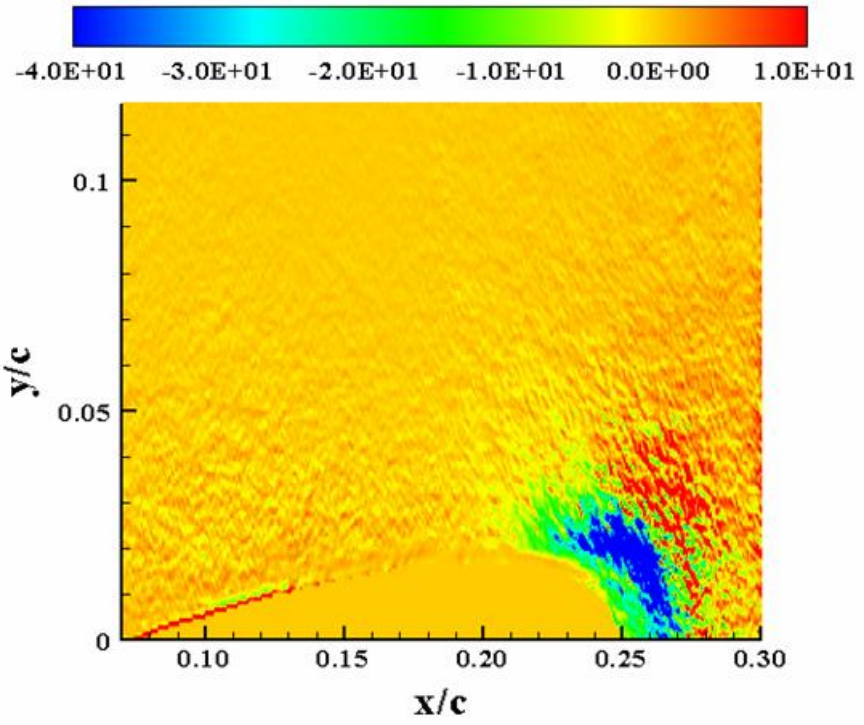

Figure C-97: $P_{yy}(M_\infty = 0.28, k = 0.1, Down, \alpha = 16^0)$

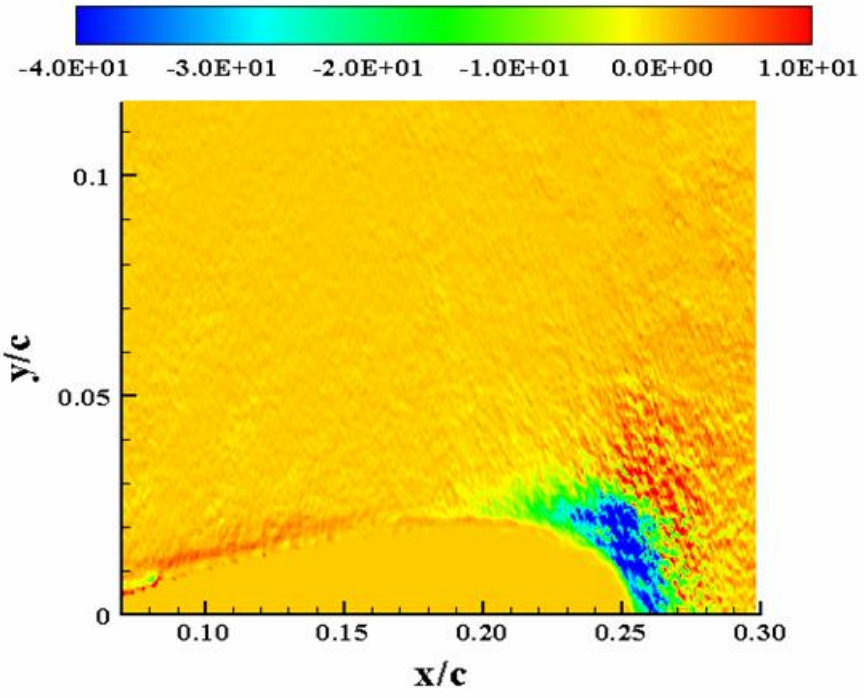

Figure C-98: $P_{yy}(M_\infty = 0.28, k = 0.1, Down, \alpha = 14^0)$

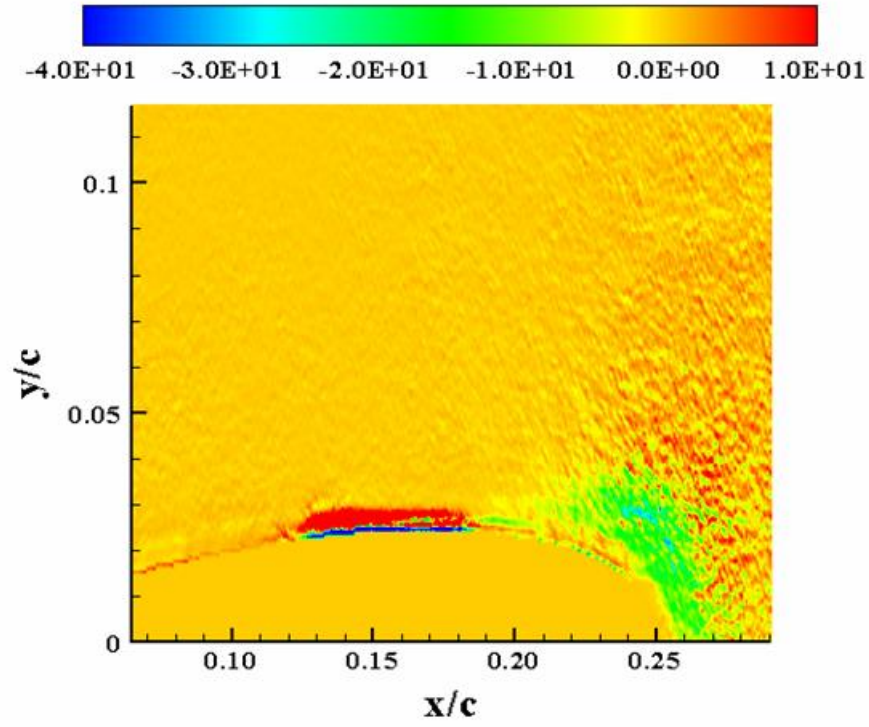

Figure C-99: $P_{yy}(M_\infty = 0.28, k = 0.1, Down, \alpha = 12^0)$

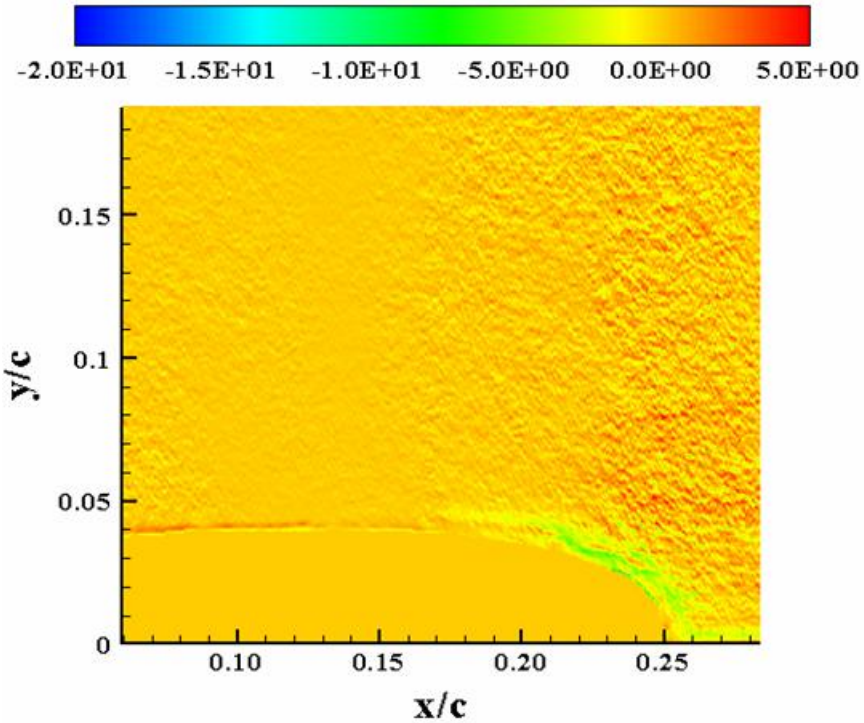

Figure C-100: $P_{yy}(M_\infty = 0.28, k = 0.1, Down, \alpha = 10^0)$

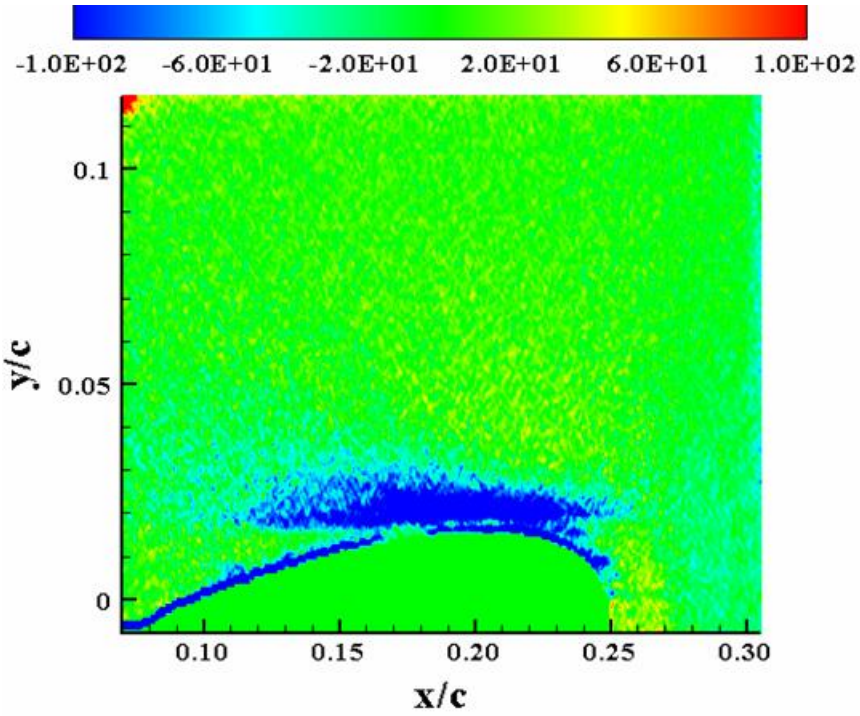

Figure C-101: $S_{xy}(M_\infty = 0.28, k = 0.1, Down, \alpha = 18^0)$

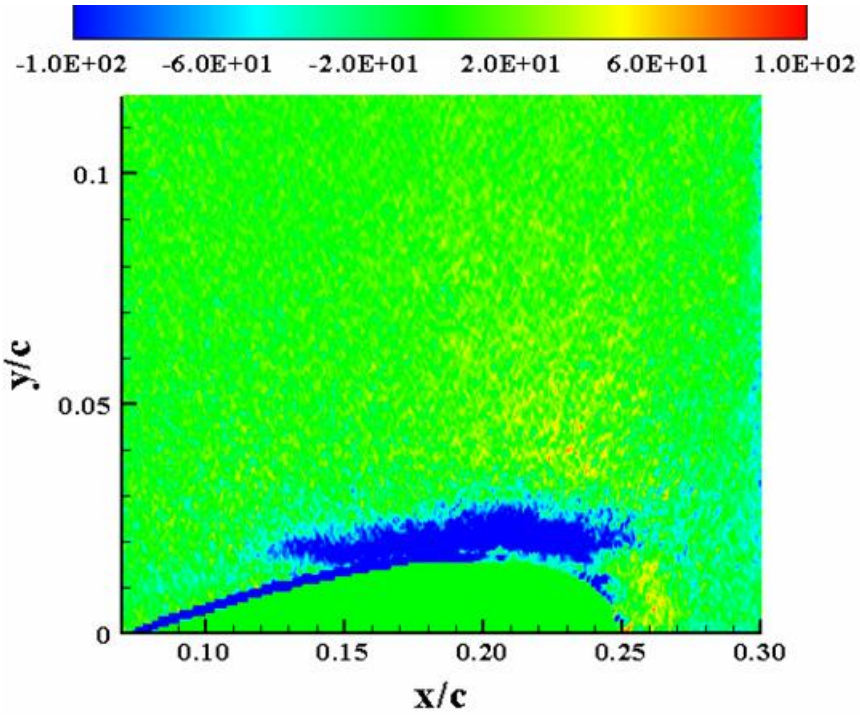

Figure C-102: $S_{xy}(M_\infty = 0.28, k = 0.1, Down, \alpha = 16^0)$

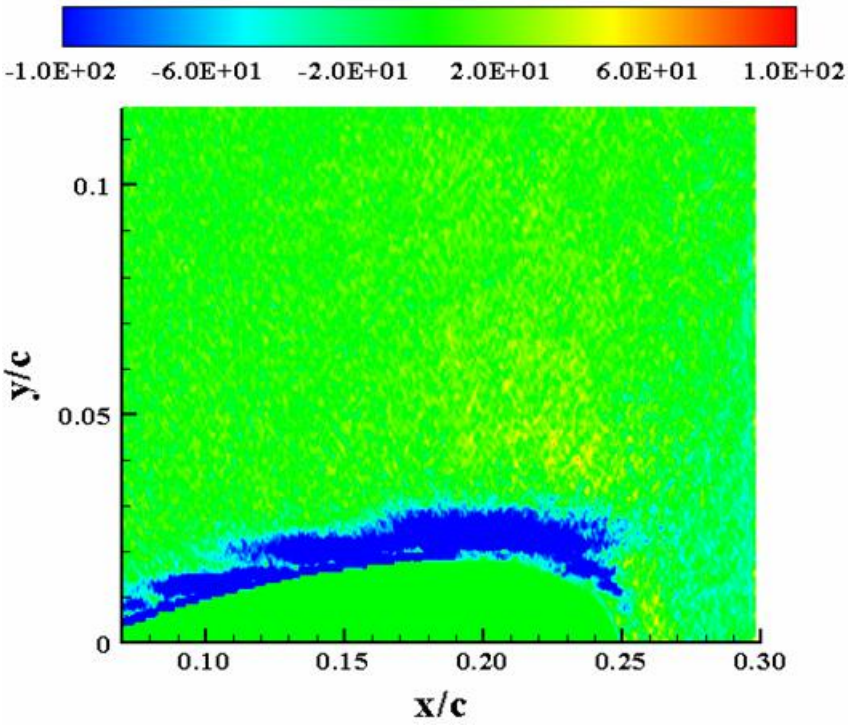

Figure C-103: $S_{xy}(M_\infty = 0.28, k = 0.1, Down, \alpha = 14^0)$

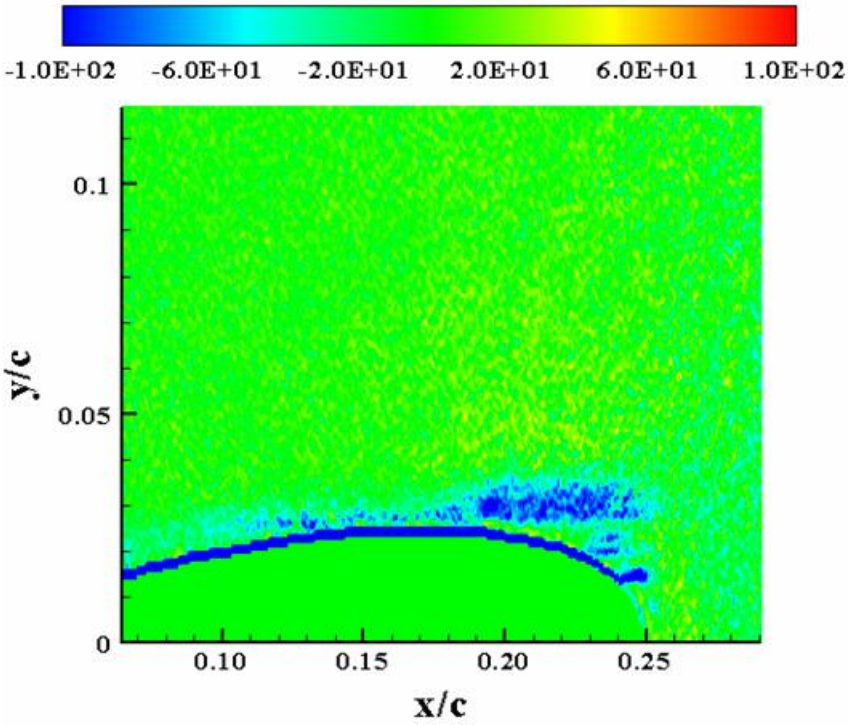

Figure C-104: $S_{xy}(M_\infty = 0.28, k = 0.1, Down, \alpha = 12^0)$

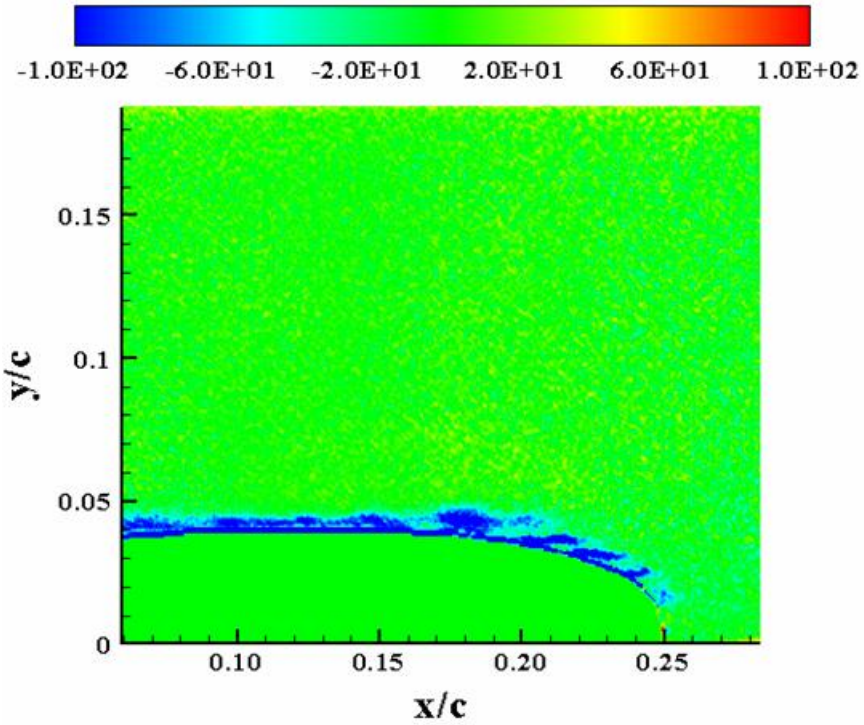

Figure C-105: $S_{xy}(M_\infty = 0.28, k = 0.1, Down, \alpha = 10^0)$

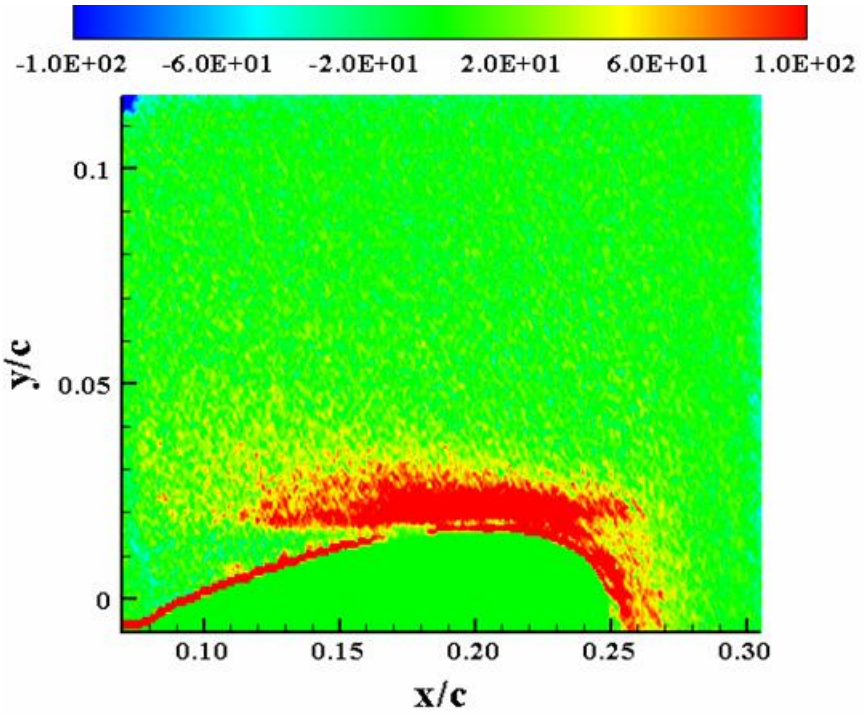

Figure C-106: $\omega_z(M_\infty = 0.28, k = 0.1, Down, \alpha = 18^0)$

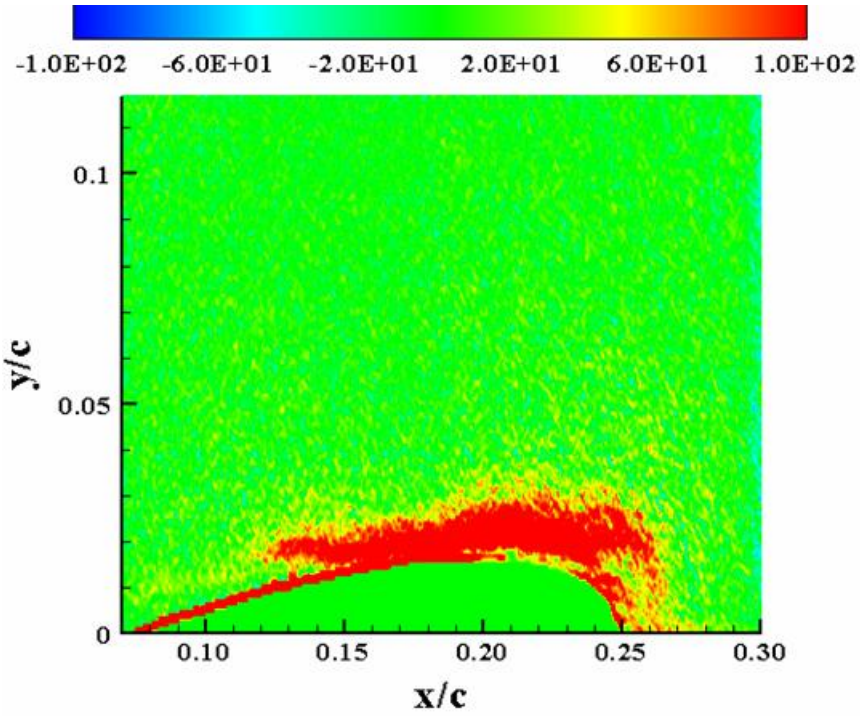

Figure C-107: $\omega_z(M_\infty = 0.28, k = 0.1, Down, \alpha = 16^0)$

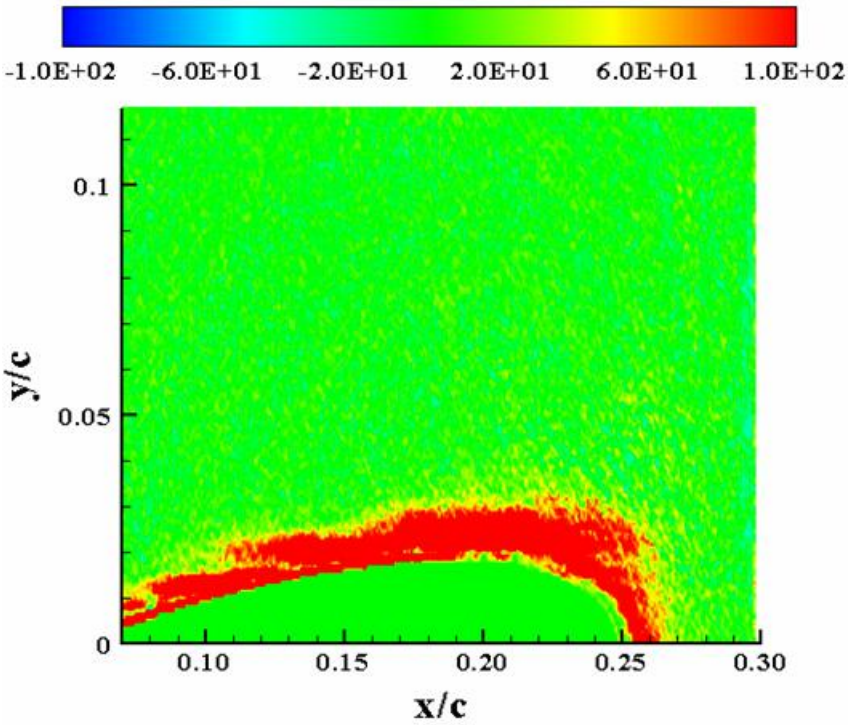

Figure C-108: $\omega_z(M_\infty = 0.28, k = 0.1, Down, \alpha = 14^0)$

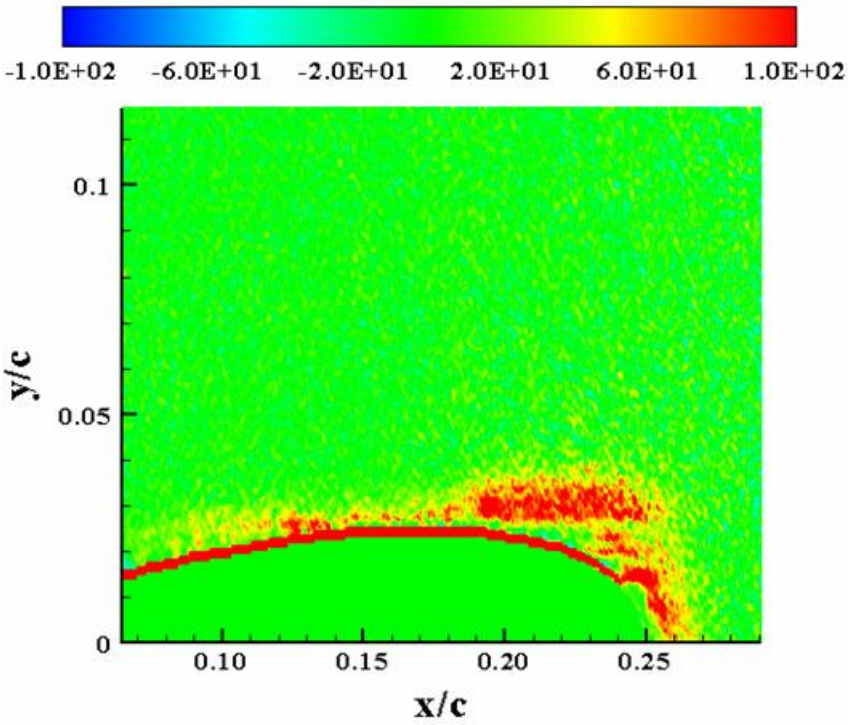

Figure C-109: $\omega_z (M_\infty = 0.28, k = 0.1, Down, \alpha = 12^0)$

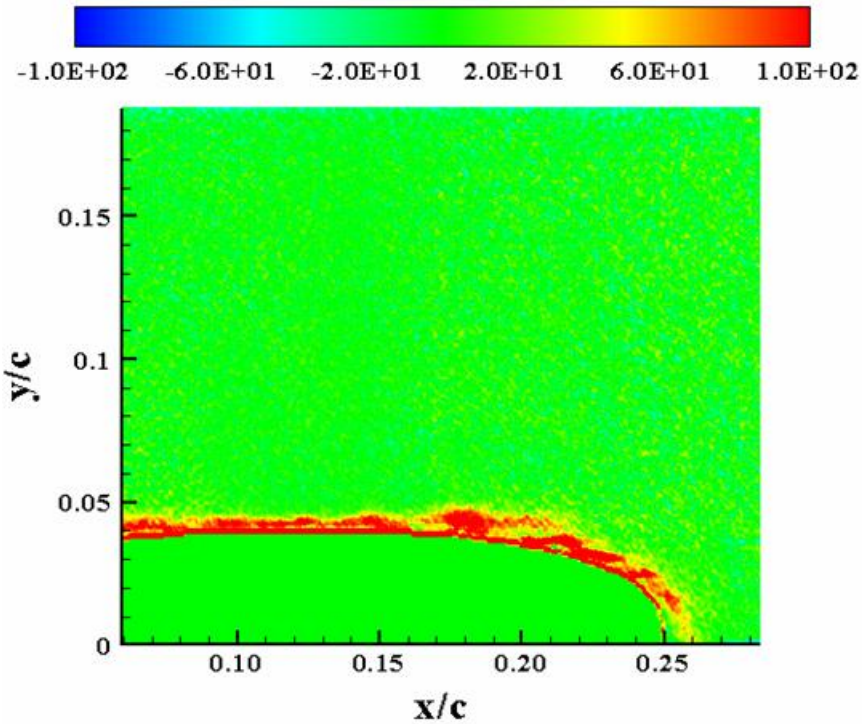

Figure C-110: $\omega_z (M_\infty = 0.28, k = 0.1, Down, \alpha = 10^0)$

APPENDIX D

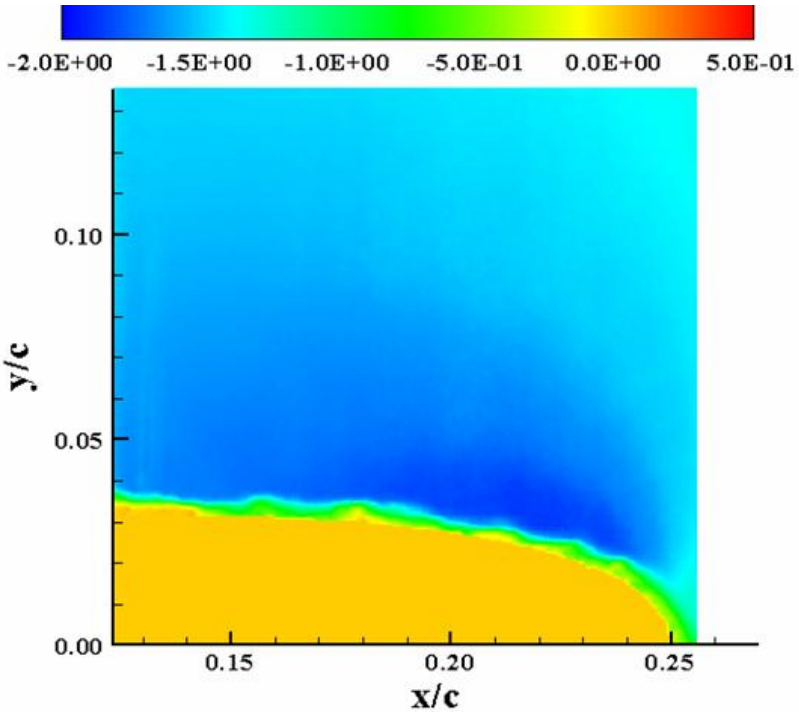

Figure D-1: $U_N\,(M_\infty = 0.2, k = 0.18, Up, \alpha = 9.19^0)$

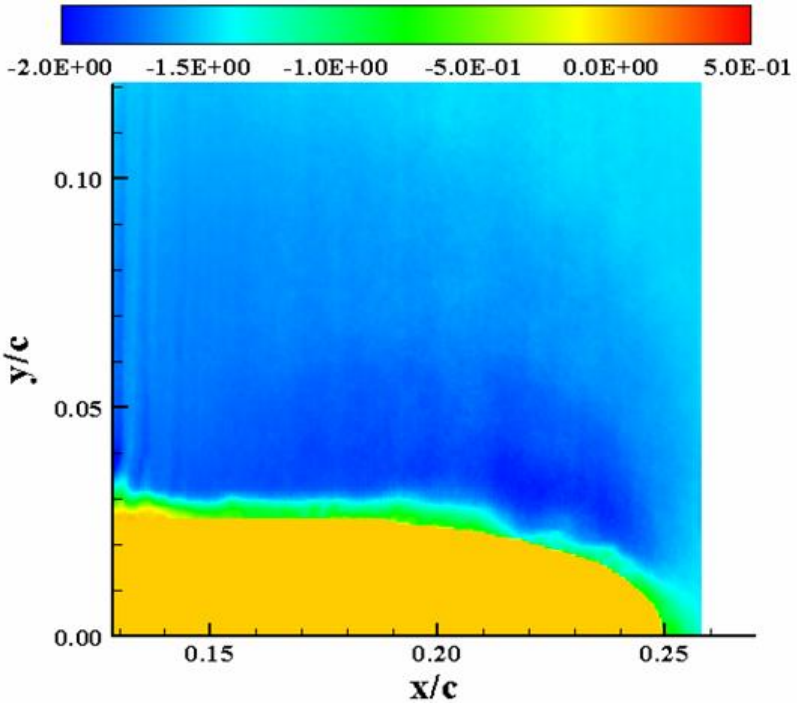

Figure D-2: $U_N\,(M_\infty = 0.2, k = 0.18, Up, \alpha = 11.1^0)$

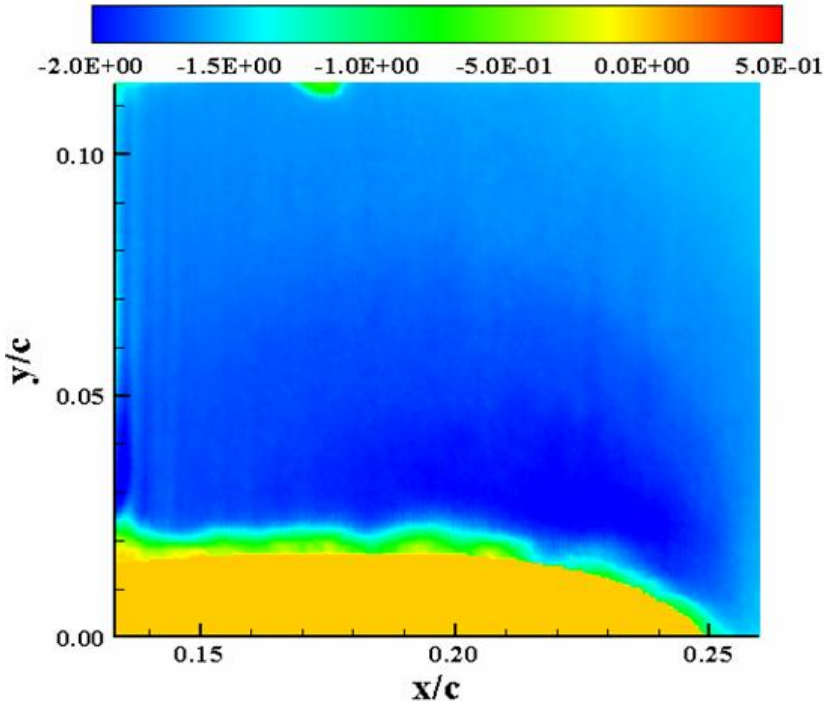

Figure D-3: $U_N\,(M_\infty = 0.2, k = 0.18, Up, \alpha = 13.02^0)$

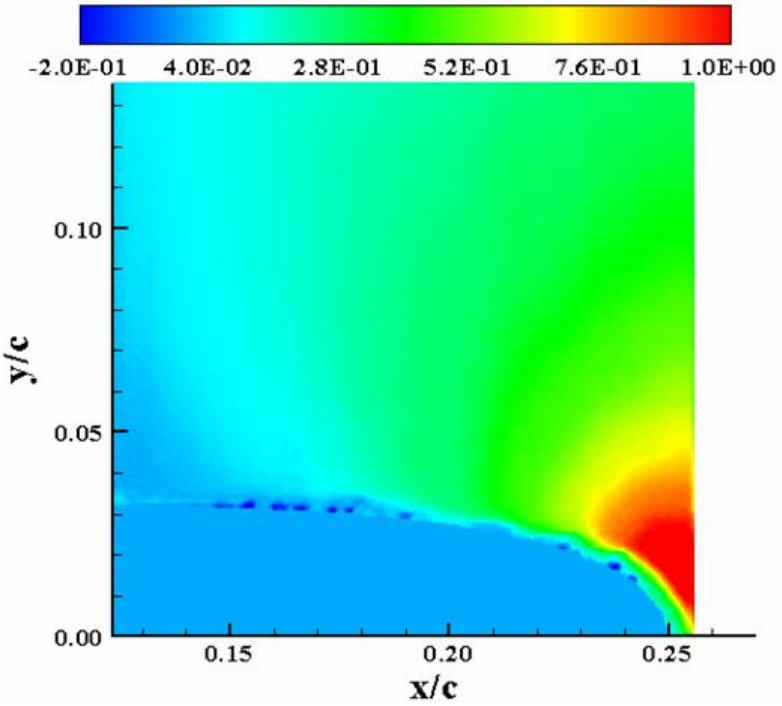

Figure D-4: $V_N\,(M_\infty = 0.2, k = 0.18, Up, \alpha = 9.19^0)$

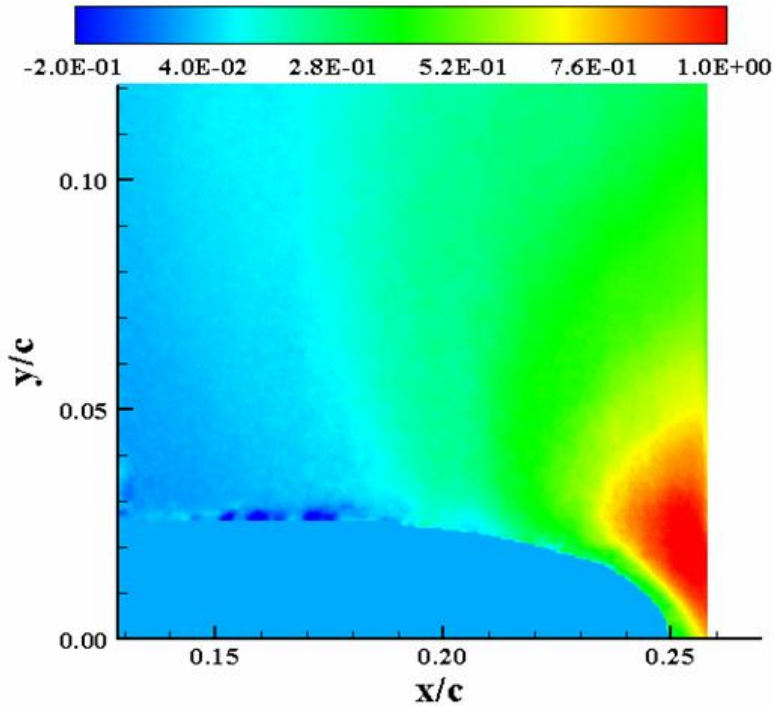

Figure D-5: $V_N\,(M_\infty = 0.2, k = 0.18, Up, \alpha = 11.1^0)$

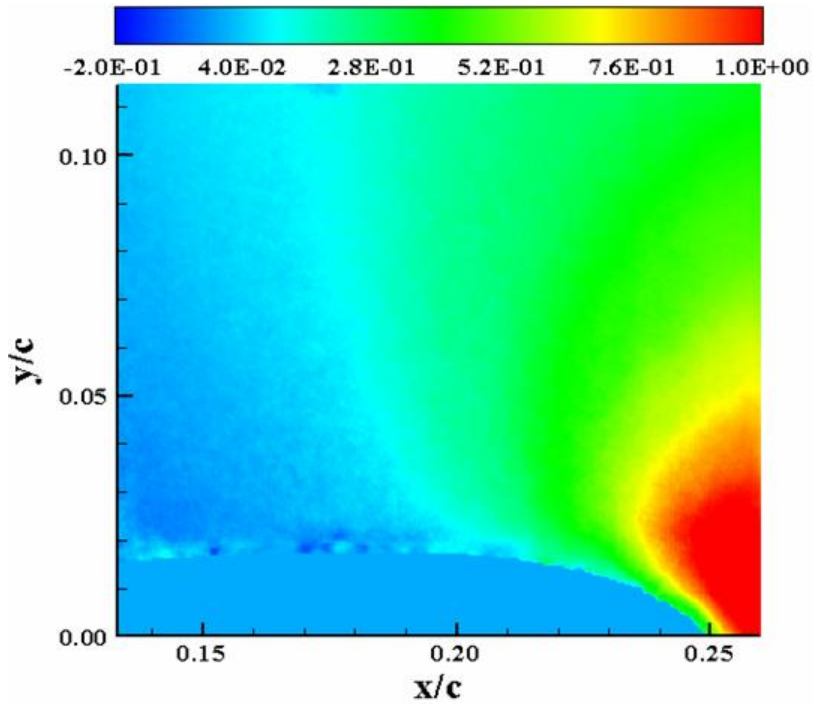

Figure D-6: $V_N\,(M_\infty = 0.2, k = 0.18, Up, \alpha = 13.02^0)$

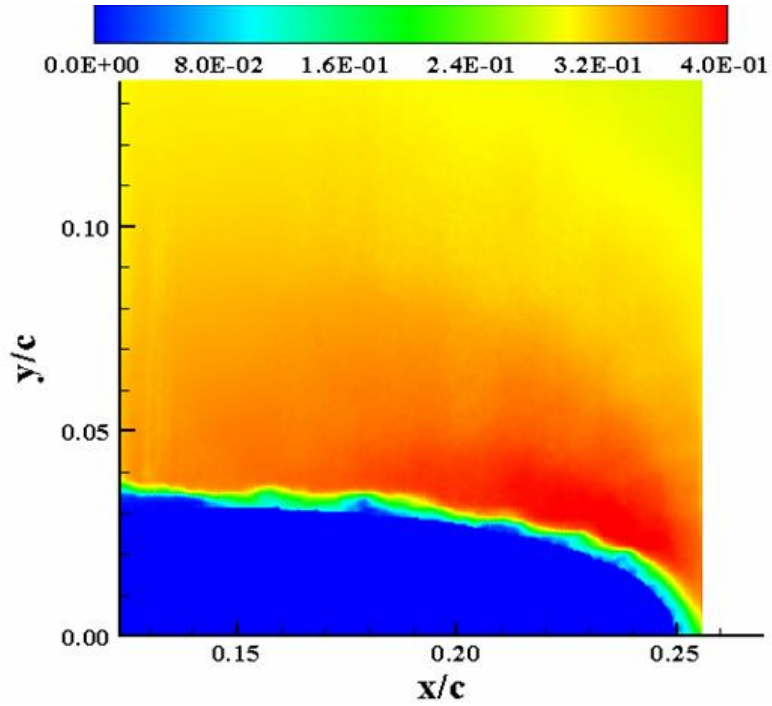

Figure D-7: $M(M_\infty = 0.2, k = 0.18, Up, \alpha = 9.19^0)$

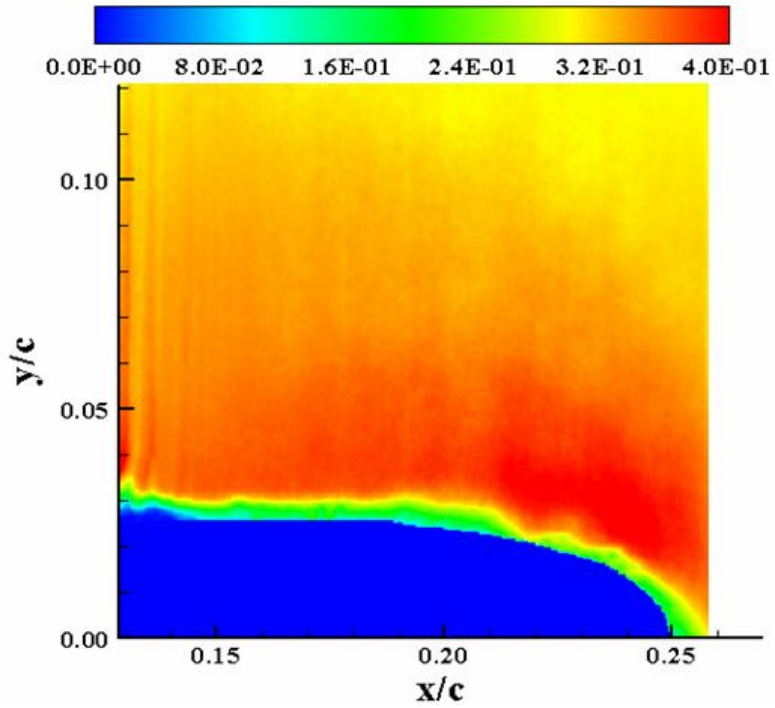

Figure D-8: $M(M_\infty = 0.2, k = 0.18, Up, \alpha = 11.1^0)$

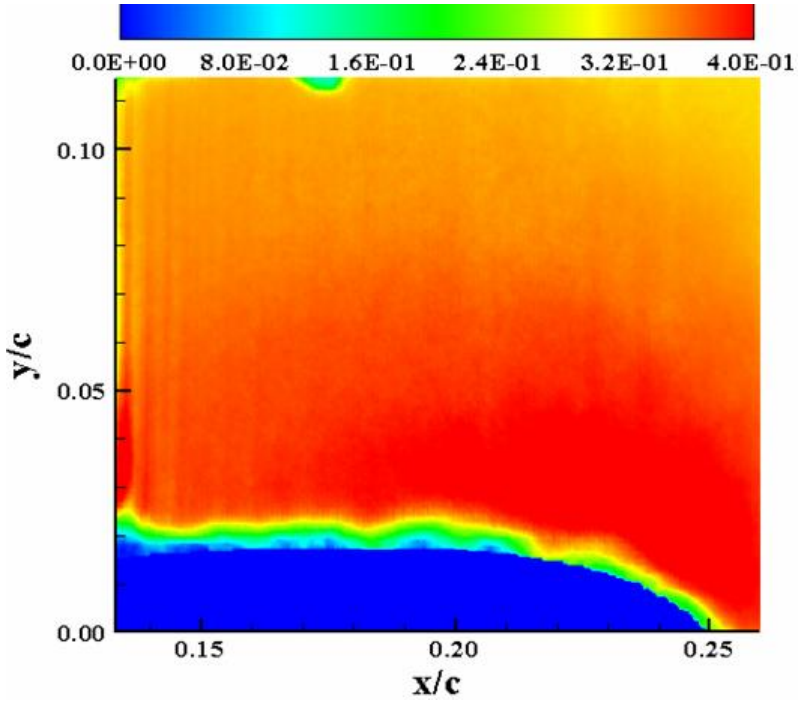

Figure D-9: $M(M_\infty = 0.2, k = 0.18, Up, \alpha = 13.02^0)$

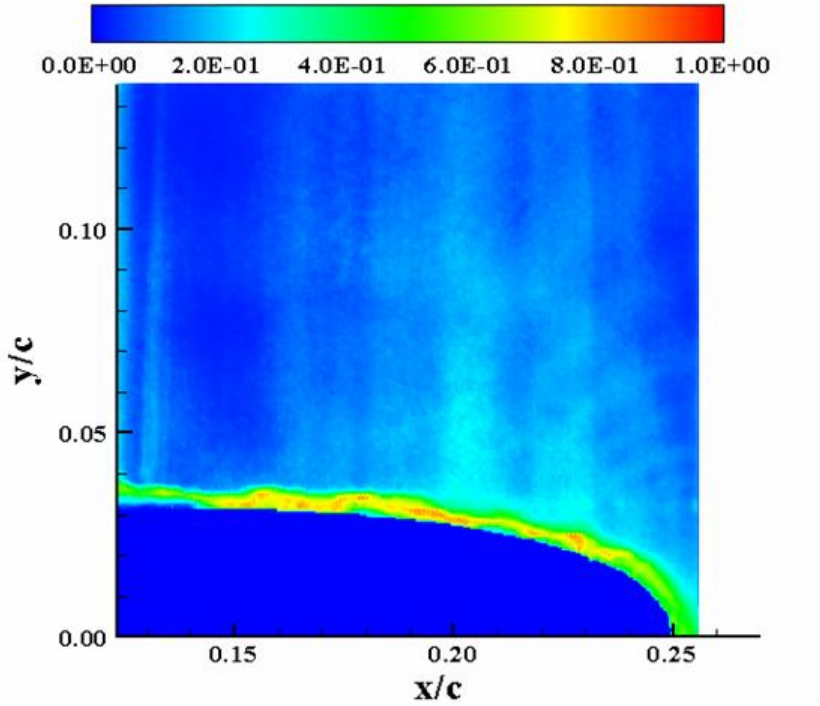

Figure D-10: $\sigma_u(M_\infty = 0.2, k = 0.18, Up, \alpha = 9.19^0)$

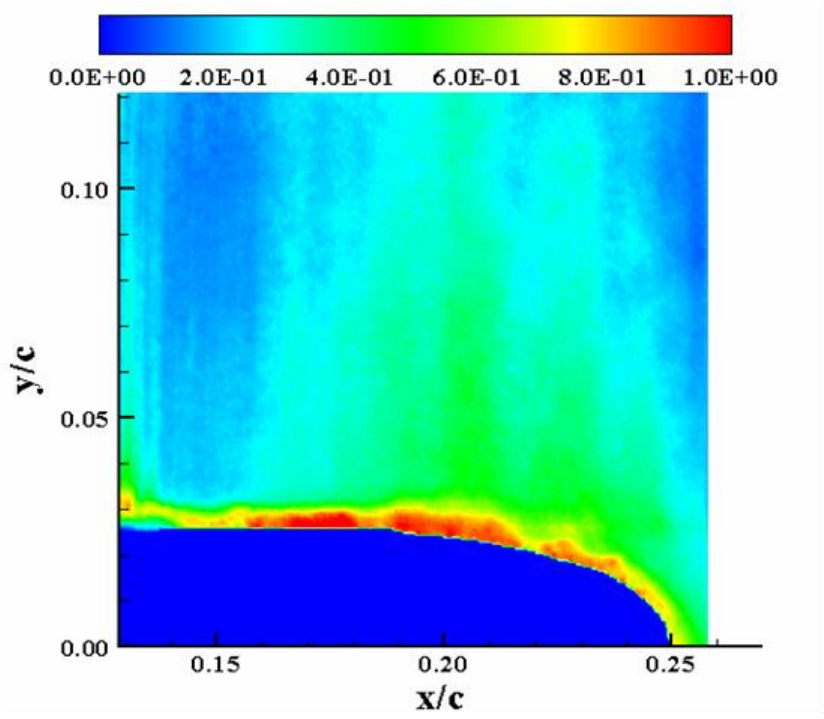

Figure D-11: $\sigma_u(M_\infty = 0.2, k = 0.18, Up, \alpha = 11.1^0)$

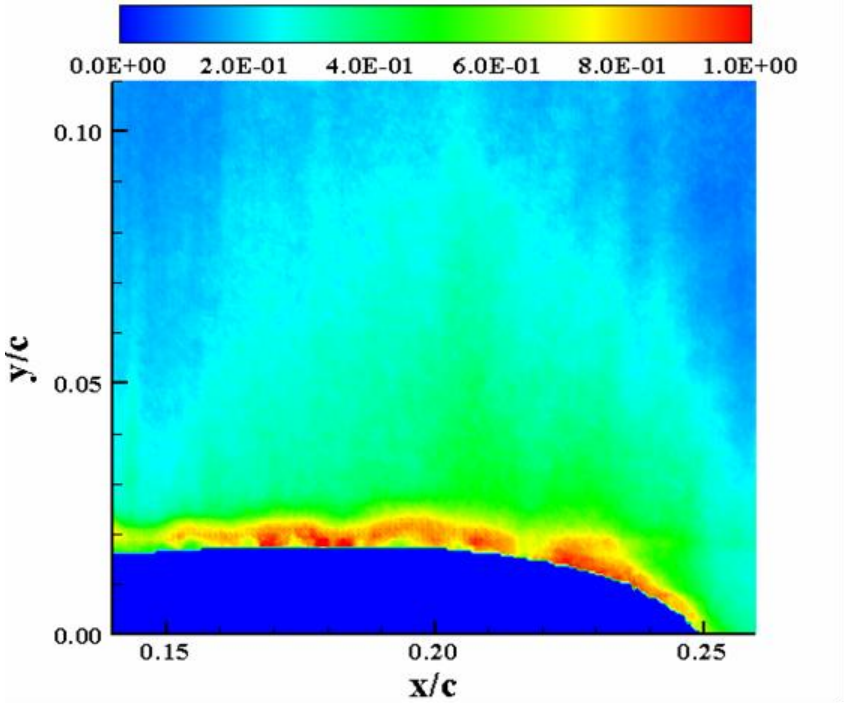

Figure D-12: $\sigma_u(M_\infty = 0.2, k = 0.18, Up, \alpha = 13.02^0)$

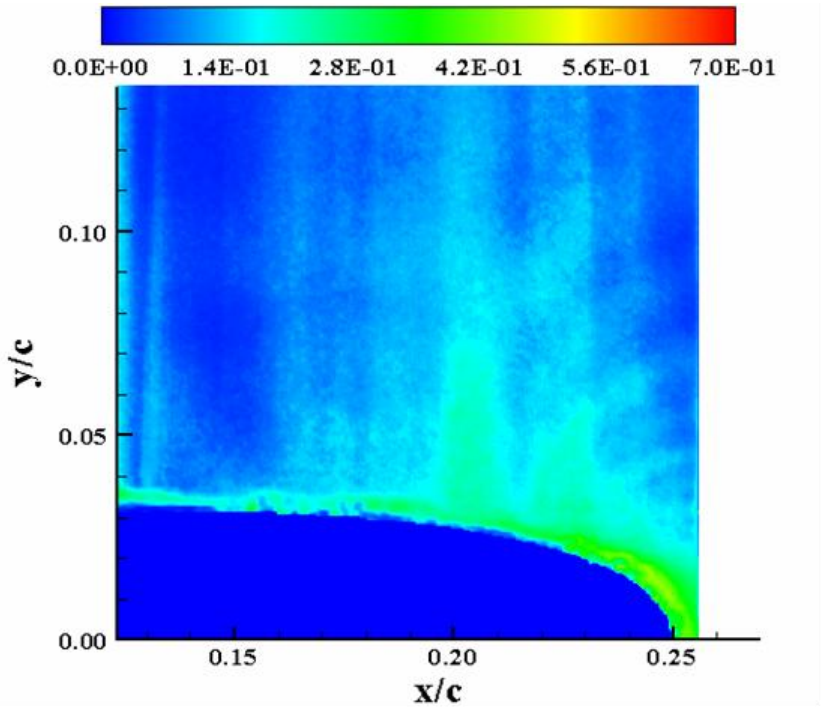

Figure D-13: $\sigma_v(M_\infty = 0.2, k = 0.18, Up, \alpha = 9.19^0)$

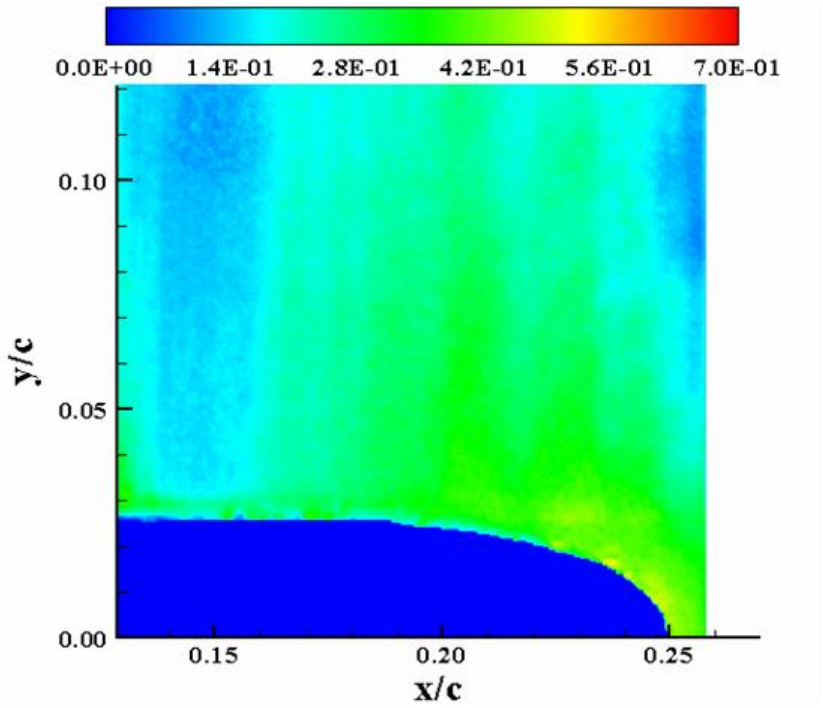

Figure D-14: $\sigma_v(M_\infty = 0.2, k = 0.18, Up, \alpha = 11.1^0)$

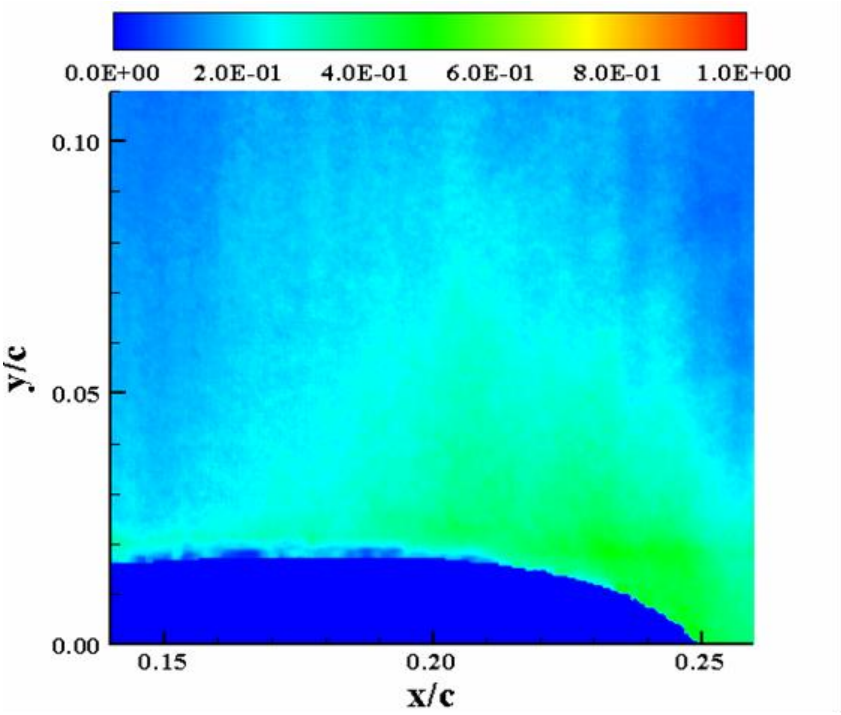

Figure D-15: $\sigma_v (M_\infty = 0.2, k = 0.18, Up, \alpha = 13.02^0)$

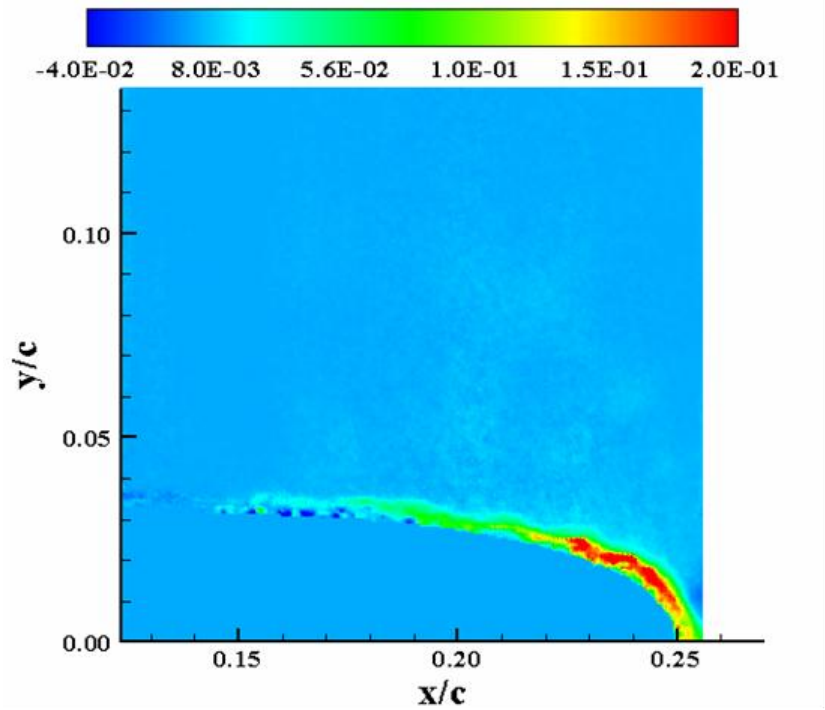

Figure D-16: $\tau_{xy} (M_\infty = 0.2, k = 0.18, Up, \alpha = 9.19^0)$

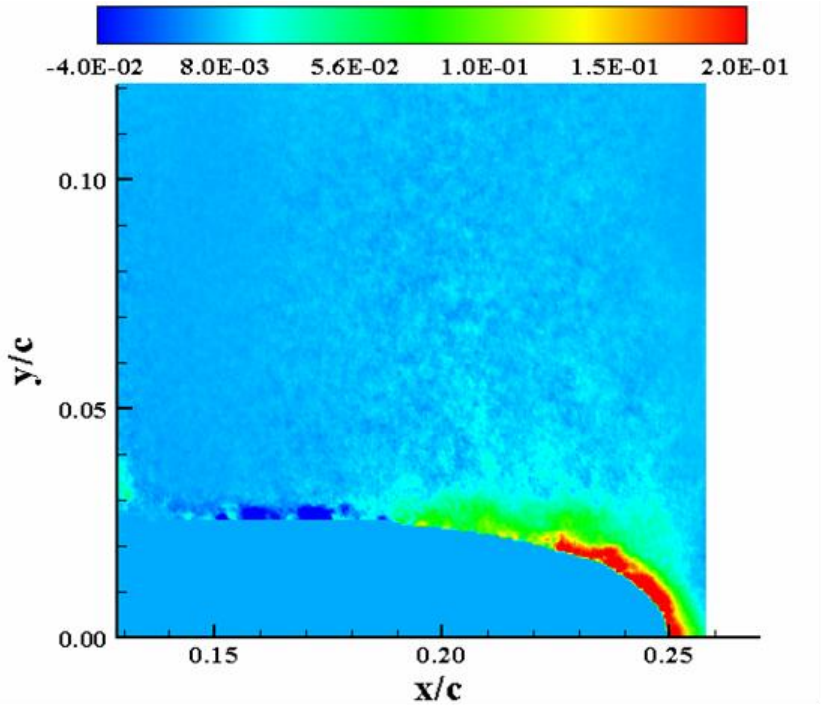

Figure D-17: $\tau_{xy}(M_\infty = 0.2, k = 0.18, Up, \alpha = 11.1^0)$

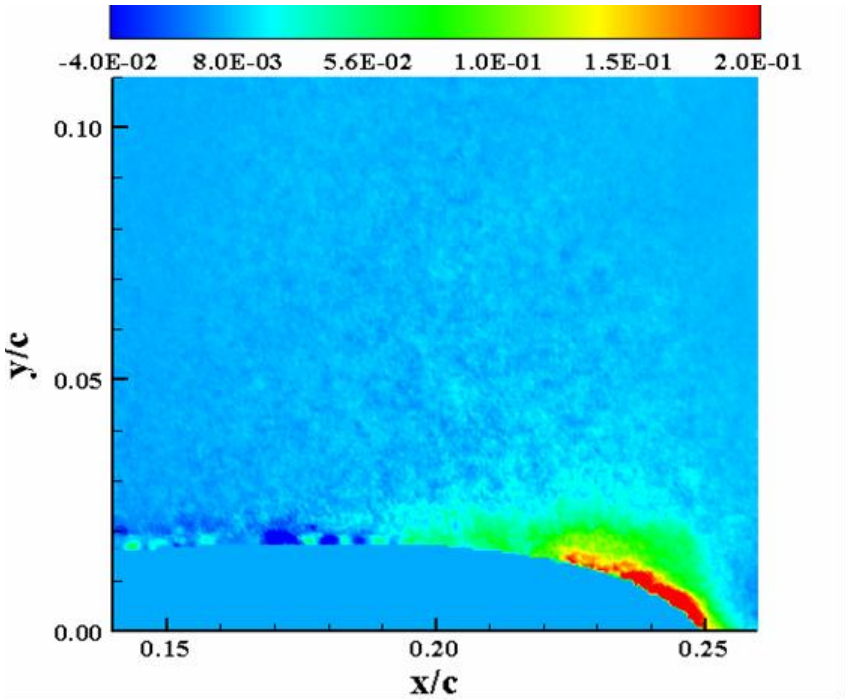

Figure D-18: $\tau_{xy}(M_\infty = 0.2, k = 0.18, Up, \alpha = 13.02^0)$

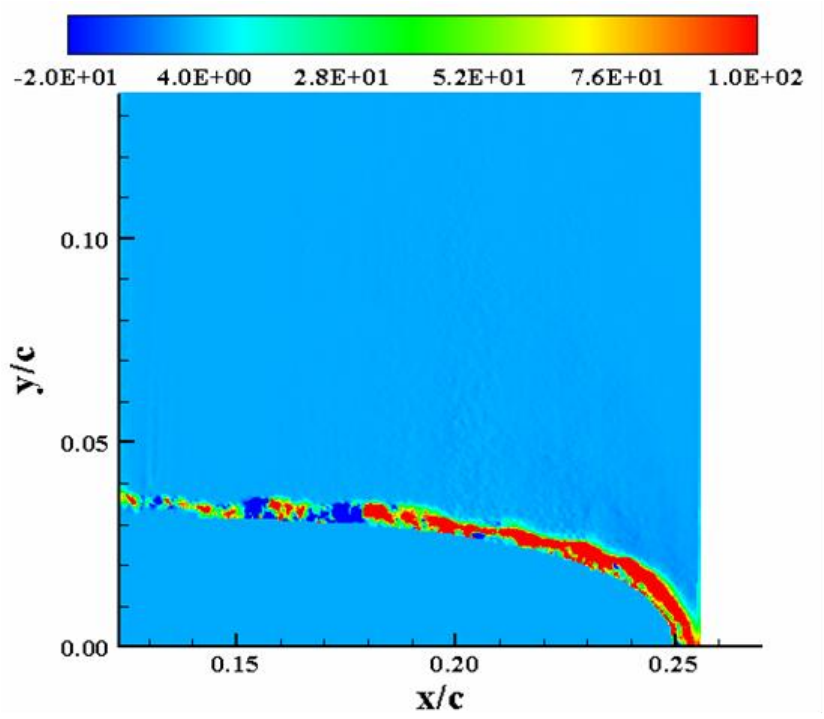

Figure D-19: $P_{xx}(M_\infty = 0.2, k = 0.18, Up, \alpha = 9.19^0)$

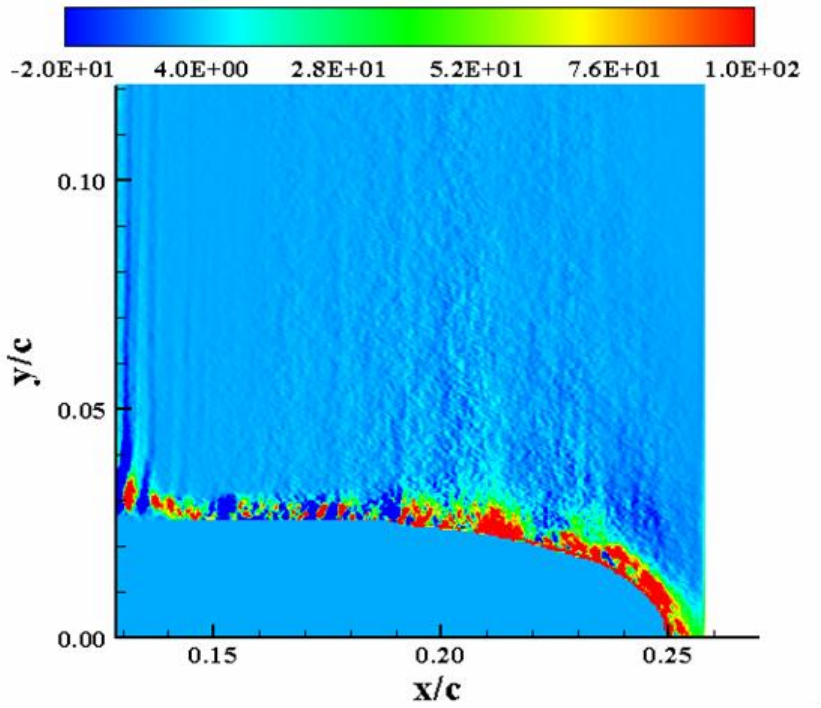

Figure D-20: $P_{xx}(M_\infty = 0.2, k = 0.18, Up, \alpha = 11.1^0)$

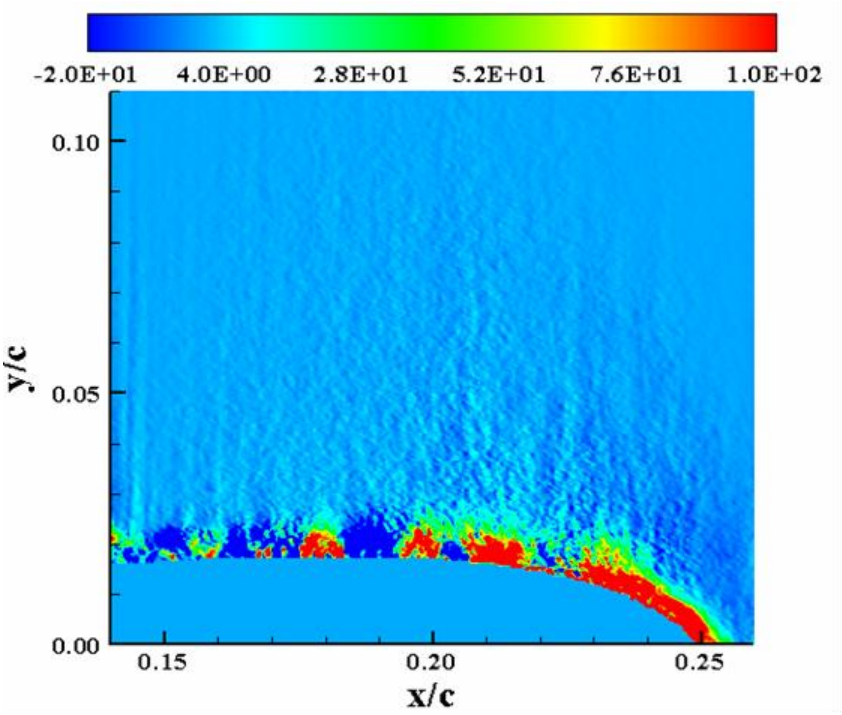

Figure D-21: $P_{xx}(M_\infty = 0.2, k = 0.18, Up, \alpha = 13.02^0)$

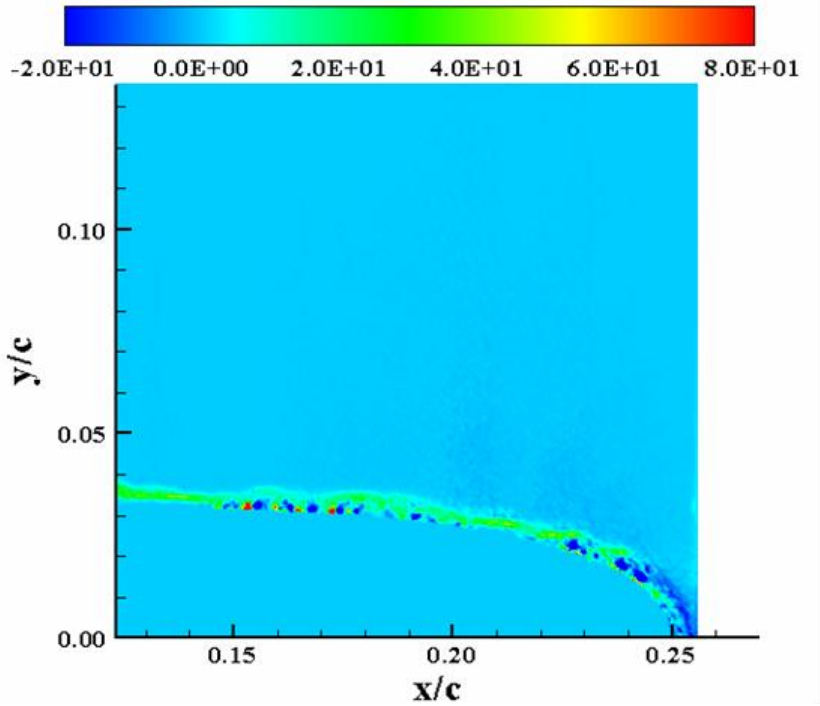

Figure D-22: $P_{xy}(M_\infty = 0.2, k = 0.18, Up, \alpha = 9.19^0)$

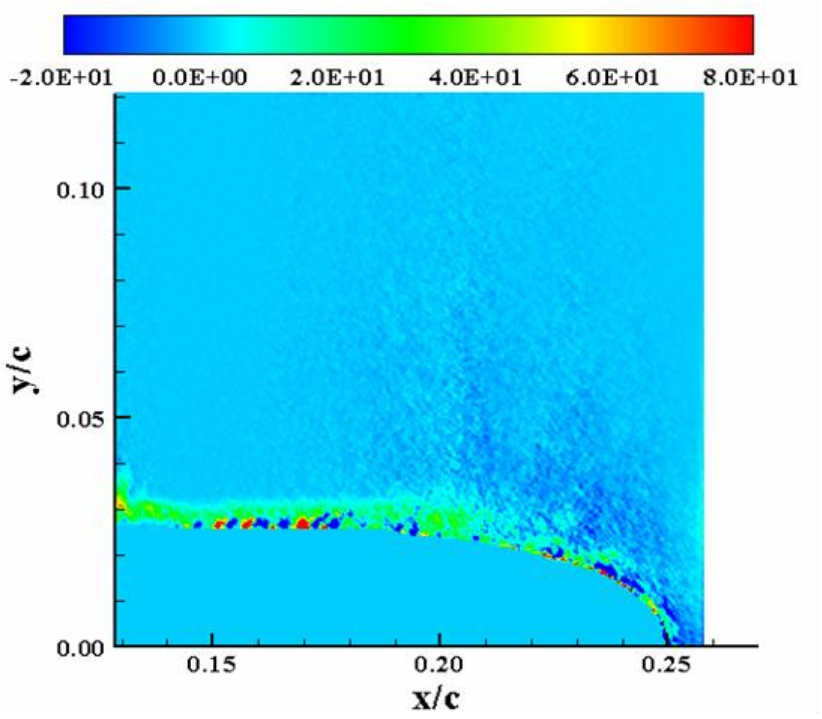

Figure D-23: $P_{xy}(M_\infty = 0.2, k = 0.18, Up, \alpha = 11.1^0)$

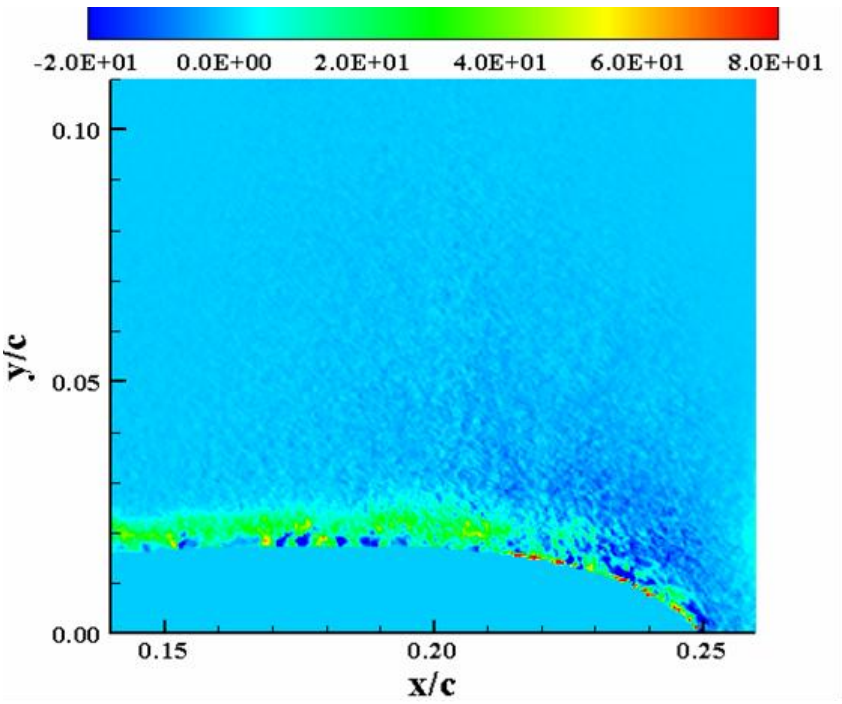

Figure D-24: $P_{xy}(M_\infty = 0.2, k = 0.18, Up, \alpha = 13.02^0)$

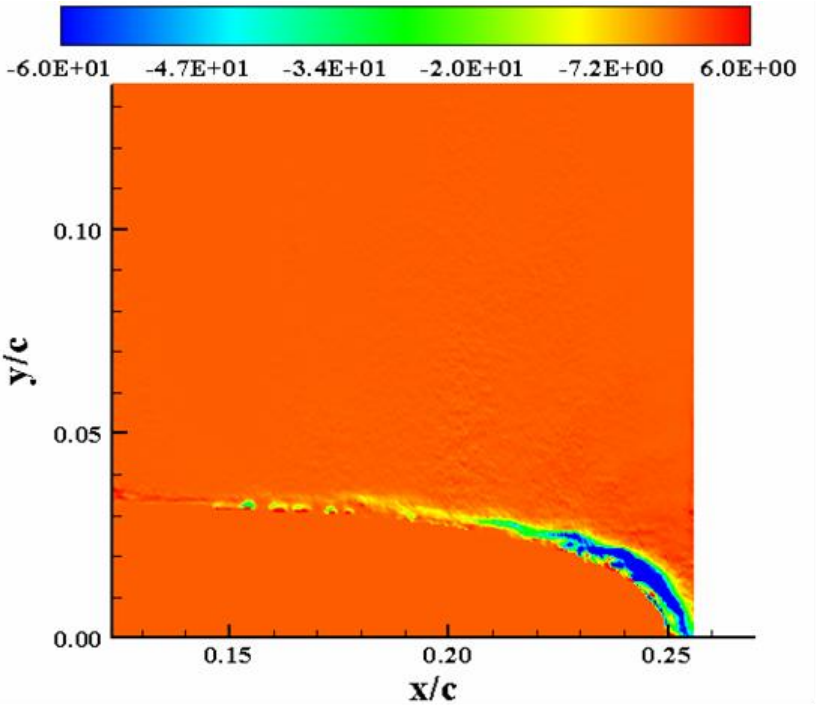

Figure D-25: $P_{yy}(M_\infty = 0.2, k = 0.18, Up, \alpha = 9.19^0)$

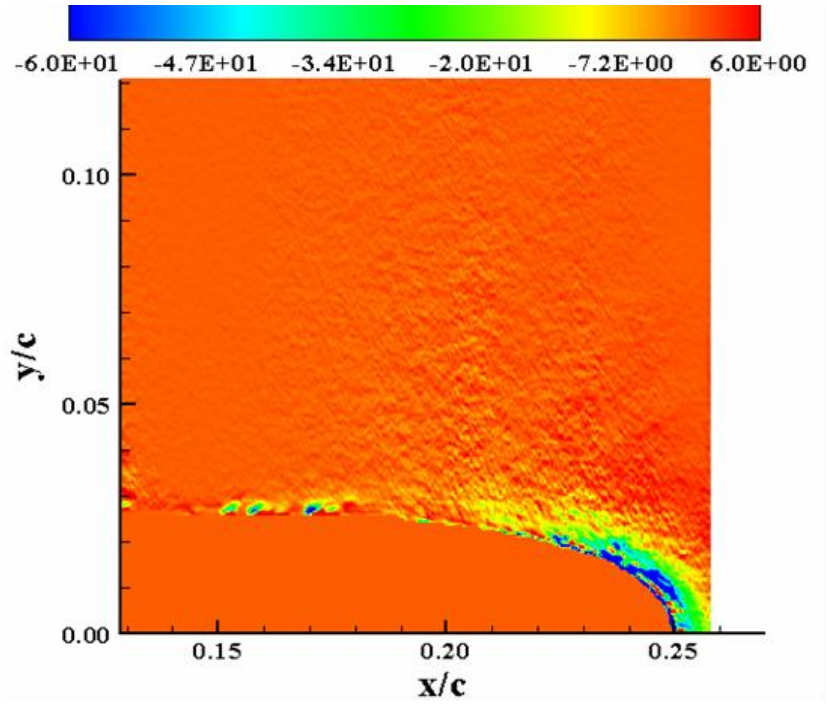

Figure D-26: $P_{yy}(M_\infty = 0.2, k = 0.18, Up, \alpha = 11.1^0)$

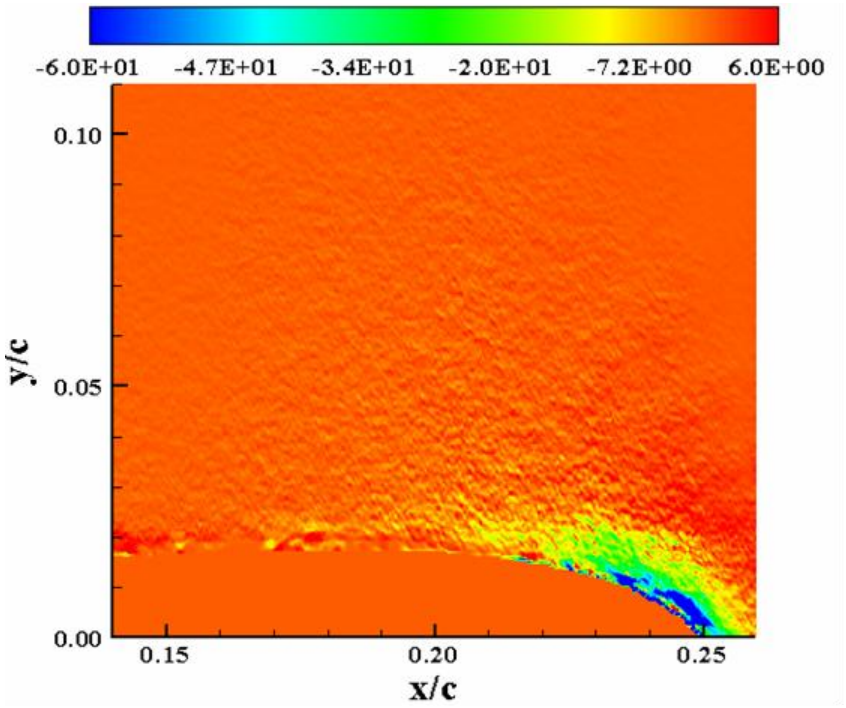

Figure D-27: $P_{yy}(M_\infty = 0.2, k = 0.18, Up, \alpha = 13.02^0)$

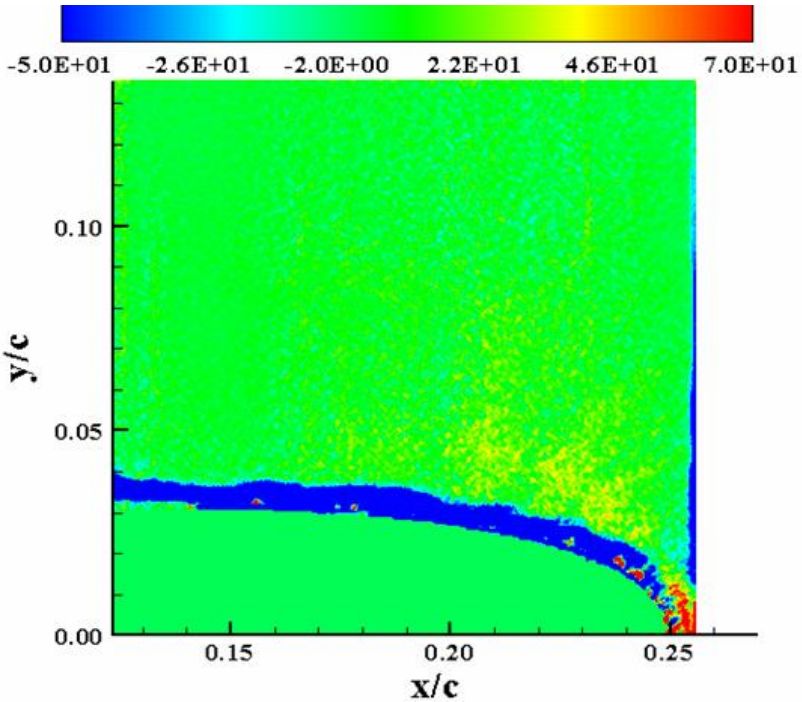

Figure D-28: $S_{xy}(M_\infty = 0.2, k = 0.18, Up, \alpha = 9.19^0)$

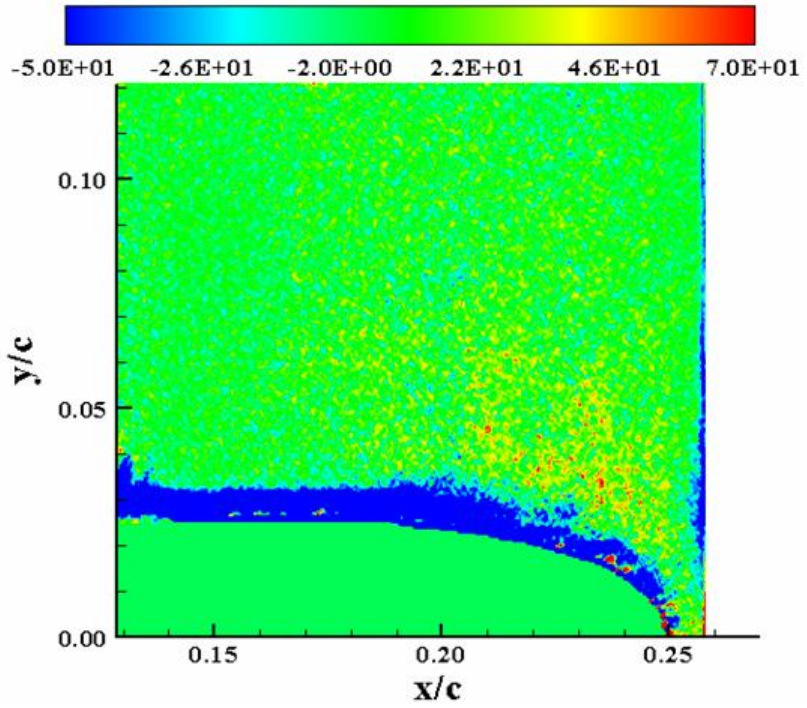

Figure D-29: $S_{xy}(M_\infty = 0.2, k = 0.18, Up, \alpha = 11.1^0)$

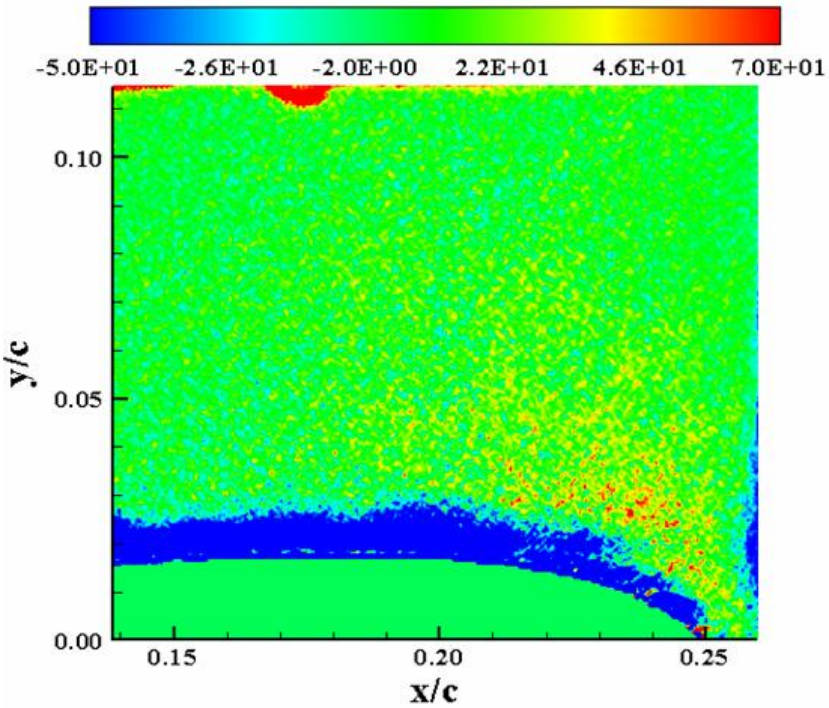

Figure D-30: $S_{xy}(M_\infty = 0.2, k = 0.18, Up, \alpha = 13.02^0)$

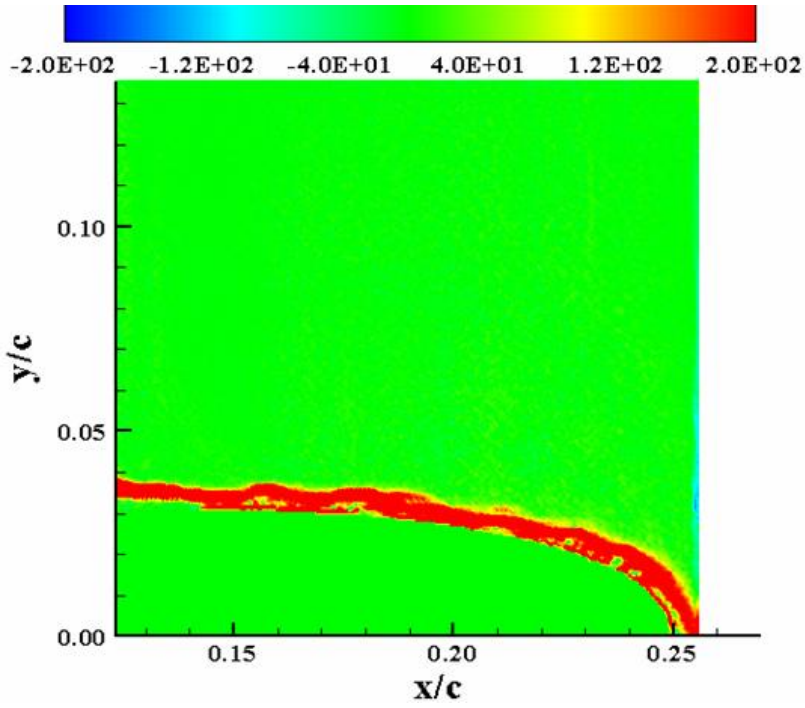

Figure D-31: $\omega_z(M_\infty = 0.2, k = 0.18, Up, \alpha = 9.19^0)$

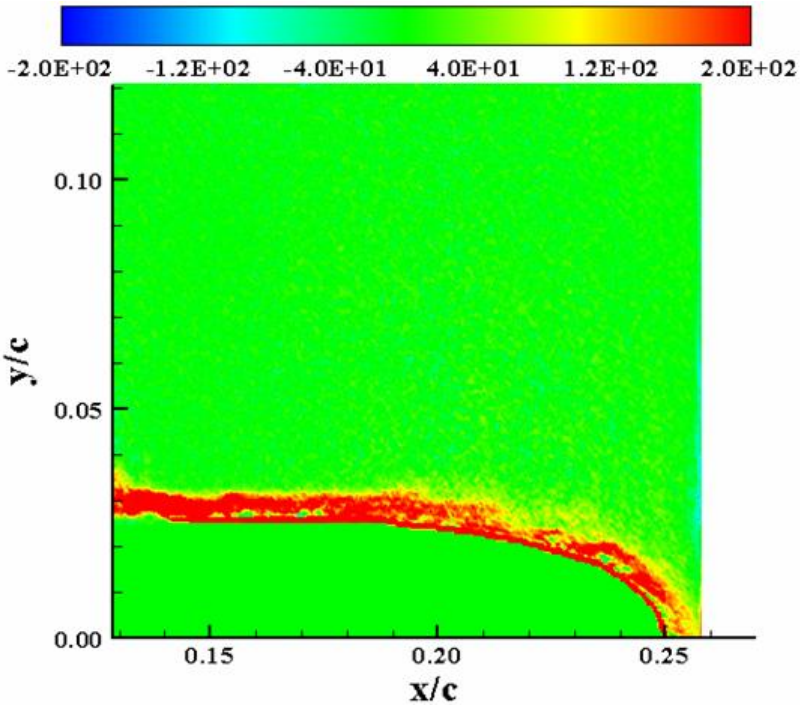

Figure D-32: $\omega_z(M_\infty = 0.2, k = 0.18, Up, \alpha = 11.1^0)$

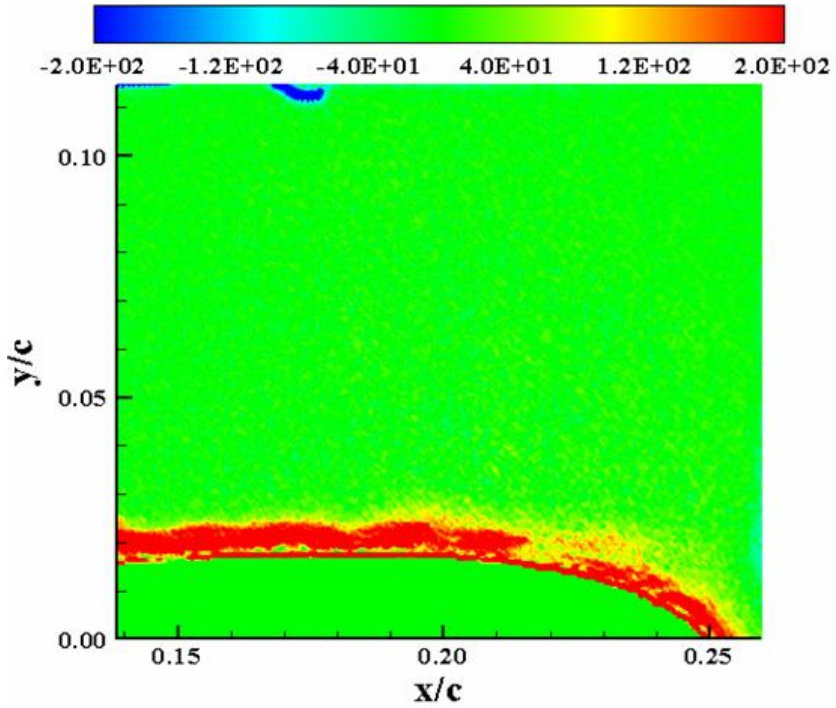

Figure D-33: $\omega_z (M_\infty = 0.2, k = 0.18, Up, \alpha = 13.02^0)$

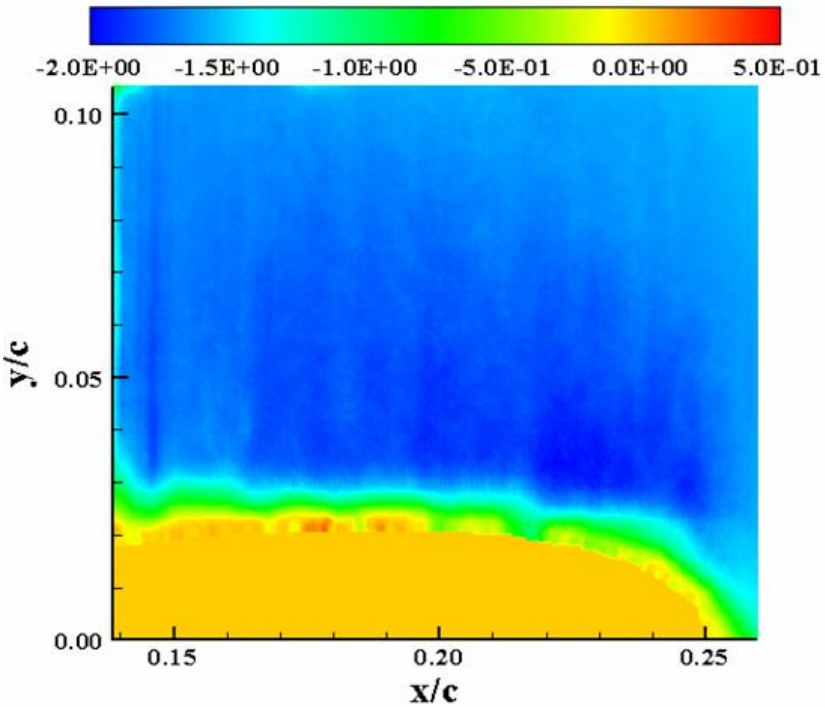

Figure D-34: $U_N (M_\infty = 0.2, k = 0.1, Down, \alpha = 13.02^0)$

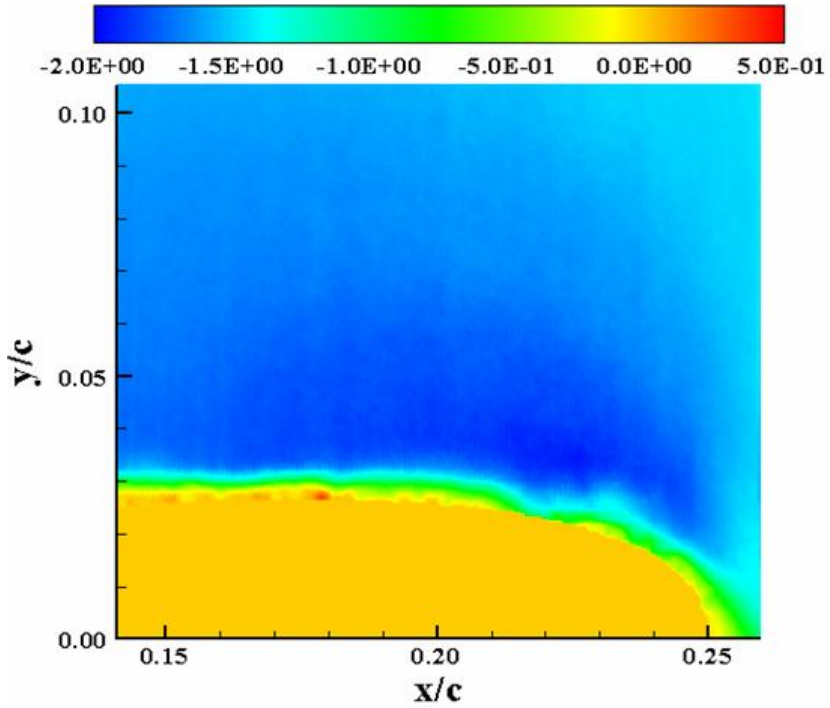

Figure D-35: $U_N(M_\infty = 0.2, k = 0.18, Down, \alpha = 11.1^0)$

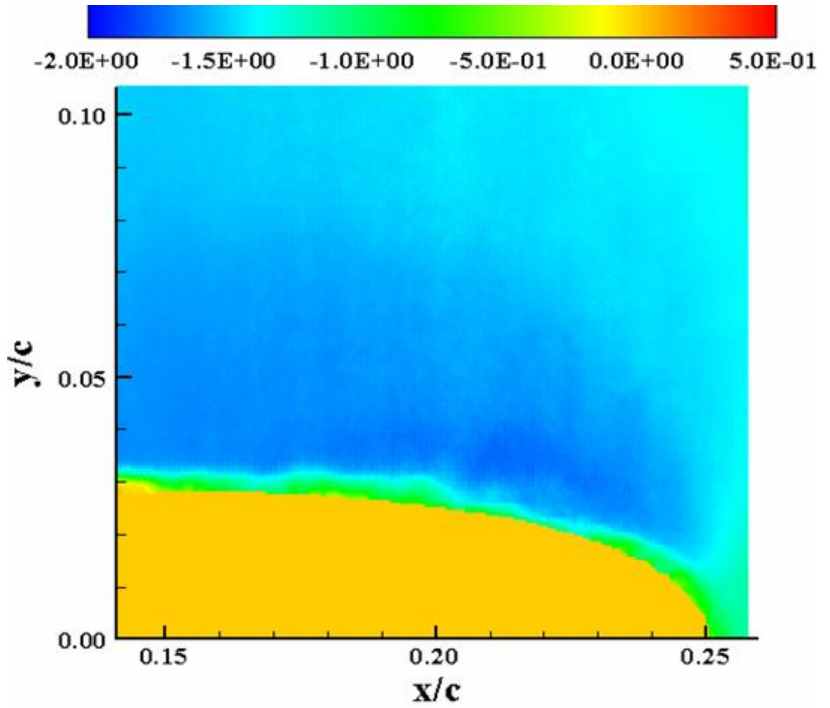

Figure D-36: $U_N(M_\infty = 0.2, k = 0.18, Down, \alpha = 9.19^0)$

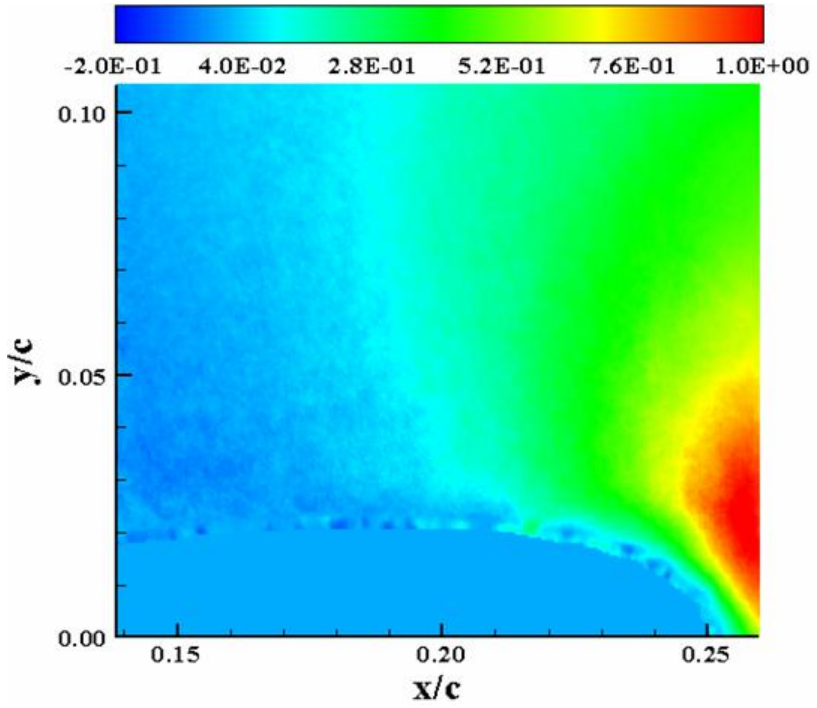

Figure D-37: $V_N\,(M_\infty = 0.2, k = 0.18, Down, \alpha = 13.02^0)$

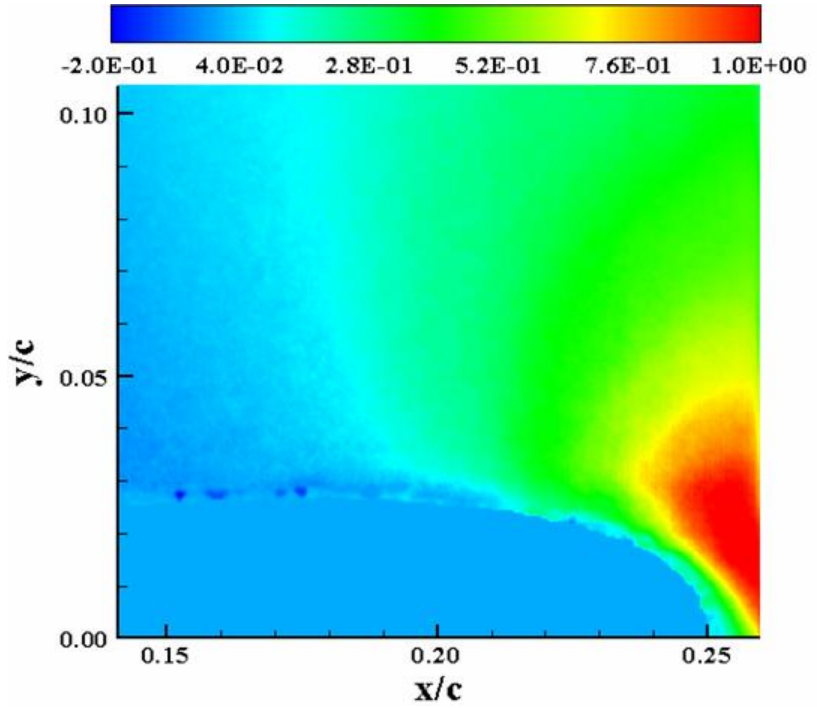

Figure D-38: $V_N\,(M_\infty = 0.2, k = 0.18, Down, \alpha = 11.1^0)$

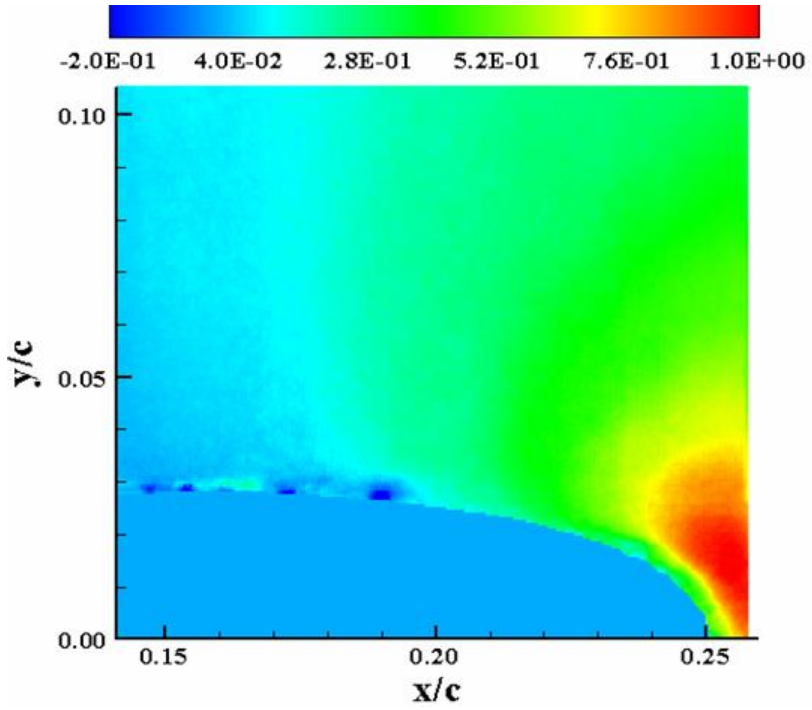

Figure D-39: $V_N\,(M_\infty = 0.2, k = 0.18, Down, \alpha = 9.19^0)$

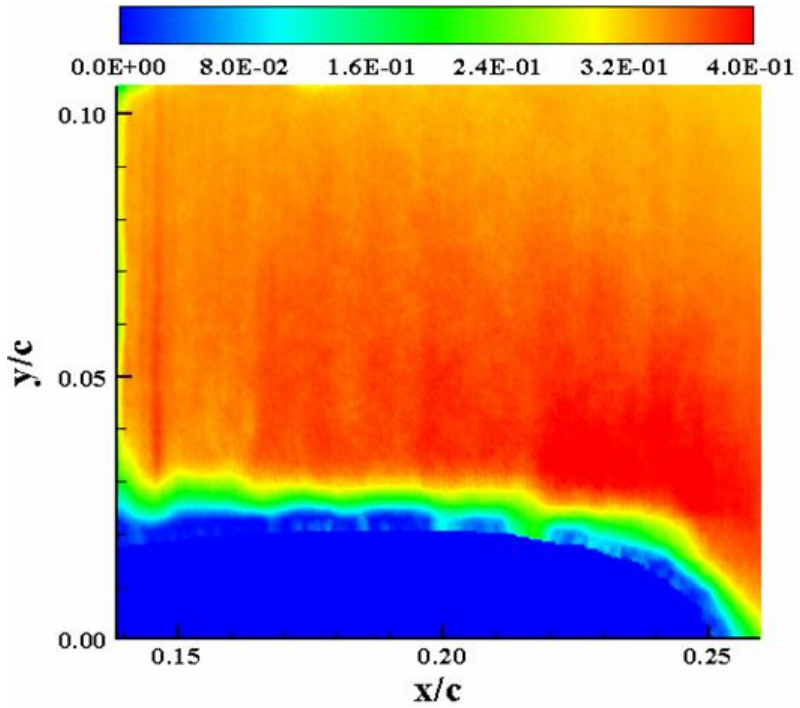

Figure D-40: $M(M_\infty = 0.2, k = 0.18, Down, \alpha = 13.02^0)$

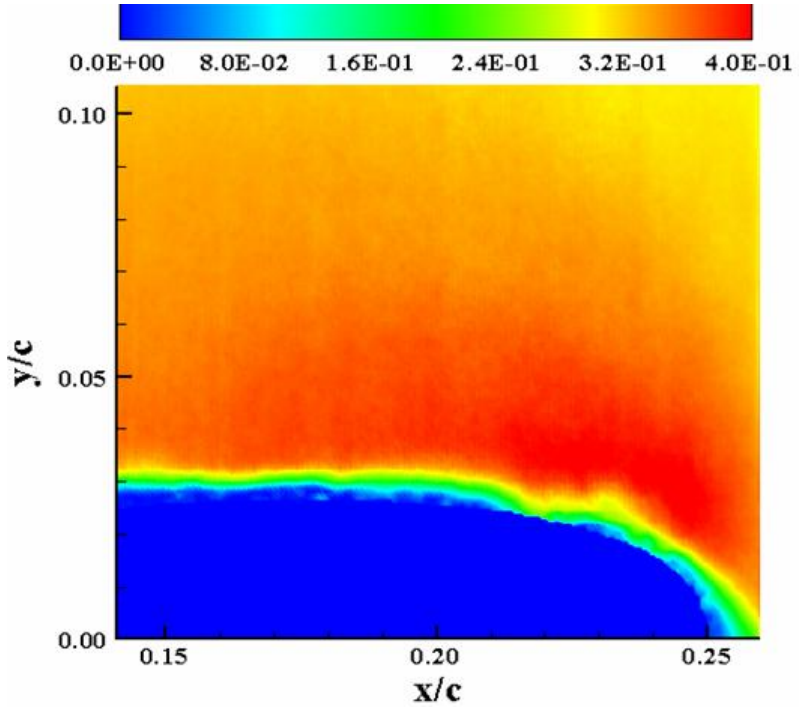

Figure D-41: $M(M_\infty = 0.2, k = 0.18, Down, \alpha = 11.1^0)$

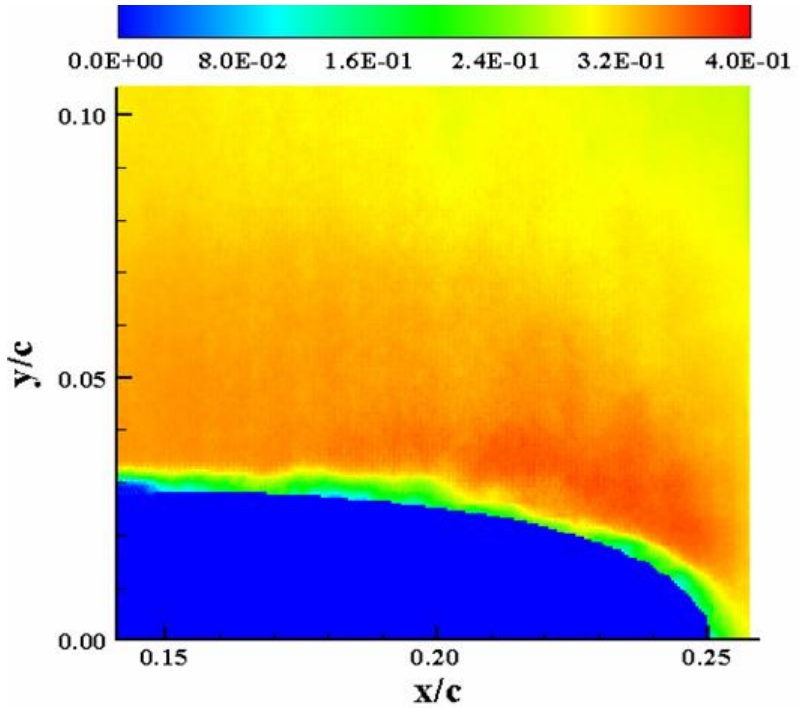

Figure D-42: $M(M_\infty = 0.2, k = 0.18, Down, \alpha = 9.19^0)$

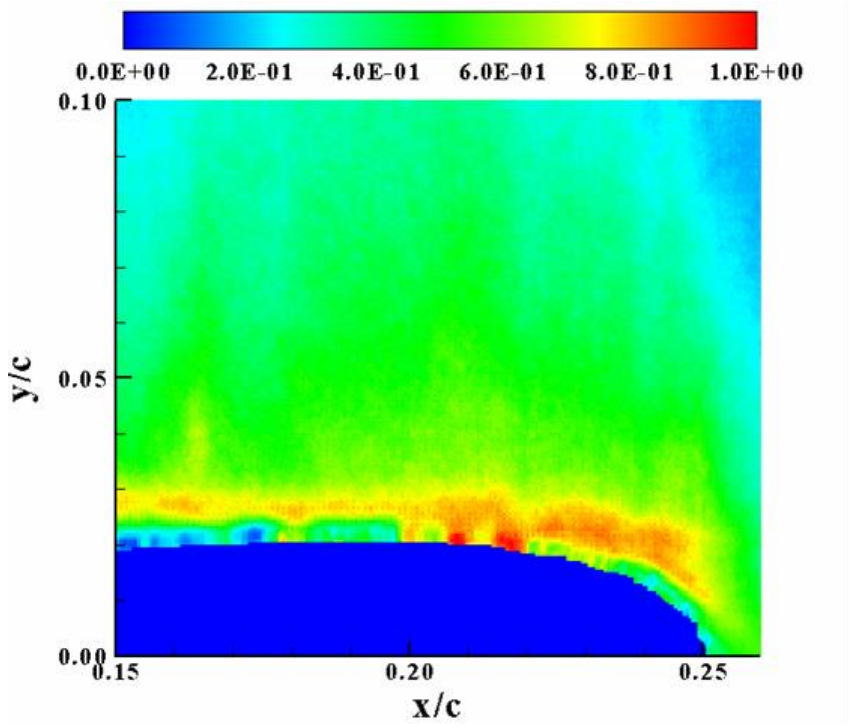

Figure D-43: $\sigma_u(M_\infty = 0.2, k = 0.18, Down, \alpha = 13.02^0)$

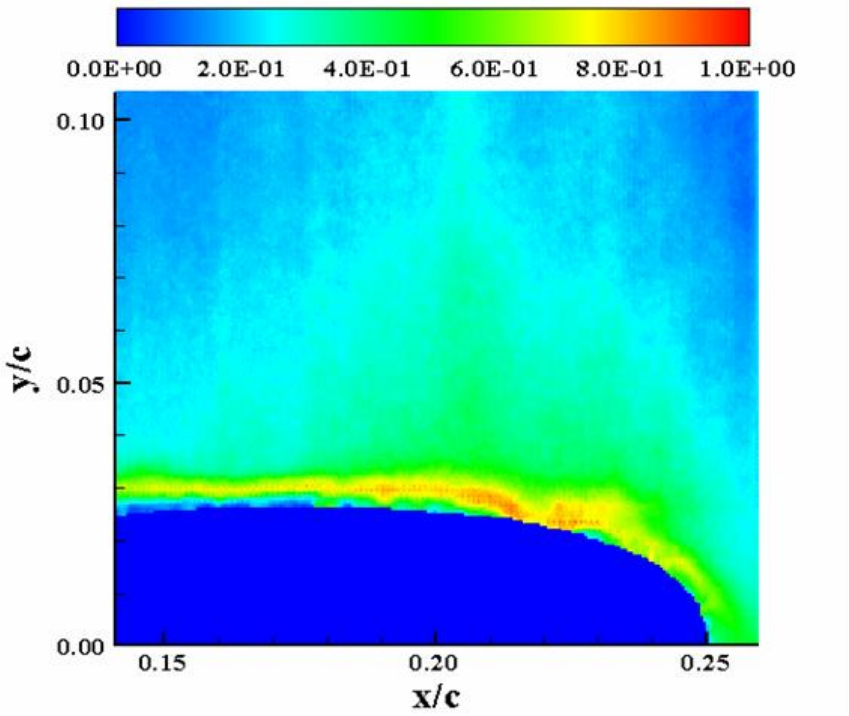

Figure D-44: $\sigma_u(M_\infty = 0.2, k = 0.18, Down, \alpha = 11.1^0)$

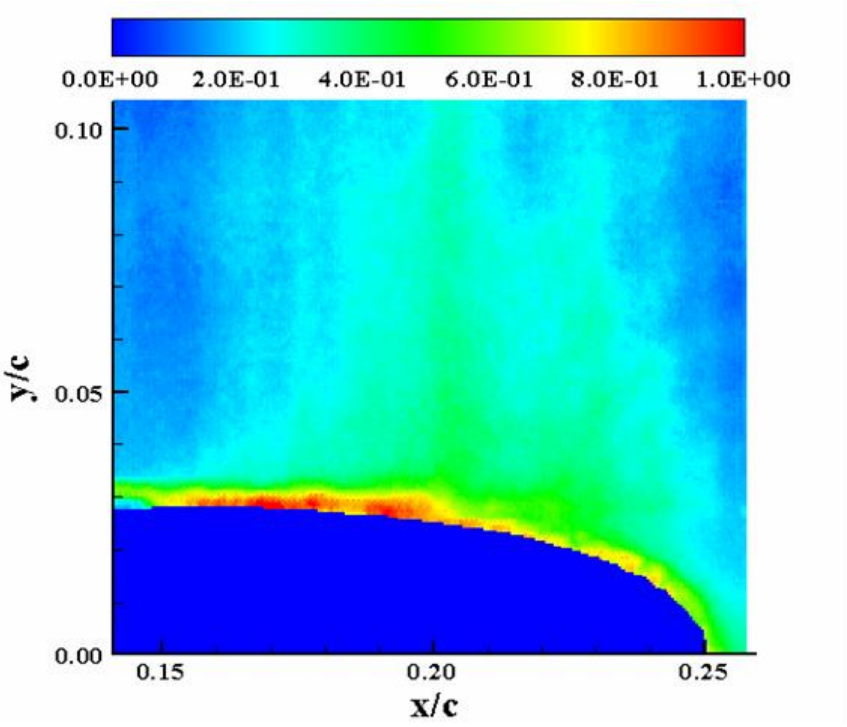

Figure D-45: $\sigma_u(M_\infty = 0.2, k = 0.18, Down, \alpha = 9.19^0)$

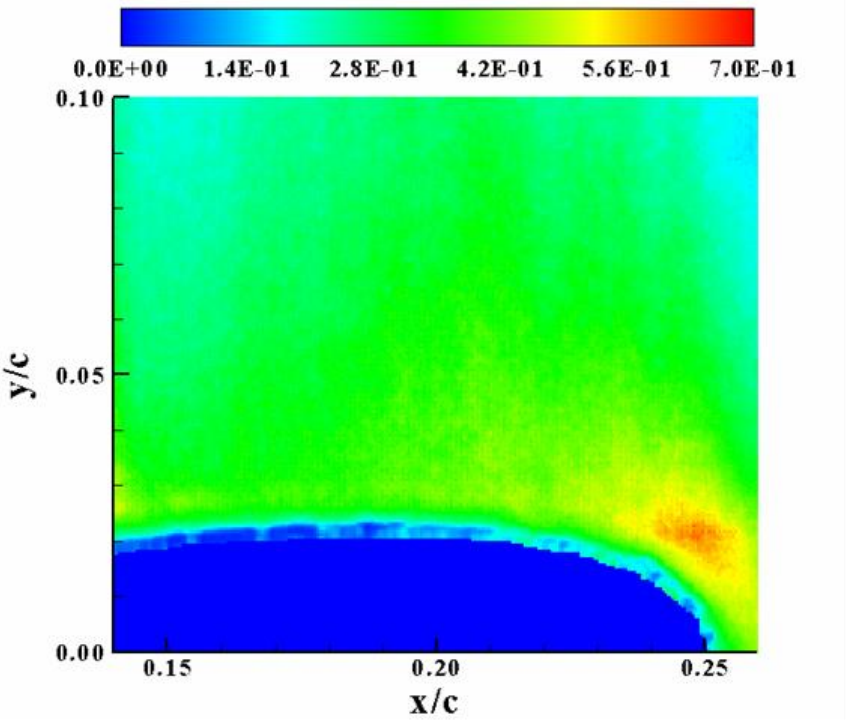

Figure D-46: $\sigma_v(M_\infty = 0.2, k = 0.18, Down, \alpha = 13.02^0)$

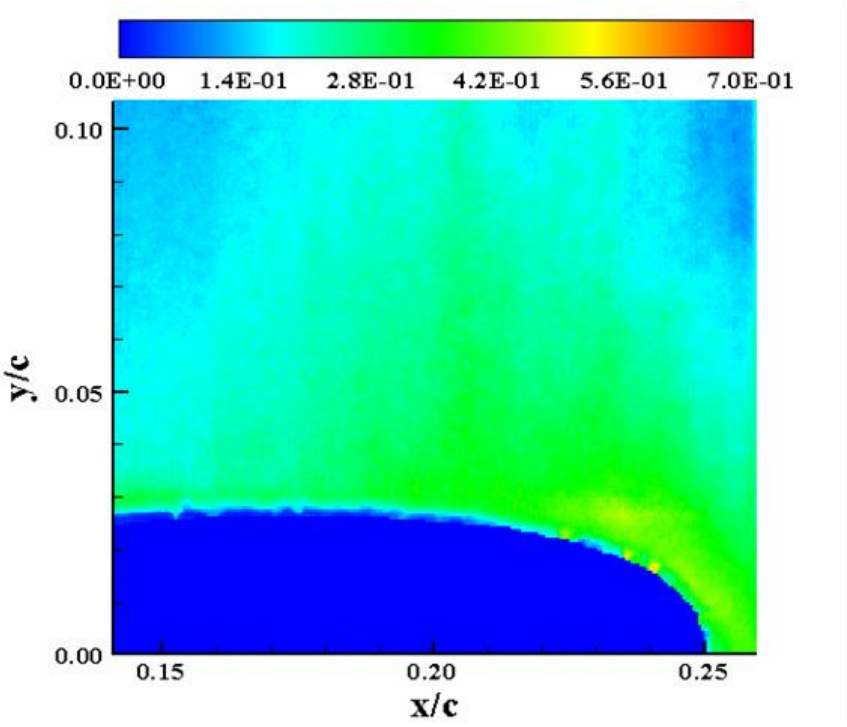

Figure D-47: $\sigma_v (M_\infty = 0.2, k = 0.18, Down, \alpha = 11.1^0)$

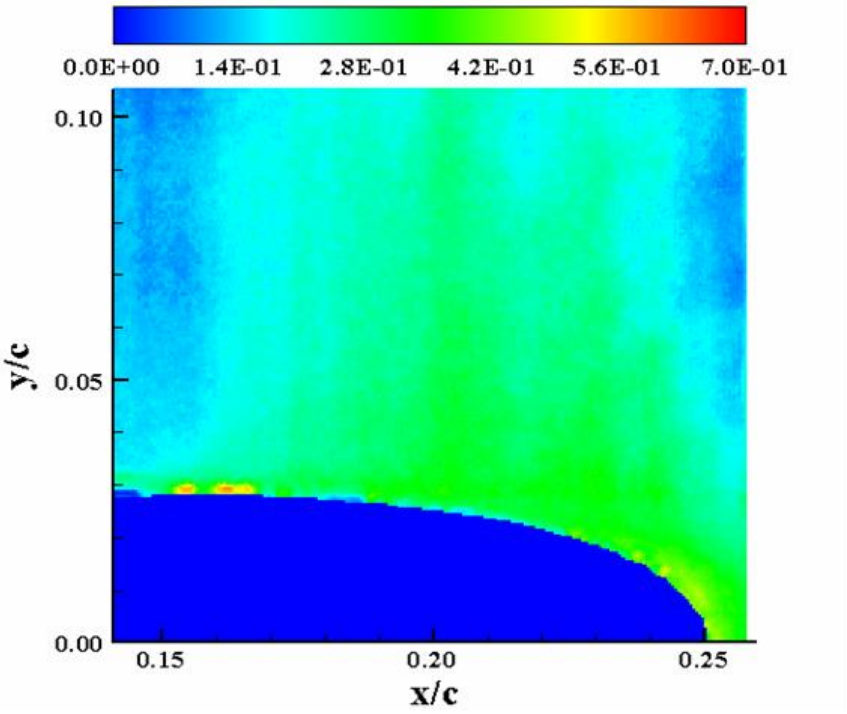

Figure D-48: $\sigma_v (M_\infty = 0.2, k = 0.18, Down, \alpha = 9.19^0)$

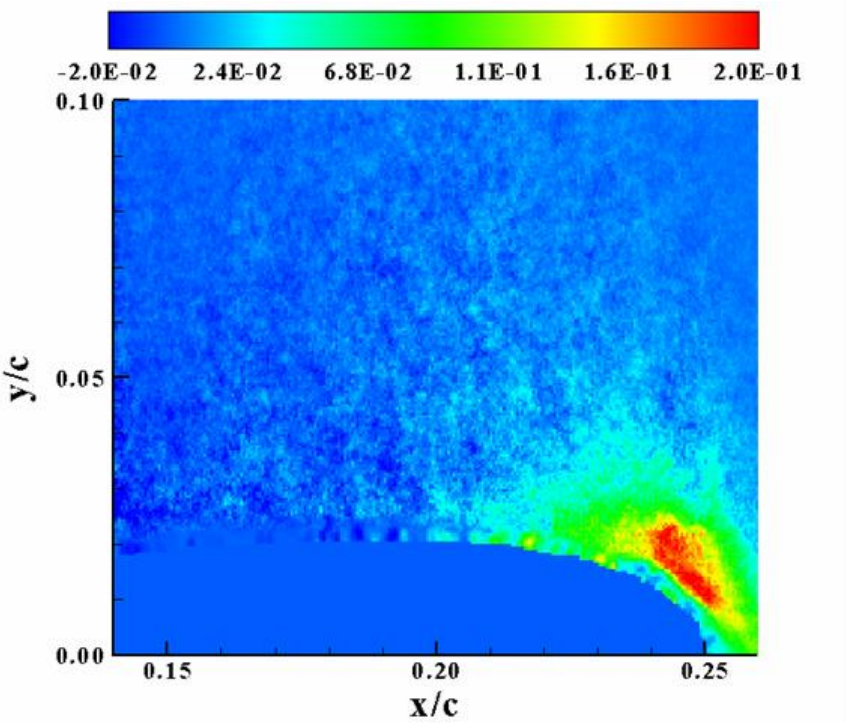

Figure D-49: $\tau_{xy}(M_\infty = 0.2, k = 0.18, Down, \alpha = 13.02^0)$

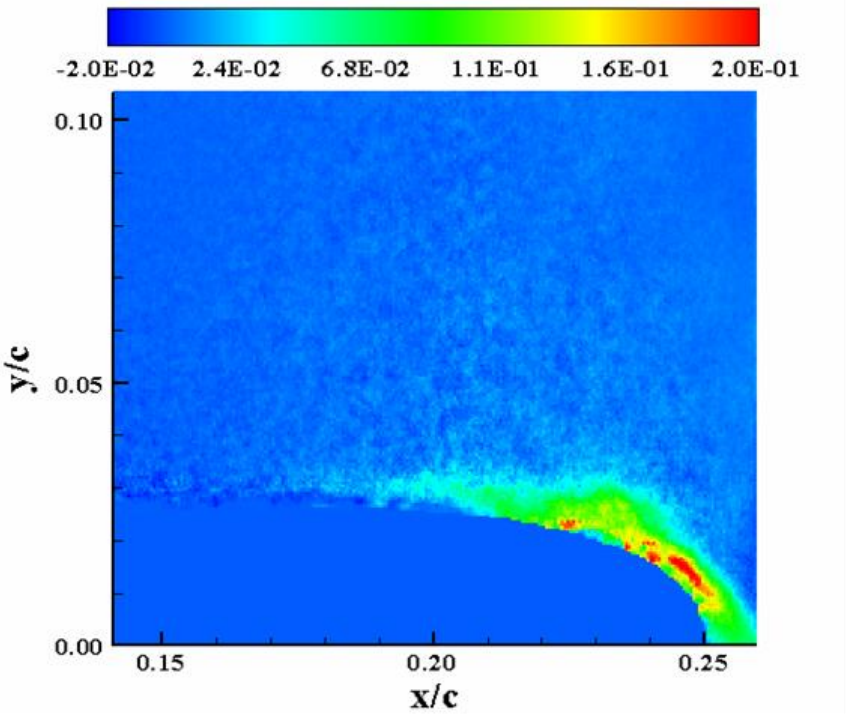

Figure D-50: $\tau_{xy}(M_\infty = 0.2, k = 0.18, Down, \alpha = 11.1^0)$

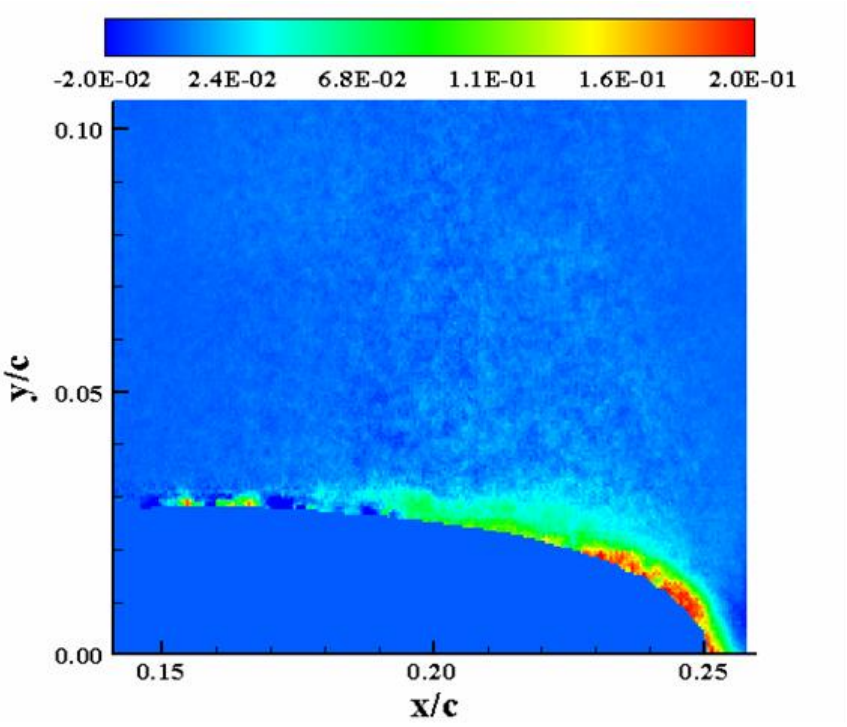

Figure D-51: $\tau_{xy}(M_\infty = 0.2, k = 0.18, Down, \alpha = 9.19^0)$

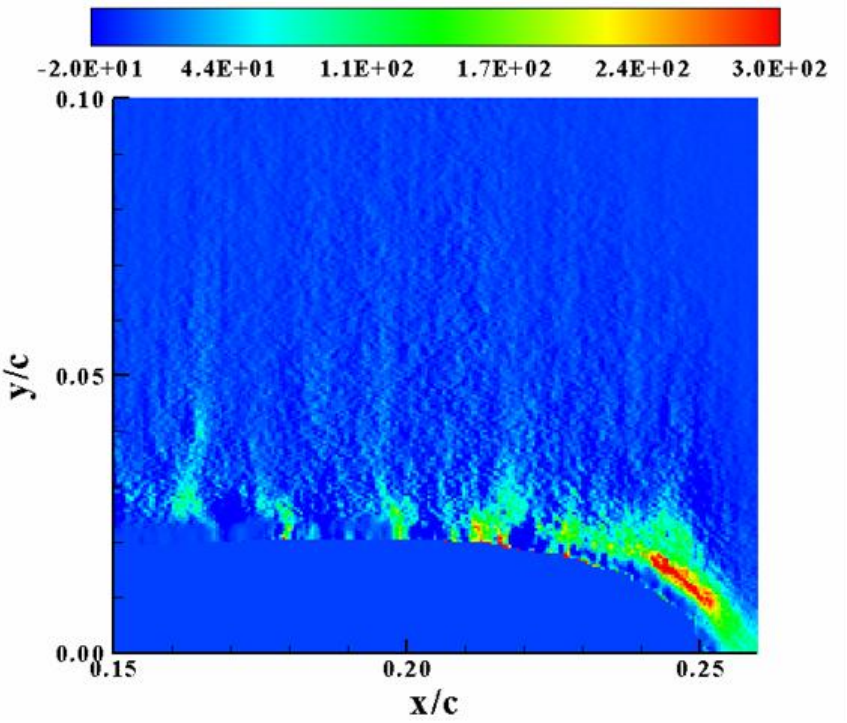

Figure D-52: $P_{xx}(M_\infty = 0.2, k = 0.18, Down, \alpha = 13.02^0)$

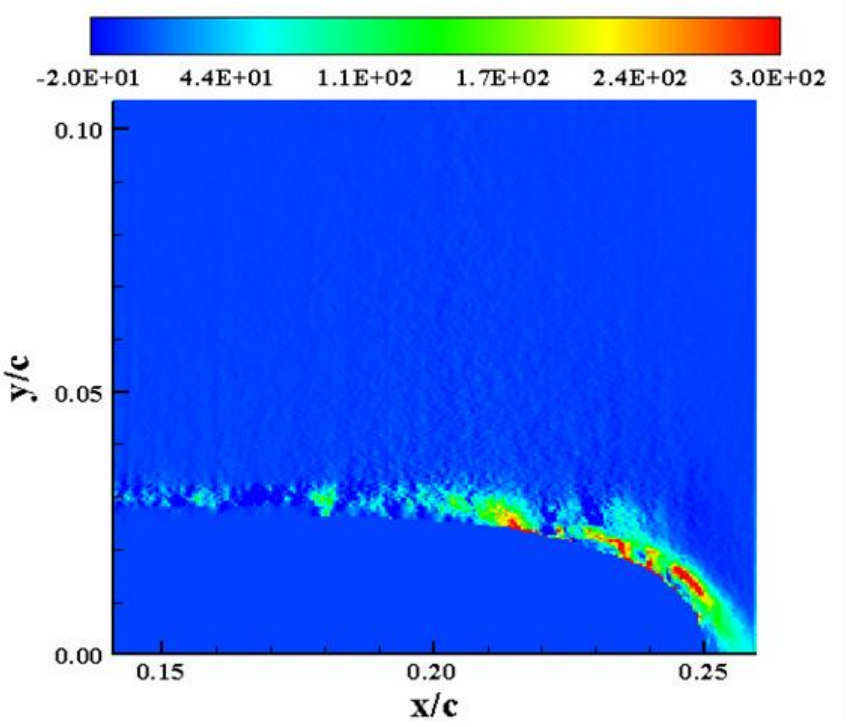

Figure D-53: $P_{xx}(M_\infty = 0.2, k = 0.18, Down, \alpha = 11.1^0)$

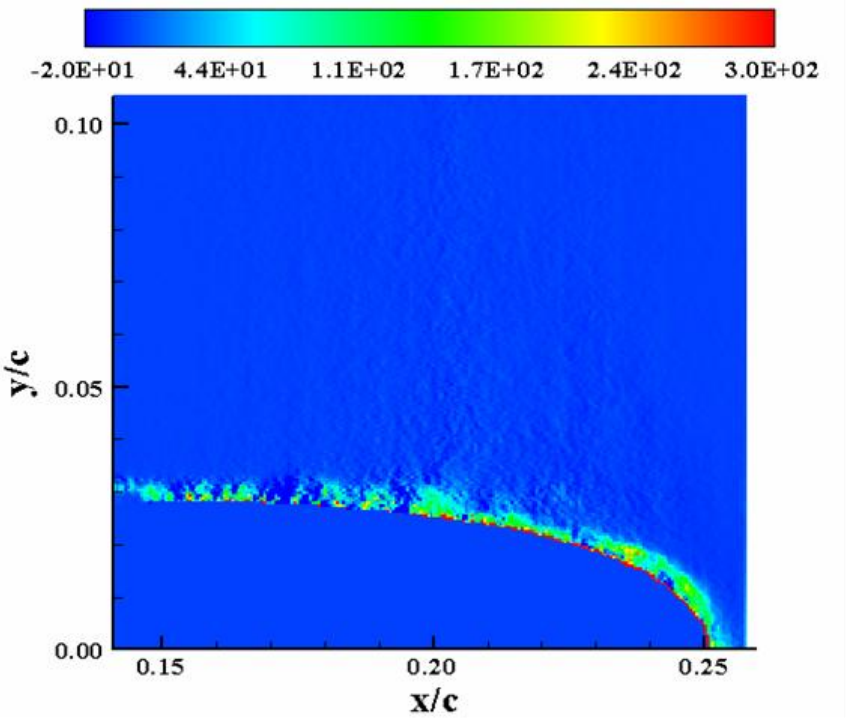

Figure D-54: $P_{xx}(M_\infty = 0.2, k = 0.18, Down, \alpha = 9.19^0)$

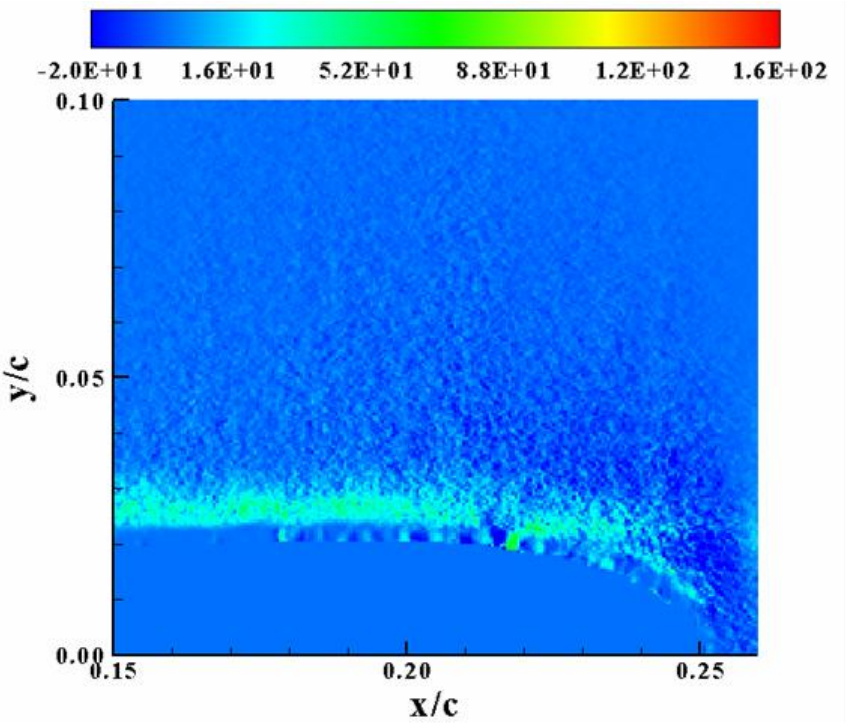

Figure D-55: $P_{xy}(M_\infty = 0.2, k = 0.18, Down, \alpha = 13.02^0)$

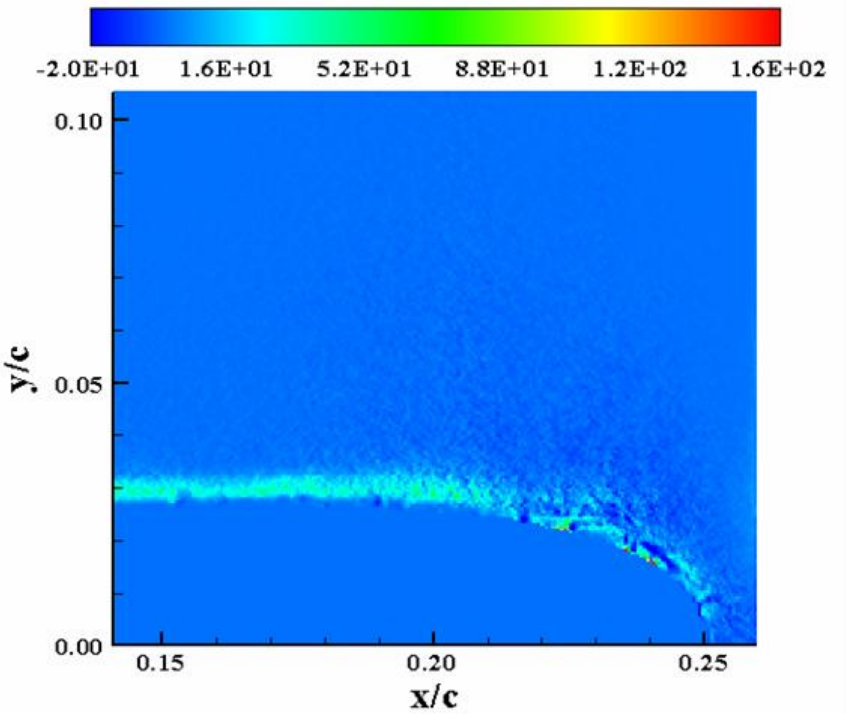

Figure D-56: $P_{xy}(M_\infty = 0.2, k = 0.18, Down, \alpha = 11.1^0)$

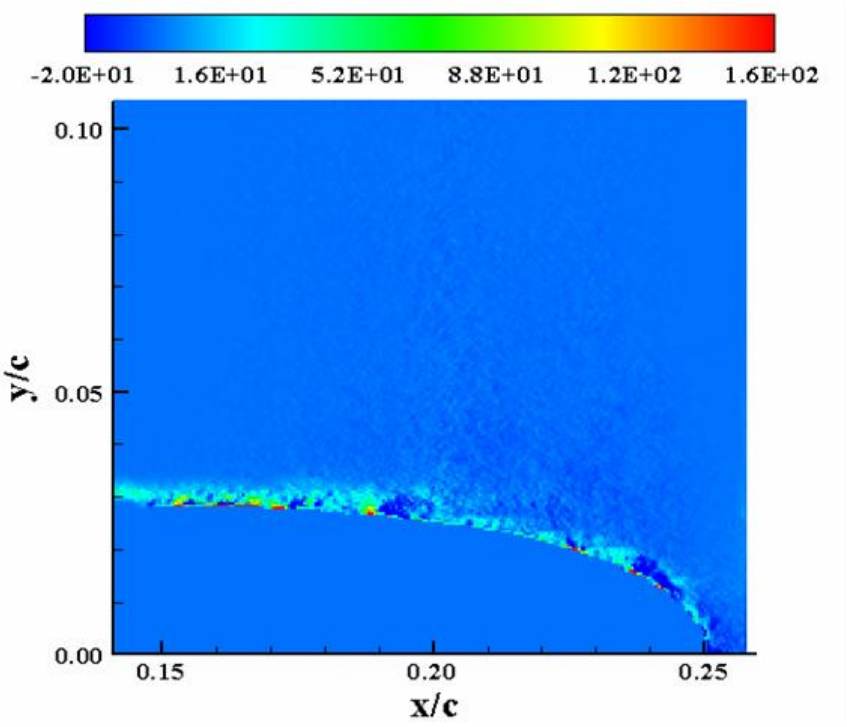

Figure D-57: $P_{xy}(M_\infty = 0.2, k = 0.18, Down, \alpha = 9.19^0)$

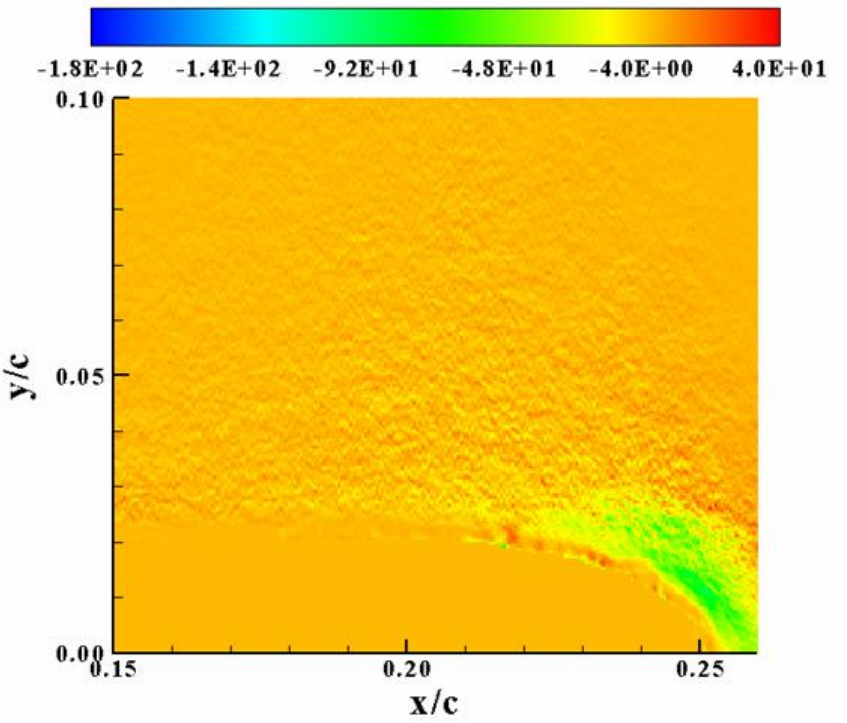

Figure D-58: $P_{yy}(M_\infty = 0.2, k = 0.18, Down, \alpha = 13.02^0)$

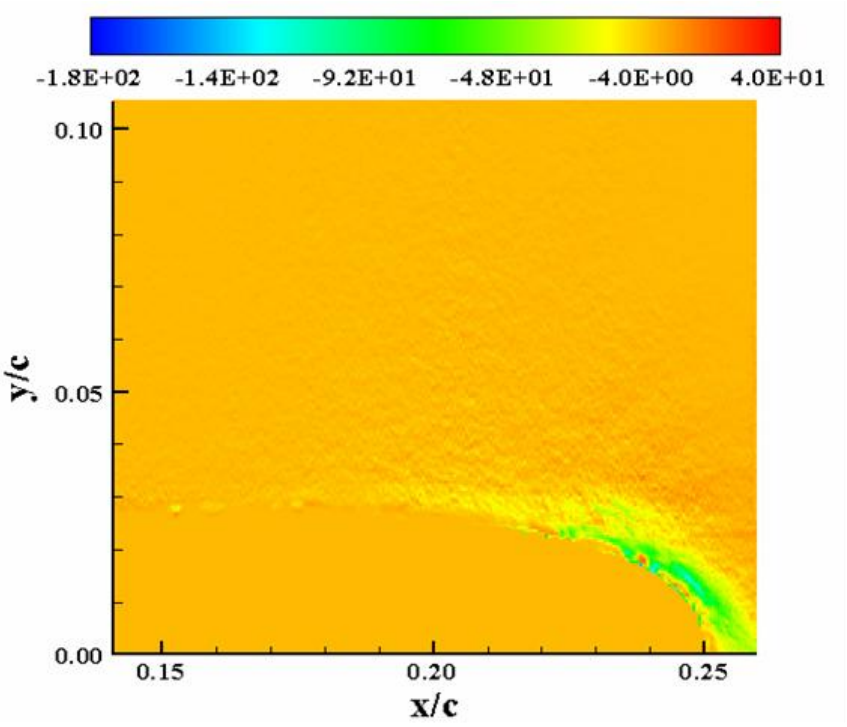

Figure D-59: $P_{yy}(M_\infty = 0.2, k = 0.18, Down, \alpha = 11.1^0)$

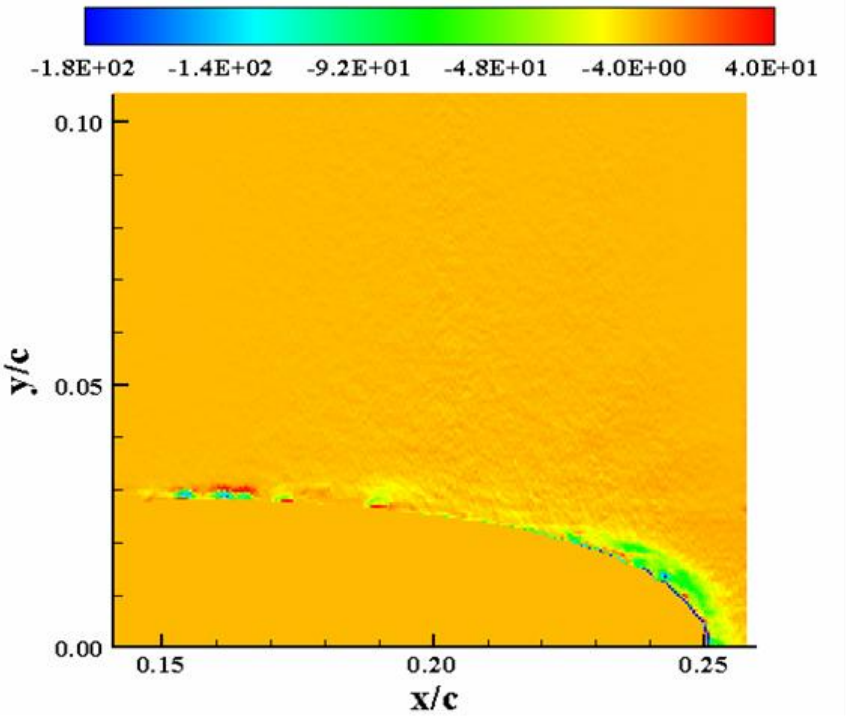

Figure D-60: $P_{yy}(M_\infty = 0.2, k = 0.18, Down, \alpha = 9.19^0)$

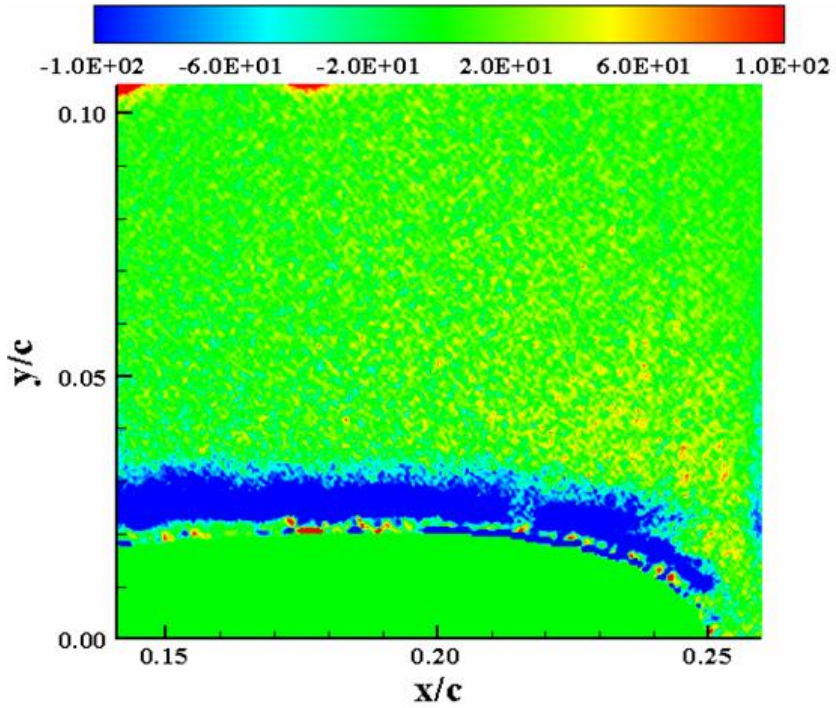

Figure D-61: $S_{xy}(M_\infty = 0.2, k = 0.18, Down, \alpha = 13.02^0)$

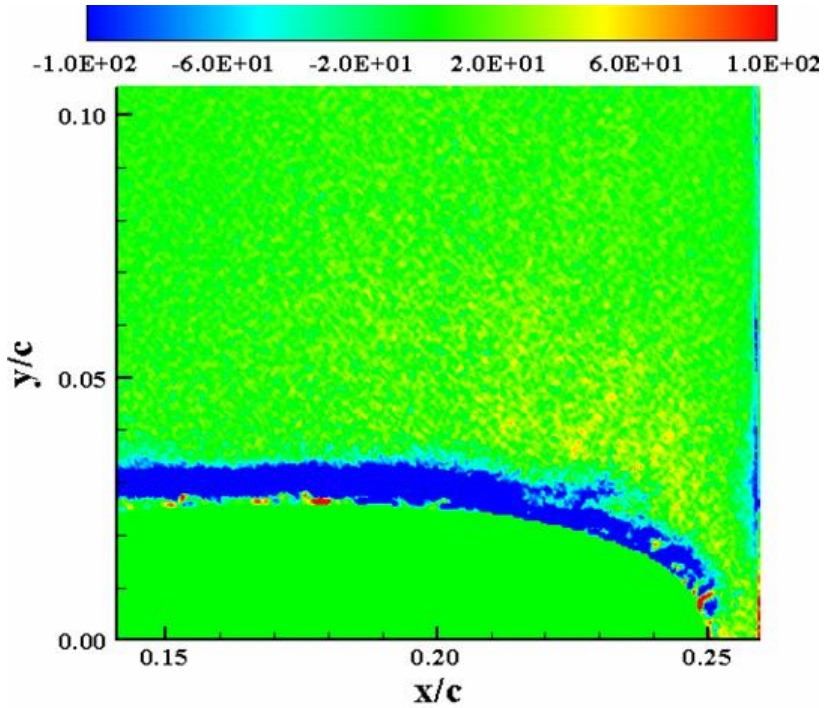

Figure D-62: $S_{xy}(M_\infty = 0.2, k = 0.18, Down, \alpha = 11.1^0)$

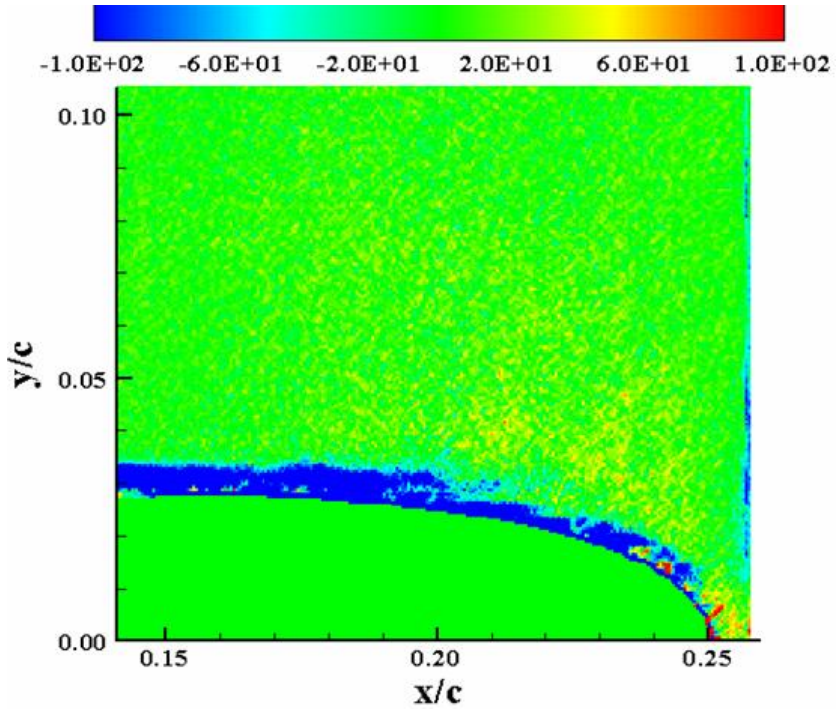

Figure D-63: $S_{xy}(M_\infty = 0.2, k = 0.18, Down, \alpha = 9.19^0)$

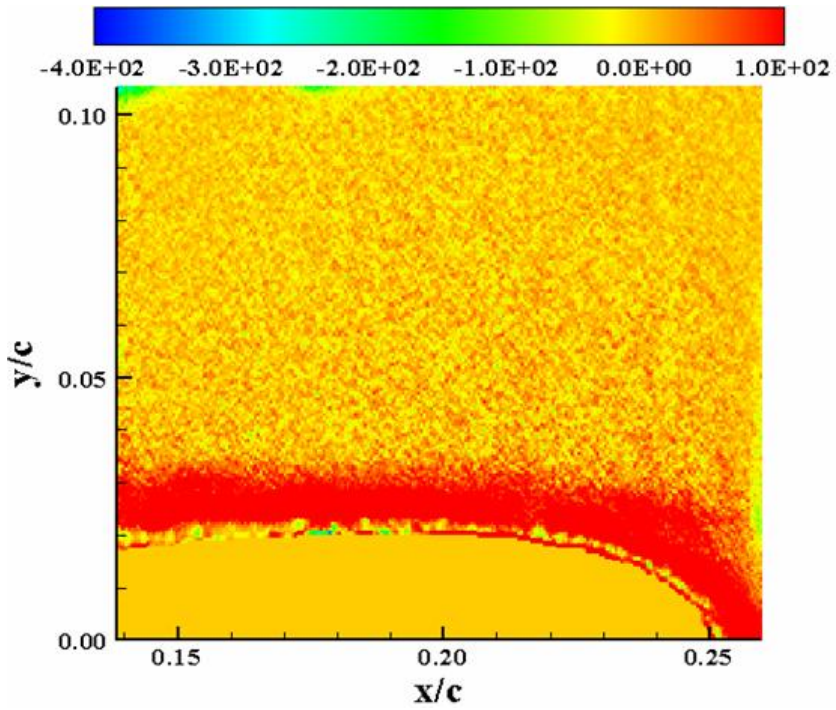

Figure D-64: $\omega_z(M_\infty = 0.2, k = 0.18, Down, \alpha = 13.02^0)$

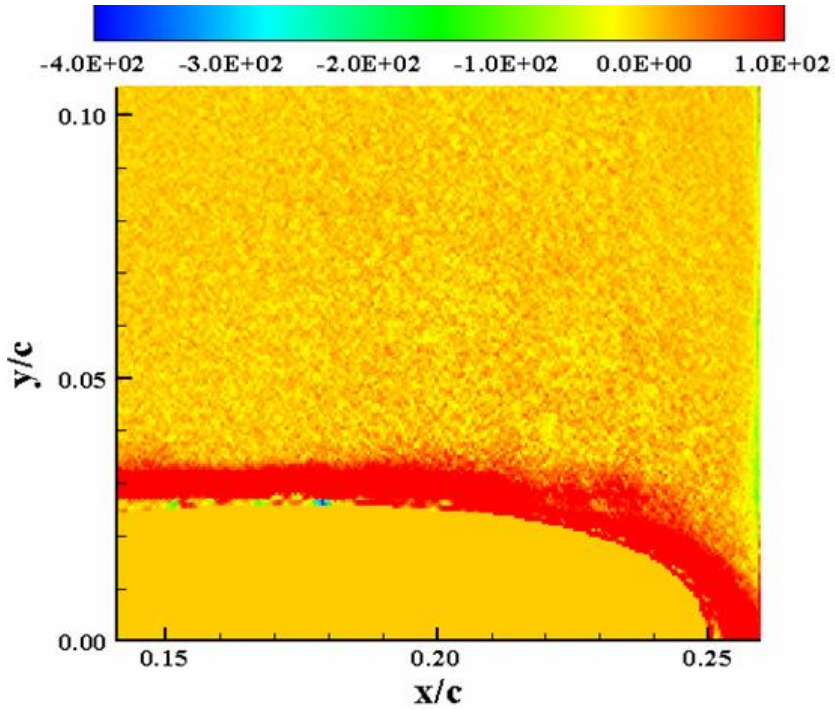

Figure D-65: $\omega_z (M_\infty = 0.2, k = 0.18, Down, \alpha = 11.1^0)$

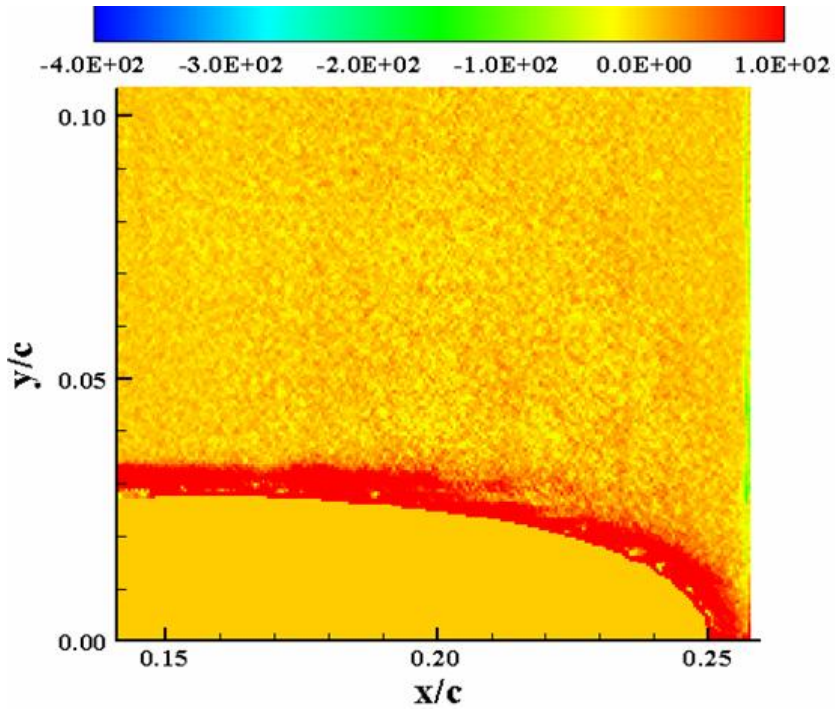

Figure D-66: $\omega_z (M_\infty = 0.2, k = 0.18, Down, \alpha = 9.19^0)$

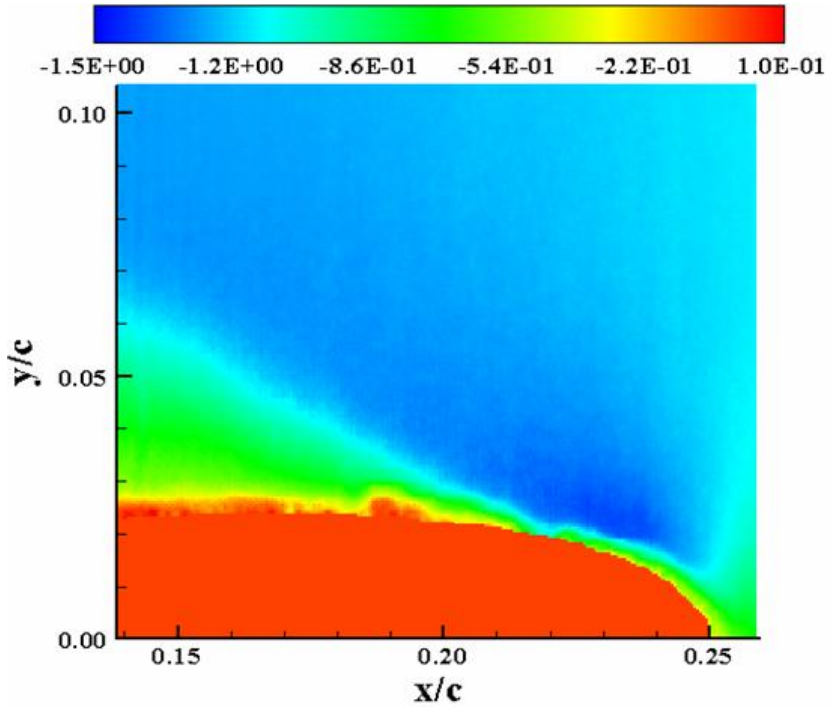

Figure D-67: $U_N(M_\infty = 0.2, k = 0.18, Up, \alpha = 13.7^0)$

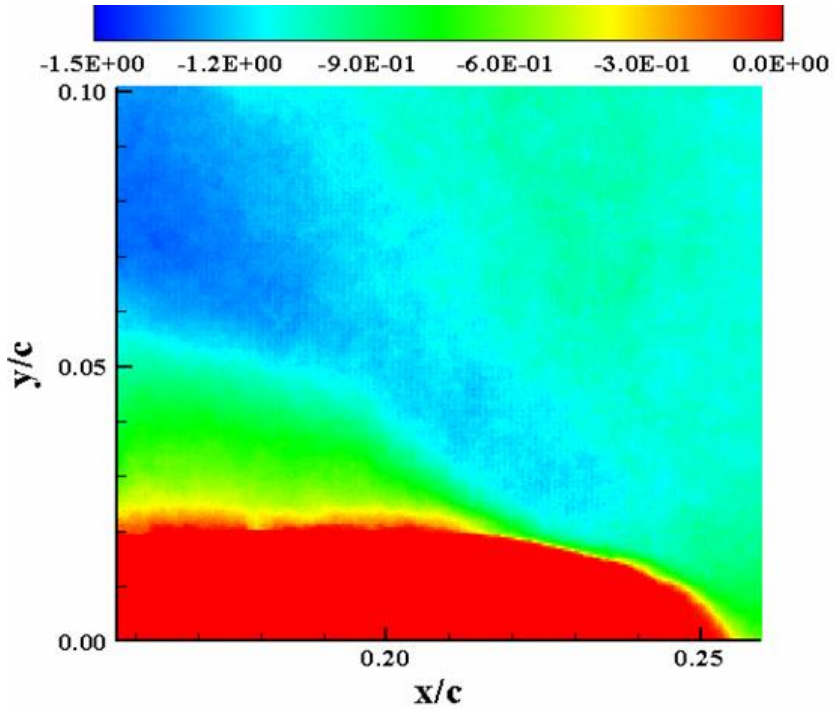

Figure D-68: $U_N(M_\infty = 0.2, k = 0.18, Up, \alpha = 15^0)$

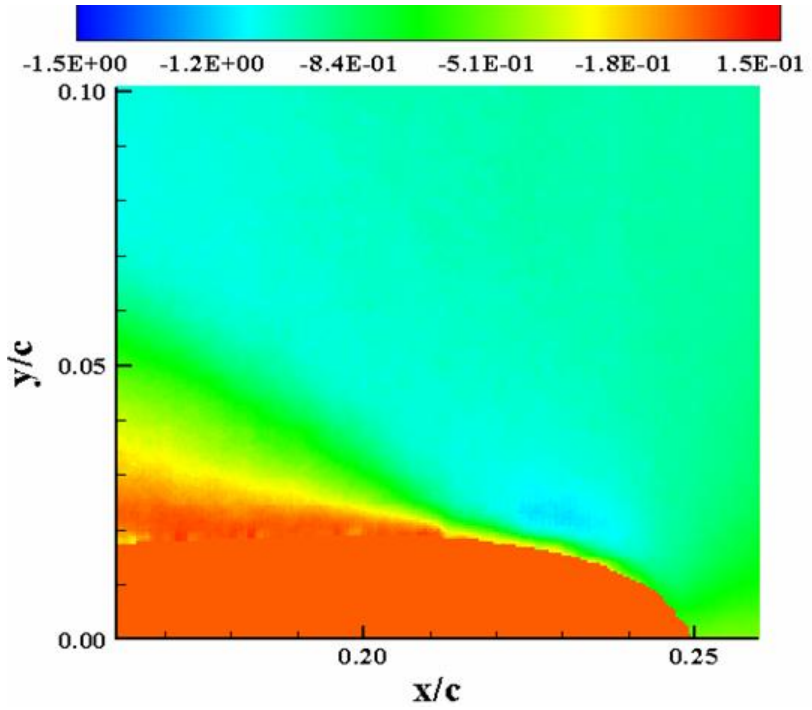

Figure D-69: $U_N\,(M_\infty = 0.2, k = 0.18, Up, \alpha = 16.88^0)$

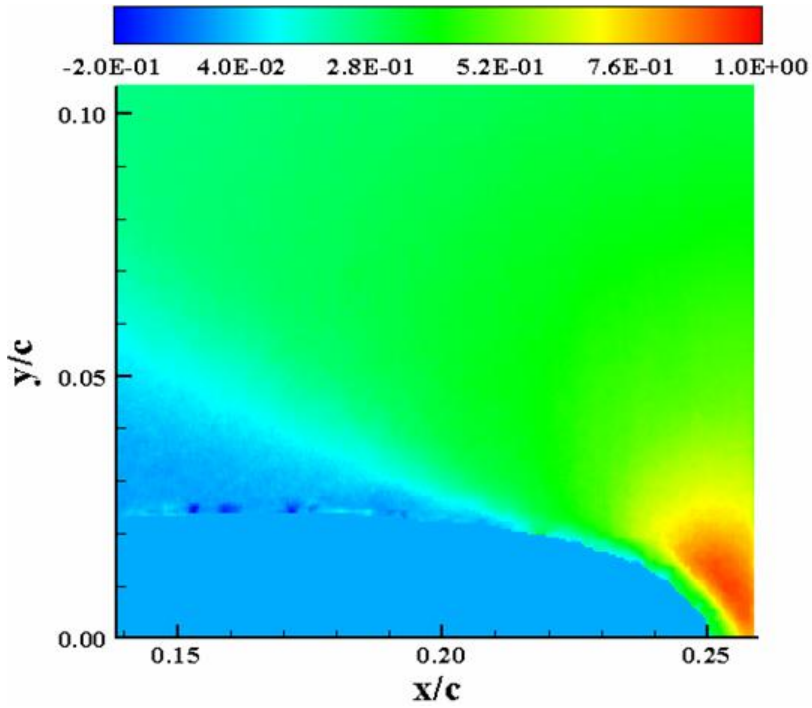

Figure D-70: $V_N\,(M_\infty = 0.2, k = 0.18, Up, \alpha = 13.7^0)$

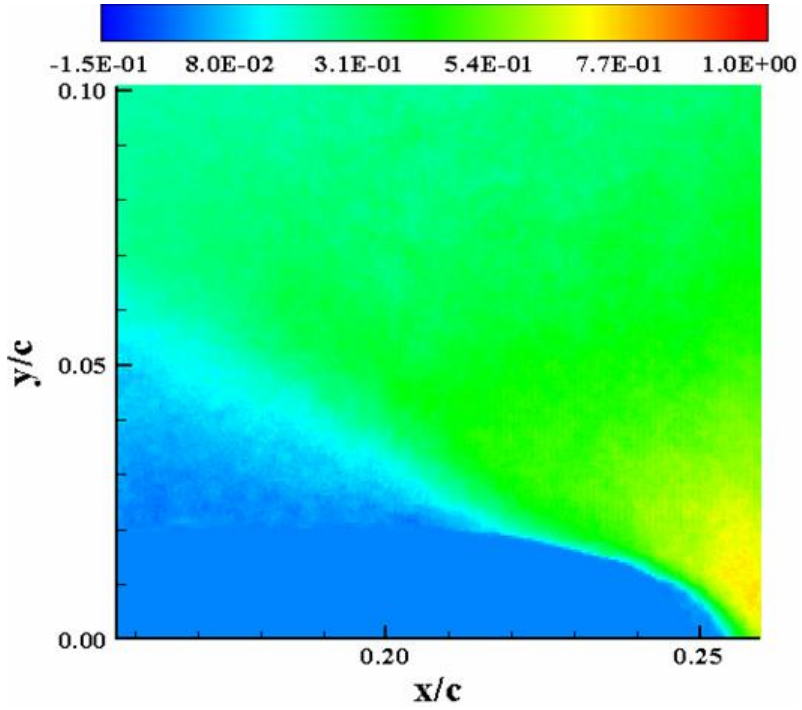

Figure D-71: $V_N\,(M_\infty = 0.2, k = 0.18, Up, \alpha = 15^0)$

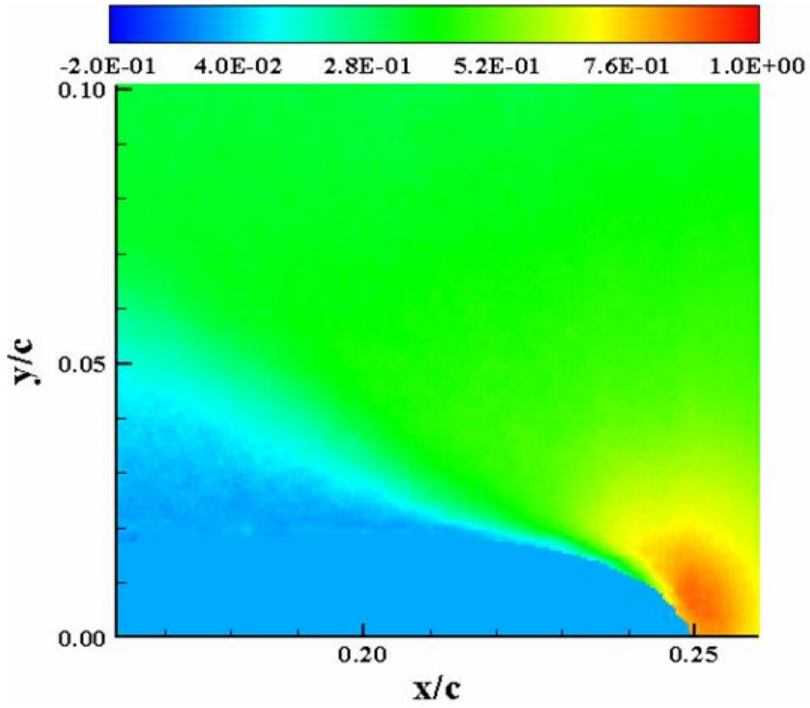

Figure D-72: $V_N\,(M_\infty = 0.2, k = 0.18, Up, \alpha = 16.88^0)$

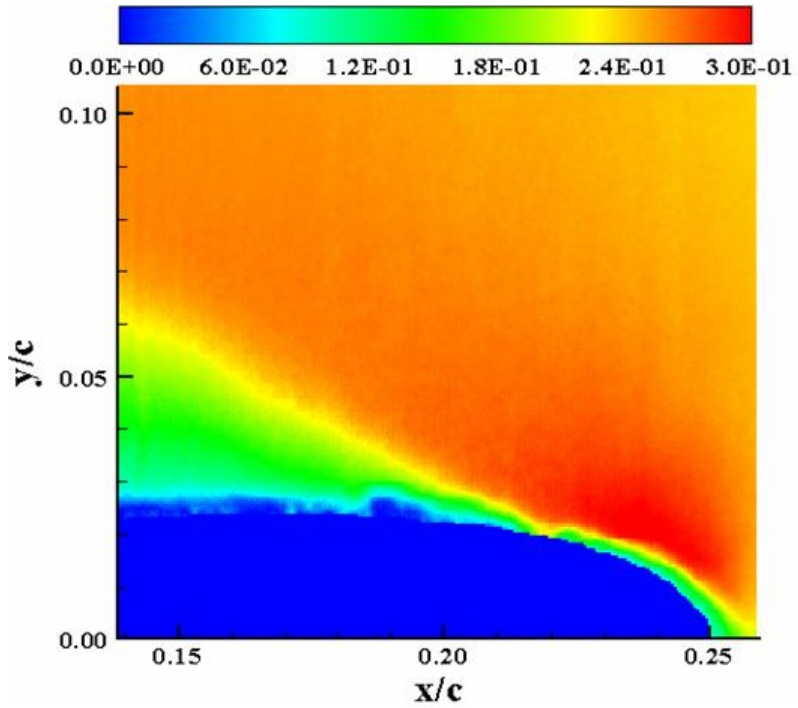

Figure D-73: $M(M_\infty = 0.2, k = 0.18, Up, \alpha = 13.7^0)$

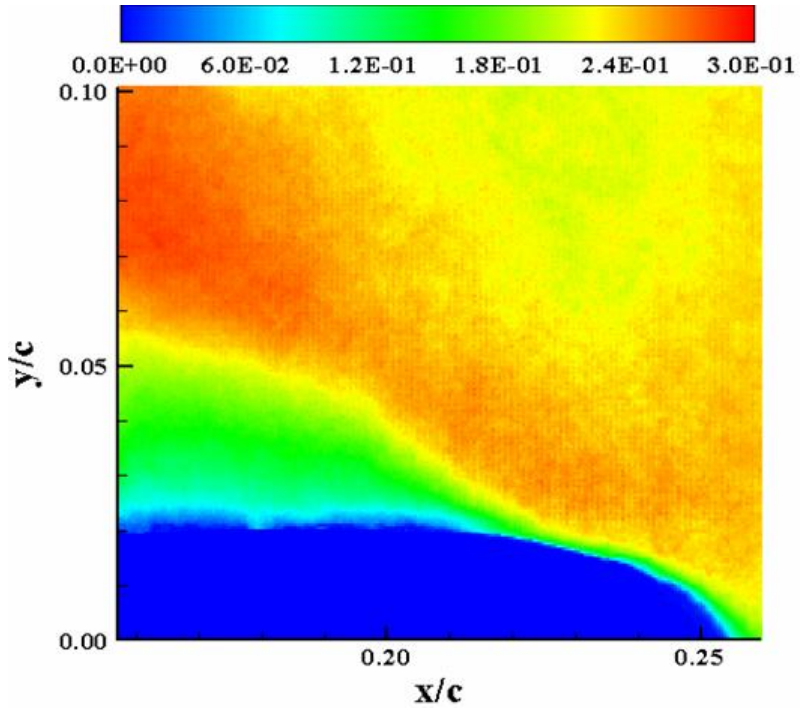

Figure D-74: $M(M_\infty = 0.2, k = 0.18, Up, \alpha = 15^0)$

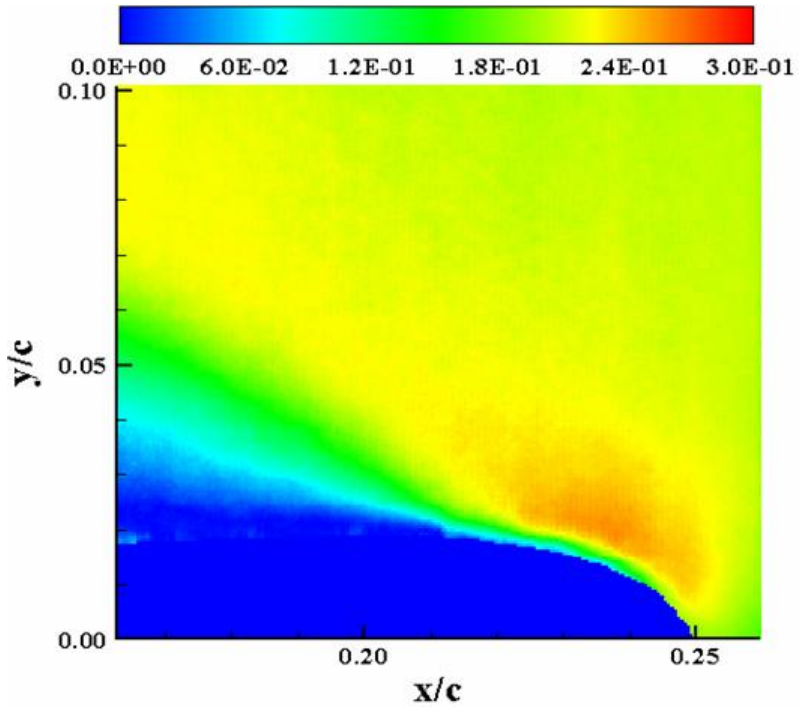

Figure D-75: $M(M_\infty = 0.2, k = 0.18, Up, \alpha = 16.88^0)$

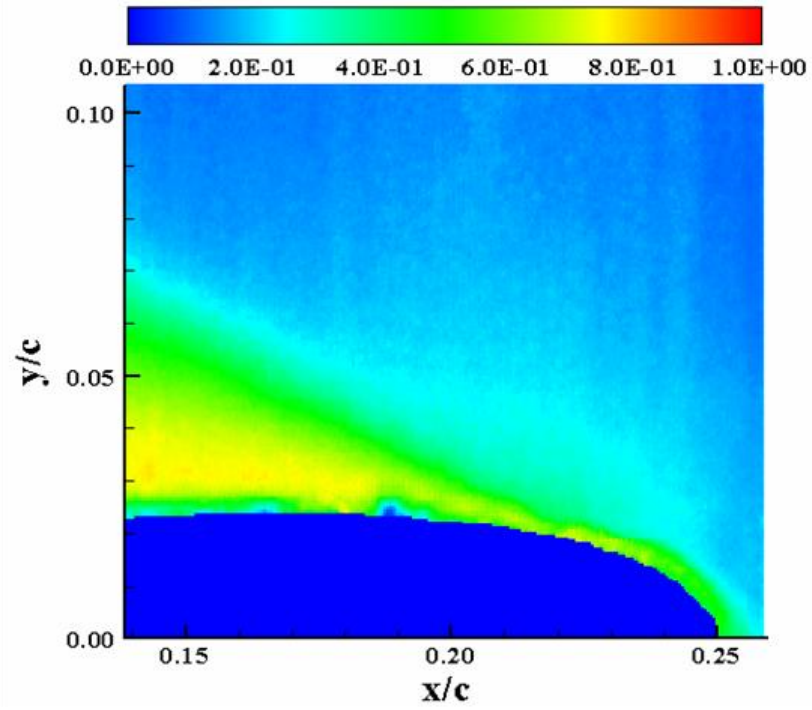

Figure D-76: $\sigma_u(M_\infty = 0.2, k = 0.18, Up, \alpha = 13.7^0)$

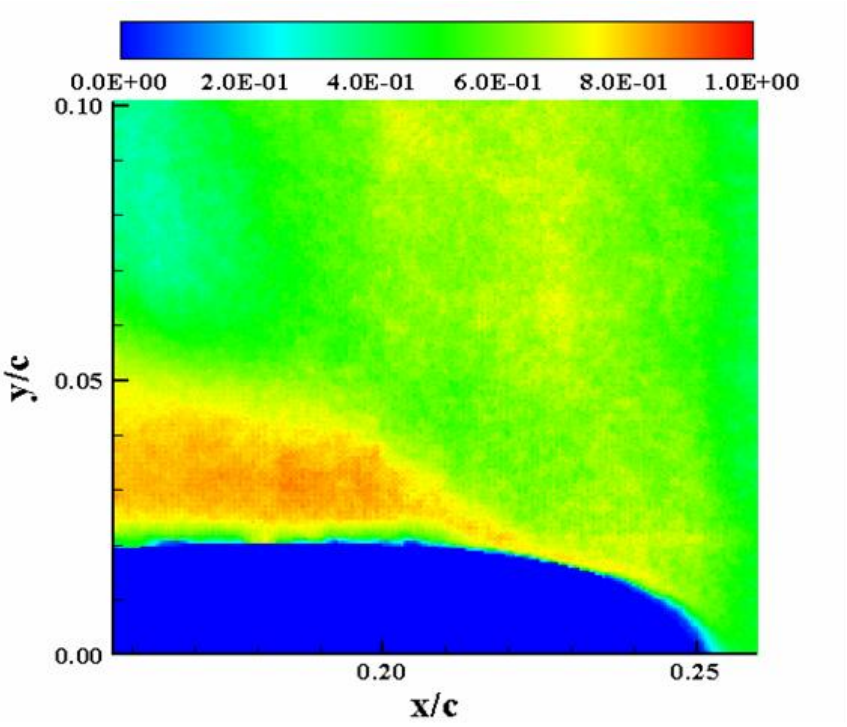

Figure D-77: $\sigma_u(M_\infty = 0.2, k = 0.18, Up, \alpha = 15^0)$

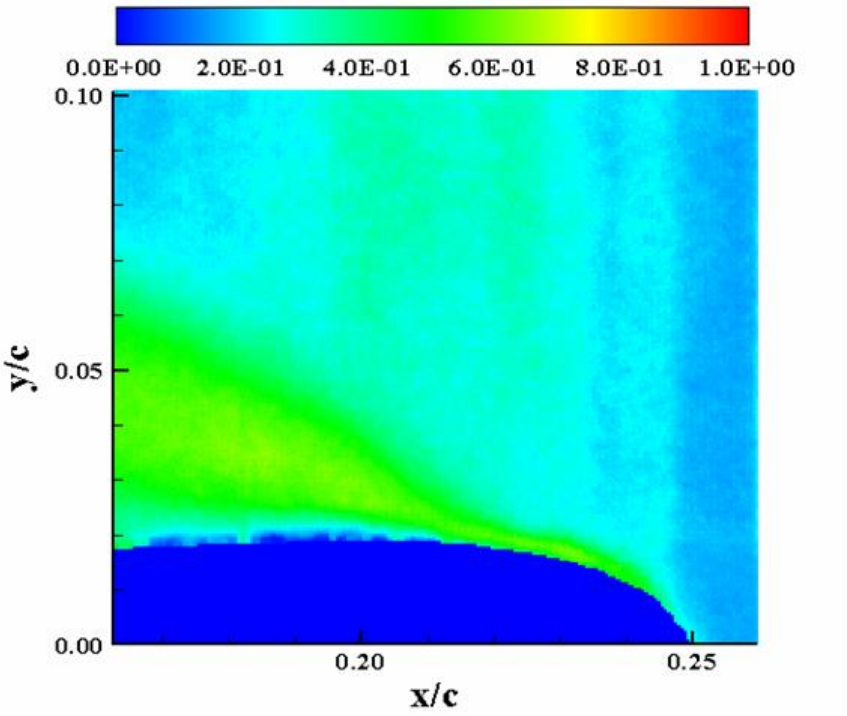

Figure D-78: $\sigma_u(M_\infty = 0.2, k = 0.18, Up, \alpha = 16.88^0)$

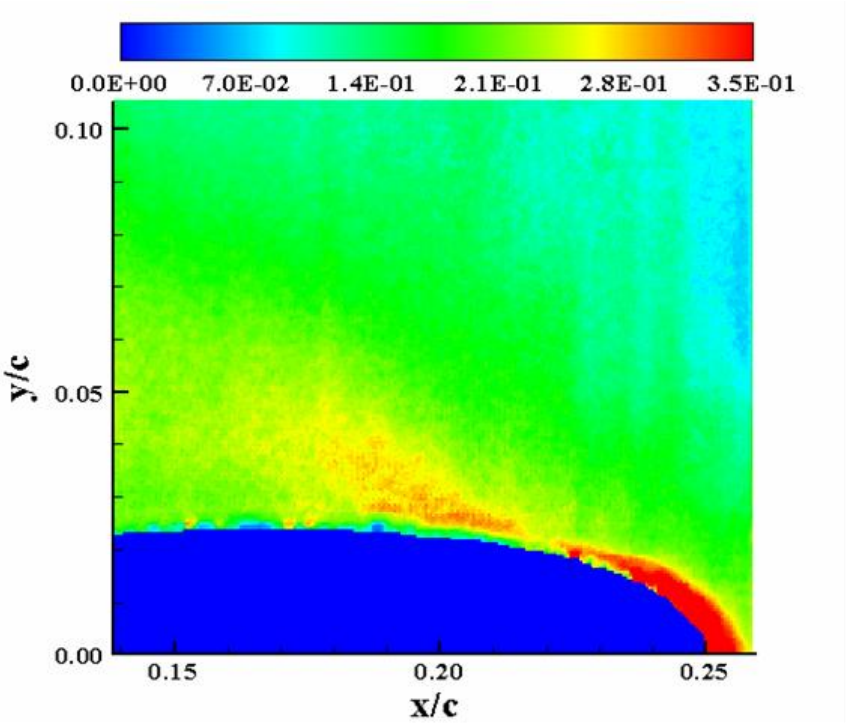

Figure D-79: $\sigma_v(M_\infty = 0.2, k = 0.18, Up, \alpha = 13.7^0)$

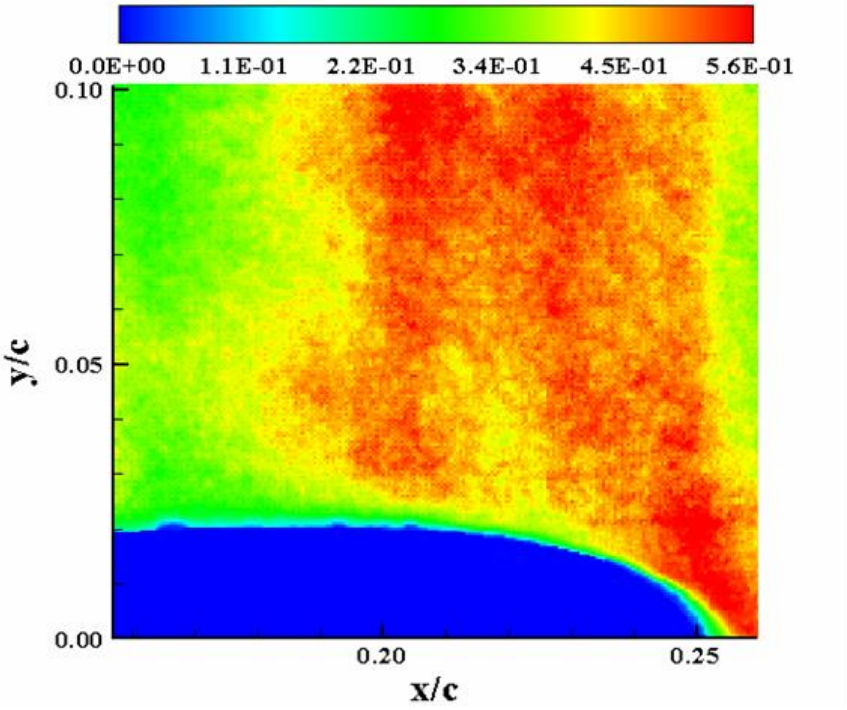

Figure D-80: $\sigma_v(M_\infty = 0.2, k = 0.18, Up, \alpha = 15^0)$

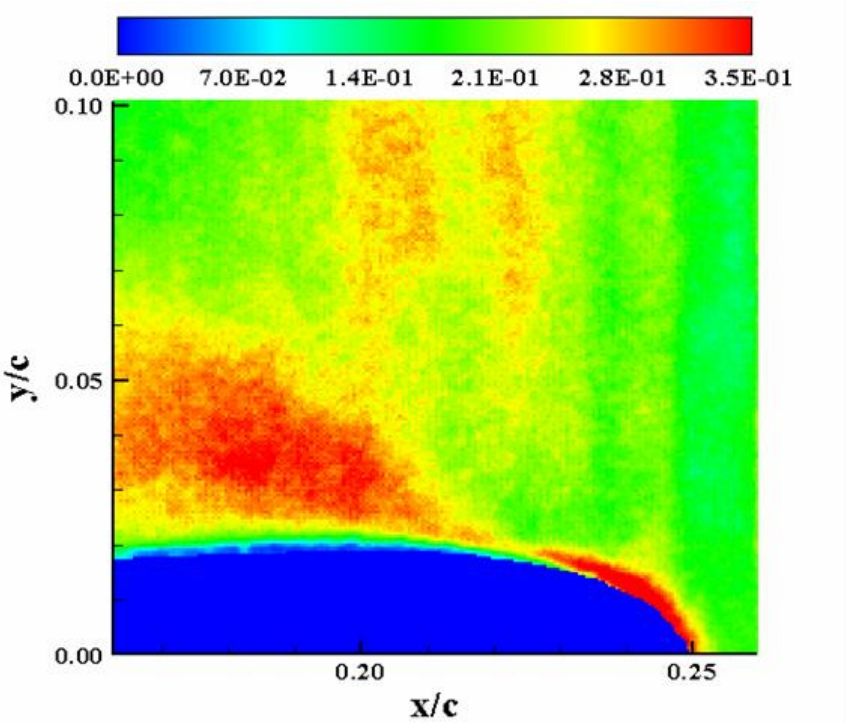

Figure D-81: $\sigma_v (M_\infty = 0.2, k = 0.18, Up, \alpha = 16.88^0)$

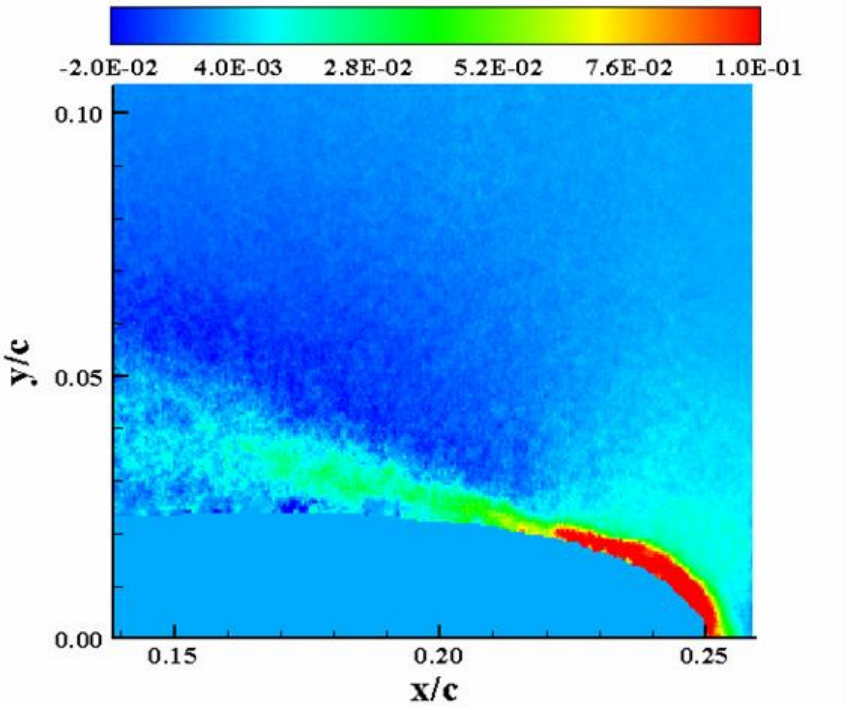

Figure D-82: $\tau_{xy} (M_\infty = 0.2, k = 0.18, Up, \alpha = 13.7^0)$

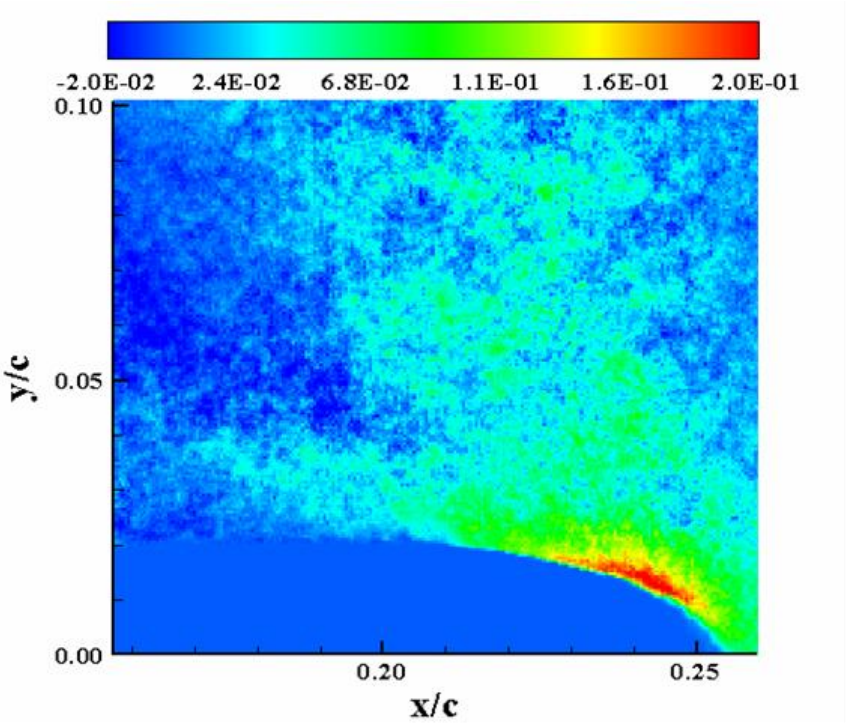

Figure D-83: $\tau_{xy}(M_\infty = 0.2, k = 0.18, Up, \alpha = 15^0)$

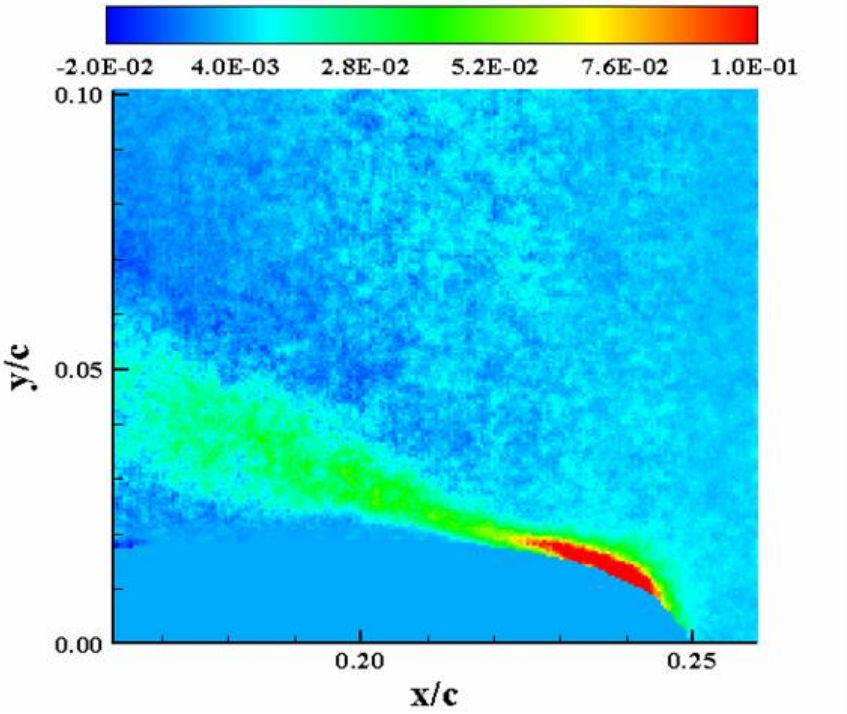

Figure D-84: $\tau_{xy}(M_\infty = 0.2, k = 0.18, Up, \alpha = 16.88^0)$

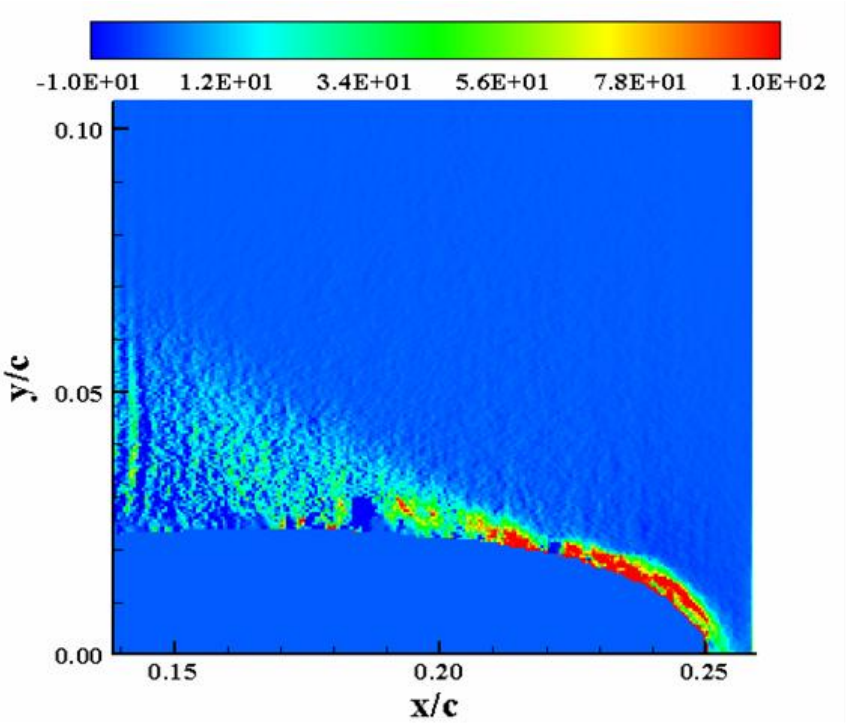

Figure D-85: $P_{xx}(M_\infty = 0.2, k = 0.18, Up, \alpha = 13.7^0)$

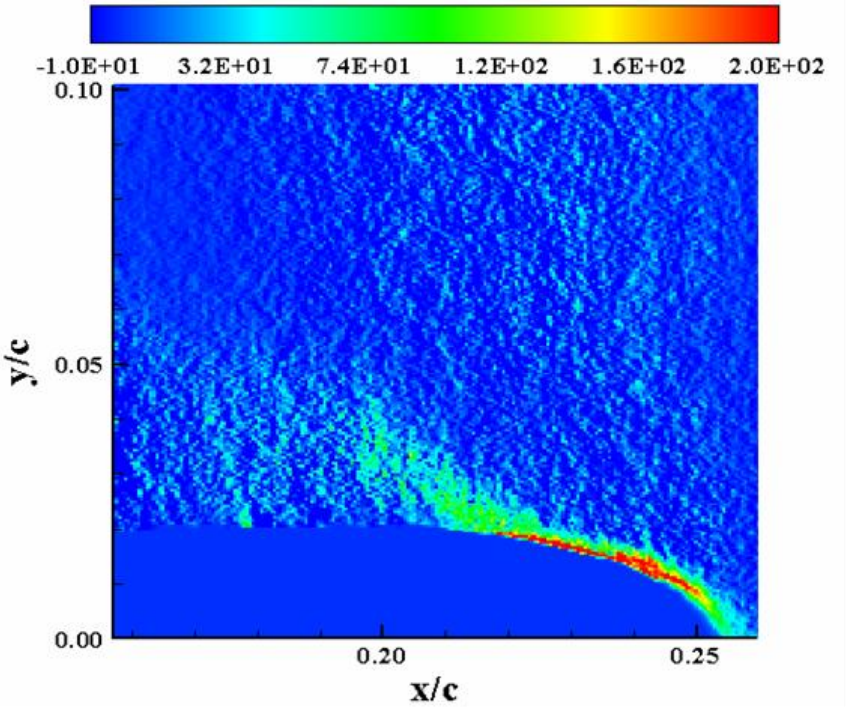

Figure D-86: $P_{xx}(M_\infty = 0.2, k = 0.18, Up, \alpha = 15^0)$

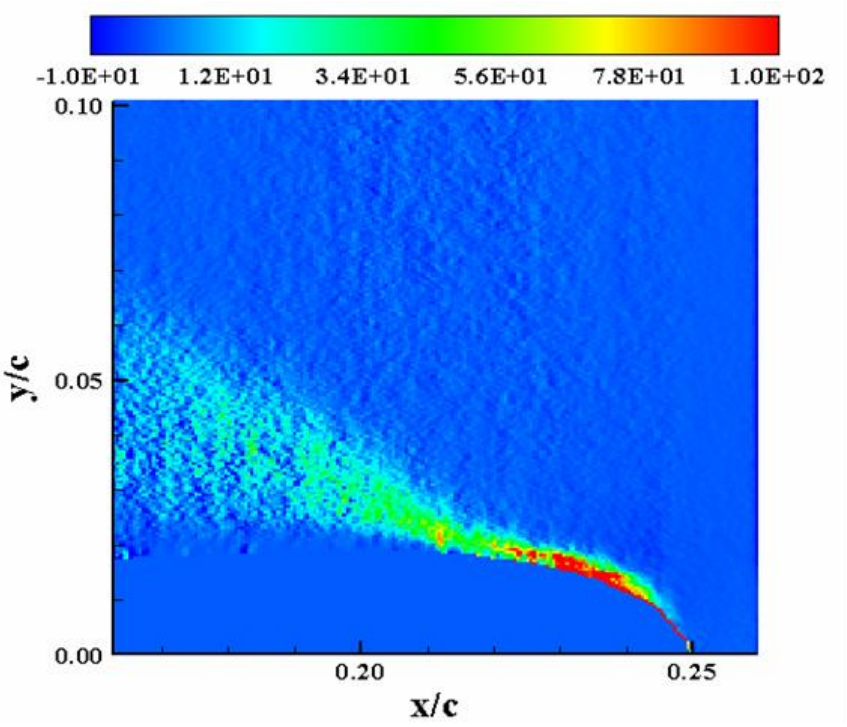

Figure D-87: $P_{xx}(M_\infty = 0.2, k = 0.18, Up, \alpha = 16.88^0)$

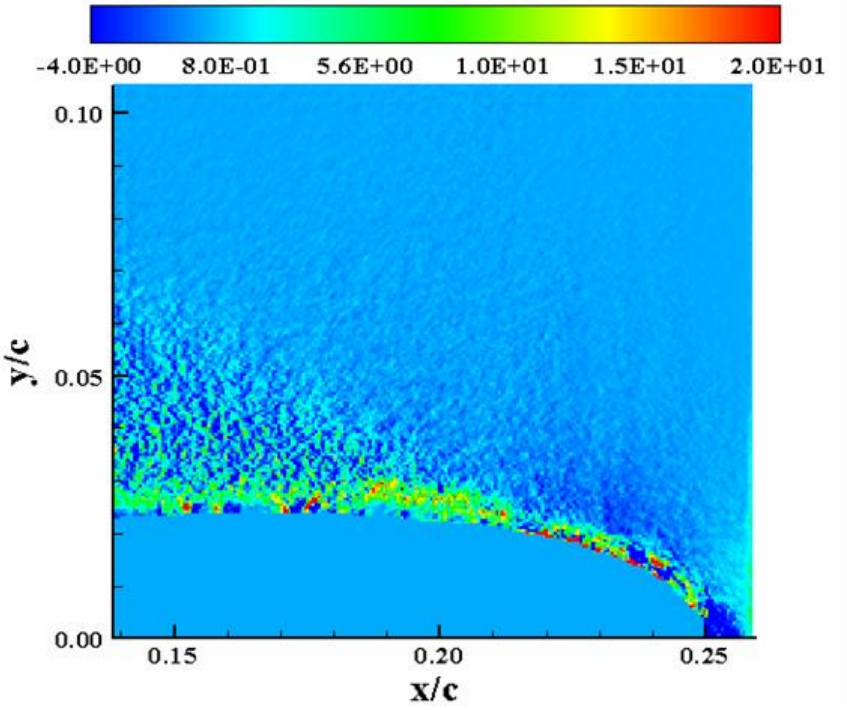

Figure D-88: $P_{xy}(M_\infty = 0.2, k = 0.18, Up, \alpha = 13.7^0)$

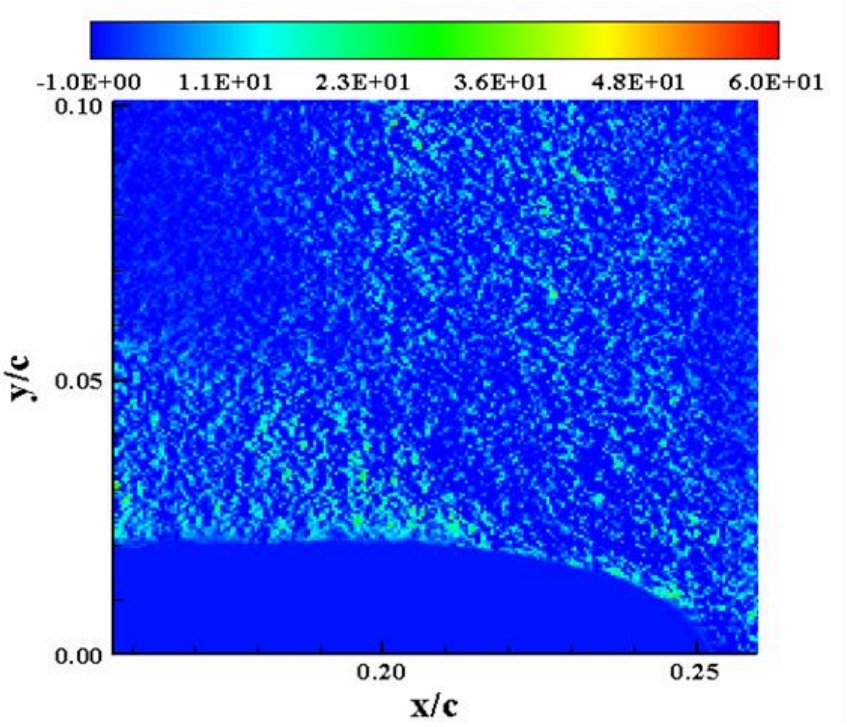

Figure D-89: $P_{xy}(M_\infty = 0.2, k = 0.18, Up, \alpha = 15^0)$

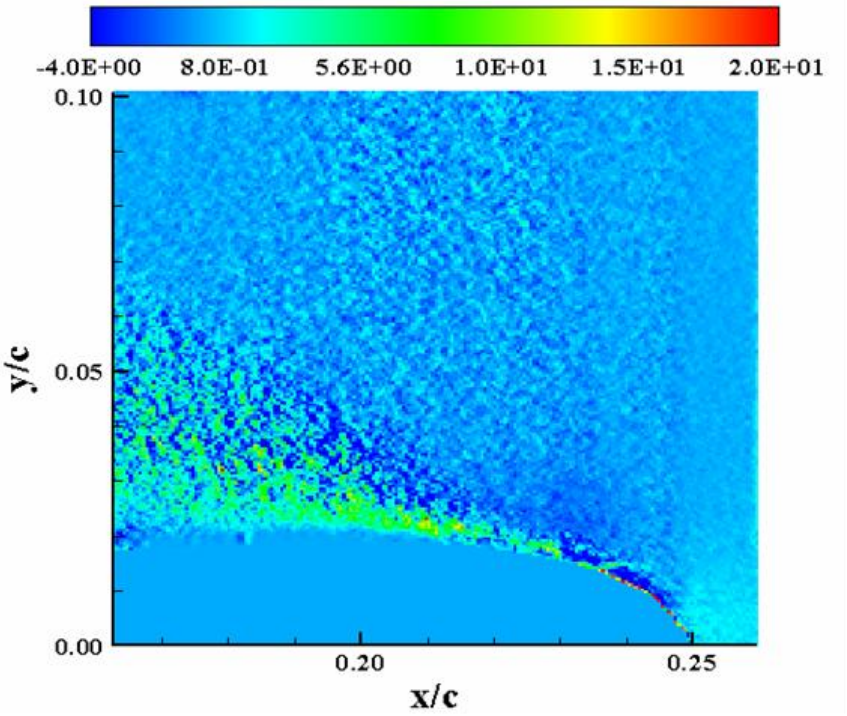

Figure D-90: $P_{xy}(M_\infty = 0.2, k = 0.18, Up, \alpha = 16.88^0)$

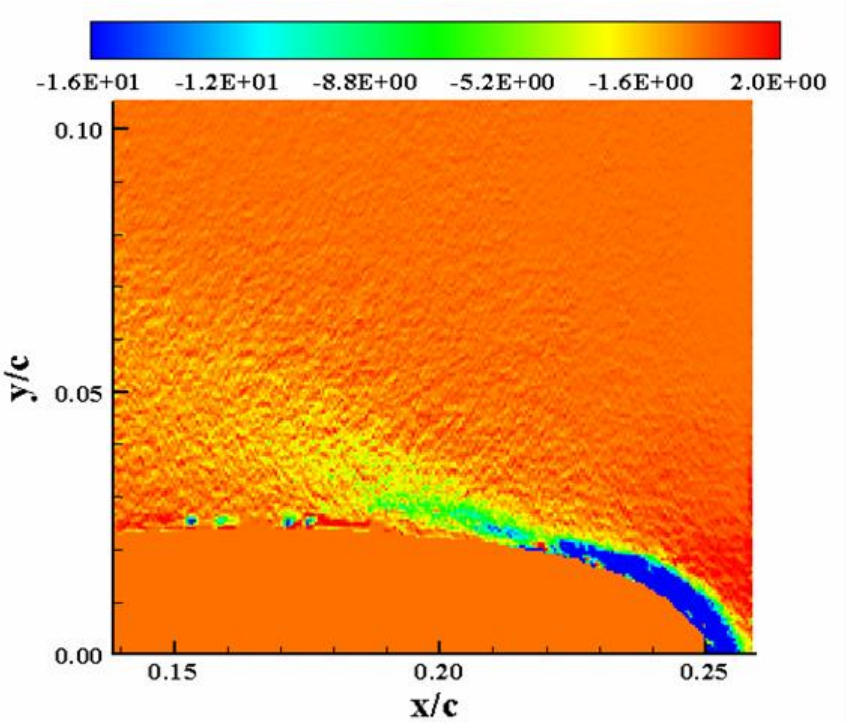

Figure D-91: $P_{yy}(M_\infty = 0.2, k = 0.18, Up, \alpha = 13.7^0)$

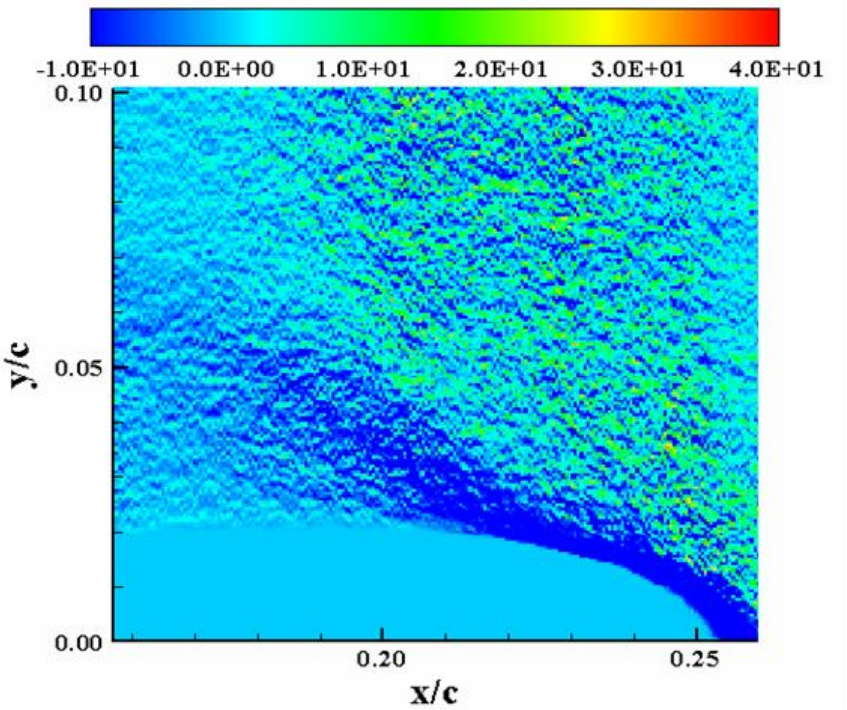

Figure D-92: $P_{yy}(M_\infty = 0.2, k = 0.18, Up, \alpha = 15^0)$

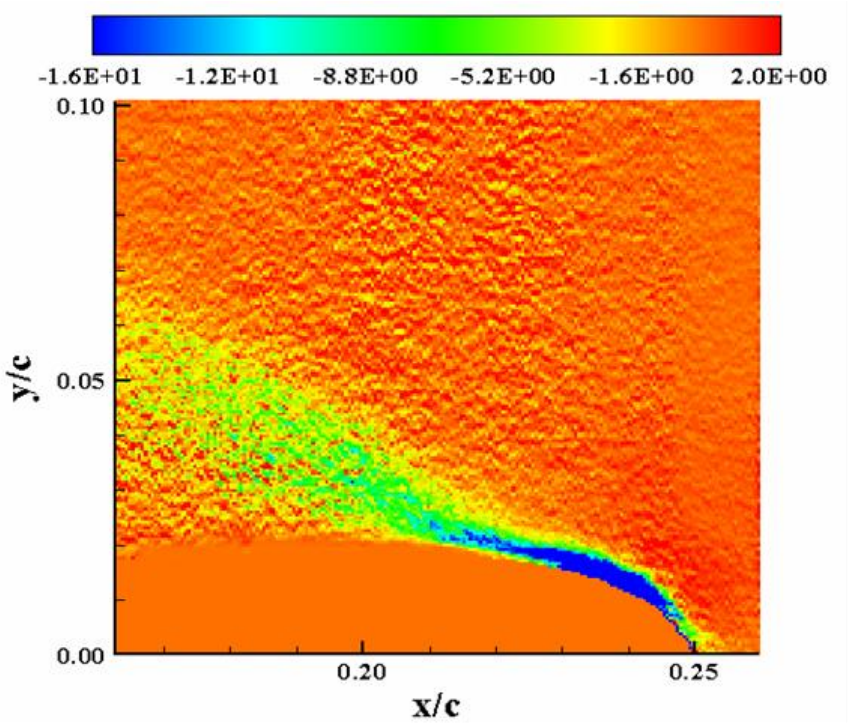

Figure D-93: $P_{yy}(M_\infty = 0.2, k = 0.18, Up, \alpha = 16.88^0)$

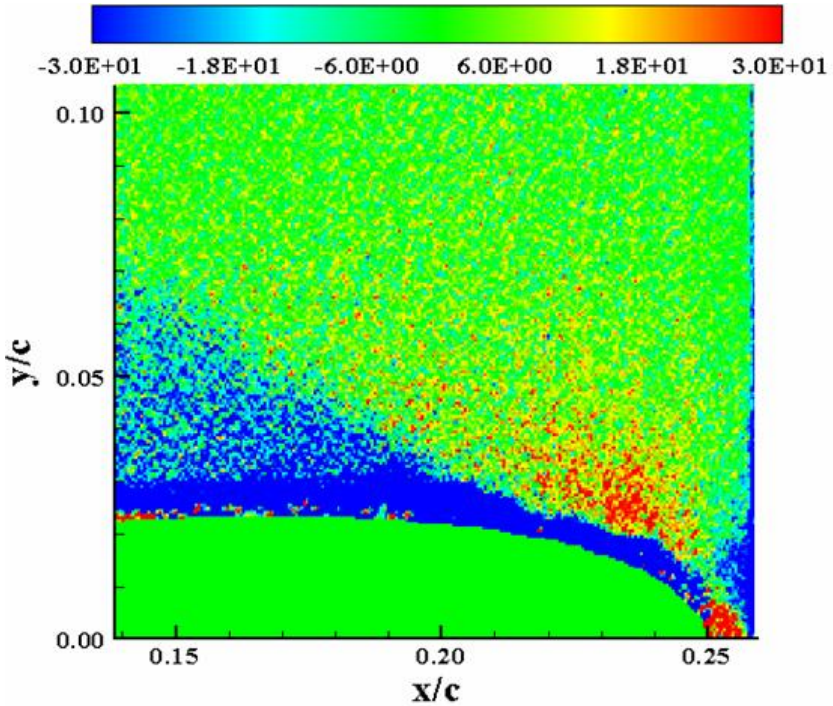

Figure D-94: $S_{xy}(M_\infty = 0.2, k = 0.18, Up, \alpha = 13.7^0)$

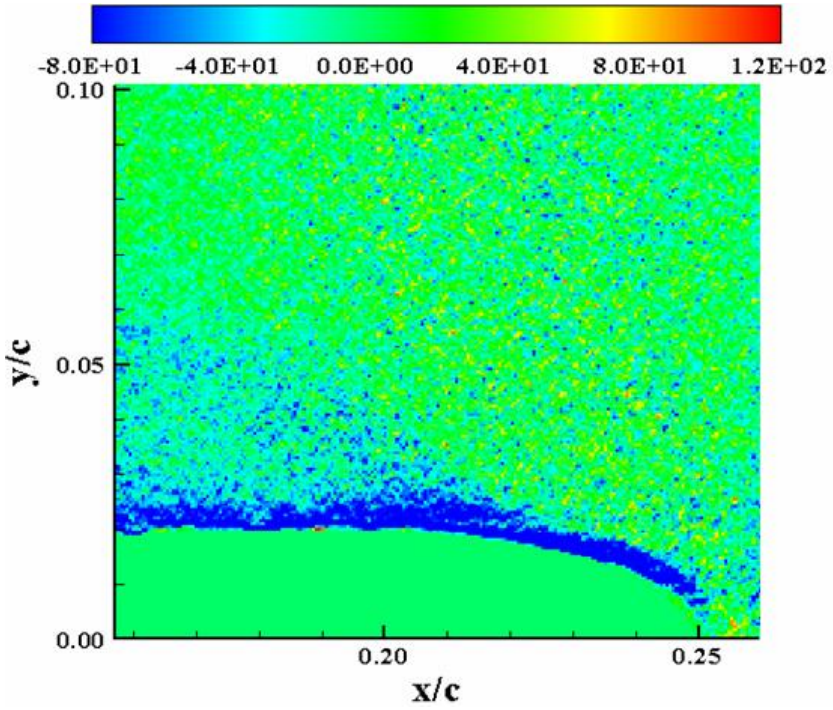

Figure D-95: $S_{xy}(M_\infty = 0.2, k = 0.18, Up, \alpha = 15^0)$

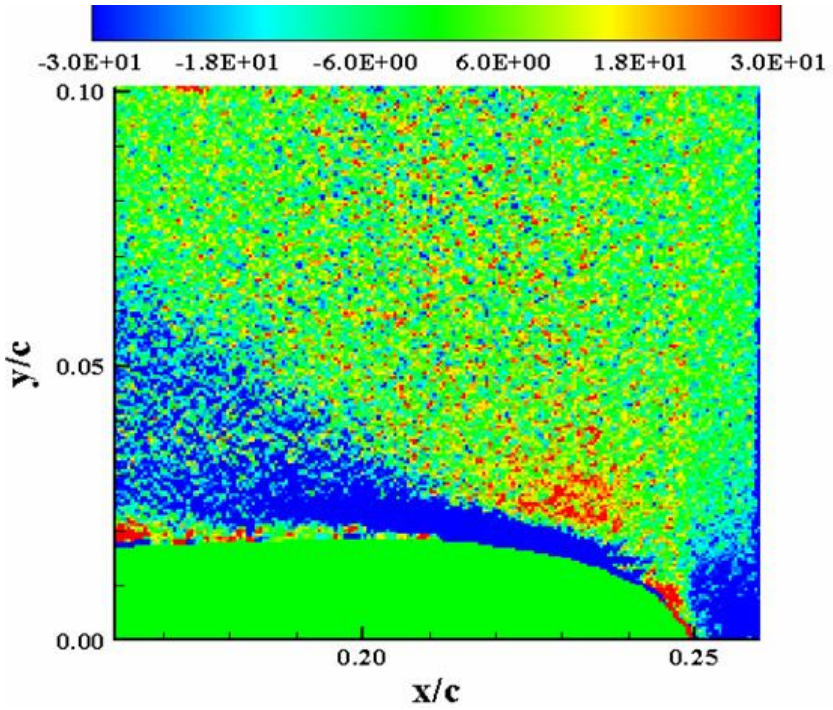

Figure D-96: $S_{xy}(M_\infty = 0.2, k = 0.18, Up, \alpha = 16.88^0)$

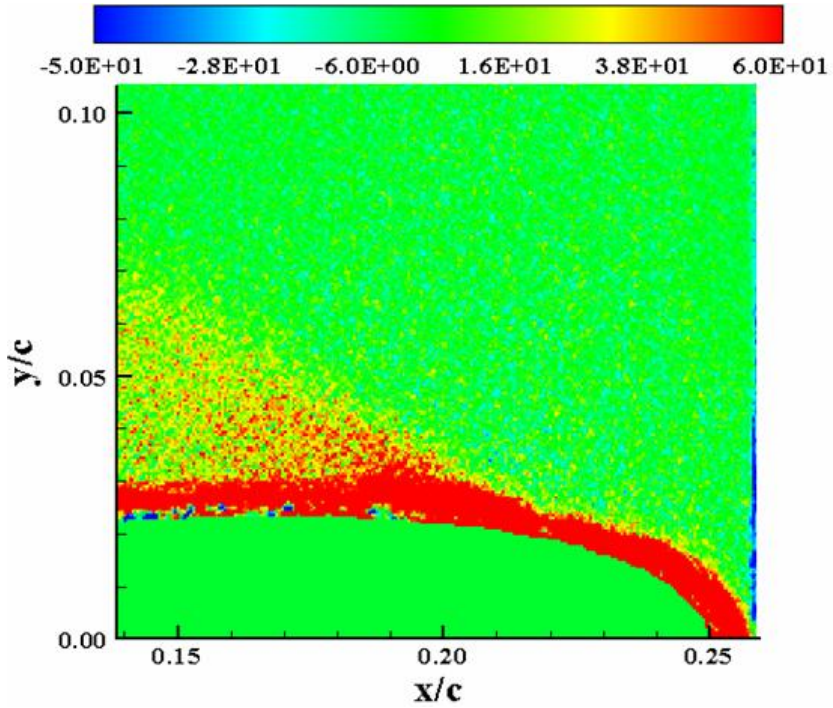

Figure D-97: $\omega_z(M_\infty = 0.2, k = 0.18, Up, \alpha = 13.7^0)$

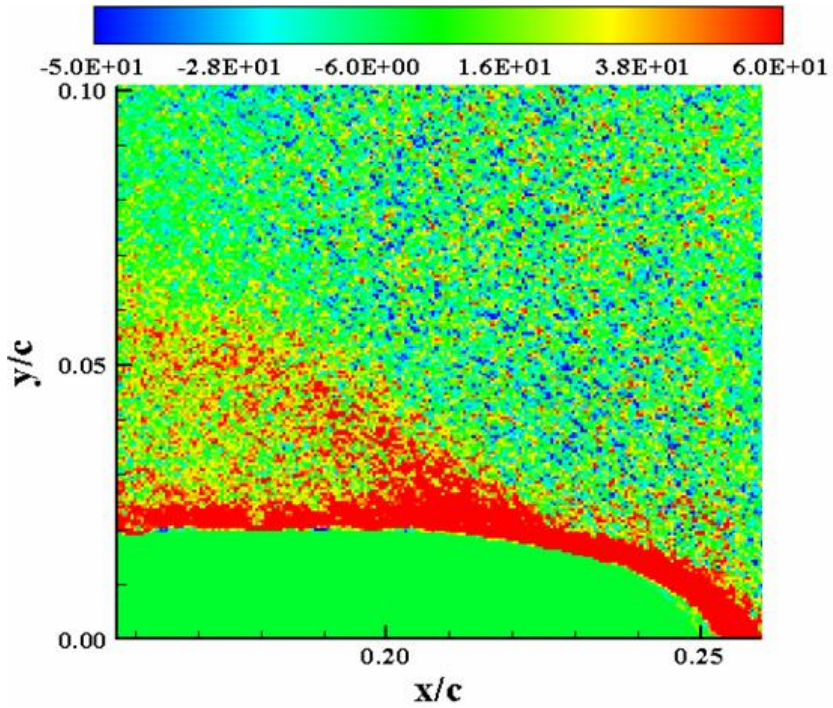

Figure D-98: $\omega_z(M_\infty = 0.2, k = 0.18, Up, \alpha = 15^0)$

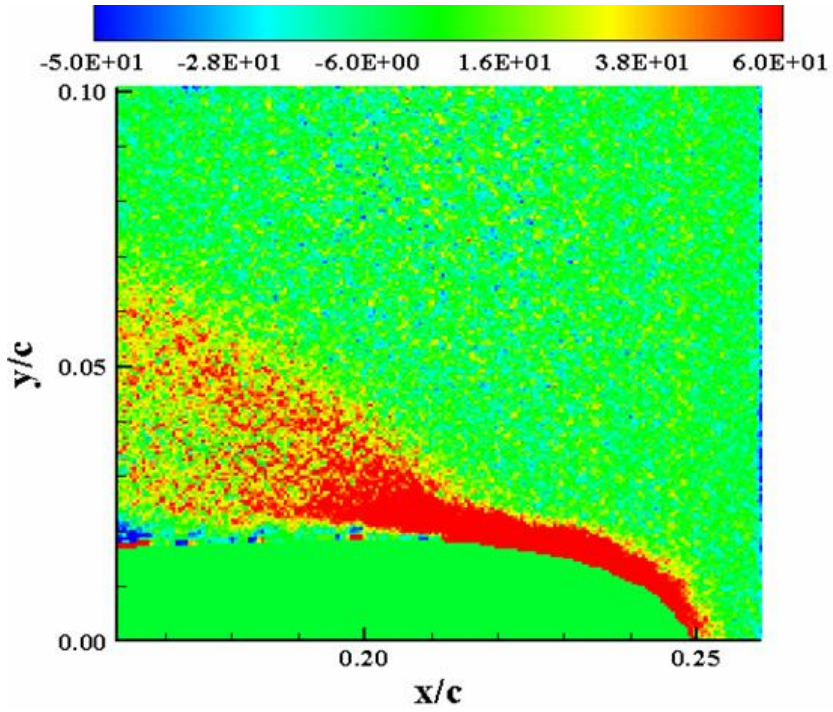

Figure D-99: $\omega_z (M_\infty = 0.2, k = 0.18, Up, \alpha = 16.88^0)$

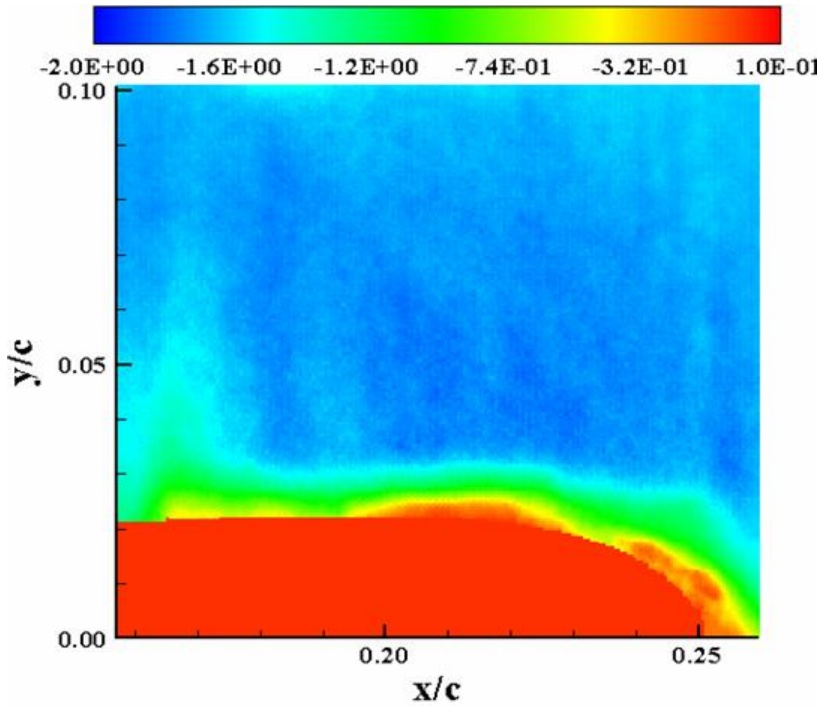

Figure D-100: $U_N (M_\infty = 0.2, k = 0.18, Down, \alpha = 15^0)$

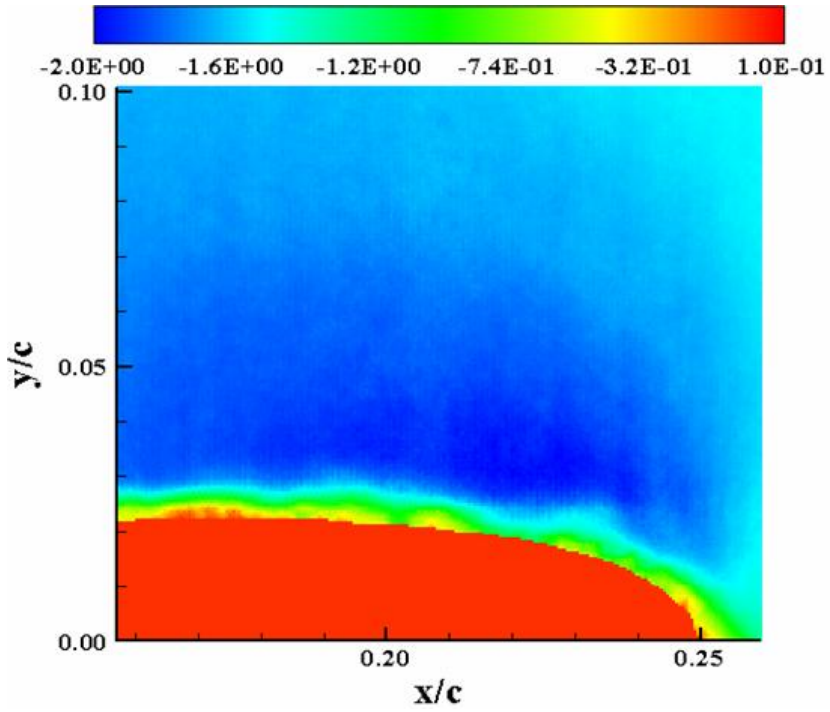

Figure D-101: $U_N\,(M_\infty = 0.2, k = 0.18, Down, \alpha = 13.7^0)$

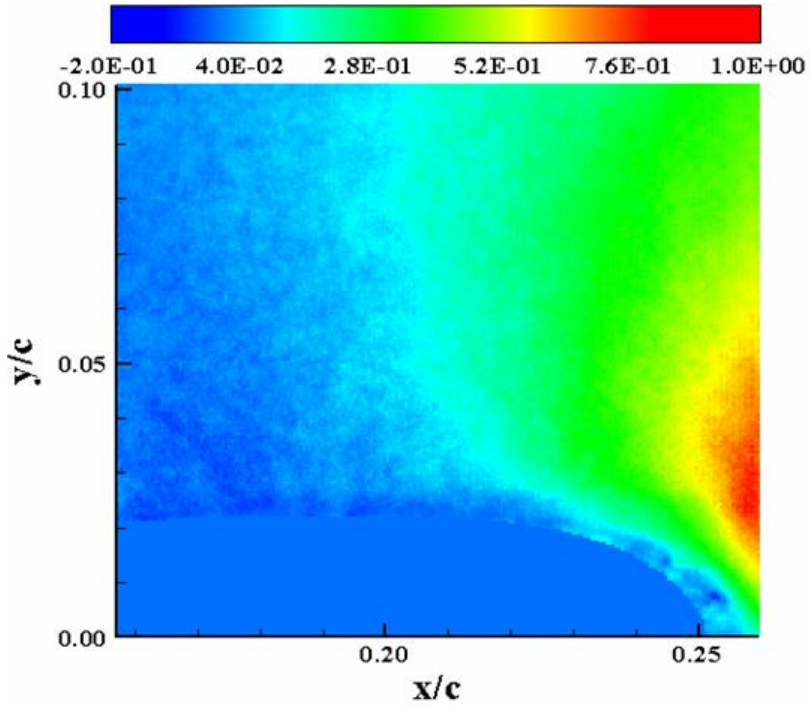

Figure D-102: $V_N\,(M_\infty = 0.2, k = 0.18, Down, \alpha = 15^0)$

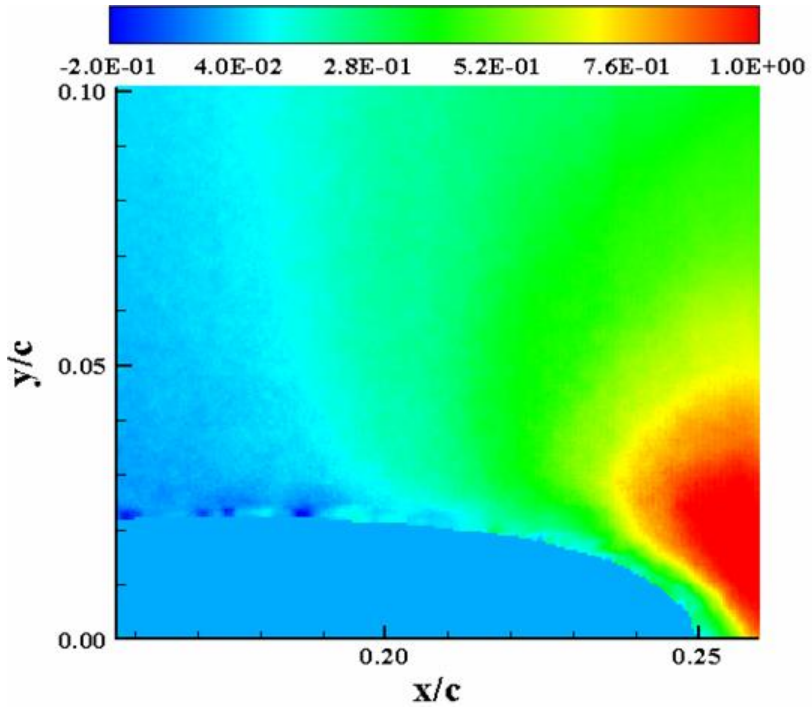

Figure D-103: V_N ($M_\infty = 0.2, k = 0.18, Down, \alpha = 13.7^0$)

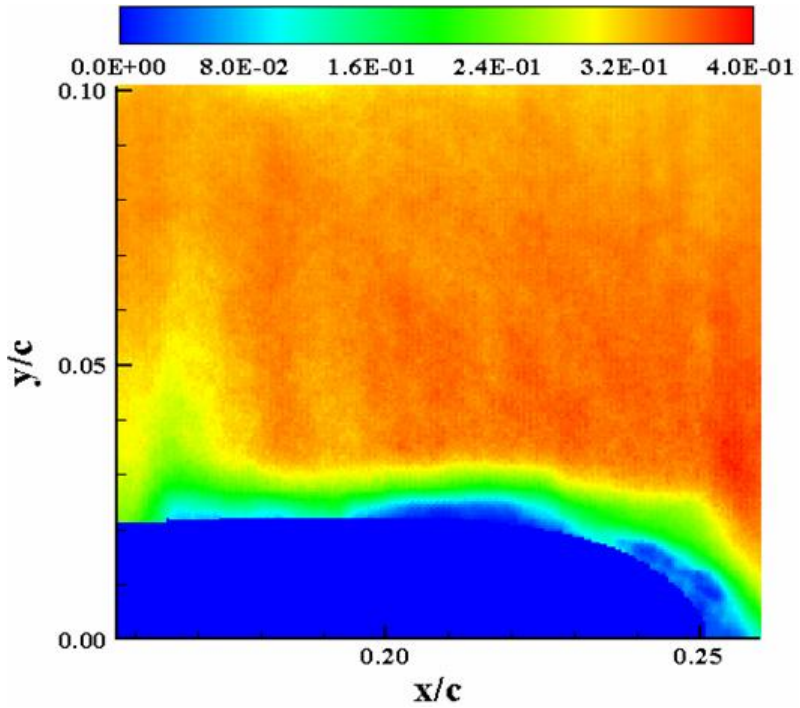

Figure D-104: M($M_\infty = 0.2, k = 0.18, Down, \alpha = 15^0$)

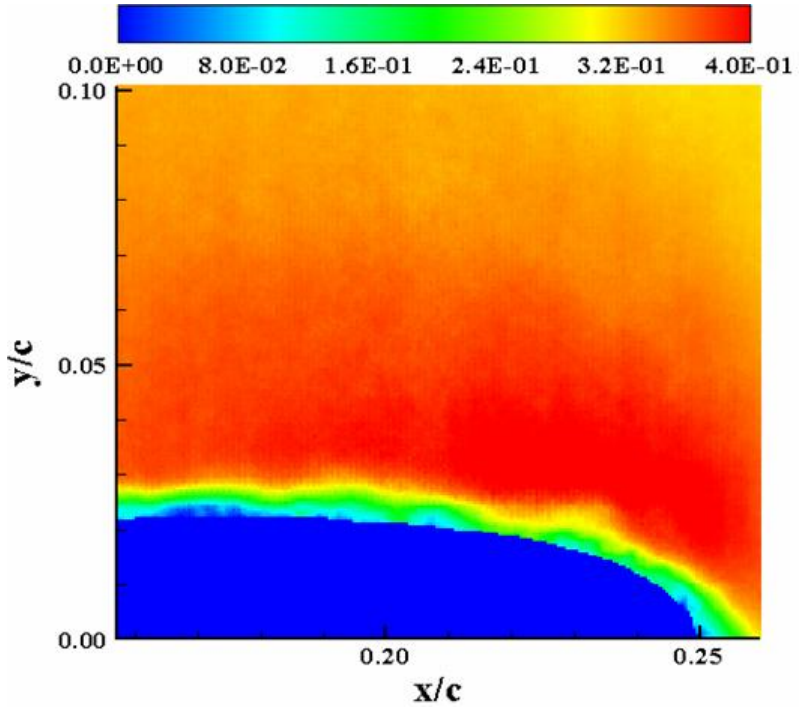

Figure D-105: $M(M_\infty = 0.2, k = 0.18, Down, \alpha = 13.7^0)$

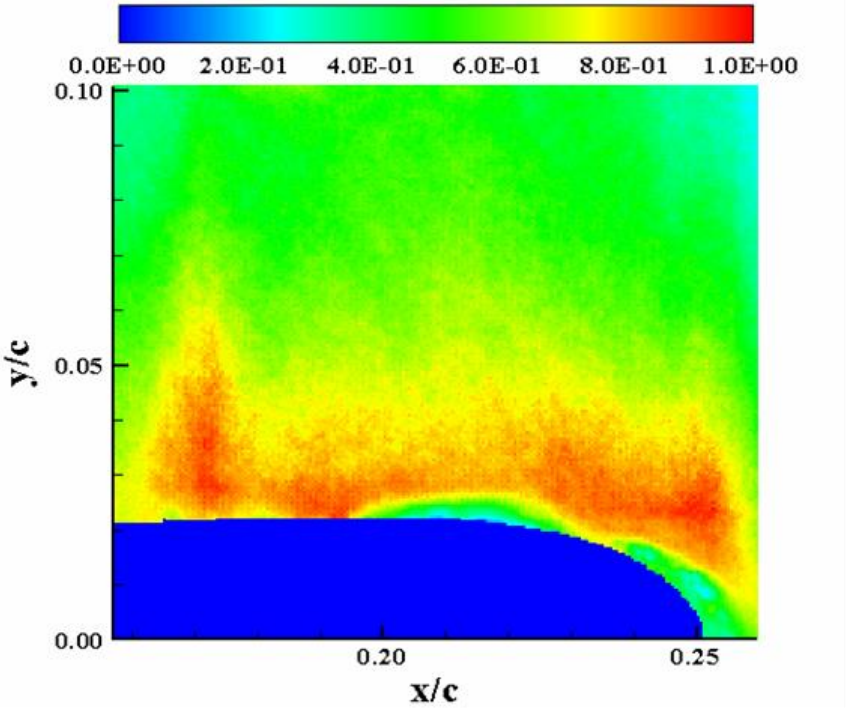

Figure D-106: $\sigma_u(M_\infty = 0.2, k = 0.18, Down, \alpha = 15^0)$

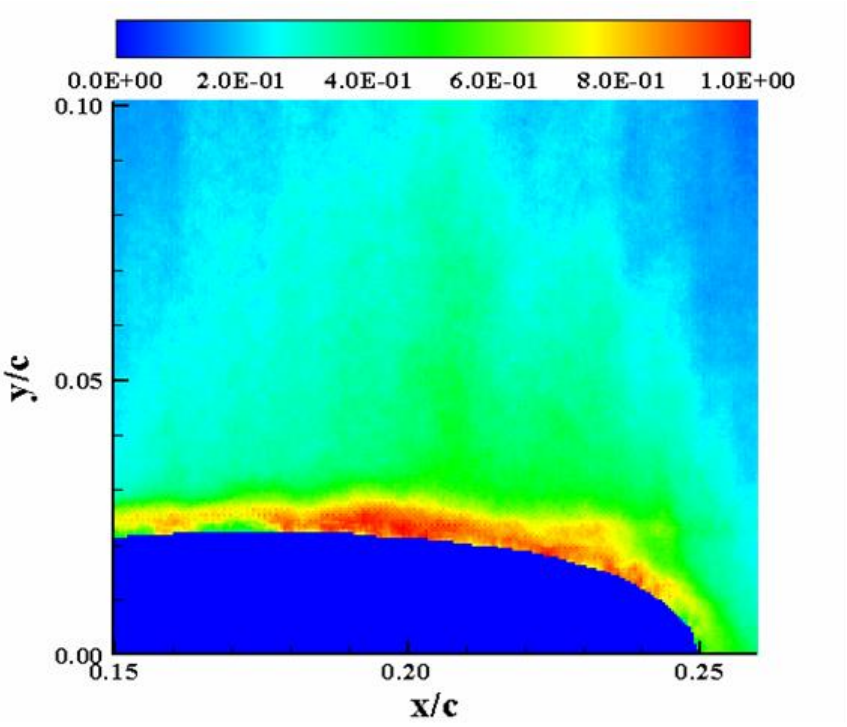

Figure D-107: $\sigma_u(M_\infty = 0.2, k = 0.18, Down, \alpha = 13.7^0)$

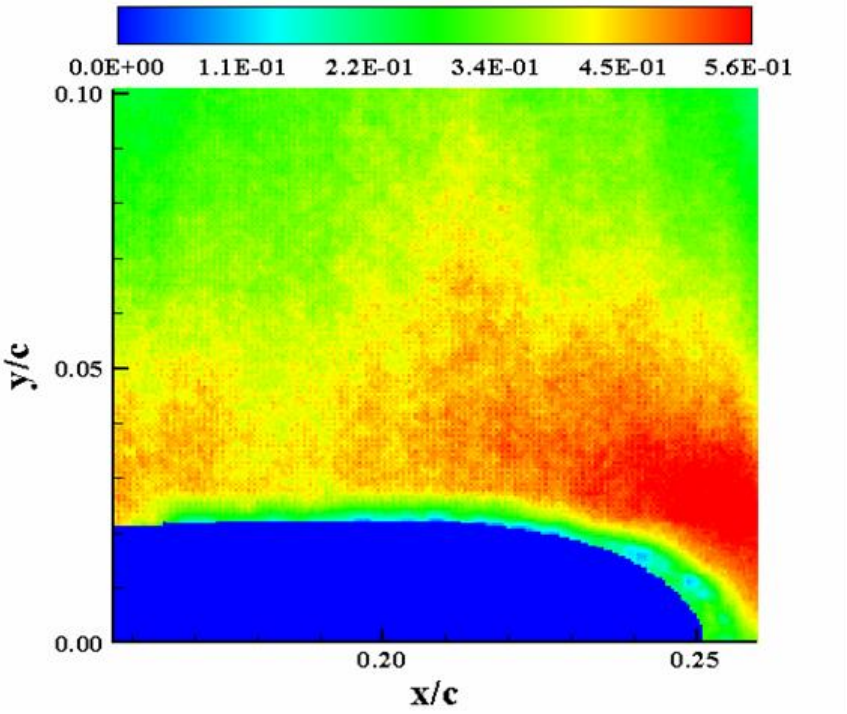

Figure D-108: $\sigma_v(M_\infty = 0.2, k = 0.18, Down, \alpha = 15^0)$

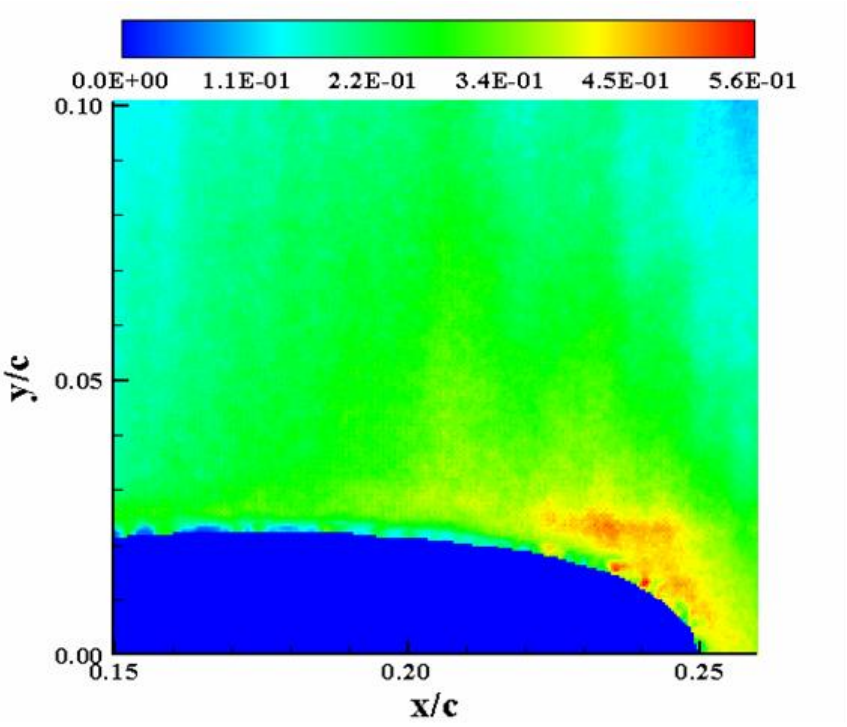

Figure D-109: $\sigma_v (M_\infty = 0.2, k = 0.18, Down, \alpha = 13.7^0)$

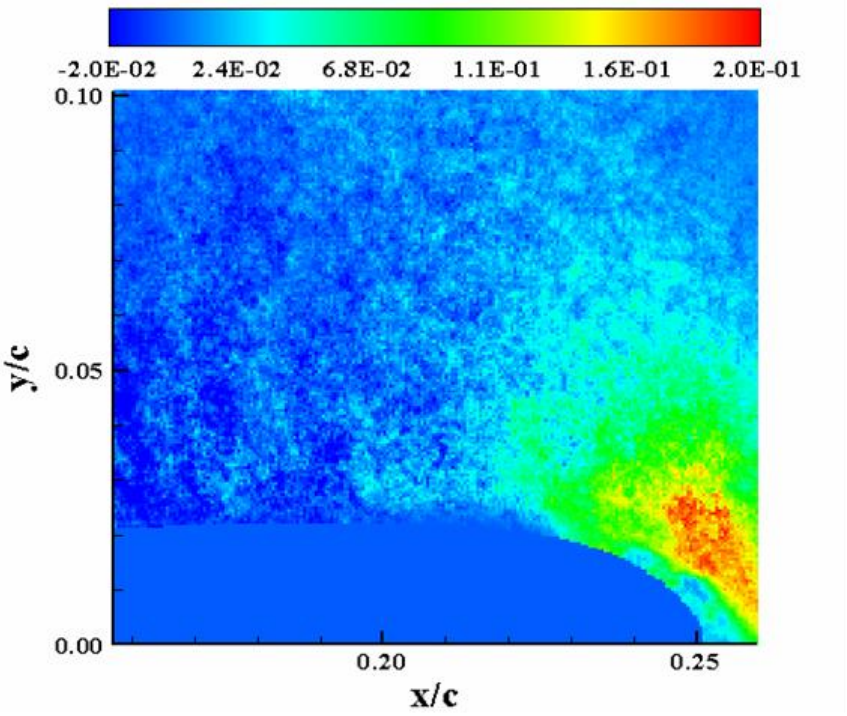

Figure D-110: $\tau_{xy} (M_\infty = 0.2, k = 0.18, Down, \alpha = 15^0)$

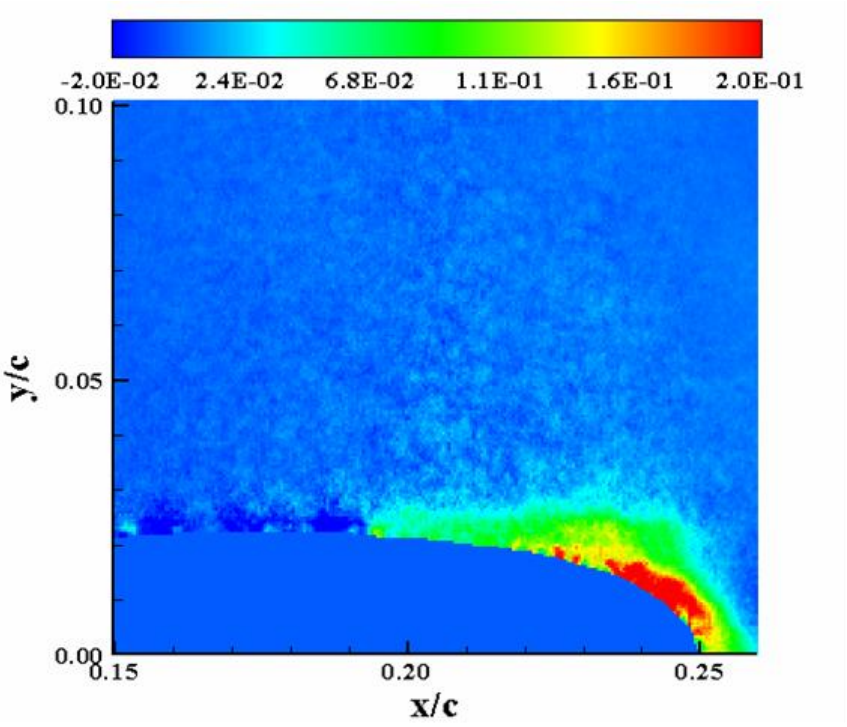

Figure D-111: $\tau_{xy}(M_\infty = 0.2, k = 0.18, Down, \alpha = 13.7^0)$

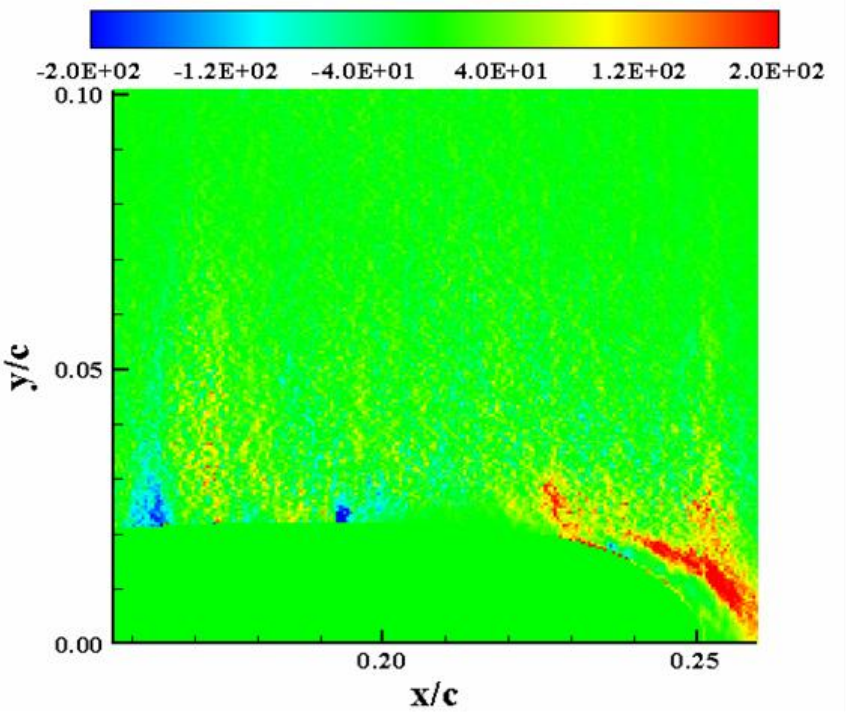

Figure D-112: $P_{xx}(M_\infty = 0.2, k = 0.18, Down, \alpha = 15^0)$

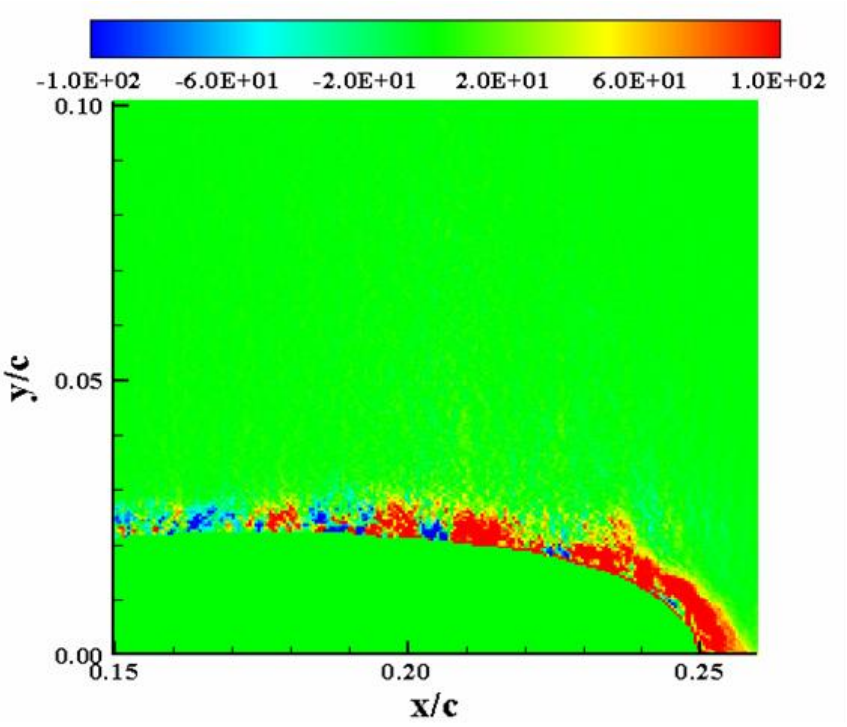

Figure D-113: $P_{xx}(M_\infty = 0.2, k = 0.18, Down, \alpha = 13.7^0)$

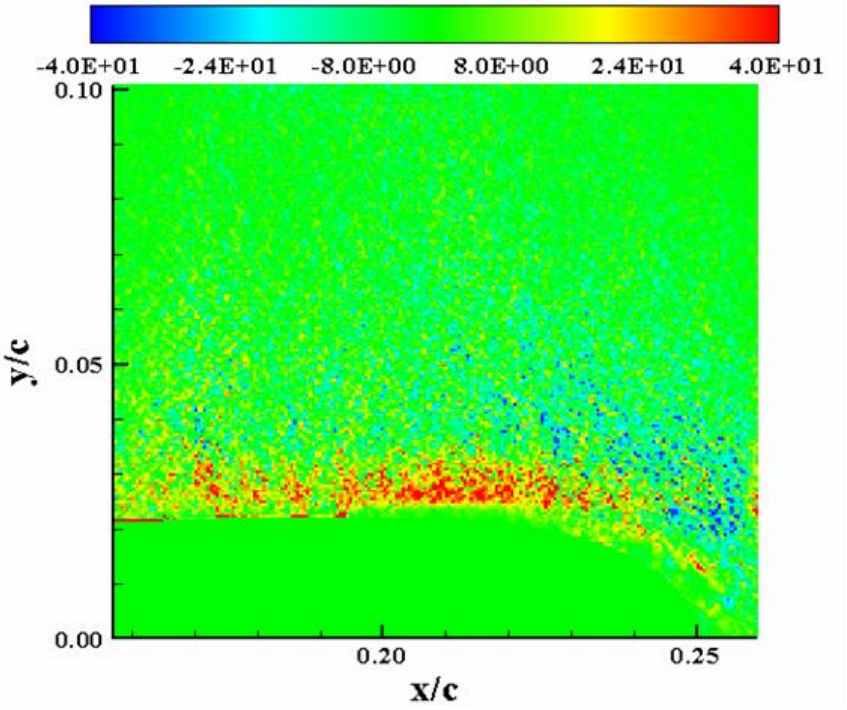

Figure D-114: $P_{xy}(M_\infty = 0.2, k = 0.18, Down, \alpha = 15^0)$

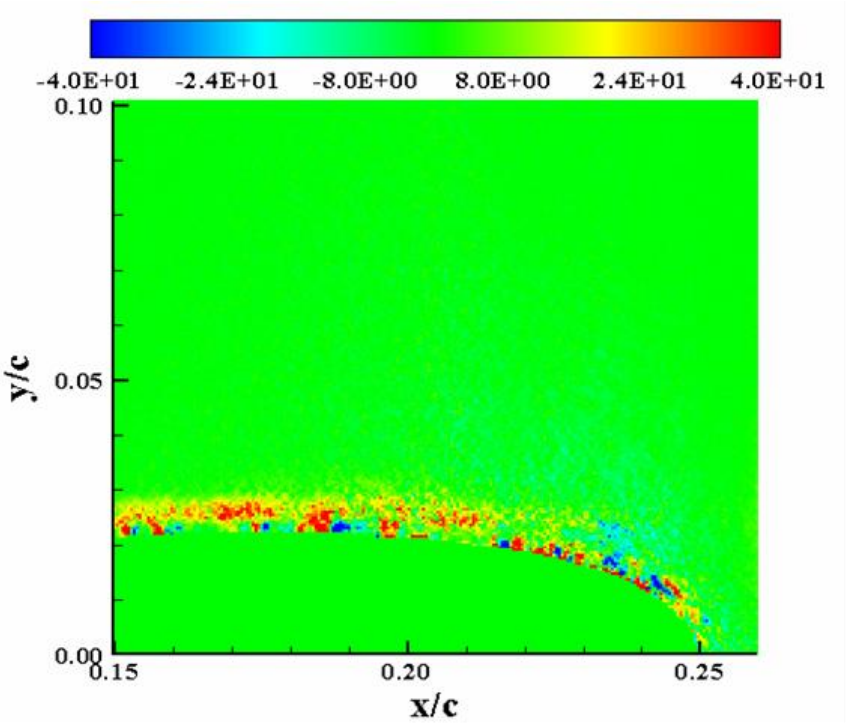

Figure D-115: $P_{xy}(M_\infty = 0.2, k = 0.18, Down, \alpha = 13.7^0)$

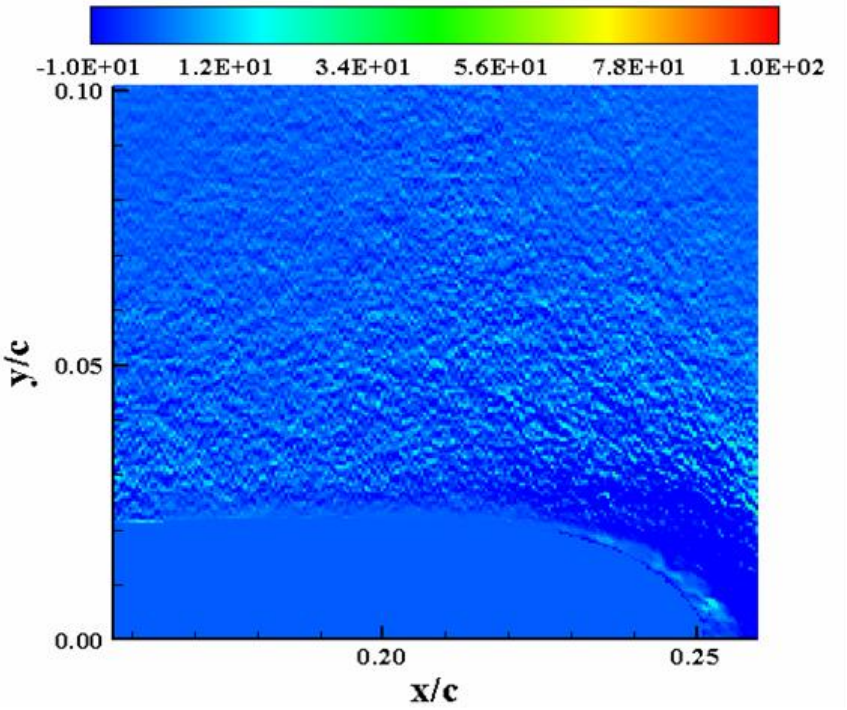

Figure D-116: $P_{yy}(M_\infty = 0.2, k = 0.18, Down, \alpha = 15^0)$

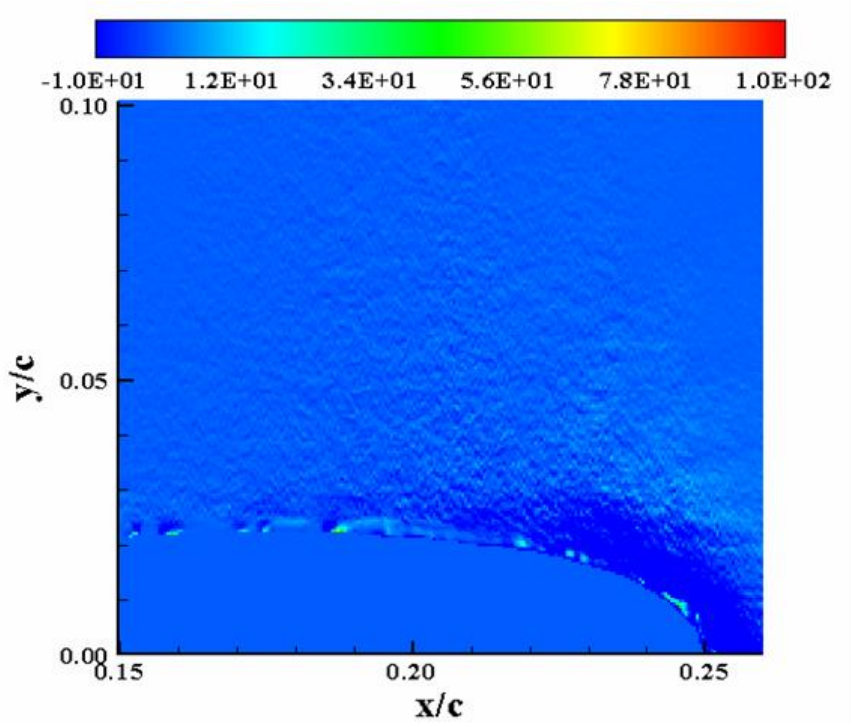

Figure D-117: $P_{yy}(M_\infty = 0.2, k = 0.18, Down, \alpha = 13.7^0)$

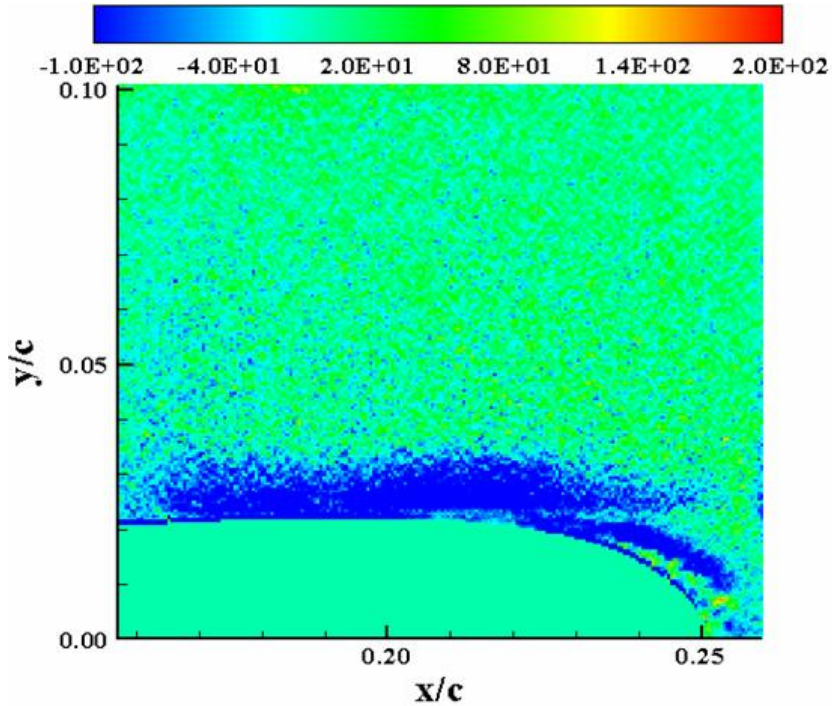

Figure D-118: $S_{xy}(M_\infty = 0.2, k = 0.18, Down, \alpha = 15^0)$

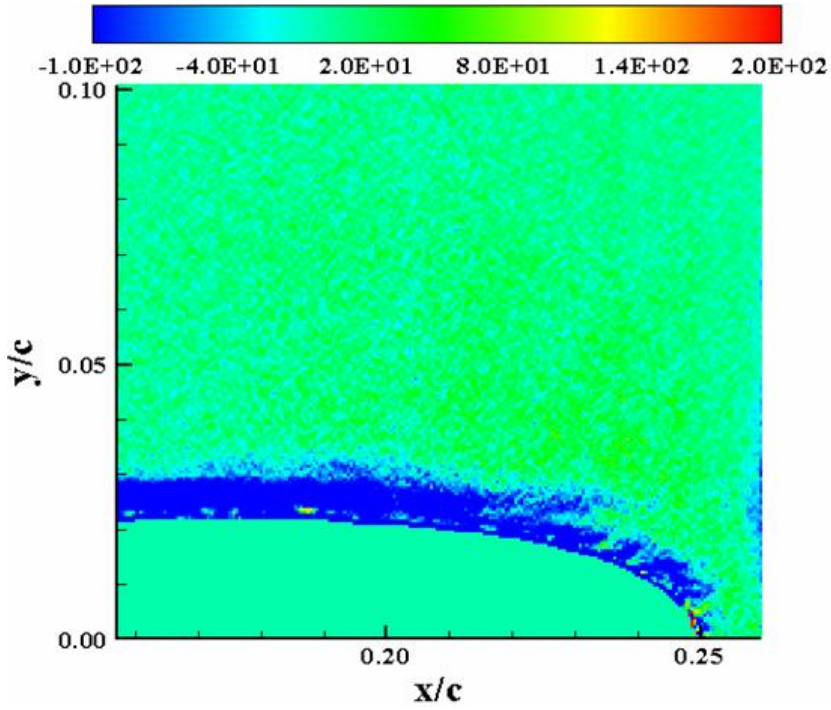

Figure D-119: $S_{xy}(M_\infty = 0.2, k = 0.18, Down, \alpha = 13.7^0)$

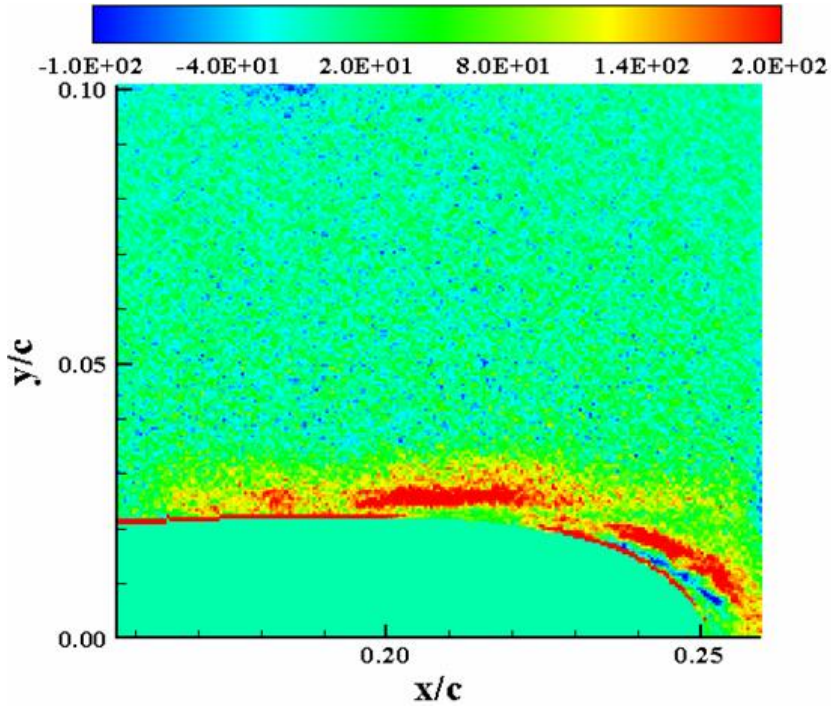

Figure D-120: $\omega_z(M_\infty = 0.2, k = 0.18, Down, \alpha = 15^0)$

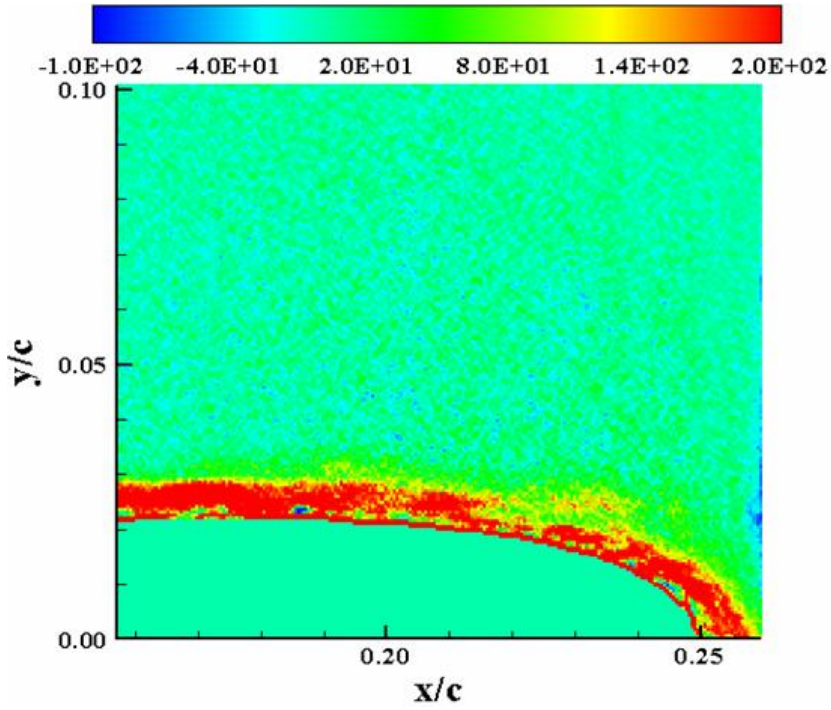

Figure D-121: $\omega_z (M_\infty = 0.2, k = 0.18, Down, \alpha = 13.7^0)$

APPENDIX E

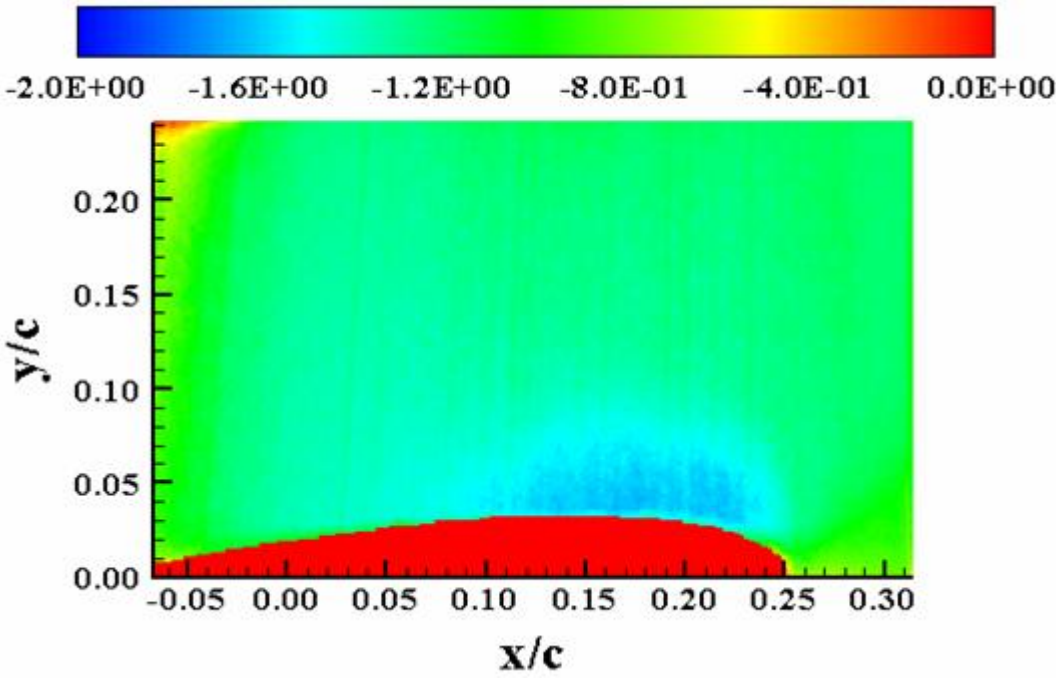

Figure E-1: $U_N(M_\infty = 0.2, k = 0, \alpha = 10^0)$

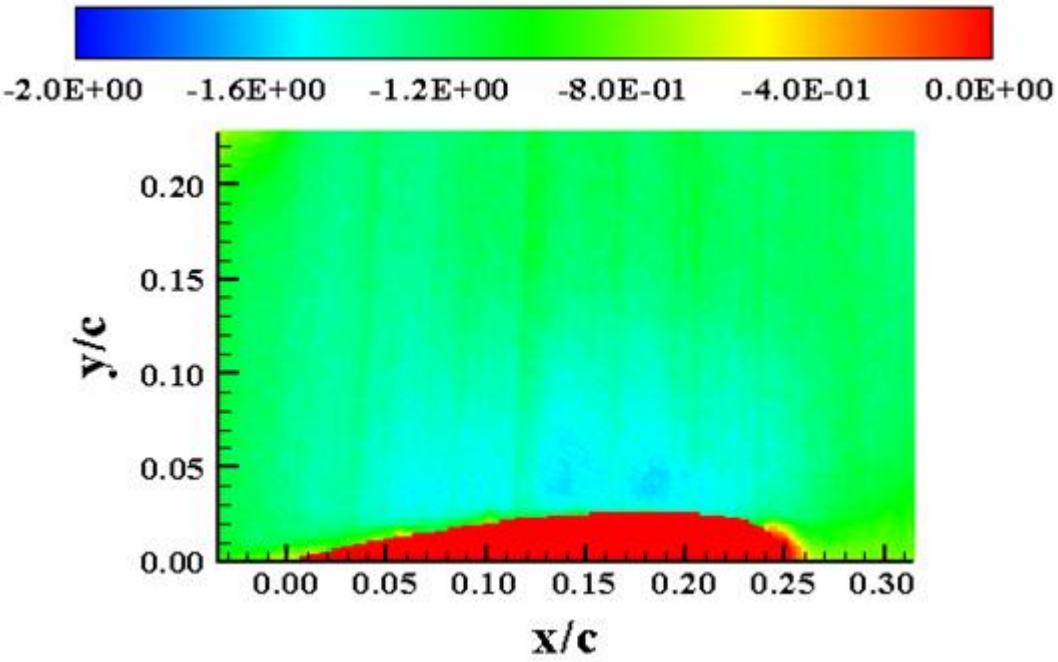

Figure E-2: $U_N(M_\infty = 0.2, k = 0, \alpha = 14^0)$

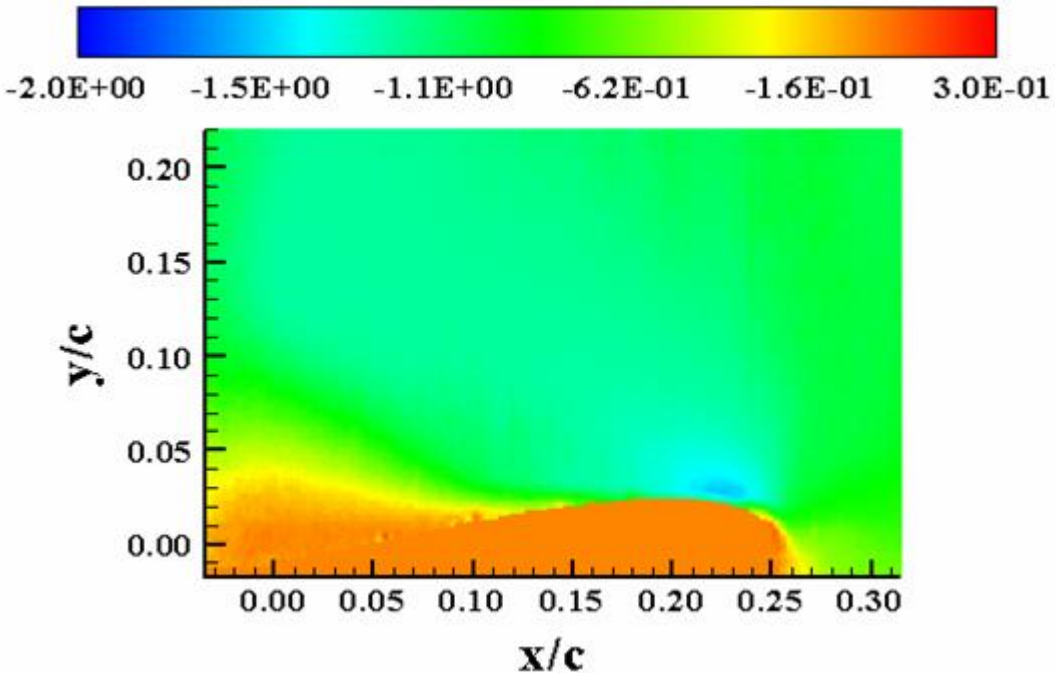

Figure E-3: $U_N(M_\infty = 0.2, k = 0, \alpha = 18^0)$

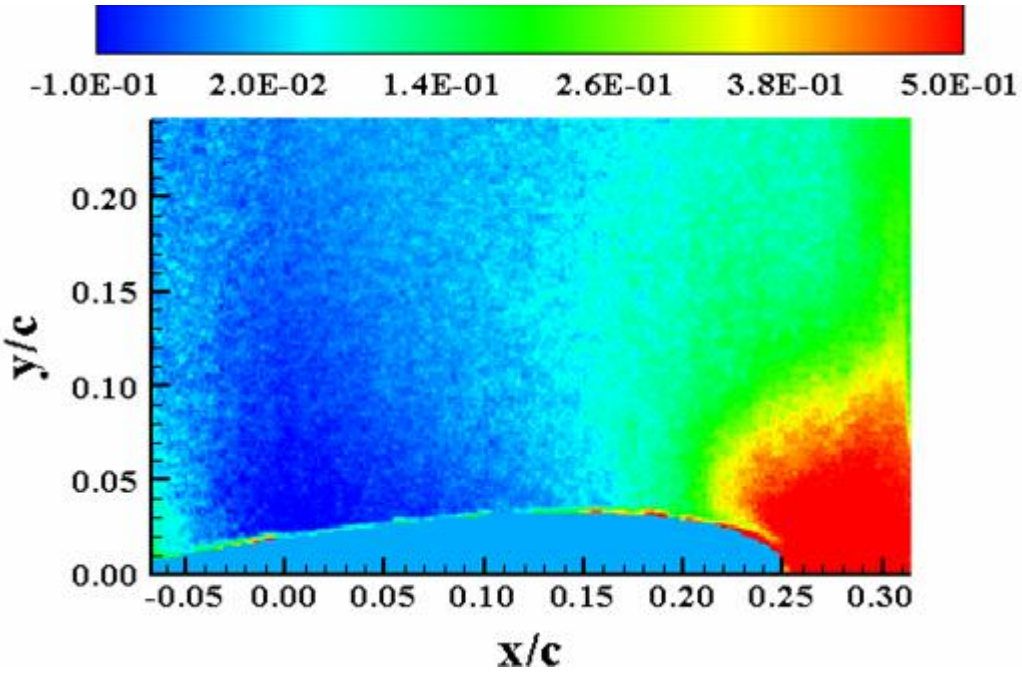

Figure E-4: $V_N(M_\infty = 0.2, k = 0, \alpha = 10^0)$

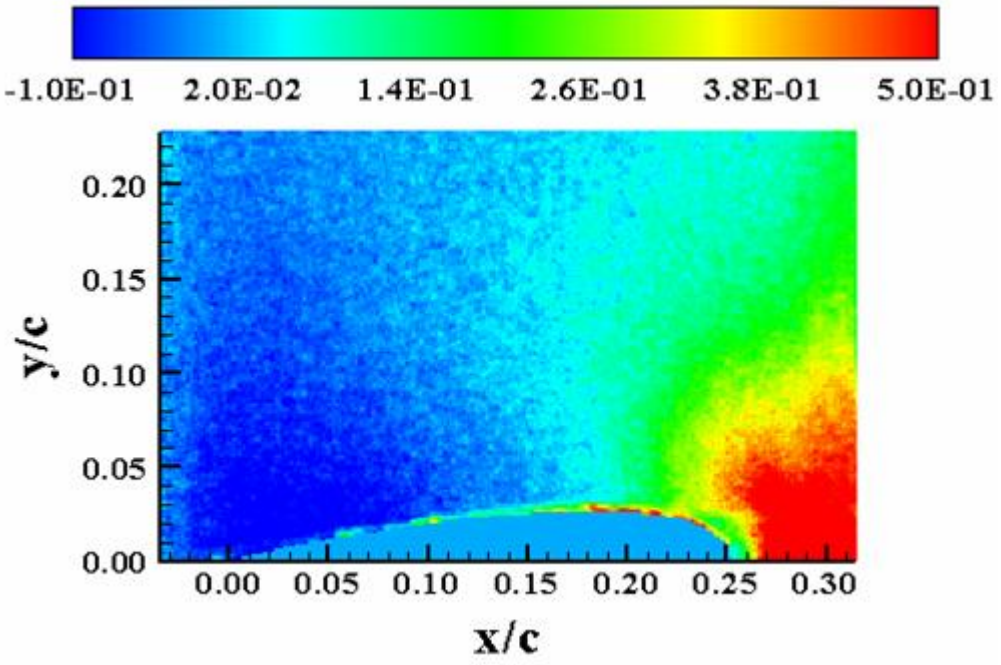

Figure E-5: $V_N\,(M_\infty = 0.2, k = 0, \alpha = 14^0)$

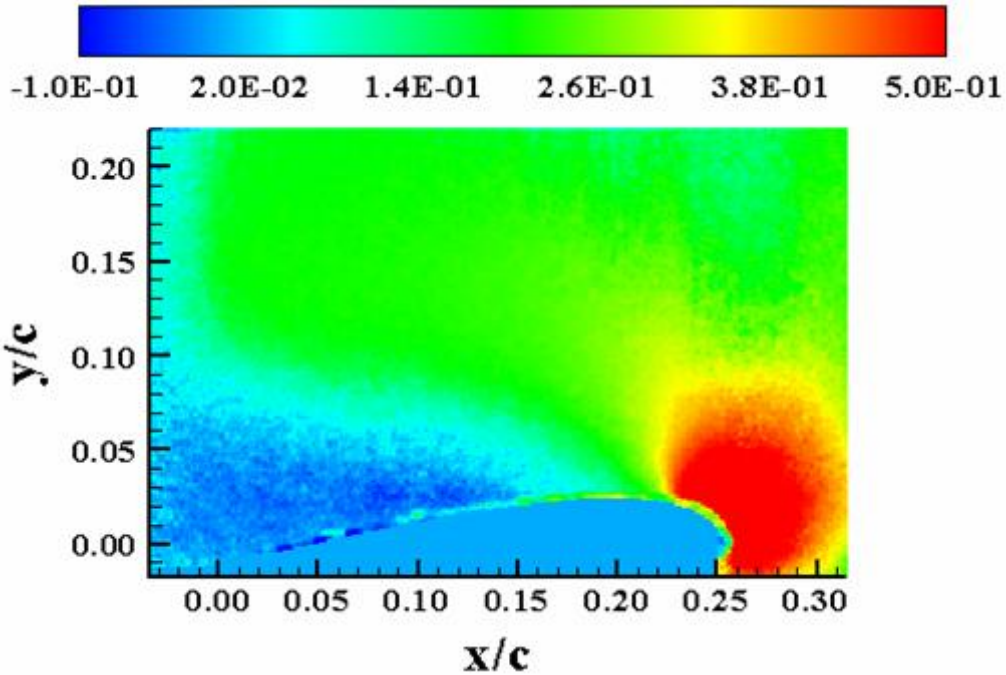

Figure E-6: $V_N\,(M_\infty = 0.2, k = 0, \alpha = 18^0)$

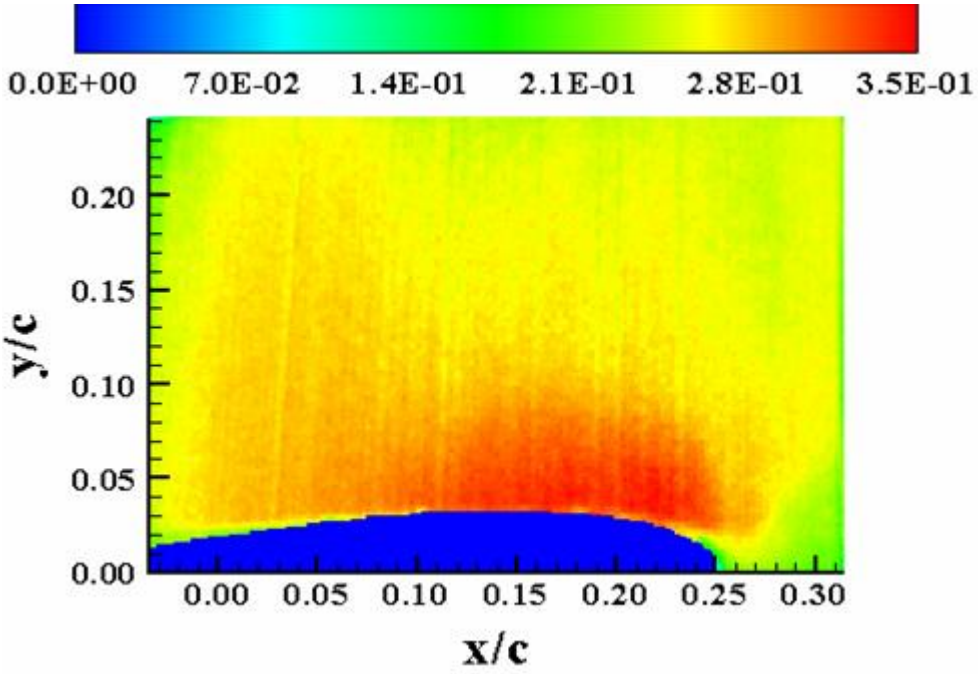

Figure E-7: $M(M_\infty = 0.2, k = 0, \alpha = 10^0)$

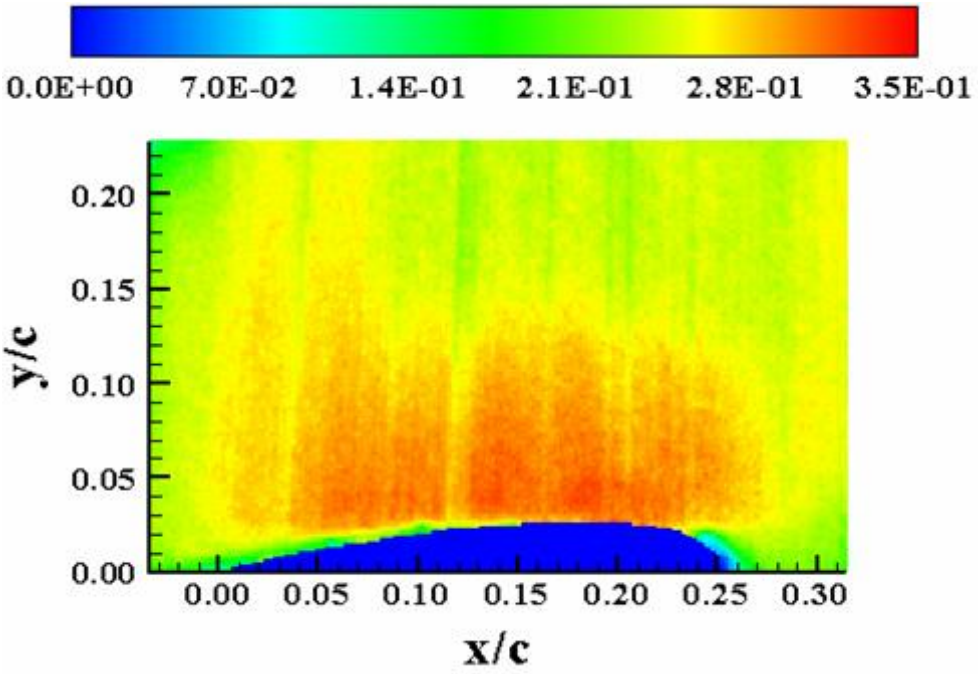

Figure E-8: $M(M_\infty = 0.2, k = 0, \alpha = 14^0)$

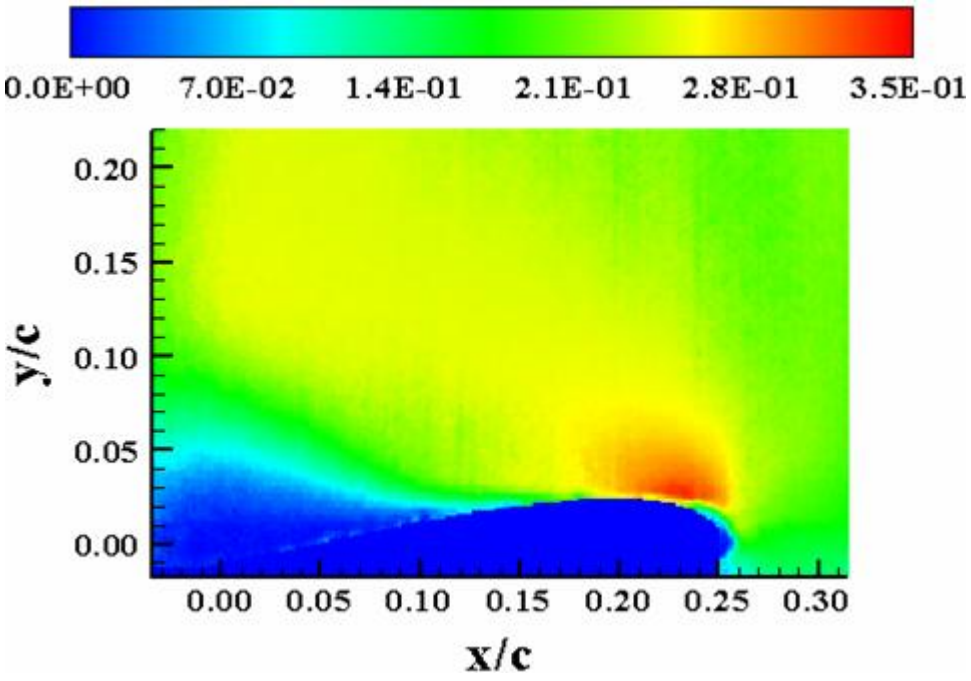

Figure E-9: $M(M_\infty = 0.2, k = 0, \alpha = 18^0)$

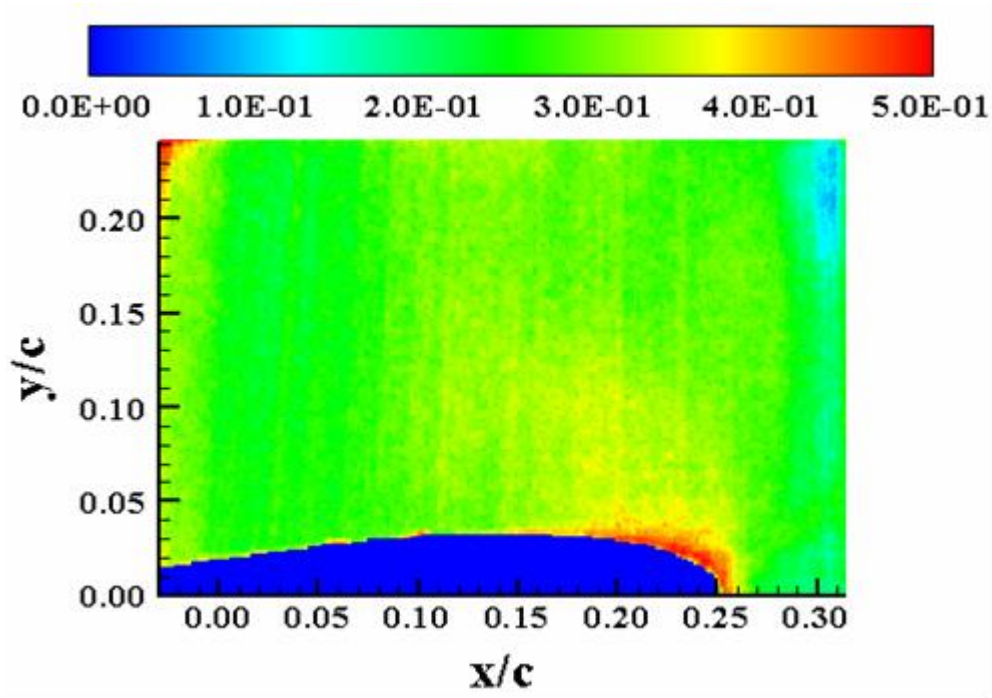

Figure E-10: $\sigma_u(M_\infty = 0.2, k = 0, \alpha = 10^0)$

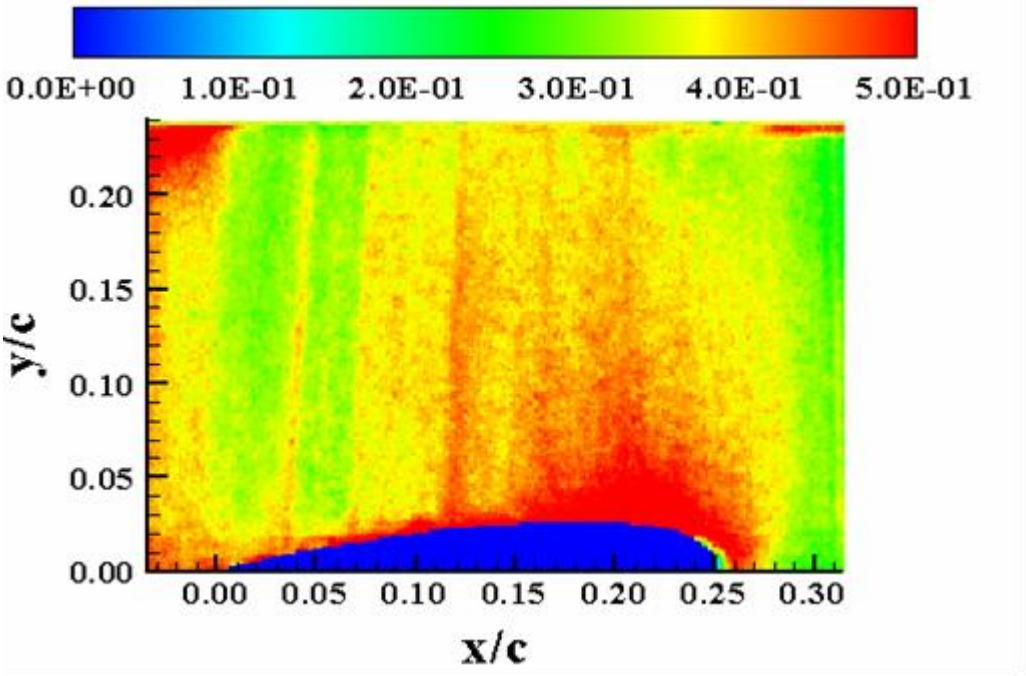

Figure E-11: $\sigma_u(M_\infty = 0.2, k = 0, \alpha = 14^0)$

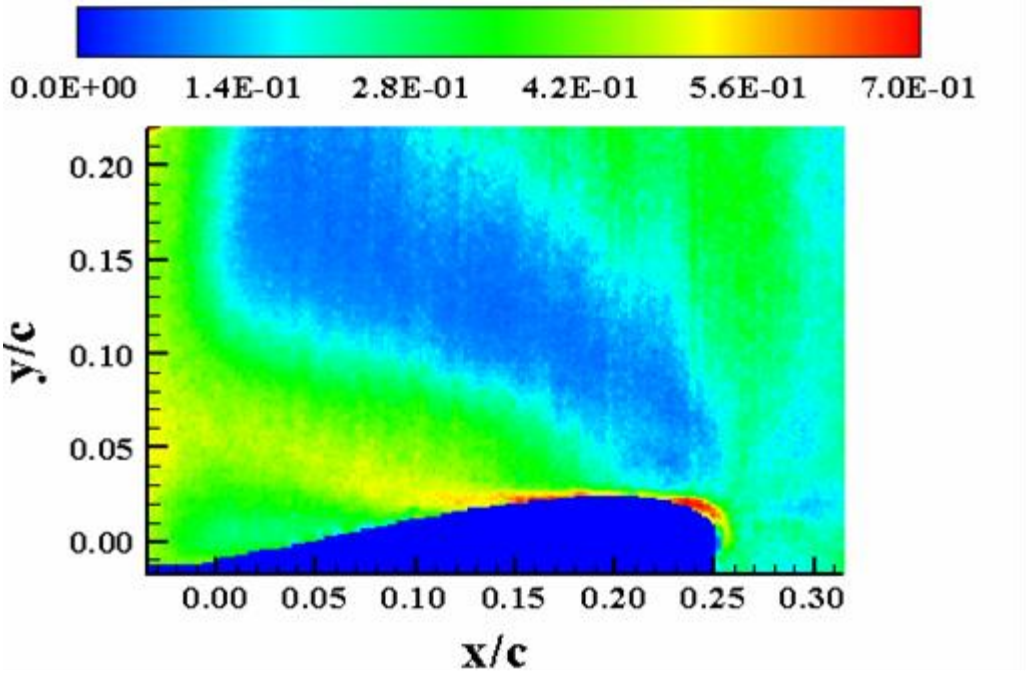

Figure E-12: $\sigma_u(M_\infty = 0.2, k = 0, \alpha = 18^0)$

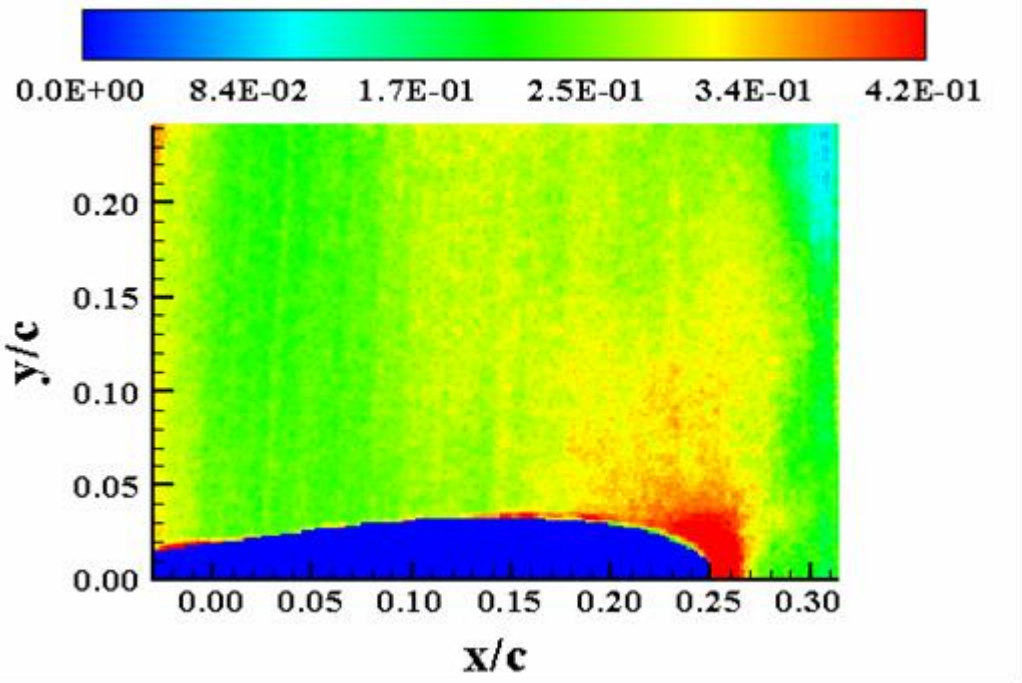

Figure E-13: $\sigma_v(M_\infty = 0.2, k = 0, \alpha = 10^0)$

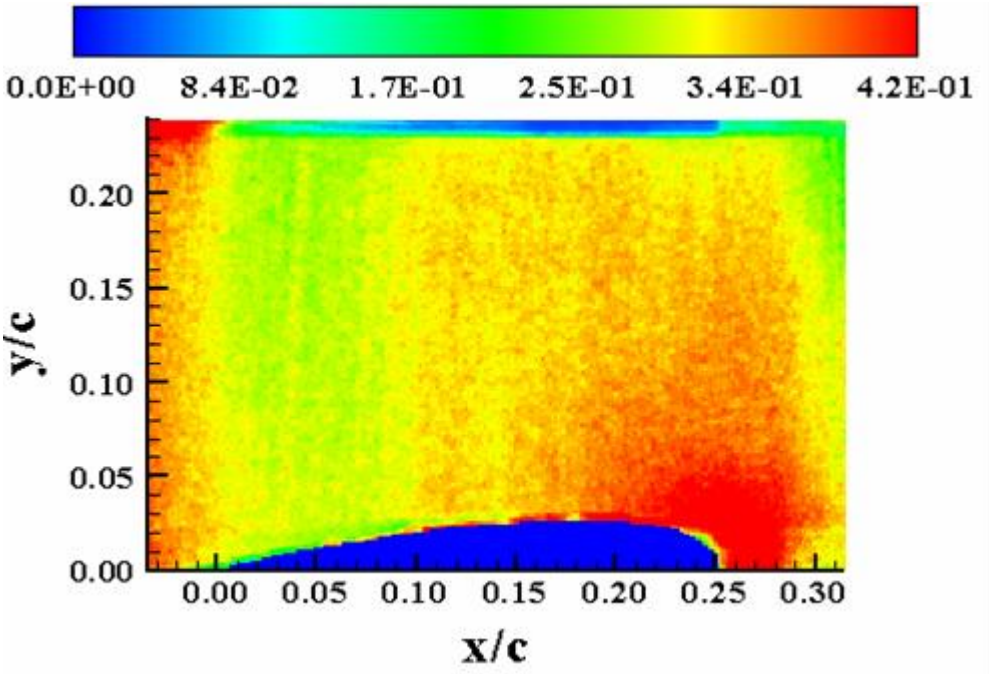

Figure E-14: $\sigma_v(M_\infty = 0.2, k = 0, \alpha = 14^0)$

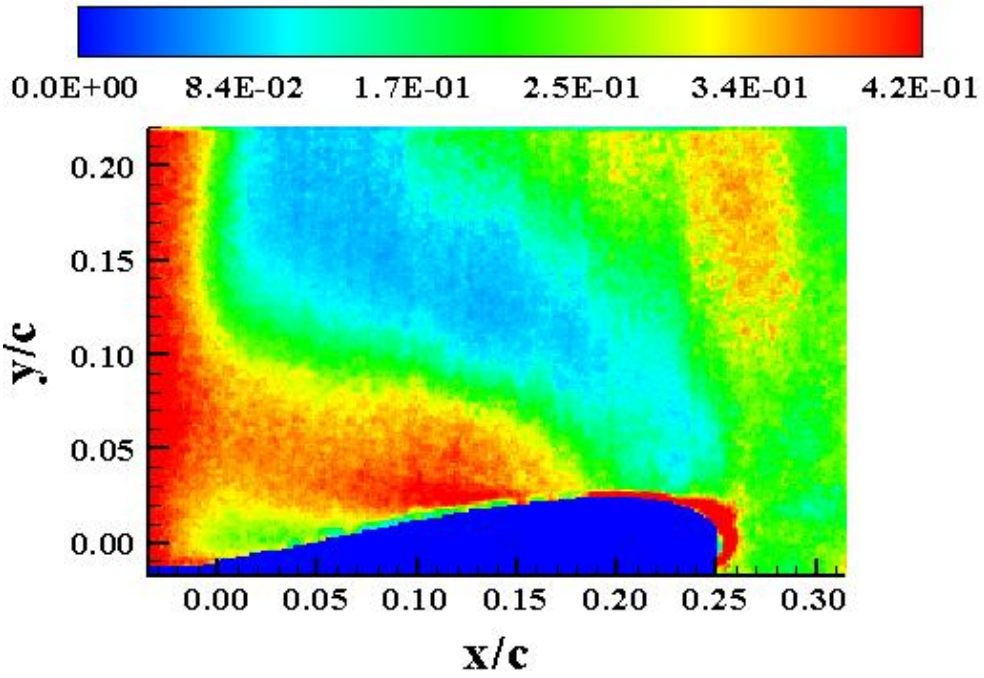

Figure E-15: $\sigma_v(M_\infty = 0.2, k = 0, \alpha = 18^0)$

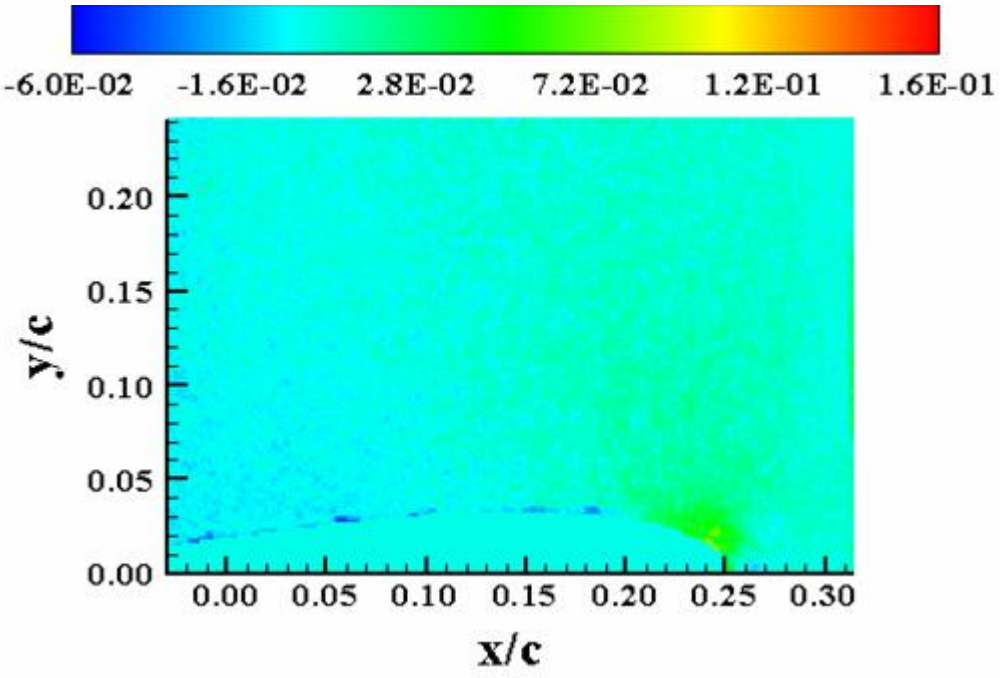

Figure E-16: $\tau_{xy}(M_\infty = 0.2, k = 0, \alpha = 10^0)$

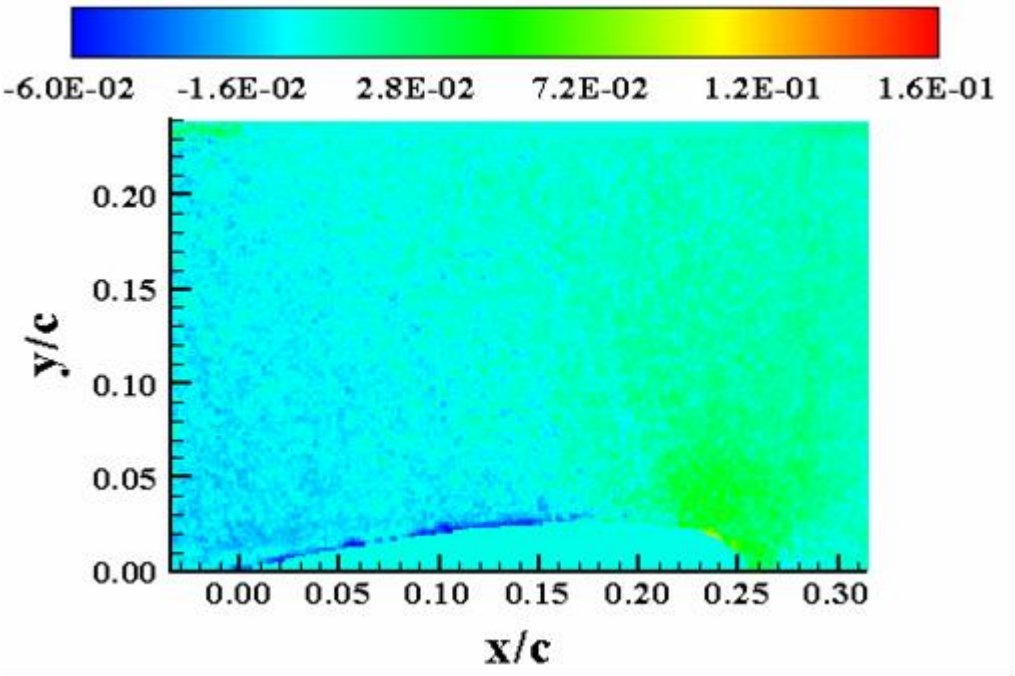

Figure E-17: $\tau_{xy}(M_\infty = 0.2, k = 0, \alpha = 14^0)$

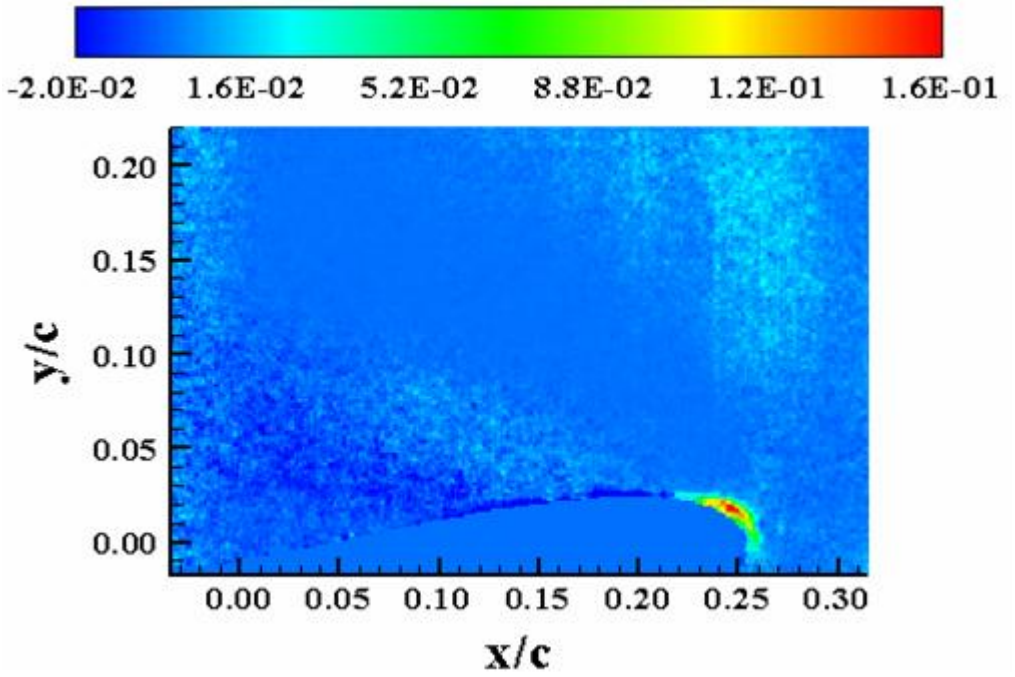

Figure E-18: $\tau_{xy}(M_\infty = 0.2, k = 0, \alpha = 18^0)$

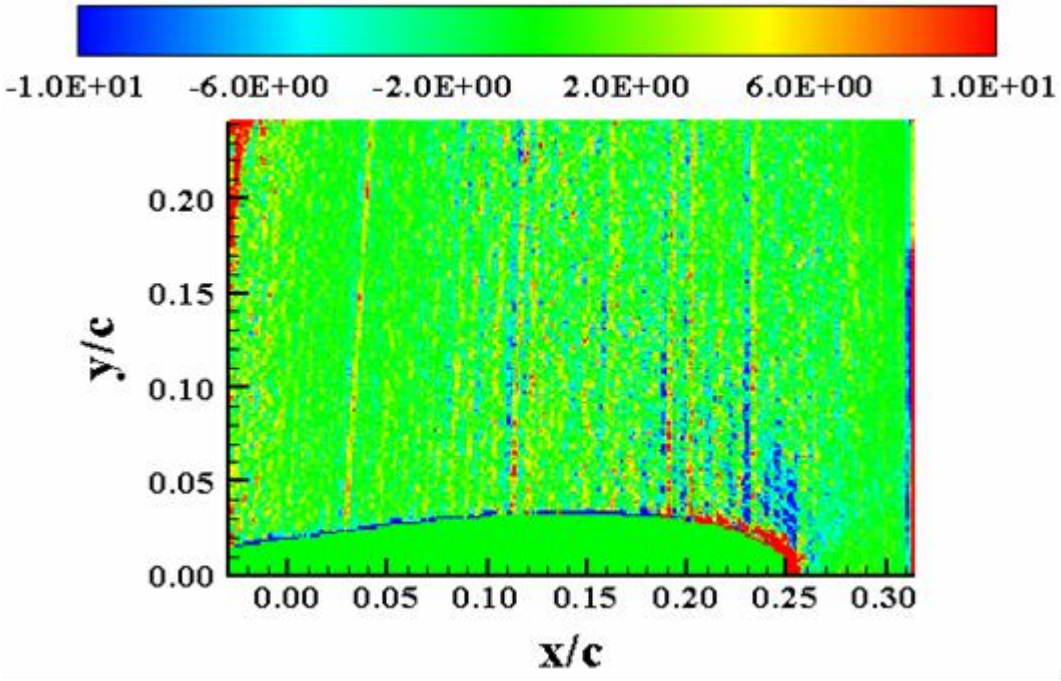

Figure E-19: $P_{xx}(M_\infty = 0.2, k = 0, \alpha = 10^0)$

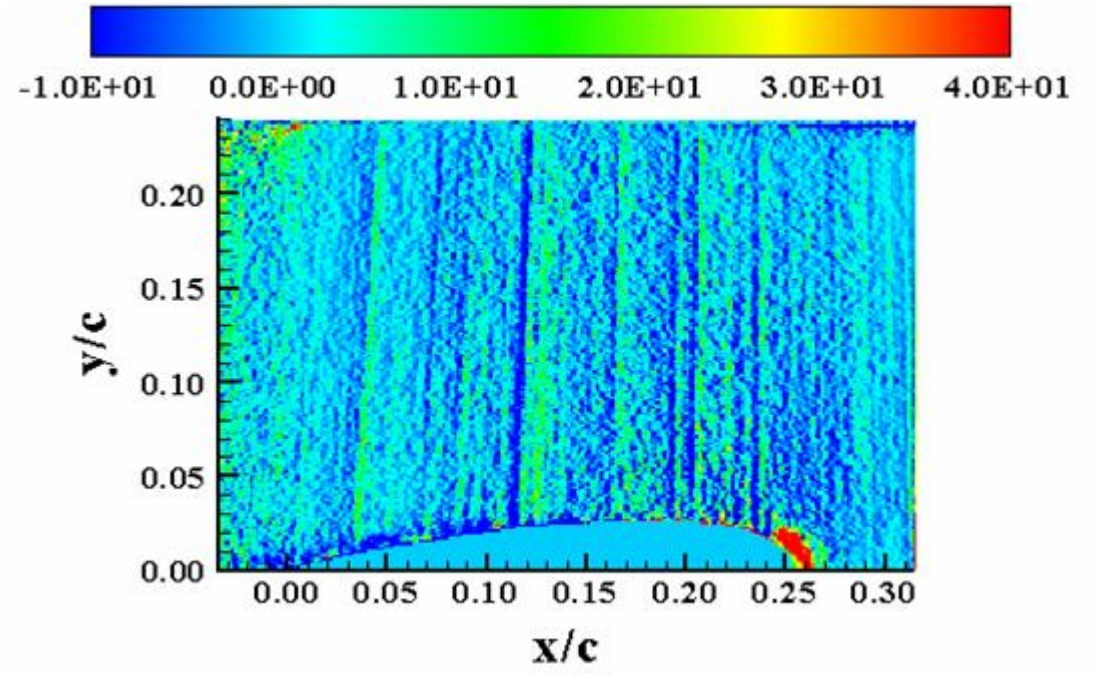

Figure E-20: $P_{xx}(M_\infty = 0.2, k = 0, \alpha = 14^0)$

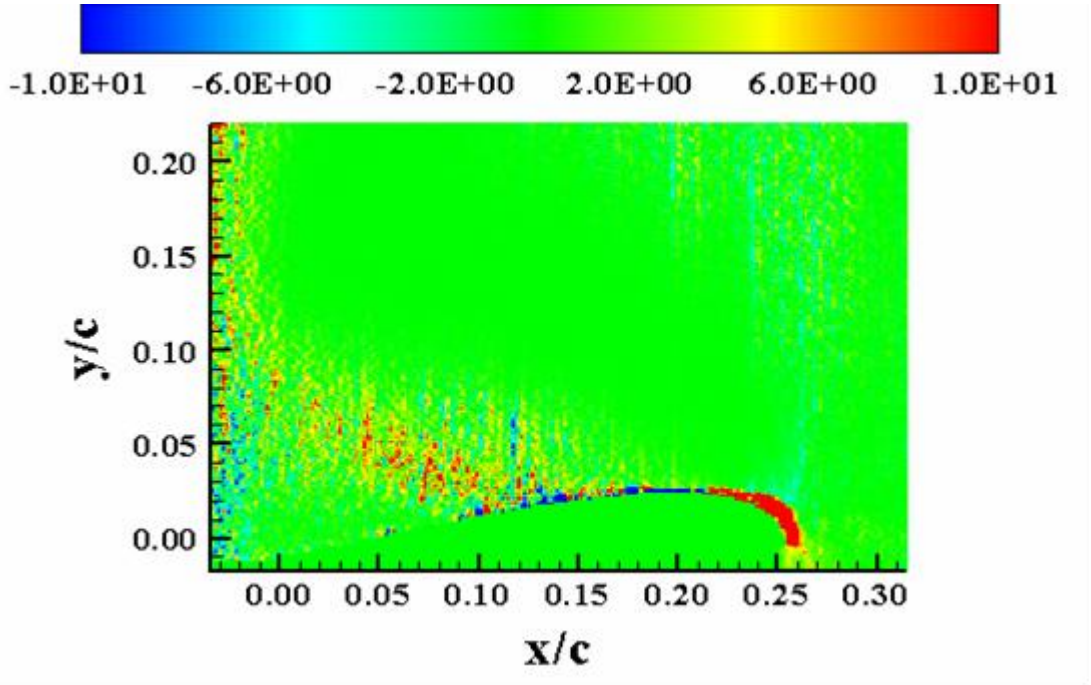

Figure E-21: $P_{xx}(M_\infty = 0.2, k = 0, \alpha = 18^0)$

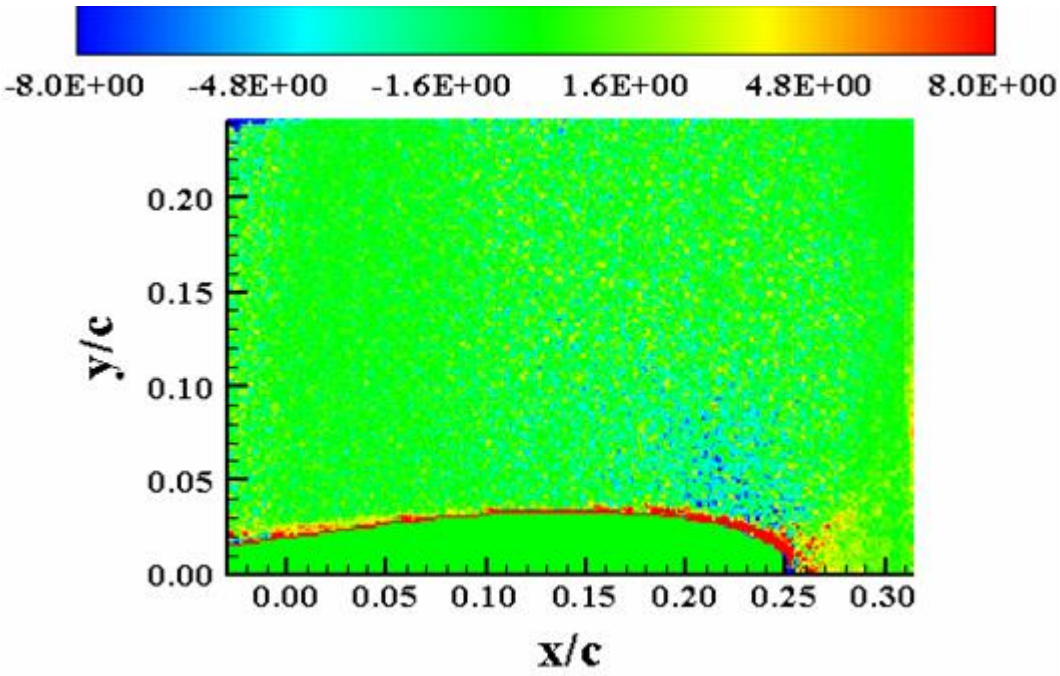

Figure E-22: $P_{xy}(M_\infty = 0.2, k = 0, \alpha = 10^0)$

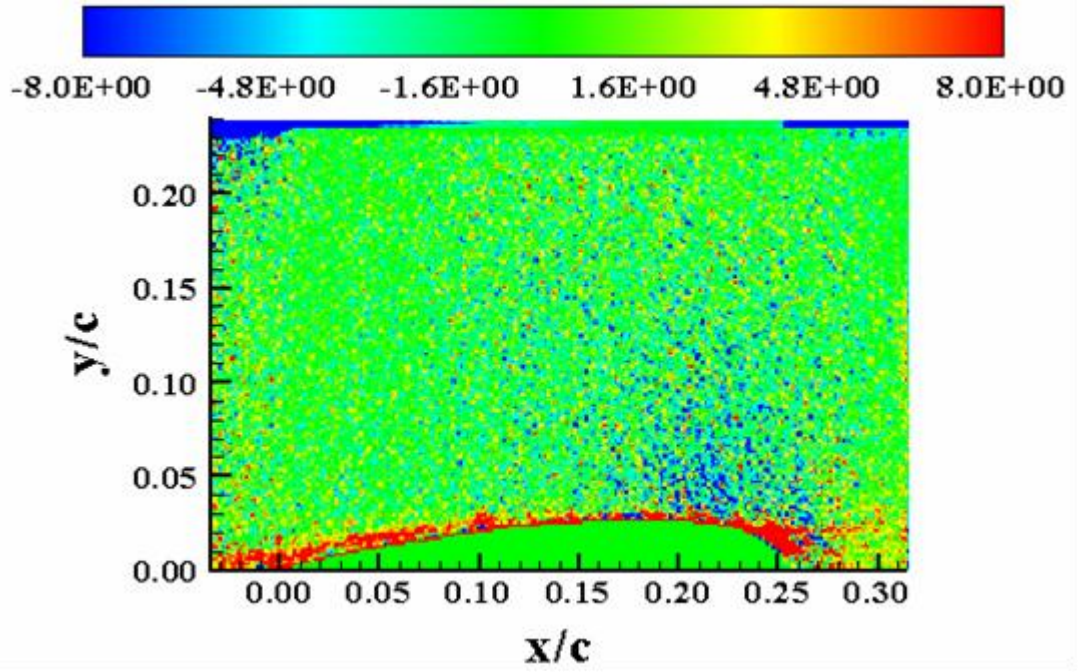

Figure E-23: $P_{xy}(M_\infty = 0.2, k = 0, \alpha = 14^0)$

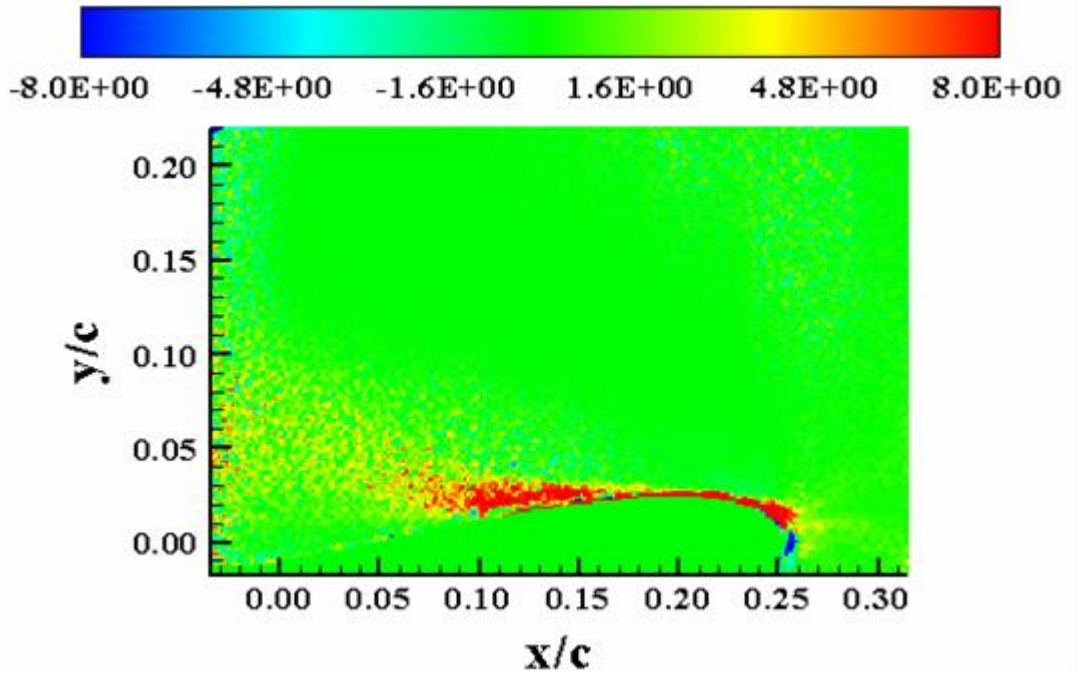

Figure E-24: $P_{xy}(M_\infty = 0.2, k = 0, \alpha = 18^0)$

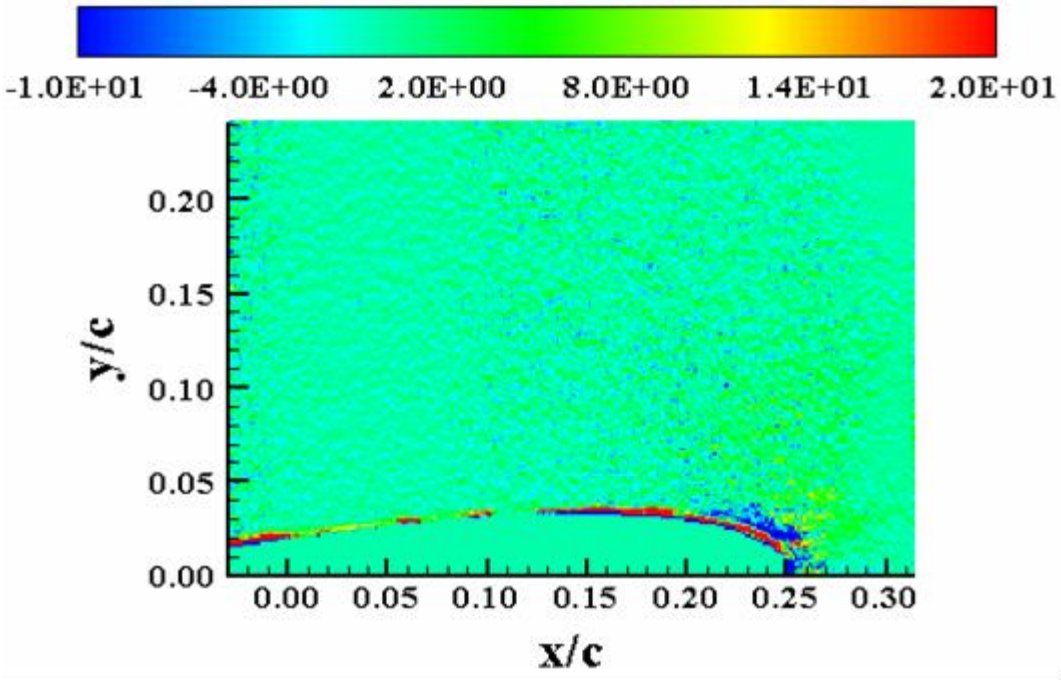

Figure E-25: $P_{yy}(M_\infty = 0.2, k = 0, \alpha = 10^0)$

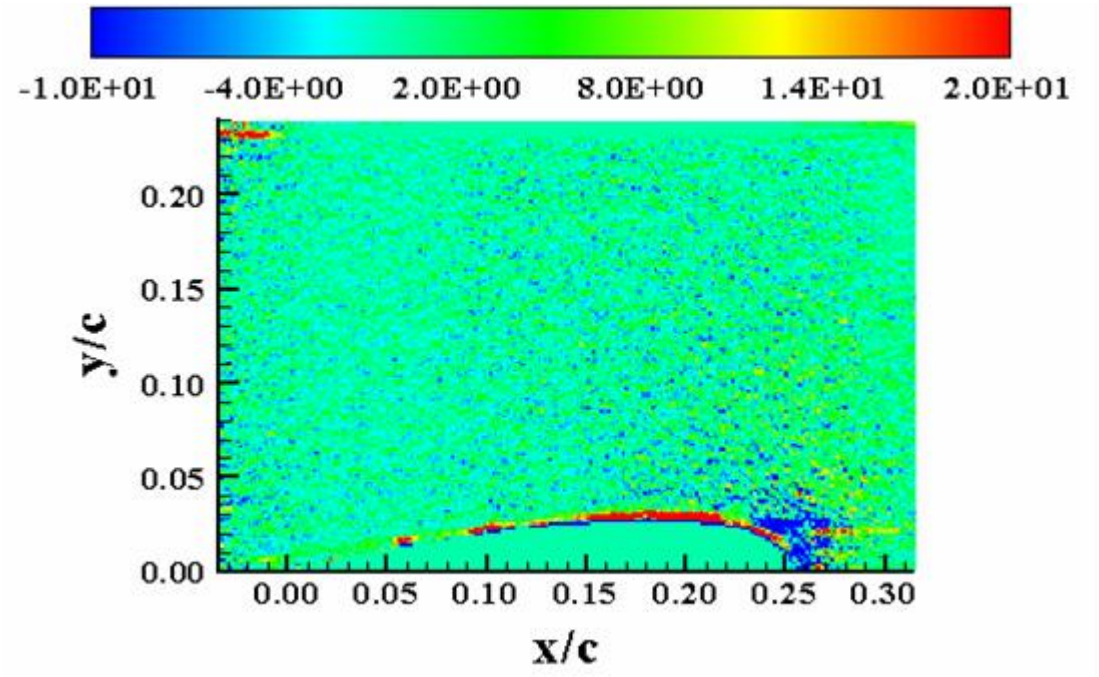

Figure E-26: $P_{yy}(M_\infty = 0.2, k = 0, \alpha = 14^0)$

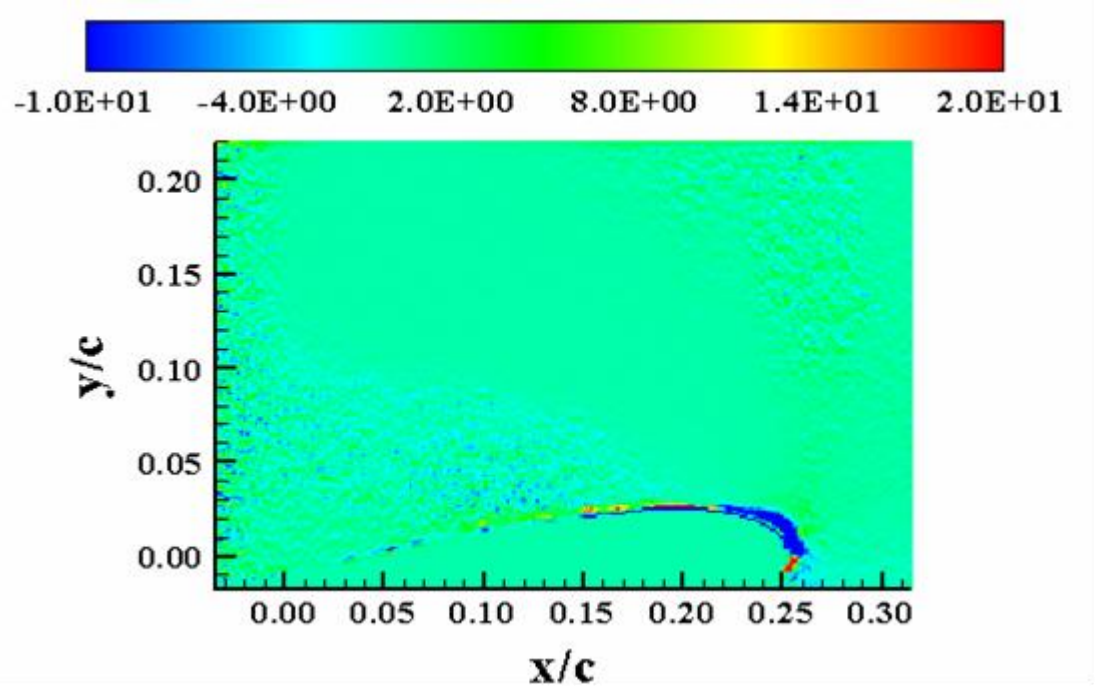

Figure E-27: $P_{yy}(M_\infty = 0.2, k = 0, \alpha = 18^0)$

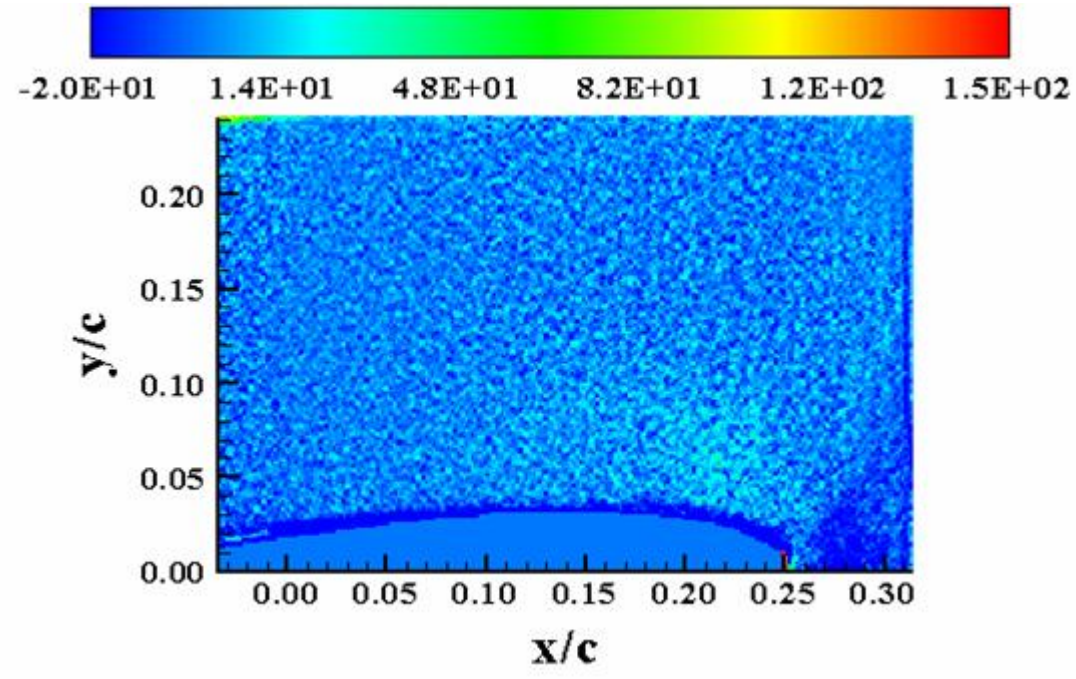

Figure E-28: $S_{xy}(M_\infty = 0.2, k = 0, \alpha = 10^0)$

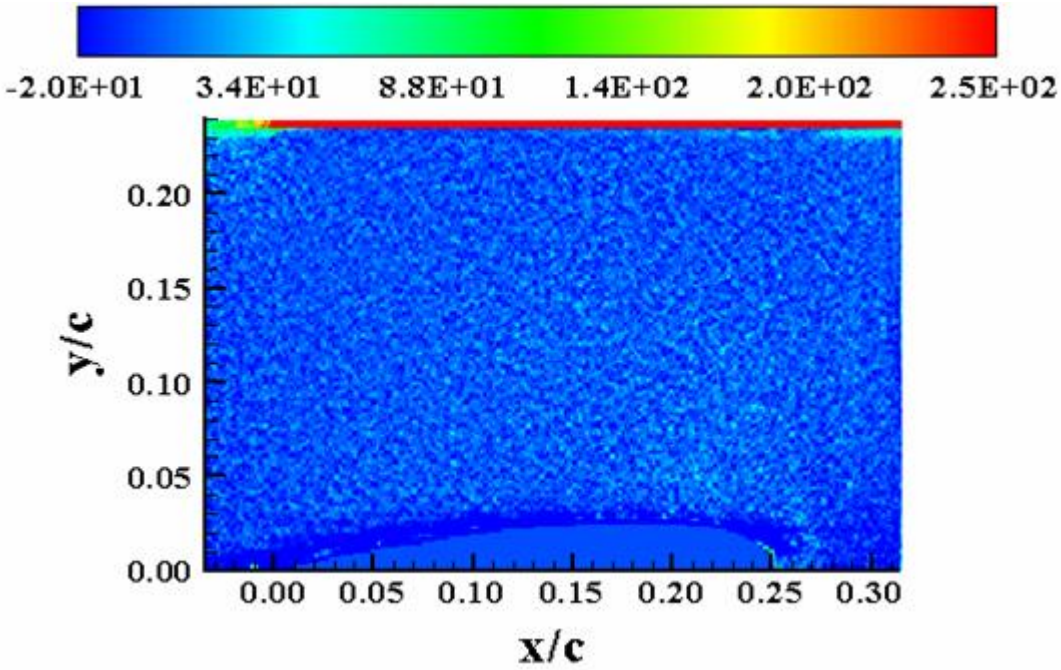

Figure E-29: $S_{xy}(M_\infty = 0.2, k = 0, \alpha = 14^0)$

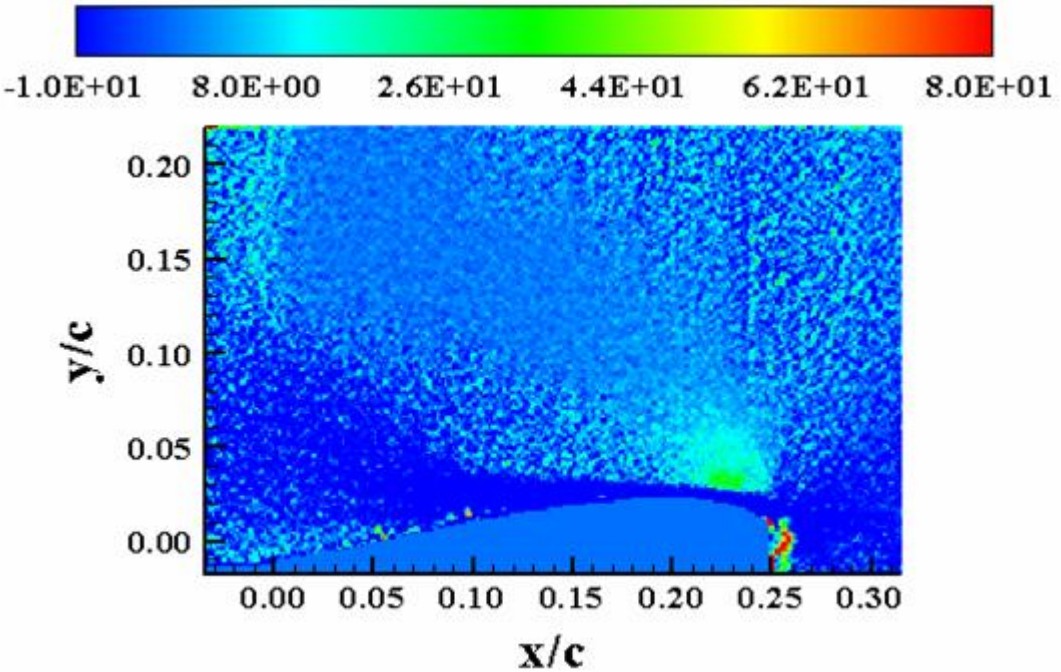

Figure E-30: $S_{xy}(M_\infty = 0.2, k = 0, \alpha = 18^0)$

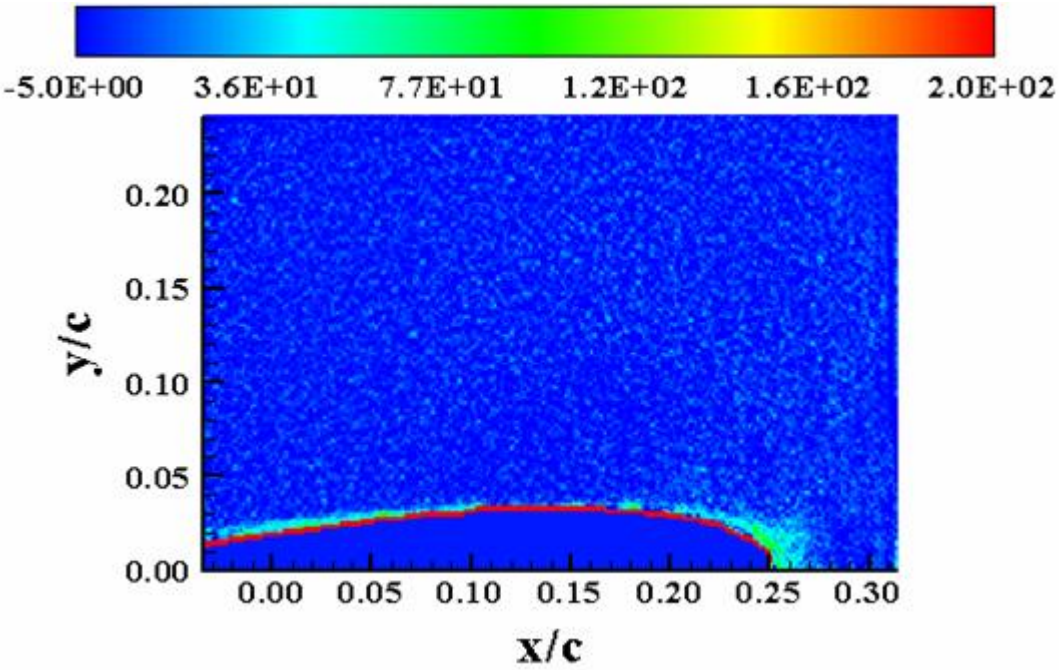

Figure E-31: $\omega_z(M_\infty = 0.2, k = 0, \alpha = 10^0)$

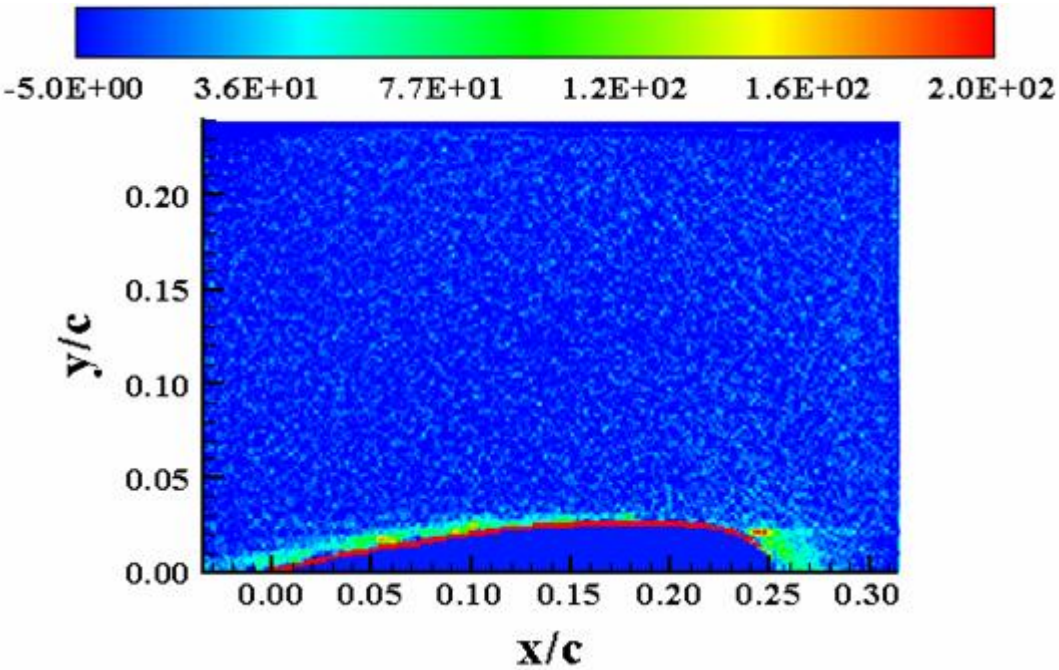

Figure E-32: $\omega_z(M_\infty = 0.2, k = 0, \alpha = 14^0)$

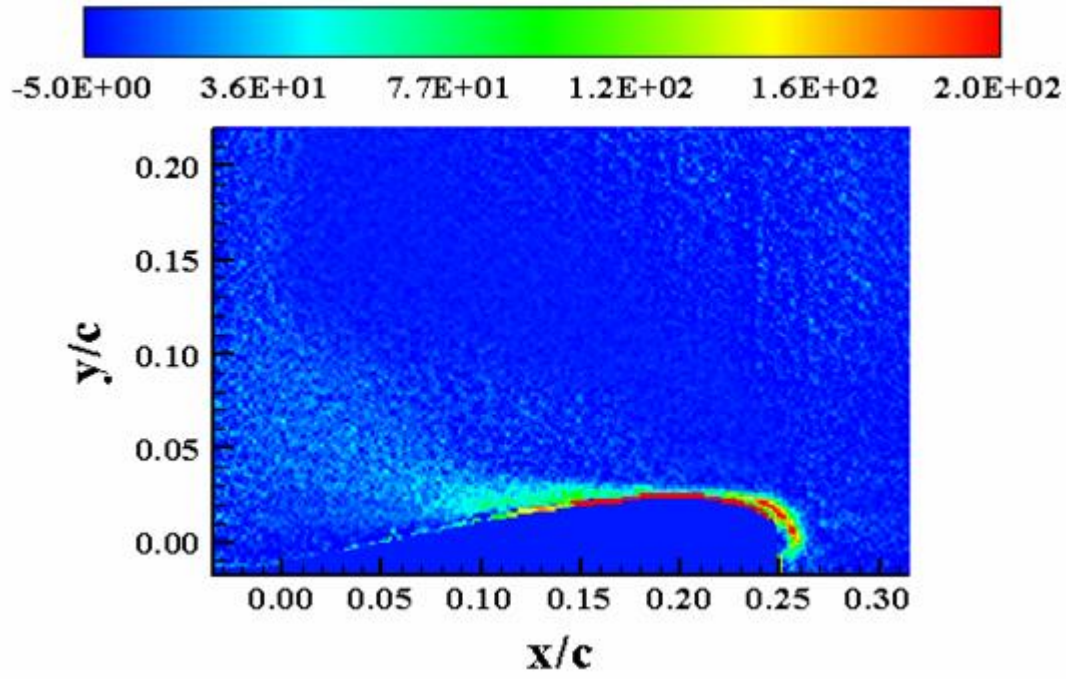

Figure E-33: $\omega_z (M_\infty = 0.2, k = 0, \alpha = 18^0)$

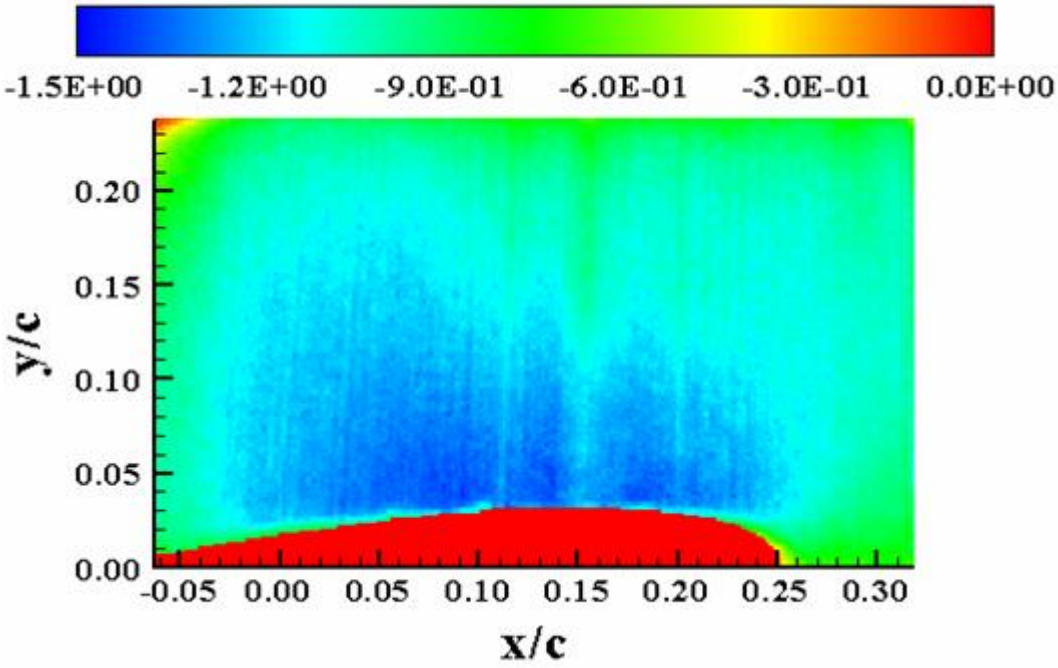

Figure E-34: $U_N (M_\infty = 0.28, k = 0, \alpha = 10^0)$

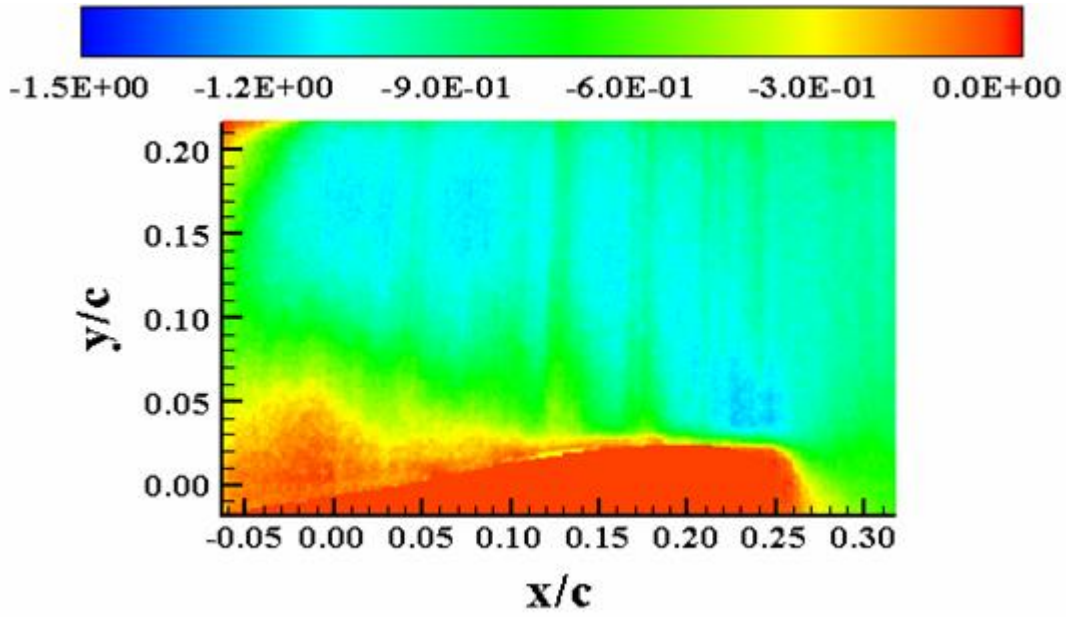

Figure E-35: $U_N\,(M_\infty = 0.28, k = 0, \alpha = 18^0)$

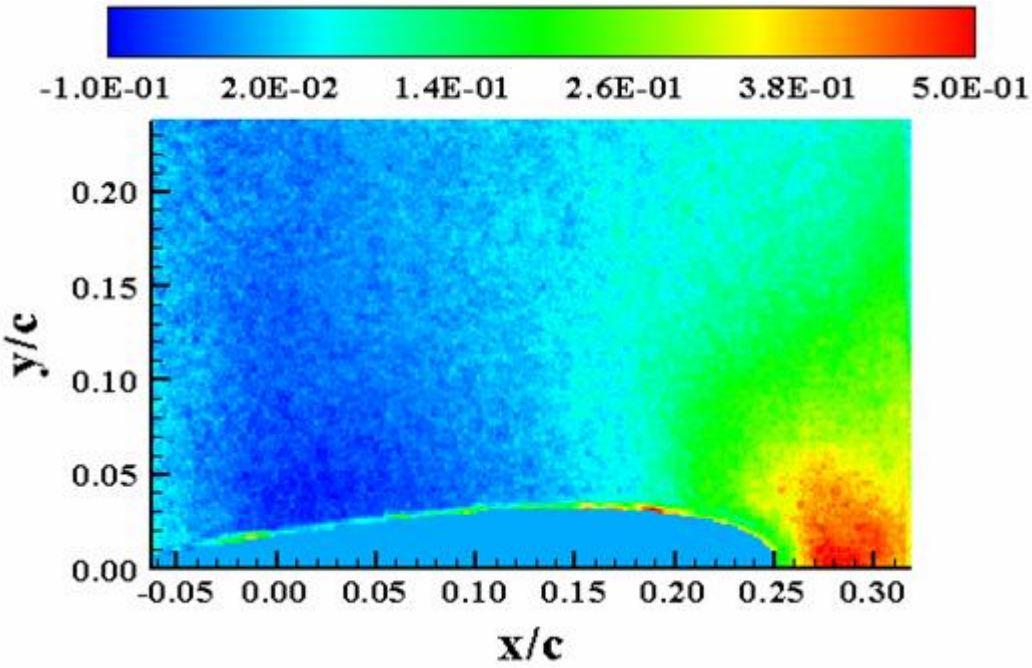

Figure E-36: $V_N\,(M_\infty = 0.28, k = 0, \alpha = 10^0)$

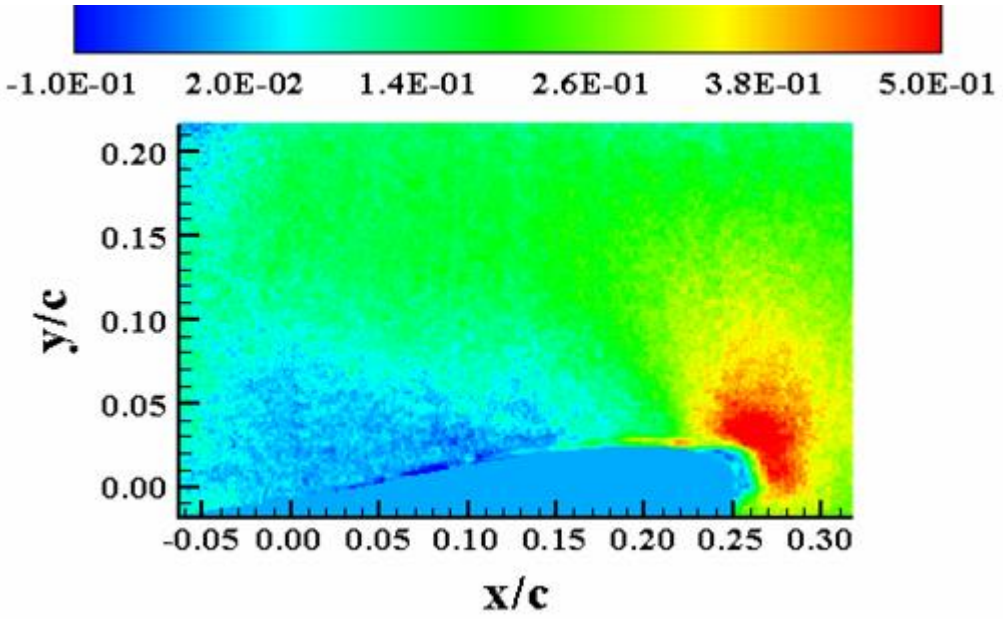

Figure E-37: $V_N(M_\infty = 0.28, k = 0, \alpha = 18^0)$

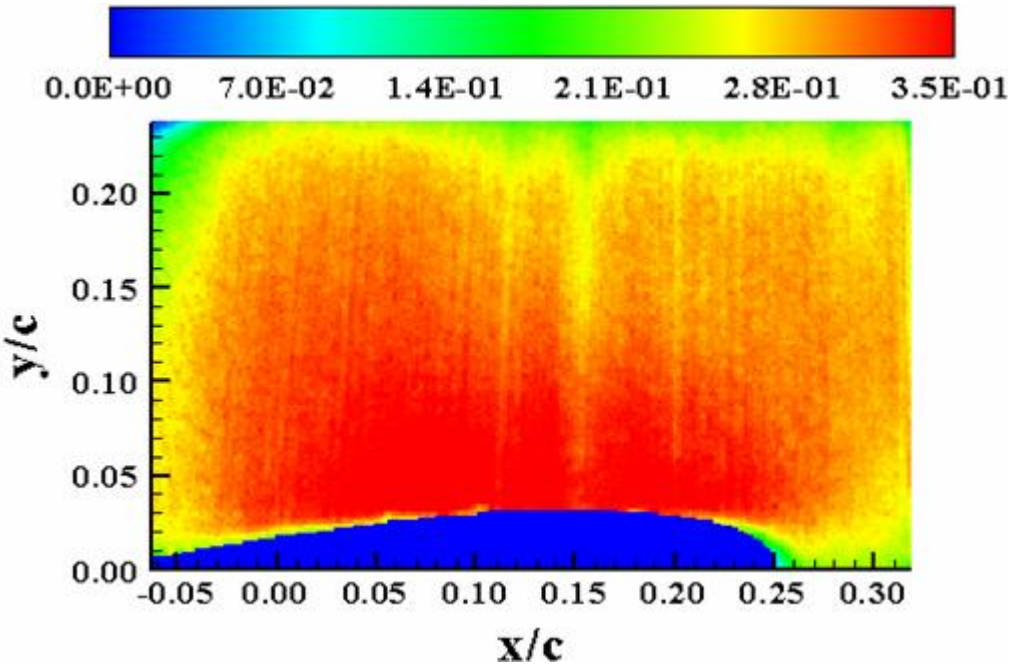

Figure E-38: $M(M_\infty = 0.28, k = 0, \alpha = 10^0)$

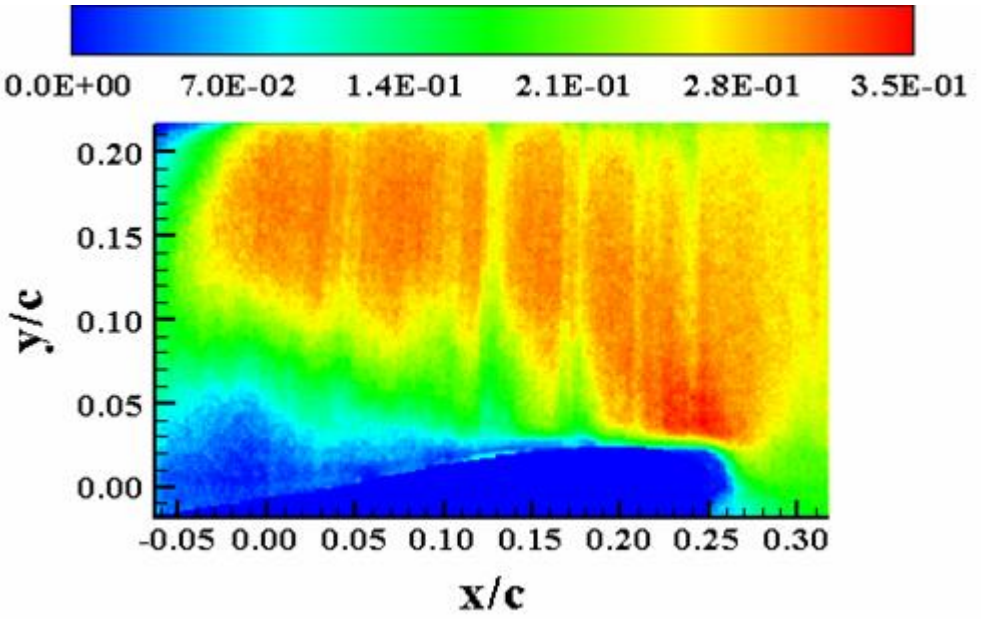

Figure E-39: $M(M_\infty = 0.28, k = 0, \alpha = 18^0)$

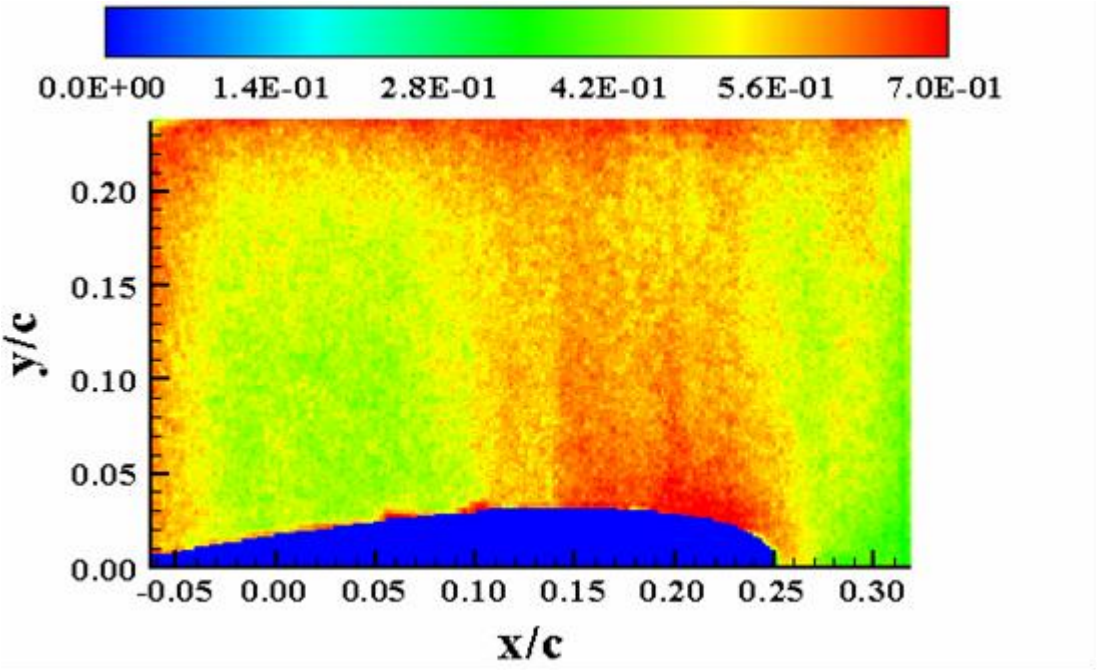

Figure E-40: $\sigma_u(M_\infty = 0.28, k = 0, \alpha = 10^0)$

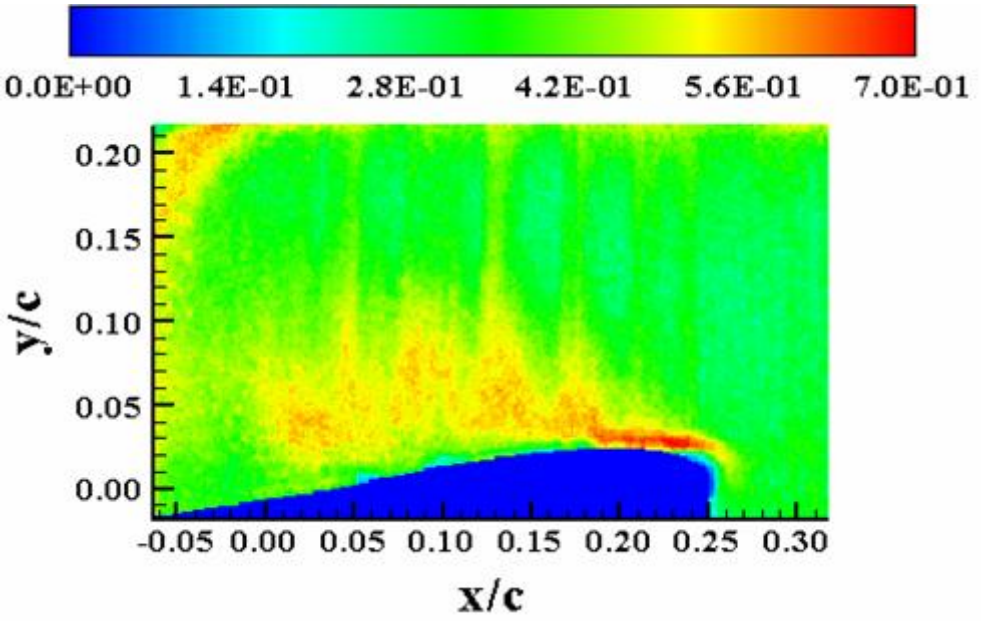

Figure E-41: $\sigma_u(M_\infty = 0.28, k = 0, \alpha = 18^0)$

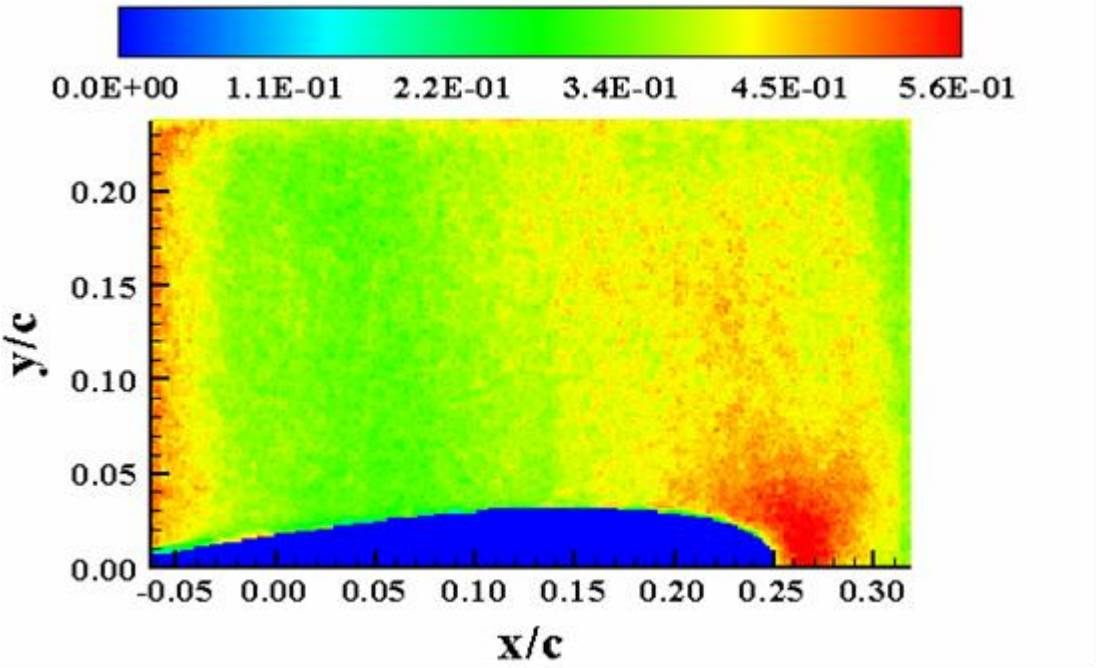

Figure E-42: $\sigma_v(M_\infty = 0.28, k = 0, \alpha = 10^0)$

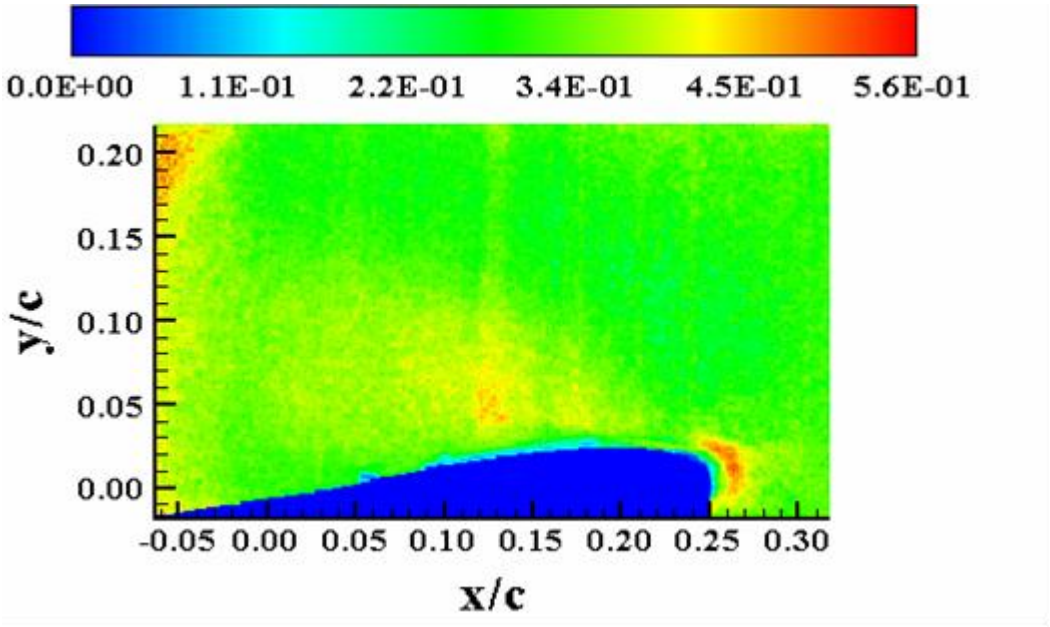

Figure E-43: $\sigma_v (M_\infty = 0.28, k = 0, \alpha = 18^0)$

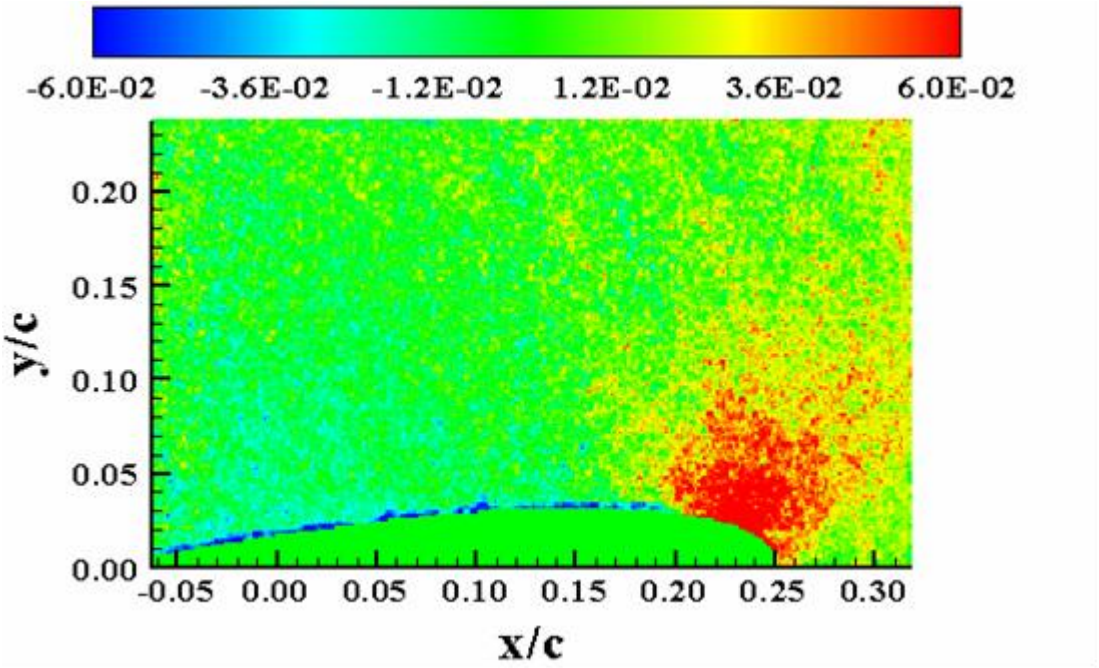

Figure E-44: $\tau_{xy} (M_\infty = 0.28, k = 0, \alpha = 10^0)$

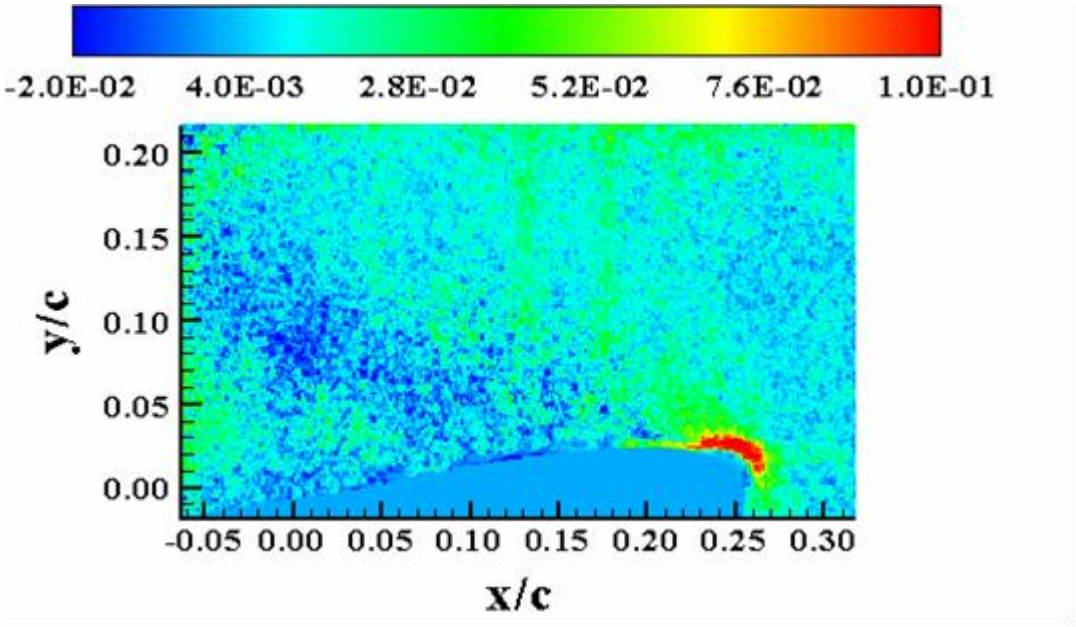

Figure E-45: $\tau_{xy}(M_\infty = 0.28, k = 0, \alpha = 18^0)$

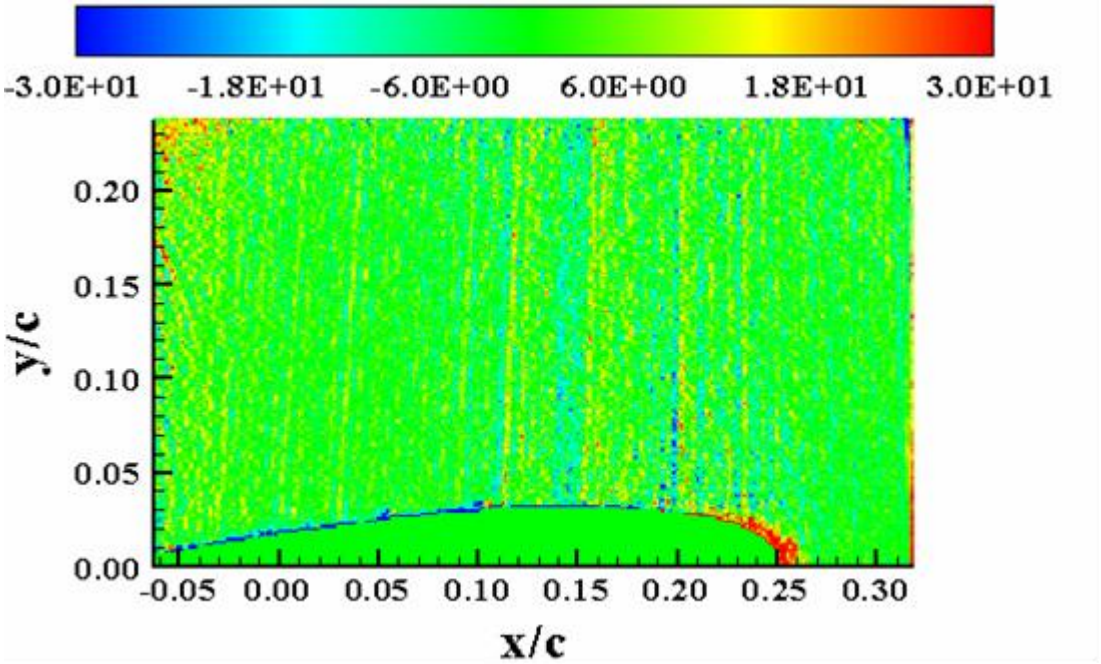

Figure E-46: $P_{xx}(M_\infty = 0.28, k = 0, \alpha = 10^0)$

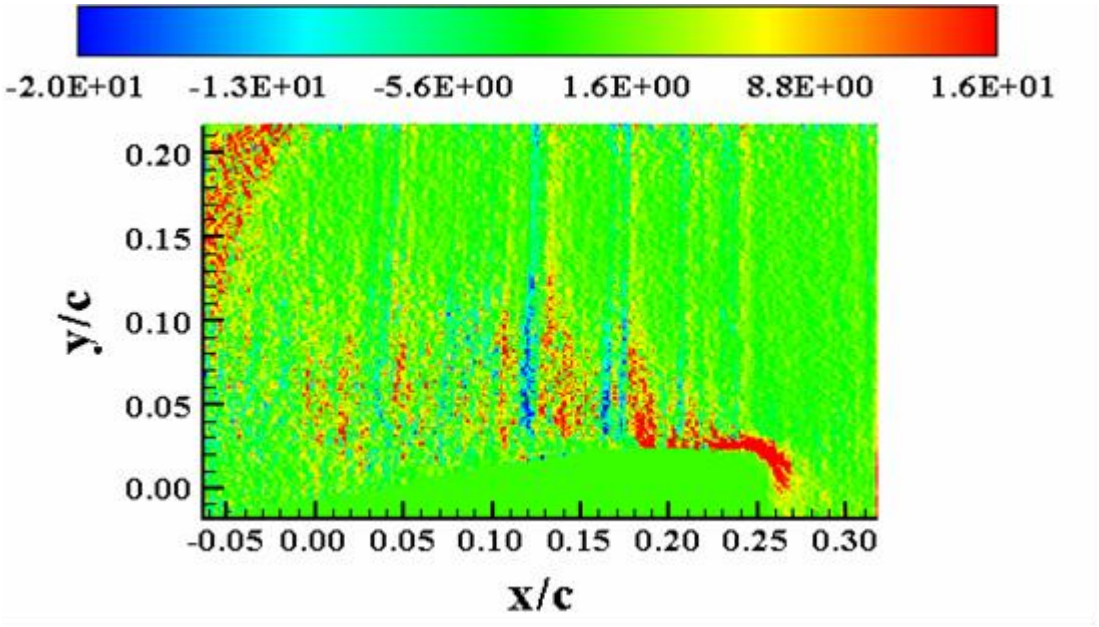

Figure E-47: $P_{xx}(M_\infty = 0.28, k = 0, \alpha = 18^0)$

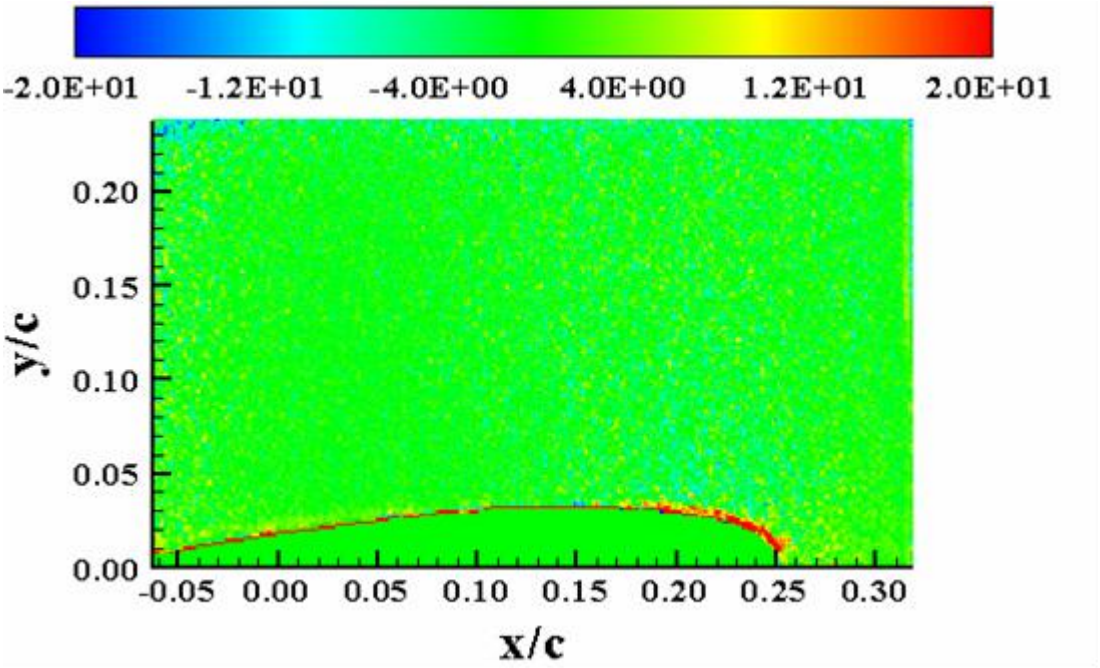

Figure E-48: $P_{xy}(M_\infty = 0.28, k = 0, \alpha = 10^0)$

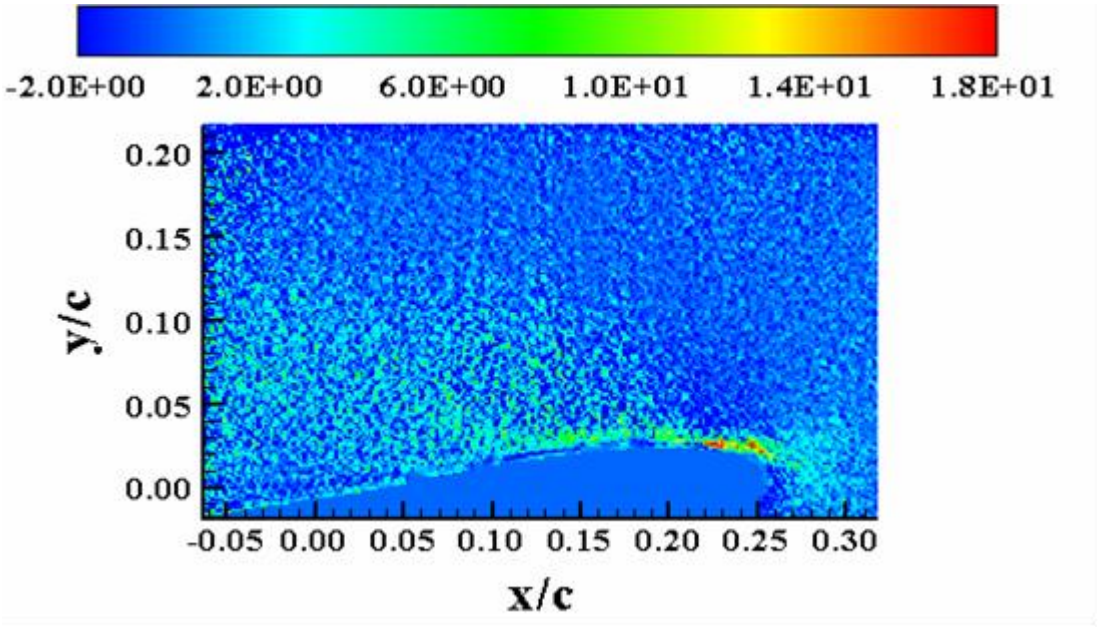

Figure E-49: $P_{xy}(M_\infty = 0.28, k = 0, \alpha = 18^0)$

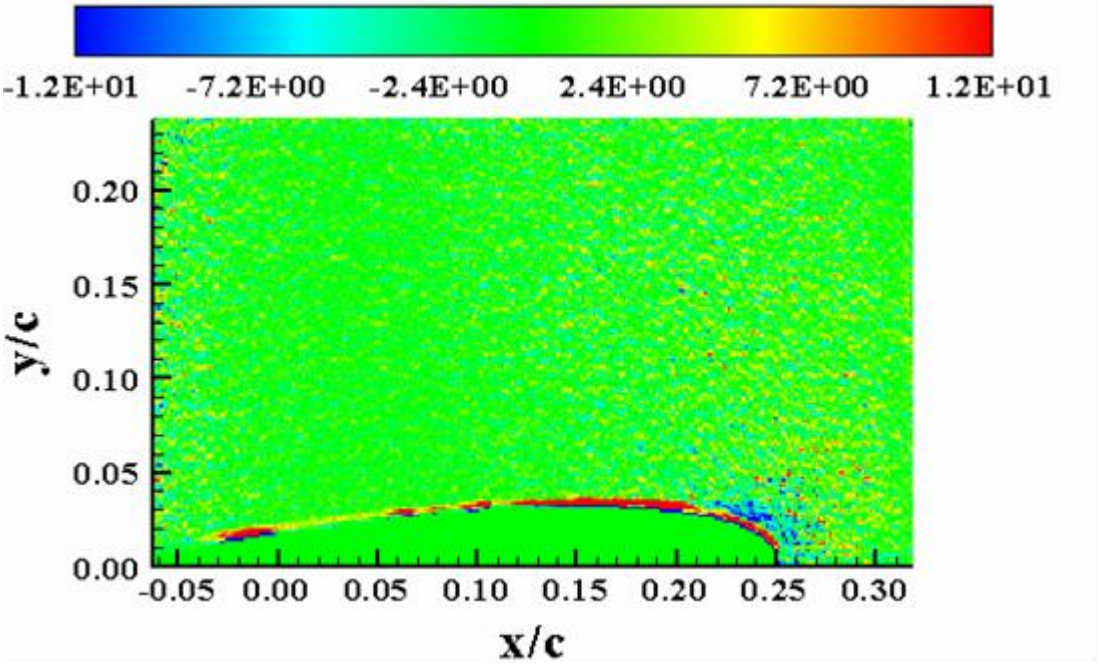

Figure E-50: $P_{yy}(M_\infty = 0.28, k = 0, \alpha = 10^0)$

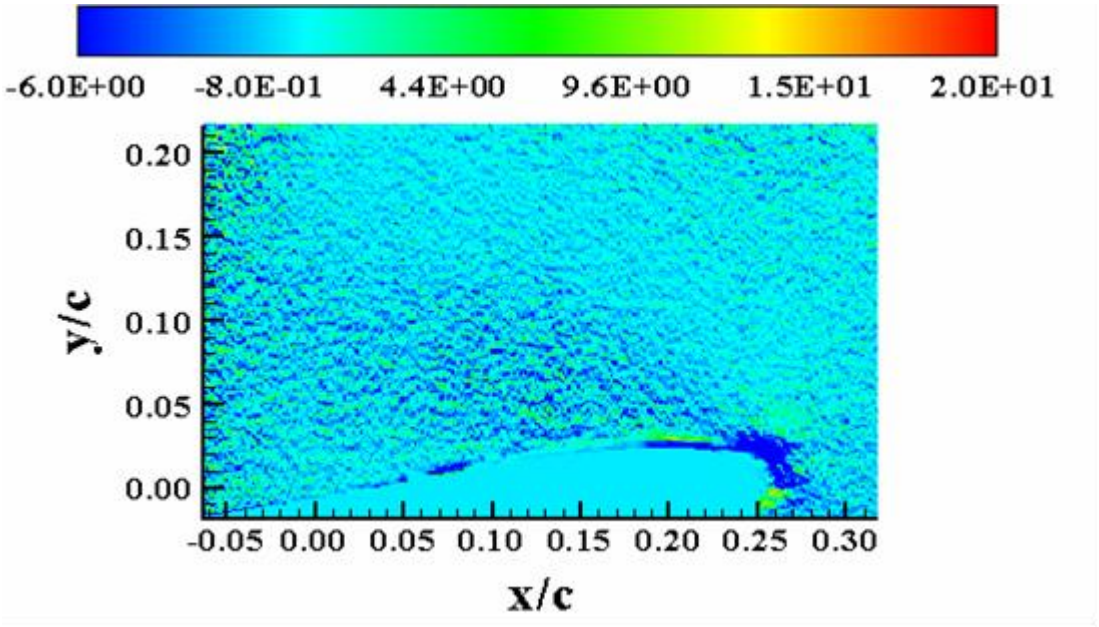

Figure E-51: $P_{yy}(M_\infty = 0.28, k = 0, \alpha = 18^0)$

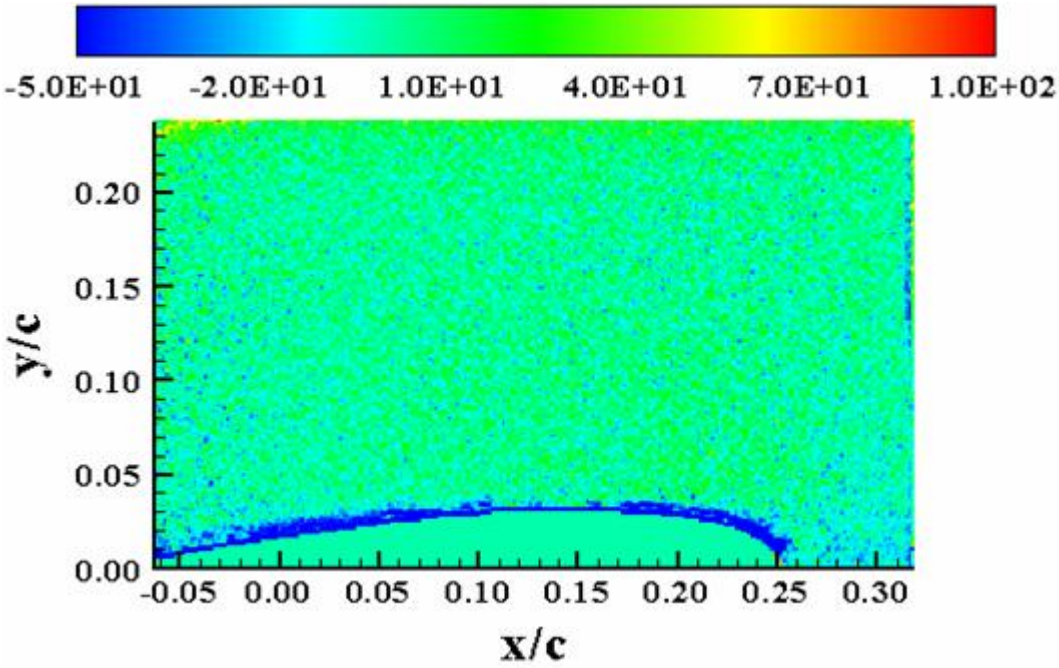

Figure E-52: $S_{xy}(M_\infty = 0.28, k = 0, \alpha = 10^0)$

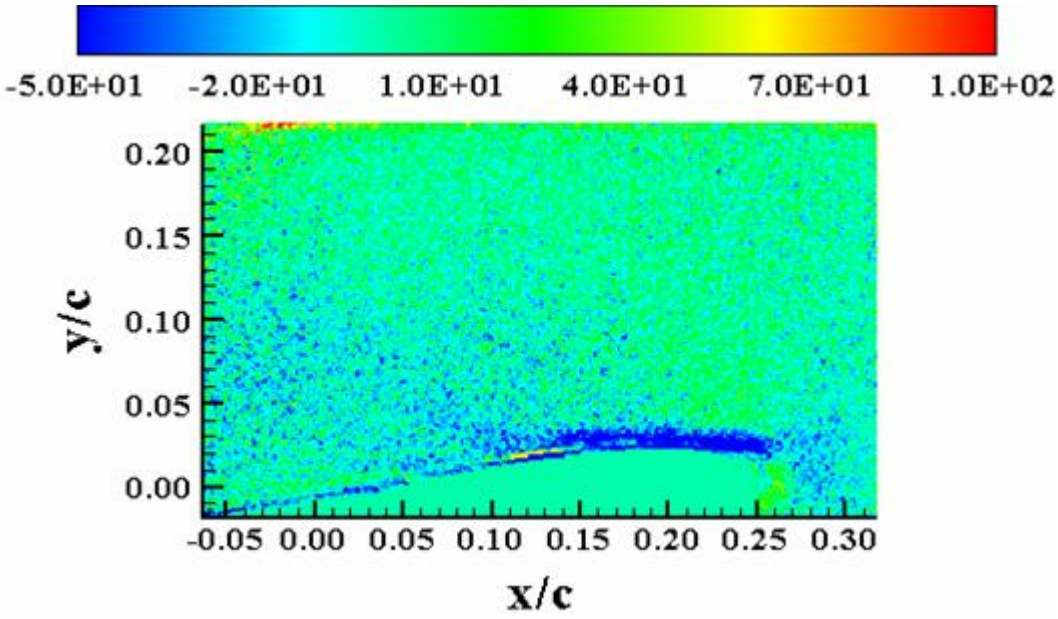

Figure E-53: $S_{xy}(M_\infty = 0.28, k = 0, \alpha = 18^0)$

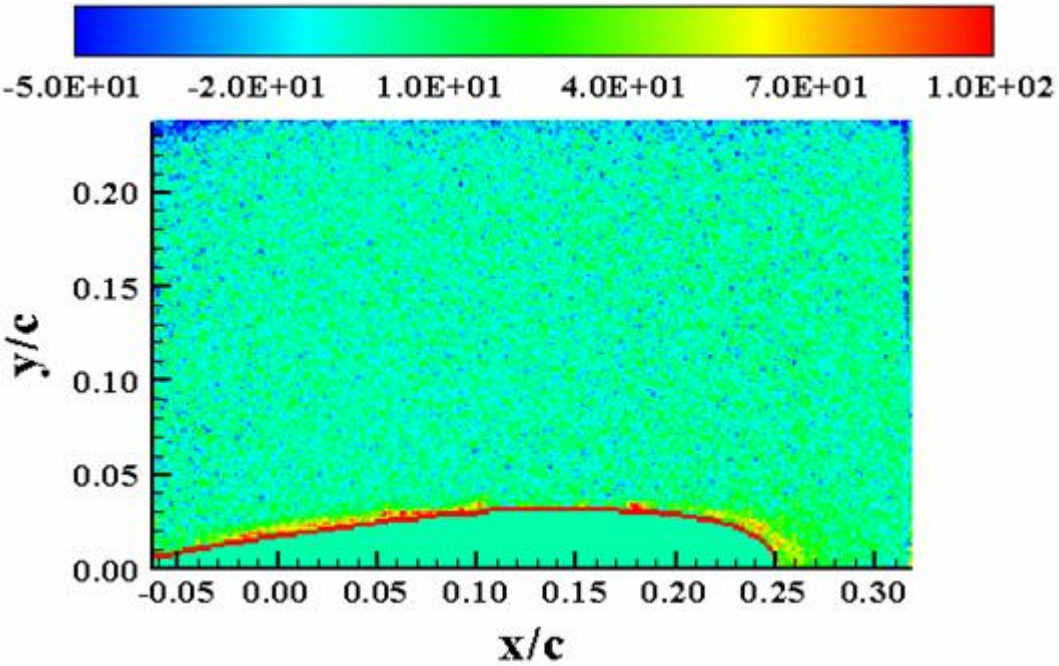

Figure E-54: $\omega_z(M_\infty = 0.28, k = 0, \alpha = 10^0)$

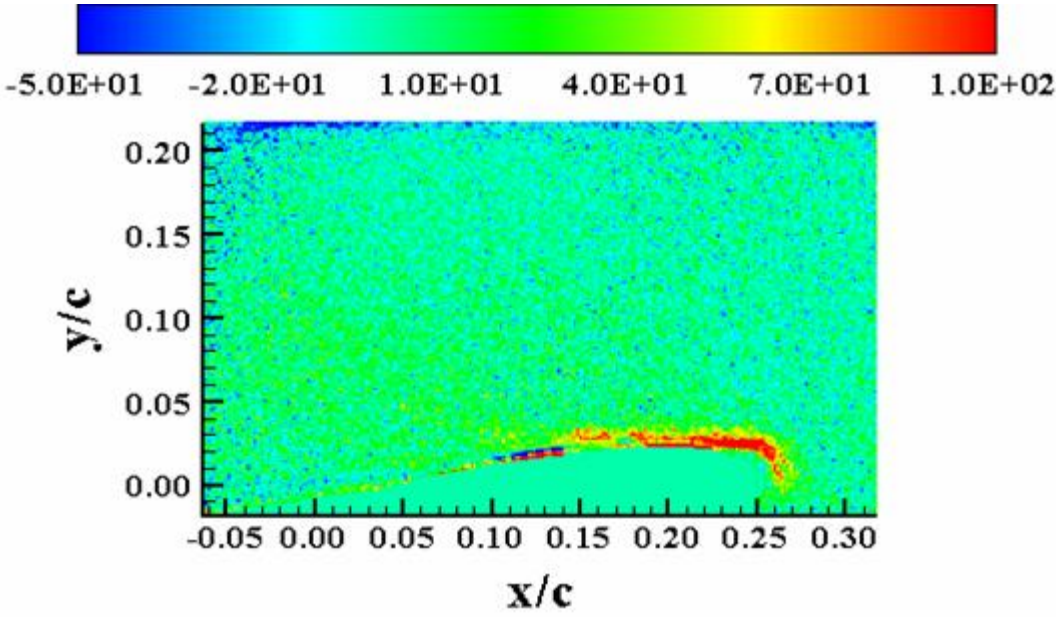

Figure E-55: $\omega_z (M_\infty = 0.28, k = 0, \alpha = 18^0)$

VITA

NAME: Dipankar Sahoo

ADDRESS: Department of Aerospace Engineering

c/o Dr. Rodney Bowersox

Texas A&M University, MS 3141

College Station, TX – 77843 - 3141

EMAIL ADDRESS: dipankar@tamu.edu

EDUCATION: B.E., Mechanical Engineering, N.I.T. Trichy, India, 1999

M.S., Aerospace Engineering, University of Alabama, 2003

Ph.D., Aerospace Engineering, Texas A&M University, 2008